Proceedings of

ICADD-2

The Second International Conference on Analysis of Discontinuous Deformation

Edited by
Yuzo Ohnishi

Proceedings of
The Second International Conference on Analysis of Discontinuous Deformation

July 10-12, 1997
(Special Workshop on July 9)
Kyoto, Japan

Organized by
School of Civil Engineering, Kyoto University
and
The Japan Institute of Systems Research

Sponsors

Kyoto University, Japan
The Japan Institute of Systems Research, Japan

International Advisory Committee

Prof. Bernard Amadei, University of Colorado, USA
Dr. Don Banks, US Army Corps, USA
Prof. Richard E. Goodman, University of California at Berkeley, USA
Prof. Jeen-Shang Lin, University of Pittsburgh, USA
Prof. A. Munjiza, Univ. of London, UK
Prof. M. Reza Salami, North Carolina A&T State University, USA
Dr. Gen-hua Shi, US Army Corps, USA
Prof. Nicolas Sitar, Univ. of California, Berkeley, USA
Prof. Chung-Yue Wang, National Central University, Taiwan

Chair of Organizing Committee

Yuzo Ohnishi, Kyoto University

Organizing Committee

Ryuzo Akai, The Japan Institute of Systems Research
Guangqi Chen, Kyoto University
Fujio Enami, Oriental Consultants Co., Ltd.
Tetsuro Esaki, Kyushu University
Masaaki Himeda, Dai-Nippon Consultant Co., Ltd.
Yoshiaki Hirakawa, Newjec Co., Ltd.
Sadayuki Ihara, Shimizu Corporation
Toshiaki Kobayashi, Taisei Corporation
Shinjuro Komata, Nippon Koei Co., Ltd.
Morito Kusabuka, Hosei University
Masao Matsuyama, Kajima Corporation
Shigeru Miki, Kiso-jiban Consultants Co., Ltd.
Koji Nakagawa, Yamaguchi University
Takumi Nakai, Geogyro Co.
Manabu Nakayama, Okumura Corporation
Tsuyoshi Nishimura, Hazama Corporation
Koichi Ono, Kyoto University
Yasunori Otsuka, OYO Corporation
Takeshi Sasaki, Kajima Corporation
Sadao Shimamura, Konoike Construction Co., Ltd.
Makoto Tanaka, Kyoto University
Masayuki Tsutsui, Tobishima Corporation
Fusakazu Yoshimi, Obayashi Corporation
Ryunoshin Yoshinaka, Saitama University

A message to the delegates from Prof. Richard Goodman

The great sweep and power of the computational methods you are demonstrating in Japan show how far we have traveled towards Terzaghi's dreams for soil and rock engineering. Many rock masses being completely discontinuous, the development of discontinuous deformation analysis, and of other numerical methods that include interface elements, becomes ever more adaptable to the hard requirements of real problems faced by constructors, miners, and engineering designers. No doubt the pace of innovation and development will continue and the state of the art will allow increasing use of numerical methods for engineering in rock.

However, we are still in a state of infancy with respect to the hurdles to be leaped in attempting to solve real wok problems on a routine basis. Most of us know the difficulties with rock, but if by any chance your previous experience has denied you this knowledge, for goodness sakes don't take another step without getting real. I think the hardest part of our problem is in posing the right questions for computer solution. The rock for the most part is inaccessible and not only don't we know where the discontinuities will be a priori but probably can never know this, except for a few highly mappable faults, or contacts. Any computing mesh that requires actual placement of discontinuities in a mesh on a deterministic basis, is only one realization of a compounded infinity of possibilities.

Furthermore, it is rare that a two-dimensional computation is meaningful in itself. Therefore, we need to find easier ways to compute in three dimensions, or to learn how to bracket our solutions in terms of intelligently combined two dimensional initiatives. We must no imagine that a single 2-D mesh with fixed joint locations is more than a gross simplification.

I believe that there will be a bright future for computational models in rock engineering, especially the emerging manifold methods that will facilitate coupling of discretized joint meshes in three dimensions, with fluid flow through the joint network. For the present, I believe the Block

Theory method has distinct advantages over the use of computational methods even though it's day has not yet come. In the United States, the use of block theory has been enormously helpful in assessing the safety of existing arch dams by the U.S. Bureau of Reclamation. The trouble with this system is that the engineer has not invest some energy to learn the methodology. (S)he can't simply choose boxes from a windows screen. Are we becoming intellectually lazy?

Whatever the limitations of modern computing when facing the enormous complexity and uncertainty of real rock masses, there can be no doubt that we are on the trail of something wonderful, and you are walking along this trail towards most exciting rewards. I wish you the best of luck.

Richard E Goodman (17 June '97)

Richard E. Goodman (June 17, 1997)

Preface

Since the first ICADD was held at Taipei, R.O.C. in 1995, the analysis of discontinuous deformation has attracted many researchers and engineers in wide range of fields. At the first conference the International Forum for Mechanics of Discontinua (IFMD) was established and then the international collaboration has been continuously taken place to motivate the further development of the powerful methods and gave birth to the 2nd ICADD at Kyoto.

Even in a short period of time, the analysis of discontinuous deformation has grown up to study on the behavior of jointed rock masses, glacier movement, granular materials, mechanica contacts, plate tectonics, blasting fragmentation and fracture extension. Various new methods have been developed and the experiences of their application to practical projects have been gained.

In the middle of two ICADD, the first International Forum on DDA was held at Berkeley, Calif., in 1996. It stimulated the academic and practical engineers in developing new theories and applying DDA to solve difficult problems. It is amazing to know that so many valuable papers are produced in such a short time.

The Second International Conference on Analysis of Discontinuous Deformation will collect efforts for developing the methods for discontinuous analyses, to make cooperate developments and information exchange, based on past experiences and theoretical backgrounds.

It should be noted that the first day of this conference is for a special workshop to educate young promising engineers and to let them understand the potentiality of analyses of discontinuous deformation. They will play a big role in creating a new world of discontinuous analyses in a very near future.

The proceeding contains papers presented at the second ICADD held at the beautiful ancient city of Japan, Kyoto during July 9-12, 1997. There are 5 papers of special lectures and 30 papers in 10 sessions, which include much of the recent work done in the field of discontinuous deformation. We hope that every participants may get some benefits for their future work.

The conference has been supported by Kyoto University, The Institute of Systems Research, many construction companies and consulting firms. Their supports are deeply appreciated. We would also like to thank all, who have devoted their work to the conference.

Yuzo Ohnishi, Conference Chairperson
Professor at School of Civil Engineering
Kyoto University, Kyoto JAPAN

TABLE OF CONTENTS

Special Lectures

Numerical manifold method
by Gen-hua Shi 1

Applicability of existing models to predict the behavior of rock joints under different boundary conditions
by Bernard Amadei and Johannes L. Wibowo 36

A packing generation scheme for the granular assemblies with 3D ellipsoidal particles
by Chung-Yue Wang, Chi-Fong Wang and Jopan Sheng 107

Simulation of 3-D concrete-frame collapse due to dynamic loading
by Motohiko Hakuno 125

Development of high order manifold method
by Guangqi Chen, Yuzo Ohnishi and Takahiro Ito 132

Discontinuous Deformation Analysis

Application of DDA to simulate fracture propagation in solid
by Te-chih Ke 155

Modeling of progressive fracture in jointed rock by DDA method
by Cheng-Yu Koo and J. C. Chern 186

Viscosity coefficient of the rockfall simulation
by Masato Shinji, Hiroyuki Ohno, Yasunori Otsuka and Guichen Ma 201

Dynamic deformation and stress field analysis of fault
by Xiaoli Deng 211

Tunnel engineering applications using discontinuous deformation analysis with finite element mesh
by Kuokai Shyu, Chiao-Tung Chang and M. Reza Salami 218

Soil slope stability analysis using DDA
by Jeen-Shang Lin and Shiou Chen 238

Large displacement and finite strain DDA: an implementation and physical verification
by Jeen-Shang Lin, Rashed Al-Zahrani, A. Munjiza and Der-Her Lee 245

DDA applied to deformation analysis of coarse granular materials (ballast)
by Tatsuya Ishikawa, Yuzo Ohnishi and Akira Namura 253

Geological survey for DDA and its application to a large rock cavern
by Hiroshi Chikahisa, Kaoru Kobayashi,
Kazunobu Matsumoto, Masayuki Tsutsui
and Yuzo Ohnishi 263

Manifold Method

Manifold methods and its applications to engineering
by Weiyuan Zhow, Qiang Yang and Xiaodong Kou 274

Crack propagation and thermal fracture analysis by manifold method
by Guo-Xin Zhang, Yasuhito Sugiura and Hiroo Hasegawa 282

Crack propagation using manifold method
by Yaw-Jeng Chiou, Rend-Jow Tsay and Wai-Lin Chuang 298

Elastic-plastic analysis of jointed rock models by manifold method
by Takeshi Sasaki, Seiji Morikawa, Daisuke Ishii
and Yuzo Ohnishi 309

Utilization of finite covers in the manifold method for accuracy control
by Hideomi Ohtsubo, Katsuyuki Suzuki, Kenjiro Terada
and Katsuyoshi Nakanishi 317

Distinct Element Method

Static contact problems of discrete systems solved by the diffuse element method
by Ming-Hong Chen, Chung-Yue Wang and Jopan Sheng 323

Analysis of loose earth pressure in trap door test by the distinct element method
by Takeshi Asano, Masao Nishimura, Hitoshi Masui
and Shigeru Kameda 343

Numerical study on support effects of cable bolt in discontinuous rock mass
by Hideo Kinashi and Satoru Amano 351

A static model of granular materials in a bin using distinct element analysis
by Jun Yoshida 359

Combined finite/discrete element method - improved contact solutions
by A. Munjiza, G. J. Huang and Jeen-Shang Lin 365

Rigid Body Spring Method

Size effect analysis of plain concrete beams by using RBSM
by Hiroaki Kitoh, Norio Takeuchi, Masatoshi Ueda,
Harunori Higuchi, Atsushi Kambayashi
and Michihiro Tomida 373

Development of discrete limit analysis and its application to the solid mechanics
by Norio Takeuchi and Tadahiko Kawai 383

Finite Element Method

Behavior and analysis of deformable continuous media containing rigid discontinuous bodies
by Chiang Shih, Yeong-Kang Wang and Edward C. Ting 391

New finite elements for the analysis of progressive discontinuity problems based on the finite volume concepts
by Hiroshi Takeda, Morito Kusabuka, Norio Takeuchi and Kazuo Sato 419

Finite element method for contact problem and its application to shield tunnel excavation analysis
by Hiroshi Takeda, Morito Kusabuka, Hiroshi Tanaka and Nobuko Kurokawa 432

Other Topics

The movement of rock joint triggered by water diffusion
by Xing-jue Shi and Dong-mei Li 442

Study of the mechanism of destruction of rock with a discrete inhomogeneity
by A. D. Alexeev, V. N. Revva, Yu. B. Gryadushchi and A. N. Kabanov 448

Selections of contact spring stiffness values in the numerical analysis for the system of rigid disks
by C. P. Wang, Jopan Sheng, Chung-Yue Wang and C. L. Lee 451

Effect of the asperity damage on the shear behaviour of irregular rock joints
by Tetsuro Esaki, Shouji Du, Yujing Jiang, Yoshinori Wada and Jun Sun 459

Research and development of new device for discontinuities' site-survey
by Tomio Fujikawa, Tosirou Aoki and Takao Hirokawa 465

Characterization and behavior evaluation of jointed rock mass in tunnelling
by Masayuki Kosugi, Yuki Onodera, Akio Tamai and Wuyi Wang 472

Numerical Manifold Method

Gen-hua Shi

Geotechnical Laboratory, US Army Engineer Waterways Experiment Station, Vicksburg, MS, USA

Abstract. For global analysis, the well known mathematical manifold is perhaps the most important subject of modern mathematics. Based upon the mathematical manifold, this numerical manifold method is a newly developed general numerical method. This method computes the movements and deformations of structures or materials. The meshes of the numerical manifold method are finite covers. These finite covers overlap each other and cover the entire material volume. On each cover, an independent cover displacement function is defined. The cover displacement function on individual covers are connected together to form a global displacement function on the entire material volume. The global displacement function is the weighted averages of the independent cover functions on the common part of several covers.

Using the finite cover system, any continuous, jointed or blocky materials can be computed in a mathematically consistent manner. The mathematical covers and physical mesh are independent. As mathematical covers can be moved, split, removed or added, the large deformations can be computed by steps. By dividing a cover onto two or more covers, jointed and blocky materials can be modeled. Both the finite element method (FEM) for continua and the discontinuous deformation analysis (DDA) for block systems are special cases of this numerical manifold method. In the current stage of development of the numerical manifold method, the extended finite element method can compute large deformations and movements of joints and blocks.

1 Finite Covers Formed by Mathematical Mesh and Physical Mesh

Physically, material objects often have different shapes. When the material volume has fractures or blocks, the shapes and boundaries become more complex. The Manifold method, by connecting many individual folded covers together, is able to study the entire material volume. The new method has separate mathematical covers and

physical meshes: the mathematical covers define only the fine or rough approximations; as the real material boundary, the physical mesh defines the integration fields. The mathematical covers are chosen by the user. The physical mesh includes the material boundaries, joints, blocks and the interfaces of different material zones. The physical mesh can not be chosen artificially. If the joints or block boundaries divide a mathematical cover onto two or more completely disconnected domains, these domains are defined as physical covers.

In Figure 1.1 and 1.2, two circles and one rectangle (indicated by thin lines) delimit three mathematical covers V_1, V_2, V_3. The thick lines indicate the material boundary and inner curved joints. In Figure 1.1, V_1 is divided by the physical mesh into two physical covers 1_1, 1_2; V_2 has two physical covers 2_1, 2_2 and V_3 has two physical covers 3_1, 3_2.

Figure 1.2 shows more joints. Mathematical cover V_2 contains two curved lines, but only two totally disconnected physical covers 2_1, 2_2 are formed. The upper curve (inside cover 2_1) can not cut through rectangle V_2 to form more physical covers, therefore cover 2_1 is a single physical cover. Similarly, mathematical cover V_3 contains two physical covers 3_1, 3_2. In both Figure 1.1 and 1.2, the common part of two or more physical covers are defined as "elements" and marked by its cover numbers.

Figure 2.1 shows a simple but often useful chain cover system. This cover system is specially convenient for long and narrow material shapes. Figure 2.2 shows a DDA block system, where each block is a mathematical cover and a physical cover. There are no overlaps between any two covers in the DDA case.

The finite element meshes can be used to define finite covers in the manifold method. Considering any node, all elements having this node form a mathematical cover (called "star" in algebraic topology). In Figure 3, there are 10 nodes, each node has a mathematical cover. Cover U_1 of node 1 has two elements $(1, 2, 5)$ and $(1, 5, 4)$. Cover U_5 of node 5 has 6 elements $(1, 5, 4)$, $(1, 2, 5)$, $(2, 6, 5)$, $(5, 6, 9)$, $(5, 9, 8)$, $(4, 5, 8)$. Any original finite element is the common area of the mathematical cover of its nodes. The element $(1, 5, 4)$ is the common area of covers U_1, U_5, U_4.

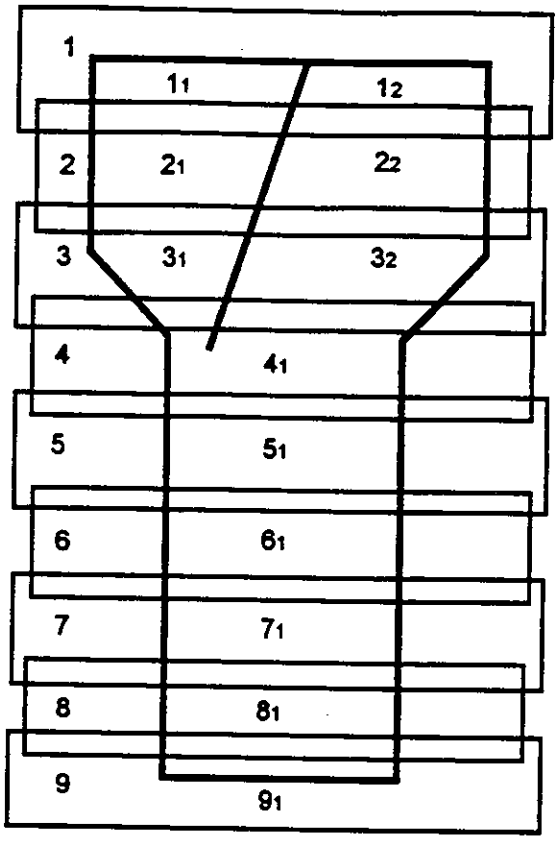

Figure 2.1 Chain cover system for narrow material shapes

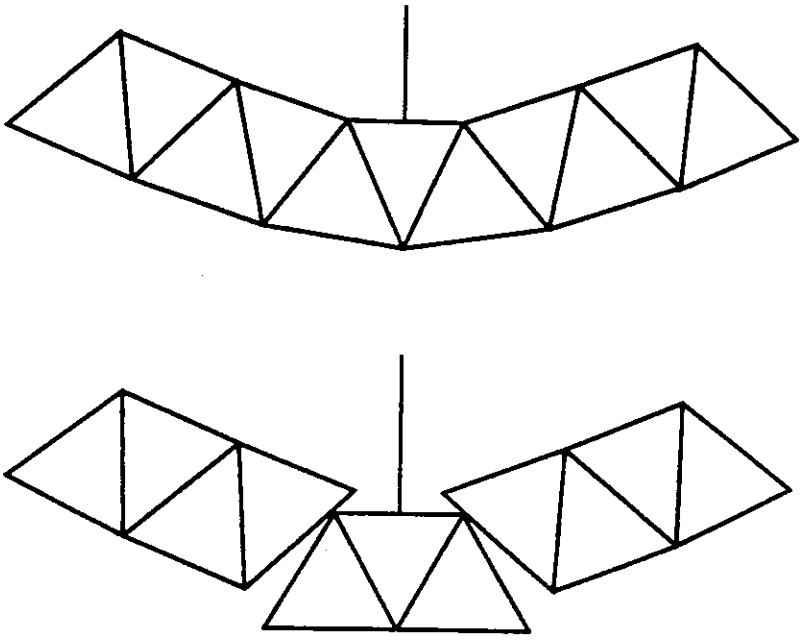

Figure 2.2 Finite covers formed by individual blocks

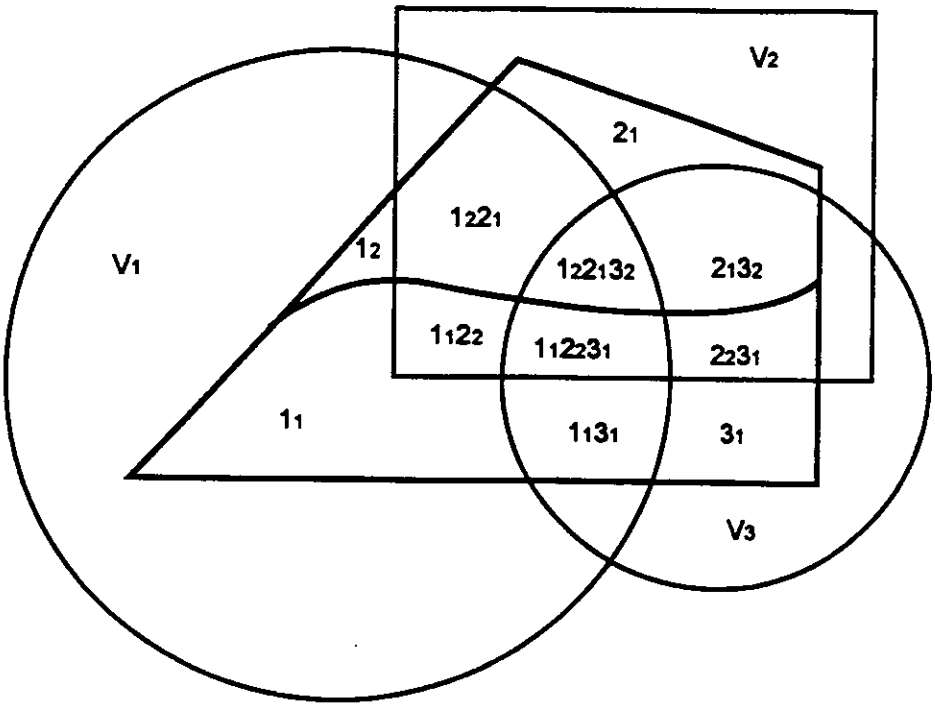

Figure 1.1 Finite covers on the materials of two blocks

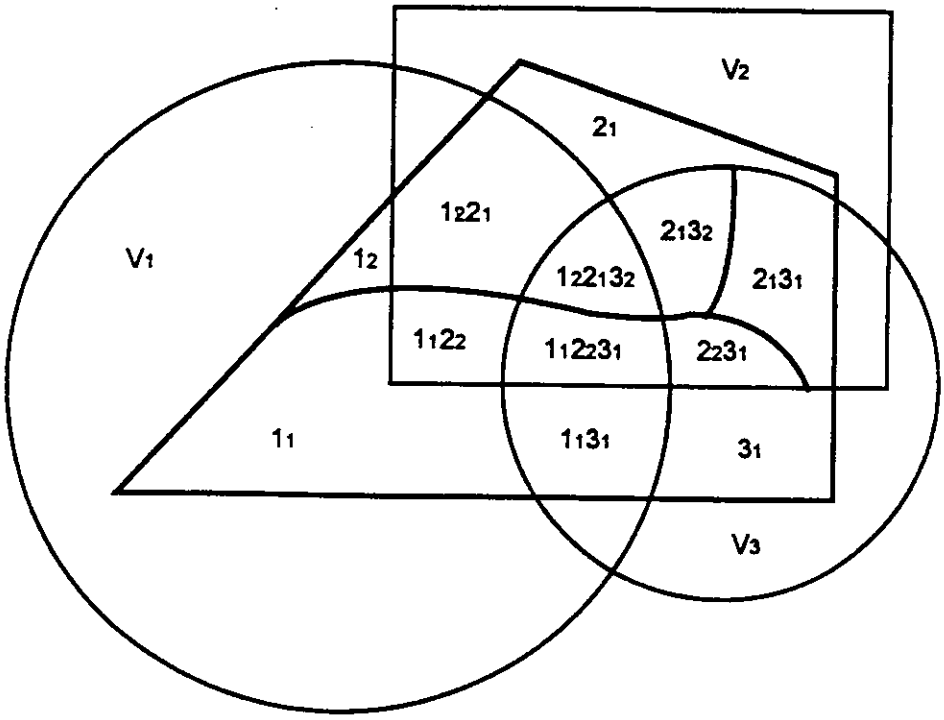

Figure 1.2 Finite covers on the materials with joints

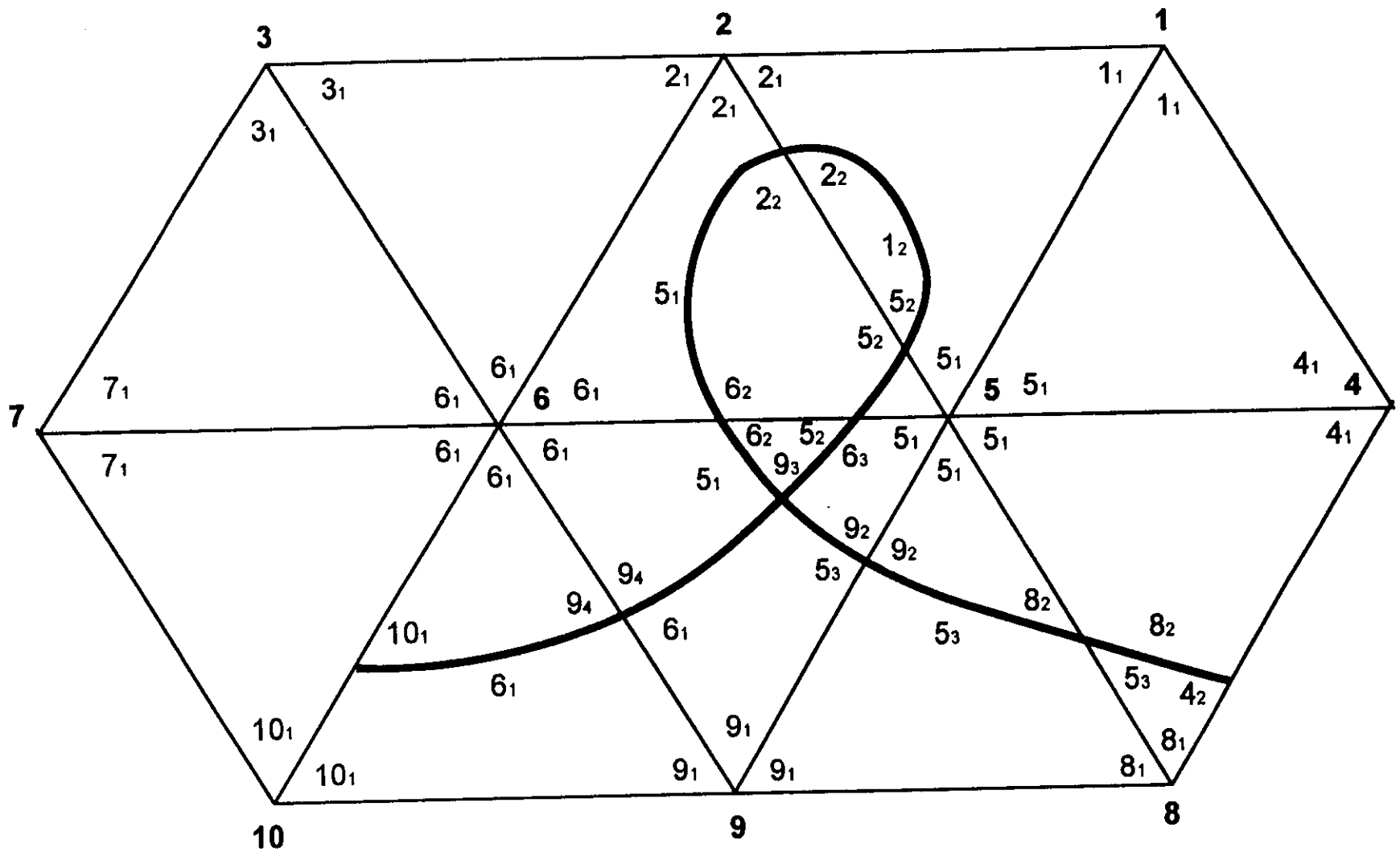

Figure 3 Finite covers formed by finite elements

The mathematical covers of Figure 3 are

math cover	element	element	element	element	element	element
U_1	1,2,5	1,5,4				
U_2	2,3,6	2,6,5	2,5,1			
U_3	2,3,6	3,7,6				
U_4	1,5,4	4,5,8				
U_5	1,5,4	1,2,3	2,6,5	5,6,9	5,9,8	4,5,8
U_6	2,6,5	2,3,6	3,7,6	6,7,10	6,10,9	6,9,5
U_7	3,7,6	6,7,10				
U_8	4,5,8	5,9,8				
U_9	5,9,8	5,6,9	6,10,9			
U_{10}	6,7,10	6,10,9				

The physical mesh of Figure 3 is the thick curved joint line, and the material boundary 1 2 3 7 10 9 8 4. Here, the material boundary is the same as the mesh boundary. In Figure 3, mathematical cover U_1 splits into two physical covers: $1_1, 1_2$; mathematical cover U_5 splits onto three physical covers: $5_1, 5_2, 5_3$. The original element $(2, 5, 6)$ splits onto three new elements $(2_1, 6_1, 5_1)$, $(2_2, 6_2, 5_2)$ and $(2_1, 6_3, 5_1)$.

The physical covers of Figure 3 are

math cover	physical cover	physical cover	physical cover	physical cover
U_1	1_1	1_2		
U_2	2_1	2_2		
U_3	3_1			
U_4	4_1	4_2		
U_5	5_1	5_2	5_3	
U_6	6_1	6_2	6_3	
U_7	7_1			
U_8	8_1	8_2		
U_9	9_1	9_2	9_3	
U_{10}	10_1			

Each physical cover is a new "node". Each "element" is a common part of exactly three physical covers. The element $(1_1, 5_1, 4_1)$ is the common part of three physical covers 1_1,5_1 and 4_1. Using the new nodes and elements, the joints can open and slide, the blocks can move away and the continuous area can still be connected. Two new elements $(1_1, 2_1, 5_1)$ and $(1_2, 2_2, 5_2)$ have no common new nodes and can be separated

after the load is applied. Therefore, the joint dividing the two elements can open or slide. The new elements $(1_2, 2_2, 5_2)$ and $(2_2, 6_2, 5_2)$ are divided by an edge $2, 5$ which is not a joint. Then the two elements have common edge $2_2, 5_2$

Before deformation take place, some nodes share the same position. This can be understood as many layers divided by discontinuities on the original simple finite element mesh. Using the manifold definition of nodes and elements, the following important conclusions can be seen directly from Figure 3:

[1] The elements are irregularly shaped;

[2] Each element has three physical cover numbers or "nodes";

[3] These three covers have one element as their common area;

[4] The adjacent elements have the same nodes along the common edge;

[5] Two elements divided by joints have different nodes.

2 Cover Functions and Weight Functions on Finite Covers

The one dimensional cover functions $u_i(x)$, defined on physical cover U_i: $u_i(x) \quad x \in U_i$ can be constant, linear, high order polynomial or locally defined series. These cover functions are connected together by the weight functions $w_i(x)$

$$w_i(x) \geq 0 \quad x \in U_i, \qquad w_i(x) = 0 \quad x \notin U_i, \qquad \sum_{x \in U_j} w_j(x) = 1$$

The weight functions $w_i(x)$ are the weighted average, which is to take a percentage from each cover function $u_i(x)$ for all physical covers U_i containing x. Using the weight functions $w_i(x)$, a global function $F(x)$ on the whole physical cover system is defined

$$F(x) = \sum_{i=1}^{n} w_i(x) u_i(x).$$

Figure 4.1 is a one dimensional example of three physical covers

$$\begin{array}{llll}
u_1(x) = A_3A_4, & U_1 = A_1A_2, & w_1(x)u_1(x) = & A_3A_5A_2, \qquad x \in U_1 \\
u_2(x) = B_3B_4, & U_2 = B_1B_2, & w_2(x)u_2(x) = & B_1B_5B_6B_2, \qquad x \in U_2 \\
u_3(x) = C_3C_4, & U_3 = C_1C_2, & w_3(x)u_3(x) = & C_2C_5C_4, \qquad x \in U_3
\end{array}$$

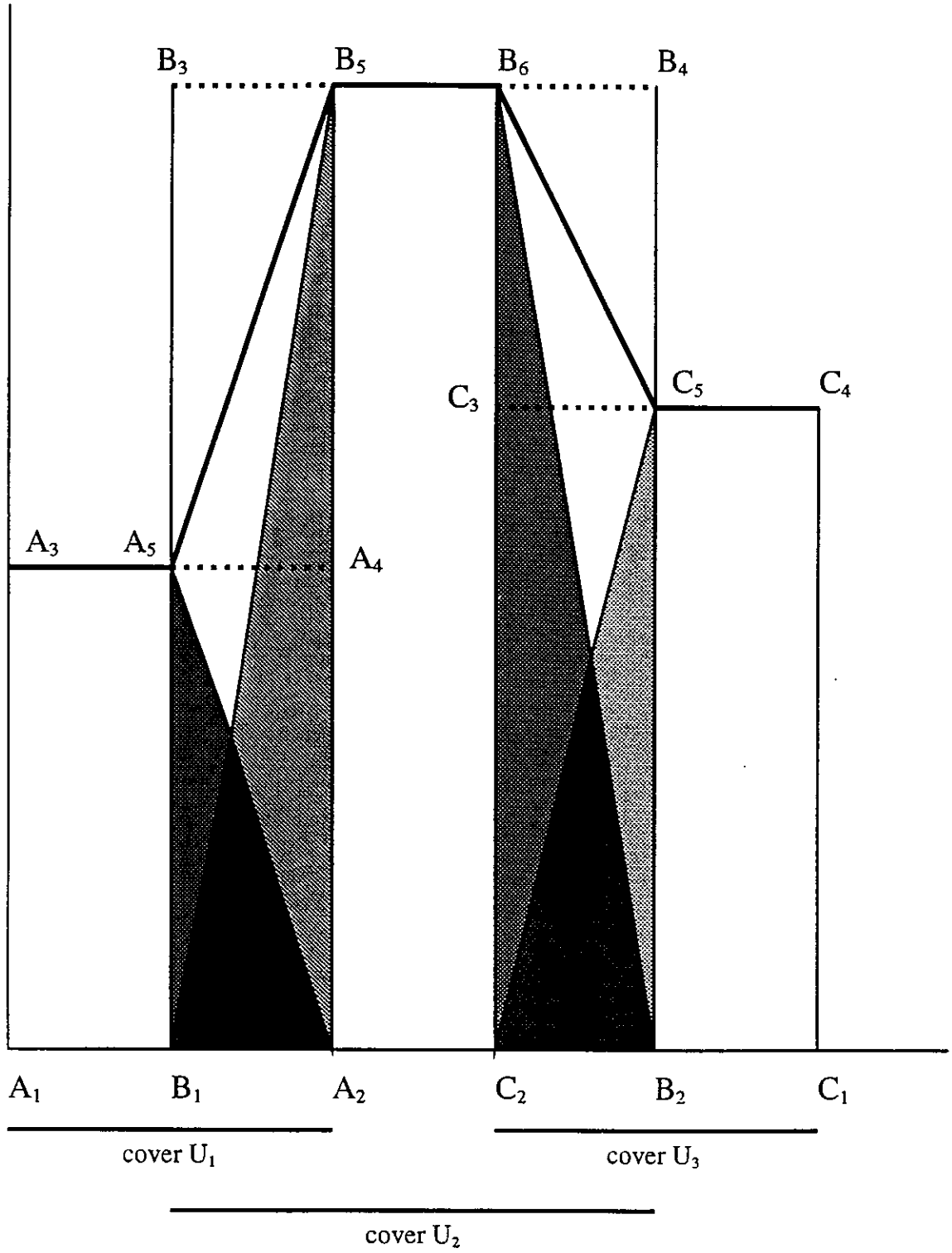

Figure 4.1 One dimensional cover functions

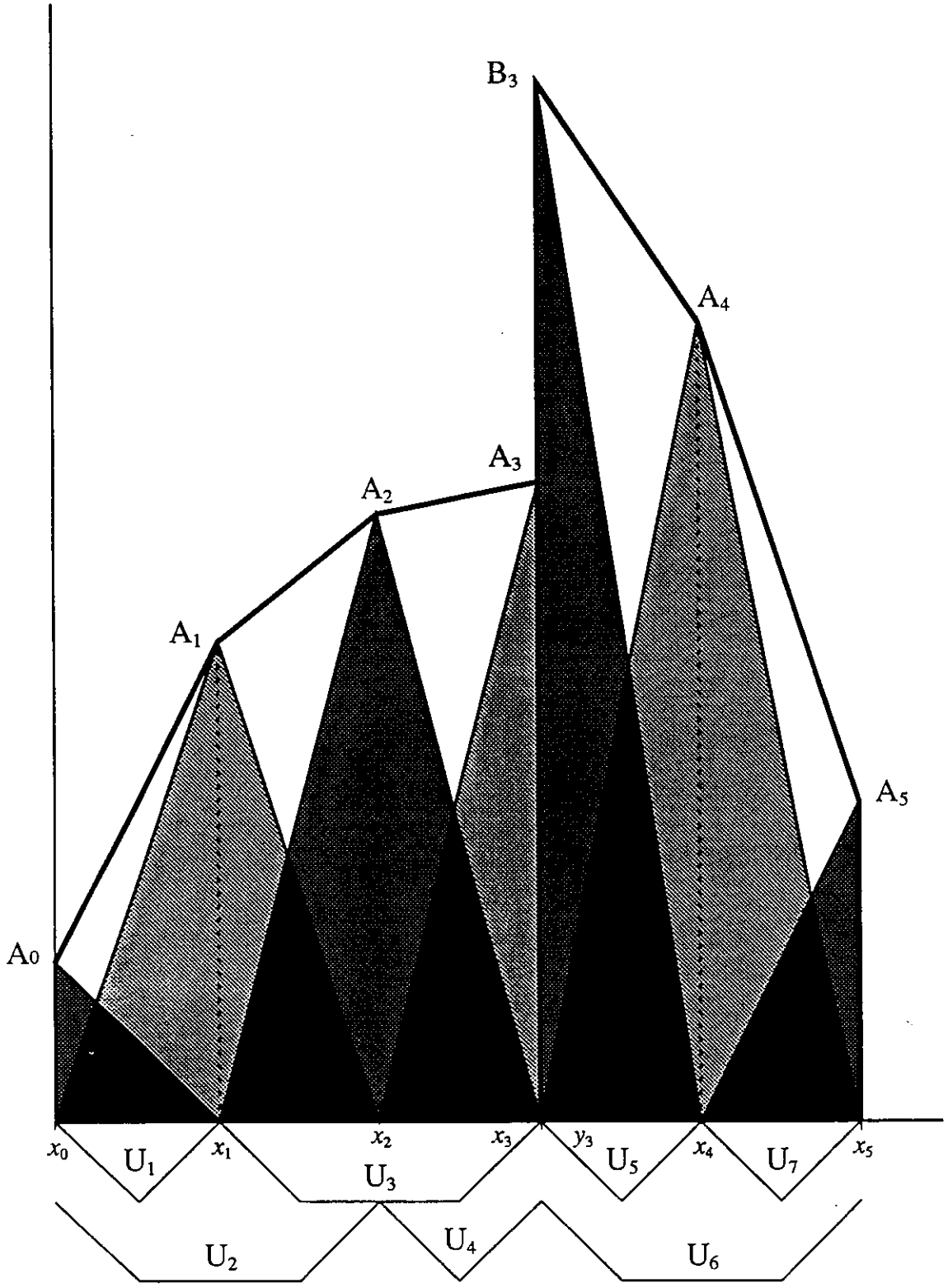

Figure 4.2 One dimensional discontinuous global function

The global function $F(x)$ is

$$F(x) = \sum_{i=1}^{n} w_i(x)u_i(x) = A_3A_5B_5B_6C_5C_4.$$

Figure 4.2 shows seven one dimensional physical covers $U_1 = x_0x_1$, $U_2 = x_0x_2$, $U_3 = x_1x_3$, $U_4 = x_2x_3$, $U_5 = y_3x_4$, $U_6 = y_3x_5$, $U_7 = x_4x_5$ Since the function has a jump at the point $x_3 = y_3$, the mathematical cover x_2x_4 was split into two physical covers $U_4 = x_2x_3$ and $U_5 = y_3x_4$.

$w_1(x)u_1(x)$	$w_2(x)u_2(x)$	$w_3(x)u_3(x)$	$w_4(x)u_4(x)$	$w_5(x)u_5(x)$	$w_6(x)u_6(x)$	$w_7(x)u_7(x)$
A_0x_1	$x_0A_1x_2$	$x_1A_2x_3$	x_2A_3	B_3x_4	$y_3A_4x_5$	x_4A_5
$x \in U_1$	$x \in U_2$	$x \in U_3$	$x \in U_4$	$x \in U_5$	$x \in U_6$	$x \in U_7$

The global function $F(x) = \sum_{i=1}^{7} w_i(x)u_i(x) = A_0A_1A_2A_3B_3A_4A_5$ is very close to the original natural curve.

For two dimensional manifold computation, the cover displacement functions $u_i(x, y)$ and $v_i(x, y)$ are defined on cover U_i.

$$\begin{Bmatrix} u_i(x,y) \\ v_i(x,y) \end{Bmatrix} = \sum_{j=1}^{m} \begin{pmatrix} f_{ij}(x,y) & 0 \\ 0 & f_{ij}(x,y) \end{pmatrix} \begin{Bmatrix} u_{ij} \\ v_{ij} \end{Bmatrix}$$
$$(x, y) \in U_i \tag{1}$$

The cover displacement functions are connected together by the weight functions $w_i(x, y)$

$$w_i(x, y) \geq 0 \quad (x, y) \in U_i, \qquad w_i(x, y) = 0 \quad (x, y) \notin U_i \tag{2}$$

with $\sum_{(x,y)\in U_j} w_j(x, y) = 1$. The global displacement function $u(x, y)$ and $v(x, y)$ on the whole physical cover system is

$$\begin{Bmatrix} u(x,y) \\ v(x,y) \end{Bmatrix} = \begin{Bmatrix} \sum_{i=1}^{n} w_i(x,y)u_i(x,y) \\ \sum_{i=1}^{n} w_i(x,y)v_i(x,y) \end{Bmatrix} = \sum_{i=1}^{n}\sum_{j=1}^{m} [T_{ij}(x,y)]\{D_{ij}\} \tag{3}$$

$$[T_{ij}(x,y)] = \begin{pmatrix} w_i(x,y)f_{ij}(x,y) & 0 \\ 0 & w_i(x,y)f_{ij}(x,y) \end{pmatrix} \quad \{D_{ij}\} = \begin{Bmatrix} u_{ij} \\ v_{ij} \end{Bmatrix}$$

For finite elements, the cover functions are the simplest functions, namely constant $m = 1$, $f_{ij}(x,y) = 1$, $u_{i1} = u_i$ and $v_{i1} = v_i$ in (3). Therefore,

$$\begin{Bmatrix} u(x,y) \\ v(x,y) \end{Bmatrix} = \sum_{i=1}^{n} [T_i(x,y)]\{D_i\}$$
$$[T_i(x,y)] = \begin{pmatrix} w_i(x,y) & 0 \\ 0 & w_i(x,y) \end{pmatrix} \quad \{D_i\} = \begin{Bmatrix} u_i \\ v_i \end{Bmatrix} \tag{4}$$

If one denotes the nodes of a triangle element e as $e(1), e(2), e(3)$, then e is the common region of three covers of its three nodes $e = U_{e(1)} \cap U_{e(2)} \cap U_{e(3)}$. On all points of this element, the only non-zero weight functions are $w_{e(1)}, w_{e(2)}, w_{e(3)}$. Denote (x_i, y_i) as the coordinates of node i, then the weight functions of element e are computed.

$$\begin{aligned} &(\, w_{e(1)}(x,y) \quad w_{e(2)}(x,y) \quad w_{e(3)}(x,y)\,) \\ &= (1 \quad x \quad y) \begin{pmatrix} 1 & x_{e(1)} & y_{e(1)} \\ 1 & x_{e(2)} & y_{e(2)} \\ 1 & x_{e(3)} & y_{e(3)} \end{pmatrix}^{-1} = (1 \quad x \quad y) \begin{pmatrix} f_{11} & f_{12} & f_{13} \\ f_{21} & f_{22} & f_{23} \\ f_{31} & f_{32} & f_{33} \end{pmatrix} \end{aligned} \tag{5}$$

For each element, the summation of three weight functions of three nodes are 1.

$$(\, w_{e(1)}(x,y) \quad w_{e(2)}(x,y) \quad w_{e(3)}(x,y)\,) \begin{pmatrix} 1 & x_{e(1)} & y_{e(1)} \\ 1 & x_{e(2)} & y_{e(2)} \\ 1 & x_{e(3)} & y_{e(3)} \end{pmatrix} = (1 \quad x \quad y)$$
$$w_{e(1)}(x,y) + w_{e(2)}(x,y) + w_{e(3)}(x,y) = 1$$

For element e and $(x,y) \in e$, equation (4) will reduce to a normal element displacement function,

$$\begin{Bmatrix} u(x,y) \\ v(x,y) \end{Bmatrix} = \sum_{r=1}^{3} [T_{e(r)}][D_{e(r)}]$$

$$[T_{e(r)}(x,y)] = \begin{pmatrix} f_{1r} + f_{2r}x + f_{3r}y & 0 \\ 0 & f_{1r} + f_{2r}x + f_{3r}y \end{pmatrix} \tag{6}$$

3 Coefficient Matrix of Equilibrium Equations

Assume the number of physical covers is n, and there are $2m$ unknowns in each physical cover, the total potential energy has the form

$$\Pi = \frac{1}{2}\,(\,D_1^T \quad D_2^T \quad D_3^T \quad \dots \quad D_n^T\,) \tag{7}$$

$$\begin{pmatrix} K_{11} & K_{12} & K_{13} & \dots & K_{1n} \\ K_{21} & K_{22} & K_{23} & \dots & K_{2n} \\ K_{31} & K_{32} & K_{33} & \dots & K_{3n} \\ \vdots & \vdots & \vdots & \ddots & \vdots \\ K_{n1} & K_{n2} & K_{n3} & \dots & K_{nn} \end{pmatrix} \begin{Bmatrix} D_1 \\ D_2 \\ D_3 \\ \vdots \\ D_n \end{Bmatrix} + (\,D_1^T \quad D_2^T \quad D_3^T \quad \dots \quad D_n^T\,) \begin{Bmatrix} F_1 \\ F_2 \\ F_3 \\ \vdots \\ F_n \end{Bmatrix} + C$$

Submatrices $[K_{ij}]$ are $2m \times 2m$ matrices. $[D_i]$ and $[F_i]$ are $2m \times 1$ submatrices, where $[D_i]$ represents the displacement variables $(d_{i1}\ d_{i2}\ d_{i3}\ d_{i4}\ \dots\ d_{i2m})^T$ of physical cover i. From the formulation of Π, equation (7) can be written as a symmetric representation, $[K_{ij}] = [K_{ji}]^T$.

The equilibrium equations are derived by minimizing the total potential energy Π. The i-th row of equation (8) consists of $2m$ linear equations

$$\frac{\partial \Pi}{\partial d_{ir}} = 0, \quad r = 1, 2, 3, 4, \dots, 2m,$$

The matrix of simultaneous equilibrium equations obtained is the same as the matrix of quadratic form (7):

$$\begin{pmatrix} K_{11} & K_{12} & K_{13} & \dots & K_{1n} \\ K_{21} & K_{22} & K_{23} & \dots & K_{2n} \\ K_{31} & K_{32} & K_{33} & \dots & K_{3n} \\ \vdots & \vdots & \vdots & \ddots & \vdots \\ K_{n1} & K_{n2} & K_{n3} & \dots & K_{nn} \end{pmatrix} \begin{Bmatrix} D_1 \\ D_2 \\ D_3 \\ \vdots \\ D_n \end{Bmatrix} = \begin{Bmatrix} F_1 \\ F_2 \\ F_3 \\ \vdots \\ F_n \end{Bmatrix} \tag{8}$$

Here $[F_i]$ is the loading on cover i. Submatrices $[K_{ii}]$ depend on the material properties of cover i and $[K_{ij}]$, where $i \neq j$ is defined by the overlapping of cover i and cover j.

For the two dimensional triangle elements, $m = 1$. The unknown $[D_i]$ and the force term $[F_i]$ of cover i are 2×1 submatrices. The coefficient submatrices $[K_{ij}]$ are 2×2.

4 Stiffness Matrix

For the FEM, the integration domains of the stiffness matrices are whole elements with standard boundaries. For the manifold method, the integration domains of the stiffness matrices are the manifold elements, which can be part of the elements.

As for the FEM method, the relationship between stress and strain on the manifold method, is given by

$$\begin{Bmatrix} \sigma_x \\ \sigma_y \\ \tau_{xy} \end{Bmatrix} = [E] \begin{Bmatrix} \epsilon_x \\ \epsilon_y \\ \gamma_{xy} \end{Bmatrix}, \qquad [E] = \frac{E}{1-\nu^2} \begin{pmatrix} 1 & \nu & 0 \\ \nu & 1 & 0 \\ 0 & 0 & \frac{1-\nu}{2} \end{pmatrix} \tag{9}$$

$E and \nu$ are the Young's modulus and Poisson's ratio, respectively. From equation (5), element strain can be computed

$$\begin{Bmatrix} \epsilon_x \\ \epsilon_y \\ \gamma_{xy} \end{Bmatrix} = \begin{Bmatrix} \frac{\partial u(x,y)}{\partial x} \\ \frac{\partial v(x,y)}{\partial y} \\ \frac{\partial u(x,y)}{\partial y} + \frac{\partial v(x,y)}{\partial x} \end{Bmatrix} = \Big([B_{e(1)}] \quad [B_{e(2)}] \quad [B_{e(3)}] \Big) \begin{Bmatrix} D_{e(1)} \\ D_{e(2)} \\ D_{e(3)} \end{Bmatrix}$$

$$[B_{e(r)}] = \begin{pmatrix} \frac{\partial w_{e(r)}}{\partial x} & 0 \\ 0 & \frac{\partial w_{e(r)}}{\partial y} \\ \frac{\partial w_{e(r)}}{\partial y} & \frac{\partial w_{e(r)}}{\partial x} \end{pmatrix} = \begin{pmatrix} f_{2r} & 0 \\ 0 & f_{3r} \\ f_{3r} & f_{2r} \end{pmatrix} \quad r = 1, 2, 3 \tag{10}$$

The strain energy Π_e, caused by the elastic stresses of element e, is the integration over the entire material area S in that element. Then

$$\Pi_e = \iint_S \frac{1}{2} \begin{pmatrix} \epsilon_x & \epsilon_y & \gamma_{xy} \end{pmatrix} \begin{Bmatrix} \sigma_x \\ \sigma_y \\ \tau_{xy} \end{Bmatrix} dx\, dy$$

$$= \frac{1}{2}\mathcal{S}\,(\,D^T_{e(1)} \quad D^T_{e(2)} \quad D^T_{e(3)}\,)\begin{pmatrix} B^T_{e(1)} \\ B^T_{e(2)} \\ B^T_{e(3)} \end{pmatrix}[E]\,(\,B_{e(1)} \quad B_{e(2)} \quad B_{e(3)}\,)\begin{Bmatrix} D_{e(1)} \\ D_{e(2)} \\ D_{e(3)} \end{Bmatrix} \tag{11}$$

Then

$$\mathcal{S}[B_{e(r)}]^T[E][B_{e(s)}] \qquad \rightarrow \qquad [K_{e(r)e(s)}], \qquad r, s = 1, 2, 3,$$

5 Initial Stress Matrix

Following the time sequence, the manifold method computes in a step by step fashion. The computed stresses of the previous time step will be the initial stresses of the next time step. Therefore the initial stresses are essential for manifold computations.

For element e, the potential energy of the initial constant stresses $\{\sigma^0\} = (\,\sigma^0_x \quad \sigma^0_y \quad \tau^0_{xy}\,)^T$ is

$$\begin{aligned} \Pi_\sigma &= \iint_{\mathcal{S}} (\,\epsilon_x \quad \epsilon_y \quad \gamma_{xy}\,)\begin{Bmatrix} \sigma^0_x \\ \sigma^0_y \\ \tau^0_{xy} \end{Bmatrix} dx\,dy \\ &= \mathcal{S}\,(\,D^T_{e(1)} \quad D^T_{e(2)} \quad D^T_{e(3)}\,)\begin{pmatrix} B^T_{e(1)} \\ B^T_{e(2)} \\ B^T_{e(3)} \end{pmatrix}\begin{Bmatrix} \sigma^0_x \\ \sigma^0_y \\ \tau^0_{xy} \end{Bmatrix} \end{aligned} \tag{12}$$

where $\mathcal{S}$ is the area of that element.

$$-\mathcal{S}[B_{e(r)}]^T\begin{Bmatrix} \sigma^0_x \\ \sigma^0_y \\ \tau^0_{xy} \end{Bmatrix} \qquad \rightarrow \qquad \{F_{e(r)}\}, \qquad r = 1, 2, 3.$$

6 Point Loading Matrix

Different from the ordinary FEM method, a load point can be applied at any point on the element. The point loading force $(\,F_x \quad F_y\,)^T$ acts on point (x_0, y_0) of element e. The potential energy due to the point loading is

$$\Pi_p = -\,(\,u(x_0, y_0) \quad v(x_0, y_0)\,)\begin{Bmatrix} F_x \\ F_y \end{Bmatrix}$$

$$= -\left(D_{e(1)}^T \quad D_{e(2)}^T \quad D_{e(3)}^T \right) \begin{pmatrix} T_{e(1)}(x_0, y_0)^T \\ T_{e(2)}(x_0, y_0)^T \\ T_{e(3)}(x_0, y_0)^T \end{pmatrix} \begin{Bmatrix} F_x \\ F_y \end{Bmatrix} \tag{13}$$

Then

$$[T_{e(r)}(x_0, y_0)]^T \begin{Bmatrix} F_x \\ F_y \end{Bmatrix} \quad \rightarrow \quad \{F_{e(r)}\}, \qquad r = 1, 2, 3,$$

7 Body Loading Matrix

Assuming that $(f_x \quad f_y)^T$ is the constant body force acting on the material area of element e. The potential energy due to the body loading is

$$\begin{aligned}
\Pi_w &= -\int\int_S (u(x,y) \quad v(x,y)) \begin{Bmatrix} f_x \\ f_y \end{Bmatrix} dx\, dy \\
&= -\left(D_{e(1)}^T \quad D_{e(2)}^T \quad D_{e(3)}^T \right) \int\int_S \begin{pmatrix} T_{e(1)}(x,y)^T \\ T_{e(2)}(x,y)^T \\ T_{e(3)}(x,y)^T \end{pmatrix} dx\, dy \begin{Bmatrix} f_x \\ f_y \end{Bmatrix} \\
&= -\left(D_{e(1)}^T \quad D_{e(2)}^T \quad D_{e(3)}^T \right) \begin{pmatrix} C_1 \\ C_2 \\ C_3 \end{pmatrix} \begin{Bmatrix} f_x \\ f_y \end{Bmatrix} dxdy \qquad (14) \\
[C_r] &= \int\int_S T_{e(r)}(x,y)^T dxdy = \int\int_S \begin{pmatrix} S_r & 0 \\ 0 & S_r \end{pmatrix} \\
S_r &= f_{1r} S + f_{2r} \int\int_S x dxdy + f_{3r} \int\int_S y dxdy
\end{aligned}$$

S_r can be computed by equations (5) and (20). Then

$$\begin{pmatrix} S_r & 0 \\ 0 & S_r \end{pmatrix} \begin{Bmatrix} f_x \\ f_y \end{Bmatrix} \quad \rightarrow \quad \{F_{e(r)}\}, \qquad r = 1, 2, 3.$$

8 Inertia Force Matrix

The inertia force matrix is equivalent to the mass matrix of the FEM and is the most important matrix of the manifold method. The inertia force matrix will control the movements of all points of the whole material volume. By small time steps, the discontinuous contact computation will be stable. From the beginning of the current time step, denote $(\,u(t) \quad v(t)\,)^T$ as the time dependent displacements of any point (x, y) of element e and $\mathcal{M}$ as the mass per unit area. The force of inertia per unit area is

$$\begin{Bmatrix} f_x(x,y) \\ f_y(x,y) \end{Bmatrix} = -\mathcal{M}\frac{\partial^2}{\partial t^2}\begin{Bmatrix} u(t) \\ v(t) \end{Bmatrix} = -\mathcal{M}\,(\,T_{e(1)} \quad T_{e(2)} \quad T_{e(3)}\,)\,\frac{\partial^2}{\partial t^2}\begin{Bmatrix} D_{e(1)}(t) \\ D_{e(2)}(t) \\ D_{e(3)}(t) \end{Bmatrix}$$

At the beginning of the time step, the node displacement $\{D_{e(i)}(0)\} = \{0\}$. At the end of the time step, the node displacement $\{D_{e(i)}(\Delta)\} = \{D_{e(i)}\}$, Δ is the time interval of this time step. Then

$$\begin{aligned} \{D_{e(r)}(\Delta)\} &= \{D_{e(r)}(0)\} + \Delta\frac{\partial\{D_{e(r)}(0)\}}{\partial t} + \frac{\Delta^2}{2}\frac{\partial^2\{D_{e(r)}(0)\}}{\partial t^2} \\ &= \Delta\frac{\partial\{D_{e(r)}(0)\}}{\partial t} + \frac{\Delta^2}{2}\frac{\partial^2\{D_{e(r)}(0)\}}{\partial t^2}, \end{aligned} \tag{15}$$

$$\begin{aligned} \frac{\partial^2\{D_{e(r)}(0)\}}{\partial t^2} &= \frac{2}{\Delta^2}\{D_{e(r)}(\Delta)\} - \frac{2}{\Delta}\frac{\partial\{D_{e(r)}(0)\}}{\partial t} = \frac{2}{\Delta^2}\{D_{e(r)}\} - \frac{2}{\Delta}\{V_{e(r)}(0)\}, \\ \{V_{e(r)}(0)\} &= \frac{\partial\{D_{e(r)}(0)\}}{\partial t}, \qquad \{D_{e(r)}\} = \{D_{e(r)}(\Delta)\} \end{aligned} \tag{16}$$

$\{V_{e(r)}(0)\}$ is the velocity at the beginning of the time step. Then the potential energy becomes

$$\begin{aligned} \Pi_i &= -\int\int_S (\,u(x,y) \quad v(x,y)\,)\begin{Bmatrix} f_x(x,y) \\ f_y(x,y) \end{Bmatrix} dxdy \\ &= \int\int_S \mathcal{M}\,(\,u(x,y) \quad v(x,y)\,)\,(\,T_{e(1)} \quad T_{e(2)} \quad T_{e(3)}\,)\,dxdy\frac{\partial^2}{\partial t^2}\begin{Bmatrix} D_{e(1)}(t) \\ D_{e(2)}(t) \\ D_{e(3)}(t) \end{Bmatrix} \\ &= \mathcal{M}\frac{2}{\Delta^2}\,(\,D^T_{e(1)} \quad D^T_{e(2)} \quad D^T_{e(3)}\,) \end{aligned}$$

$$\int\int_S \begin{pmatrix} T_{e(1)}(x,y)^T \\ T_{e(2)}(x,y)^T \\ T_{e(3)}(x,y)^T \end{pmatrix} \begin{pmatrix} T_{e(1)} & T_{e(2)} & T_{e(3)} \end{pmatrix} dxdy \begin{Bmatrix} D_{e(1)} - \Delta V_{e(1)}(0) \\ D_{e(2)} - \Delta V_{e(2)}(0) \\ D_{e(3)} - \Delta V_{e(3)}(0) \end{Bmatrix} \quad (17)$$

$$\int\int_S [T_{e(r)}]^T [T_{e(s)}] dxdy = \begin{pmatrix} t_{e(r)e(s)} & 0 \\ 0 & t_{e(r)e(s)} \end{pmatrix} \quad (18)$$

$$\begin{aligned} t_{e(r)e(s)} &= \int\int_S w_{e(r)} w_{e(s)} dxdy \\ &= \int\int_S (f_{1r} + f_{2r}x + f_{3r}y)(f_{1s} + f_{2s}x + f_{3s}y) dxdy \end{aligned}$$

Number $t_{e(r)e(s)}$ can be computed by equations (5) and (20). Then the final equation is

$$\frac{2\mathcal{M}}{\Delta^2} \begin{pmatrix} t_{e(r)e(s)} & 0 \\ 0 & t_{e(r)e(s)} \end{pmatrix} \quad \rightarrow \quad [K_{e(r)e(s)}], \qquad r, s = 1, 2, 3,$$

$$\frac{2\mathcal{M}}{\Delta} \begin{pmatrix} t_{e(r)e(s)} & 0 \\ 0 & t_{e(r)e(s)} \end{pmatrix} \{V_{e(s)}(0)\} \quad \rightarrow \quad \{F_{e(r)}\}, \qquad r, s = 1, 2, 3,$$

9 Fixed Point Matrix

Assume the fixed point is (x, y) at element e. There are two springs which are along the x and y directions respectively. The stiffness of the springs is p. The spring forces are

$$\begin{Bmatrix} f_x \\ f_y \end{Bmatrix} = -p \begin{Bmatrix} u(x,y) \\ v(x,y) \end{Bmatrix}$$

The strain energy of the springs is

$$\begin{aligned} \Pi_f &= \frac{p}{2} \begin{pmatrix} u(x,y) & v(x,y) \end{pmatrix} \begin{Bmatrix} u(x,y) \\ v(x,y) \end{Bmatrix} \\ &= \frac{p}{2} \begin{pmatrix} D_{e(1)}^T & D_{e(2)}^T & D_{e(3)}^T \end{pmatrix} \begin{pmatrix} T_{e(1)}^T \\ T_{e(2)}^T \\ T_{e(3)}^T \end{pmatrix} \begin{pmatrix} T_{e(1)} & T_{e(2)} & T_{e(3)} \end{pmatrix} \begin{Bmatrix} D_{e(1)} \\ D_{e(2)} \\ D_{e(3)} \end{Bmatrix} \\ p[T_{e(r)}][T_{e(s)}] &\quad \rightarrow \quad [K_{e(r)e(s)}], \qquad r, s = 1, 2, 3. \end{aligned} \quad (19)$$

10 Simplex Integration

As an element of the manifold method is a generally shaped polygon, $P_1\ P_2\ \ldots\ P_{m-1}\ P_m\ P_1$, $P_1 = P_{m+1}$, $P_i = (x_i, y_i)$ are its ordered vertices rotating from axis x to axis y. As a arbitrary chosen point, $P_0 = (0, 0)$. The following integrations are analytical solutions

$$
\begin{aligned}
S &= \frac{1}{2}\sum_{i=1}^{m}\begin{vmatrix} x_i & y_i \\ x_{i+1} & y_{i+1} \end{vmatrix}, \\
S_x &= \frac{S}{3}\sum_{i=1}^{m}(x_i + x_{i+1}), \\
S_y &= \frac{S}{3}\sum_{i=1}^{m}(y_i + y_{i+1}), \\
S_{xx} &= \frac{S}{6}\sum_{i=1}^{m}(x_i^2 + x_{i+1}^2 + x_i x_{i+1}), \\
S_{yy} &= \frac{S}{6}\sum_{i=1}^{m}(y_i^2 + y_{i+1}^2 + y_i y_{i+1}), \\
S_{xy} &= \frac{S}{12}\sum_{i=1}^{m}(2x_i y_i + 2x_{i+1}y_{i+1} + x_i y_{i+1} + x_{i+1}y_i).
\end{aligned} \tag{20}
$$

11 Definition of Entrances

Thus far, only individual covers and elements were considered. For the movements of discontinuous boundaries, no tension and no penetration must be satisfied between two contact sides. The entrances are defined in the beginning of each time step.

[1] An entrance consists of two contact sides with their minimum distance is less than 2ρ. Here ρ is the maximum step displacement.

[2] When one entrance side translates to the other side without rotation, the maximum overlapping angle is less than 2δ. Here $\delta = 1.5$ is the maximum step rotation.

Figure 5.2 shows two complex blocks. As defined by this contact criteria, there are only two contacts even if the distance limit 2ρ is lager than the block diameters.

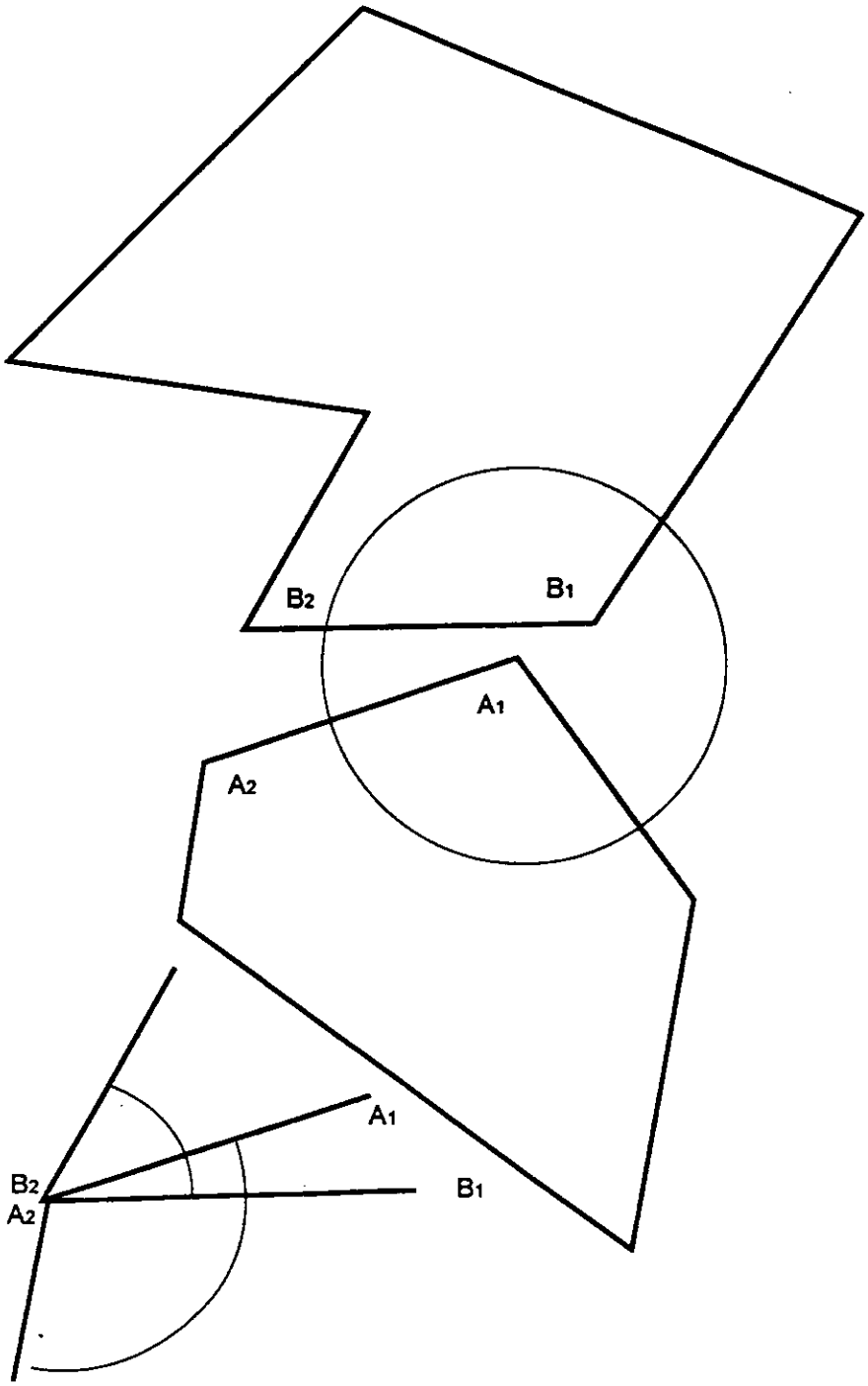

Figure 5 Entrance positions between two blocks

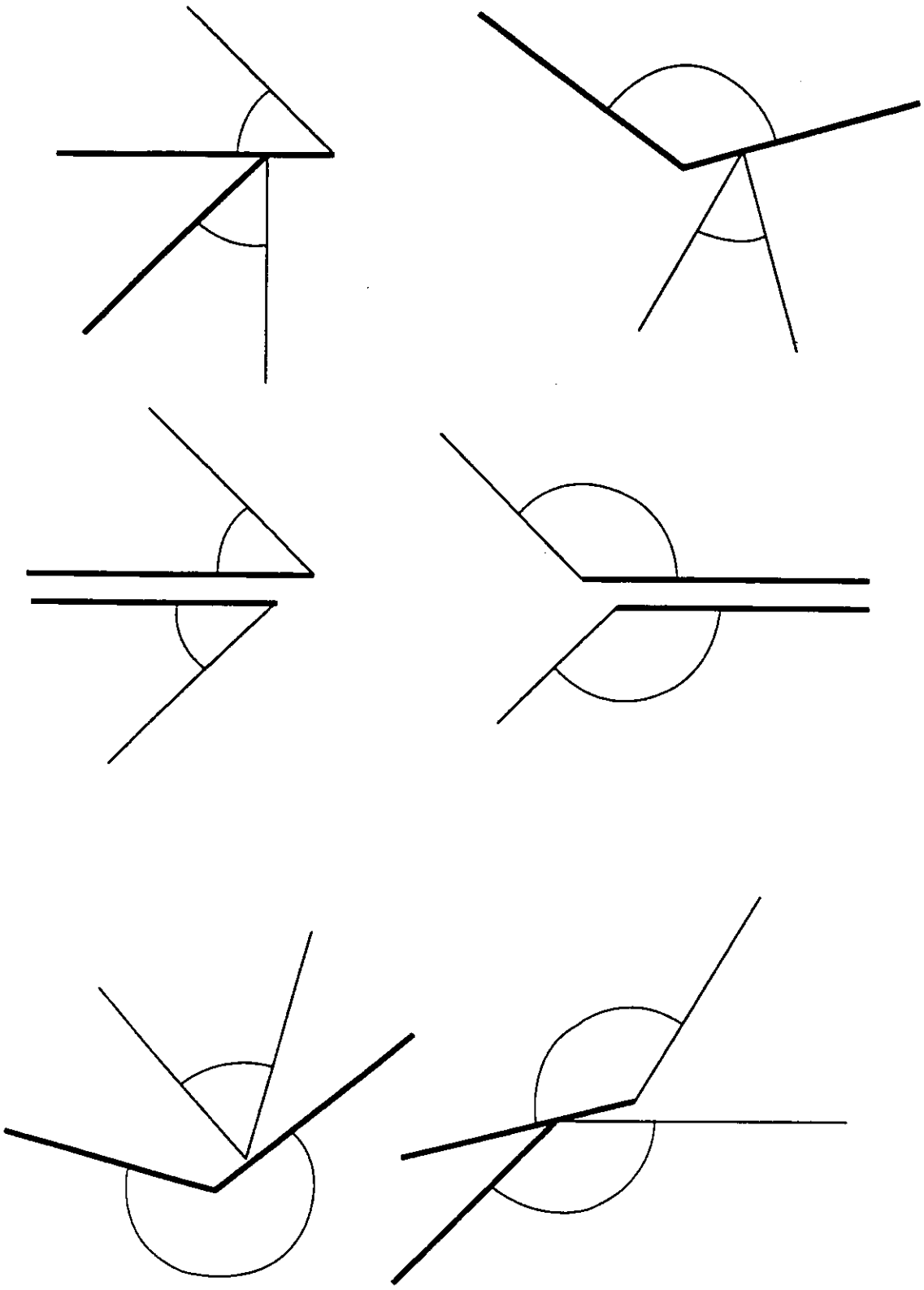

Figure 6.1 Entrance lines between two angles

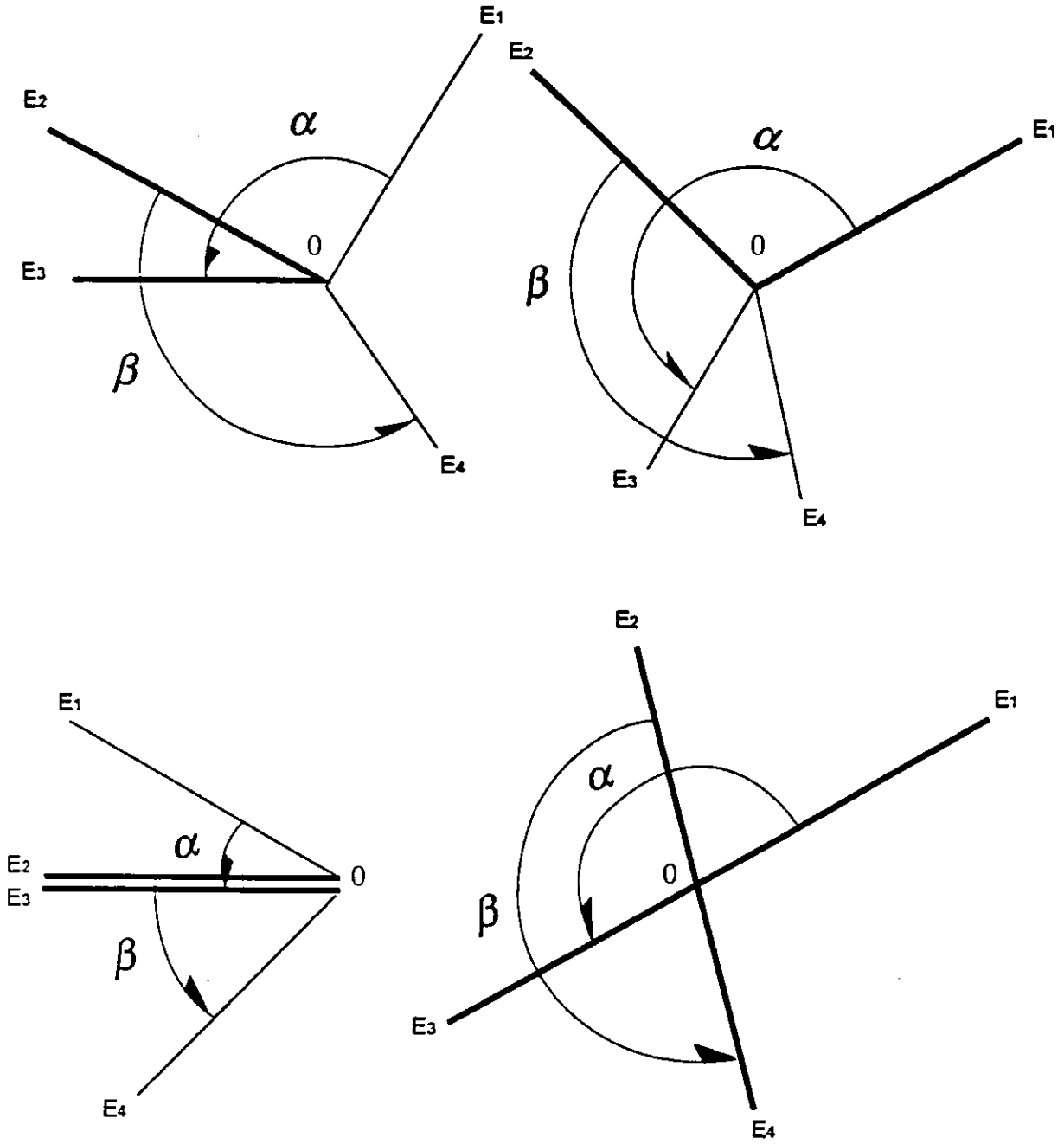

Figure 6.2 Criteria of entrance lines

The kinematics can be imposed on the global equations by adding stiff springs in the entrance positions.

[1] For the angle to angle entrance, if both angles are less than 180°, the two entrance lines are defined as the two thick lines shown by Figure 6.1 and 6.2. according to the following table:

	two entrance lines		
$\alpha \leq 180°$	$\beta \leq 180°$	OE_3	OE_2
$\alpha \leq 180°$	$\beta > 180°$	OE_3	OE_4
$\alpha > 180°$	$\beta \leq 180°$	OE_1	OE_2
$\alpha > 180°$	$\beta > 180°$	OE_1	OE_4

Penetration will occur if the two entrance lines are passed by the vertices of the other angles. A normal stiff spring is attached between the vertex and its entrance line where the entrance occurs first.

[2] For an angle to angle entrance, if a angle is larger than 180°, the two entrance lines are the two edges of the angle greater than 180°. If an entrance line has been passed by the vertex of another angle, a normal stiff springs is applied to the vertex and its entrance line. If two entrance lines have been passed, two springs are applied to the two entrance lines.

[3] For the angle to edge contact, the only entrance line is the edge, as showing by Figure 7. If the vertex passes its entrance line, a normal stiff spring is applied to the entrance line.

The definition of entrance line is still correct even if edges of two sides of the entrance are parallel or slightly penetrated.

12 Entrance Distances

Assume P_1 is a point before deformation which moves to point P_1' after deformation; P_2P_3 is the entrance line and (x_i, y_i) and (u_i, v_i) are the coordinates and displacement increments of $P_i, i = 1, 2, 3$ respectively. If points P_1, P_2 and P_3 rotate in the same sense as the rotation of ox to oy (see Figure 7.1 and 7.2), then P_1' has passed line P_2P_3 and is stated by the inequality:

$$\Delta = \begin{vmatrix} 1 & x_1 + u_1 & y_1 + v_1 \\ 1 & x_2 + u_2 & y_2 + v_2 \\ 1 & x_3 + u_3 & y_3 + v_3 \end{vmatrix} < 0, \tag{21}$$

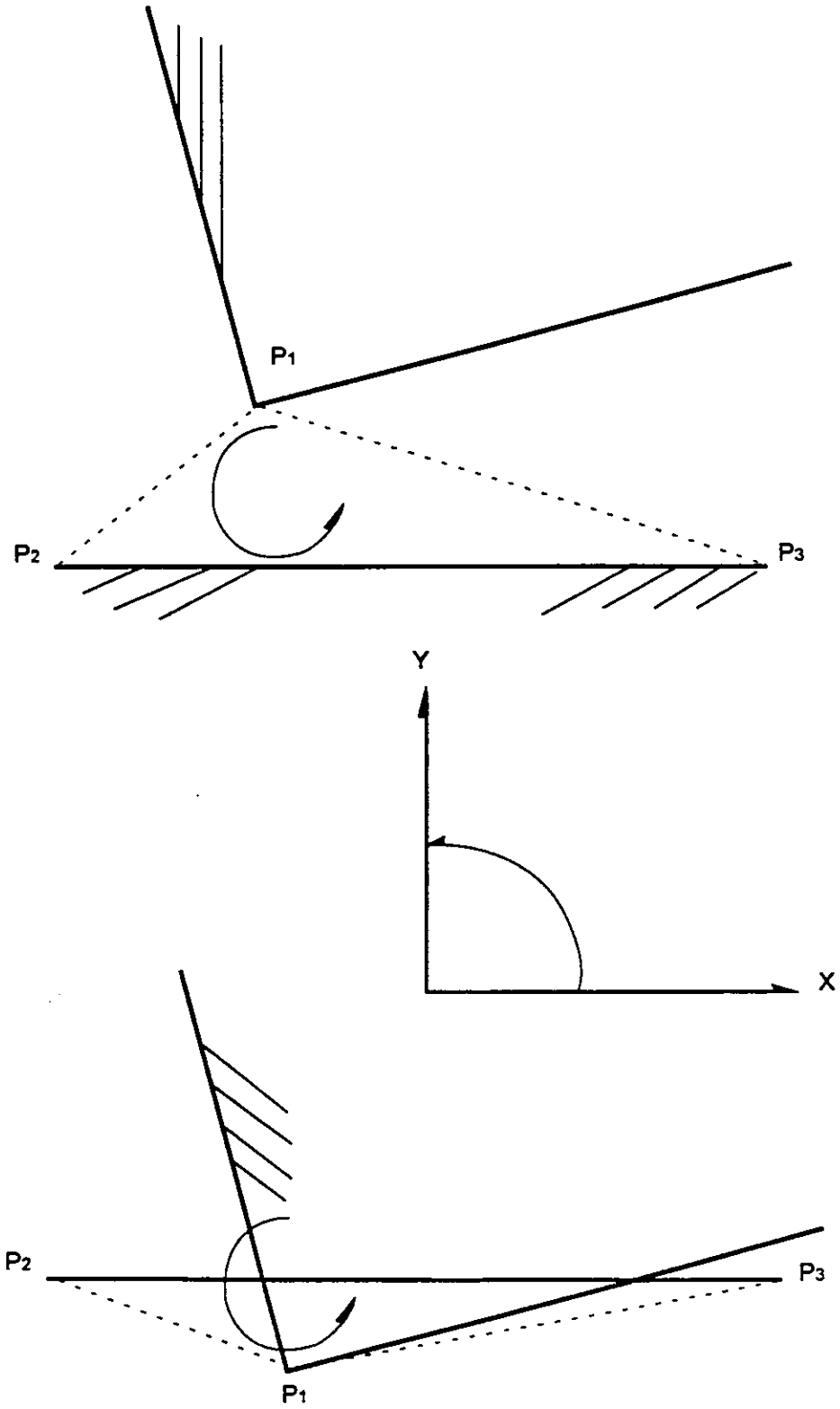

Figure 7 Penetration judgement

This simple equation is still correct even when these three points move simultaneously.

Since Δ is small, distance formula can be simplified

$$\begin{aligned} d &= \frac{\Delta}{\sqrt{(x_2+u_2-x_3-u_3)^2+(y_2+v_2-y_3-v_3)^2}} \\ &= \frac{\Delta}{\sqrt{(x_2-x_3)^2+(y_2-y_3)^2}} \end{aligned} \tag{22}$$

The friction law or Coloumb's law is also an inequality. $\mathcal{F} \leq \mathcal{N}\tan(\phi) + \mathcal{C}$.

If an entrance is open in the beginning of a time step and is closed in the end of the same time step, the entrance time and position in this time step can be computed. Assume $t = 0$ in the beginning of the time step, and $t = 1$ in the end of the time step, and

$$\Delta(t) = \begin{vmatrix} 1 & x_1+tu_1 & y_1+tv_1 \\ 1 & x_2+tu_2 & y_2+tv_2 \\ 1 & x_3+tu_3 & y_3+tv_3 \end{vmatrix} \tag{23}$$

then $\Delta(0) > 0$ *and* $\Delta(1) < 0$. The entrance time t_0 satisfies the equation $\Delta(t_0) = 0$. Neglecting the second order terms, the entrance time t_0 and the entrance position (x_0, y_0) can be computed by the simpler equation:

$$t_0 = -\begin{vmatrix} 1 & x_1 & y_1 \\ 1 & x_2 & y_2 \\ 1 & x_3 & y_3 \end{vmatrix} \left(\begin{vmatrix} 1 & u_1 & y_1 \\ 1 & u_2 & y_2 \\ 1 & u_3 & y_3 \end{vmatrix} + \begin{vmatrix} 1 & x_1 & v_1 \\ 1 & x_2 & v_2 \\ 1 & x_3 & v_3 \end{vmatrix} \right)^{-1}, \quad \begin{Bmatrix} x_0 \\ y_0 \end{Bmatrix} = \begin{Bmatrix} x_1+u_1t_0 \\ y_1+v_1t_0 \end{Bmatrix} \tag{24}$$

These equations are still correct even when the three points move simultaneously.

13 Normal Springs

From equation (22), the distance d from P_1 of element i to the entrance line P_2P_3 of element j is $d = \frac{\Delta}{\sqrt{(x_2-x_3)^2+(y_2-y_3)^2}}$, d should be *zero* if P_1 passed edge P_2 P_3. Let

$$S_0 = \begin{vmatrix} 1 & x_1 & y_1 \\ 1 & x_2 & y_2 \\ 1 & x_3 & y_3 \end{vmatrix}, \qquad l = \sqrt{(x_2-x_3)^2+(y_2-y_3)^2}$$

Neglecting the second order terms, the distance d can be expressed a linear function of $\{D_i\}$:

$$
\begin{aligned}
d &= \frac{1}{l}S_0 + \frac{1}{l}\begin{vmatrix} 1 & u_1 & y_1 \\ 1 & u_2 & y_2 \\ 1 & u_3 & y_3 \end{vmatrix} + \frac{1}{l}\begin{vmatrix} 1 & x_1 & v_1 \\ 1 & x_2 & v_2 \\ 1 & x_3 & v_3 \end{vmatrix} \\
&= \frac{1}{l}S_0 + \frac{1}{l}\begin{pmatrix} u_1 & v_1 \end{pmatrix}\begin{Bmatrix} y_2 - y_3 \\ x_3 - x_2 \end{Bmatrix} \\
&+ \frac{1}{l}\begin{pmatrix} u_2 & v_2 \end{pmatrix}\begin{Bmatrix} y_3 - y_1 \\ x_1 - x_3 \end{Bmatrix} + \frac{1}{l}\begin{pmatrix} u_3 & v_3 \end{pmatrix}\begin{Bmatrix} y_1 - y_2 \\ x_2 - x_1 \end{Bmatrix} \\
&= \frac{S_0}{l} + \begin{pmatrix} D^T_{i(1)} & D^T_{i(2)} & D^T_{i(3)} \end{pmatrix}\begin{Bmatrix} H_1 \\ H_2 \\ H_3 \end{Bmatrix} + \begin{pmatrix} D^T_{j(1)} & D^T_{j(2)} & D^T_{j(3)} \end{pmatrix}\begin{Bmatrix} G_1 \\ G_2 \\ G_3 \end{Bmatrix}
\end{aligned}
\tag{25}
$$

where

$$
\begin{aligned}
\{H_r\} &= \frac{1}{l}[T_{i(r)}(x_1, y_1)]^T \begin{Bmatrix} y_2 - y_3 \\ x_3 - x_2 \end{Bmatrix}, \qquad r = 1, 2, 3, \\
\{G_s\} &= \frac{1}{l}[T_{j(s)}(x_2, y_2)]^T \begin{Bmatrix} y_3 - y_1 \\ x_1 - x_3 \end{Bmatrix} \\
&+ \frac{1}{l}[T_{j(s)}(x_3, y_3)]^T \begin{Bmatrix} y_1 - y_2 \\ x_2 - x_1 \end{Bmatrix}, \qquad s = 1, 2, 3,
\end{aligned}
\tag{26}
$$

The potential energy of the normal spring is

$$
\begin{aligned}
\Pi_s = \frac{p}{2}d^2 &= \frac{p}{2}\begin{pmatrix} D^T_{i(1)} & D^T_{i(2)} & D^T_{i(3)} \end{pmatrix}\begin{Bmatrix} H_1 \\ H_2 \\ H_3 \end{Bmatrix}\begin{pmatrix} H^T_1 & H^T_2 & H^T_3 \end{pmatrix}\begin{Bmatrix} D_{i(1)} \\ D_{i(2)} \\ D_{i(3)} \end{Bmatrix} \\
&+ \frac{p}{2}\begin{pmatrix} D^T_{j(1)} & D^T_{j(2)} & D^T_{j(3)} \end{pmatrix}\begin{Bmatrix} G_1 \\ G_2 \\ G_3 \end{Bmatrix}\begin{pmatrix} G^T_1 & G^T_2 & G^T_3 \end{pmatrix}\begin{Bmatrix} D_{j(1)} \\ D_{j(2)} \\ D_{j(3)} \end{Bmatrix} \\
&+ p\begin{pmatrix} D^T_{i(1)} & D^T_{i(2)} & D^T_{i(3)} \end{pmatrix}\begin{Bmatrix} H_1 \\ H_2 \\ H_3 \end{Bmatrix}\begin{pmatrix} G^T_1 & G^T_2 & G^T_3 \end{pmatrix}\begin{Bmatrix} D_{j(1)} \\ D_{j(2)} \\ D_{j(3)} \end{Bmatrix}
\end{aligned}
$$

$$+p\frac{S_0}{l}\left(D^T_{i(1)} \quad D^T_{i(2)} \quad D^T_{i(3)}\right)\begin{Bmatrix} H_1 \\ H_2 \\ H_3 \end{Bmatrix}$$

$$+p\frac{S_0}{l}\left(D^T_{j(1)} \quad D^T_{j(2)} \quad D^T_{j(3)}\right)\begin{Bmatrix} G_1 \\ G_2 \\ G_3 \end{Bmatrix} + \frac{p}{2}\left(\frac{S_0}{l}\right)^2 \tag{27}$$

Then

$$\begin{aligned}
p\{H_r\}\{H_s\}^T &\rightarrow [K_{i(r)i(s)}], && r,s=1,2,3,\\
p\{H_r\}\{G_s\}^T &\rightarrow [K_{i(r)j(s)}], && r,s=1,2,3,\\
p\{G_r\}\{H_s\}^T &\rightarrow [K_{j(r)i(s)}], && r,s=1,2,3,\\
p\{G_r\}\{G_s\}^T &\rightarrow [K_{j(r)j(s)}], && r,s=1,2,3,\\
-p\left(\frac{S_0}{l}\right)\{H_r\} &\rightarrow \{F_{i(r)}\}, && r=1,2,3,\\
-p\left(\frac{S_0}{l}\right)\{G_r\} &\rightarrow \{F_{j(r)}\}, && r=1,2,3,
\end{aligned} \tag{28}$$

14 Shear Springs

In Figure 8, (x_0, y_0) is on the edge P_2P_3 and is the assumed contact point of vertex P_1. The shear spring is on the direction P_2P_3, and connects vertices P_1 and P_0. Denote

$$S_0 = \left(x_3 - x_2 \quad y_3 - y_2\right)\begin{Bmatrix} x_1 - x_0 \\ y_1 - y_0 \end{Bmatrix} \tag{29}$$

Since P_0P_1 is small, the shear displacement of P_0 and P_1 along line P_2P_3 is

$$\begin{aligned}
d &= \frac{1}{l}\overrightarrow{P_0P_1}\cdot\overrightarrow{P_2P_3} \\
&= \frac{1}{l}\left(x_3 - x_2 \quad y_3 - y_2\right)\begin{Bmatrix} x_1 + u_1 - x_0 - u_0 \\ y_1 + v_1 - y_0 - v_0 \end{Bmatrix}
\end{aligned} \tag{30}$$

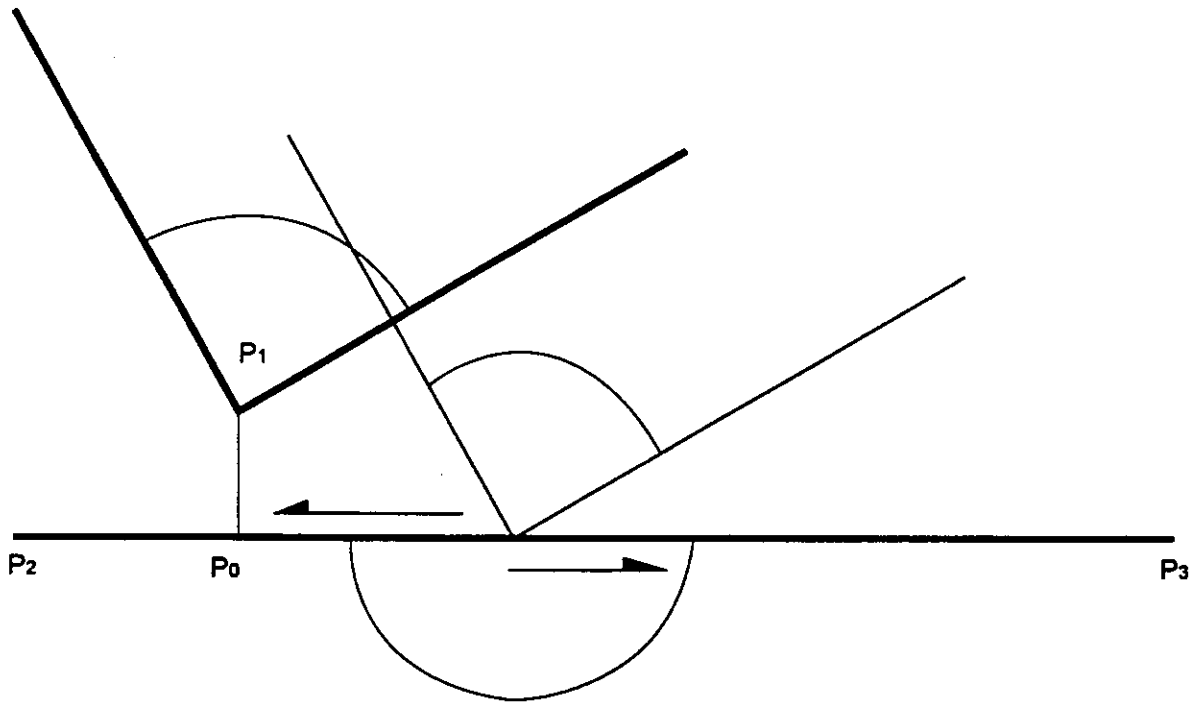

Figure 8 Position of shear spring

$$= \frac{S_0}{l} + \frac{1}{l}\begin{pmatrix} u_1 & v_1 \end{pmatrix}\begin{Bmatrix} x_3 - x_2 \\ y_3 - y_2 \end{Bmatrix} + \frac{1}{l}\begin{pmatrix} u_0 & v_0 \end{pmatrix}\begin{Bmatrix} x_2 - x_3 \\ y_2 - y_3 \end{Bmatrix} \tag{31}$$

$$= \frac{S_0}{l} + \begin{pmatrix} D^T_{i(1)} & D^T_{i(2)} & D^T_{i(3)} \end{pmatrix}\begin{Bmatrix} H_1 \\ H_2 \\ H_3 \end{Bmatrix} + \begin{pmatrix} D^T_{j(1)} & D^T_{j(2)} & D^T_{j(3)} \end{pmatrix}\begin{Bmatrix} G_1 \\ G_2 \\ G_3 \end{Bmatrix}$$

$$\{H_r\} = \frac{1}{l}[T_{i(r)}(x_1, y_1)]^T \begin{Bmatrix} x_3 - x_2 \\ y_3 - y_2 \end{Bmatrix}, \qquad r = 1, 2, 3,$$

$$\{G_s\} = \frac{1}{l}[T_{j(s)}(x_0, y_0)]^T \begin{Bmatrix} x_2 - x_3 \\ y_2 - y_3 \end{Bmatrix}, \qquad s = 1, 2, 3, \tag{32}$$

The equation of the potential energy of the shear spring is same as equation (27); the submatrices contributing to simultaneous equations are also the equation (28) accept that the definition of H_r, G_s, S_0 are different.

15 Friction Force Matrix

When the Coulomb's law allows sliding between two sides of the entrances, there exist the couple of friction forces on the two sliding sides. The friction force is calculated from the normal compressive force, $F = pd\tan(\phi)$, where d is the normal penetration distance, $\tan(\phi)$ is the friction coefficient. The directions of the friction force couple are against the movement of P_1 relative to P_0 in the direction $\pm\overrightarrow{P_2P_3}$.

The potential energy of friction force pair is

$$\Pi_f = \frac{F}{l}\begin{pmatrix} u_1 & v_1 \end{pmatrix}\begin{Bmatrix} x_3 - x_2 \\ y_3 - y_2 \end{Bmatrix} - \frac{F}{l}\begin{pmatrix} u_0 & v_0 \end{pmatrix}\begin{Bmatrix} x_3 - x_2 \\ y_3 - y_2 \end{Bmatrix}$$

$$= F\begin{pmatrix} D^T_{i(1)} & D^T_{i(2)} & D^T_{i(3)} \end{pmatrix}\begin{Bmatrix} H_1 \\ H_2 \\ H_3 \end{Bmatrix} - \mathcal{F}\begin{pmatrix} D^T_{j(1)} & D^T_{j(2)} & D^T_{j(3)} \end{pmatrix}\begin{Bmatrix} G_1 \\ G_2 \\ G_3 \end{Bmatrix} \tag{33}$$

where

$$\{H_r\} = \frac{1}{l}[T_{i(r)}(x_1, y_1)]^T \begin{Bmatrix} x_3 - x_2 \\ y_3 - y_2 \end{Bmatrix}, \qquad r = 1, 2, 3,$$

$$\{G_s\} = \frac{1}{l}[T_{j(s)}(x_0, y_0)]^T \begin{Bmatrix} x_3 - x_2 \\ y_3 - y_2 \end{Bmatrix}, \qquad s = 1, 2, 3, \tag{34}$$

The loading matrix of the coupled friction forces are

$$-F\{H_r\} \quad \rightarrow \quad \{F_{i(r)}\}, \qquad r = 1, 2, 3,$$

$$+F\{G_r\} \quad \rightarrow \quad \{F_{j(r)}\}, \qquad r = 1, 2, 3,$$

16 Equation Solver and Open-Close Iterations

The manifold method computations follow the time steps. The following items are transferred from the end of the previous time step to the beginning of the next time step: stresses, strains and velocities of each element, current geometry, contact positions, contact forces and contact states.

The current version of the manifold code is a simple version. In the beginning of a time step, the dynamic computations inherit the velocity at the end of the last step. For static computations, the initial velocity of each time step is zero.

Within each time step, the global equations are solved repeatedly while adding and removing stiff springs. These open-close iterations ensues no-penetration in the open contacts, and no-tension in the contacts with normal springs. If the two conditions are not fulfilled for all entrances after five times of open-close iterations, the time step will be reduced to one third, and the open-close iteration continues.

The principles of choosing time steps Δ are: Δ is small enough, so that the second order displacements are neglected; Δ is small enough, so that the SOR iteration will converge in less than 30 iterations; Δ is small enough, so that the open-close iterations will converge in less than 5 iterations. But Δ should be large enough, so that the computation will represent significant time span and the displacements are stabilized if possible.

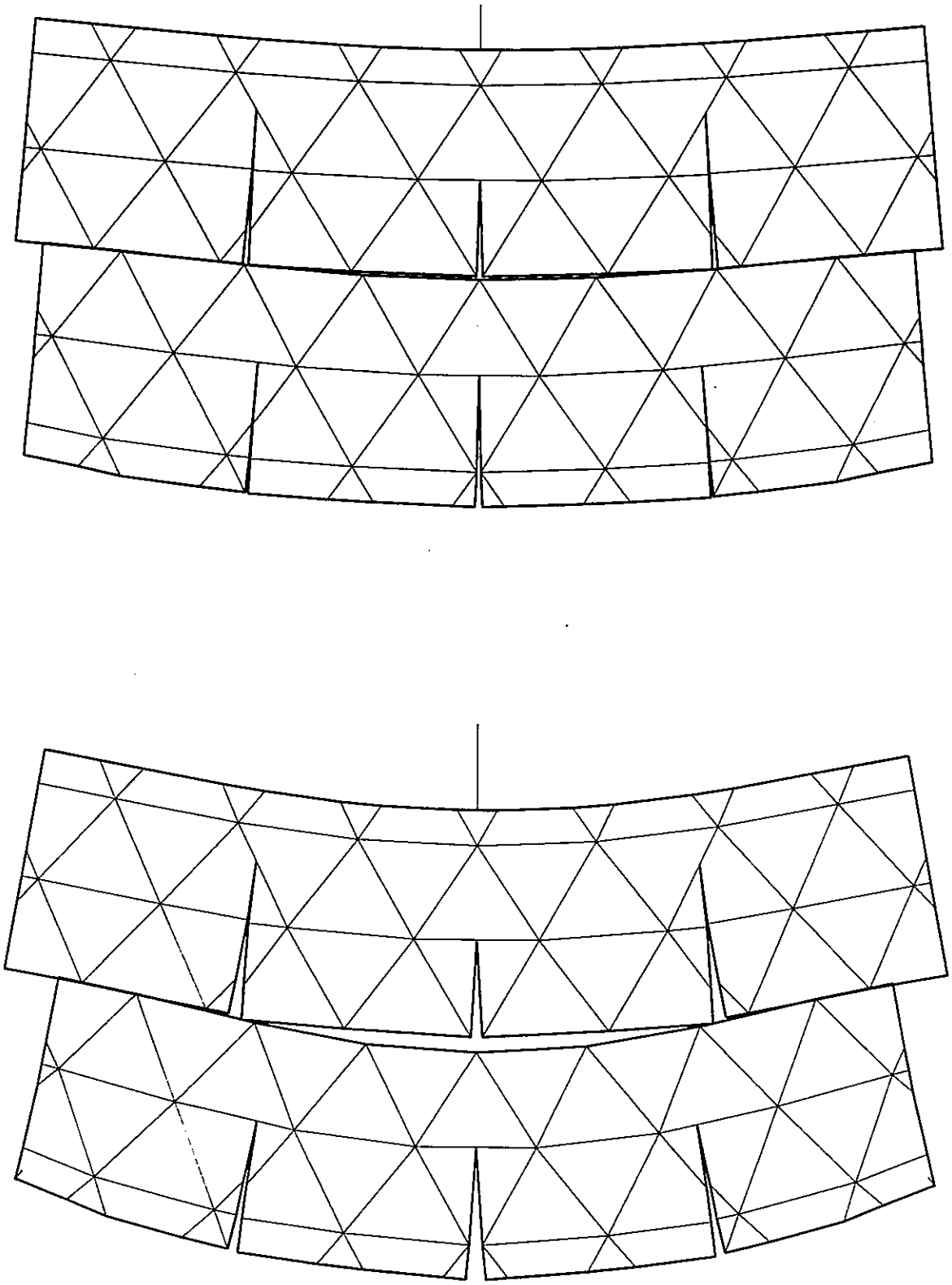

Figure 9.1 Deformation of double simply supported beams

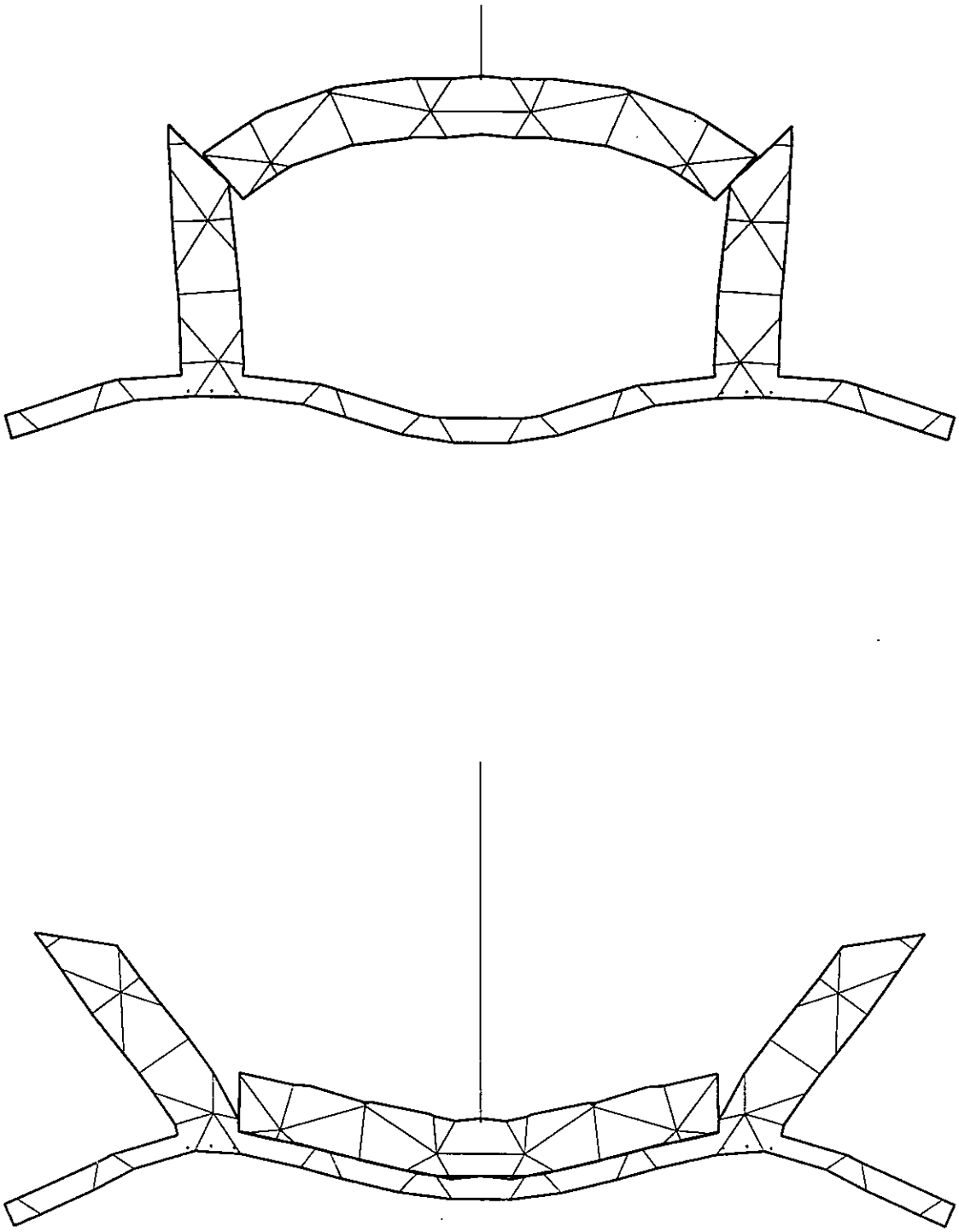

Figure 9.2 Failure of a tunnel lining under point loads

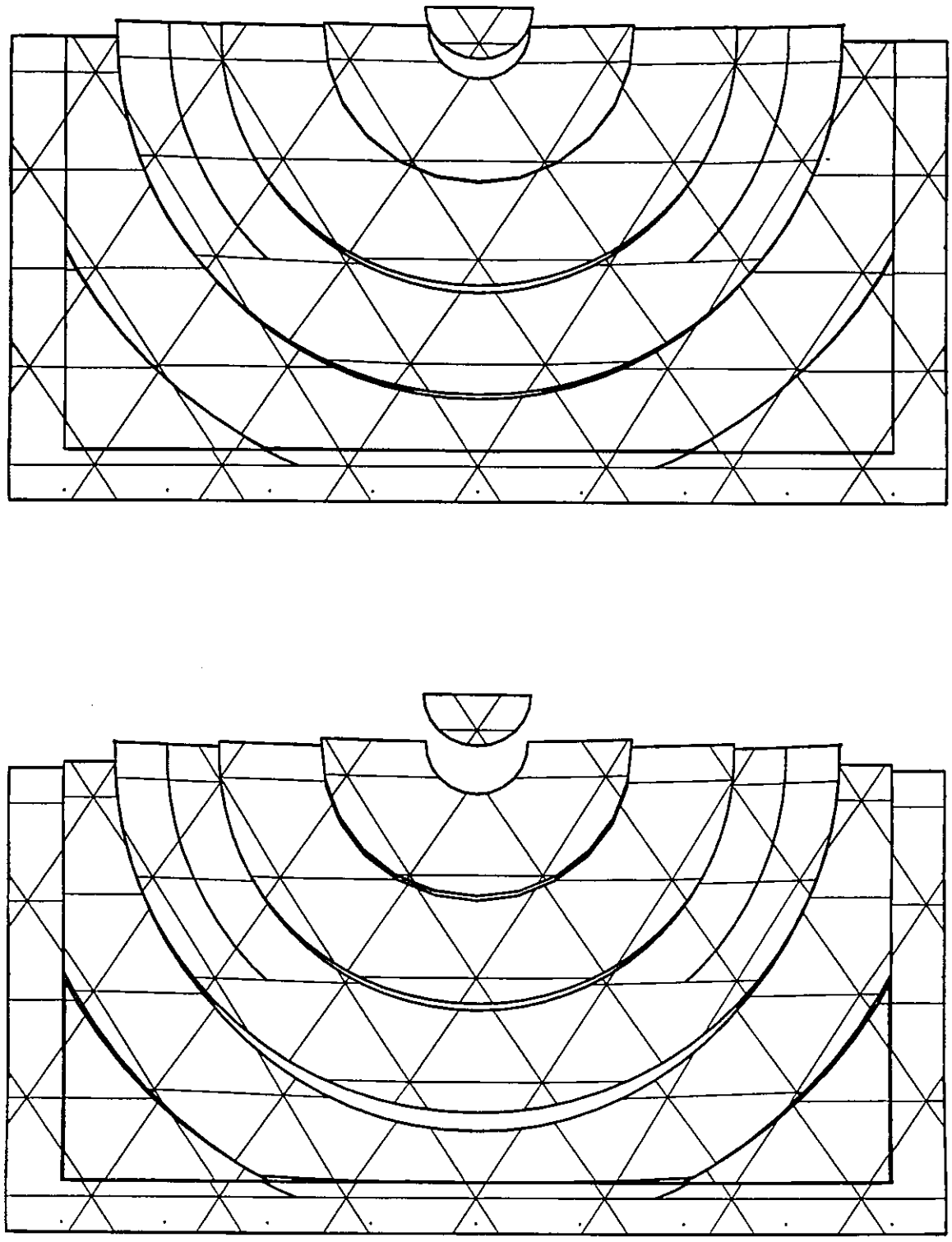

Figure 9.3 Ground movements under horizontal force

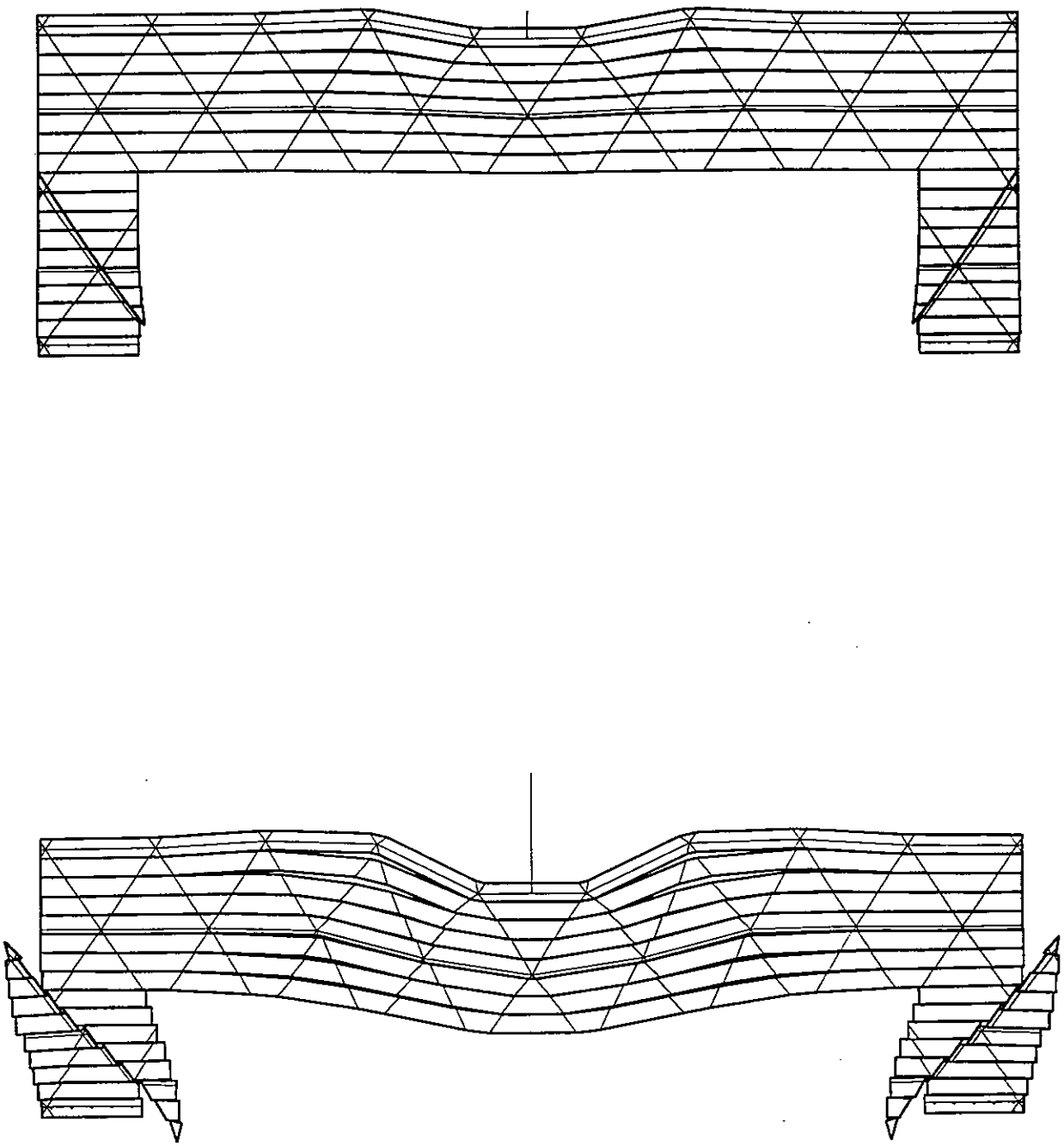

Figure 9.4 Failure of rocks with horizontal bedding planes

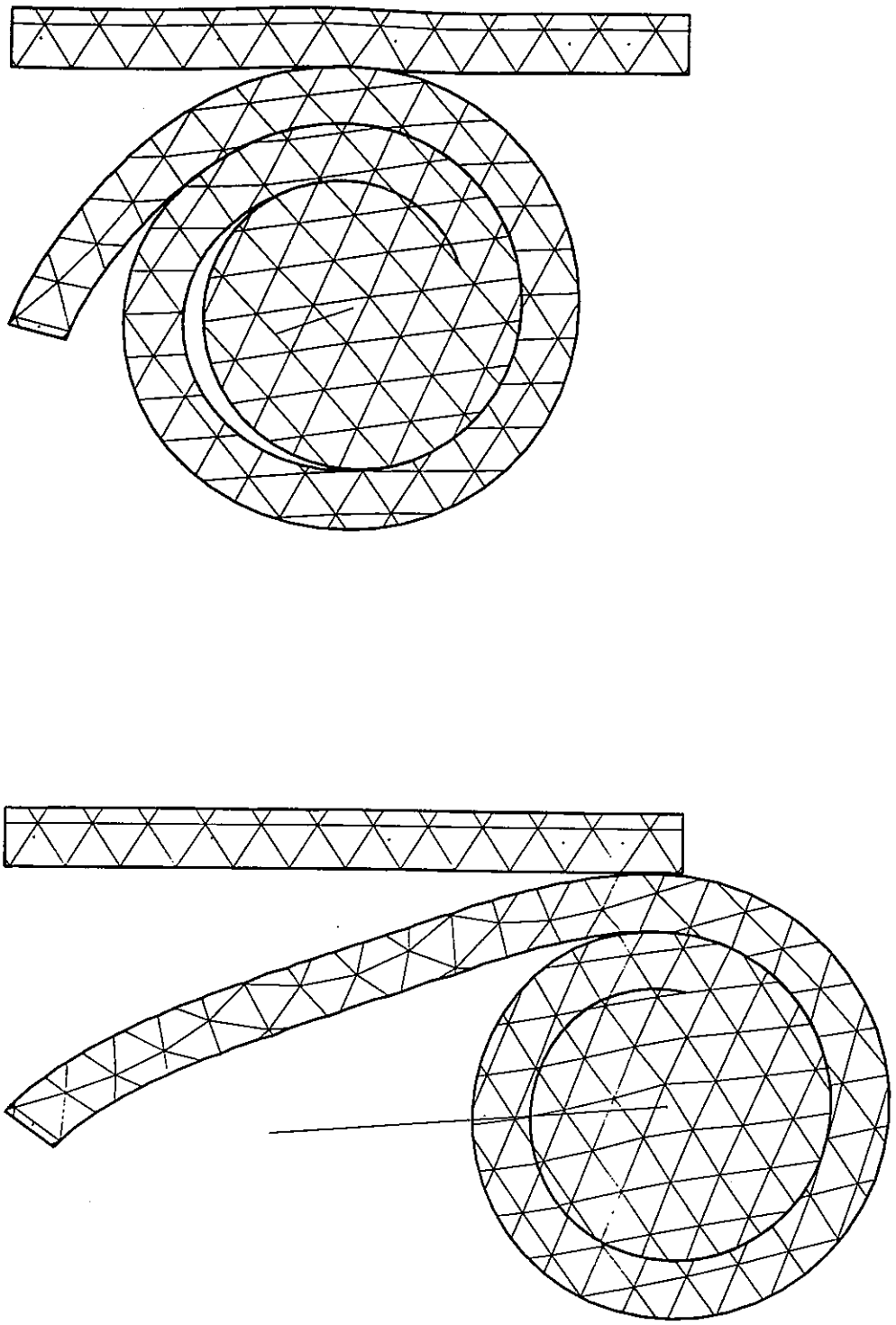

Figure 9.5 Computation of a spiral joint

17 Applications of Numerical Manifold Method

Figure 9.1 shows the deformation of the joints and the continuous materials of double simply supported beams. Figure 9.2 shows the failure of a tunnel lining under the point load on the arch top. Figure 9.3 shows the ground movements under a horizontal force. Figure 9.4 shows the failure of rock with horizontal bedding planes. Figure 9.5 shows the deformations of a domain with a spiral joint.

Acknowledgement This study was made possible through fundings provide by the U. S. Army Corps of Engineers, Office of the Chief of Engineers, under the Civil Works Research and Development Program. The study was conducted by the US Army Engineer Waterways Experiment Station, Geotechnical Laboratory, Soil and Rock Mechanics Division.

References

[1] K. J. Bathe and E. D. Wilson 1976. "Numerical Methods in Finite Element Analysis." (PRENTICE-HALLL, INC., Englewood Cliffs, New Jersey).

[2] Gen-hua Shi, 1992. "Modeling Rock Joints and Blocks by Manifold Method," *Rock Mechanics Proceedings of the 33rd U. S. Symposium*, pp. 639-648 (Santa Fe, New Mexico).

[3] Gen-hua Shi, 1992. " Manifold Method of Material Analysis," *Transactions of the Ninth Army Conference on Applied Mathematics and Computing*, pp. 51-76 (Minneapolis, Minnesoda).

[4] Shi, Gen-hua 1993. "Block system modeling by discontinuous deformation analysis." (Southampton UK and Boston USA).

Applicability of Existing Models to Predict the Behavior of Rock Joints under Different Boundary Conditions

B. Amadei[+] and J. Wibowo*

[+]Department of Civil, Environmental, and Architectural Engineering
University of Colorado at Boulder, Boulder, Colorado 80309-0428

*Geotechnical Lab., US Army Engineer Waterways
Experiment Station, Vicksburg MS 39180-6199

ABSTRACT: The response of a rough joint (or a fracture) to shear loading depends on its surface properties as well as the boundary conditions that are applied by the surrounding rock mass. In this paper, we present the results of cyclic direct shear experiments conducted on replicas of three natural fractures and a laboratory-developed tensile fracture of welded tuff. The tests were carried out under constant normal loads or constant normal stiffnesses with different initial normal load levels. Each test consisted of five cycles of forward and reverse shear motion. The results of the constant normal load shear experiments are analyzed using several constitutive models proposed in the rock mechanics literature for joint shear strength, dilatancy, and joint surface damage. It is shown that some of the existing models have limitations. New constitutive models are proposed and are included in a mathematical analysis tool that can be used to predict joint behavior under various boundary conditions.

1. INTRODUCTION

The response of a rough joint (or a fracture) to shear loading depends on its surface properties as well as the boundary conditions that are applied by the surrounding rock mass. These boundary conditions can exist in a variety of forms as shown in Fig. 1. A constant normal load (stress) boundary condition can be used, for instance, in rock slope stability problems to model the sliding of a block along a critical joint plane [Fig. 1(a)]. On the other hand, if a system of rock bolts or cables is installed to stabilize the same block as shown in Fig. 1(b), the dilatancy of the joint is now constrained and controlled by the stiffness of the reinforcement. Similarly, a rock block constrained between dilatant joints that slides into an underground excavation, as shown in Fig. 1(c), does not move as freely as in Fig. 1(a). As the block moves, dilation of the joints is restricted by the surrounding rock mass, and the joint shear behavior is controlled by the rock mass stiffness, i.e., the capacity of the rock mass to deform.

The range of joint normal loading conditions shown in Fig. 1 can best be represented by assuming that the reinforcement in Fig. 1(b) and the rock mass surrounding the joints in Fig. 1(c) are modelled by a spring with stiffness, K, defined as the ratio between the increments in joint normal load (stress) and the increments in joint normal displacement. The applied stiffness may vary between zero for a constant normal load (stress) condition and infinity for a constant

normal displacement condition. The applied stiffness is constant if the change in joint normal load (stress) remains proportional to the change in joint normal displacement during shearing. However, the applied stiffness may also vary with the load history of the rock mass. Note that the applied stiffness, K, is a property of the rock mass or the reinforcement system and should not be confused with the joint normal stiffness.

In general, joint shear strength under constant (nonzero) or variable normal stiffness is higher than joint shear strength under constant normal load (stress). The main reason for the increase in shear strength is that under constant or variable normal stiffness boundary conditions, joint dilatancy created by the joint surface roughness is inhibited and joint normal load (stress) increases as shear takes place. The effect of normal stiffness boundary conditions on the shear behavior of rock joints has been investigated either theoretically or experimentally in the rock mechanics literature [1-10].

In two publications, Saeb [11] and Amadei and Saeb [12] proposed mathematical and graphical methods to predict the shear behavior of a rock joint under constant or variable normal stiffness boundary condition from the results of conventional constant normal load (stress) direct shear tests. An experimental research program was initiated to test these methods using the data collected on several fractures. Cyclic direct shear tests and normal compression tests were conducted on replicas of three natural fractures and a laboratory-developed tensile fracture of welded tuff. A total of 20 direct shear tests were carried out under constant normal loads ranging between 2.7 and 113.9 kN (equivalent to nominal normal stresses ranging between 0.3 and 5.5 MPa). Also 15 direct shear tests were carried out under constant normal stiffnesses ranging between 25.9 and 328.4 kN/cm with different initial normal loads. Each direct shear test consisted of five cycles of forward and reverse shear motion.

In this paper, the results of the shear tests conducted under constant normal load are analyzed using several constitutive models proposed in the rock mechanics literature for joint shear strength, dilatancy, and joint surface damage (models of Goodman, Ladanyi and Archambault, Barton, Schneider, and Jing). Some of the existing models appear to have limitations. New constitutive models are proposed and are included in a mathematical analysis tool that can be used to predict joint behavior under various boundary conditions.

2. EXPERIMENTAL WORK

2.1 Specimen Preparation

Four rectangular joint samples of welded tuff were investigated in this study:

a. A 10.2 cm x 20.3 cm natural joint sample which is referred to as G2.

b. An artificially created joint sample created by tensile splitting of a welded tuff block. The size of the sample was approximately 7.6 cm x 15.2 cm. This sample is referred to as F2.

c. A 7.6 cm x 15.2 cm natural joint sample which is referred to as F3.

d. A 7.6 cm x 15.2 cm natural joint sample which is referred to as F4.

All four joints originated from several large and irregular blocks of welded tuff. To obtain a natural joint sample and create a regular external configuration with the size mentioned above, the big blocks were cut using a diamond bit masonry saw. The mean plane of the joint coincided with the center plane of the block.

In order to perform several shear tests on fracture surfaces with duplicated initial roughness, replicas of the four joint surfaces were made using gypsum cement. Two steps were followed in making the replicas. First, the negative images of the joint surfaces (top and bottom) were created by pouring silicon rubber on the surfaces of the original joints. After 48 hours of hardening, the half-inch-thick negative images were strong enough to be used as negative molds for the joint replicas. Then, twelve to fifteen joint replicas were reproduced using a water-to-gypsum cement ratio of 20%. With this mixture, the unconfined compressive strength of the gypsum cement was measured as approximately 27.6 MPa.

The bottom portion of each joint replica was placed at the center of the lower shear box specimen holder. Spacers were placed at the bottom of the sample in order to keep the mean joint surfaces horizontal. The mean joint surfaces were adjusted to a horizontal plane by using the air bubble of a 5.1 cm x 20.3 cm level placed longitudinally across the joint surfaces. A gypsum cement mixture was then poured into the lower specimen holder to maintain the replica in place. Following hardening of the gypsum cement, the top part of each joint replica was placed and kept in a mated position above the corresponding bottom part. Then, the assembly consisting of the top and bottom parts of the joint replica and the bottom specimen holder were turned over and placed at the center of the top specimen holder. The upper and lower specimen holders were positioned in a manner that ensured initially parallel alignment. The top part of the joint replica was held in place using gypsum cement.

Bevelled miniature berms or embankments made of gypsum cement were placed along the periphery and up to the surfaces of samples F3 and F4 in order to prevent their edges from breaking off during shear, especially under high normal loads. This helped in keeping most of the test specimen edges intact during shear. For the G2 and F2 samples no slope embankments were constructed. The joint surfaces were then ready for the following test sequence: profilometer recording before shear (one set of profiles for each joint), normal compression before shear (one test for each joint), cyclic shear, normal compression after shear, and profilometer recording after shear.

2.2 Direct Shear Tests

Direct shear tests were conducted using the direct shear machine available in the Department of Civil, Environmental, and Architectural Engineering at the University of Colorado at Boulder. For each direct shear test, six steps were followed:

- identification of each joint specimen,
- placement of joint specimen with the specimen holders on the platens of the direct shear machine,

- application of initial normal load across the joint surfaces,
- cyclic normal compression,
- shearing with five cycles, and
- cyclic normal compression.

Direct Shear Apparatus

The direct shear experiments were conducted using a servo-controlled direct shear apparatus. Figs. 2 and 3 show the different components of the apparatus including two independent Minnesota Testing System (MTS) actuators (used to transmit normal and shear loads), reaction frames, loading fixtures, and shear box specimen holders. The MTS actuators used to apply normal and shear loads have a capacity of 734 kN and 156 kN, respectively, and can be operated independently in load or displacement control modes. The actuators are equipped with load cells to measure applied forces and have internal LVDTs for monitoring displacement (stroke). Both actuators are powered by independent, closed-loop continuous flow systems powered by a 76 lpm generator pump. For cyclic shearing, a function generator provides a sinusoidal reference voltage to the shear load actuator in the displacement control mode. The sinusoidal reference voltage was chosen to avoid a sudden change of shear rate at the maximum shear displacement. Although this sinusoidal reference voltage caused the shear rate to be variable, the shear load response does not show significant difference as explained by Gould [13]. A detailed description of the apparatus and its performance characteristics is given by Gould [13].

Instrumentation

The applied loads were measured using the MTS actuator load cells; a 978 kN cell mounted on the normal actuator and a 156 kN cell mounted on the shear actuator. The range or amplification for the normal load cell was changed between times-one (100% of capacity) and times-ten (10% of capacity) depending on the test condition. The shear load cell was always operated in a times-one (100% of capacity) mode. Since the actuators' internal LVDTs were not sensitive enough and were located too far away from the test specimens to monitor displacements accurately, two external horizontal LVDTs (Schaevitz 1000 HRDC) were used to monitor the relative shear displacements. They had a 2.5 cm maximum stroke and were of the DC type. Aluminum rods (2.5 mm dia.) were cemented into the top and bottom parts of each specimen using heavy duty epoxy. Collars were used to connect the rods to the tips of the LVDTs in order to provide a solid mechanical connection during shear direction reversal. The two LVDTs were supported by an unstressed external stand placed on the structural test floor.

In addition, three external vertical LVDTs were used to monitor the normal joint displacement. Two of those LVDTs were Schaevitz 1000 HRDC with a 2.5 cm maximum stroke. The third LVDT was a Schaevitz 500 HRDC with a 1.3 cm maximum stroke. The normal displacement LVDTs were mounted on holder assemblies made of heavy steel bars, which were attached to supports that were firmly bolted to the thick steel base plate of the direct shear apparatus.

For the constant stiffness tests, a more precise Schaevitz 200 HR LVDT (AC type), with a 5.1 mm maximum stroke, was also used to monitor the normal displacement of the joints. A special

holder was constructed that allowed that particular LVDT to be placed between the hydraulic cylinder and the load cell of the vertical actuator. An initial load had to be applied across the joint surfaces before that LVDT was adjusted into zero position in order to prevent it from going out of range.

Test Control for Normal Stiffness Tests

For the joints sheared under constant normal stiffness, their dilatancy caused an additional normal load proportional to the applied stiffness. Direct shear tests under constant normal stiffness were performed following a procedure similar to the constant normal load shear tests with an additional computer system appended to the existing system. The dilatancy monitored by the Schaevitz 200 HR LVDT (AC type) was converted to digital data and manipulated by a computer program to maintain the value of applied stiffness to a predetermined value. As dilatancy occurred, the additional normal load due to stiffness was reconverted to an analog signal, and these additional voltages were added to the existing load applied by the MTS system. Details of the constant stiffness tests have been described by Hutson [5].

Data Acquisition System

An IBM-XT personal computer with a Tecmar board A/D (analog to digital) converter was used for data collection. Various voltage ranges are software selectable. The MTS system works on a +/- 10 v circuit. Since the load cell readings were being supplied by this system, all channels were set for a +/- 10 v range. A data acquisition computer program written in Turbo Pascal provided adequate speed, along with good organization and readability.

Testing

The upper half of each joint sample with the specimen holder was attached to the shear machine first. The upper platen was raised to its full height under displacement control and low hydraulic pressure. The upper half of the sample was then inserted, supported by a padded block, and the upper platen was lowered and secured with 13 cap screws. The lower half of the joint specimen was then inserted and bolted into the lower platen with the same number of cap screws. The two specimen holders were brought into contact and the normal actuator was shifted into load control. A small normal load of 0.9 kN was applied to keep the two specimen halves in contact and to remove any mechanical slack. The data acquisition program, which displayed the channel voltage output, was started. Each LVDT was positioned and adjusted so that its voltage output was in the appropriate range to prevent going off scale. Hydraulic pressure was turned to high pressure and the appropriate normal load was applied. The function generator and the test control computer were started.

Two series of direct shear tests were carried out on the joint replicas. An example of experiment schedule for the F4 samples is summarized in Table 1. The first series was conducted at different constant normal load levels ranging between 2.7 and 113.9 kN (equivalent to nominal normal stresses ranging between 0.3 and 5.5 MPa). The second series of direct shear tests was conducted at different levels of initial normal load ranging between 16.0 and 32.0 kN and constant normal stiffness ranging between 25.9 and 328.4 kN/cm. Each direct shear test

consisted of five continuous loading cycles with a sinusoidal pattern, a frequency of 2.8×10^{-4} Hz and an amplitude of 4.1 cm for test series G2, and a frequency of 3.7×10^{-4} Hz and an amplitude of 3.1 cm for test series F2, F3, and F4. The nominal shear displacement rate was 1.3 mm/min.

2.3 Normal Compression Tests

Before and after shear, joint surfaces were subjected to five cycles of normal loading and unloading to characterize their normal stress vs. normal displacement response. The tests were conducted using the normal load actuator of the direct shear machine. The maximum normal stress applied during the first cycle was 0.7 MPa. This was followed by four cycles with maximum normal stresses of 1.4, 2.8, 5.5, and 6.9 MPa. The loading rate was 0.7 MPa/min. Normal load and normal displacement were measured using the normal load actuator's load cell and the three external vertical HRDC LVDTs, respectively. For each normal compression test, three steps were followed:

- identification of each joint specimen,
- application of a small initial normal load,
- normal loading and unloading with five cycles.

Before the shear experiments were conducted, a normal compression test was performed on one replica of each joint in order to determine its initial normal deformability. After shear, normal compression tests were conducted on all replicas.

2.4 Profilometer Measurements

Surface roughness affects all aspects of mechanical properties of rock joints. Depending on the boundary conditions across the joint surfaces, shear through the joint surface asperities or overriding of the asperities can take place. Joint surface roughness also affects joint dilatancy. If the dilatancy is completely or partially suppressed due to the controlled boundary conditions, then normal stresses further increase during shear and the joint has a higher shear strength than if the joint is free to dilate. Measurement of joint surface roughness prior to and after shearing can be useful in assessing joint surface damage and its relation to joint shear strength.

Joint surface roughness profiling was carried out using a mechanical profilometer. A detailed description of the equipment can be found in Farrington [14] and Gamal-Eldin [15]. Basically, the apparatus consists of a table on which two systems of steel rods are installed. An LVDT attached to one set of rods can travel in a horizontal X-Y plane covering the joint surface. The cone apex angle of the profilometer tip is 18°, and the tip radius is about 0.05 mm. The joint sample is placed on a levelling plate below the table. At each selected X,Y point, the height of a point on the sample is measured relative to a reference height with the LVDT.

Before and after the shear tests, the bottom and top joint surfaces were profiled along four lines 2.5 cm apart for the G2 specimens and along four lines 2.0 cm apart for the F2, F3, and F4 specimens. The horizontal distance between two consecutive sampling points was 0.25 mm. All X,Y,Z data were recorded by the same data acquisition system used for the direct shear tests. Four steps were followed in each profilometer test:

- identification of each joint specimen,
- placement of joint specimen on levelling plate under profilometer table,
- alignment of X and Y axes on joint surface,
- measurement of surface roughness.

The profiles are called X1, X2, X3, and X4, with X1 and X4 being the closest to the side edges of the test specimens. Before the shear tests, one profilometer test was carried out on both surfaces of one replica of each joint. After shear, profilometer tests were performed on all replica surfaces.

3. TEST RESULTS

3.1 Direct Shear Test Results

All direct shear test results are presented in the form of shear load vs. shear displacement response curves, and normal displacement (dilatancy) vs. shear displacement curves. From these curves, the following data were collected:

- peak and residual shear loads for forward and reverse shear in each cycle,
- initial shear stiffness for the forward part of the first cycle calculated with data between 25% and 75% of the peak shear load,
- slope of the dilatancy curve (*tan i*) for forward and reverse shear in each cycle measured between 0.25 and 1.0 cm of shear displacement.

Figs. 4 through 7 and Tables 2 through 5 show typical response curves and test data for some of the F4 specimens. Figs. 4a and 4b show the shear load vs. shear displacement and dilatancy vs. shear displacement curves, respectively, for specimen R2F4 tested under a constant normal load of 16.0 kN. The peak and residual shear loads in both forward and reverse shear directions decrease as the number of shear cycles increases, but approach a steady state level (Fig. 4a). Joint dilatancy decreases gradually in both shear directions as the number of cycles increases (Fig. 4b), also approaching steady state behavior. Figs. 5a and 5b show examples of response curves for specimen KR10F4 tested under a constant normal stiffness of 315.1 kN/cm with an initial normal load of 16.0 kN. Fig. 5a shows that under constant normal stiffness, there is no specific peak and residual shear loads as displayed in Fig. 4a. Instead, a hardening form of behavior can be observed.

The first cycle, forward shear load - shear displacement response curves for all F4 test specimens are summarized in Fig. 6a. The corresponding dilatancy curves are shown in Fig. 6b. Specimen R2F4 was tested under a constant normal load of 16.0 kN (or zero normal stiffness). Specimens KR7F4, KR9F4, and KR10F4 tested under constant normal stiffnesses of 31.5, 94.6, and 315.1 kN/cm respectively, with the same initial normal load as R2F4, carry larger shear loads than R2F4 and experience less dilatancy.

Figs. 7a and 7b show the paths followed by the F4 specimens tested under constant normal stiffness in a shear load vs. normal load space for the forward and reverse parts of the first shear load cycle only. In this figure, the peak and residual shear failure envelopes determined from

the constant normal load shear tests are also shown for comparison.

Table 2 gives the values of the peak and residual shear loads and the shear stiffness for the F4 samples tested under constant normal load, for forward shear only. Table 3 shows the data for the samples tested under constant normal stiffness. For those samples tested under constant normal stiffness and showing hardening, the peak and residual shear loads are replaced by the shear loads at 1.0 cm of shear displacement. Tables 4 and 5 give the slopes (*tan i*) of the corresponding dilatancy curves for forward and reverse shear.

A complete listing of direct shear test results can be found in a report by Wibowo *et al.* [16], which includes:

- shear load vs. shear displacement response curves and normal displacement (dilatancy) vs. shear displacement response curves for all test specimens,
- combination of response curves for the forward and reverse parts of each shear cycle,
- values of peak and residual shear loads for the forward and reverse parts of each cycle and the values of the shear stiffness for the forward part of the first shear cycle,
- values of the slope of the dilatancy curves for the forward and reverse parts of each shear cycle, and the path followed by the test specimens tested under constant normal stiffness in the shear load vs. normal load space for the forward and reverse parts of each shear cycle.

3.2 Normal Compression Test Results

The normal compression test results are presented in the form of normal load vs. normal displacement response curves. The actual joint closure is determined from these response curves after subtracting the deformation of the intact gypsum cement and the system from the total measured normal displacement (as shown in Fig. 8). The intact gypsum cement behavior was obtained from a gypsum cement block sample with the same size as the joint replica and also the same height of potting cement. Using the model of Bandis *et al.* [17], the initial joint normal stiffness k_{ni} and maximum closure V_m were determined from the envelope to the five loading/unloading cycles of the joint closure curves. In this model, the normal stress σ and joint closure v are related as follows

$$\sigma = \frac{v\, k_{ni}\, V_m}{V_m - v} \tag{1}$$

Both k_{ni} and V_m can be determined by regression analysis of $1/\sigma$ versus $1/v$. As an example, Table 6 gives the values of the initial stiffness and maximum joint closure for all F3 samples. Values of those two parameters for all samples can be found in [16].

3.3 Profilometer Measurement Results

As an example, a set of two profiles is presented in Fig. 9. One of the profiles was taken on the

bottom half of sample R1F4 before shear (profile R1F4X3) and the other on the bottom half of sample R3F4 after shear under a constant normal load of 32.0 kN (profile R3F4X3). The profiles before and after shear show minor differences in micro-roughness. The macro-roughness (large undulations) remains essentially the same.

4. DATA ANALYSIS

4.1 Definitions and Assumptions

In the previous section, the results of the cyclic direct shear experiments and the normal compression tests were presented in terms of normal or shear loads and displacements. On the other hand, most constitutive models of rock joints available in the literature use normal or shear stresses and displacements. The normal and shear stresses mentioned in this paper are all nominal stresses and are calculated using the normal and shear loads divided by the initial cross-sectional areas of the joints. The error in neglecting the change in joint area during shear was investigated. An example is shown in Fig. 10 for sample R1F4, where two shear stress vs. shear displacement response curves have been plotted for the same shear test under a constant normal load of 3.2 kN. One curve assumes a constant area during shear whereas the other has been obtained after area correction. The difference in shear stress at 1.5 cm of shear displacement is 27.6 kN/m^2 or about 10% of the value of shear stress for constant area.

For data analysis, the shear stress vs. shear displacement response curves under constant normal load are idealized, as shown in Fig. 11(a), and consist of three regions: prepeak, peak and postpeak. The slope of the prepeak region for data ranging between 25% and 75% of the peak shear load is defined as the *joint shear stiffness* k_s. It is only defined for the forward part of the first shear cycle. The shear stresses and displacements for the peak and residual conditions are defined as (τ_p, u_p) and (τ_r, u_r), respectively. In this data analysis, the residual shear displacement is assumed to be independent of the normal load and equal to the maximum forward or reverse shear displacement of 1.3 cm for samples F2, F3, and F4, and 1.5 cm for sample G2. Thus, the shear stresses observed at 1.3 cm or 1.5 cm of shear displacement are assumed to represent the residual shear strengths.

From the normal displacement, v, vs. shear displacement, u, response curves measured during the constant normal load direct shear tests, three angles of dilatancy are defined as shown in Fig. 11(b): (1) an *average dilation angle*, i_{av}, between 0.25 and 1.0 cm of shear displacement, (2) *a peak secant dilation angle*, i_s, at the peak shear stress, and (3) *a peak tangent dilation angle*, i_p, at the peak shear stress.

4.2 Variation of Peak Shear Displacement and Shear Stiffness with Normal Stress

Goodman [2] recommended two models shown in Fig. 12 to represent the variation of joint shear stress with shear displacement under constant normal stress. One model [Fig. 12(a)] assumes that the joint shear stiffness, k_s, is independent of the normal stress (constant stiffness model), whereas the second model [Fig. 12(b)] assumes that the peak and residual shear displacements u_p and u_r are constant (constant displacement model). Both models show an increase in peak and residual shear strengths with normal stress. Based on the shape of the shear load vs. shear

displacement response curves presented in the previous section and in the data report by Wibowo *et al.* [16], it is shown below that neither constant stiffness model nor constant displacement model, by itself, fits the observed behavior.

Peak Shear Displacement

The peak shear displacement measured in the experiments was found to increase with the normal load or stress. A linear relation was used to describe the variation of the peak displacement, u_p, with the applied normal stress, σ_n, as follows:

$$u_p = a + b\sigma_n \tag{2}$$

As an example, Fig. 13(a) and 13(b) show the variation of the peak displacement with the normal stress for samples F3 and for the forward and reverse parts of the first shear cycle. Similar variations for samples F4, F2, and G2 can be found in [18]. Coefficients a and b in equation (2) were determined by linear regression analysis. Their values are listed in Table 7. This table indicates that in general, peak shear displacement increases with the normal stress.

It is noteworthy that equation (2) was used to describe the variation of the peak displacement with the normal stress for the first shear cycle only. For the other four cycles, the peak displacement was sometimes poorly defined and it was difficult to separate the peak and residual displacements because of accumulated joint surface damage. This resulted in more scatter in the plots of peak shear displacement vs. normal stress. An example of such a plot is shown in Fig. 14 for forward shear of samples F4.

In general, the peak shear displacements were found to be small. The ratio u_p/L between the peak displacement, u_p, and the length of each test sample, L, was found to vary between 0.001 and 0.047 (Table 8). This indicates that the peak shear stress is mobilized after a small amount of shear displacement.

Shear Stiffness

A linear relation was used to describe the variation of the shear stiffness, k_s, with the applied normal stress, σ_n, as follows

$$k_s = c + d\sigma_n \tag{3}$$

Fig. 15 shows an example of variation of the shear stiffness with the normal stress for samples F4. Similar variations for samples F3, F2, and G2 can be found in [18]. Coefficients c and d in equation (3) were determined by linear regression analysis. Their values are listed in Table 9. This table indicates that, in general, the shear stiffness increases with the normal stress.

4.3 Variation of the Ratio of Residual to Peak Shear Strengths with Normal Stress

Goodman [2] proposed an equation describing the variation of the ratio between the residual shear strength, τ_r, and the peak shear strength, τ_p, of a rock joint with the normal stress σ_n, e.g.

$$\frac{\tau_r}{\tau_p} = B_o + (1 - B_o)\frac{\sigma_n}{\sigma_T} \tag{4}$$

when $\sigma_n < \sigma_T$ and

$$\tau_r = \tau_p \tag{5}$$

when $\sigma_n \geq \sigma_T$. In equation (4), B_o ($0 \leq B_o \leq 1$) is the ratio of residual to peak shear strengths at zero normal stress and σ_T (N_T divided by the initial joint area) is a transitional stress beyond which the peak shear strength is always equal to the residual shear strength.

The peak and residual shear loads obtained from the constant normal load direct shear tests on samples F4, F3, F2, and G2 were used to determine the values of B_o and σ_T for the forward and reverse parts of each shear cycle. Linear regression analyses were carried out between the ratios of residual to peak shear loads (also equal to τ_r/τ_p) and the applied constant normal loads.

As an example, Fig. 16(a) and 16(b) show the variation of τ_r/τ_p with the normal stress σ_n for samples F4 for the forward and reverse parts of the five shear cycles, respectively. The corresponding values of B_o and σ_T for each one of the five shear cycles are given in Tables 10a and 10b. Using a similar analysis, the values B_o and σ_T for samples F3, F2, and G2 can be found in [18].

Figs. 16(a) and 16(b) and the plots presented in [18] indicate that the linear model of Goodman defined in equation (4) gives a fair representation of the observed increase in τ_r/τ_p with the normal stress σ_n. Tables 10a and 10b indicate that for a given joint sample, B_o and σ_T are not constant, but vary from one shear cycle to another and have different values for forward and reverse motions. It appears that B_o approaches unity as the number of cycles increases, that is, the peak shear strength approaches its residual value as more damage occurs along the joint surfaces during shear. For a given joint sample, the smallest values of B_o are always obtained for the first shear cycle for which the difference between peak and residual shear loads is the largest.

Goodman [2] suggested that the uniaxial compressive strength of the intact material q_u in the joint walls can be used as an estimate of σ_T. Here q_u for the gypsum cement is equal to 27.6 MN/m^2. The test results in Tables 10a & 10b and in [18] indicate that the value of σ_T/q_u is not equal to one but varies between 0.22 and 0.47 for samples F4, 0.23 and 0.34 for samples F3, 0.24 and 0.61 for samples F2, and 0.22 and 1.12 for samples G2. The value of σ_T/q_u varies and depends on the joint profile and the number of cycles.

4.4 Variation of Dilatancy with Normal Stress

The models of Ladanyi and Archambault [19], Barton and Choubey [20], Schneider [21] and Jing [22] were used to analyze the variation of joint dilatancy with normal load (stress). In these models, different dilation angles were used. Referring to Fig. 11(b), Barton and Choubey [20] used the peak secant dilation angle, i_s, (also called initial dilation angle), and the peak tangent dilation angle, i_p. Based on their experimental results, Barton and Choubey found that the peak secant dilation angle is about one-third of the peak tangent dilation angle. Ladanyi and Archambault [19], Schneider [21], and Jing [22] considered the peak tangent dilation angle only.

Based on the present experimental results, the three dilatancy rates $tan(i_s)$, $tan(i_p)$, and $tan(i_{av})$ were determined for samples F2, F3, F4, and G2. Their values can be found in [18]. As an example, Table 11 gives the values of the three rates of dilatancy for the forward and reverse parts of the first shear cycle for samples F4. Under relatively small normal stresses of 0.3 and 1.4 MPa, the three dilatancy rates differ with larger values for the peak tangent dilatancy rate. Under larger normal stresses ranging between 2.8 and 5.5 MPa, the three dilatancy rates are about the same.

Fig. 17 shows the variation of $tan(i_{av})$ with the applied constant normal stress for the forward and reverse parts of each one of the five shear cycles for samples F4. Due to the anisotropic behavior of the joint surfaces, joint dilatancy is not the same in the forward and reverse directions, and varies from one cycle to another. It also decreases as the applied normal stress increases. Plots similar to those presented in Fig. 17 for samples F3, F2, and G2 can be found in [18]. The models of Ladanyi and Archambault [19], Barton and Choubey [20], Schneider [21], and Jing [22] were used to fit the observed variation of the peak tangent dilatancy rate, $tan(i_p)$, with the normal stress σ_n.

Model of Ladanyi and Archambault

Ladanyi and Archambault [19] proposed the following expression between the peak tangent dilatancy rate and the applied normal stress σ_n

$$\tan(i_p) = (1-\frac{\sigma_n}{\sigma_T})^{k_2}\tan(i_{po}) \qquad (6)$$

where k_2 is an empirical coefficient, σ_T is a transitional stress beyond which no further dilatancy takes place and $tan(i_{po})$ is the peak rate of dilatancy at zero normal stress. Using the values of σ_T defined in Tables 10a and 10b and in [18], the values of k_2 and $tan(i_{po})$ were determined by linear regression analysis between $log(tan(i_p))$ and $log(1- \sigma_n/\sigma_T)$. As an example, Table 12 gives the values of k_2 and $tan(i_{po})$ for the forward and reverse parts of each shear cycle for joint samples F4. In general, $tan(i_{po})$ decreases as the number of cycles increases, with most or all of the decrease following the first cycle. The value of k_2 decreases as the number of cycles increases. Tables similar to Table 12 for samples F3, F2, and G2 can be found in [18]. In general, it was found that the values of k_2 range between 0.25 and 3.55 and are less than the

value of 4 initially suggested by Ladanyi and Archambault [19]. The value of k_2 was found to be influenced by the joint surface roughness.

Model of Barton and Choubey

Barton and Choubey [20] proposed the following expression between the peak tangent dilatancy rate and the applied normal stress σ_n

$$\tan(i_p) = \tan(JRC \log_{10}\frac{JCS}{\sigma_n}) \tag{7}$$

where JRC is the *Joint Roughness Coefficient* and JCS is the *Joint Wall Compressive Strength* (equal to q_u for unweathered rock surface i.e., 27.6 MPa for gypsum cement). According to Barton and Choubey [20], equation (7) is valid as long as σ_n < JCS.

Knowing the values of JCS, the applied normal stress and the peak tangent dilatancy rate, JRC was back-calculated directly from equation (7) for each joint sample and for the forward and reverse parts of each shear cycle. For clarity, JRC determined from the peak dilatancy rates is defined here as JRC_{ptd}.

The values of JRC_{ptd} for the first shear cycle are plotted as a function of normal stress in Fig. 18(a) and 18(b) for forward shear motion and reverse shear motion, respectively. These two figures show that JRC_{ptd} is not constant for a given joint sample, but is relatively independent of normal stress (except for sample G2 at a normal stress of 5.5 MPa in Fig. 18(a) and sample F2 in Fig. 18b). The average values of JRC_{ptd} for the forward and reverse parts of the five shear cycles are given in Table 13 for joint samples F4. Similar tables for joint samples F2, F3, and G2 can be found in [18]. In general, the test results indicate that the average value of JRC_{ptd} back-calculated from the dilatancy curves decreases significantly between the first and second cycles and remains essentially constant for the other three cycles, indicating a major degradation in the joint surface asperities during the first shear cycle.

Using the initial and final joint surface roughness profiles X2 and X3, the values of JRC at the beginning of the first shear cycle and at the end of the fifth shear cycle were determined for all joint samples using the methods of Tse and Cruden [23] and modified by Yu and Vayssade [24]. These authors proposed an empirical regression equation between the joint roughness coefficient, defined here as JRC_{pr}, and the root-mean-square (RMS) of the first derivative of the profile, Z_2. Yu and Vayssade [24] recommended the following equation

$$JRC_{pro} = 60.32\ Z_2 - 4.51 \tag{8}$$

for profiles with a sampling interval of 0.25 mm. The value of Z_2 is defined as follows

$$Z_2 = \sqrt{\frac{1}{M(Dx)^2}\sum (y_{i+1}-y_i)^2} \tag{9}$$

where M is the number of sampling intervals, Dx is the interval size, and y_i is the asperity height along the profile. The value of JRC_{pr} is then corrected for scale effect as suggested by Barton and Bandis [25] using the following equation

$$JRC_{pr} = JRC_{pro}\left(\frac{L_n}{L_o}\right)^{-0.02JRC_{pro}} \tag{10}$$

where JRC_{pro} is the value of JRC before correction corresponding to a joint sample length L_o of 10 cm, and JRC_{pr} is the value of JRC after correction for the actual length L_n of the joint profiles. The average values of JRC_{pr} calculated using that method are presented in Table 13 and other tables in [18]. The test results seem to reveal that the average values of JRC_{pr} determined from the initial profiles at the beginning of the direct shear tests are similar to those back-calculated from the dilatancy curves. However, the average values of JRC_{pr} determined from the final profiles at the end of the shear tests are much smaller.

Model of Schneider

Schneider [21] proposed the following relationship between the peak tangent dilation angle and the normal stress σ_n

$$i_p = i_{po} e^{-k\sigma_n} \tag{11}$$

where k is an empirical coefficient and i_{po} is the peak tangent dilation angle at zero normal stress. The values of k and i_{po} were determined by linear regression analysis between $log(i_p)$ and $log(\sigma_n)$. They are given in Table 14 for the forward and reverse parts of each shear cycle for samples F4. Similar tables for samples F2, F3, and G2 can be found in [18]. Schneider [21] found that the value of coefficient k depends on the joint surface roughness and material type. In Schneider's experiments on limestone, sandstone and granite the coefficient k was found to range between 0.29 and 1.89 MPa^{-1}. In our experiments, with a much weaker material (gypsum), coefficient k was found to vary between 7.25 and 15.95 MPa^{-1} for all samples (first shear cycle forward motion).

Model of Jing

Jing [22] proposed another relationship between the peak tangent dilation angle and the normal

stress σ_n as follows

$$i_p = i_{po}(1-\frac{\sigma_n}{q_u})^k \tag{12}$$

where k is another empirical coefficient, i_{po} is the peak tangent dilation angle at zero normal stress and q_u is the uniaxial compressive strength of the intact material in the joint walls. Using the values of σ_T defined in Tables 10a and 10b and in [18] instead of q_u, the values of k and i_{po} were determined by linear regression analysis between $log(i_p)$ and $log(\sigma_n)$. They are given in Table 15 for the forward and reverse parts of each shear cycle for samples F4. Similar tables for samples F2, F3, and G2 can be found in [18]. Jing *et al.* [26] suggested values of k ranging between 0.2 and 5. In our experiments, the coefficient k was found to vary between 0.65 and 3.52 for all samples (first shear cycle forward motion).

Summary

An overall comparison between the peak dilatancy rates measured on all joint samples and those predicted using the models of Ladanyi and Archambault, Barton and Choubey, Schneider, and Jing can be found in [18]. An example of such comparison is shown in Figs. 19(a) and 19(b) for samples F4 and for the forward and reverse parts of the first shear cycle, respectively. In general, good agreement is found between predictions and observations. In particular, the dilatancy model of Schneider was found to fit the experimental results the best. The second best fit was obtained with Barton and Choubey's model using the average values of JRC_{ptd} reported in Table 13.

Proposed Model

The variation of the average dilatancy rate $tan(i_{av})$ with the normal stress was analyzed using the following equation,

$$\tan(i_{av}) = (1-\frac{\sigma_n}{\sigma_T})^{k_3}\tan(i_{avo}) \tag{13}$$

which is similar to equation (6). In equation (13), k_3 is an empirical coefficient, σ_T is a transitional stress beyond which no further dilatancy takes place and $tan(i_{avo})$ is the average rate of dilatancy at zero normal stress. Using the values of σ_T defined in Tables 10a and 10b and in [18], the values of k_3 and $tan(i_{avo})$ were determined by linear regression analysis between $log(tan(i_{av}))$ and $log(1- \sigma_n/\sigma_T)$. Table 16 gives the values of k_3 and $tan(i_{avo})$ for the forward and reverse parts of each shear cycle for samples F4. Comparison between model and actual test results for samples F4 are shown in Figs. 20(a) and 20(b), for forward and reverse shear motion respectively. Similar comparison for the other samples can be found in [18].

4.5 Peak Shear Strength Envelope

The joint failure criteria of Saeb [27] and Barton [28] were used to determine the variation of the peak shear strength τ_p with the normal stress σ_n for the direct shear tests conducted under constant normal load.

Modified Ladanyi and Archambault Criterion

Saeb [27] modified the failure criterion of Ladanyi and Archambault [19] which is now expressed as follows

$$\tau_p = \sigma_n \tan(\phi_u + i)(1 - a_s) + a_s s_r \tag{14}$$

where a_s is the proportion of total joint area sheared through the asperities and $(1-a_s)$ is the proportion on which sliding takes place. In equation (14), ϕ_u is the angle of friction for sliding along the asperities. The angle, i, is the peak tangent dilation angle, i_p, of Fig. 11b. and s_r represents the shear strength of the intact rock in the asperities. As suggested by Ladanyi and Archambault [19], s_r can be approximated by the Mohr-Coulomb criterion:

$$s_r = s_o + \sigma_n \tan\phi_o \tag{15}$$

or Fairhurst's parabolic criterion (Fairhurst[29]):

$$s_r = q_u \frac{\sqrt{(1+n)} - 1}{n} (1 + n\frac{\sigma_n}{q_u}) \tag{16}$$

In equation (15), s_o and ϕ_o are the intact rock cohesion and internal friction angle, respectively. In equation (16), q_u is the intact rock compressive strength and n is the ratio between the rock compressive and tensile strengths.

According to Ladanyi and Archambault [19], a_s and $tan(i)$ are normal stress dependent such that

$$a_s = 1 - (1 - \frac{\sigma_n}{\sigma_T})^{k_1} \tag{17}$$

and

$$\tan(i) = (1-\frac{\sigma_n}{\sigma_T})^{k_2}\tan(i_{po}) \tag{18}$$

In addition to unconfined compression experiments, triaxial tests were conducted on two cylindrical samples of gypsum cement at confining stresses of 3.4 and 6.9 MPa. Using the Mohr-Coulomb criterion, it was found that s_o=7.7 MPa and ϕ_o=31.5°. Fairhurst failure envelope was obtained with q_u=27.6 MPa and n=10. The value of ϕ_u was determined from four shear tests conducted on smooth gypsum cement surfaces under normal stresses ranging between 0.3 and 5.5 MPa. It was found to be approximately 30°. The values of k_2 and $tan(i_{po})$ in equation (17) were taken directly from Table 12.

Since it was not possible to determine the proportion of total joint area, a_s, sheared at the end of the forward and reverse parts of each shear cycle (except at the end of the fifth shear cycles), coefficient k_1 in equation (17) was varied until equation (14) would fit the experimental results. As an example, Fig. 21 shows that for samples F4, k_1=0.25 gives the best fit for the forward part of the first shear cycle. The values of k_1 for the five shear cycles for sample F4 are summarized in Table 17. Similar tables for samples F2, F3, and G2 can be found in [18].

The test results on all samples indicate that for the forward part of the first shear cycle, k_1 varies between 0.05 and 0.3 which is much smaller than the value of 1.5 initially suggested by Ladanyi and Archambault [19]. For the other four cycles, k_1 is equal to 0 except for the reverse part of the second and third shear cycles of samples F4. According to equation (17), if k_1=0 then a_s=0, and the second term in equation (14) vanishes. This means that, in most cases, starting on the second shear cycle, sliding (and not shearing) is dominant along the joint surfaces.

Barton Failure Criterion

Barton [28] proposed the following joint failure criterion

$$\tau_p = \sigma_n\tan(\phi_u + JRC\log_{10}\frac{JCS}{\sigma_n}) \tag{19}$$

where JRC is the *Joint Roughness Coefficient* and JCS is the *Joint Wall Compressive Strength* (for an unweathered joint this is equal to 27.6 MPa for gypsum cement). In equation (19), ϕ_u is the basic friction angle which is equal to 30° for all cases.

The peak shear strength envelope was predicted for the forward and reverse parts of each shear cycle and for each joint sample using the average JRC_{ptd} values determined from the dilatancy curves presented in Table 13 and other tables in [18]. The peak shear strength was also predicted for the forward part of the first shear cycle only using the average values of JRC_{pr} determined from the initial joint surface profiles. Figs. 22(a) and 22(b) show two examples of comparison between predicted and measured shear strengths for forward and reverse motions for the first

shear cycle of shear on samples F4 and F3, respectively. Comparison between predicted and observed peak shear strengths for the other shear cycles and for joint samples F2 and G2 can be found in [18]. For samples F4, the predicted shear strengths are less than the measured ones. However, for samples F3, measured and predicted shear strengths are similar for forward motion, but slightly different for reverse motion.

Because of some of the discrepancies between the measured and predicted shear strengths, JRC in equation (19) was also back-calculated from the measured peak shear strengths. Its values are presented as JRC_{ps} in Table 18 for the forward part of the first shear cycle for samples F4 and in other tables in [18] for the other shear cycles and joint samples.

At the beginning of the first shear cycle for each test, JRC was also determined from tilt tests following the methodology recommended by Barton and Choubey [20]. The measured values are presented as JRC_t in Table 18.

The JRC values reported in Tables 13, and 18, and other tables in [18] indicate that when using the model of Barton and Choubey [20], significantly different values of the *Joint Roughness Coefficient* JRC can be obtained for a same rock joint with different methods.

5. A MATHEMATICAL MODEL FOR JOINT BEHAVIOR

Based on the test results presented in the report by Wibowo *et al.*[16] and the data analysis presented above, a non-linear joint mathematical model was developed to predict joint behavior under various boundary conditions. The model is an extension of that proposed by Saeb [11] and Amadei and Saeb [12] and incorporates the different constitutive models presented in this paper.

5.1 Assumptions

Joint Normal Behavior

The hyperbolic model of Bandis *et al.* [17] shown as curve 1 in Fig. 23 is used to describe joint behavior under increasing normal load (stress). The normal stress σ_n and joint normal displacement, v, are related as follows

$$\sigma_n = \frac{v k_{ni} V_m}{V_m + v} \tag{20}$$

or

$$v = \frac{\sigma_n V_m}{k_{ni} V_m - \sigma_n} \tag{21}$$

In equations (20) and (21), compressive stresses and joint opening are assumed to be positive, V_m is the maximum joint closure and k_{ni} is the initial normal stiffness of the joint which is

negative for the sign convention adopted here. At any other normal stress level, the joint tangent normal stiffness is equal to

$$k_{nn} = \frac{\partial \sigma_n}{\partial v} = k_{ni}\left(\frac{k_{ni}V_m - \sigma_n}{k_{ni}V_m}\right)^2 \tag{22}$$

Also, the joint is assumed to have zero tensile strength.

Joint Shear and Dilatant Behavior

For the geometry of Figs. 11(a), the shear stress and shear displacement are related as follows

$$\tau = \frac{u}{\frac{u_p}{\tau_p} + B(u - u_p)} \quad \textit{for } u < u_p \tag{23}$$

$$\tau = \left(\frac{\tau_p - \tau_r}{u_p - u_r}\right)u + \left(\frac{\tau_r u_p - \tau_p u_r}{u_p - u_r}\right) \quad \textit{for} \quad u_p \le u \le u_r \tag{24}$$

$$\tau = \tau_r \quad \textit{for} \quad u > u_r \tag{25}$$

The variation of u_p with the normal stress is defined by equation (2). The residual displacement is assumed to be independent of the normal stress. The variation of peak shear strength, τ_p, with the normal stress is defined by the modified Ladanyi and Archambault's failure criterion [equation (14)] or Barton's failure criterion [equation (19)]. The variation of the ratio between the residual and peak shear strengths with the normal stress is defined by equations (4) and (5). The coefficient B in equation (23) is the positive root of the following second-degree polynomial

$$\frac{3}{16}B^2\tau_p^{\,2} - B(\tau_p - u_p k_s) + \left(1 - \frac{u_p}{\tau_p}k_s\right) = 0 \tag{26}$$

The variation of k_s with the normal stress is defined by equation (3). Note that B in equation (26) depends on the normal stress.

Using an approach similar to that of Goodman and St.John [30], the dilatancy rate $tan(i) = \partial v/\partial u$ is assumed to be independent of the shear displacement for $0 \le u \le u_r$ and to vanish for $u >$

u_r. It depends on the normal stress only according to equations (6), (7), or (13).

5.2 Formulation

Consider a rock joint undergoing first normal compression followed by shear. Combining equations (6) or (7) and equation (21), the total normal displacement of the joint is then equal to

$$v = u(1-\frac{\sigma_n}{\sigma_T})^{k_2}\tan(i_{po}) + \frac{\sigma_n V_m}{k_{ni}V_m-\sigma_n} \tag{27}$$

or

$$v = u\tan(JRC\log_{10}\frac{JCS}{\sigma_n}) + \frac{\sigma_n V_m}{k_{ni}V_m-\sigma_n} \tag{28}$$

If equation (13) is used instead of (6), then k_2 and $tan(i_{po})$ in equation (27) must be replaced by k_3 and $tan(i_{avo})$, respectively.

Equations (27) and (28) are valid as long as $u \leq u_r$. When $u > u_r$ and $\sigma_n < \sigma_T$ or $\sigma_n <$ JCS, the joint ceases to dilate and v is equal to its value obtained by substituting $u=u_r$ in equations (27) or (28). When $\sigma_n \geq \sigma_T$ or $\sigma_n \geq$ JCS, the first term in equation (27) or (28) vanishes and no dilation is possible during shearing.

If the first term on the right-hand side of equations (27) and (28) is called, w, then after rearrangement, those equations take the more general form

$$\sigma_n = \frac{(v-w)k_{ni}V_m}{V_m+(v-w)} \tag{29}$$

Comparing equations (29) and (20), it appears that v-w has now been substituted for v. In other words, equation (29) models the normal stress-displacement behavior of the joint after having been sheared by an amount equal to u. Equation (29) has been plotted as curve 2 in Fig. 23 for a value of u less than or equal to u_r. Curves 1 and 2 are a distance w apart as long as $\sigma_n < \sigma_T$ or $\sigma_n <$ JCS and coincide when $\sigma_n \geq \sigma_T$ or $\sigma_n \geq$ JCS. Fig. 23 shows that as more shear develops, the joint becomes more deformable in the normal direction.

An incremental formulation can be obtained by differentiating equations (27) and (28) which, after rearrangement, can be written in a more compact form as follows

$$d\sigma_n = k_{nn}dv + k_{nt}du \tag{30}$$

where $k_{nn}=\partial\sigma_n/\partial v$ and $k_{nt}=\partial\sigma_n/\partial u$ are two normal stiffness coefficients equal to

$$k_{nn} = \frac{1}{-\frac{uk_2}{\sigma_T}(1-\frac{\sigma_n}{\sigma_T})^{k_2-1}\tan(i_{po}) + \frac{V_m{}^2k_{ni}}{(k_{ni}V_m-\sigma_n)^2}} \tag{31}$$

and

$$k_{nt} = \frac{-(1-\frac{\sigma_n}{\sigma_T})^{k_2}\tan(i_{po})}{-\frac{uk_2}{\sigma_T}(1-\frac{\sigma_n}{\sigma_T})^{k_2-1}\tan(i_{po}) + \frac{V_m{}^2k_{ni}}{(k_{ni}V_m-\sigma_n)^2}} \tag{32}$$

when using the modified Ladanyi and Archambault's criterion. If Barton's criterion is used instead, equations (31) and (32) are replaced by

$$k_{nn} = \frac{1}{-\frac{u}{\sigma_n}\frac{JRC}{\ln(10)}[1+\tan^2(JRC\log_{10}\frac{JCS}{\sigma_n})] + \frac{V_m{}^2.k_{ni}}{(k_{ni}V_m-\sigma_n)^2}} \tag{33}$$

and

$$k_{nt} = \frac{-\tan(JRC\log_{10}\frac{JCS}{\sigma_n})}{-\frac{u}{\sigma_n}\frac{JRC}{\ln(10)}[1+\tan^2(JRC\log_{10}\frac{JCS}{\sigma_n})] + \frac{V_m{}^2k_{ni}}{(k_{ni}V_m-\sigma_n)^2}} \tag{34}$$

Note that equations (31) and (33) provide an analytical expression for the joint tangent normal stiffness (slope of curve 2 in Fig. 23) when the joint has been sheared by an amount equal to u. Both equations reduce to equation (22) when $u=0$. Also equations (31)-(34) are valid as long as $u \leq u_r$ and $\sigma_n < \sigma_T$ or $\sigma_n <$ JCS. When $u > u_r$ or $\sigma_n \geq \sigma_T$ or $\sigma_n \geq$ JCS, k_{nt} vanishes.

Because the shear stress τ depends on u and v, increments of shear stress are related to increments of normal and shear displacements, as follows

$$d\tau = k_{tn}dv + k_{tt}du \tag{35}$$

where $k_{tn}=\partial\tau/\partial v$ and $k_{tt}=\partial\tau/\partial u$ are two shear stiffness coefficients that are equal to

(i) <u>for $u < u_p$</u>

$$k_{tn} = -\frac{u}{Den}[k_{nn}\frac{d}{d\sigma_n}(\frac{u_p}{\tau_p})+k_{nn}(u-u_p)\frac{dB}{d\sigma_n}] \tag{36}$$

$$k_{tt} = \frac{1}{Den}[\frac{u_p}{\tau_p}-Bu_p-uk_{nt}\frac{d}{d\sigma_n}(\frac{u_p}{\tau_p})-uk_{nt}(u-u_p)\frac{dB}{d\sigma_n}] \tag{37}$$

with $Den=((u_p/\tau_p)+B(u-u_p))^2$.

(ii) <u>for $u_p \leq u \leq u_r$</u>

$$k_{tt} = k_{ss}+k_{nt}[(u-u_p)\frac{dk_{ss}}{d\sigma_n}+\frac{d\tau_p}{d\sigma_n}-k_{ss}\frac{du_p}{d\sigma_n}] \tag{38}$$

$$k_{tn} = k_{nn}[(u-u_p)\frac{dk_{ss}}{d\sigma_n}+\frac{d\tau_p}{d\sigma_n}-k_{ss}\frac{du_p}{d\sigma_n}] \tag{39}$$

with $k_{ss}=(\tau_p-\tau_r)/(u_p-u_r)$.

(iii) <u>for $u > u_r$</u>

$$k_{tt} = k_{nt}[(1-B_o)\frac{\tau_p}{\sigma_T}+(B_o+(1-B_o)\frac{\sigma_n}{\sigma_T})\frac{d\tau_p}{d\sigma_n}] = 0 \tag{40}$$

$$k_{tn} = k_{nn}[(1-B_o)\frac{\tau_p}{\sigma_T}+(B_o+(1-B_o)\frac{\sigma_n}{\sigma_T})\frac{d\tau_p}{d\sigma_n}] \tag{41}$$

When $\sigma_n \geq \sigma_T$ or $\sigma_n \geq$ JCS, $k_{tt}=\tau_p/u_p$ when $u < u_p$ and k_{tt} vanishes when $u \geq u_p$.

In equations (36)-(41), the derivative $du_p/d\sigma_n$ is equal to the coefficient b in equation (1). The expression of the derivative $d\tau_p/d\sigma_n$ depends on the selected peak shear strength criterion. For instance, for the modified Ladanyi and Archambault's criterion [equation (14)] with a Mohr

Coulomb's criterion for the intact rock shear strength (equation (15)), $d\tau_p/d\sigma_n$ is equal to

$$\frac{d\tau_p}{d\sigma_n} = (1-a_s)\tan(\phi_u+i) - \frac{\sigma_n}{\sigma_T}\frac{(1-a_s)k_2}{\cos^2(\phi_u+i)}$$

$$\frac{1}{1+(1-\frac{\sigma_n}{\sigma_T})^{2k_2}\tan^2(i_{po})}\tan(i_{po})(1-\frac{\sigma_n}{\sigma_T})^{k_2-1} \tag{42}$$

$$-\frac{\sigma_n}{\sigma_T}k_1\tan(\phi_u+i)(1-\frac{\sigma_n}{\sigma_T})^{k_1-1}+\frac{s_r}{\sigma_T}k_1(1-\frac{\sigma_n}{\sigma_T})^{k_1-1}+a_s\tan\phi_o$$

For Barton's criterion (equation (19)), $d\tau_p/d\sigma_n$ is now equal to

$$\frac{d\tau_p}{d\sigma_n} = \tan(\phi_u+JRC\log_{10}\frac{JCS}{\sigma_n}) - \frac{JRC}{\ln(10)}[1+\tan^2(\phi_u+JRC\log_{10}\frac{JCS}{\sigma_n})] \tag{43}$$

Combining equations (29) and (35), an incremental formulation can be written relating the increments of normal and shear stresses to the increments of normal and shear displacements.

5.3 Joint Response Under Applied Stiffness Boundary Conditions

As a direct application of the formulation in previous section, the shear response of a rock joint under applied stiffness boundary conditions can be predicted. This can be done by writing that $d\sigma_n$ and dv must be related as follows

$$d\sigma_n = Kdv \tag{44}$$

where K is the applied stiffness that can be constant or vary with u or σ_n. Substituting equation (44) into (29), gives two relationships between the increments of normal stress and normal displacement and the increment of shear displacement, e.g.

$$d\sigma_n = \frac{Kk_{nt}}{K-k_{nn}}du \tag{45}$$

and

$$dv = \frac{k_{nt}}{K-k_{nn}}du \tag{46}$$

Similarly, using equation (35), the increments of shear stress are related to the increments of shear displacement as follows

$$d\tau = [\frac{k_{tn}k_{nt}}{K-k_{nn}}+k_{tt}]du \tag{47}$$

As a special case, consider the case when the applied stiffness K is equal to zero, corresponding to a constant normal stress condition ($d\sigma_n=0$). Then, equation (46) reduces to $dv=-(k_{nt}/k_{nn})du$. Using equations (36)-(41) and equation (47), it follows that $d\tau=[u_p/\tau_p-Bu_p]/[(u_p/\tau_p)+B(u-u_p)]^2du$ when $u<u_p$, $d\tau=k_{ss}du$ when $u_p < u < u_r$ and $d\tau=0$ when $u>u_r$. If K is now equal to infinity, corresponding to a constant normal displacement boundary condition ($dv=0$), it follows from equation (45) that $d\sigma_n=k_{nt}du$ and $d\tau=k_{tt}du$.

In general, knowing the initial stress across a dilatant joint and its shear displacement and dilatancy curves at different normal stress levels, equations (45)-(47) can be used to predict the joint shear response under various boundary conditions.

5.4 Illustrative Example

As an illustrative example, it is proposed to predict the shear response of samples F4 under constant normal stiffness from the results of the constant normal load direct shear tests for the forward part of the first shear cycle. In order to use the present model, some of the experimental data reported by Wibowo *et al.* [16] and presented in this paper were selected, e.g:

- joint maximum closure V_m=0.074 cm,
- joint initial stiffness k_{ni}=-135.7 MPa/cm,
- joint basic friction angle ϕ_u=30°,
- ratio of residual to peak shear strengths B_o=0.48,
- transitional stress σ_T=12.8 MPa,
- a=0.064 cm in equation (2),
- b=0.029 cm/MPa in equation (2),
- c=205.4 MPa/cm in equation (3),
- d=6.57 cm^{-1} in equation (3),
- residual displacement of 1.27 cm.

Further, if the modified Ladanyi and Archambault's criterion is used for the peak shear strength and dilatancy, the following data must also be input:

- k_1=0.25 in equation (17),

- k_2=0.81 in equation (18) or k_3=0.58 in equation (13),
- initial dilatancy rate $tan(i_{po})$=0.18 or $tan(i_{avo})$=0.15,
- intact rock cohesion s_o=7.7 MPa,
- intact rock friction angle ϕ_o=31.5°.

If on the other hand, Barton's criterion is used, the following data must be input:

- joint roughness coefficient JRC=15.5 (back calculated from peak shear equation), or JRC=6.6 (back calculated from dilatancy equation),
- joint wall compressive strength JCS=27.6 MPa.

Figs. 24a, 24b and 24c show respectively, the predicted and observed shear load versus shear displacement curves, the dilatancy curves and the shear load versus normal load paths for the F4 samples tested under an initial normal load of 16.0 kN (initial nominal normal stress of 1.4 MPa) with constant applied stiffness, K, equal to 0, 2.7, 8.1 and 27.1 MPa/cm, k_3 = 0.58 and $tan(i_{avo})$=0.15. Figs. 25(a), 25(b), and 25(c) show similar predicted and observed response curves for the samples tested under an initial normal load of 32.0 kN (initial nominal normal stress of 2.8 MPa). In Figs. 24 and 25, the modified Ladanyi and Archambault's criterion was used in the predictions. These figures show that the predicted curves agree relatively well with the experimental observations. In particular, the mathematical model is able to predict postpeak softening at low applied stiffnesses and hardening as the applied stiffness increases. Comparison between observed and predicted response curves for samples F3, F2, and G2 can be found in [18].

Figs. 26(a), 26(b), and 26(c) show, respectively, the predicted and observed shear load versus shear displacement curves, the dilatancy curves and the shear load versus normal load paths for the F4 samples tested under an initial normal load of 16.0 kN (initial nominal normal stress of 1.4 MPa) with constant applied stiffness equal to 0, 2.7, 8.1 and 27.1 MPa/cm, and JRC=15.5. Figs. 27(a), 27(b), and 27(c) show similar predicted and observed response curves for the samples tested under the same conditions, except that JRC is now equal to 6.6. In both Figs. 26 and 27, Barton's criterion was used in the predictions.

Figs. 26(a)-(c) indicate that using Barton's criterion with JRC=15.5 (back calculated from peak shear equation) overestimates joint shear strength and dilatancy. On the other hand, for JRC=6.6 (back calculated from dilatancy equation), Figs. 27(a)-(c) show that the predicted joint shear strengths are lower than the actual test results, but the predicted joint dilatancy agrees quite well with the experimental observations. Figs. 26 and 27 show that the mathematical predictions using Barton's model are very sensitive to the input value of JRC. Comparison between observed and predicted response curves for samples F3, F2, and G2 can be found in [18].

6. CONCLUSIONS

In this paper, several existing constitutive models were used to describe the constant normal load cyclic direct shear test results obtained by Wibowo *et al.* [16]. The analysis of the test results was done for the forward and reverse part of each shear cycle.

For the forward part of the first shear cycle, the shear load vs. shear displacement response curves show an increase in peak shear displacement and shear stiffness with the applied normal load (stress). Thus, the constant displacement and stiffness models initially proposed by Goodman [2] are inadequate to describe the observed behavior. Note that in this paper, and contrary to existing models in the literature, the prepeak region of the shear load versus shear displacement curves was assumed to be nonlinear and the shear stiffness was defined for data ranging from 25 to 75% of the peak shear load. The increase in peak shear displacement and shear stiffness with normal load was observed for the forward part of the first shear cycle only. For the other four cycles, the peak displacement was found to be poorly defined. It was difficult to separate the peak and residual displacements because of accumulated joint surface damage.

The model of Goodman [2] predicting a linear increase of the ratio between the residual and peak shear strengths with normal load (or stress) was found to describe the experimental observations relatively well for forward and shear motions and all shear cycles. As the number of cycles increases and joint surface damage accumulates, the peak shear strength rapidly approaches its residual value.

Joint dilatancy decreases with increasing normal load (stress). For a given normal load, it decreases rapidly as the number of cycles increases. The models of Ladanyi and Archambault [19], Barton and Choubey [20], Schneider [21], and Jing [22] were found to fit the observed variation of joint dilatancy with normal load (stress). The model of Schneider was found to fit the experimental results the best. The second best fit was obtained using Barton and Choubey's model.

The modified Ladanyi and Archambault's failure criterion proposed by Saeb [27] and that of Barton [28] were used to model the variation of peak shear strength with normal load (stress) for the forward and reverse parts of each shear cycle. The modified Ladanyi and Archambault's criterion fits the experimental data quite well. This criterion implies that both shearing of surface asperities and sliding occurs simultaneously along joint surfaces during shear. It was found that starting with the second shear cycle, sliding is dominant along the joint surfaces.

Barton's failure criterion requires knowledge of the joint roughness coefficient JRC. Several methods were explored in this paper to determine JRC, e.g., (1) from the tangent dilatancy rate at the peak shear stress, (2) from initial joint surface profiles, (3) from measured peak shear strengths, and (4) from tilt tests. It was found that those methods lead to different values of JRC. A value of JRC determined with one of those methods may give a good prediction of dilatancy, but a poor prediction of shear strength and vice versa.

A mathematical model for joint shear response under various boundary conditions was proposed. In this model, joint normal behavior is represented by the hyperbolic formulation of Bandis *et al.* [17]. Joint shear behavior is represented by the modified Ladanyi and Archambault's criterion or Barton's criterion and joint dilatant behavior is represented using the model of Goodman and St. John [30]. Comparison between predicted joint response under constant normal stiffness and test results revealed that Ladanyi and Archambault's criterion can model relatively well the gain in shear strength of rock joints during shear and their dilatant response under constant applied normal stiffness. On the other hand, the mathematical predictions using Barton's

model were found to be very sensitive to the input value of JRC and not as good as the predictions with Ladanyi and Archambault's criterion.

7. REFERENCES

1. Leichnitz W. Mechanical properties of rock joints. *Int. J. Rock Mech. Min. Sci. & Geomech. Abstr.* **22**, 313-321 (1985).

2. Goodman R. E. *Methods of Geological Engineering in Discontinuous Rocks.* West Publ. Company, St. Paul, MN (1976).

3. Obert L., Brady B. T., and Schmechel F. H. The effect of normal stiffness on the shear resistance of rock. *Rock Mech.* **8**, 57-72 (1976).

4. Goodman R. E. and Boyle W. Non-linear analysis for calculating the support of a rock block with dilatant joint faces. Presented at the 34th Geomechanics Colloquy, Salzburg, Austria (1985).

5. Hutson R. W. Preparation of duplicate rock joints and their changing dilatancy under cyclic shear. Ph.D. dissertation, Northwestern University, Evanston, IL (1987).

6. Archambault G., Fortin M., Gill D. E., Aubertin M., and Ladanyi B. Experimental investigations for an algorithm simulating the effect of variable normal stiffness on discontinuities shear strength. *Proc. Int. Conf. on Rock Joints*, Loen, Norway. A.A. Balkema, Rotterdam. pp. 141-148 (1990).

7. Bandis S. C. Mechanical properties of rock joints. *Proc. Int. Conf. on Rock Joints*, Loen, Norway. A.A. Balkema, Rotterdam. pp. 125-140 (1990).

8. Benmokrane B., Bouraoui M., and Mouchaorab K. S. Shearing behaviour of rock discontinuities under constant or variable normal stiffness conditions. Addendum to *Proc. of the 32nd U.S. Symp. in Rock Mech.* Norman, Oklahoma (1991).

9. Ohnishi Y. and Dharmaratne P. G. R. Shear behaviour of physical models of rock joints under constant normal stiffness conditions. *Proc. Int. Conf. on Rock Joints*, Loen, Norway. A.A. Balkema, Rotterdam. pp. 267-273 (1990).

10. Skinas C. A., Bandis S. C., and Demiris C.A. Experimental investigation and modeling of rock joint behaviour under constant stiffness. *Proc. Int. Conf. on Rock Joints*, Loen, Norway. A.A. Balkema, Rotterdam. pp. 301-308 (1990).

11. Saeb. S. Effect of boundary condition on the behavior of a dilatant rock joint. Ph.D. dissertation, Univ. of Colorado at Boulder, CO (1989).

12. Amadei B. and Saeb S. Constitutive models of rock joints. *Proc. Int. Conf. on Rock Joints*,

Loen, Norway. A.A. Balkema, Rotterdam. pp. 581-594 (1990).

13. Gould M. C. Development of a high capacity dynamic direct shear apparatus and its application to testing sandstone rock joints. M.S. Thesis, Univ. of Colorado at Boulder, CO (1982).

14. Farrington J. J. On the characterization of rock joint roughness. MS Thesis, Department of Civil, Environmental, and Architectural Engineering, Univ. of Colorado at Boulder, CO (1983).

15. Gamal-Eldin N. A. Fractal and statistical analysis of crack surface and their use in fracture mechanics of concrete dams. Ph. D. dissertation, Department of Civil Eng., Colorado State University, CO (1989).

16. Wibowo J., Amadei B., Sture S., Price R.H. and Robertson A. B. Effect of Boundary Conditions on the Strength and Deformability of Replicas of Natural Fractures in Welded Tuff: Data Report. Technical Report SAND 92-1853, SNL, Albuquerque, NM (1993).

17. Bandis S. C., Lumsden A. C., and Barton N.R. Fundamentals of Rock Joint Deformation. *Int. J. Rock Mech. Min. Sci. & Geomech. Abstr.* **20**, 249-268 (1983).

18. Wibowo J., Amadei B., Sture S. and Price R. H. Effect of Boundary Conditions on the Strength and Deformability of Replicas of Natural Fractures in Welded Tuff: Data Analysis. Technical Report SAND 93-7079, SNL, Albuquerque, NM (1994).

19. Ladanyi B., and Archambault G. Simulation of Shear Behavior of a Jointed Rock Mass, *Proc. 11th Symp. on Rock Mech.* Berkeley, California, SME/AIME, pp. 105-125 (1970).

20. Barton N. and Choubey V. The Shear Strength of Rock Joints in Theory and Practice. *Rock Mechanics.* **10**, 1-54 (1977).

21. Schneider H. J. The Friction and Deformation Behaviour of Rock Joints. *Rock Mech*anics. **8**, 169-185 (1976).

22. Jing L. Numerical Modelling of Jointed Rock Masses by Distinct Element Method for Two, and Three Dimensional Problems. Ph.D. Dissertation, Division of Rock Mechanics, Lulea University of Technology, Lulea, Sweden (1990).

23. Tse R, and Cruden D. M. Estimating Joint Roughness Coefficients. *Int. J. Rock Mech. Min. Sci. & Geomech. Abstr.* **16**, 303-307 (1979).

24. Yu X., and Vayssade B. Technical Note: Joint Profiles and Their Roughness Parameter. *Int. J. Rock Mech. Min. Sci. & Geomech. Abstr.* **28**, 333-336 (1991).

25. Barton N. and Bandis S. C. Review of Predictive Capabilities of JRC-JCS Model in Engineering Practice. *Proc. Int. Conf. on Rock Joints*, Loen, Norway. A.A. Balkema,

Rotterdam. pp. 603-610 (1990).

26. Jing L., Nordlund E., and Stephansson O. An Experimental Study on the Anisotropy and Stress-Dependency of the Strength and Deformability of Rock Joints. *Int. J. Rock Mech. Min. Sci & Geomech. Abstr.* **29**, 535-542 (1992).

27. Saeb S. A Variance on the Ladanyi and Archambault's Shear Strength Criterion. *Proc. Int. Conf. on Rock Joints*, Loen, Norway, A.A. Balkema, Rotterdam. pp. 701-705 (1990).

28. Barton N. Rock Mechanics Review, The Shear Strength of Rock and Rock Joints. *Int. J. Rock Mech. Min. Sci & Geomech. Abstr.* **13**, 255-279 (1976).

29. Fairhurst C. On the Validity of Brazilian Test for Brittle Materials. *Int. J. Rock Mech. Min. Sci & Geomech. Abstr.* **1**, pp. 535-546 (1964).

30. Goodman R. E., and St. John C. Finite Element Analysis for Discontinuous Rocks. *Numerical Methods in Geotechnical Engineering* (Desai, C. S., and Christian, J. T. editors). McGraw-Hill, New York, pp. 148-175 (1977).

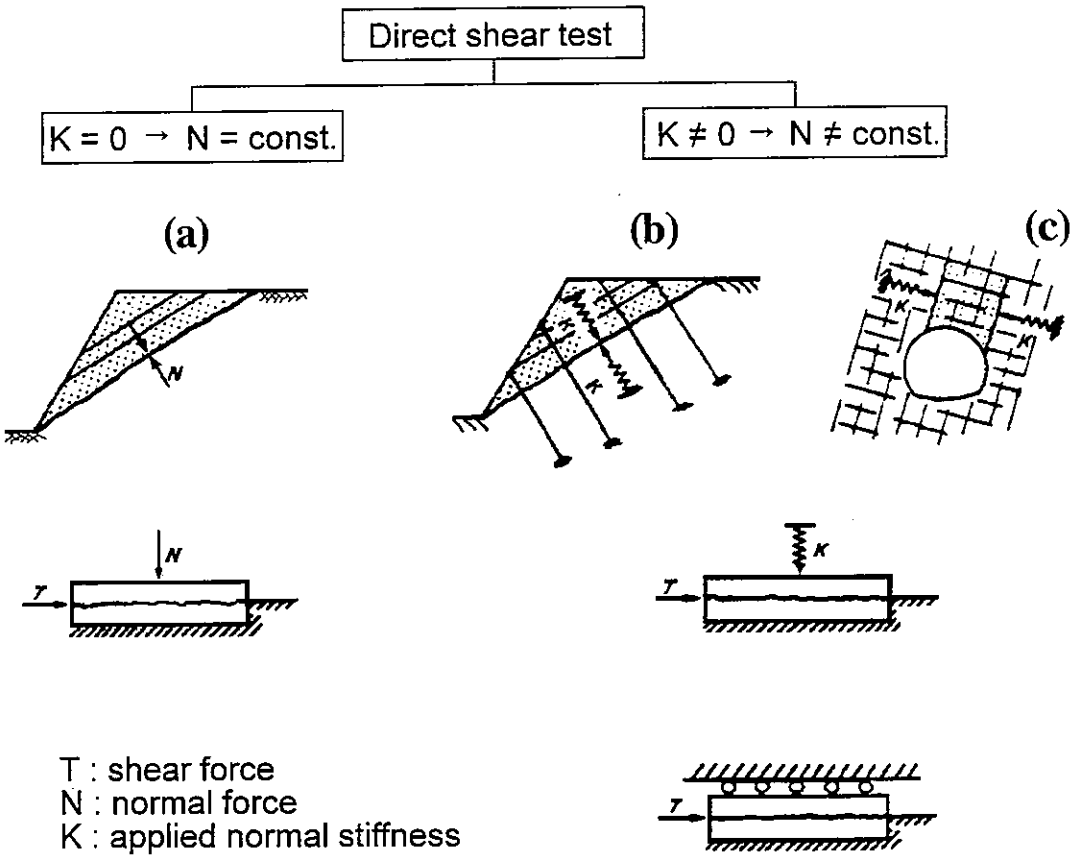

Figure 1. Simulation of different *in situ* boundary conditions in direct shear tests (adapted from Leichnitz [1]).

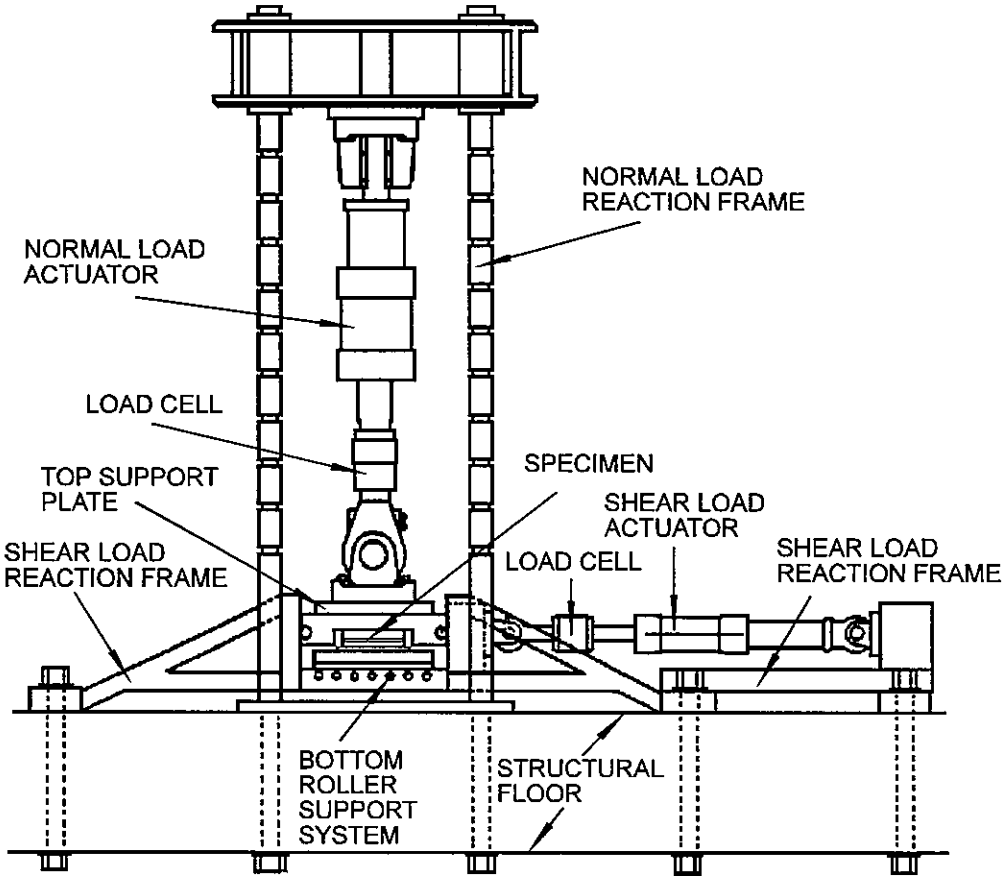

Figure 2. Direct shear apparatus (Schematic side view), (after Gould [13]).

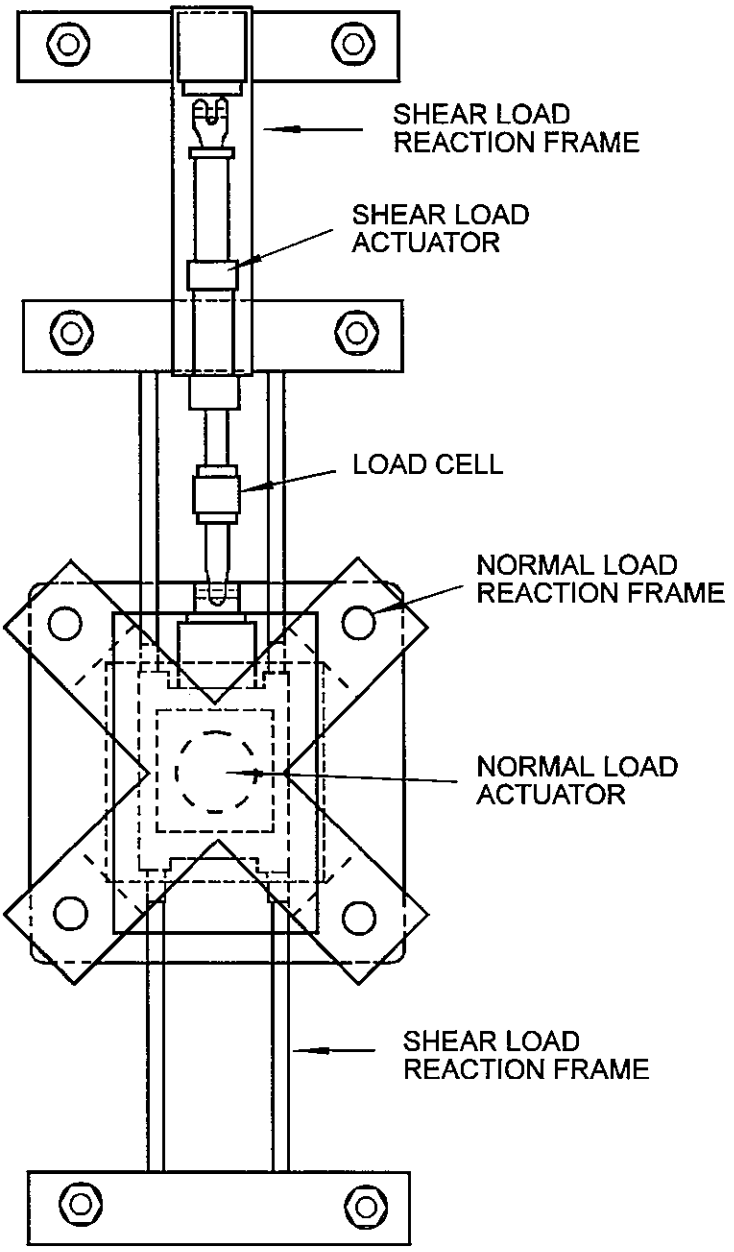

Figure 3. Direct shear apparatus (Schematic overhead view), (after Gould [13]).

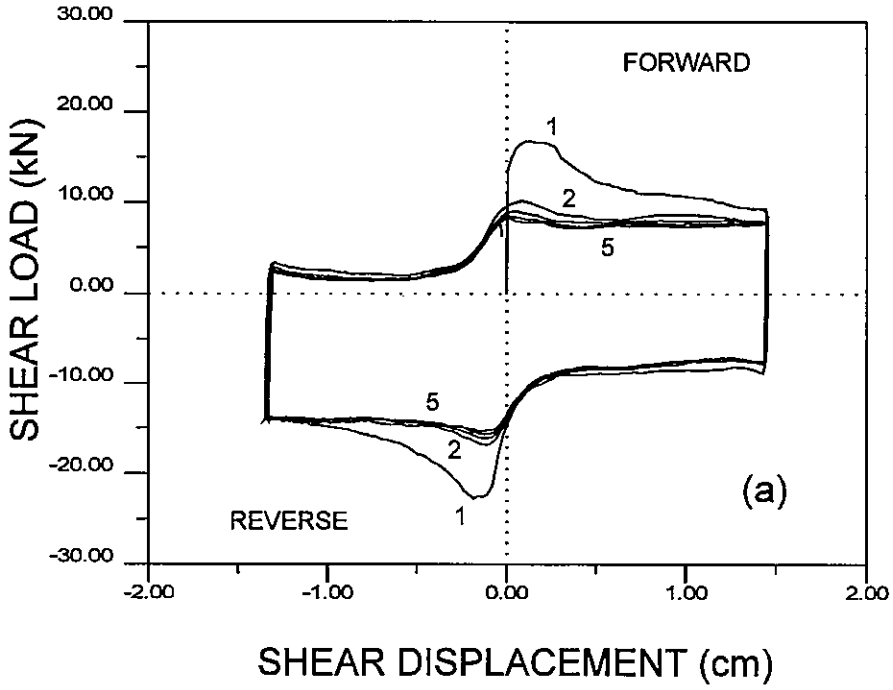

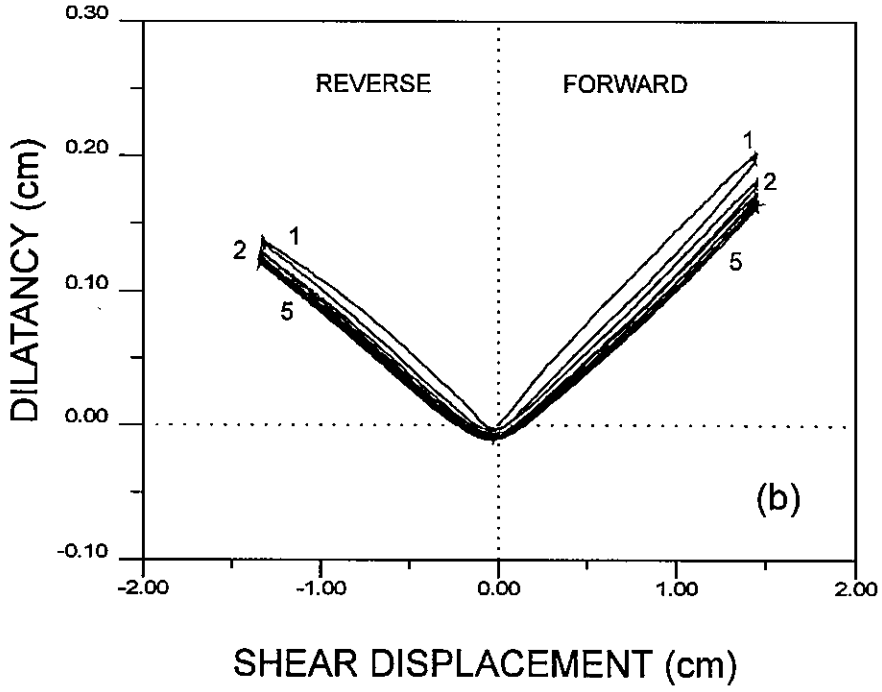

Figure 4. (a) Shear load vs. shear displacement, (b) Dilatancy vs. shear displacement. Specimen R2F4, constant normal load N_0=16.0 kN.

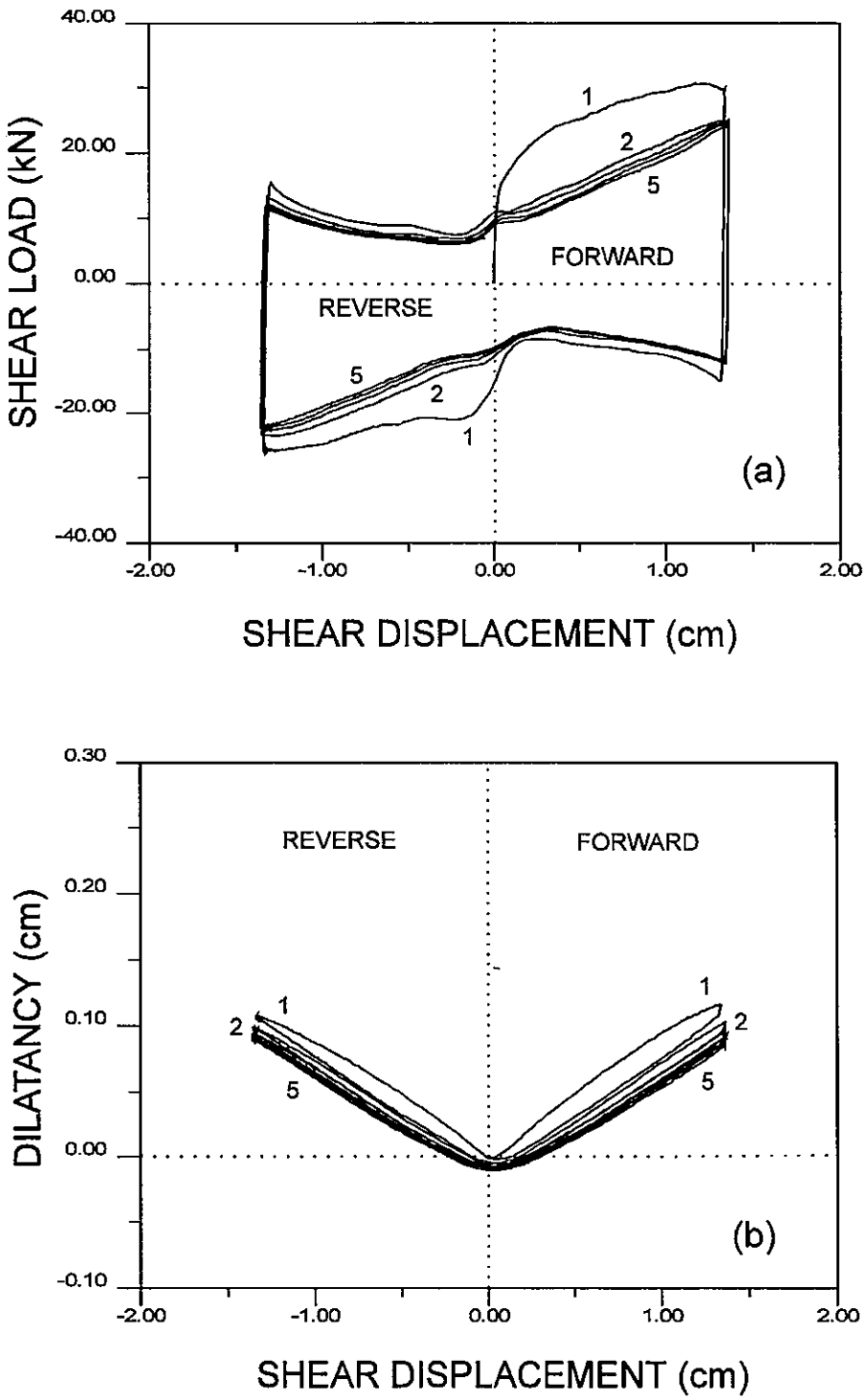

Figure 5. (a) Shear load vs. shear displacement, (b) Dilatancy vs. shear displacement. Specimen KR10F4, constant normal stiffness K=315.1 kN/cm and initial normal load N_0=16.0 kN.

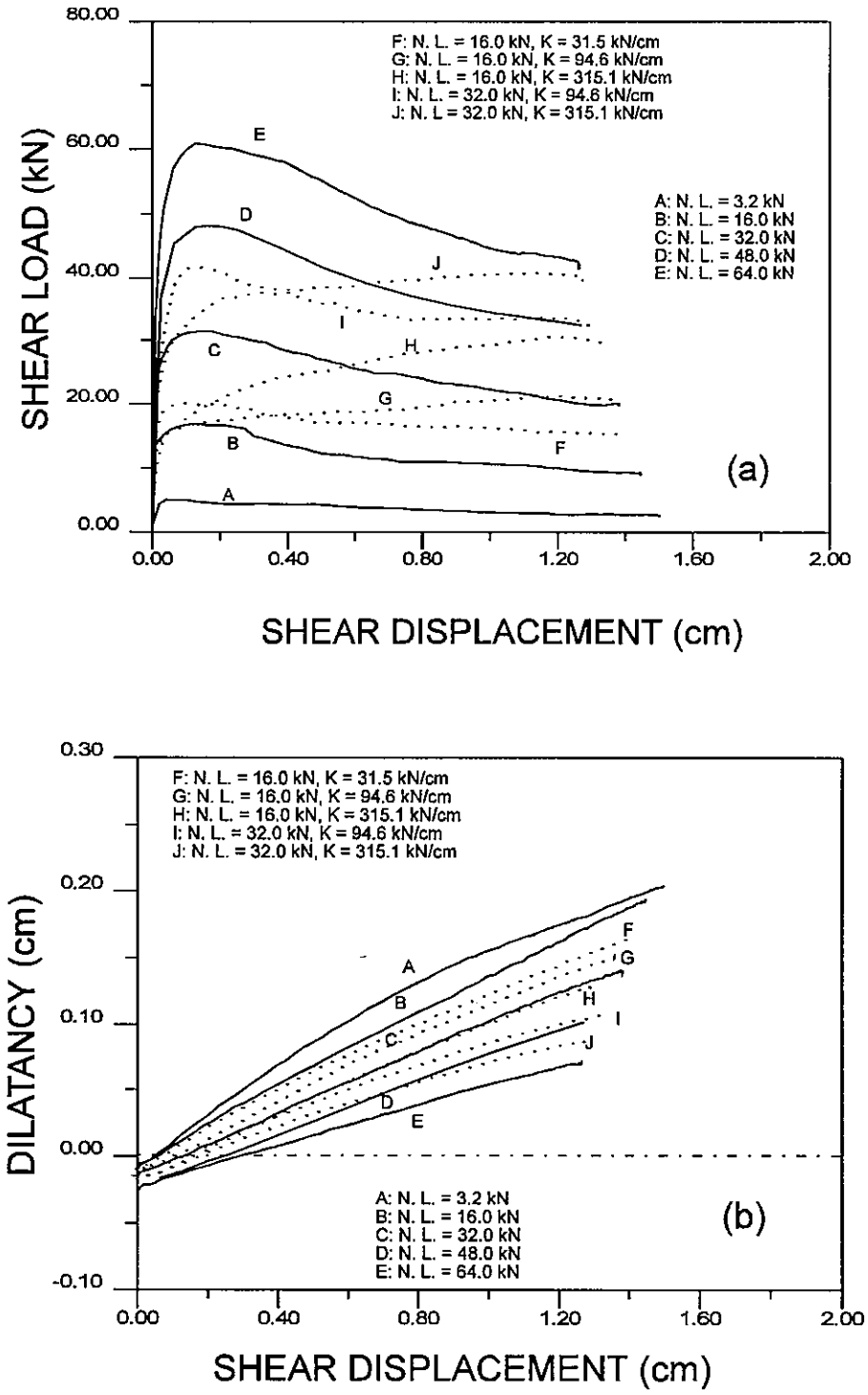

Figure 6. (a) Shear load vs. shear displacement, (b) Dilatancy vs. shear displacement. First cycle forward shear of F4 samples. Solid lines for constant normal load tests and dashed lines for constant stiffness tests under initial normal loads N_0=16.0 kN or N_0=32.0 kN. (line A=specimen R1F4, B=R2F4, C=R3F4, D=R4F4, E=R5F4, F=KR7F4, G=KR9F4, H=KR10F4, I=KR11F4, and J=KR12F4)

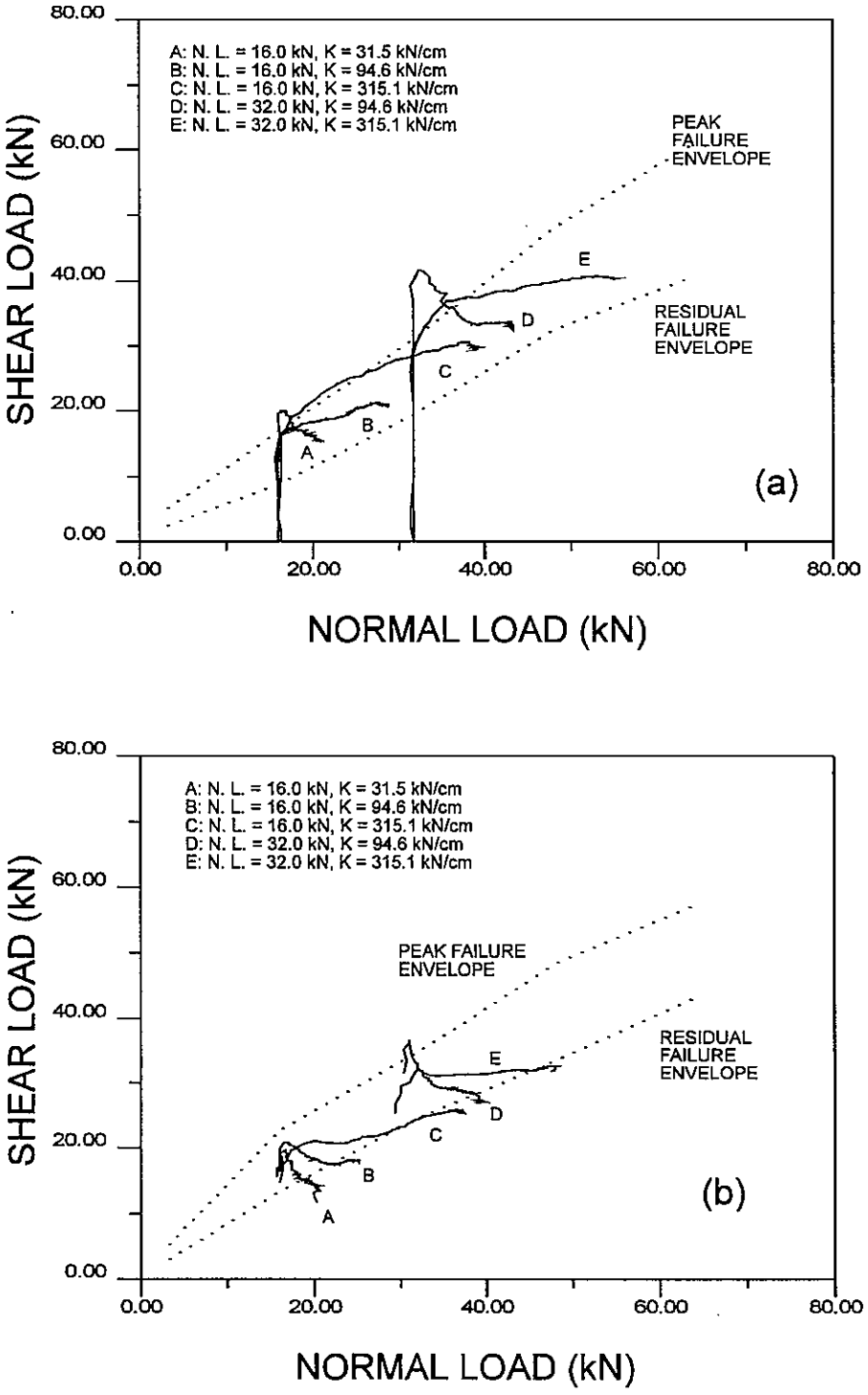

Figure 7. Load paths for constant normal stiffness tests on F4 samples in the shear load vs. normal load space, (a) first cycle forward shear load paths, and (b) first cycle reverse shear load paths. The peak and residual envelopes determined from the constant normal load tests are also shown. (line A=specimen KR7F4, B=KR9F4, C=KR10F4, D=KR11F4, and E=KR12F4)

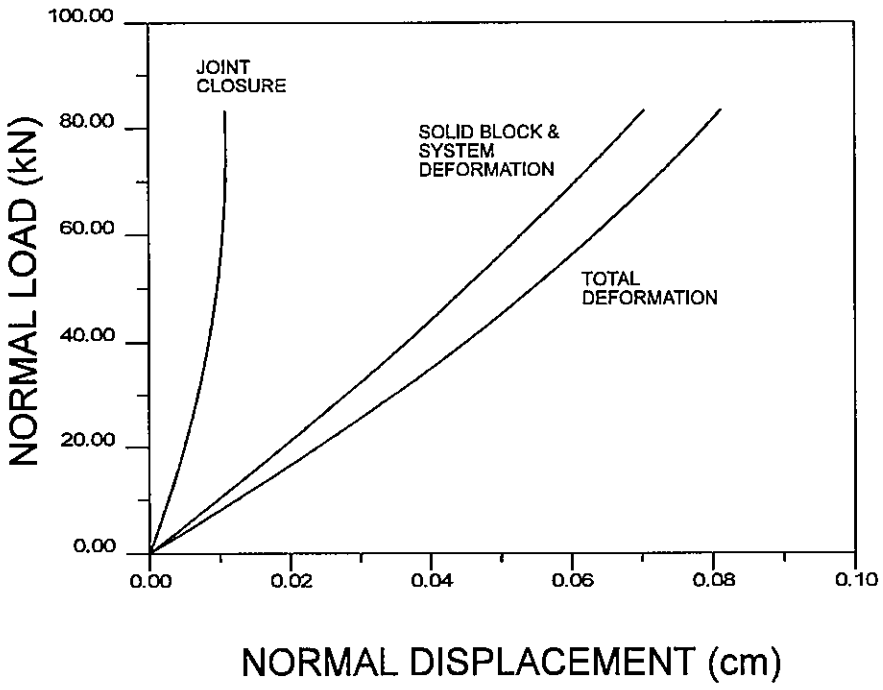

Figure 8. Joint closure of specimen R5F3 after shear testing under constant normal load N_0=66.7 kN.

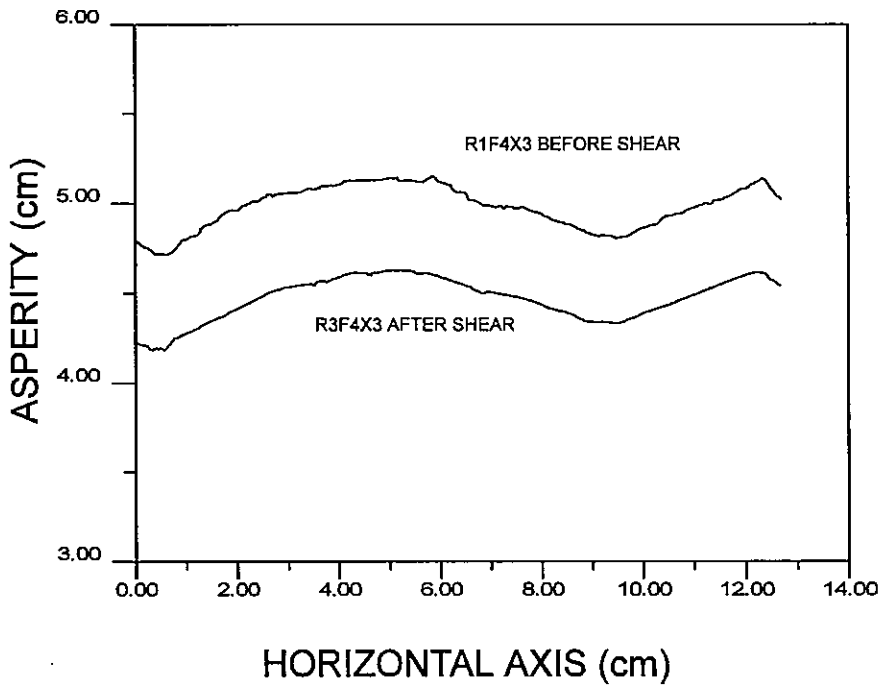

Figure 9. Comparison of profile X3 taken on the bottom half of sample R1F4 before shear and profile X3 taken on the bottom half of sample R3F4 after shear (offset -5.1 mm). Sample R3F4 was tested under a constant normal load N_0=32.0 kN.

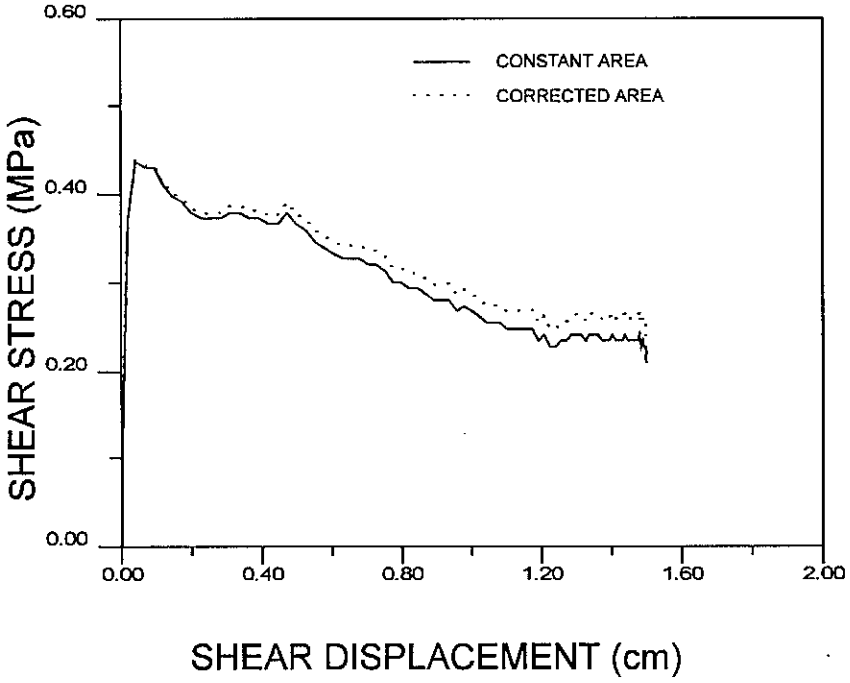

Figure 10. Comparison between shear stress vs. shear displacement curves using initial and corrected areas for samples R1F4 and forward shear motion.

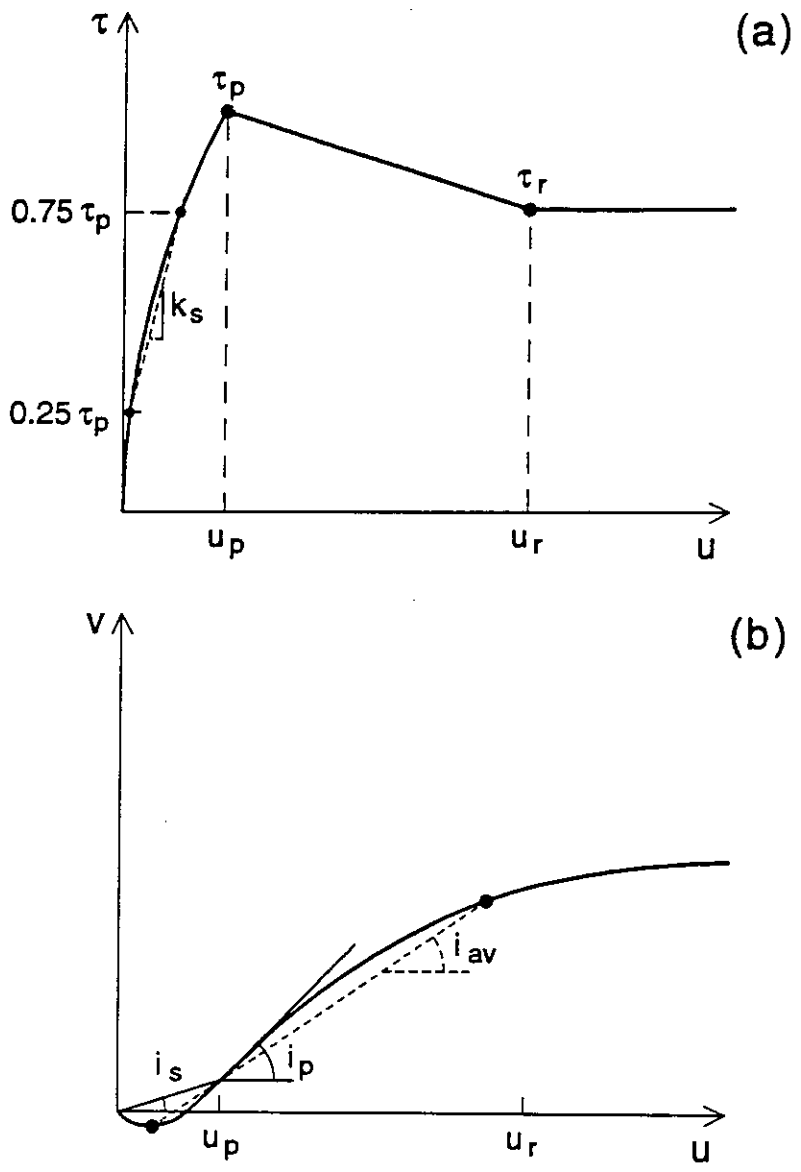

Figure 11. (a) Idealized shear stress vs. shear displacement curve, (b) Idealized normal displacement (dilatancy) vs. shear displacement curve.

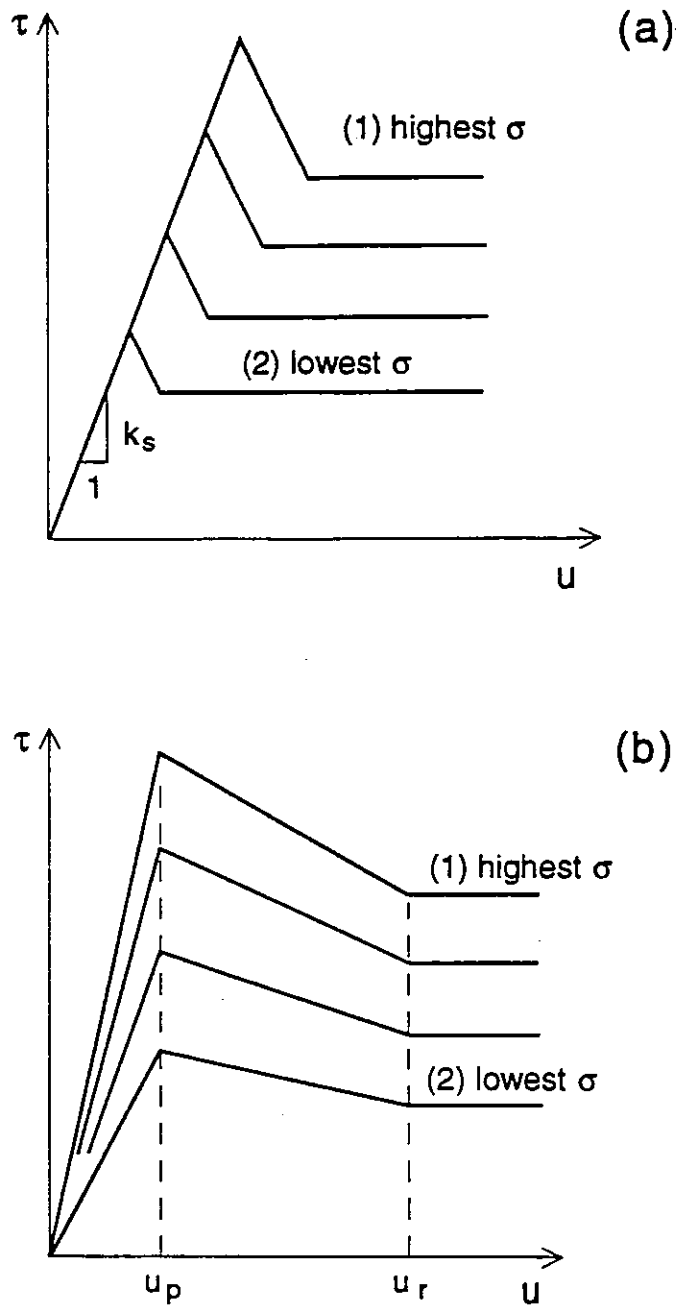

Figure 12. (a) Constant stiffness, and (b) Constant peak displacement models (adapted from Goodman [2]).

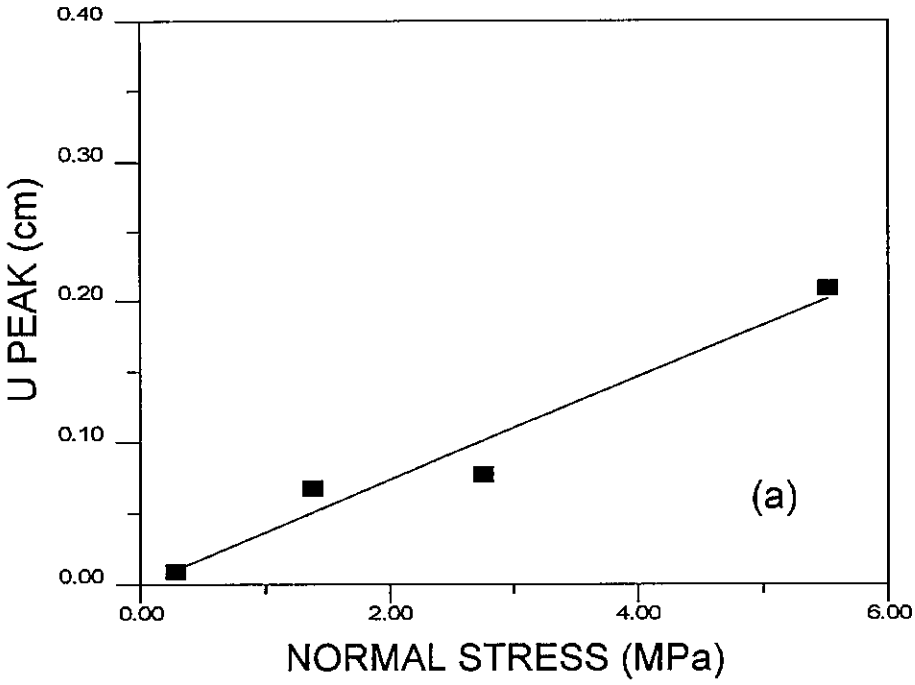

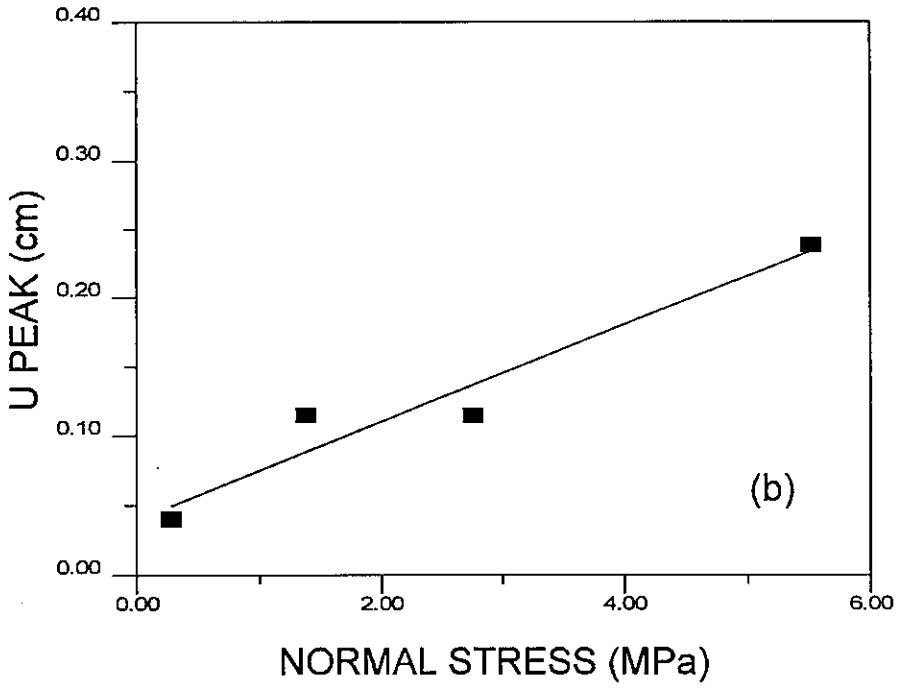

Figure 13. Peak shear displacement vs. normal stress for samples F3, (a) forward shear motion, and (b) reverse shear motion.

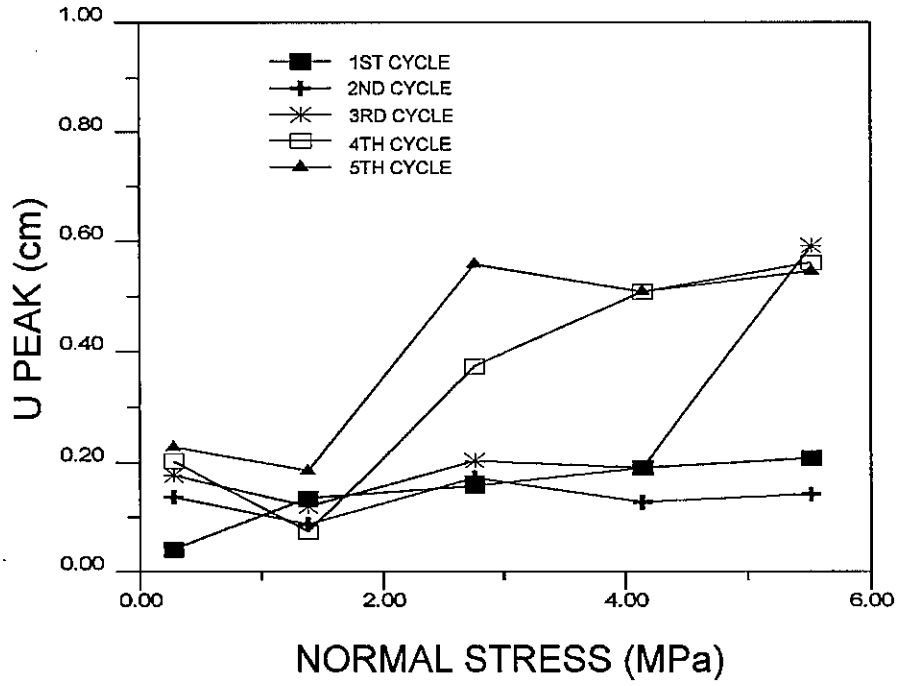

Figure 14. Peak shear displacement vs. normal stress for samples F4, forward shear motion (all cycles).

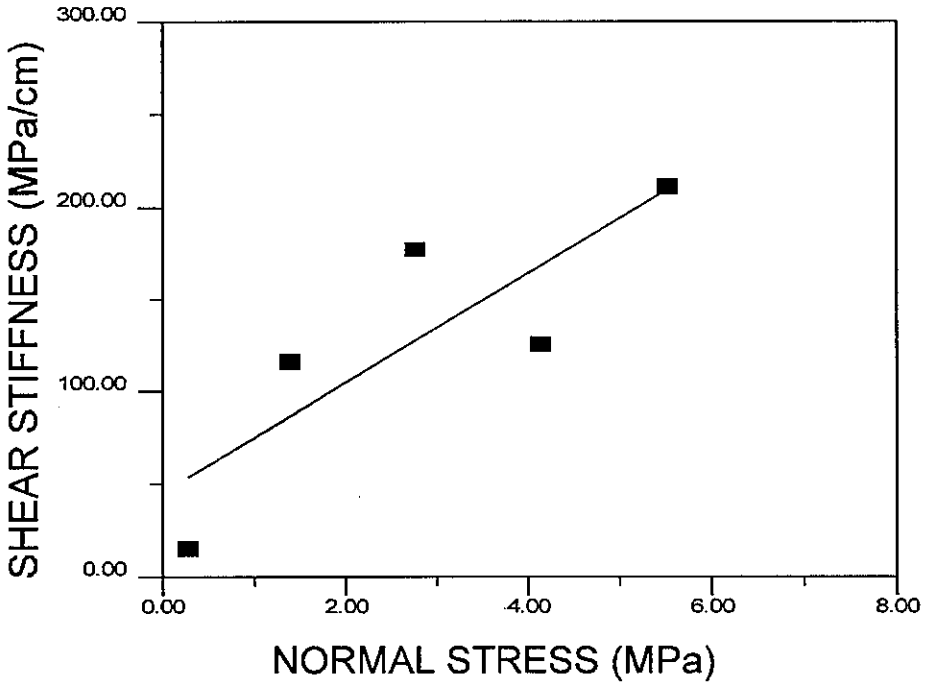

Figure 15. Shear stiffness vs. normal stress for samples F4.

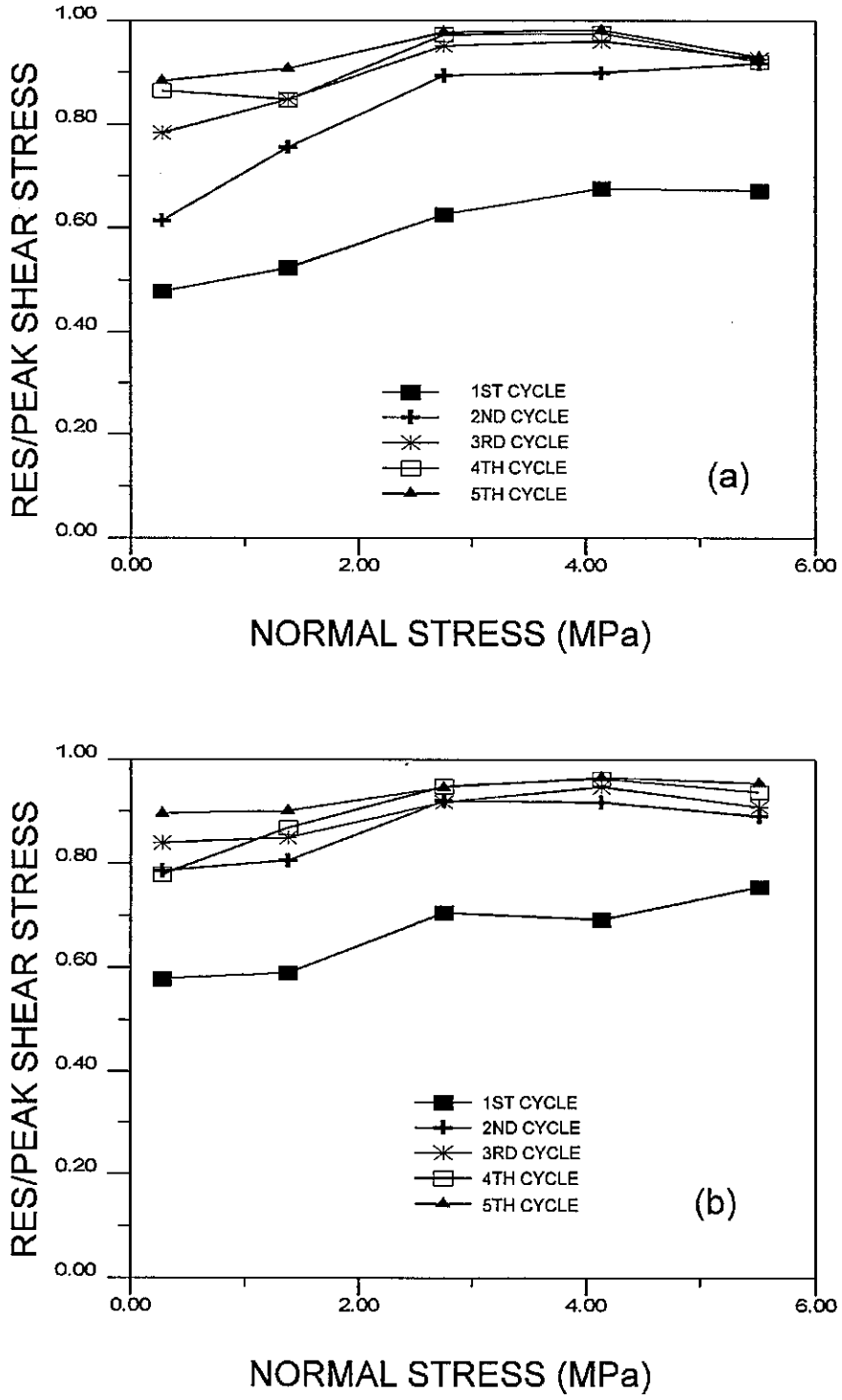

Figure 16. Ratio of residual to peak shear strengths vs. normal stress for samples F4, (a) forward shear motion, and (b) reverse shear motion.

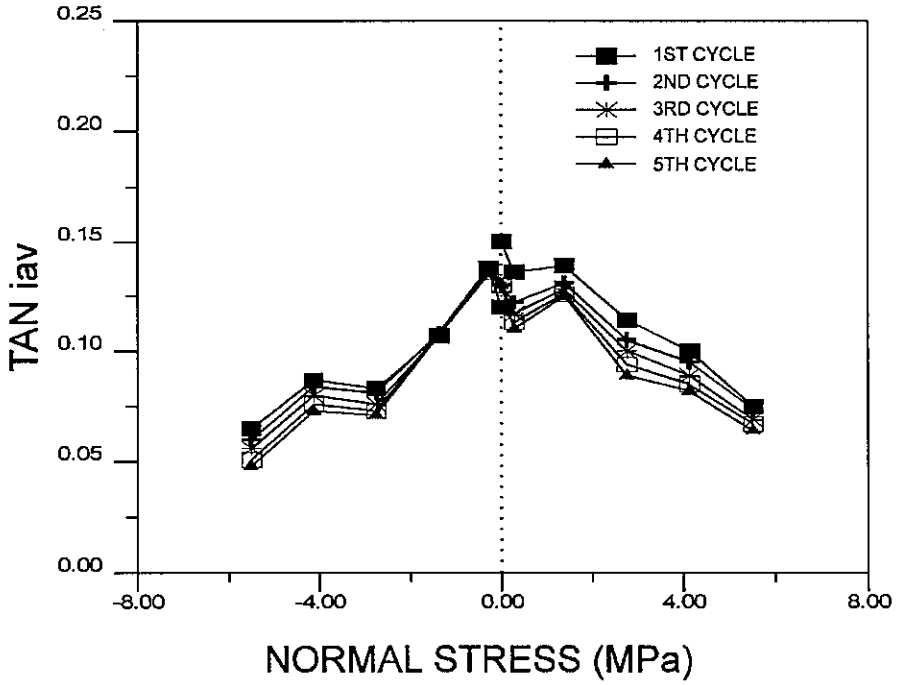

Figure 17. Average dilatancy vs. normal stress for samples F4.

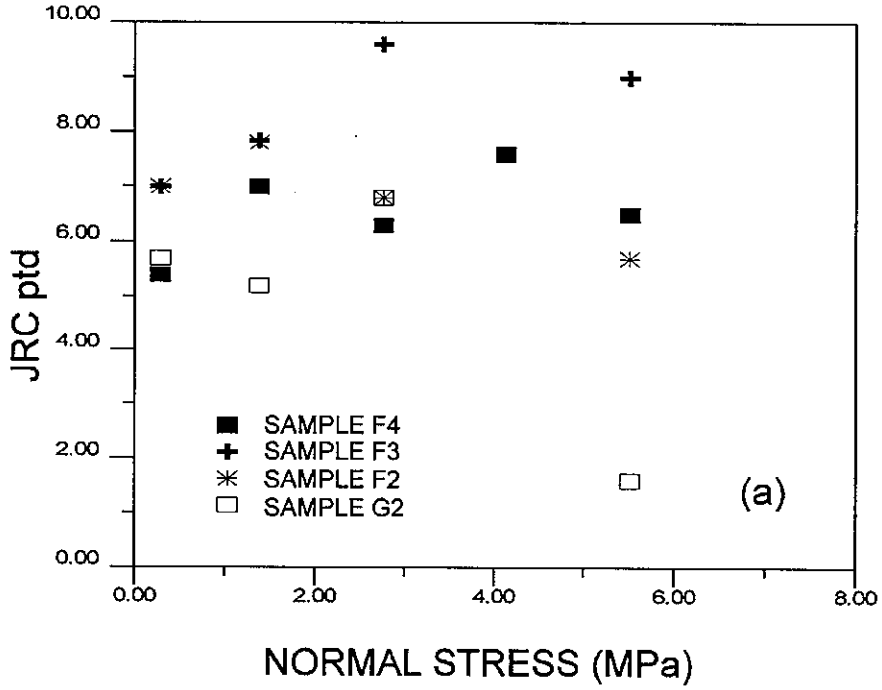

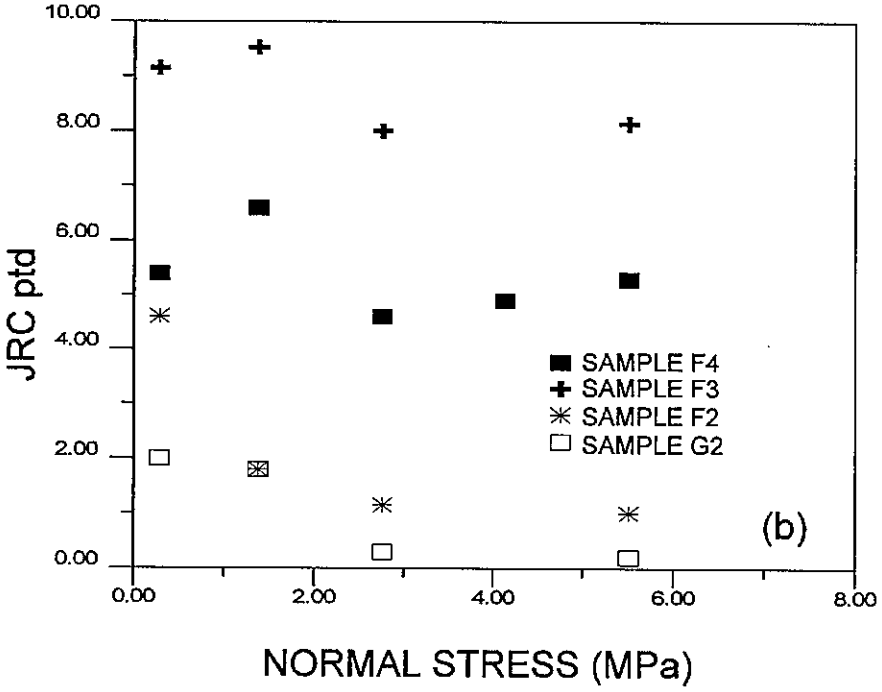

Figure 18. Joint Roughness Coefficient vs. normal stress, (a) first cycle forward shear motion, and (b) first cycle reverse shear motion.

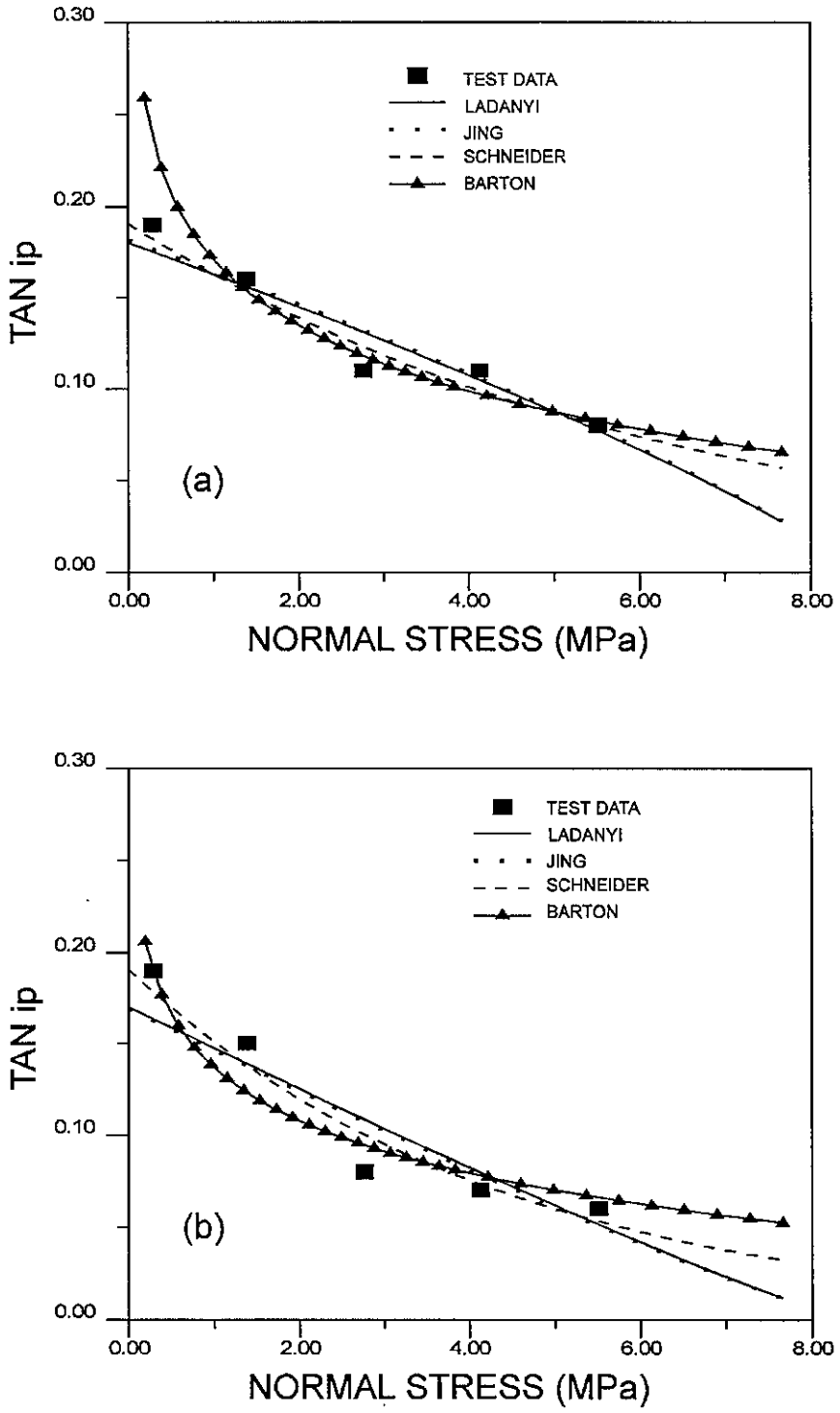

Figure 19. Comparison between the different dilatancy models for samples F4, (a) first cycle forward shear motion, and (b) first cycle reverse shear motion.

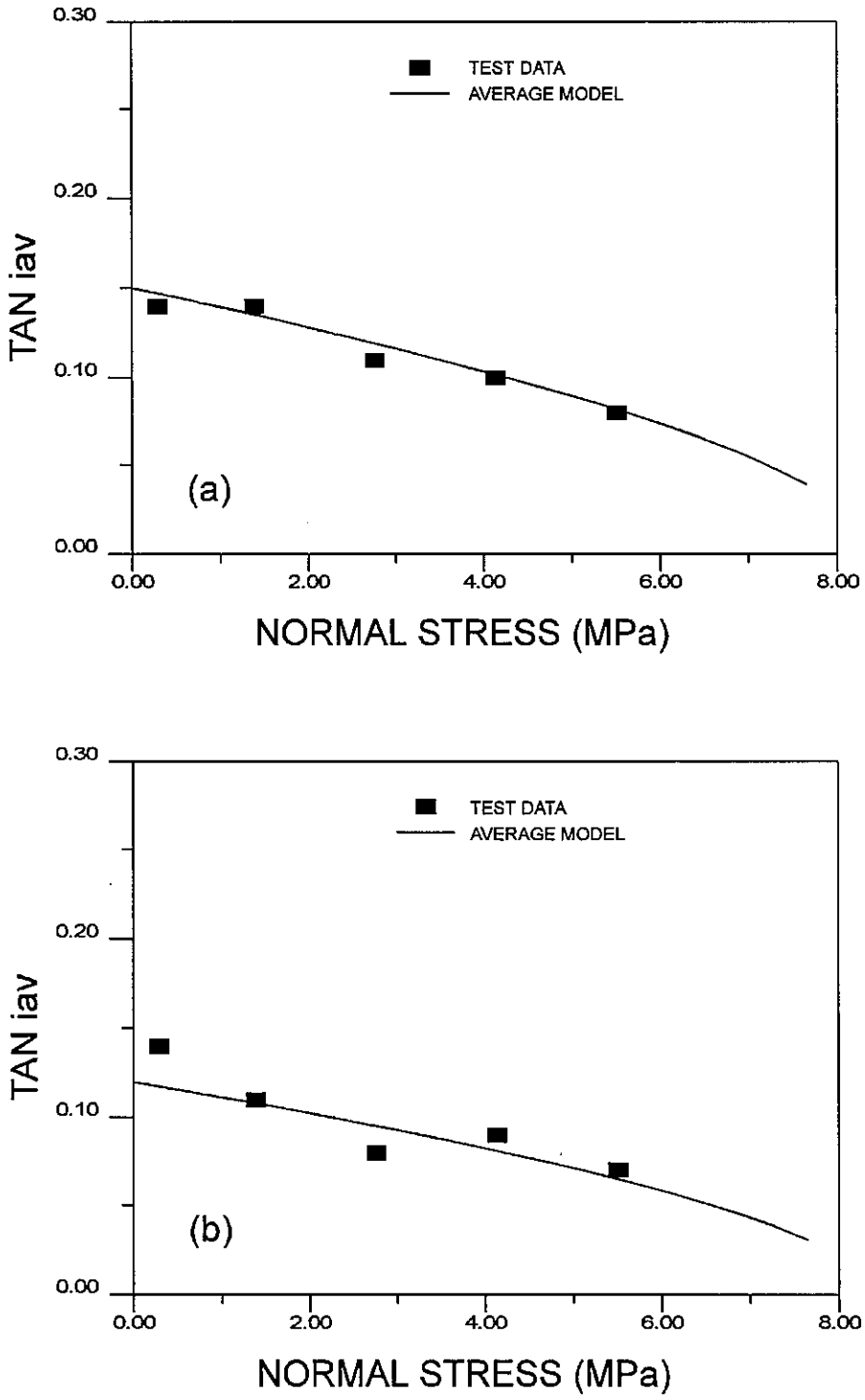

Figure 20. Comparison between average dilatancy model and actual test results for samples F4, (a) first cycle forward shear motion, and (b) first cycle reverse shear motion.

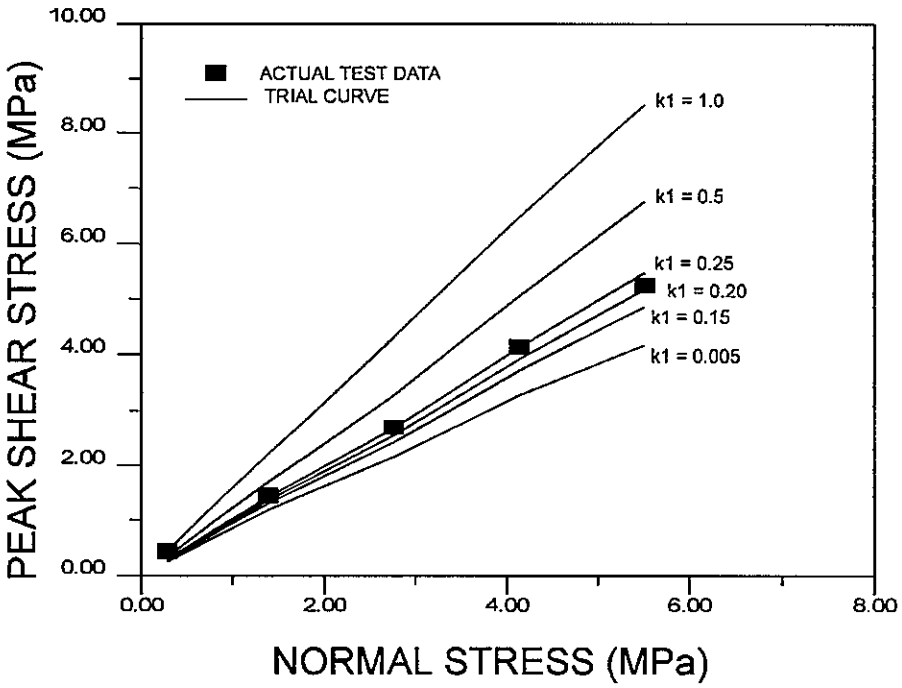

Figure 21. Trial values of k_1 for samples F4 and first shear cycle.

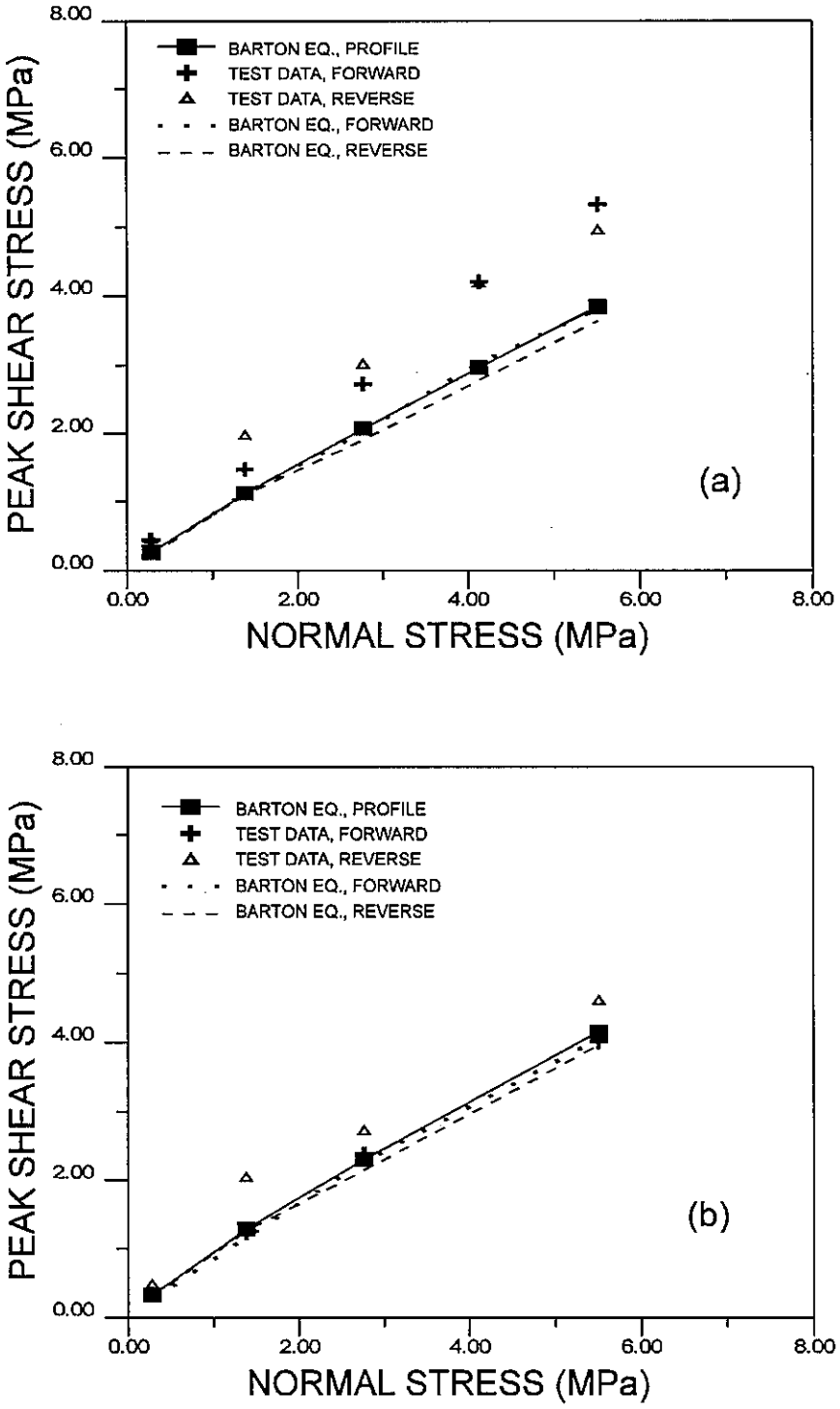

Figure 22. Comparison between Barton's peak shear strengths and observed peak shear strengths, (a) for samples F4 first cycle, and (b) for samples F3 first cycle.

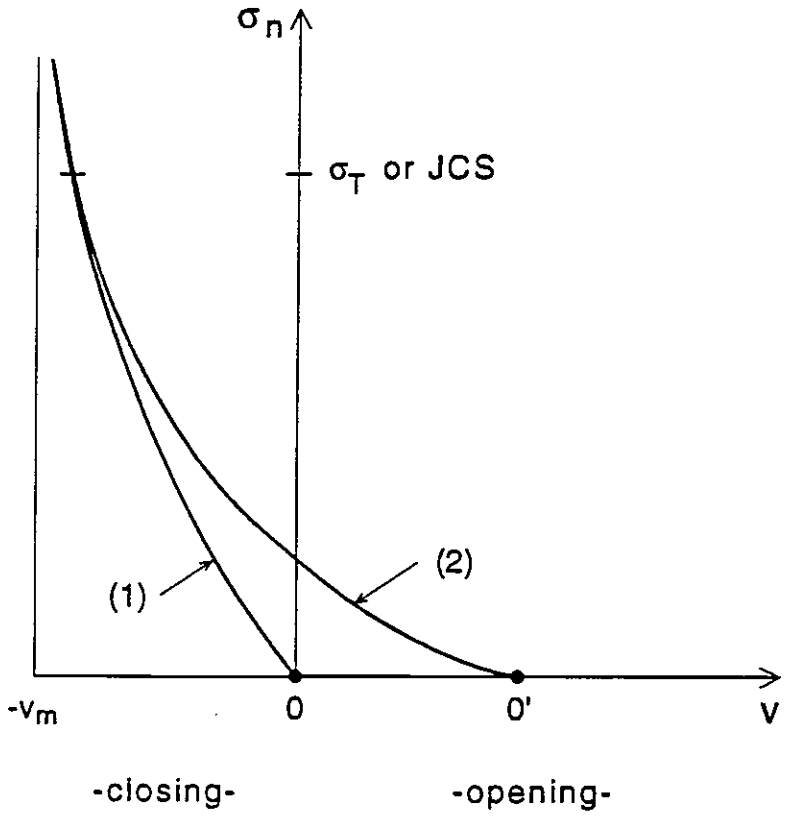

Figure 23. Normal stress vs. normal displacement curves for zero shear displacement (curve 1) and for shear displacement $u \leq u_r$ (curve 2).

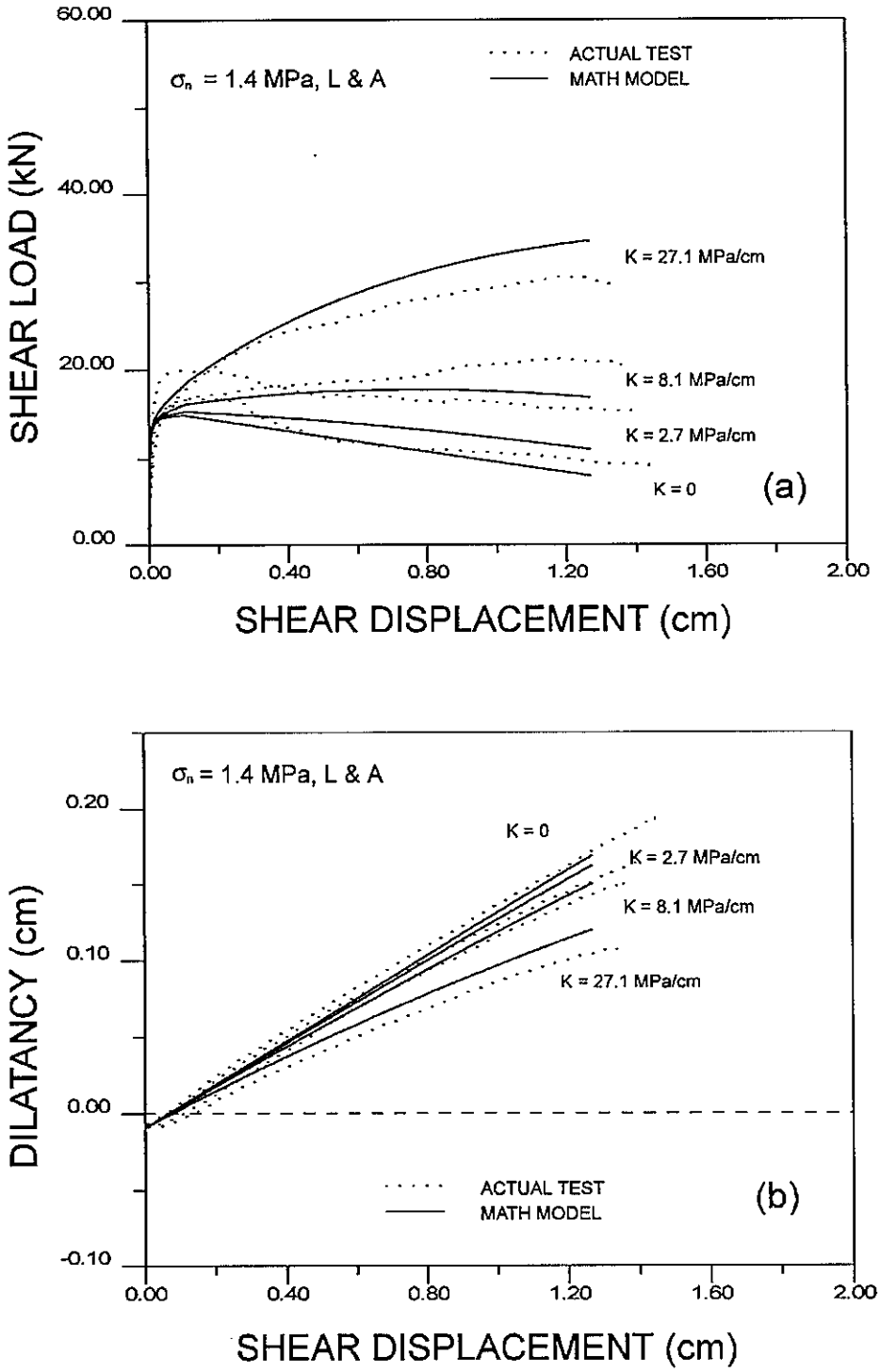

Figure 24. Predicted and observed shear load vs. shear displacement curves, dilatancy curves and shear load vs. normal load paths in (a)-(c), respectively, for K=0, 2.7, 8.1, and 27.1 MPa/cm, k_3=0.58 and $\tan(i_{avo})$=0.15. Samples F4, first shear cycle forward motion with initial normal stress =1.4 MPa. The mathematical model is based on Ladanyi and Archambault's criterion.

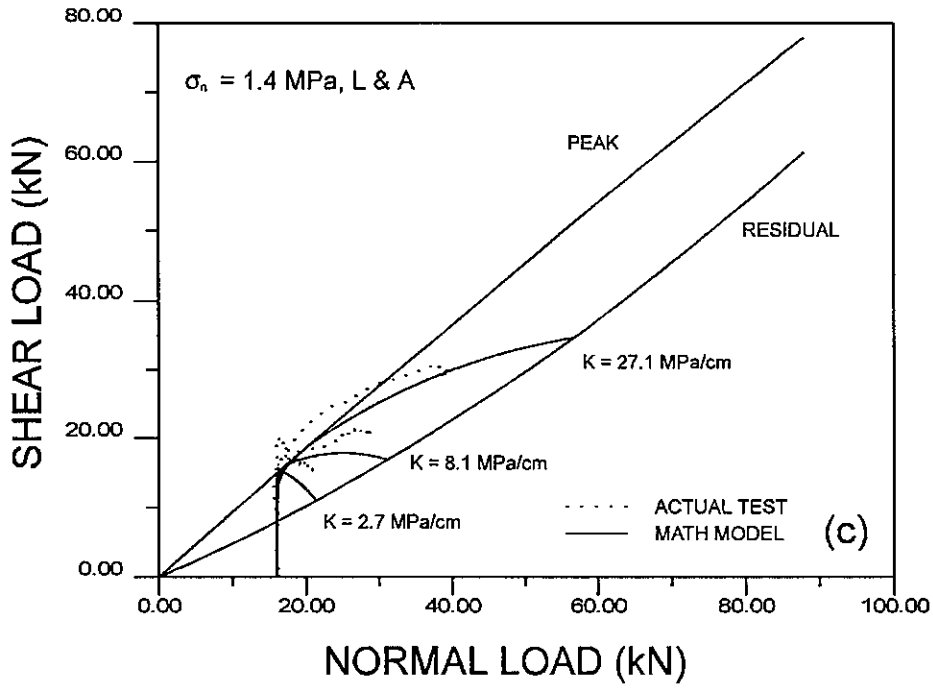

Figure 24 (continued).

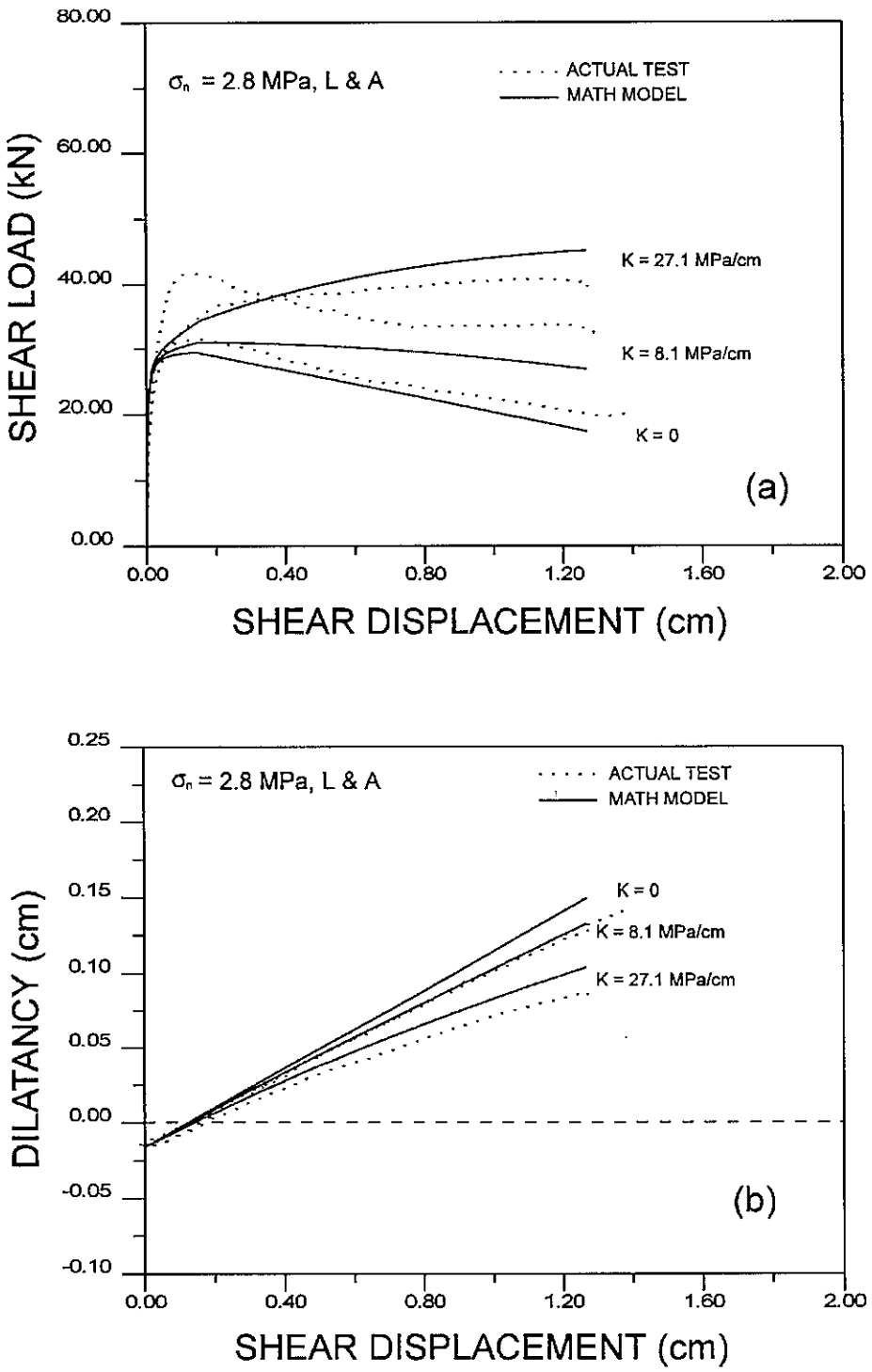

Figure 25. Predicted and observed shear load vs. shear displacement curves, dilatancy curves and shear load vs. normal load paths in (a)-(c), respectively, for K=0, 8.1, and 27.1 MPa/cm, k_3=0.58 and tan(i_{avo})=0.15. Samples F4, first shear cycle forward motion with initial normal stress =2.8 MPa. The mathematical model is based on Ladanyi and Archambault's criterion.

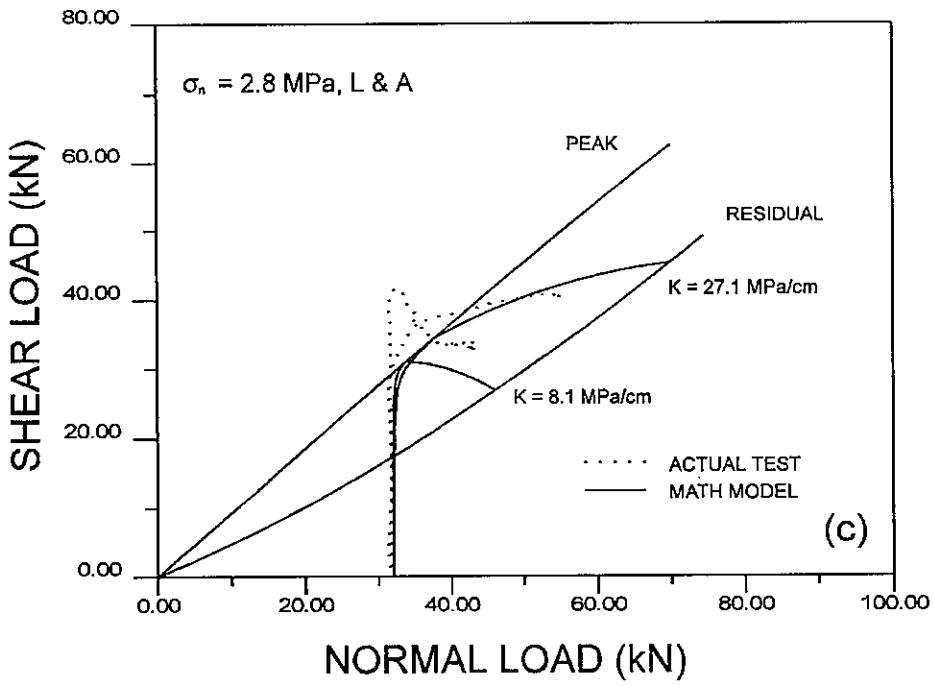

Figure 25 (continued)

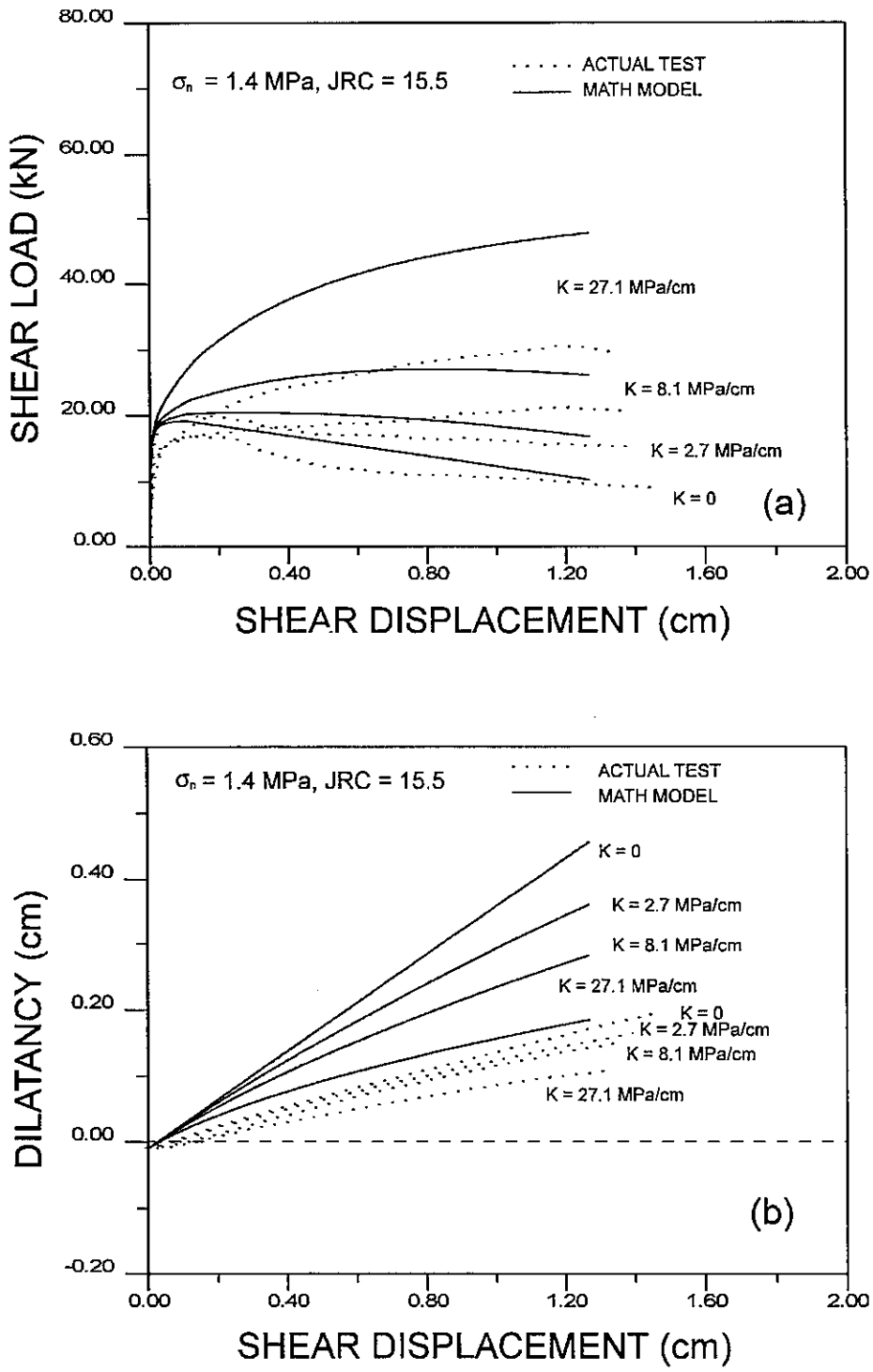

Figure 26. Predicted and observed shear load vs. shear displacement curves, dilatancy curves and shear load vs. normal load paths in (a)-(c), respectively, for K=0, 2.7, 8.1, and 27.1 MPa/cm and JRC=15.5. Samples F4, first shear cycle forward motion with initial normal stress = 1. 4 MPa. The mathematical model is based on Barton's criterion.

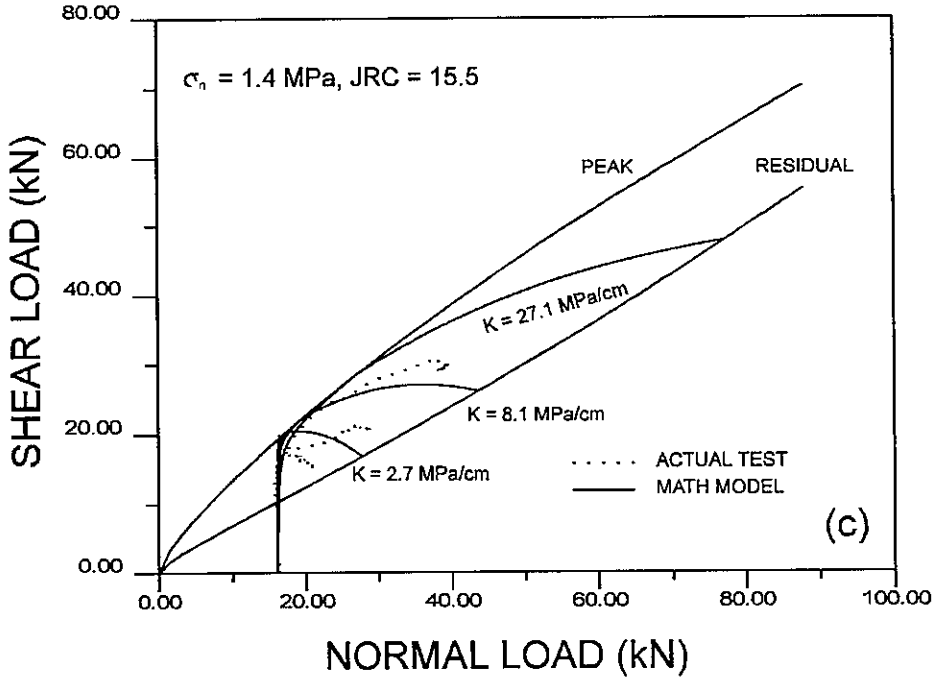

Figure 26 (continued).

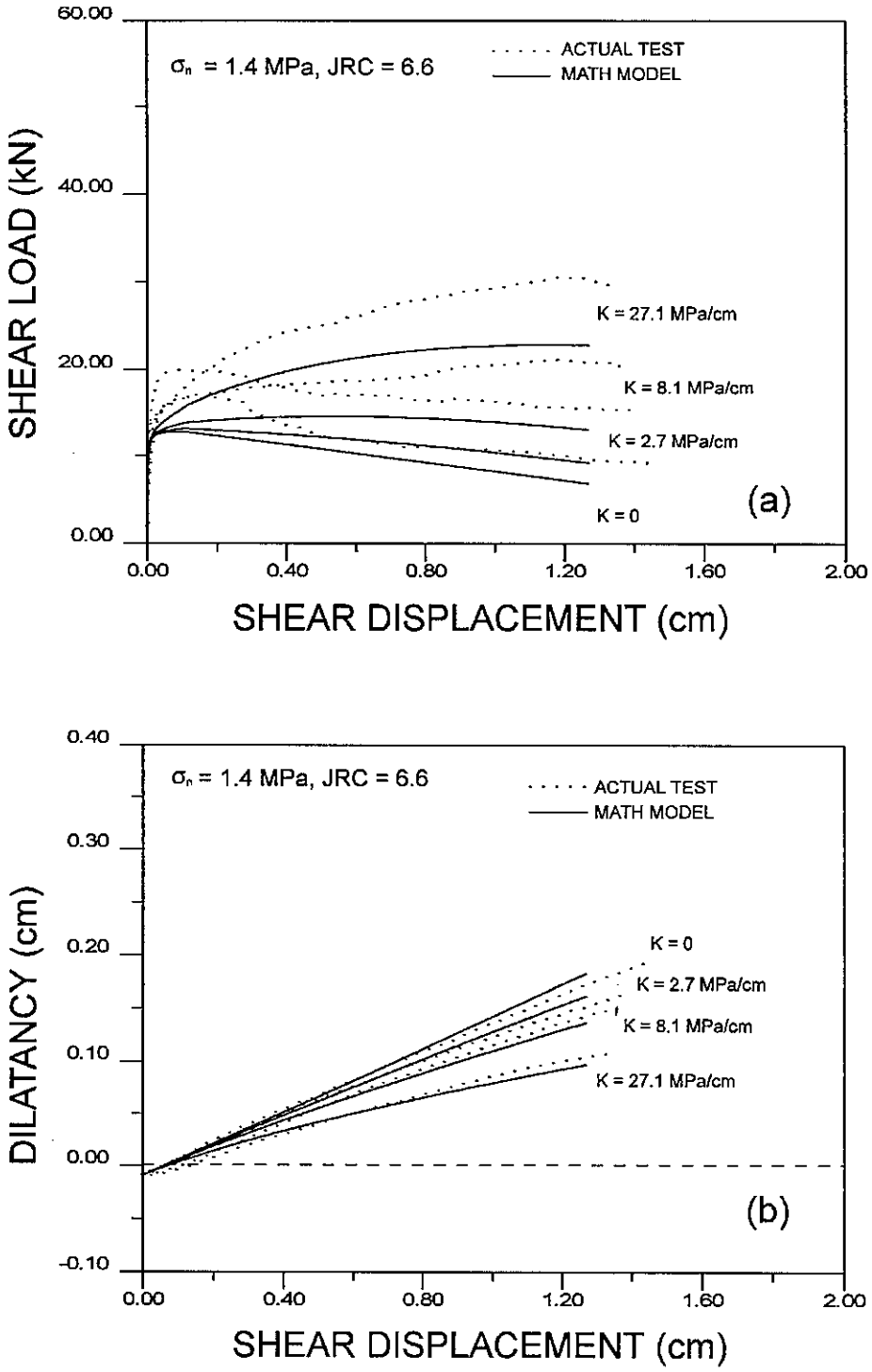

Figure 27. Predicted and observed shear load vs. shear displacement curves, dilatancy curves and shear load vs. normal load paths in (a)-(c), respectively, for K=0, 2.7, 8.1, and 27.1 MPa/cm and JRC=6.6. Samples F4, first shear cycle forward motion with initial normal stress = 1.4 MPa. The mathematical model is based on Barton's criterion.

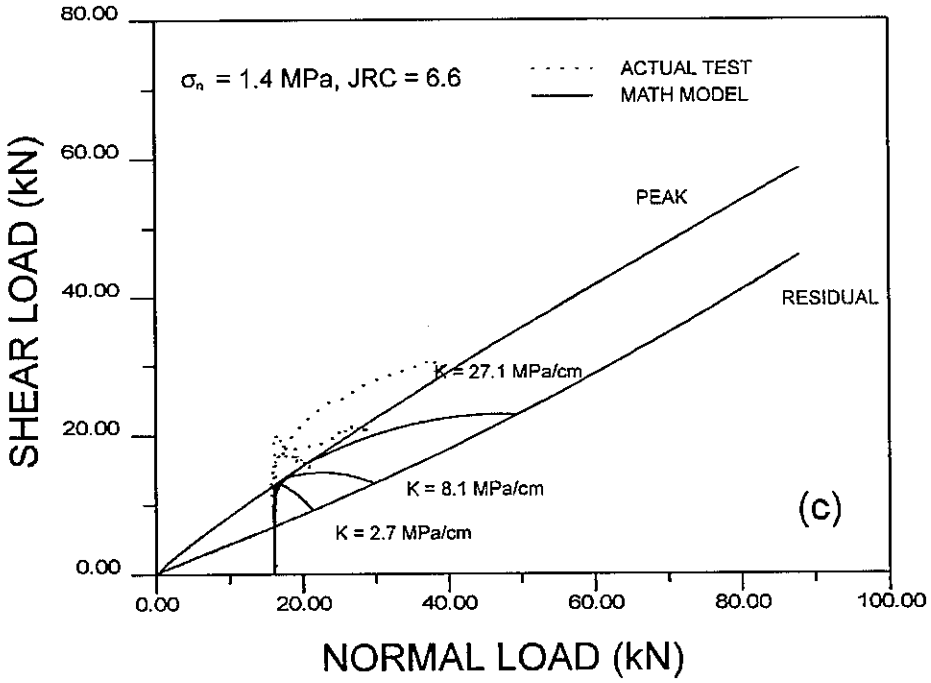

Figure 27 (continued).

Table 1. Experiment schedule for F4 specimens.

Sample	Normal Load (kN)	Init. Normal Stress (MPa)*	Const. Stiffness (kN/cm)
R1F4	3.2	0.3	0
R2F4	16.0	1.4	0
R3F4	32.0	2.8	0
R4F4	48.0	4.1	0
R5F4	64.0	5.5	0
R6F4	48.0	4.1	0
R8F4	48.0	4.1	0
R13F4	16.0	1.4	0
KR7F4	16.0	1.4	31.5
KR9F4	16.0	1.4	94.6
KR10F4	16.0	1.4	315.1
KR11F4	32.0	2.8	94.6
KR12F4	32.0	2.8	315.1

* Area = 116.1 cm^2

Note that in Table:

- R6F4 and R8F4 are repetitions of R4F4; a shear test under constant normal load of 48.0 kN. This was done to observe the reproducibility of the testing procedure and the sensitivity of the shear apparatus.

- R13F4 is a repetition of R2F4; a shear test under constant normal load of 16.0 kN. However, shearing was started in the opposite direction.

Table 2. Peak and residual shear loads for F4 samples, constant normal load, forward direction.

Cycle	Constant Normal Load (kN)	Peak Shear Load (kN)	Residual Shear Load (kN)	Shear Stiffness (kN/cm)
1st Forward	3.2	5.1	2.4	175.1
	16.0	16.9	8.9	1371.2
	32.0	31.4	19.7	2091.0
	48.0	48.1	32.5	1453.5
	64.0	60.9	40.9	1619.9
2nd Forward	3.2	3.3	2.0	
	16.0	10.2	7.7	
	32.0	20.1	17.9	
	48.0	32.8	29.5	
	64.0	40.3	37.0	
3rd Forward	3.2	2.5	2.0	
	16.0	9.0	7.6	
	32.0	18.3	17.4	
	48.0	30.6	29.4	
	64.0	38.5	35.7	
4th Forward	3.2	2.3	2.0	
	16.0	8.5	7.2	
	32.0	17.4	16.9	
	48.0	29.6	28.9	
	64.0	38.6	35.5	
5th Forward	3.2	2.2	2.5	
	16.0	8.2	7.4	
	32.0	17.1	16.7	
	48.0	29.3	28.8	
	64.0	38.2	35.5	

Table 3. Peak and residual shear loads or shear loads at 1.0 cm of shear displacement for F4 samples, constant normal stiffness, forward direction.

Cycle	Initial Normal Load (kN)	Constant Normal Stiffness (kN/cm)	Peak Shear Load (kN)	Residual Shear Load (kN)	Shear Load at 1.0 cm of Shear Displ. (kN)
1st Forward	16.0	31.5	20.1	15.2	
	16.0	94.6			20.7
	16.0	315.1			29.3
	32.0	94.6	41.7	32.5	
	32.0	315.1			40.7
2nd Forward	16.0	31.5			13.6
	16.0	94.6			17.4
	16.0	315.1			21.8
	32.0	94.6			29.3
	32.0	315.1			32.0
3rd Forward	16.0	31.5			13.0
	16.0	94.6			16.1
	16.0	315.1			20.7
	32.0	94.6			28.5
	32.0	315.1			30.0
4th Forward	16.0	31.5			12.8
	16.0	94.6			15.4
	16.0	315.1			20.1
	32.0	94.6			28.3
	32.0	315.1			28.8
5th Forward	16.0	31.5			12.4
	16.0	94.6			15.1
	16.0	315.1			19.1
	32.0	94.6			28.2
	32.0	315.1			-

Table 4. Slope of dilatancy curves (*tan i*) for F4 samples, constant normal load tests.

	Initial Normal Load (kN)	tan i 1st cycle	tan i 2nd cycle	tan i 3rd cycle	tan i 4th cycle	tan i 5th cycle
Forward Shear	3.2	0.14	0.12	0.12	0.11	0.11
	16.0	0.14	0.13	0.13	0.13	0.13
	32.0	0.11	0.11	0.10	0.09	0.09
	48.0	0.10	0.10	0.09	0.09	0.08
	64.0	0.08	0.07	0.07	0.07	0.06
Reverse Shear	3.2	0.14	0.14	0.14	0.14	0.14
	16.0	0.11	0.11	0.11	0.11	0.11
	32.0	0.08	0.08	0.08	0.07	0.07
	48.0	0.09	0.08	0.08	0.08	0.07
	64.0	0.07	0.06	0.06	0.05	0.05

Table 5. Slope of dilatancy curves (*tan i*) for F4 samples, constant normal stiffness tests.

	Initial Normal Load (kN)	Constant Normal Stiffness (kN/cm)	tan i 1st cycle	tan i 2nd cycle	tan i 3rd cycle	tan i 4th cycle	tan i 5th cycle
For-ward Shear	16.0	31.5	0.13	0.12	0.11	0.11	0.11
	16.0	94.6	0.13	0.12	0.11	0.11	0.11
	16.0	315.1	0.10	0.09	0.08	0.08	0.08
	32.0	94.6	0.12	0.11	0.10	0.10	0.10
	32.0	315.1	0.08	0.08	0.08	0.07	
Re-verse Shear	16.0	31.5	0.11	0.11	0.11	0.10	0.10
	16.0	94.6	0.10	0.10	0.09	0.09	0.09
	16.0	315.1	0.08	0.09	0.08	0.08	0.08
	32.0	94.6	0.08	0.09	0.08	0.08	0.08
	32.0	315.1	0.06	0.06	0.06	0.06	-

Table 6. Maximum closure and initial normal stiffness for samples F3.

	Sample	Maximum Closure V_m ($x10^{-2}$ cm)	Initial Normal Stiffness k_{ni} (x 10^2 MPa/cm)
Before Shear		0.5	5.1
After Shear	R1F3	2.3	3.5
	R6F3	3.3	3.2
	R4F3	0.5	5.4
	R5F3	3.0	3.2
	KR7F3	8.1	2.4
	KR8F3	1.3	5.1
	KR9F3	6.1	1.6
	KR10F3	6.1	2.2
	KR11F3	6.3	2.2

Table 7. Variation of coefficients *a* and *b* for samples F4, F3, F2, and G2. Forward and reverse parts of the first shear cycle.

Sample	1st cycle Forward Motion			1st cycle Reverse Motion		
	Coeff. a (cm)	Coeff. b (cm/MPa)	Coeff. of Corr.	Coeff. a (cm)	Coeff. b (cm/MPa)	Coeff. of Corr.
F4	0.064	0.029	0.93	0130	0.001	0.31
F3	0.000	0.036	0.98	0.041	0.035	0.97
F2	0.041	0.014	0.86	0.064	0.008	0.56
G2	0.114	0.050	0.99	0.612	0.072	0.88

Table 8. Range of u_p/L for samples F4, F3, F2, and G2.

Sample	Range of u_p/L
F4	0.003 - 0.014
F3	0.001 - 0.016
F2	0.003 - 0.009
G2	0.006 - 0.047

Table 9. Variation of coefficients *c* and *d* for samples F4, F3, F2, and G2. Forward part of the first shear cycle.

Sample	1st cycle Forward Motion		
	Coeff. c (MPa/cm)	Coeff. d (1/cm)	Coeff. of Corr.
F4	205.4	6.57	0.84
F3	167.4	7.10	0.87
F2	162.6	4.94	0.98
G2	95.4	2.57	0.67

Table 10a. Values of B_o, N_T, σ_T, and σ_T/q_u for samples F4. Forward part of the five shear cycles.

Sample F4	Forward Motion				
Cycle #	B_o	N_T (kN)	σ_T (MPa)	σ_T/q_u	Coeff. of Correlation.
1st	0.48	149.5	12.82	0.47	0.95
2nd	0.66	71.2	6.07	0.22	0.90
3rd	0.81	74.7	6.41	0.23	0.81
4th	0.87	87.2	7.45	0.27	0.63
5th	0.90	93.9	8.07	0.29	0.59

Table 10b. Values of B_o, N_T, σ_T, and σ_T/q_u for samples F4. Reverse part of the five shear cycles.

Sample F4	Reverse Motion				
Cycle #	B_o	N_T (kN)	σ_T (MPa)	σ_T/q_u	Coeff. of Correlation
1st	0.57	146.3	12.62	0.46	0.94
2nd	0.80	98.3	8.48	0.31	0.79
3rd	0.84	104.1	8.83	0.32	0.80
4th	0.81	71.2	6.14	0.22	0.83
5th	0.89	90.7	7.79	0.28	0.90

Table 11. Secant, tangential, and average rates of dilatancy for samples F4. Forward and reverse parts of the first shear cycle.

Normal Stress (MPa)	$\tan(i_s)$	$\tan(i_p)$	$\tan(i_{av})$
Forward			
0.3	0.12	0.19	0.14
1.4	0.16	0.16	0.14
2.8	0.12	0.11	0.11
4.1	0.09	0.11	0.10
5.5	0.09	0.08	0.08
Reverse			
0.3	0.16	0.19	0.14
1.4	0.10	0.15	0.11
2.8	0.06	0.08	0.08
4.1	0.07	0.07	0.09
5.5	0.06	0.06	0.07

Table 12. Coefficients k_2 and $tan(i_{po})$ in Ladanyi and Archambault's equation, samples F4.

Sample F4	Forward Motion		Reverse Motion	
Cycle #	k_2	$\tan(i_{po})$	k_2	$\tan(i_{po})$
1st	0.81	0.18	1.14	0.17
2nd	0.73	0.12	0.65	0.10
3rd	0.40	0.10	0.39	0.10
4th	0.25	0.10	0.39	0.10
5th	0.38	0.10	0.49	0.11

Table 13. Comparison between average JRC_{ptd} back-calculated from the dilatancy curves and average JRC_{pr} determined from roughness profiles on samples F4.

	Cycle Motion	JRC_{ptd} (back-calculated from dilatancy curves)	JRC_{pr} (from profiles)
Forward Motion	1st	6.6	6.7
	2nd	4.6	
	3rd	4.6	
	4th	4.6	
	5th	4.6	
Reverse Motion	1st	5.4	
	2nd	4.0	
	3rd	4.5	
	4th	4.7	
	5th	4.6	1.5

Table 14. Coefficients k and i_{po} in Schneider's equation, for samples F4.

Sample F4	Forward Motion		Reverse Motion	
Cycle #	k (MPa^{-1})	i_{po} (degrees)	k (MPa^{-1})	i_{po} (degrees)
1st	8.70	10.8	12.76	10.8
2nd	7.98	7.4	7.69	6.4
3rd	4.79	6.2	4.35	6.0
4th	2.90	5.7	4.64	6.3
5th	4.21	6.0	5.37	6.3

Table 15. Coefficients k and i_{po} in Jing's equation, for samples F4.

Sample F4	Forward Motion		Reverse Motion	
Cycle #	k	i_{po} (degrees)	k	i_{po} (degrees)
1st	0.80	10.3	1.14	9.6
2nd	0.73	6.9	0.66	5.9
3rd	0.39	5.8	0.38	5.8
4th	0.24	5.4	0.40	6.0
5th	0.38	5.8	0.50	6.1

Table 16. Coefficients k_3 and $tan(i_{avo})$ in the proposed dilatancy model for samples F4.

Sample F4	Forward Motion		Reverse Motion	
Cycle #	k_3	$tan(i_{avo})$	k_3	$tan(i_{avo})$
1st	0.58	0.15	0.59	0.12
2nd	0.56	0.13	0.76	0.13
3rd	0.59	0.13	0.76	0.13
4th	0.52	0.12	0.91	0.13
5th	0.69	0.13	0.95	0.13

Table 17. Coefficients k_1 in Ladanyi and Archambault's equation for samples F4, forward and reverse shear motions.

Cycle #	k_1 (forward)	k_1 (reverse)
1st	0.25	0.30
2nd	0.00	0.10
3rd	0.00	0.05
4th	0.00	0.00
5th	0.00	0.00

Table 18. JRC values for samples F4. Forward motion for first shear cycle.

N Load (kN)	JRC_{ps} (τ_p)	JRC_{ptd} (i_p)	JRC_{pr} (profile)	JRC_t (tilt test)
3.2	13.9	5.4	6.7	4.7
16.0	12.7	7.0		
32.0	14.4	6.3		
48.0	18.3	7.6		
64.0	19.4	6.5		
	(av = 15.5)	(av = 6.6)		

A Packing Generation Scheme for the Granular Assemblies with 3D Ellipsoidal Particles

Chung-Yue Wang, Chi-Fong Wang and Jopan Sheng

Department of Civil Engineering
National Central University
Chungli, 32054, Taiwan, R. O. C.

ABSTRACT

Keywords: granule, packing, ellipsoidal particle, contact detection

In this paper, a new generator algorithm and computer program are introduced for 3D numerical simulation of packing configuration in a granular assemblies composed of ellipsoidal particles of different a/b aspect ratios. Each ellipsoidal particle is approximated by the revolution of an ellipse, formed by four connected arcs, about the major axis passing through its centroid. Coordinates of the centroid, direction of the major axis and lengths of major and minor axes are the essential data for the packing generation and associated contact detection. The domain to be filled with particles can be a polyhedron of any shape. The packing program was coded based on a newly proposed scheme which obeying the no inter-penetration kinematics of solid bodies.

A new contact detection algorithm for any two ellipsoids in the packing space is developed. This algorithm is simple but can effectively determine the contact condition and the contact point without solving the simultaneous equations of two ellipsoidal surfaces. By given boundaries of the packing domain, numbers and geometrical information of particles to be generated, the packing location of each particle and the coordinates of contact points together with three dimensional packing graphs can be generated as the outputs.

Simulation results show that this new algorithm can provide a quite reasonable packing model as a required initial input for the analysis of the mechanics of granular material. This generation scheme has potential to be applied to explore the complex 3D behaviors of material composed of discrete particles.

INTRODUCTION

Granular materials are commonly describe as a collection of distinct particles which can displace from one another with some degree of independence and which interact basically through contact mechanisms. The discrete nature of such materials establishes noncontinuous and discrete load transfer behavior which can be related to the material microstructure or fabric [1,2]. Packing fabric measures have included branch vectors, normal contact vectors, coordination or contact numbers, void characterizations, etc. These fabric measures determined primarily by the particle shape, packing geometry, particle material and contact surface conditions. Many researchers [1-7] are continuously working on the linkage of fabric to the mechanical response of particulate media.

Numerical simulation of granular assemblies has been used for some time to gain an insight into micro mechanical behavior and to facilitate development of micromechanics-based constitutive model of discrete materials. Also unlike physical and analytical modeling, numerical simulation can provide essentially any desired piece of information (stresses, strain and detailed micro-mechanical statistics and spatial distribution of fabric parameters) at any time step throughout loading. For any numerical simulation of the behaviors of particulate media, the packing of the granular assembly is required as the essential input configuration. The existence of an automatic packing generator can save the researcher's energy of inputting the geometrical data of the granular congregated medium. The generated packing can also be more similar to the natural material. But, it is worth pointing out that the research on packing thus far have mostly focused on developing disk and sphere-based numerical codes for simplicity. BALL [8], TRUBAL [9], CONBAL [10], GLUE [11] and DISC [12] are some of the available codes for circular shape particles. The main drawback of using monotonous rounded particle system in modeling some real material is the particle rolling can dominate as a deformational mechanism, resulting in very low shear resistance. Therefore, replacing circular shapes with elliptical shapes have been investigated by some researchers [13-17]. However, in order to study the real behaviors of general particle system, the developing of numerical code based on 3D ellipsoidal elements has its own meaning.

In this paper, a packing generation program ELLIPSOID for the granular assemblies with 3D ellipsoidal particles is presented. Based on the 4-arc approximation theory of ellipse as developed by the first author [14], an approximation of ellipsoid is

constructed. A three dimensional contact detection theory of any two ellipsoids in space is developed as the core of any computational method in the particulate mechanics.

APPROXIMATION OF AN ELLIPSOID

The first author has derived a 4-arc approximation method of an ellipse with major and minor axes of length 2a and 2b [14]. In this method, each ellipse is described by four connected arcs with unique outward normal and no singularity at any point on the particle boundary. As shown in the Fig. 1, point C is the centroid of the ellipse, while the points I, J, G, F are the center of radius of arcs KAL, LEM, MBH and HDK respectively. The associate formulae of for this approximation method are summarized as follows (see Fig. 1):

$$\overline{AC} = \overline{CB} = a \tag{1}$$

$$\overline{DC} = \overline{CE} = b \tag{2}$$

$$\overline{CG} = \frac{(a^2 - b^2)\, c + (a^2 + b^2)\, d}{2ac} \tag{3}$$

$$\overline{CF} = \frac{(a^2 - b^2)\, c + (a^2 + b^2)\, d}{2bc} \tag{4}$$

where

$$c = \sqrt{a^2 + b^2} \tag{5}$$

$$d = a - b \tag{6}$$

$$\alpha = \tan^{-1}\left(\frac{\overline{CF}}{\overline{CG}}\right) = \tan^{-1}\left(\frac{a}{b}\right) \tag{7}$$

$$\overline{GB} = \overline{GH} = \overline{GM} = \overline{AI} = \overline{AK} = \overline{AL} = R_1 = a - \overline{CG} \tag{8}$$

$$\overline{FK} = \overline{FD} = \overline{FH} = \overline{JL} = \overline{JE} = \overline{JM} = R_2 = b + \overline{CF} \tag{9}$$

Based on the above fundamental equations, the coordinates of the end points and center of radius of each arc for any ellipse translation from origin with a rotation respect to horizontal axis, can be easily obtained by superimposing the associated rigid body mode.

A special type of ellipsoid with minor axes of equal length (i.e. b=c) can be generated by revolving the major axis of the 4-arc approximated ellipse as shown by the Fig. 2. Therefore, an ellipsoid is formed by two spherical surfaces I, II and a curved surface III. Surfaces I and II are formed by the revolving of arcs KAL and MBH respectively. While the curved surface III is formed by revolving arcs KH and LM about the major axis. A surrounding ring IV with central axis matched the major axis is formed as the trace of the radius centers J, F during the revolving of the 4-arc ellipse. The radius r of this circle IV is equal to the length of CF as expressed by Eq.(4). For an ellipsoid in space as shown by Fig. 3, major axis directed in $\mathbf{n} = (n_x, n_y, n_z)$, the coordinates of a point located on the surrounding ring IV can be derived as

$$x = C_x + r\cos\theta\left(\frac{n_z n_x}{R_{xy}}\right) - r\sin\theta\left(\frac{n_y}{R_{xy}}\right) \tag{10}$$

$$y = C_y + r\cos\theta\left(\frac{n_z n_y}{R_{xy}}\right) + r\sin\theta\left(\frac{n_x}{R_{xy}}\right) \tag{11}$$

$$z = C_Z - r R_{xy}\cos\theta \tag{12}$$

where the θ is measured counter clockwise from the point with the minimum z coordinate and

$$R_{xy} = \sqrt{n_x^2 + n_y^2} \tag{13}$$

$$r = \frac{(a^2 - b^2)\sqrt{a^2 + b^2} + (a^2 + b^2)(a - b)}{2b\sqrt{a^2 + b^2}} \tag{14}$$

Since any point on the ellipsoidal surface has an arc passing through it, the contact detection of any two ellipsoids in the packing space can be easily conducted by checking the distance between the corresponding radius centers. This is the main feature of our contact detection scheme which is different from the way of solving geometric equations of 3D ellipsoidal to detect contacts as some researchers proposed.

CONTACT DETECTION

The contact conditions of ellipsoidal particles inside a container can be identified as the following five conditions:

(1) spherical surface (I or III) of a particle contacts a plane (Fig. 4a),

(2) curved surface (II) of a particle contacts a plane (Fig. 4b),

(3) spherical surface (I or III) of a particle contacts the spherical surface (I or III) of another particle (Fig. 4c),

(4) spherical surface (I or III) of a particle contacts the curved surface (II) of another particle (Fig. 4d),

(5) curved surface (II) of a particle contacts the curved surface (II) of another particle (Fig. 4e).

The contact detection between two spherical surfaces can be made by comparing the distance between centers with the sum of the radius of the two spheres. While the contact detection between a sphere and a plane can be conducted by checking the distance of the spherical center to the plane with the radius of the sphere. Any three dimensional contact detection related to the curved surface II is somewhat complicated. It can be seen that the curved surface is composed of many arcs with different radius centers. If we can find which arc on this surface will contact with other arc or plane, then the contact detection can be proceeded by comparing the distance between the center of this arc and the other arc center or plane with the impenetrability condition. The contact detection methods between surfaces relating curved surface are discussed in the following sections.

Contact Detection Between Two Curved Surfaces

Fig. 5 shows two curved surfaces from separate ellipsoids in the packing space contact at point P. There is only one tangent plane passing through point P for both curved surfaces. Since both vector AP and vector BP normal to this tangent plane, one can conclude that the points A, P and B are on a straight line. Points G and H are the

intersection points of line AB with major axis of the ellipsoid, respectively. The point A and point B are the centers of the arc passing point P on each curved surface. According to the Eqs. (10)-(14), the location of point A (or point B) on the surrounding ring can be determined by only one parameter θ_A (or θ_B). The length of the line AC_1 is equal to the radius of the surrounding arc. Hence, one can understand that the planes AGC_1 and plane BHC_2 are on a plane. From these two properties, we have the following two vector equations to find the coordinates of the points A and B:

$$(\overrightarrow{AC_1} \times \overrightarrow{n_1}) \bullet \overrightarrow{AB} = 0 \tag{15}$$

$$(\overrightarrow{BC_2} \times \overrightarrow{n_2}) \bullet \overrightarrow{AB} = 0 \tag{16}$$

After applying the Eqs. (10)-(14) into the Eqs. (15)-(16), a set of nonlinear simultaneous equations of the following form are obtained.

$$\begin{aligned} &a_1 \cos\theta_A + a_2 \sin\theta_A + a_3 \sin\theta_A \sin\theta_B + a_4 \sin\theta_A \cos\theta_B \\ &+ a_5 \cos\theta_A \sin\theta_B + a_6 \cos\theta_A \cos\theta_B = 0 \end{aligned} \tag{17}$$

$$\begin{aligned} &b_1 \cos\theta_B + b_2 \sin\theta_B + b_3 \sin\theta_A \sin\theta_B + b_4 \sin\theta_A \cos\theta_B \\ &b_5 \cos\theta_A \sin\theta_B + b_6 \cos\theta_A \cos\theta_B = 0 \end{aligned} \tag{18}$$

where the coefficients a_i, b_i ($i = 1,6$) are constants determined by the directional cosines of vectors $\mathbf{n}_1$ and $\mathbf{n}_2$ of the major axes, coordinates of the centroid of both ellipsoids and the radii of the surrounding rings.

Instead of solving these nonlinear equations for θ_A and θ_B, we used the following iteration method to find the positions of A and B on each surrounding ring. As shown by the Fig. 6, it can be seen that A is the point farthest from the contact point P. The same conclusion is for point B on the other surrounding ring. Since points A, P and B are in a line, then we can prove that the distance between points A and B in the Fig. 5 is the largest one among any pair of points selected separately from those surrounding rings. An iterative method is used to find the pair of points with largest distance. First we choose three points on each ring with 120 degree divided angle. Then, there are 9 combinations to be evaluated to find the pair ($A^{(1)}$, $B^{(1)}$) with largest distance. In the second iteration step, we find another two points on each ring by adding and subtracting 60 degree from the

coordinate $\theta_{A(1)}$ (or $\theta_{B(1)}$) just obtained. Therefore, the pair of points with largest distance needs to be picked out from these 9 new combinations. After few iterations, it will converge to two points with absolute largest distance For n iteration steps were proceeded, the error is equal to $\pm 60 / (2^{(n-1)})$ degree. The value of the largest distance obtained will compare with the sum of the radii of the two rings to check whether these two ellipsoids contact or not.

Contact Detection of a Curved Surface with a Spherical Surface

Fig. 8 shows the contact between a spherical surface of ellipsoid C1 and the curved surface of the ellipsoid C2. The point Z is the center of the sphere and the P is the contact point of these two ellipsoids. It is seen that points B, P and Z are on the same line and point B is the point on the surrounding ring having largest distance with point Z. Using the iterative method as mentioned in the previous section, the location of point B can be found. The existence of contact condition can be determined by comparing the distance between points Z and B with the sum of the radius of the sphere and the radius of the surrounding ring.

Contact Detection of a Curved Surface with a Plane

Fig. 7 shows the ellipsoid contacts a plane at point P. Point C is the centroid of the ellipsoid and the θ is the angle between the normal vector **N** of the plane and the direction vector **n** of the major axis of the ellipsoid. From the Fig. 8, it can be derived that when the ellipsoid having contact with a plane, the distance between the centroid and the plane is equal to

$$\overline{CH} = b + \frac{(a^2 - b^2)\sqrt{a^2+b^2} + (a^2+b^2)(a-b)}{2b\sqrt{a^2+b^2}}(1 - \sin\theta) \tag{19}$$

Then, the contact detection criterion for the curved surface with a plane is by checking the distance between the centroid and the plane with the value obtained from Eq. (19).

Determination of the Contact Detection Type

Since there are five types of contact condition that an ellipsoid may admit during the packing or motion. It is necessary to set up some rules for analysts to determine which contact detection type is the one needed further evaluation in order to accelerate the

simulation speed. Followings are the summarized rules for the determination of contact detection type:

(I) Contact with plane

If θ is defined as the angle between the direction vector **n** of the major axis and the normal vector **N** of the plane (see Fig. 8), then

(a) when $\theta > \alpha$, the curve surface of the ellipsoid contacts with the plane,

(b) when $\theta < \alpha$, the spherical surface of the ellipsoid contacts the plane.

(II) Contact between two ellipsoids

For any two ellipsoids in space, the points A and B located on the surrounding ring of separate ellipsoid, with farthest distance can be determined first. Hence, the angle between the major axis direction and the line AB of each ellipsoid can be calculated (see Fig. 9), then

(a) when $\theta_1 > \alpha_1$ and $\theta_2 > \alpha_2$, the curved surface of ellipsoid-1 contacts the curved surface of ellipsoid-2.

(b) when $\theta_1 > \alpha_1$ and $\theta_2 < \alpha_2$, the curved surface of ellipsoid-1 contacts the spherical surface of ellipsoid-2.

(c) when $\theta_1 < \alpha_1$ and $\theta_2 > \alpha_2$, the spherical surface of ellipsoid-1 contacts the curved surface of ellipsoid-2.

(d) when $\theta_1 < \alpha_1$ and $\theta_2 < \alpha_2$, the spherical surface of ellipsoid-1 contacts the spherical surface of ellipsoid-2.

IMPLEMENTATION AND EXAMPLE

Based on the theories developed in the previous sections, a computer simulation code ELLIPSOID applying the Auto-CAD -Release 12 version was coded. This program contains the following subroutines:

(1) Formation of ellipsoids with different sizes, direction angles, initial translation velocities and angular velocities;

(2) Particles moving (translating and rotating) in the packing space;

(3) Contact detections;

(4) Rest the new coming particle on a packing position by checking the stabilization criteria;

(5) Find the velocity vector and angular velocity vector for unstable particle after each impact;

(6) Output the data (centroid coordinates, direction vectors of major axes, particle sizes and coordinates of contact points);

(7) Graphic display.

Fig. 10 to Fig. 11 show the packing process and final result of 50 ellipsoids inside a box. The packing state can be viewed from different angles. From these figures, it seems that the ELLIPSOID code can generate a reasonable packing configuration.

CONCLUSIONS

A packing scheme for 3D ellipsoidal particles is presented in this paper. The ellipsoids are formed by revolving 4-arc approximated ellipse about its major axis. All the contact detection is based on the comparison of distance between arcs and the associated impenetrability condition. Methods of finding the corresponding arcs to check whether contact or not are presented in detail. These methods are very efficient compared with solving highly nonlinear geometrical equations of ellipsoids in 3D space. Packing of ellipsoids with different shapes and sizes can be generated within a given space. The generated packing configuration can be used as the initial state for the numerical analysis of granular material behaviors.

ACKNOWLEDGEMENTS

This research was supported by the National Science Council, Taiwan, R. O. C. under Grant NSC-86-2815-C008-005E. This support is gratefully acknowledged.

REFERENCES

1. Oda, M.; S. Nemat-Nasser and M. M. Mehrabadi, " A Statical Study of Fabric in a Random Assembly of Spherical Granules," Journal for Numerical and Analytical Methods in Geomechanics, Vol. 6, pp. 77-94 (1982).
2. Tai, Qiming and M. H. Sadd, " A Discrete Element Study of the Relationship of Fabric to Wave Propagational Behaviours in Granular Materials, " Journal for Numerical and Analytical Methods in Geomechanics, Vol. 21, pp. 295-311 (1997).

4. Bathurst, R. J. and L. Rothenburg, "Micromechanical Aspects of Isotropic Granular Assemblies with Linear Contact Interactions," J. Appl. Mech., 55, pp. 17-23 (1988).
5. Satake, M., "A Discrete-Mechanical Approach to Granular Materials," Int. J. Eng. Sci., 30, pp. 1525-153 (1992).
6. Walton, O. "The Effective Elastic Moduli of a Random Packing of Spheres," J. Mech. Phys. Solids, 35, pp.213-226 (1987).
7. Chang, C. S. and L. Ma, "Modelling of Discrete Granulates as Micropolar Continua," J. Eng. Mech., 116, pp. 213-226 (1987).
8. Strack, O. D. L. and P. A. Cundall "The Distinct Element Method as a Tool for Research in Granular Material," Part II , Report to NSF, University of Minnesota, Minneapolis, Minnesota (1978).
9. Cundall, P. A. and O. D. L. Strack "A Discrete Numerical Model for Granular Assemblies," Geotechnique, 29, No. 1, pp. 47-65 (1979).
10. Ng. T. T. "Numerical Simulation of Granular Soils under Monotonic and Cyclic Loading: A Particulate Mechanics Approach," Ph.D. Dissertation, Department of Civil Engineering, Rensselaer Polytechnic Institute, Troy, NY, U. S. A. (1989).
11. Bathurst, R. J. and L. Rothenburg "Investigation of Micromechanical Features of Idealized Granular Assemblies using DEM," Proceedings, 1st U. S. Conference on Discrete Element Methods, Golden, Colorado, U. S. A. (1989).
12. Ting, J. M.; B. T. Corkum; C. R. Kauffman and C. Greco "Discrete Numerical Model for Soil Mechanics," J. Geotechnical Engineering, ASCE, No. 3, pp. 379-398 (1989).
13. Ng, Tang-Tat and Xiaoshan Lin "Numerical Simulations of Naturally Deposited Granular Soil with Ellipsoidal Elements," Proceedings, 2nd Int. Conf. on Discrete Element Methods (DEM), IESL Publications, pp. 557-567 (1993).
14. Wang, Chung-Yue and Vei-Chung Liang, "A Packing Generation Scheme for the Granular Assemblies with Planar Elliptical Particles," International Journal for Numerical and Analytical Methods in Geomechanics, Vol. 21, pp. 347-358 (1997).
15. Rothenburg, L. and R. J. Bathurst "Numerical Simulation of Idealized Granular Assemblies with Plane Elliptical Particles," Comput. Geotech., 11, pp. 315-329 (1991).
16. Rothenburg, L. and R. J. Bathurst "Micromechanical Features of Granular Assemblies with Planar Elliptical Particles," Geotechnique, 42, pp. 79-95 (1992).

17. Ting, J. M. " A Robust Algorithm for Ellipse-Based Discrete Element Modelling of Granular Materials," Comput. Geotech., 13, pp. 175-186 (1992).

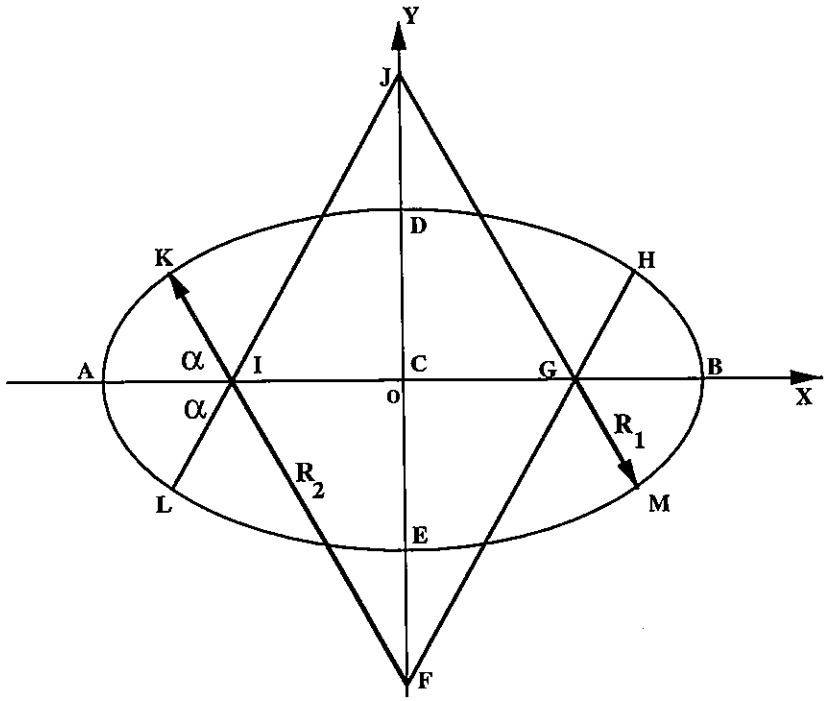

Fig. 1 Approximation of an ellipse by four connected arcs.

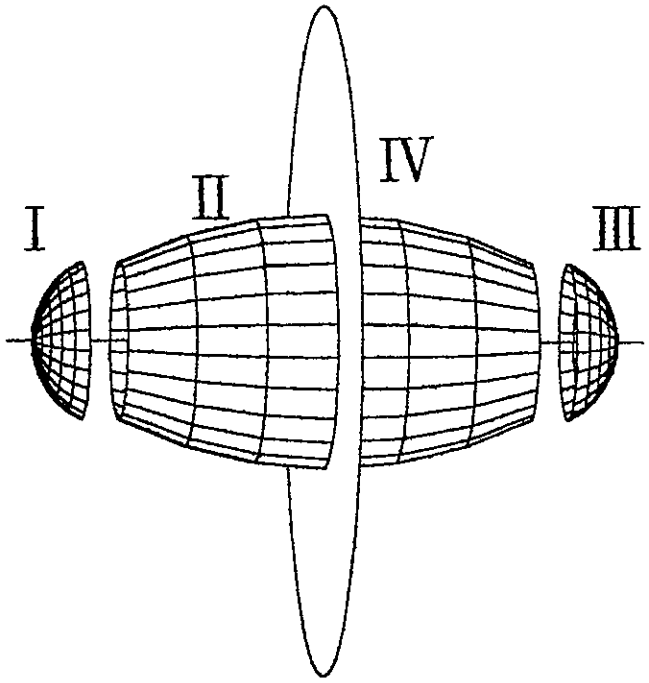

Fig. 2 An ellipsoid formed by revolving the 4-arc approximated ellipse.

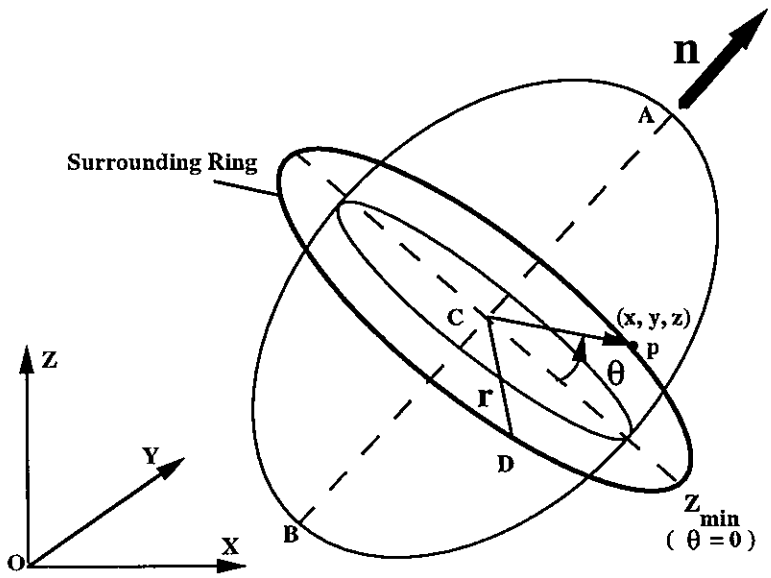

Fig. 3 Cartesian coordinates of a point p located on the surrounding ring of an ellipsoid in space.

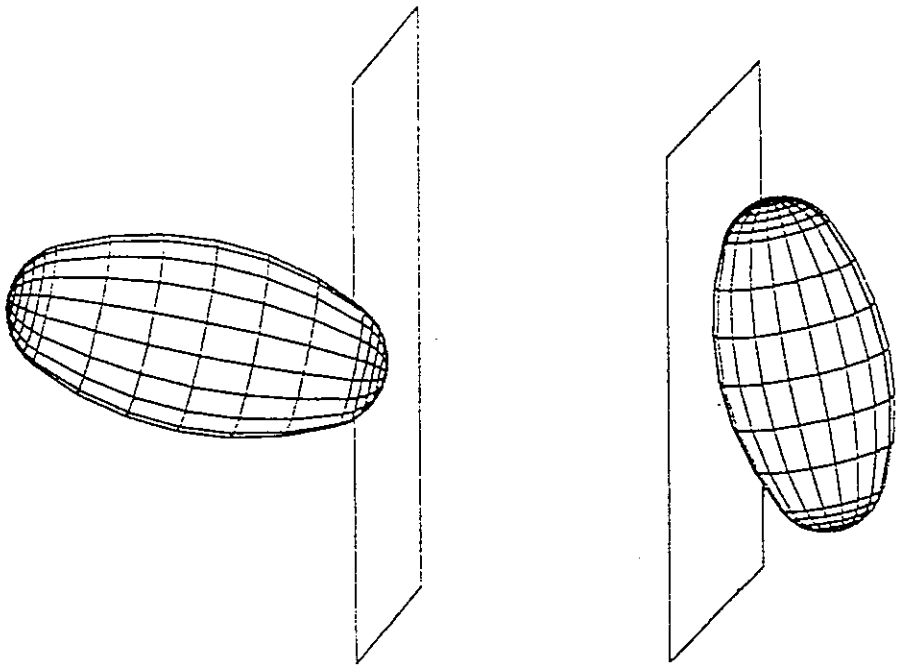

Fig. 4 Contact conditions for particles inside a container, (a) sphere – plane, (b) curved surface – plane,

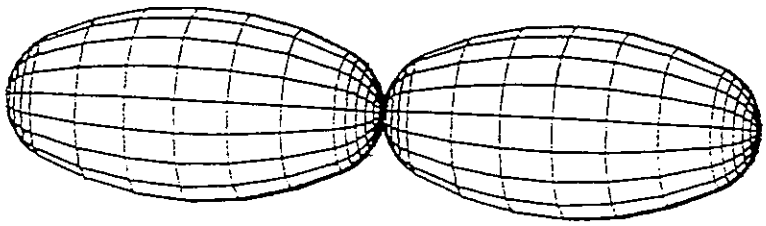

(c)

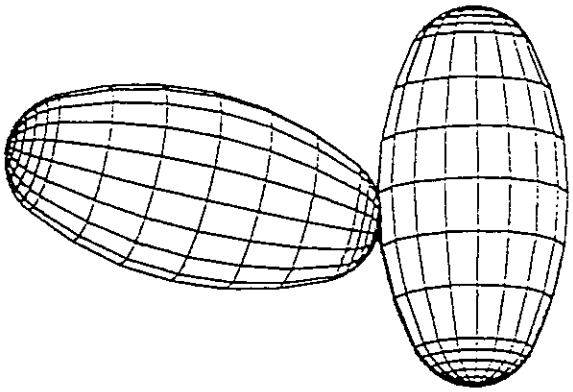

(d)

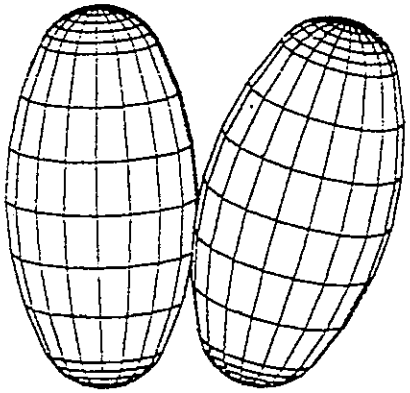

(e)

Fig. 4 Contact conditions for particles inside a container, (c) sphere – sphere, (d) sphere – curved surface, (e) curved surface – curved surface.

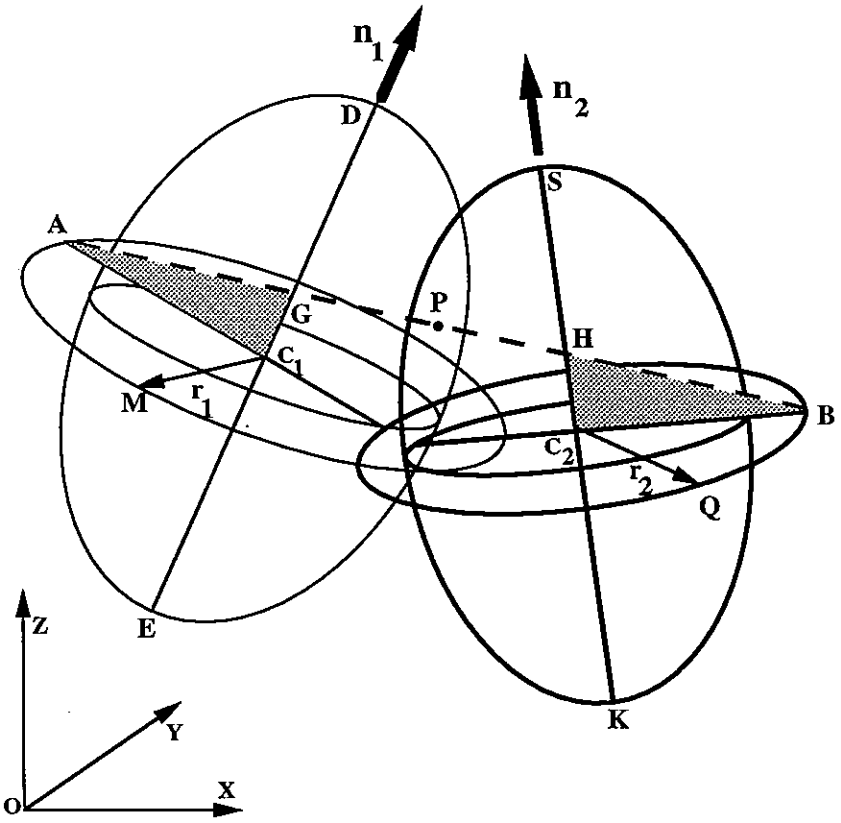

Fig. 5 Co-plane condition of plane AGC_1 and plane BHC_2.

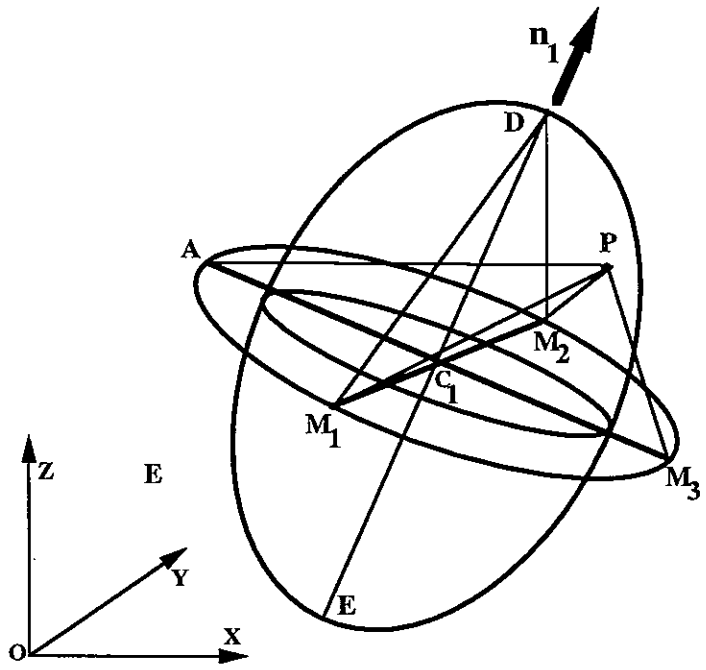

Fig. 6 Point on the surrounding ring having largest distance with the contact point P.

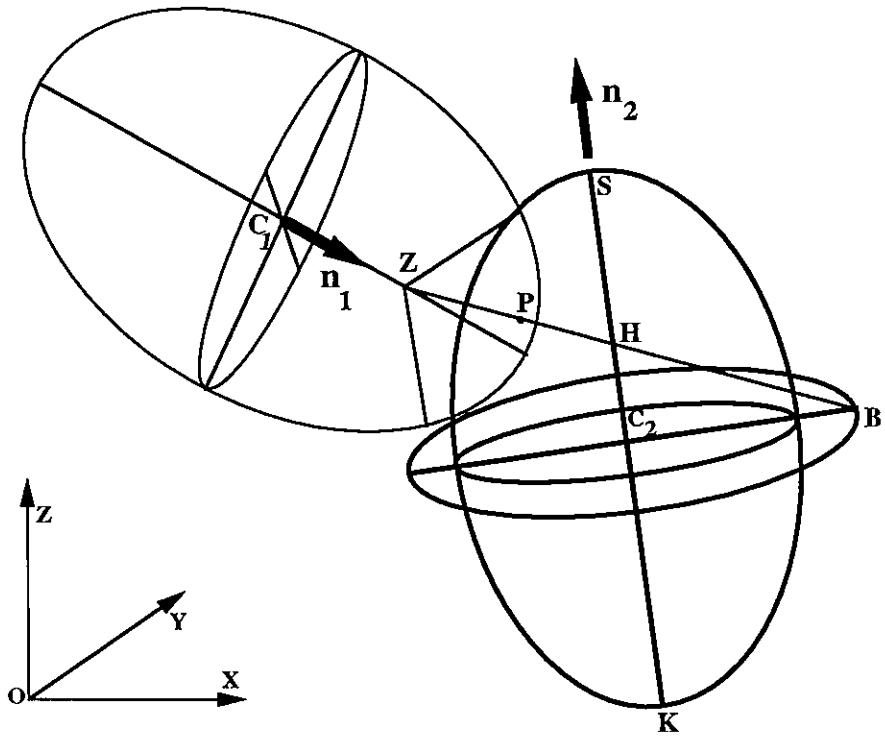

Fig. 7 Contact detection between spherical surface and curved surface.

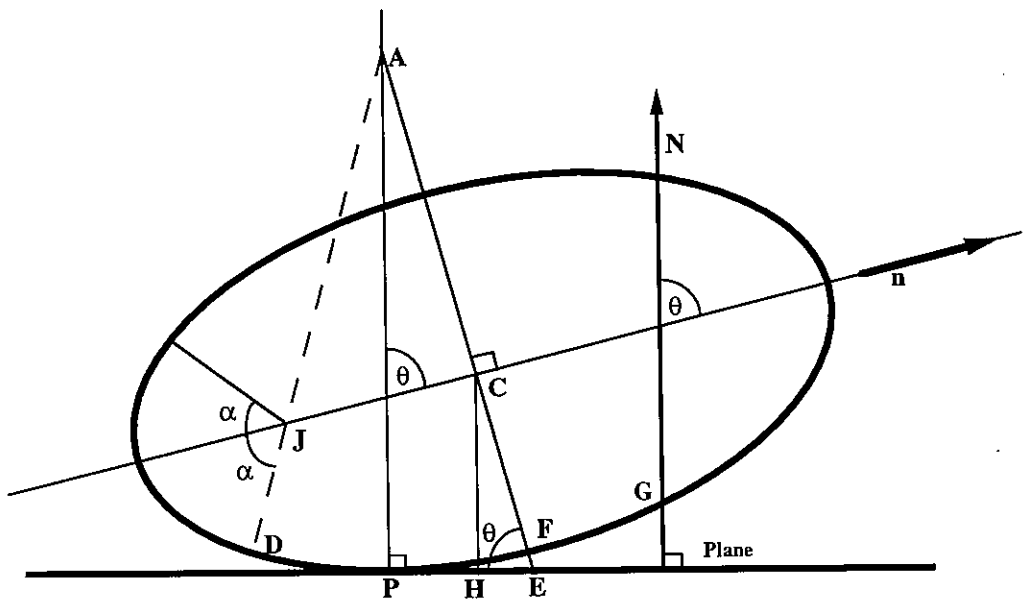

Fig. 8 Contact detection between a curved surface and a plane.

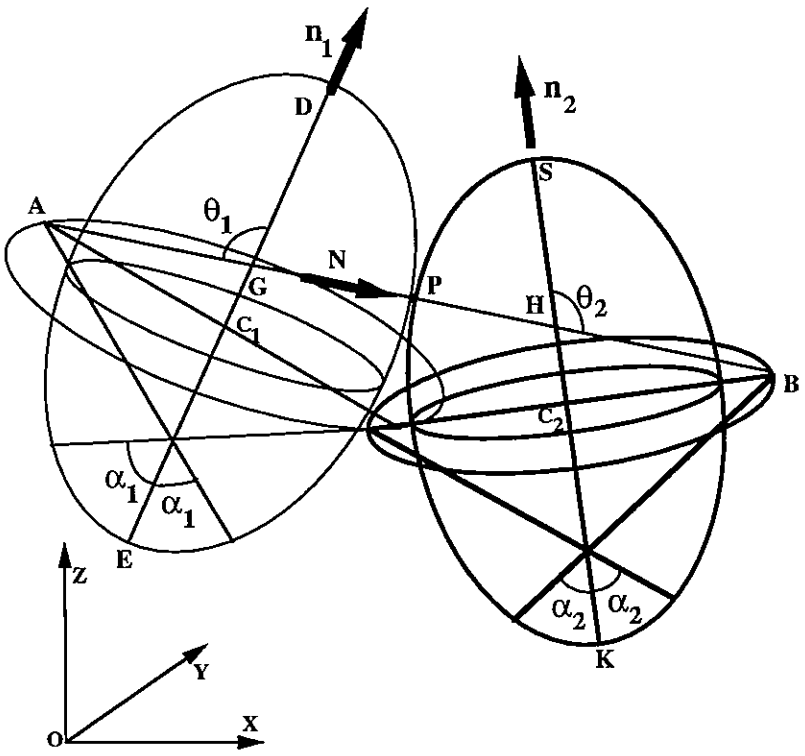

Fig. 9 Angles used for the determination of the contact detection type.

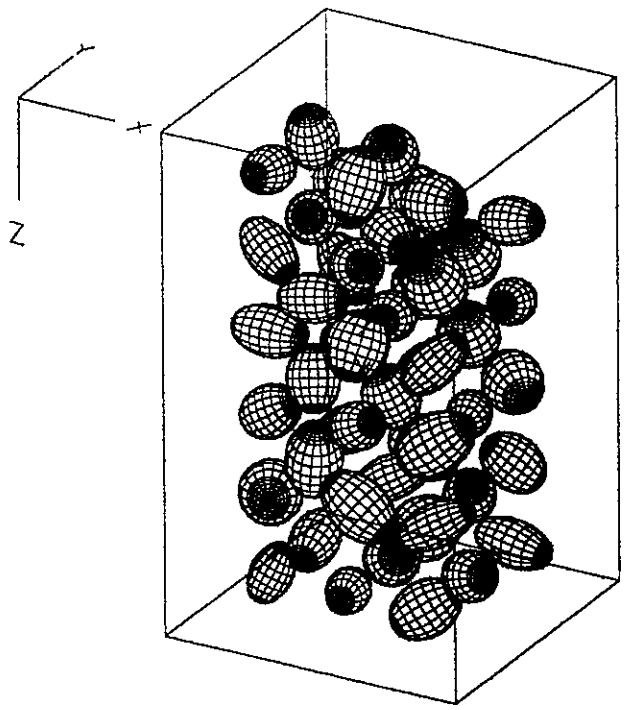

Fig. 10 Initial state of 50 freely droped ellipsoids.

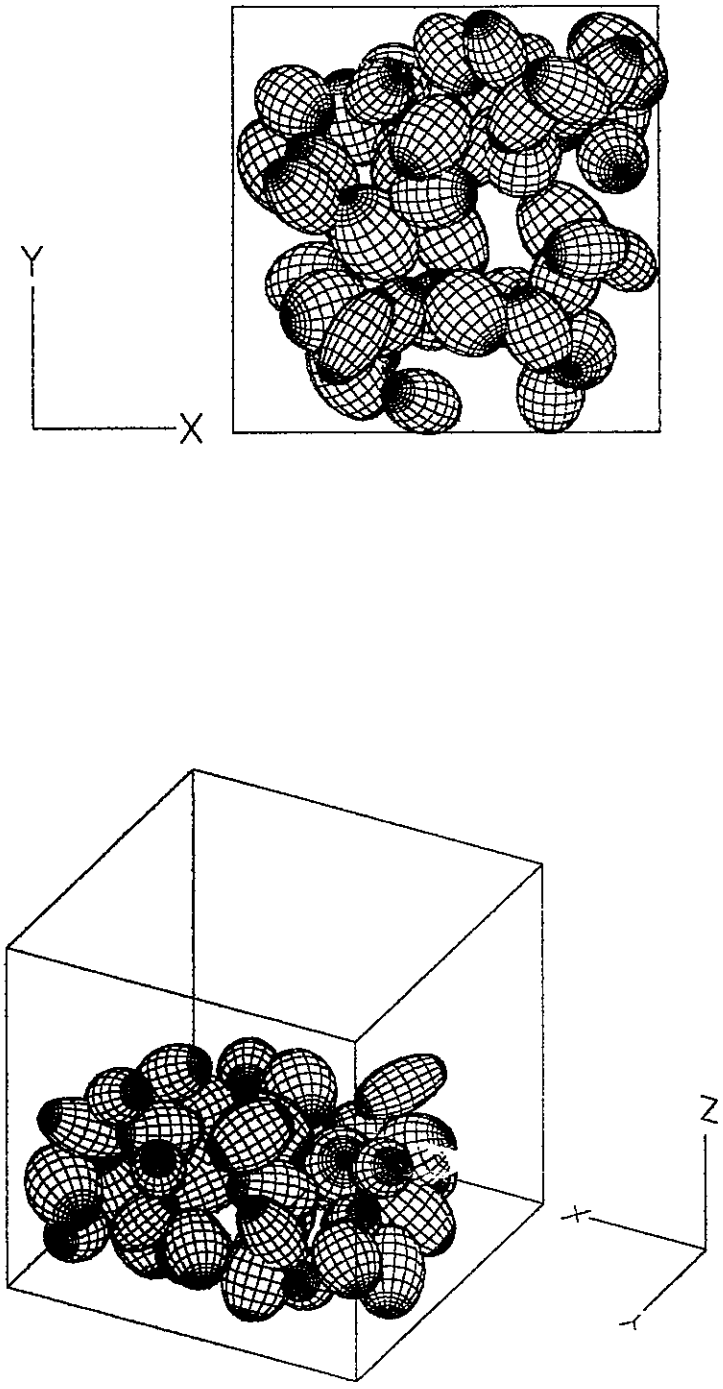

Fig. 11 Final packing states viewed from different angles.

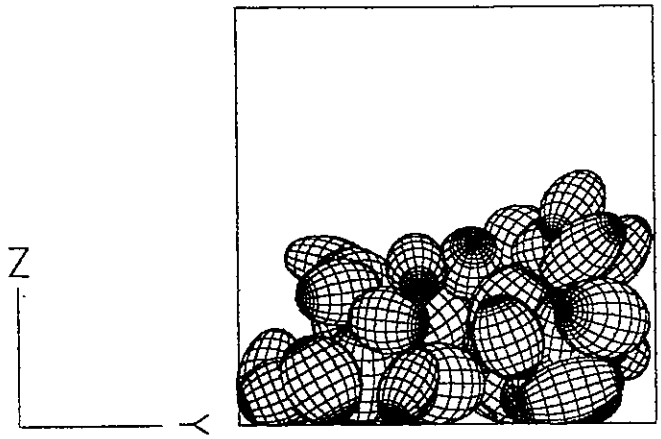

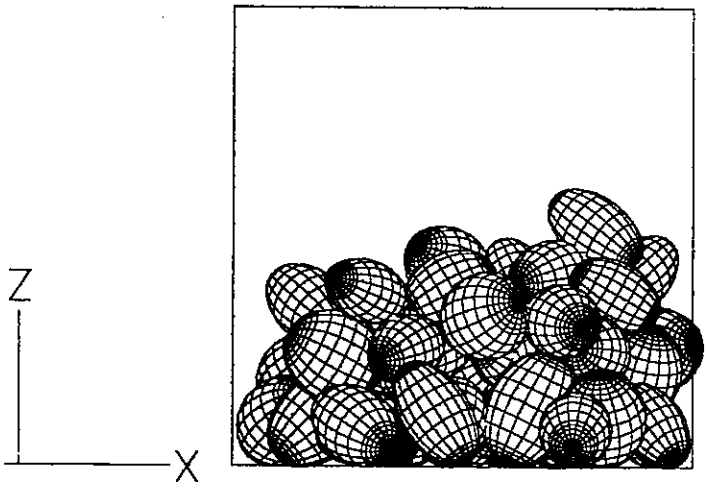

Fig. 11 (continue) Final packing states viewed from different angles .

Simulation of 3-D Concrete-Frame Collapse due to Dynamic Loading

Motohiko Hakuno
Prof., Dept. of Civil and Environmental Engineering, Toyo University
2,100 Kujirai, Kawagoe City, Saitama 350 JAPAN

INTRODUCTION

Iwashita and Hakuno(1990) proposed the extended distinct-element method (EDEM) as a modification of Cundall's distinct-element method by adding pore springs to such pore material as clay between particles or mortar and Hakuno proposed that an aggregate of circular elements and mortar constituent pore springs would satisfy the conditions of fracture . Under these assumptions, we established a model for concrete by setting these pore springs among elements and then followed the fracture process.(Fig.1)

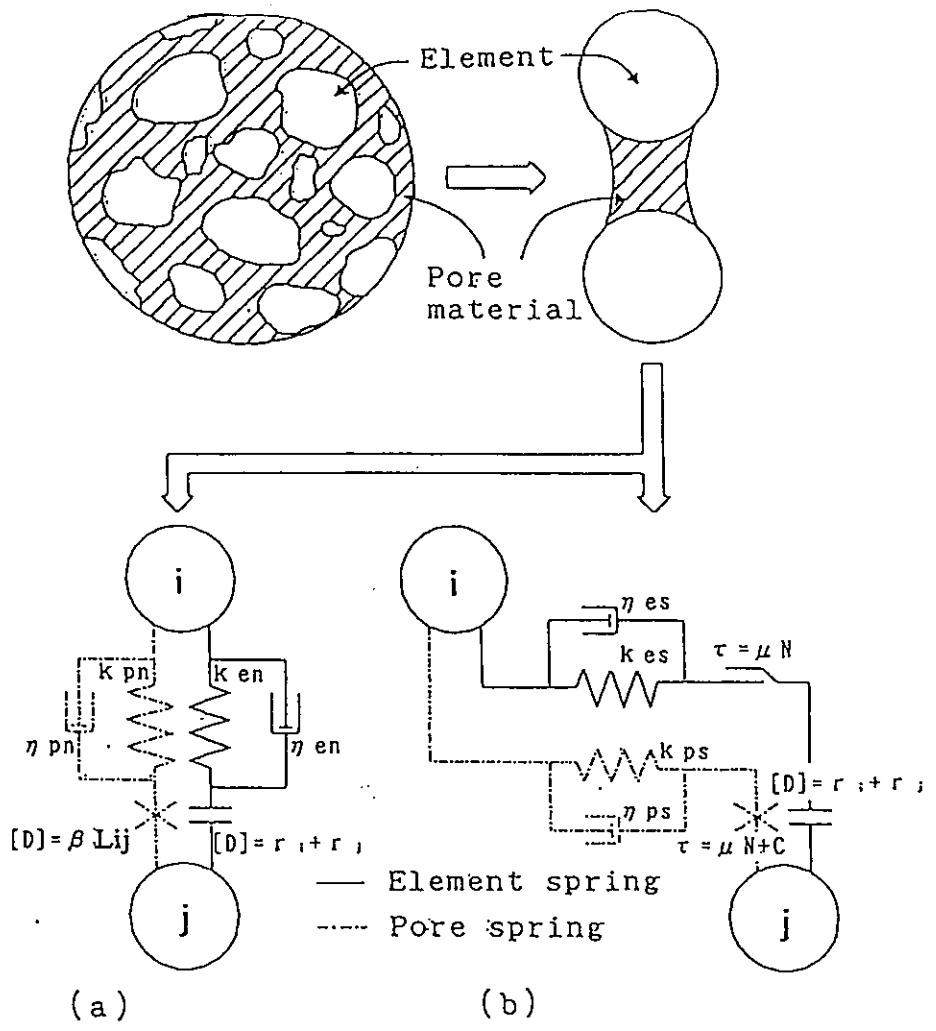

Fig. 1. EDEM Modeling of Concrete: (a)Normal Direction; (b)Tangential Direction

NUMERICAL RESULTS

Case1: Bending Fracture Test of Concrete Specimen

The EDEM was used to simulate a bending fracture test of the concrete specimen modeled in Fig.s 2 and 3. The specimen was bent under a constant rate of deformation. The fracture process during bending is shown in Fig. 4, which also shows the mortar spring distribution and the position of the intact mortar. During stage 1, no cracks occur in the spring locations. Should a crack occur, the mortar spring at the corresponding site would be eliminated. The cracks in Fig.4 are all tensile cracks. Although the test system is completely symmetric, the crack produced is not symmetric. We believe this is because of accumulated computational error due to cancelling for no initial imperfections were prescribed for the pore springs.

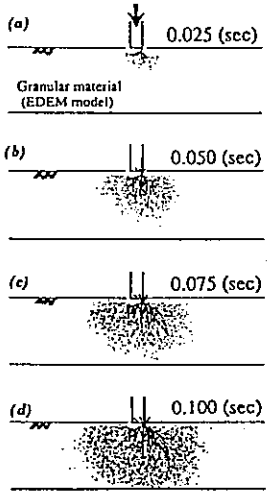

Fig. 2. Propagation of Wave in EDEM Model

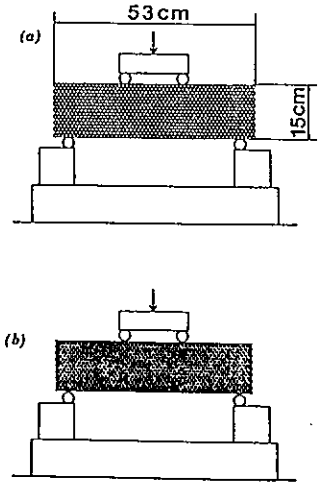

Fig. 3. Model of Concrete Specimen (Bending Test Model): (a)Particle Distribution; (b)Mortar Spring Distribution

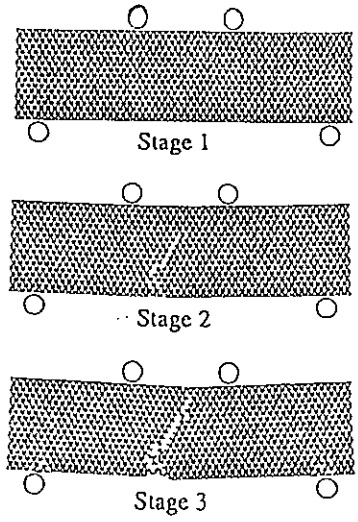

Fig. 4. EDEM Simulation of Bending Test under Vertical, Constant-Rate Deformation(Mortar Spring Distribution)

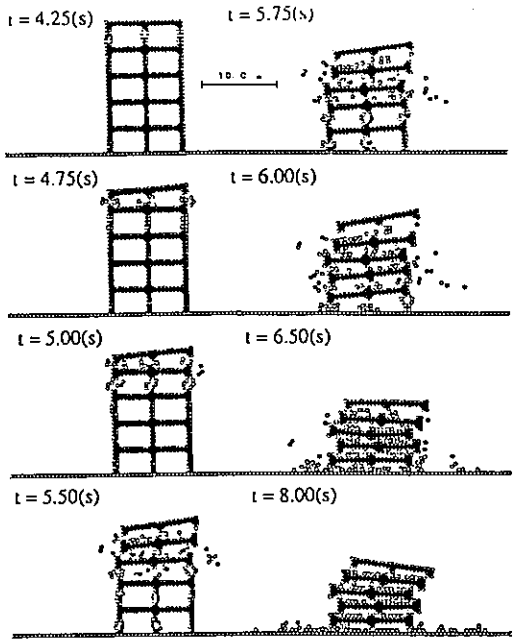

Fig. 5. Upper-Story Fracture and Pancake Collapse of Five-Story Building because of Horizontal Seismic Loading(Element and Pore Spring Distribution)

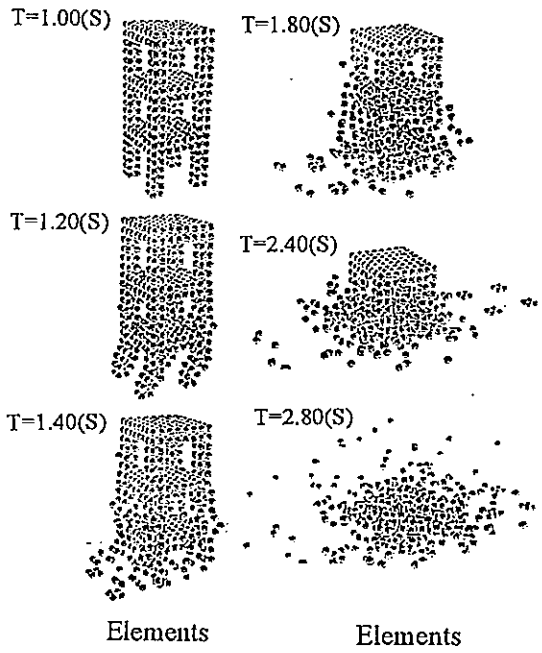

Fig. 6. Complete Collapse of Three-Story Building due to Horizontal Seismic Loading

Case2: Collapse Simulation of Concrete Frames by Horizontal Seismic Oscillation

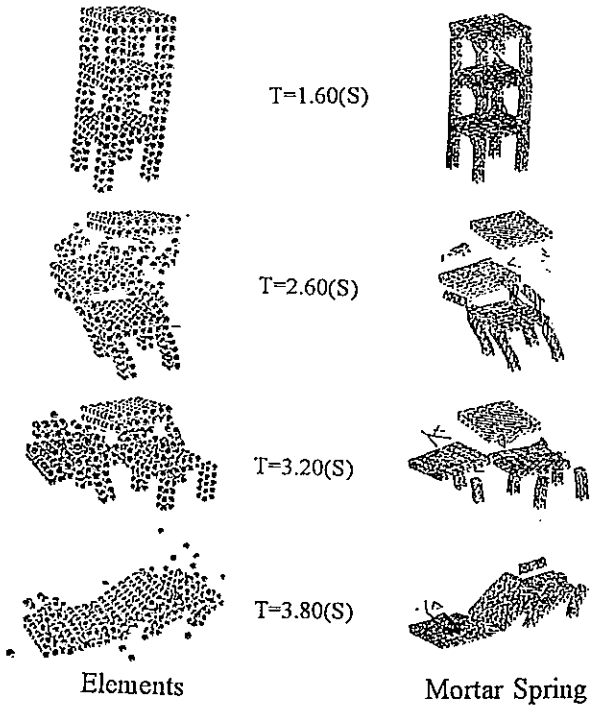

Fig. 7. Pancake Collapse of Three-Story Building

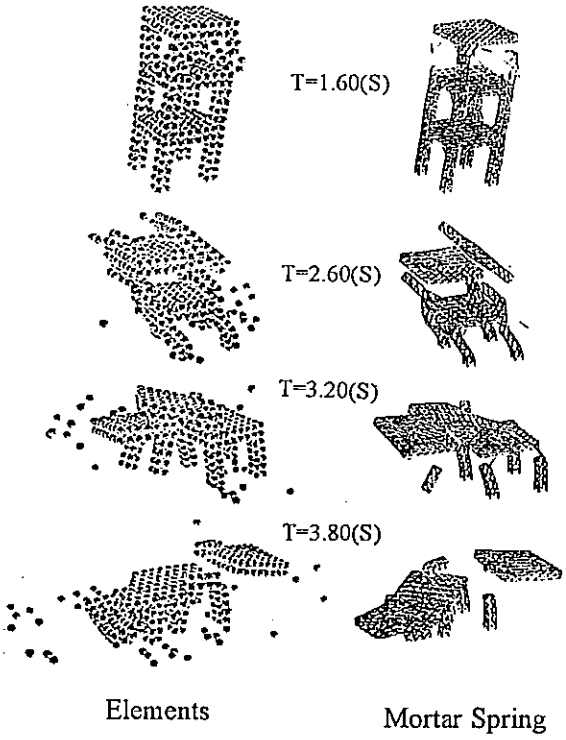

Fig. 8. Pancake Collapse of Three-Story Building

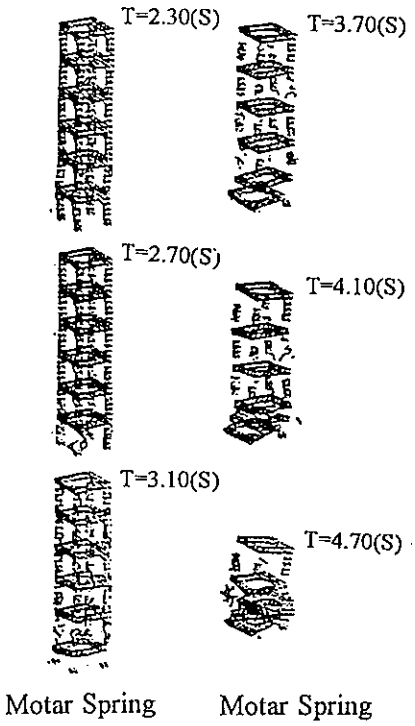

Fig. 9. Pancake Collapse of Six-Story Building

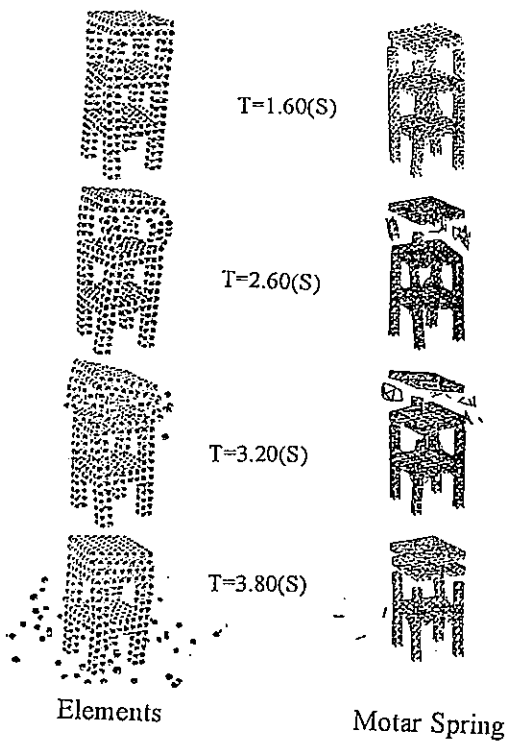

Fig. 10. Collapse of Concrete-Frame due to Twisting Load

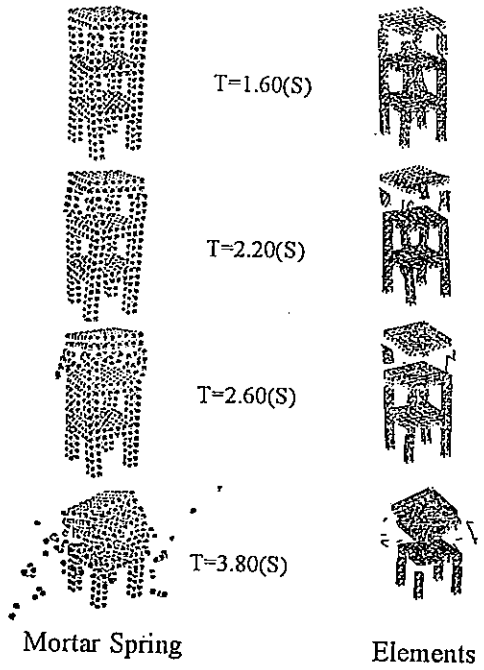

Fig. 11. Collapse of Concrete-Frame due to Twisting Load

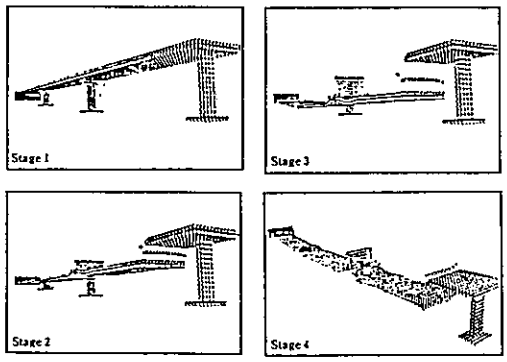

Fig. 12. Collapse Simulation of a Bridge

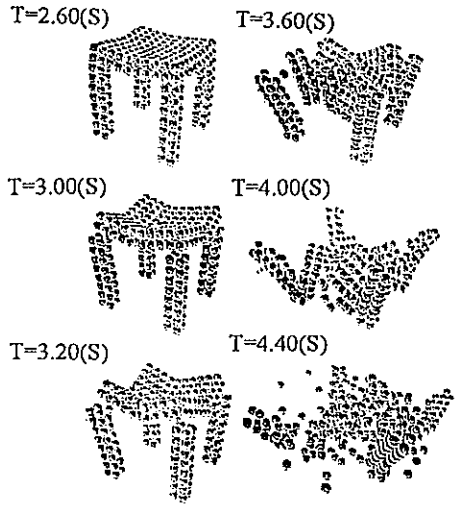

Fig. 13. Collapse of a Bridge

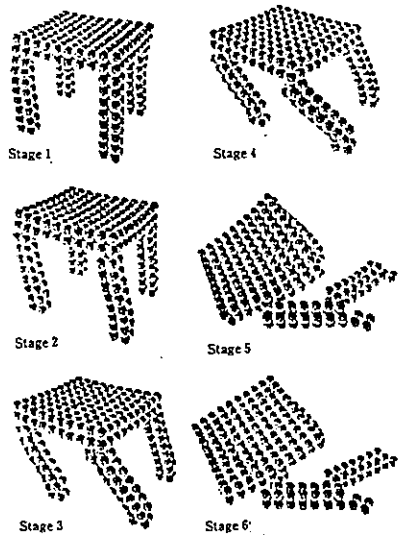

Fig. 14. Collapse of a Bridge

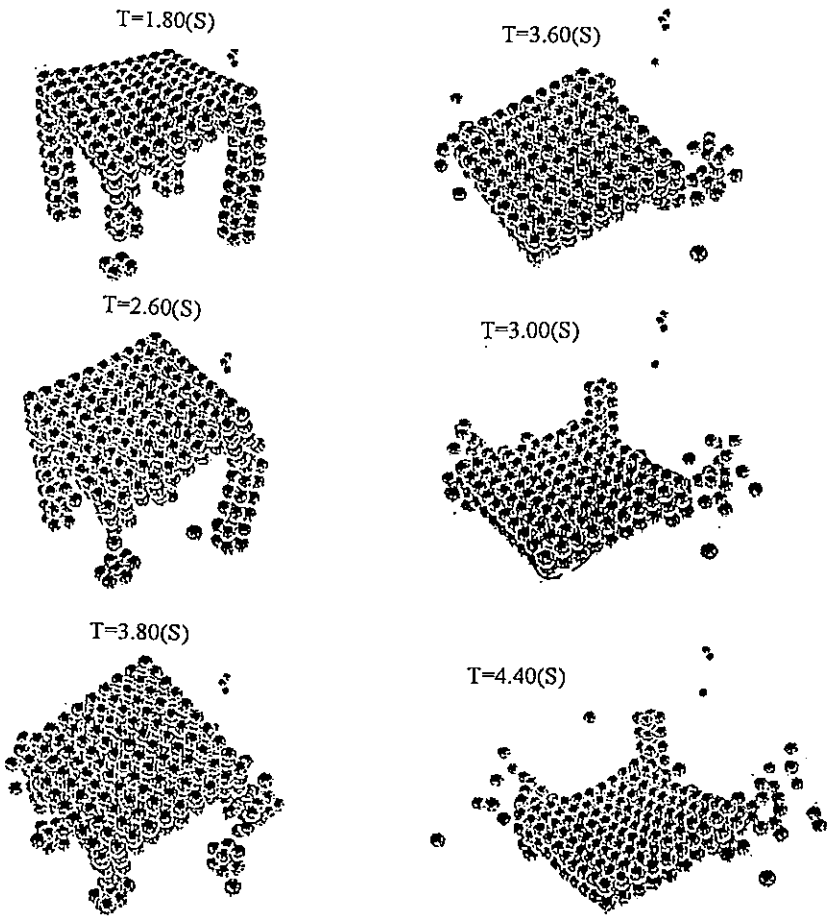

Fig. 15. Collapse by Blasting of a Column

References: Hakuno, M. and Meguro, K. (1993). "Simulation of Concrete-Frame Collapse Due to Dynamic Loading", Jounal of EM, ASCE, Vol.119, No.9, pp1709-1723.

Development of High Order Manifold Method

Guangqi CHEN, Yuzo OHNISHI and Takahiro ITO

Kyoto University, Kyoto 606-01, Japan

Abstract

The Manifold Method of Material Analysis (MM) with high order displacement functions has been derived based on triangular meshes for the requirement of high accurate calculations from practical applications. The matrices of equilibrium equations for the second order MM have been given in detail for program coding. The derivation of the method is made by means of approximation theory and very few new mathematical concepts are used in this paper. So, it may be easily understood by most engineering researchers. By close comparison with widely used Finite Element Method, the advantages of MM can be seen very clearly in the following aspects: 1) the capability of processing large deformation and handing discontinuities like block oriented Discontinuous Deformation Analysis method; 2) making element meshes easily and 3) using high order displacement functions easily.

The C program codes for the second order MM has been developed, and it has been applied to the example of a beam bending under a central point loading. The calculated results are quite good in agreement with theoretical solutions. By contrast, the results for the same example calculated by the original first order MM are far from the theoretical solutions. Therefore, it is obviously very important and necessary to develop high order Manifold Method for the complicated deformation problems.

1 Introduction

The Manifold Method of Material Analysis (MM) is a very flexible numerical analysis method, which contains and combines widely used Finite Element Method (FEM) and joint or block oriented Discontinuous Deformation Analysis (DDA) method in a unified form (Shi, 1991, 1992). The first order MM for two dimensional problems has been highly developed in both the theory and program codes. Now, it is the time to develop high order MM since many practical applications need much higher accurate calculations that the original first order MM can not meet. In this paper, the MM with high order displacement functions is derived based on triangular meshes and the details for the second order displacement function are given for program coding.

Since the derivation of the method is made by means of approximation theory and very few new mathematical concepts are used in this paper, it may be easily understood by most engineering researchers. In addition, by close comparison with widely used Finite Element Method, the advantages of MM can be seen very clearly in the following aspects: 1) the capability of processing large deformation and handing discontinuities like block oriented Discontinuous Deformation Analysis method; 2) making element meshes easily and 3) using high order displacement functions easily.

The C program codes for the second order MM has been developed, and it is used to calculate a beam bending problem under a central point loading. The calculated results are quite good in agreement with the theoretical solutions. Also, the same problem is calculated by the original first order MM and the calculated results are far from the theoretical solutions. Therefore, it is obviously very important and necessary to develop high order Manifold Method for the complicated deformation problems.

2 The theory of manifold method

In order to handle a complicated function $f(x,y)$ defined in a field F, it is common to divide the whole field into finite small regions ($C_i, \quad i = 1, \cdots, n$), and use a simple function $u_i(x,y)$ (e.g. constant, linear or some order polynomial functions) approaching to $f(x,y)$ within each small region C_i in general numerical analysis methods.

For example, in FEM, these small regions are elements. All the elements are pieced together covering the whole field without overlapping. In order to ensure the continuity of displacements from an element to its adjacent element, the simple function in an element is constrained at its boundary points called nodes. As a result, the order of the simple function used in an element is limited by the number of the nodes of the element.

In MM, such a small region C_i is called a *cover*, and the corresponding simple function $u_i(x,y)$ is called *cover function* here. Unlike FEM, MM covers can overlap each other (Fig. 1). A *common area* of the overlapped covers corresponds to an element in FEM, which is defined in such a way that the number of the overlapped covers keeps constant everywhere within the area. It is obvious that all the common areas are pieced together covering the whole field completely without overlapping.

Supposing that m overlapped covers ($C_i, \quad i = 1, \cdots, m$) have a common area E, the optimal estimation of $f(x,y)$ in the area, i.e. the function $u(x,y)$, can be obtained by taking the weighted average of the m cover functions:

$$u(x,y) = \sum_{i=1}^{m} w_i(x,y) u_i(x,y), \qquad (x,y) \in E, \tag{1}$$

where $w_i(x,y)$ is called *cover weighting function*

$$0 \leq w_i(x,y) \leq 1, \qquad (x,y) \in C_i \tag{2}$$

and

$$\sum_{i=1}^{m} w_i(x,y) \equiv 1, \qquad (x,y) \in E. \tag{3}$$

Since the whole field F will be completely covered by common areas without overlapping, the complicated function $f(x,y)$ can be approximately expressed by piecewise functions $u(x,y)$ defined in each element.

It is obvious that the key points for practical application of MM theory are 1). how to choose the cover shape; 2). how to choose the cover functions; 3). how to determine cover weighting functions.

3 Covers and weighting functions

In theory, any shapes of covers can be used in MM. However, since the weighting function, the common area and integration are related to the cover shape, a reasonable choice of cover shapes is very important.

It is very convenient to use triangular meshes as shown in Fig. 2, where each intersection point of the meshes is right the center point of a cover and called a star. All the triangles around the star form a hexagonal cover.

With this kind of covers, both the common areas and weighting functions can be easily determined by the following way.

A triangle in Fig. 2 is exactly the common area of three covers with the center points at three vertices of the triangle.

The weighting function in a hexagonal cover is defined as shown in Fig.3. It is equal to 1 at the center point and declines linearly to 0 to all the sides of the cover. That is, the weighting function is a piecewise function of six linear functions corresponding to six triangles of the cover.

It is worth mentioning that a MM cover can span discontinuity boundaries, and can be partially out of the material volume. So, the same size and shape to all the covers are always available no matter how complicated the geometric shapes of material volumes and joint distributions are. This is one of the major advantages of MM, which makes it very easy to create MM covers automatically and to handle discontinuity.

In a triangular common area, it is easy to show that the three weighting functions of the three covers forming the area are exactly equal to the shape functions of the corresponding FEM triangular element.

Suppose that three covers i, j and k have a triangular common area E (Fig. 4), also called element in this paper, the corresponding three linear weighting functions in the area can be written as

$$\begin{aligned} w_l(x,y) &= a_l + b_l\, x + c_l\, y, \qquad (x,y) \in E, \\ l &= i,j,k\,. \end{aligned} \tag{4}$$

At the three center points of the covers, i.e. three vertices of the triangle $((x_m, y_m),\ m = i,j,k)$, there should be

$$w_l(x_m, y_m) = \delta_{lm}, \qquad (l, m = i,j,k) \tag{5}$$

where

$$\delta_{lm} = \begin{cases} 1 & for \quad l = m \\ 0 & for \quad l \neq m \end{cases} \tag{6}$$

Substituting (4) into (5) we can solve the unknowns $(a_l, b_l, c_l,\ \ l = i,j,k)$ and obtain

$$\begin{pmatrix} w_i(x,y) \\ w_j(x,y) \\ w_k(x,y) \end{pmatrix} = \frac{1}{\Delta} \begin{pmatrix} x_j y_k - x_k y_j & y_j - y_k & x_k - x_j \\ x_k y_i - x_i y_k & y_k - y_i & x_i - x_k \\ x_i y_j - x_j y_i & y_i - y_j & x_j - x_i \end{pmatrix} \begin{pmatrix} 1 \\ x \\ y \end{pmatrix} \tag{7}$$

where

$$\Delta = (x_j - x_i)(y_k - y_i) - (x_k - x_i)(y_j - y_i) \tag{8}$$

It can be seen that the right side of (7) is the same as the shape function of the element E in FEM.

4 The displacement functions in the common area

According to (1), the displacement functions in an element E shown in Fig. 4 can be written as

$$\begin{cases} u(x,y) = w_i(x,y)u_i(x,y) + w_j(x,y)u_j(x,y) + w_k(x,y)u_k(x,y) \\ v(x,y) = w_i(x,y)v_i(x,y) + w_j(x,y)v_j(x,y) + w_k(x,y)v_k(x,y) \end{cases} \tag{9}$$

where $(u_l(x,y), v_l(x,y),\ \ l = i,j,k)$ are cover displacement functions; $(w_l(x,y),\ \ l = i,j,k)$ are corresponding weighting functions given by (7).

It is easy to verify

$$w_i(x,y) + w_j(x,y) + w_k(x,y) \equiv 1 \quad (x,y) \in E \tag{10}$$

The weighting and cover displacement functions can be also expressed as

$$w_l(x,y) = \mathbf{W}_l\, \mathbf{L}(x,y) \tag{11}$$

$$u_l(x,y) = \mathbf{B}_l(x,y)\, \mathbf{U}_l \tag{12}$$

$$v_l(x,y) = \mathbf{B}_l(x,y)\, \mathbf{V}_l \tag{13}$$

$$l = i,j,k$$

where

$$\begin{pmatrix} \mathbf{W}_i \\ \mathbf{W}_j \\ \mathbf{W}_k \end{pmatrix} = \frac{1}{\Delta} \begin{pmatrix} x_j y_k - x_k y_j & y_j - y_k & x_k - x_j \\ x_k y_i - x_i y_k & y_k - y_i & x_i - x_k \\ x_i y_j - x_j y_i & y_i - y_j & x_j - x_i \end{pmatrix}, \quad \mathbf{L}(x,y) = \begin{pmatrix} 1 \\ x \\ y \end{pmatrix}, \tag{14}$$

and ($\mathbf{B}_l(x,y), \mathbf{U}_l, \mathbf{V}_l, \quad l = i,j,k$) are just the split expression of $(u_l(x,y), v_l(x,y), \quad l = i,j,k)$, which depend on the choices of the three cover displacement functions and will be discussed late.

Considering (11), (12), (13), displacement functions (9) in the common area can be written as

$$\begin{pmatrix} u(x,y) \\ v(x,y) \end{pmatrix} = \begin{pmatrix} \mathbf{F}_i(x,y) & 0 & \mathbf{F}_j(x,y) & 0 & \mathbf{F}_k(x,y) & 0 \\ 0 & \mathbf{F}_i(x,y) & 0 & \mathbf{F}_j(x,y) & 0 & \mathbf{F}_k(x,y) \end{pmatrix} \begin{pmatrix} \mathbf{U}_i \\ \mathbf{V}_i \\ \mathbf{U}_j \\ \mathbf{V}_j \\ \mathbf{U}_k \\ \mathbf{V}_k \end{pmatrix}, \tag{15}$$

where

$$\mathbf{F}_l(x,y) = \mathbf{W}_l \, \mathbf{L}(x,y) \, \mathbf{B}_l(x,y), \quad l = i,j,k \tag{16}$$

(15) can be still further expressed as

$$\begin{pmatrix} u(x,y) \\ v(x,y) \end{pmatrix} = \begin{pmatrix} \mathbf{T}_i(x,y) & \mathbf{T}_j(x,y) & \mathbf{T}_k(x,y) \end{pmatrix} \begin{pmatrix} \mathbf{D}_i \\ \mathbf{D}_j \\ \mathbf{D}_k \end{pmatrix} = \{\mathbf{T}\}\{\mathbf{D}\}, \tag{17}$$

where

$$\mathbf{T}_l(x,y) = \begin{pmatrix} \mathbf{F}_l(x,y) & 0 \\ 0 & \mathbf{F}_l(x,y) \end{pmatrix}, \quad \mathbf{D}_l = \begin{pmatrix} \mathbf{U}_l \\ \mathbf{V}_l \end{pmatrix}, \quad l = i,j,k \tag{18}$$

It is worth to notice that cover displacement functions can be arbitrary chosen as long as they can expressed as (12) and (13). As a result, it is not necessary to add nodes to the element for increasing the order of the displacement function.

When the displacement functions of each common area are obtained, the total potential energy of the whole field can be expressed as the function of $(\mathbf{D}_l, \ l = 1, 2, \cdots, n)$. The equilibrium equations can be derived from minimizing the total potential energy, and then, the coefficients of each cover displacement function can be obtained by solving the equilibrium equations (Shi, 1991, 1992).

4.1 Constant cover displacement functions

If three cover displacement functions are taken as constants, i.e.

$$\begin{cases} u_l(x,y) = u_l \\ v_l(x,y) = v_l \end{cases} \quad l = i,j,k \tag{19}$$

the corresponding $\mathbf{B}, \mathbf{U}$ and $\mathbf{V}$ are

$$\begin{cases} \mathbf{B}_l(x,y) = 1 \\ \mathbf{U}_l = u_l \\ \mathbf{V}_l = v_l \end{cases} \quad l = i,j,k \tag{20}$$

Then,

$$\mathbf{F}_l(x,y) = \mathbf{W}_l \, \mathbf{L}(x,y) = w_l(x,y) \quad l = i,j,k \tag{21}$$

As a result, the displacement functions in the element become

$$\begin{pmatrix} u(x,y) \\ v(x,y) \end{pmatrix} = \begin{pmatrix} w_i(x,y) & 0 & w_j(x,y) & 0 & w_k(x,y) & 0 \\ 0 & w_i(x,y) & 0 & w_j(x,y) & 0 & w_k(x,y) \end{pmatrix} \begin{pmatrix} u_i \\ v_i \\ u_j \\ v_j \\ u_k \\ v_k \end{pmatrix} \tag{22}$$

It can be seen that constant cover displacement functions generate the linear displacement functions of the element, which are the same as that of a triangular element in FEM. In this case, the constant cover displacements correspond to the node displacements in FEM. Please refer to Shi (1991 and 1992) for the details about the first order MM.

4.2 Linear cover displacement functions

If three cover displacement functions are taken as linear functions

$$\begin{cases} u_l(x,y) = u_{l0} + u_{l1}\ x + u_{l2}\ y \\ v_l(x,y) = v_{l0} + v_{l1}\ x + v_{l2}\ y \end{cases} \qquad l = i,j,k, \tag{23}$$

where $(u_{lm}, v_{lm},\ m = 0,1,2)$ are unknown coefficients, the corresponding $\mathbf{B}, \mathbf{U}$ and $\mathbf{V}$ are

$$\mathbf{B}_l = \begin{pmatrix} 1 & x & y \end{pmatrix}, \quad \mathbf{U}_l = \begin{pmatrix} u_{l0} \\ u_{l1} \\ u_{l2} \end{pmatrix}, \quad \mathbf{V}_l = \begin{pmatrix} v_{l0} \\ v_{l1} \\ v_{l2} \end{pmatrix}, \quad l = i,j,k \tag{24}$$

And then, we have

$$\mathbf{F}_l(x,y) = \mathbf{W}_l \begin{pmatrix} 1 & x & y \\ x & x^2 & xy \\ y & xy & y^2 \end{pmatrix} \qquad l = i,j,k \tag{25}$$

$$\mathbf{D}_l = \begin{pmatrix} u_{l0} & u_{l1} & u_{l2} & v_{l0} & v_{l1} & v_{l2} \end{pmatrix}^T \tag{26}$$

It can be seen that the linear cover displacement functions generate the second order displacement functions in an element while the meshes remain unchanged. The details about the second order MM are given in the next section.

4.3 General high order cover displacement functions

When three cover displacement functions are taken as n order functions

$$\begin{cases} u_l(x,y) = u_{l0} + u_{l1}x + u_{l2}y + u_{l3}x^2 + u_{l4}xy + u_{l5}y^2 + \cdots + u_{lr}x^n + \cdots + u_{lm}y^n \\ v_l(x,y) = v_{l0} + v_{l1}x + v_{l2}y + v_{l3}x^2 + v_{l4}xy + v_{l5}y^2 + \cdots + v_{lr}x^n + \cdots + v_{lm}y^n \\ \qquad\qquad l = i,j,k, \end{cases} \tag{27}$$

where $(u_{lk}, v_{lk},\ k = 0,1,2,\cdots,m)$ are m unknown coefficients, the corresponding $\mathbf{B}, \mathbf{U}$ and $\mathbf{V}$ are

$$\mathbf{B}_l = \begin{pmatrix} 1 & x & y & x^2 & xy & y^2 & \cdots & x^n & \cdots & y^n \end{pmatrix},$$

$$\mathbf{U}_l = \begin{pmatrix} u_{l0} \\ u_{l1} \\ u_{l2} \\ \vdots \\ u_{lm} \end{pmatrix}, \quad \mathbf{V}_l = \begin{pmatrix} v_{l0} \\ v_{l1} \\ v_{l2} \\ \vdots \\ v_{lm} \end{pmatrix}, \quad l = i,j,k$$

According to (16), we have

$$\mathbf{F}_l(x,y) = \mathbf{W}_l \begin{pmatrix} 1 & x & y & x^2 & xy & y^2 & \cdots & x^n & \cdots & y^n \\ x & x^2 & xy & x^3 & x^2y & xy^2 & \cdots & x^{n+1} & \cdots & xy^n \\ y & xy & y^2 & x^2y & xy^2 & y^3 & \cdots & x^ny & \cdots & y^{n+1} \end{pmatrix} \quad l = i,j,k \tag{28}$$

and

$$\mathbf{D}_l = \begin{pmatrix} \mathbf{U}_l \\ \mathbf{V}_l \end{pmatrix} \quad l = i,j,k$$

It can be seen that n order cover displacement functions generate $n+1$ order displacement functions of the element without changing the meshes.

Therefore, the following advantages of the method over FEM can be summarized:

1. the order of displacement functions of an element is independent on the meshes, that is, the same meshes can be used by both th first order and high order MM. By contrast, the order of displacement functions are limited by the number of element nodes in FEM, (e.g. linear function needs 3 nodes and second order function needs 6 nodes).

2. It is possible to use different orders of cover displacement functions together in an element for processing stress concentration area.

5 Handling discontinuities

As mentioned before, one of important features in MM is that whether and how a cover displacement function contributes to the displacement function of its common area depends on the corresponding weighting function. With this feature, the discontinuities involved in a field can be easily handled in MM.

Case one: If a cover is partially out of the field (Fig. 5), the cover function should be only effective in the inside part Ω of the cover. For this purpose, we just let the weighting function of the cover $w_i(x,y)$ be zero for the outside part

$$\begin{cases} w_i(x,y) \geq 0, & (x,y) \in \Omega \\ w_i(x,y) \equiv 0, & (x,y) \notin \Omega \end{cases} \tag{29}$$

Here, we call the inside part Ω the *effective region* of the cover C_i, and say that the cover C_i is an effective cover of the region Ω. Any cover has and only has one effective region, and the weighting function of the cover is identically equal to zero for the outside of its effective region.

Case two: When a cover is divided into two completely disconnected domains by a discontinuity boundary (Fig. 6a), it is obvious that a simple cover function is not reasonable for the whole cover because of the apparent discontinuity. In this case, two covers C_i and C_m with the same shape and position are needed. Cover C_i has the effective region of Ω_i while C_m has the effective region of Ω_m.

This is very nature when we consider that two parts Ω_i and Ω_m may move apart (Fig. 6b).

In general, if a cover is divided into m completely disconnected domains by discontinuity boundaries, m independent covers with the same shape are needed there. Each cover takes one domain as its effective region.

In addition, when discontinuity is involved, a triangle may be divided into several completely disconnected domains by discontinuities. In this case, it can be seen that each domain inside the material volumes is exactly the common area of three effective covers. That is, each domain is an element.

An example is shown in Fig. 7 in which figures inside circles indicate cover numbers (e.g. covers 16, 17 and 18 have the same shape and positions). It can be seen that each element has exactly three effective covers.

6 Matrices of equilibrium equations for the second order MM

The matrices of equilibrium equations for the second order MM are derived in this section. The displacements in an element can be written as

$$\begin{pmatrix} u(x,y) \\ v(x,y) \end{pmatrix} = ([\mathbf{T}_1]\ [\mathbf{T}_2]\ [\mathbf{T}_3]) \begin{pmatrix} \mathbf{D}_1 \\ \mathbf{D}_2 \\ \mathbf{D}_3 \end{pmatrix} = \{\mathbf{T}\}\{\mathbf{D}\} \tag{30}$$

where

$$[\mathbf{T}_l] = \begin{pmatrix} F_{l1} & F_{l2} & F_{l3} & 0 & 0 & 0 \\ 0 & 0 & 0 & F_{l1} & F_{l2} & F_{l3} \end{pmatrix}, \qquad \mathbf{D}_l = \begin{pmatrix} \mathbf{U}_l \\ \mathbf{V}_l \end{pmatrix},$$

and

$$\begin{pmatrix} F_{l1} \\ F_{l2} \\ F_{l3} \end{pmatrix} = \begin{pmatrix} f_{l1} + f_{l2}x + f_{l3}y \\ f_{l1}x + f_{l2}x^2 + f_{l3}xy \\ f_{l1}y + f_{l2}xy + f_{l3}y^2 \end{pmatrix}, \quad l = 1,2,3$$

Then, the strains in the element can be obtained as follows:

$$\begin{pmatrix} \varepsilon_x \\ \varepsilon_y \\ \gamma_{xy} \end{pmatrix} = \begin{pmatrix} \frac{\partial u}{\partial x} \\ \frac{\partial v}{\partial y} \\ \frac{\partial u}{\partial y} + \frac{\partial v}{\partial x} \end{pmatrix} = ([\mathbf{G}_1]\ [\mathbf{G}_2]\ [\mathbf{G}_3]) \begin{pmatrix} \mathbf{D}_1 \\ \mathbf{D}_2 \\ \mathbf{D}_3 \end{pmatrix} = \{\mathbf{G}\}\{\mathbf{D}\} \tag{31}$$

where

$$[\mathbf{G}_l] = \begin{pmatrix} f_{l2} & f_{l1} + 2xf_{l2} + yf_{l3} & yf_{l2} & 0 & 0 & 0 \\ 0 & 0 & 0 & f_{l3} & xf_{l3} & f_{l1} + xf_{l2} + 2yf_{l3} \\ f_{l3} & xf_{l3} & f_{l1} + xf_{l2} + 2yf_{l3} & f_{l2} & f_{l1} + 2xf_{l2} + yf_{l3} & yf_{l2} \end{pmatrix}$$
$$l = 1,2,3 \tag{32}$$

The total potential energy can be expressed as following

$$\Pi = \frac{1}{2}\begin{pmatrix} \mathbf{D}_1^T & \mathbf{D}_2^T & \cdots & \mathbf{D}_n^T \end{pmatrix} \begin{pmatrix} \mathbf{K}_{11} & \mathbf{K}_{12} & \cdots & \mathbf{K}_{1n} \\ \mathbf{K}_{21} & \mathbf{K}_{22} & \cdots & \mathbf{K}_{2n} \\ \vdots & \vdots & \ddots & \vdots \\ \mathbf{K}_{n1} & \mathbf{K}_{n2} & \cdots & \mathbf{K}_{nn} \end{pmatrix} \begin{pmatrix} \mathbf{D}_1 \\ \mathbf{D}_2 \\ \vdots \\ \mathbf{D}_n \end{pmatrix}$$
$$+ \begin{pmatrix} \mathbf{D}_1^T & \mathbf{D}_2^T & \cdots & \mathbf{D}_n^T \end{pmatrix} \begin{pmatrix} \mathbf{F}_1 \\ \mathbf{F}_2 \\ \vdots \\ \mathbf{F}_n \end{pmatrix} + C \tag{33}$$

where the coefficient submatrix $\mathbf{K}_{ij}$ can be written as a symmetric representation:

$$\mathbf{K}_{ij} = \mathbf{K}_{ji}^T$$

Minimizing the total potential energy Π, we can obtain simultaneous equilibrium equations as follows:

$$\begin{pmatrix} \mathbf{K}_{11} & \mathbf{K}_{12} & \cdots & \mathbf{K}_{1n} \\ \mathbf{K}_{21} & \mathbf{K}_{22} & \cdots & \mathbf{K}_{2n} \\ \vdots & \vdots & \ddots & \vdots \\ \mathbf{K}_{n1} & \mathbf{K}_{n2} & \cdots & \mathbf{K}_{nn} \end{pmatrix} \begin{pmatrix} \mathbf{D}_1 \\ \mathbf{D}_2 \\ \vdots \\ \mathbf{D}_n \end{pmatrix} = \begin{pmatrix} \mathbf{F}_1 \\ \mathbf{F}_2 \\ \vdots \\ \mathbf{F}_n \end{pmatrix}. \tag{34}$$

For the material analysis, $\mathbf{F}_i$ is called loading matrix. The coefficient submatrix $\mathbf{K}_{ij}$ and the loading matrix $\mathbf{F}_i$ for the second order MM are derived in the follwing subsections.

6.1 Stiffness matrix

The strain energy Π_e done by the elastic stresses of element e is

$$\Pi_e = \int\int_A \frac{1}{2} \begin{pmatrix} \varepsilon_x & \varepsilon_y & \gamma_{xy} \end{pmatrix} \begin{pmatrix} \sigma_x \\ \sigma_y \\ \tau_{xy} \end{pmatrix} dxdy \tag{35}$$

Considering the relationship between stress and strain

$$\begin{pmatrix} \sigma_x \\ \sigma_y \\ \tau_{xy} \end{pmatrix} = \mathbf{E} \begin{pmatrix} \varepsilon_x \\ \varepsilon_y \\ \gamma_{xy} \end{pmatrix}, \tag{36}$$

where

$$\mathbf{E} = \frac{E}{1-\upsilon^2} \begin{pmatrix} 1 & \upsilon & 0 \\ \upsilon & 1 & 0 \\ 0 & 0 & (1-\upsilon)/2 \end{pmatrix},$$

E and υ are the Young's modulus and Poisson's ratio respectively.

Substituting (31) and (36) into (35), we can obtain the element stiffness matrix as follows:

$$\int\int_A [\mathbf{G}_r]^T \mathbf{E} [\mathbf{G}_s] dxdy \quad \longrightarrow \quad [\mathbf{K}_{i(r)i(s)}]$$

$$r, s = 1, 2, 3 \tag{37}$$

where

$$i(c) = \begin{cases} i_1, & c = 1, \ \textit{the number of the first cover} \\ i_2, & c = 2, \ \textit{the number of the second cover} \\ i_3, & c = 3, \ \textit{the number of the third cover} \end{cases}$$

The details of the stiffness matrix (37) are given in the appendix section.

6.2 Initial stress matrix

Since the computed stresses of previous time step will be the initial stresses of the next time step, the initial stress matrix is essential for MM computation. In the first order MM, the stresses in an element are constants. However, in high order MM, the strains and stresses are no longer constants because the matrix $[G_l]$ is the function of x and y.

Since strains are linear functions within an element in the second order MM, they can be expressed as following:

$$\begin{pmatrix} \varepsilon_x \\ \varepsilon_y \\ \gamma_{xy} \end{pmatrix} = \begin{pmatrix} A_{11} & A_{12} & A_{13} \\ A_{21} & A_{22} & A_{23} \\ A_{31} & A_{32} & A_{33} \end{pmatrix} \begin{pmatrix} 1 \\ x \\ y \end{pmatrix}. \tag{38}$$

Then, the stresses can be expresses as

$$\begin{pmatrix} \sigma_x \\ \sigma_y \\ \tau_{xy} \end{pmatrix} = \begin{pmatrix} S_{11} & S_{12} & S_{13} \\ S_{21} & S_{22} & S_{23} \\ S_{31} & S_{32} & S_{33} \end{pmatrix} \begin{pmatrix} 1 \\ x \\ y \end{pmatrix} \tag{39}$$

where

$$\begin{pmatrix} S_{11} & S_{12} & S_{13} \\ S_{21} & S_{22} & S_{23} \\ S_{31} & S_{32} & S_{33} \end{pmatrix} = \mathbf{E} \begin{pmatrix} A_{11} & A_{12} & A_{13} \\ A_{21} & A_{22} & A_{23} \\ A_{31} & A_{32} & A_{33} \end{pmatrix}$$

Since the initial stresses are the accumulation of the computed stresses from previous steps, we have

$$\begin{pmatrix} \sigma_x^0 \\ \sigma_y^0 \\ \tau_{xy}^0 \end{pmatrix} = \begin{pmatrix} N_{11} & N_{12} & N_{13} \\ N_{21} & N_{22} & N_{23} \\ N_{31} & N_{32} & N_{33} \end{pmatrix} \begin{pmatrix} 1 \\ x \\ y \end{pmatrix} \tag{40}$$

where, for the step n,

$$N_{ij} = \sum_{k=1}^{n-1} S_{ij}^k.$$

Denote

$$\mathbf{N} = \begin{pmatrix} N_{11} & N_{12} & N_{13} \\ N_{21} & N_{22} & N_{23} \\ N_{31} & N_{32} & N_{33} \end{pmatrix}, \mathrm{L} = \begin{pmatrix} 1 \\ x \\ y \end{pmatrix},$$

the potential energy of the initial constant stresses in an element

$$\Pi_e = \int\int_A \begin{pmatrix} \varepsilon_x & \varepsilon_y & \gamma_{xy} \end{pmatrix} \begin{pmatrix} \sigma_x^0 \\ \sigma_y^0 \\ \tau_{xy}^0 \end{pmatrix}$$

becomes as following:

$$\Pi_e = \mathbf{D}_l^T \int\int_A \mathbf{G}_l^T \mathbf{N}\mathrm{L} dxdy$$

Therefore, the initial stress matrix belongs to the load matrix, we have

$$-\int\int_A \mathbf{G}_l^T \mathbf{N}\mathrm{L} dxdy \quad \longrightarrow \quad [\mathbf{F}_{i(l)}] \quad l = 1, 2, 3 \tag{41}$$

6.3 Point loading matrix

Suppose that a loading force P with $(F_x,\ F_y)$ acts on the point $(x,\ y)$ of an element e, the potential energy due to P is

$$\Pi_p = -(F_x u + F_y v) = -\mathbf{D}_e^T [\mathbf{T}_e]^T \begin{pmatrix} F_x \\ F_y \end{pmatrix} \tag{42}$$

(42) is of the loading matrix form. Therefore, we have

$$[\mathbf{T}_c]^T \begin{pmatrix} F_x \\ F_y \end{pmatrix} \quad \longrightarrow \quad [\mathbf{F}_{i(c)}] \quad c = 1, 2, 3 \tag{43}$$

6.4 Body loading matrix

When constant body force $(Gx,\ Gy)$ acts on the material area of element e, the corresponding potential energy is

$$\Pi_w = -\int\int_A \begin{pmatrix} u & v \end{pmatrix} \begin{pmatrix} G_x \\ G_y \end{pmatrix} dxdy = -\mathbf{D}_e^T \left[\int\int_A [\mathbf{T}_e]^T dxdy\right] \begin{pmatrix} G_x \\ G_y \end{pmatrix} \tag{44}$$

(44) is of the loading matrix form. Therefore, we have

$$\int\int_A [\mathbf{T}_c]^T dxdy \begin{pmatrix} G_x \\ G_y \end{pmatrix} \quad \longrightarrow \quad [\mathbf{F}_{i(c)}] \quad c = 1, 2, 3 \tag{45}$$

It can be shown that

$$\int\int_A [\mathbf{T}_c]^T dxdy] = \begin{pmatrix} [\mathbf{R}_c] & 0 \\ 0 & [\mathbf{R}_c] \end{pmatrix} \tag{46}$$

where

$$[\mathbf{R}_c] = \begin{pmatrix} f_{c1}S^e + f_{c2}S^e_x + f_{c3}S^e_y \\ f_{c1}S^e_x + f_{c2}S^e_{xx} + f_{c3}S^e_{xy} \\ f_{c1}S^e_y + f_{c2}S^e_{xy} + f_{c3}S^e_{yy} \end{pmatrix}$$

Please refer to the Appendix section for the details of S^e, S^e_x, S^e_y, S^e_{xx}, S^e_{xy} and S^e_{yy}.

6.5 Inertia force matrix

Denote $(u(t),\ v(t))$ as the time dependent displacements of any point $(x,\ y)$ in element e, the force of inertia per unit area is

$$\begin{pmatrix} f_x \\ f_y \end{pmatrix} = -\rho\frac{\partial^2}{\partial t^2}\begin{pmatrix} u(t) \\ v(t) \end{pmatrix} = -\rho[\mathbf{T}_e]\frac{\partial^2 \mathbf{D}_e(t)}{\partial t^2}$$

where ρ is the mass per unit area.

The potential energy of the inertial force of an element e is

$$\Pi_i = -\int\int_A \begin{pmatrix} u & v \end{pmatrix}\begin{pmatrix} f_x \\ f_y \end{pmatrix} dxdy = \int\int_A \rho \mathbf{D}_e^T[\mathbf{T}_e]^T[\mathbf{T}_e]\frac{\partial^2 \mathbf{D}_e(t)}{\partial t^2}dxdy \tag{47}$$

It is easy to show that the inertial force matrix is of the same form as that for the first order MM (Shi, 1996). Then, we have

$$\frac{2\rho}{\Delta t^2}\int\int_A [\mathbf{T}_r]^T[\mathbf{T}_s]dxdy \quad\longrightarrow\quad [\mathbf{K}_{i(r)i(s)}], \qquad r,s = 1,2,3 \tag{48}$$

$$\frac{2\rho}{\Delta t}\left[\int\int_A [\mathbf{T}_r]^T[\mathbf{T}_e]dxdy\right]\mathbf{V}_e(0) \quad\longrightarrow\quad [\mathbf{F}_{i(r)}], \qquad r = 1,2,3 \tag{49}$$

where Δt is time interval of a step; $(V_e(0),\ e = 1,2,3)$ is the velocity of previous time step.

It is worth to be noted that the integration

$$\int\int_A [\mathbf{T}_r]^T[\mathbf{T}_s]dxdy \tag{50}$$

is much different from the first order MM, which is given in the appendix.

6.6 Fixed point matrix

When a point $(x,\ y)$ in an element e is to be fixed, a very strong constraint spring is used at the point. The energy of the constraint spring can be expressed as

$$\Pi_f = \frac{p}{2}\mathbf{D}_e^T[\mathbf{T}_e]^T[\mathbf{T}_e]\mathbf{D}_e$$

where p is the stiffness of the constraint spring. Then, we have

$$p[\mathbf{T}_r]^T[\mathbf{T}_s] \quad\longrightarrow\quad [\mathbf{K}_{i(r)i(s)}], \quad r,s = 1,2,3 \tag{51}$$

It is easy to obtain that

$$[\mathbf{T}_r]^T[\mathbf{T}_s] = \mathbf{W}_{rs}\begin{pmatrix} 1 & 0 \\ 0 & 1 \end{pmatrix}$$

where

$$\mathbf{W}_{rs} = \begin{pmatrix} F_{r1}F_{s1} & F_{r1}F_{s2} & F_{r1}F_{s3} \\ F_{r2}F_{s1} & F_{r2}F_{s2} & F_{r2}F_{s3} \\ F_{r3}F_{s1} & F_{r3}F_{s2} & F_{r3}F_{s3} \end{pmatrix}$$

6.7 Normal contact matrix

A normal spring is used at a contact point between discontinuous boundaries in order to prevent penetration. It is the same as the first order MM that the potential energy of the normal spring is

$$\Pi_s = \frac{1}{2}pd^2$$

where p is the stiffness of the normal spring, d is the length

$$d = \{\mathbf{H}\}^T\{\mathbf{D}_i\} + \{\mathbf{G}\}^T\{\mathbf{D}_j\} + \frac{S_0}{l}$$

Then, $p\{\mathbf{H}\}\{\mathbf{H}\}^T$, $p\{\mathbf{H}\}\{\mathbf{G}\}^T$, $p\{\mathbf{G}\}\{\mathbf{H}\}^T$ and $p\{\mathbf{G}\}\{\mathbf{G}\}^T$ are the $[\mathbf{K}_e]$ matrices, $-p\frac{S_0}{l}\{\mathbf{H}\}$ and $-p\frac{S_0}{l}\{\mathbf{G}\}$ are the load matrices. That is, we have

$$\begin{aligned}
p\mathbf{H}_r\mathbf{H}_s^T &\longrightarrow [\mathbf{K}_{i(r)i(s)}], \quad r,s = 1,2,3 \\
p\mathbf{H}_r\mathbf{G}_s^T &\longrightarrow [\mathbf{K}_{i(r)j(s)}], \quad r,s = 1,2,3 \\
p\mathbf{G}_r\mathbf{H}_s^T &\longrightarrow [\mathbf{K}_{j(r)i(s)}], \quad r,s = 1,2,3 \\
p\mathbf{G}_r\mathbf{G}_s^T &\longrightarrow [\mathbf{K}_{j(r)j(s)}], \quad r,s = 1,2,3 \\
-p\frac{S_0}{l}\mathbf{H}_r &\ [\mathbf{F}_{i(r)}], \quad r = 1,2,3 \\
-p\frac{S_0}{l}\mathbf{G}_r &\ [\mathbf{F}_{j(r)}], \quad r = 1,2,3
\end{aligned}$$

where

$$\mathbf{H}_r = \frac{1}{l}\begin{pmatrix} F_{r1}(x_1,\ y_1) & F_{r2}(x_1,\ y_1) & F_{r3}(x_1,\ y_1) & 0 & 0 & 0 \\ 0 & 0 & 0 & F_{r1}(x_1,\ y_1) & F_{r2}(x_1,\ y_1) & F_{r3}(x_1,\ y_1) \end{pmatrix}^T \begin{pmatrix} y_2 - y_3 \\ x_3 - x_2 \end{pmatrix},$$

$$\mathbf{G}_r = \frac{1}{l}\begin{pmatrix} F_{r1}(x_2,\ y_2) & 0 \\ F_{r2}(x_2,\ y_2) & 0 \\ F_{r3}(x_2,\ y_2) & 0 \\ 0 & F_{r1}(x_2,\ y_2) \\ 0 & F_{r2}(x_2,\ y_2) \\ 0 & F_{r3}(x_2,\ y_2) \end{pmatrix} \begin{pmatrix} y_3 - y_1 \\ x_1 - x_3 \end{pmatrix} + \frac{1}{l}\begin{pmatrix} F_{r1}(x_3,\ y_3) & 0 \\ F_{r2}(x_3,\ y_3) & 0 \\ F_{r3}(x_3,\ y_3) & 0 \\ 0 & F_{r1}(x_3,\ y_3) \\ 0 & F_{r2}(x_3,\ y_3) \\ 0 & F_{r3}(x_3,\ y_3) \end{pmatrix} \begin{pmatrix} y_1 - y_2 \\ x_3 - x_1 \end{pmatrix}$$

$$S_0 = \begin{vmatrix} 1 & x_1 & y_1 \\ 1 & x_2 & y_2 \\ 1 & x_3 & y_3 \end{vmatrix}, \quad l = \sqrt{(x_2 - x_3)^2 + (y_2 - y_3)^2}$$

where $(x_1,\ y_1)$ is the contact vertex, $(x_2,\ y_2)$ and (x_3, y_3) are the two ends of the entrance line.

6.8 Shear contact matrix

A shear spring is used for simulating the coupling effect between discontinuous boundaries. It is the same as the first order MM that the potential energy of the shear spring is

$$\Pi_s = \frac{1}{2}p_s d^2$$

where p_s is the stiffness of the shear spring, d is the length

$$d = \{\mathbf{H}\}^T\{\mathbf{D}_i\} + \{\mathbf{G}\}^T\{\mathbf{D}_j\} + \frac{S_0}{l}$$

Then, $p\{\mathbf{H}\}\{\mathbf{H}\}^T$, $p_s\{\mathbf{H}\}\{\mathbf{G}\}^T$, $p_s\{\mathbf{G}\}\{\mathbf{H}\}^T$ and $p_s\{\mathbf{G}\}\{\mathbf{G}\}^T$ are the $[\mathbf{K}_e]$ matrices, $-p_s\frac{S_0}{l}\{\mathbf{H}\}$ and $-p_s\frac{S_0}{l}\{\mathbf{G}\}$ are the load matrices. That is, we have

$$
\begin{aligned}
p_s\mathbf{H}_r\mathbf{H}_s^T &\longrightarrow [\mathbf{K}_{i(r)i(s)}], \quad r,s=1,2,3\\
p_s\mathbf{H}_r\mathbf{G}_s^T &\longrightarrow [\mathbf{K}_{i(r)j(s)}], \quad r,s=1,2,3\\
p_s\mathbf{G}_r\mathbf{H}_s^T &\longrightarrow [\mathbf{K}_{j(r)i(s)}], \quad r,s=1,2,3\\
p_s\mathbf{G}_r\mathbf{G}_s^T &\longrightarrow [\mathbf{K}_{j(r)j(s)}], \quad r,s=1,2,3\\
-p_s\frac{S_0}{l}\mathbf{H}_r &\longrightarrow [\mathbf{F}_{i(r)}], \quad r=1,2,3\\
-p_s\frac{S_0}{l}\mathbf{G}_r &\longrightarrow [\mathbf{F}_{j(r)}], \quad r=1,2,3
\end{aligned}
$$

where

$$
\mathbf{H}_r = \frac{1}{l}\begin{pmatrix} F_{r1}(x_1,\ y_1) & F_{r2}(x_1,\ y_1) & F_{r3}(x_1,\ y_1) & 0 & 0 & 0 \\ 0 & 0 & 0 & F_{r1}(x_1,\ y_1) & F_{r2}(x_1,\ y_1) & F_{r3}(x_1,\ y_1) \end{pmatrix}^T \begin{pmatrix} x_3 - x_2 \\ y_3 - y_2 \end{pmatrix},
$$

$$
\mathbf{G}_r = \frac{1}{l}\begin{pmatrix} F_{r1}(x_0,\ y_0) & 0 \\ F_{r2}(x_0,\ y_0) & 0 \\ F_{r3}(x_0,\ y_0) & 0 \\ 0 & F_{r1}(x_0,\ y_0) \\ 0 & F_{r2}(x_0,\ y_0) \\ 0 & F_{r3}(x_0,\ y_0) \end{pmatrix} \begin{pmatrix} x_2 - x_3 \\ y_2 - y_3 \end{pmatrix}
$$

$$
S_0 = \begin{pmatrix} x_1 - x_0 & y_1 - y_0 \end{pmatrix} \begin{pmatrix} x_3 - x_2 \\ y_3 - y_2 \end{pmatrix}
$$

where $(x_0,\ y_0)$ is on the edge of the entrance line and is the assumed contact point of the vertex $(x_1,\ y_1)$; $(x_2,\ y_2)$ and (x_3, y_3) are the two ends of the entrance line.

6.9 Friction force matrix

The Coulomb's law is used to judge the dislocation movements of the discontinuous boundaries. When the shear force F

$$F < N\tan(\phi) + C,$$

a shear spring is applied for the coupling status. When

$$F \geq N\tan(\phi) + C,$$

dislocation movement will happen and friction force should be taken into account. In the above formula, N is the normal force on the contact boundary, ϕ and C are the friction angle and cohesion respectively.

The friction force is

$$F = pd\tan(\phi)$$

where pd is the normal force on the contact point. Then, the potential energy of friction force F on element i is

$$\Pi_f = Fu_1(x_3 - x_2)/l + Fv_1(y_3 - y_2)/l = F\{D_i\}^T\{\mathbf{H}\},$$

where

$$\mathbf{H}_r = \frac{1}{l}\begin{pmatrix} F_{r1}(x_1,\ y_1) & F_{r2}(x_1,\ y_1) & F_{r3}(x_1,\ y_1) & 0 & 0 & 0 \\ 0 & 0 & 0 & F_{r1}(x_1,\ y_1) & F_{r2}(x_1,\ y_1) & F_{r3}(x_1,\ y_1) \end{pmatrix}^T \begin{pmatrix} x_3 - x_2 \\ y_3 - y_2 \end{pmatrix},$$

Therefore, we have

$$-F\mathbf{H}_r \longrightarrow [\mathbf{F}_{i(r)}], \qquad r = 1, 2, 3$$

It is the same for the element j, we have

$$-F\mathbf{G}_r \longrightarrow [\mathbf{F}_{j(r)}], \qquad r = 1, 2, 3$$

where

$$\mathbf{G}_r = \frac{1}{l}\begin{pmatrix} F_{r1}(x_0,\ y_0) & F_{r2}(x_0,\ y_0) & F_{r3}(x_0,\ y_0) & 0 & 0 & 0 \\ 0 & 0 & 0 & F_{r1}(x_0,\ y_0) & F_{r2}(x_0,\ y_0) & F_{r3}(x_0,\ y_0) \end{pmatrix}^T \begin{pmatrix} x_3 - x_2 \\ y_3 - y_2 \end{pmatrix},$$

7 Example

The C program codes of the second order MM has been developed and a beam bending problem as shown in Fig. 8 has been solved by both the second order MM as well as the original first order MM programs so as to compare the accuracy.

In Fig. 8, a point loading $P = 200N$ acts on the central point of the beam which is $10m$ long and $1m$ wide and is supported at the two ends. The Young's modulus and Poisson's ratio of the beam are $E = 1.0 \times 10^5 N/m^2$ and $\upsilon = 0.24$ respectively. The points indicated by A, B, C, D, and E are check points for comparing the results from the theoretical solution, the second order MM and the first order MM calculations.

The model for MM calculation is shown in Fig. 9, in which the left bottom end point is fixed and the right end is laid on another fixed block so as to allow the horizontal deformation of the beam. Triangular meshes are used and total 14 elements are formed. It is worth mentioning that both the first order and second order MM use the same model.

The stiffness of the spring for both normal and shear directions is $2.5 \times 10^7 N/m$. The maximum allowed displacement ratio in a step is 0.01%.

2000 steps with time step interval $\Delta t = 0.01sec$ have been calculated for the whole deformation. Fig. 10 and Fig. 11 show the final deformation results from the first order and second order MM respectively. The vertical displacements of the check points are listed in Table 1. From the table, we can see that it is quite good in agreement between the results from the second order MM and the

The Check Points	Theoretical solutions	The Results from Second order MM	The Results from First Order MM
$A(x = 0.00m)$	$0.000m$	$0.000m$	$0.000m$
$B(x = 2.50m)$	$0.344m$	$0.351m$	$0.053m$
$C(x = 5.00m)$	$0.500m$	$0.508m$	$0.076m$
$D(x = 7.50m)$	$0.344m$	$0.349m$	$0.051m$
$E(x = 10.0m)$	$0.000m$	$0.000m$	$0.000m$

Table 1: The vertical displacements of check points

theoretical solutions although this is a three order deformation problem from the theoretical solution formula:

$$v(x) = -\frac{P}{12EI}x^3 + \frac{Pl^2}{16EI}x \quad (0 \leq x \leq \frac{1}{2})$$

where I is the moment and l is the length of the beam.

By contrast, the results from the first order MM are far from the theoretical solution, that is, the first order MM can not meet the requirement of this kind of problems. Therefore, it has been shown that it is very important and necessary to develop high order MM for the complicated deformation applications.

8 Conclusions

High order Manifold Method of Material Analysis have been derived based on triangular meshes for the requirement of high accurate calculations from practical applications. The matrices of equilibrium equations for the second order MM have been given in detail for program coding.

Since the derivation is made by means of approximation theory and very few new mathematical concepts are used in this paper, it can be easily understood by most engineering researchers. In addition, by close comparison with widely used Finite Element Method, the advantages of MM can be seen very clearly in the following aspects:

1. it can process large deformation problems like block oriented Discontinuous Deformation Analysis.
2. It can easily hand discontinuities. If a cover is divided into m completely disconnected domains by discontinuity boundaries, m independent covers with the same shape will be used. Each cover takes one domain as its effective region.
3. It is easy to generate MM meshes. Since MM covers can span discontinuous boundaries, regular meshes are always available no matter how complicated the geometrical shapes of material volumes are. Therefore, it is very suitable to generate meshes automatically. By contrast, the geometrical shapes of material volumes must be taken into account when FEM meshes are made.
4. It is easy to use high order displacement functions since high order MM and the first order MM use the same meshes. By contrast, in FEM, the orders of displacement functions are limited by the number of the element nodes. Namely, increasing the orders of displacement functions should increase the number of the nodes in an element.

The C program codes for the second order MM has been developed, and it has been applied to the example of a beam bending under a central point loading. The calculated results are quite good in agreement with the theoretical solutions. On the other hand, the results for the same example from the original first order MM are far from the theoretical solutions. That is, the original first order MM can not meet the requirement of the complicated non-linear deformation problems. Therefore, it has been shown that it is very important and necessary for us to develop high order MM and to apply it to complicated deformation problems.

References

[Shi G.] (1991): Manifold Method of Material Analysis, Transactions of the Ninth Army Conference on Applied Mathematics and Computing, 57-76 (Minneapolis, Minnesota).

[Shi G.] (1992): Modeling Rock Joints and Blocks by Manifold Method, Rock Mechanics Proceedings of the 33rd U. S. Symposium, 639-648 (Santa Fe, New Mexico).

Appendix

1. The details of the stiffness matrix (35)

$$\int \int_A [G_r]^T [E][G_s]\, dxdy = \begin{pmatrix} [C_{11}][C_{12}][C_{13}] \\ [C_{21}][C_{22}][C_{23}] \\ [C_{31}][C_{32}][C_{33}] \end{pmatrix}$$

where

$$[C_{rs}] = [E] \begin{pmatrix} t_{rs}(1,1) & t_{rs}(1,2) & t_{rs}(1,3) & t_{rs}(1,4) & t_{rs}(1,5) & t_{rs}(1,6) \\ t_{rs}(2,1) & t_{rs}(2,2) & t_{rs}(2,3) & t_{rs}(2,4) & t_{rs}(2,5) & t_{rs}(2,6) \\ t_{rs}(3,1) & t_{rs}(3,2) & t_{rs}(3,3) & t_{rs}(3,4) & t_{rs}(3,5) & t_{rs}(3,6) \\ t_{rs}(4,1) & t_{rs}(4,2) & t_{rs}(4,3) & t_{rs}(4,4) & t_{rs}(4,5) & t_{rs}(4,6) \\ t_{rs}(5,1) & t_{rs}(5,2) & t_{rs}(5,3) & t_{rs}(5,4) & t_{rs}(5,5) & t_{rs}(5,6) \\ t_{rs}(6,1) & t_{rs}(6,2) & t_{rs}(6,3) & t_{rs}(6,4) & t_{rs}(6,5) & t_{rs}(6,6) \end{pmatrix}$$

and

$$t_{rs}(1,1) = \left(f_{r2}f_{s2} + \frac{1-\nu}{2} f_{r3}f_{s3}\right) S^e$$

$$t_{rs}(2,1) = (f_{r1}f_{s2})\, S^e + \left(2f_{r2}f_{s2} + \frac{1-\nu}{2} f_{r3}f_{s3}\right) S_x^e + (f_{r3}f_{s2})\, S_y^e$$

$$t_{rs}(1,2) = (f_{r2}f_{s1})\, S^e + \left(2f_{r2}f_{s2} + \frac{1-\nu}{2} f_{r3}f_{s3}\right) S_x^e + (f_{r2}f_{s3})\, S_y^e$$

$$t_{rs}(3,1) = \left(\frac{1-\nu}{2} f_{r1}f_{s3}\right) S^e + \left(\frac{1-\nu}{2} f_{r2}f_{s3}\right) S_x^e + (f_{r2}f_{s2} + (1-\nu)\, f_{r3}f_{s3})\, S_y^e$$

$$t_{rs}(1,3) = \left(\frac{1-\nu}{2} f_{r3}f_{s1}\right) S^e + \left(\frac{1-\nu}{2} f_{r3}f_{s2}\right) S_x^e + (f_{r2}f_{s2} + (1-\nu)\, f_{r3}f_{s3})\, S_y^e$$

$$t_{rs}(4,1) = \left(\nu f_{r3}f_{s2} + \frac{1-\nu}{2} f_{r2}f_{s3}\right) S^e$$

$$t_{rs}(1,4) = \left(\nu f_{r2}f_{s3} + \frac{1-\nu}{2} f_{r3}f_{s2}\right) S^e$$

$$t_{rs}(5,1) = \left(\frac{1-\nu}{2} f_{r1}f_{s3}\right) S^e + (\nu f_{r3}f_{s2} + (1-\nu)\, f_{r2}f_{s3})\, S_x^e + \left(\frac{1-\nu}{2} f_{r3}f_{s3}\right) S_y^e$$

$$t_{rs}(1,5) = \left(\frac{1-\nu}{2} f_{r3}f_{s1}\right) S^e + (\nu f_{r2}f_{s3} + (1-\nu)\, f_{r3}f_{s2})\, S_x^e + \left(\frac{1-\nu}{2} f_{r3}f_{s3}\right) S_y^e$$

$$t_{rs}(6,1) = (\nu f_{r1}f_{s2})\, S^e + (\nu\, f_{r2}f_{s2})\, S_x^e + \left(2\nu f_{r3}f_{s2} + \frac{1-\nu}{2} f_{r2}f_{s3}\right) S_y^e$$

$$t_{rs}(1,6) = (\nu f_{r2} f_{s1})\, S^e + (\nu\, f_{r2} f_{s2})\, S^e_x + \left(2\nu f_{r2} f_{s3} + \frac{1-\nu}{2}\, f_{r3} f_{s2}\right) S^e_y$$

$$t_{rs}(2,2) = (f_{r1} f_{s1})\, S^e + (2 f_{r1} f_{s2} + 2 f_{r2} f_{s1})\, S^e_x + (f_{r1} f_{s3} + f_{r3} f_{s1})\, S^e_y + \left(4 f_{r2} f_{s2} + \frac{1-\nu}{2} f_{r3} f_{s3}\right) S^e_{xx}$$
$$+ (f_{r3} f_{s3})\, S^e_{yy} + (2 f_{r2} f_{s3} + 2 f_{r3} f_{s2})\, S^e_{xy}$$

$$t_{rs}(3,2) = \left(\frac{1-\nu}{2} f_{r1} f_{s3}\right) S^e_x + (f_{r2} f_{s1})\, S^e_y + \left(\frac{1-\nu}{2} f_{r2} f_{s3}\right) S^e_{xx} + (f_{r2} f_{s3})\, S^e_{yy} + (2 f_{r2} f_{s2} + (1-\nu) f_{r3} f_{s3})\, S^e_{xy}$$

$$t_{rs}(2,3) = \left(\frac{1-\nu}{2} f_{r3} f_{s1}\right) S^e_x + (f_{r1} f_{s2})\, S^e_y + \left(\frac{1-\nu}{2} f_{r3} f_{s2}\right) S^e_{xx} + (f_{r3} f_{s2})\, S^e_{yy} + (2 f_{r2} f_{s2} + (1-\nu) f_{r3} f_{s3})\, S^e_{xy}$$

$$t_{rs}(4,2) = (\nu f_{r3} f_{s1})\, S^e + \left(\frac{1-\nu}{2}\, f_{r2} f_{s3} + 2\nu f_{r3} f_{s2}\right) S^e_x + (\nu f_{r3} f_{s3})\, S^e_y$$

$$t_{rs}(2,4) = (\nu f_{r1} f_{s3})\, S^e + \left(\frac{1-\nu}{2}\, f_{r3} f_{s2} + 2\nu f_{r2} f_{s3}\right) S^e_x + (\nu f_{r3} f_{s3})\, S^e_y$$

$$t_{rs}(5,2) = \left(\nu f_{r3} f_{s1} + \frac{1-\nu}{2}\, f_{r1} f_{s3}\right) S^e_x + (2\nu f_{r3} f_{s2} + (1-\nu) f_{r2} f_{s3})\, S^e_{xx} + \left((\nu + \frac{1-\nu}{2})\, f_{r3} f_{s3}\right) S^e_{xy}$$

$$t_{rs}(2,5) = \left(\nu f_{r1} f_{s3} + \frac{1-\nu}{2}\, f_{r3} f_{s1}\right) S^e_x + (2\nu f_{r2} f_{s3} + (1-\nu) f_{r3} f_{s2})\, S^e_{xx} + \left((\nu + \frac{1-\nu}{2})\, f_{r3} f_{s3}\right) S^e_{xy}$$

$$t_{rs}(6,2) = (\nu f_{r1} f_{s1})\, S^e + (2\nu f_{r1} f_{s2} + \nu f_{r2} f_{s1})\, S^e_x + (\nu f_{r1} f_{s3} + 2\nu f_{r3} f_{s1})\, S^e_y$$
$$+ (2\nu f_{r2} f_{s2})\, S^e_{xx} + (2\nu f_{r3} f_{s3})\, S^e_{yy} + \left((\nu + \frac{1-\nu}{2}) f_{r2} f_{s3} + 4\nu f_{r3} f_{s2}\right) S^e_{xy}$$

$$t_{rs}(2,6) = (\nu f_{r1} f_{s1})\, S^e + (2\nu f_{r2} f_{s1} + \nu f_{r1} f_{s2})\, S^e_x + (\nu f_{r3} f_{s1} + 2\nu f_{r1} f_{s3})\, S^e_y$$
$$+ (2\nu f_{r2} f_{s2})\, S^e_{xx} + (2\nu f_{r3} f_{s3})\, S^e_{yy} + \left((\nu + \frac{1-\nu}{2}) f_{r3} f_{s2} + 4\nu f_{r2} f_{s3}\right) S^e_{xy}$$

$$t_{rs}(3,3) = \left(\frac{1-\nu}{2}\, f_{r1} f_{s1}\right) S^e + \left(\frac{1-\nu}{2}\, f_{r1} f_{s2} + \frac{1-\nu}{2}\, f_{r2} f_{s1}\right) S^e_x + ((1-\nu)\, f_{r1} f_{s3} + (1-\nu)\, f_{r3} f_{s1})\, S^e_y$$
$$+ \left(\frac{1-\nu}{2}\, f_{r2} f_{s2}\right) S^e_{xx} + (2(1-\nu)\, f_{r3} f_{s3} + f_{r2} f_{s2})\, S^e_{yy} + ((1-\nu)\, f_{r2} f_{s3} + (1-\nu)\, f_{r3} f_{s2})\, S^e_{xy}$$

$$t_{rs}(4,3) = \left(\frac{1-\nu}{2}\, f_{r2} f_{s1}\right) S^e + \left(\frac{1-\nu}{2}\, f_{r2} f_{s2}\right) S^e_x + ((1-\nu)\, f_{r2} f_{s3} + \nu f_{r3} f_{s2})\, S^e_y$$

$$t_{rs}(3,4) = \left(\frac{1-\nu}{2}\, f_{r1} f_{s2}\right) S^e + \left(\frac{1-\nu}{2}\, f_{r2} f_{s2}\right) S^e_x + ((1-\nu)\, f_{r3} f_{s2} + \nu f_{r2} f_{s3})\, S^e_y$$

$$t_{rs}(5,3) = \left(\frac{1-\nu}{2}\, f_{r1} f_{s1}\right) S^e + \left(\frac{1-\nu}{2}\, f_{r1} f_{s2} + (1-\nu)\, f_{r2} f_{s1}\right) S^e_x + \left((1-\nu)\, f_{r1} f_{s3} + \frac{1-\nu}{2}\, f_{r3} f_{s1}\right) S^e_y$$
$$+ ((1-\nu)\, f_{r2} f_{s2})\, S^e_{xx} + ((1-\nu)\, f_{r3} f_{s3})\, S^e_{yy} + \left(2(1-\nu)\, f_{r2} f_{s3} + (\nu + \frac{1-\nu}{2})\, f_{r3} f_{s2}\right) S^e_{xy}$$

$$t_{rs}(3,5) = \left(\frac{1-\nu}{2}\, f_{r1} f_{s1}\right) S^e + \left(\frac{1-\nu}{2}\, f_{r2} f_{s1} + (1-\nu)\, f_{r1} f_{s2}\right) S^e_x + \left((1-\nu)\, f_{r3} f_{s1} + \frac{1-\nu}{2}\, f_{r1} f_{s3}\right) S^e_y$$
$$+ ((1-\nu)\, f_{r2} f_{s2})\, S^e_{xx} + ((1-\nu)\, f_{r3} f_{s3})\, S^e_{yy} + \left(2(1-\nu)\, f_{r3} f_{s2} + (\nu + \frac{1-\nu}{2})\, f_{r2} f_{s3}\right) S^e_{xy}$$

$$t_{rs}(6,3) = \left(\nu f_{r1} f_{s2} + \frac{1-\nu}{2}\, f_{r2} f_{s1}\right) S^e_y + (2\nu f_{r3} f_{s2} + (1-\nu) f_{r2} f_{s3})\, S^e_{yy} + \left((\nu + \frac{1-\nu}{2})\, f_{r2} f_{s2}\right) S^e_{xy}$$

$$t_{rs}(3,6) = \left(\nu f_{r2} f_{s1} + \frac{1-\nu}{2}\, f_{r1} f_{s2}\right) S^e_y + (2\nu f_{r2} f_{s3} + (1-\nu) f_{r3} f_{s2})\, S^e_{yy} + \left((\nu + \frac{1-\nu}{2})\, f_{r2} f_{s2}\right) S^e_{xy}$$

$$t_{rs}(4,4) = \left(\frac{1-\nu}{2} f_{r2}f_{s2} + f_{r3}f_{s3}\right) S^e$$

$$t_{rs}(5,4) = \left(\frac{1-\nu}{2} f_{r1}f_{s2}\right) S^e + ((1-\nu) f_{r2}f_{s2} + f_{r3}f_{s3}) S_x^e + \left(\frac{1-\nu}{2} f_{r3}f_{s2}\right) S_y^e$$

$$t_{rs}(4,5) = \left(\frac{1-\nu}{2} f_{r2}f_{s1}\right) S^e + ((1-\nu) f_{r2}f_{s2} + f_{r3}f_{s3}) S_x^e + \left(\frac{1-\nu}{2} f_{r2}f_{s3}\right) S_y^e$$

$$t_{rs}(6,4) = (f_{r1}f_{s3}) S^e + (f_{r2}f_{s3}) S_x^e + \left(\frac{1-\nu}{2} f_{r2}f_{s2} + 2f_{r3}f_{s3}\right) S_y^e$$

$$t_{rs}(4,6) = (f_{r3}f_{s1}) S^e + (f_{r3}f_{s2}) S_x^e + \left(\frac{1-\nu}{2} f_{r2}f_{s2} + 2f_{r3}f_{s3}\right) S_y^e$$

$$\begin{aligned} t_{rs}(5,5) = {} & \left(\frac{1-\nu}{2} f_{r1}f_{s1}\right) S^e + ((1-\nu) f_{r1}f_{s2} + (1-\nu) f_{r2}f_{s1}) S_x^e + \left(\frac{1-\nu}{2} f_{r1}f_{s3} + \frac{1-\nu}{2} f_{r3}f_{s1}\right) S_y^e \\ & + (2(1-\nu) f_{r2}f_{s2} + f_{r3}f_{s3}) S_{xx}^e + \left(\frac{1-\nu}{2} f_{r3}f_{s3}\right) S_{yy}^e + ((1-\nu) f_{r2}f_{s3} + (1-\nu) f_{r3}f_{s2}) S_{xy}^e \end{aligned}$$

$$\begin{aligned} t_{rs}(6,5) = {} & (f_{r1}f_{s3}) S_x^e + \left(\frac{1-\nu}{2} f_{r2}f_{s1}\right) S_y^e + (f_{r2}f_{s3}) S_{xx}^e + \left(\frac{1-\nu}{2} f_{r2}f_{s3}\right) S_{yy}^e \\ & + ((1-\nu) f_{r2}f_{s2} + 2f_{r3}f_{s3}) S_{xy}^e \end{aligned}$$

$$\begin{aligned} t_{rs}(5,6) = {} & (f_{r3}f_{s1}) S_x^e + \left(\frac{1-\nu}{2} f_{r1}f_{s2}\right) S_y^e + (f_{r3}f_{s2}) S_{xx}^e + \left(\frac{1-\nu}{2} f_{r3}f_{s2}\right) S_{yy}^e \\ & + ((1-\nu) f_{r2}f_{s2} + 2f_{r3}f_{s3}) S_{xy}^e \end{aligned}$$

$$\begin{aligned} t_{rs}(6,6) = {} & (f_{r1}f_{s1}) S^e + (f_{r1}f_{s2} + f_{r2}f_{s1}) S_x^e + (2f_{r1}f_{s3} + 2f_{r3}f_{s1}) S_y^e \\ & + (f_{r2}f_{s2}) S_{xx}^e + \left(\frac{1-\nu}{2} f_{r2}f_{s2} + 4f_{r3}f_{s3}\right) S_{yy}^e + (2f_{r2}f_{s3} + 2f_{r3}f_{s2}) S_{xy}^e \end{aligned}$$

$$S^e = \int \int_A dxdy$$

$$S_x^e = \int \int_A xdxdy$$

$$S_y^e = \int \int_A ydxdy$$

$$S_{xy}^e = \int \int_A xydxdy$$

$$S_{xx}^e = \int \int_A x^2dxdy$$

$$S_{yy}^e = \int \int_A y^2dxdy$$

2. The integration in inertia force matrix

$$\iint_A F_{r1}F_{s1}dxdy = \iint_A (f_{r1} + f_{r2}x + f_{r3}y)(f_{s1} + f_{s2}x + f_{s3}y)dxdy$$
$$= (f_{r1}f_{s1})\, S^e + (f_{r1}f_{s2} + f_{r2}f_{s1})\, S^e_x + (f_{r1}f_{s3} + f_{r3}f_{s1})\, S^e_y$$
$$+ (f_{r2}f_{s2})\, S^e_{xx} + (f_{r3}f_{s3})\, S^e_{yy} + (f_{r2}f_{s3} + f_{r3}f_{s2})\, S^e_{xy}$$

$$\iint_A F_{r2}F_{s1}dxdy = \iint_A (f_{r1}x + f_{r2}x^2 + f_{r3}xy)(f_{s1} + f_{s2}x + f_{s3}y)dxdy$$
$$= (f_{r1}f_{s1})\, S^e_x + (f_{r1}f_{s2} + f_{r2}f_{s1})\, S^e_{xx} + (f_{r1}f_{s3} + f_{r3}f_{s1})\, S^e_{xy}$$
$$+ (f_{r2}f_{s2})\, S^e_{xxx} + (f_{r3}f_{s3})\, S^e_{xyy} + (f_{r2}f_{s3} + f_{r3}f_{s2})\, S^e_{xxy}$$
$$= \iint_A F_{r1}F_{s2}dxdy$$

$$\iint_A F_{r3}F_{s1}dxdy = \iint_A (f_{r1}y + f_{r2}xy + f_{r3}y^2)(f_{s1} + f_{s2}x + f_{s3}y)dxdy$$
$$= (f_{r1}f_{s1})\, S^e_y + (f_{r1}f_{s2} + f_{r2}f_{s1})\, S^e_{xy} + (f_{r1}f_{s3} + f_{r3}f_{s1})\, S^e_{yy}$$
$$+ (f_{r2}f_{s2})\, S^e_{xxy} + (f_{r3}f_{s3})\, S^e_{yyy} + (f_{r2}f_{s3} + f_{r3}f_{s2})\, S^e_{xyy}$$
$$= \iint_A F_{r1}F_{s3}dxdy$$

$$\iint_A F_{r2}F_{s2}dxdy = \iint_A (f_{r1}x + f_{r2}x^2 + f_{r3}xy)(f_{s1}x + f_{s2}x^2 + f_{s3}xy)dxdy$$
$$= (f_{r1}f_{s1})\, S^e_{xx} + (f_{r1}f_{s2} + f_{r2}f_{s1})\, S^e_{xxx} + (f_{r1}f_{s3} + f_{r3}f_{s1})\, S^e_{xxy}$$
$$+ (f_{r2}f_{s2})\, S^e_{xxxx} + (f_{r3}f_{s3})\, S^e_{xxyy} + (f_{r2}f_{s3} + f_{r3}f_{s2})\, S^e_{xxxy}$$

$$\iint_A F_{r2}F_{s3}dxdy = \iint_A (f_{r1}x + f_{r2}x^2 + f_{r3}xy)(f_{s1}y + f_{s2}xy + f_{s3}y^2)dxdy$$
$$= (f_{r1}f_{s1})\, S^e_{xy} + (f_{r1}f_{s2} + f_{r2}f_{s1})\, S^e_{xxy} + (f_{r1}f_{s3} + f_{r3}f_{s1})\, S^e_{xyy}$$
$$+ (f_{r2}f_{s2})\, S^e_{xxxy} + (f_{r3}f_{s3})\, S^e_{xyyy} + (f_{r2}f_{s3} + f_{r3}f_{s2})\, S^e_{xxyy}$$
$$= \iint_A F_{r3}F_{s2}dxdy$$

$$\iint_A F_{r3}F_{s3}dxdy = \iint_A (f_{r1}y + f_{r2}xy + f_{r3}y^2)(f_{s1}y + f_{s2}xy + f_{s3}y^2)dxdy$$
$$= (f_{r1}f_{s1})\, S^e_{yy} + (f_{r1}f_{s2} + f_{r2}f_{s1})\, S^e_{xyy} + (f_{r1}f_{s3} + f_{r3}f_{s1})\, S^e_{yyy}$$
$$+ (f_{r2}f_{s2})\, S^e_{xxyy} + (f_{r3}f_{s3})\, S^e_{yyyy} + (f_{r2}f_{s3} + f_{r3}f_{s2})\, S^e_{xyyy}$$

where

$$S^e = \frac{1}{2}\sum_{i=1}^{m} \begin{vmatrix} 1 & 0 & 0 \\ 1 & x_i & y_i \\ 1 & x_{i+1} & y_{i+1} \end{vmatrix}$$

$$S^e_x = \frac{S^e}{3}\sum_{i=1}^{m} (x_i + x_{i+1})$$

$$S_y^e = \frac{S^e}{3}\sum_{i=1}^{m}(y_i + y_{i+1})$$

$$S_{xx}^e = \frac{S^e}{6}\sum_{i=1}^{m}(x_i{}^2 + x_{i+1}{}^2 + x_i x_{i+1})$$

$$S_{yy}^e = \frac{S^e}{6}\sum_{i=1}^{m}(y_i{}^2 + y_{i+1}{}^2 + y_i y_{i+1})$$

$$S_{xy}^e = \frac{S^e}{12}\sum_{i=1}^{m}(2x_i y_i + 2x_{i+1}y_{i+1} + x_i y_{i+1} + x_{i+1}y_i)$$

$$S_{xxx}^e = \iint_A x^3 dxdy = \frac{S^e}{10}\sum_{i=1}^{m}(x_i^3 + x_i^2 x_{i+1} + x_i x_{i+1}^2 + x_{i+1}^3)$$

$$S_{yyy}^e = \iint_A y^3 dxdy = \frac{S^e}{10}\sum_{i=1}^{m}(y_i^3 + y_i^2 y_{i+1} + y_i y_{i+1}^2 + y_{i+1}^3)$$

$$S_{xxxx}^e = \iint_A x^4 dxdy = \frac{S^e}{15}\sum_{i=1}^{m}(x_i^4 + x_i^3 x_{i+1} + x_i^2 x_{i+1}^2 + x_i x_{i+1}^3 + x_{i+1}^4)$$

$$S_{yyyy}^e = \iint_A y^4 dxdy = \frac{S^e}{15}\sum_{i=1}^{m}(y_i^4 + y_i^3 y_{i+1} + y_i^2 y_{i+1}^2 + y_i y_{i+1}^3 + y_{i+1}^4)$$

$$S_{xxy}^e = \iint_A x^2 y\, dxdy$$

$$= \frac{S^e}{30}\sum_{i=1}^{m}(3x_i^2 y_i + 2x_i x_{i+1} y_i + x_{i+1}^2 y_i + x_i^2 y_{i+1} + 2x_i x_{i+1} y_{i+1} + 3x_{i+1}^2 y_{i+1})$$

$$S_{xyy}^e = \iint_A xy^2 dxdy$$

$$= \frac{S^e}{30}\sum_{i=1}^{m}(3y_i^2 x_i + 2y_i y_{i+1} x_i + y_{i+1}^2 x_i + y_i^2 x_{i+1} + 2y_i y_{i+1} x_{i+1} + 3y_{i+1}^2 x_{i+1})$$

$$S_{xxxy}^e = \iint_A x^3 y\, dxdy$$

$$= \frac{S^e}{60}\sum_{i=1}^{m}\big(4x_i^3 y_i + 3x_i^2 x_{i+1} y_i + 2x_i x_{i+1}^2 y_i + x_{i+1}^3 y_i$$
$$+ x_i^3 y_{i+1} + 2x_i^2 x_{i+1} y_{i+1} + 3x_i x_{i+1}^2 y_{i+1} + 4x_{i+1}^3 y_{i+1}\big)$$

$$S_{xyyy}^e = \iint_A xy^3 dxdy$$

$$= \frac{S^e}{60}\sum_{i=1}^{m}\big(4y_i^3 x_i + 3y_i^2 y_{i+1} x_i + 2y_i y_{i+1}^2 x_i + y_{i+1}^3 x_i$$
$$+ y_i^3 x_{i+1} + 2y_i^2 y_{i+1} x_{i+1} + 3y_i y_{i+1}^2 x_{i+1} + 4y_{i+1}^3 x_{i+1}\big)$$

$$
\begin{aligned}
S^e_{xxyy} &= \iint_A x^2y^2\,dxdy \\
&= \frac{S^e}{90}\sum_{i=1}^{m}\big(6x_i^2y_i^2 + 3x_i^2y_iy_{i+1} + x_i^2y_{i+1}^2 + 3x_ix_{i+1}y_i^2 + 4x_ix_{i+1}y_iy_{i+1} \\
&\qquad + 3x_ix_{i+1}y_{i+1}^2 + x_{i+1}^2y_i^2 + 3x_{i+1}^2y_iy_{i+1} + 6x_{i+1}^2y_{i+1}^2\big)
\end{aligned}
$$

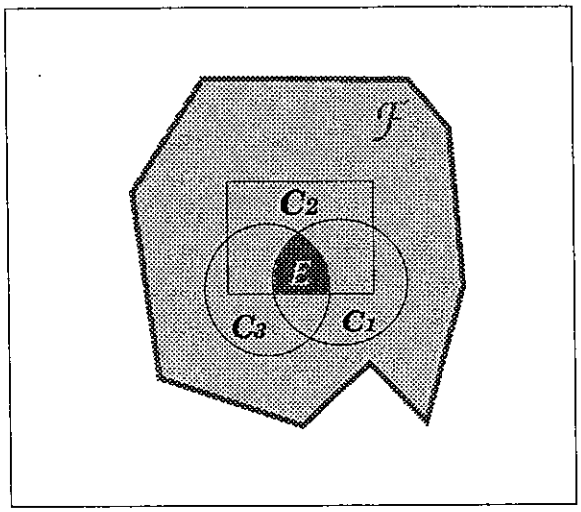

Fig. 1 Three overlapped covers C_1, C_2 and C_3 have a common area E.

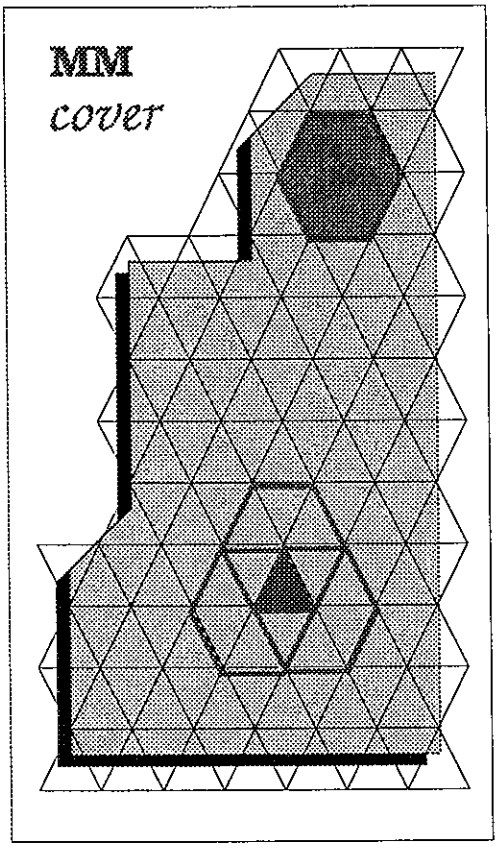

Fig. 2 MM covers formed from triangular meshes.

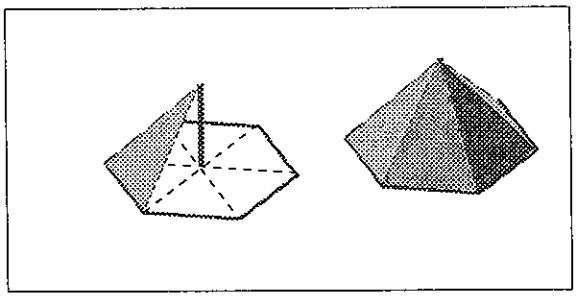

Fig. 3 Weighting functions defined in a cover.

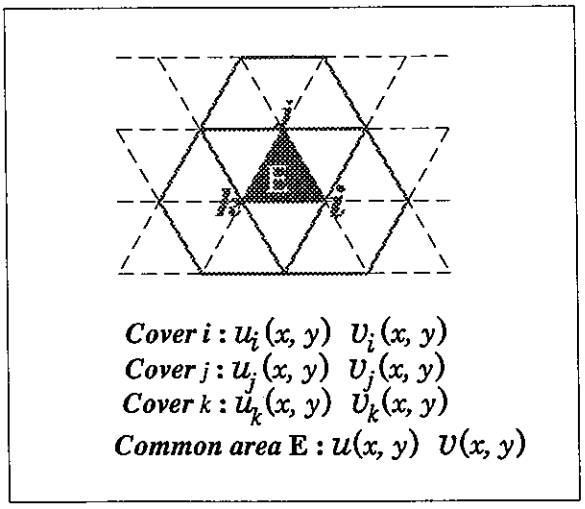

Fig. 4 The displacement functions in three covers and their common area.

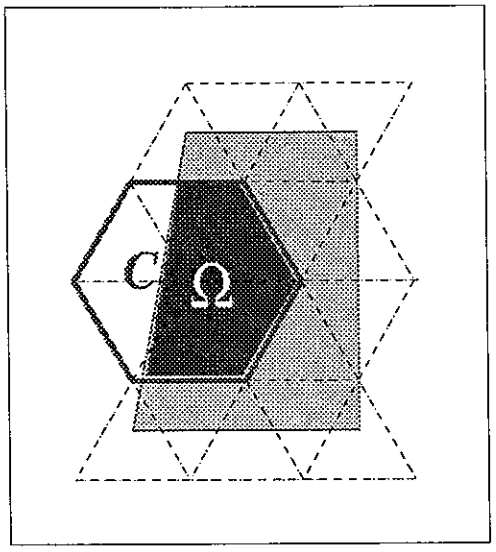

Fig. 5 A cover is partially out of the material volume.

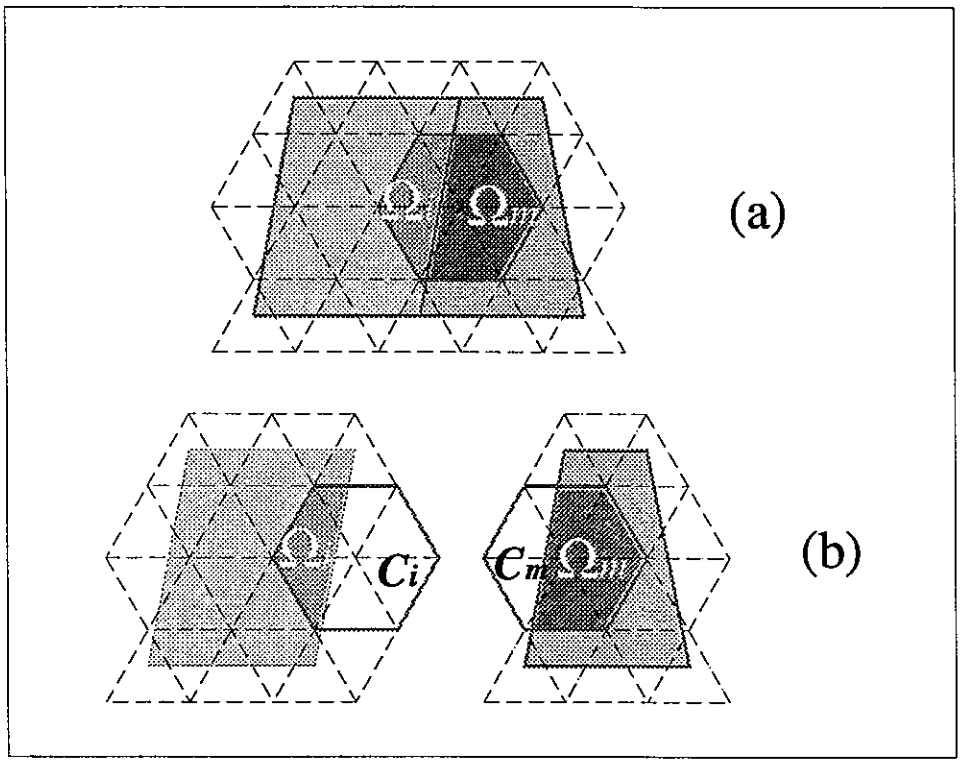

Fig. 6 A cover spans a discontinuity boundary.

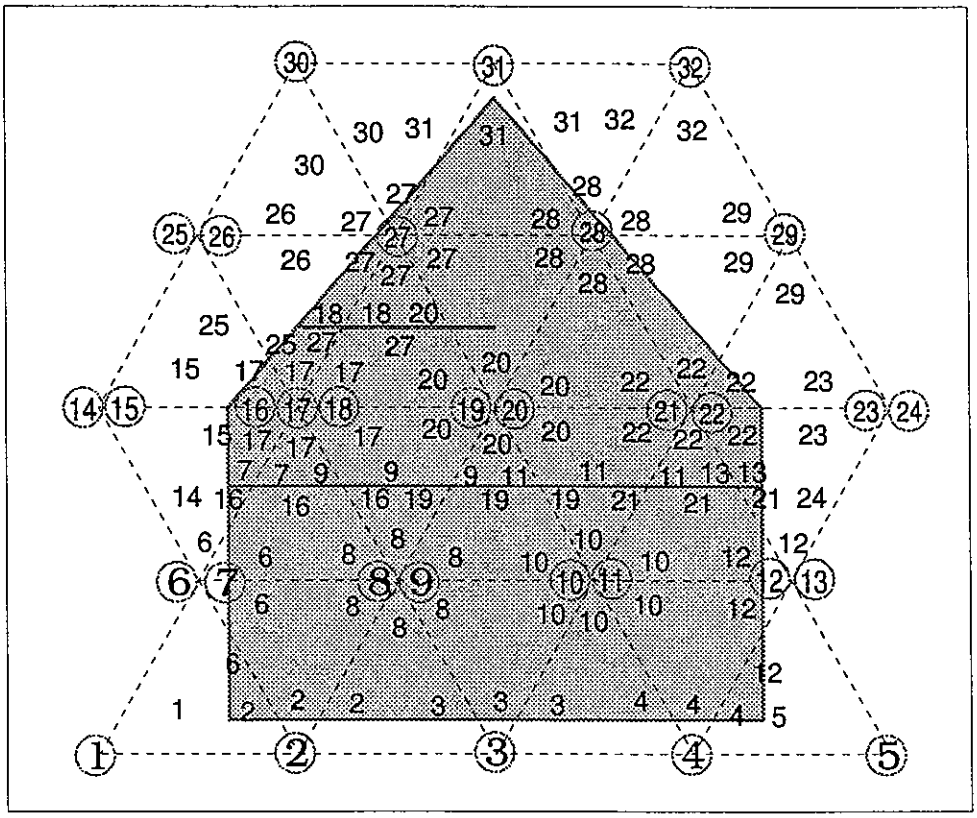

Fig. 7 An example of MM covers.

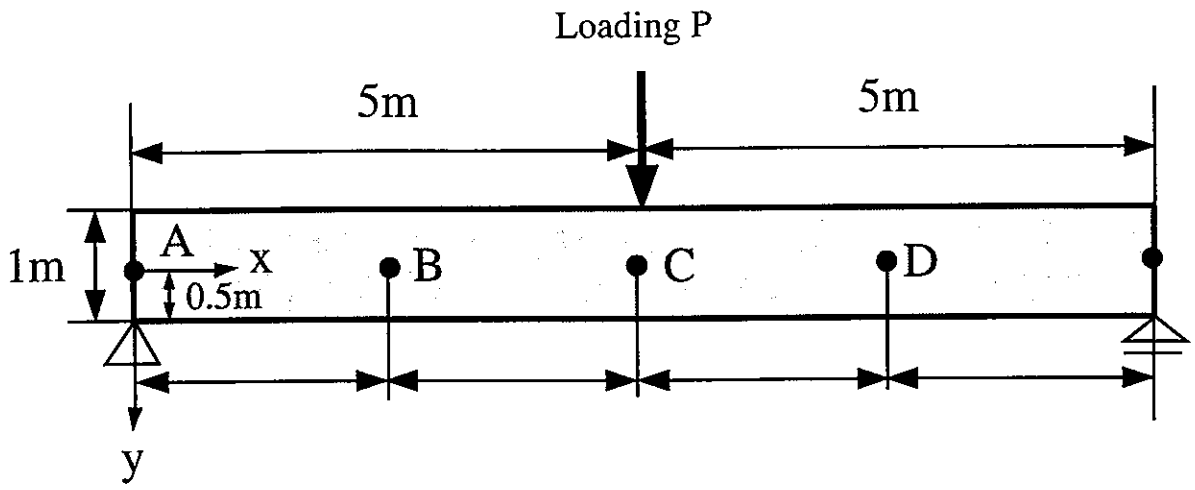

Fig. 8 Beam bending problem under central loading

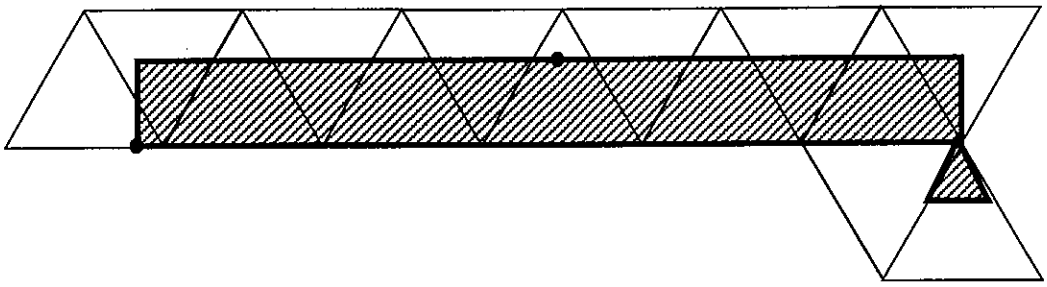

Fig. 9 The model of beam bending for both the first order and second order MM

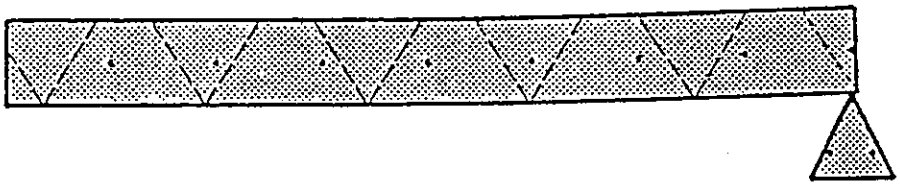

Fig. 10 The deformation of the beam calculated by using the first order MM

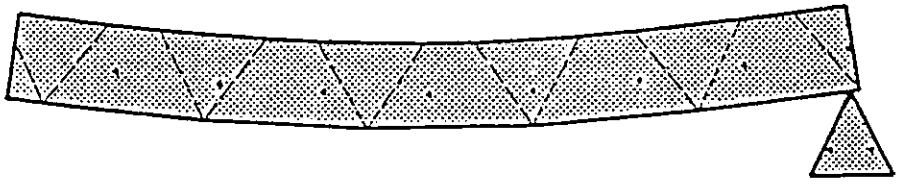

Fig. 11 The deformation of the beam calculated by using the second order MM

Application of DDA to simulate fracture propagation in solid

Te-Chih Ke

Department of Civil Engineering, Chung Yuan University
Chungli, Taiwan 32023

ABSTRACT: *Fracture propagation* is a fantastic subject in the field of solid mechanics. Its importance relies upon not only the theoretical interest, but also the variety of its engineering applications. This paper is intended to utilize the revised *DDA* code in conjunction with the *artificial joint concept*, to numerically simulate the fracture propagation of a solid column subjected to uniaxial tension. The simulation results indicate that the micro-texture and -strength in solid both affect the corresponding fracturing behavior. Besides, a brief discussion on the various analyses for this subject are also addressed.

1 INTRODUCTION

Fracture propagation is always a fantastic and challenging subject in the field of solid mechanics. Its importance relies upon not only the theoretical interest (tracing back to the birth of classic mechanics), but also the variety of its engineering applications. For example, its developing history has been well connected with civil engineering materials like concrete and rock, mechanical materials like metal, electronic materials like silicon chips, as well as transportation vehicle and military industries. Although its related theories like damage/fracture mechanics and model testing were continuously in progress, some problems still remain unsolved.

The main goal of this paper is to utilize the revised *DDA* code in conjunction with the artificial joint concept, to numerically simulate the fracture propagation in solids as well as to provide insight into the influences of micro-texture and micro-strength of solids. Before achieving this objective, the basic view of fracture propagation problems and the corresponding analyses available today are discussed in the following.

1.1 RESEARCH BACKGROUND

1.1.1 Mechanical nature of fracture propagation

Intact solid, in a macro scale, can be regarded as "continuum", and fracture propagation is a progressive breaking process, converting the initial *continuous* state into the *discontinuous* one. The so-called fracture is essentially a discontinuity, across which the displacement and strain fields are not continuous, and whose stiffness and strength are both lower than those of the solid part. Figure 1 depicts the developing cracks through the solid domain, which are finally divided into three pieces.

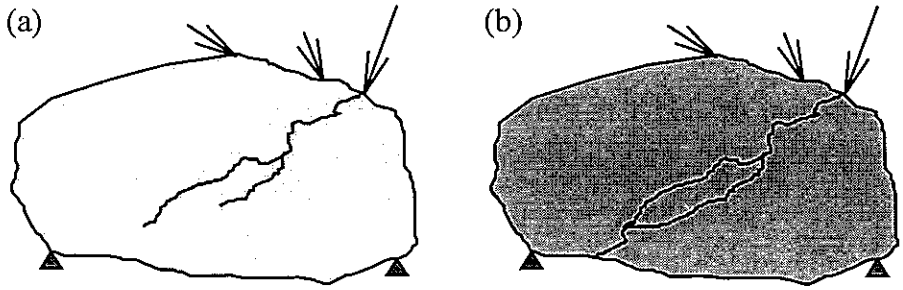

Figure 1. Illustration of fracture propagation: a) in progress; b) into three pieces

How does fracture propagation happen? A fracture always takes the weakest spot in solid to initiate or to propagate toward. That is at a certain time and under an external force field, the resultant stress field $\{\sigma\}$ and corresponding strength distribution $\{S\}$ appear within a solid, in which a new fracture always initiates wherever $\sigma \geq S$, followed by the redistribution of stress/strength field and the search of the next propagating path for the current fracture. This statement seems to be simple, but it implies the following four questions to resolve (what to be known): 1) the stress distribution within a solid; 2) the strength distribution within a solid corresponding to a certain failure mechanism; 3) all the relevant input data like geometry, material properties, and loadings; 4) the energy loss caused by fracturing. Only the third of the above relies upon the matter of measurement technology, and the rest highly depend on the capabilities of the fracturing analyses to be used. So, what are the minimum requirements for a sound fracturing analysis?

1.1.2 Minimum requirements for a sound fracturing analysis

If all the relevant input data like geometry, material properties, and loadings are known for a problem, from the author's point view, a *sound* fracturing analysis must be capable of:

1) computing the initiating point of a fracture as well as the stress/strength distributions within a solid;
2) computing the subsequent fracturing path, including the direction and length (according to some physical laws or measurements);
3) treating the energy loss caused by fracturing (according to some physical laws or measurements);
4) treating the discontinuous interactions along the existing fractures.

These four requirements are used to compare the differences among several fracturing analyses currently available today as follows. Table 1 pre-summarizes the comparison results.

Table 1. Comparison among current fracturing analyses

Fracturing analysis	Crack initiating point	Propagating direction/length	Fracture-induced energy loss	Discontinuous interactions
Fracture mechanics	*X*	*C/N*	*N*	*N*
Continuum computation	*G*	*C/P*	*N*	*N*
Lattice model	*C*	*C*	*N*	*N*
Model test	*C*	*C*	*P*	-
Discontinuous computation	*P*	*C*	*P*	*G*

G: excellent; *C*: capable; *P*: possible with extension; *N*: unable; *X*: given as a *priori*.

1.1.3 Comparisons of current fracturing analyses

According to mathematics, a crack tip in solid is really a *singular* point. By assuming elasticity and static loading, the theory of fracture mechanics [1] and the like can explain the stress concentration near a crack tip and predict the possible direction of crack propagation (Figure 2a), but are unable to deal with the initial condition of no crack tips, estimate of propagation length, energy loss, and discontinuous interactions along existing cracks.

Continuum computational methods like *finite element method* (*FEM*) and *boundary element method* (*BEM*) need to discretize the solid domain or boundary of a problem into elements, which are mutually connected at nodes to satisfy the continuous condition (Figure 2b). The method of this kind has been extensively applied to various continuous problems, and with certain modifications it can also treat contact/discontinuous problems reasonably [2]. However, as the number of discontinuities increases, continuum methods become intractable, perhaps yielding no solution. Besides, the *remeshing* scheme after cracking and the treatment of fracture-induced energy loss are the great burdens needed to dig out carefully.

Under the framework of *lattice model*, a solid domain is converted into an "equivalent" assemblage of beam-columns (Figure 2c) [3]. Whenever the stress of a beam-column exceeds as limit, it will "disappear" without energy loss on the next step, leading to the subsequent stress redistribution and the breakage of another beam-column. This model can merely be adopted for a solid mainly subjected to tension, because it is unable to handle the contact interactions between two adjacent beam-columns.

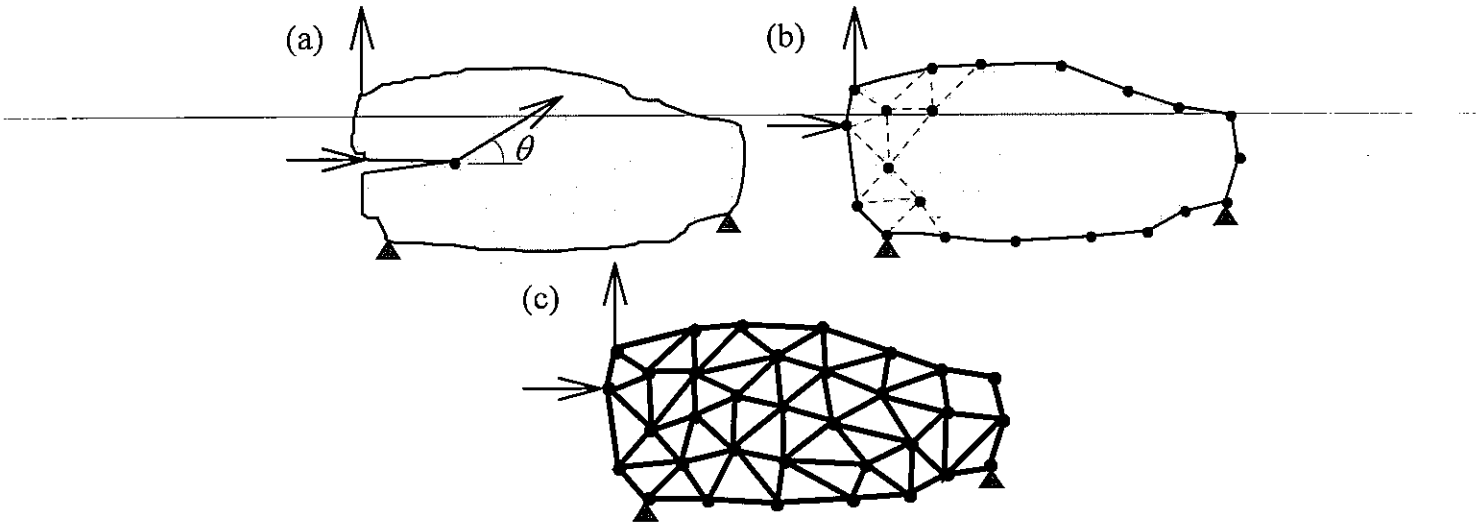

Figure 2. Three fracturing analyses: a) fracture mechanics; b) finite element or boundary element methods; c) lattice-model method

Model tests can qualitatively or semi-quantitatively capture the fracturing behavior of a solid, but at least it has the following limitations: 1) current surveying technology is not capable enough to provide detailed data on material properties for a precise feedback analysis; 2) two common specimens seldom exist in nature or can not be manufactured, leading to the low reproductivity of test results; 3) the scale effect of specimens and boundary effect of test machine are difficult to control; 4) precise equipment plus high cost is required.

It is known that once a fracture appears, the solid is no longer continuous and must be treated as discontinuum. The so-called discrete element method [4] represents all the discontinuum computational methods developed recently to deal with a discontinuous system composed of discrete blocks as shown in Figure 3. According to the view point of the author ,

the method of this kind at least possesses the following capabilities: 1) allowing finite displacement/rotation of a block, and separation of two blocks; 2) automatic detection of block contacts as computation proceeds; 3) fulfillment of block contact constraints (no penetration and no tension); 4) rational computation of contact forces; 5) satisfaction of dynamic equilibrium condition at any time. However, not every existing discrete element method owns the above five capabilities. The distinct element method (*DEM*) developed by Cundall [5] appeared first, which is a force method and an explicit method. Adding some material failure criteria, *DEM* allows the breakage of one block instantly into several pieces without energy loss. Recently, a coupled *DEM-FEM* program was developed by Munjiza etc. [6], which seems to handle the fracture propagation problems more realistically. The discontinuous deformation analysis (*DDA*) pioneered by Shi [7] is the latest version of discrete element methods. Because *DDA* owns one of the best schemes to deal with block kinematics, continuous efforts have been made toward its improvements. Today, *DDA* has become another powerful tool to analyze the complex interactions among blocks.

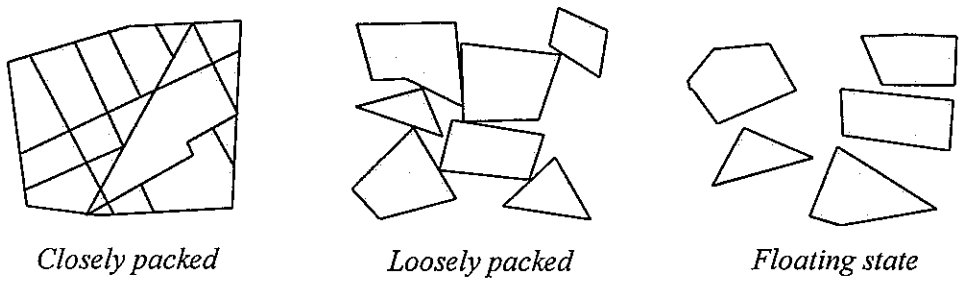

Figure 3 Discontinuous block systems

1.2 RESEARCH APPROACH

Considering the research budget and repeatability of analysis results, numerical analysis is preferred. According to the discussion of the previous sub-section, *DDA* was selected to be the main research tool in this paper. However, the original form of *DDA* did not possess the ability of simulating fracture propagation yet, and the *artificial joint concept* proposed by the author was adopted to enhance it and to revise its code. With fundamental verifications, this revised *DDA* code is then used to numerically study the fracturing behavior of a solid column under uniaxial tension, especially the influences of micro-fabric and micro-strength in solid. Besides, as an illustrative example, the impact behavior of an imaginary military is also examined. The future developments regarding the subject of this research are addressed in the concluding remarks.

2 BRIEF INTRODUCTION TO DDA

Since the invention of *DDA* in 1988, there have been two international conferences on its name to promote the use of *DDA*: 1) The First International Conference on Analysis of Discontinuous Deformation (*ICADD1*)was held in Chungli, Taiwan, in 1995; 2) The First Forum on *DDA* (*IFDDA1*) was held at Berkeley, California, USA, in 1996. It is believed that the full developments and the ultimate recognition of *DDA* within our engineering society will come out soon. The following sub-sections briefly describe the origination, theoretical background, computation flowchart, and recent developments of *DDA*.

2.1 ORIGINATION

In fact, *DDA* includes the forward analysis and backward analysis, both of which were developed by Shi and Goodman. In the backward analysis [8], the material properties or initial stresses of blocks can be computed for the given displacements or strains of blocks. On the other hand, the forward analysis usually represents what is the so-called *DDA*, in which the displacements, velocities, and stresses of blocks are computed according to the input of block geometry, material properties, and loading. Unlike *DEM*, *DDA* is a displacement method and an implicit method, which involves establishing and solving of simultaneous equations.

Dr. Shi thought that *DDA* has the following five features [7]: 1) complete block kinematics and its numerical realization; 2) perfect first-order displacement approximation; 3) strict postulate of equilibrium; 4) correct energy consumption; 5) high computing efficiency. Besides, the author suggests the three advantages of *DDA* over the other analyses: 1) to establish equilibrium equations based on the minimization of potential energy; 2) to seek right contact states by use of open-close iterations; 3) to provide closed-form solutions to block integrations.

The prototype of *DDA* was based on the following assumptions: 1) two-dimensional, and plain-stress blocks; 2) linearly-elastic, unbreakable, constant strain and non-internally cracked blocks; 3) linearly elastic, *Mohr-Coulomb*'s, and frictional block contacts; 4) static loading like body force, point load, and block initial stress. Of course, some of the above assumptions have been relaxed to accommodate new capability to date.

2.2 THEORETICAL BACKGROUND

Some important theoretical background of *DDA* is stated in this sub-section. Detailed formulation can be found in [7,9,10].

2.2.1 First-order displacement function

Figure 4 shows the positions of $P(x,y)$ with Block i at *Steps* j and $j+1$. Its displacement increments (u, v) can be expressed as

$$\begin{pmatrix} u \\ v \end{pmatrix}^{i}_{(x,y)} = [T_i]_{(x,y)} \, [D_i] \tag{1}$$

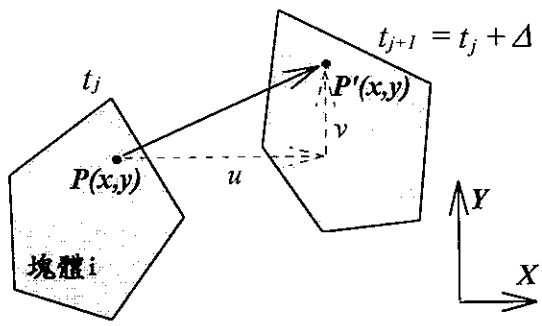

Figure 4. Displacement increments (u, v) of $P(x,y)$ within Block i

in which $[T_i]_{(x,y)}$ is the first-order displacement function, given by

$$[T_i]_{(x,y)} = \begin{pmatrix} 1 & 0 & -(y-y_0) & x-x_0 & 0 & (y-y_0)/2 \\ 0 & 1 & x-x_0 & 0 & (y-y_0) & (x-x_0)/2 \end{pmatrix} \tag{2}$$

(x_0, y_0) represents the centroid of Block i, and $[D_i]$ is the displacement vector of Block i,

$$\begin{aligned} [D_i]^T &= \begin{pmatrix} d_1 & d_2 & d_3 & d_4 & d_5 & d_6 \end{pmatrix} \\ &= \begin{pmatrix} u_0 & v_0 & \gamma_0 & \varepsilon_x & \varepsilon_y & \gamma_{xy} \end{pmatrix} \end{aligned} \tag{3}$$

where (u_0, v_0, γ_0) are the two rigid-body translations and one rotation with respect to the centroid, and $(\varepsilon_x, \varepsilon_y, \gamma_{xy})$ are the 2D strain components.

2.2.2 Equilibrium equations and minimization of potential energy

For a system of N blocks, its dynamic equilibrium equations can be given by

$$\begin{pmatrix} [K_{11}] & [K_{12}] & \cdots & [K_{1N}] \\ [K_{21}] & [K_{22}] & \cdots & [K_{2N}] \\ \vdots & \vdots & \ddots & \vdots \\ [K_{N1}] & [K_{N2}] & \cdots & [K_{NN}] \end{pmatrix} \begin{pmatrix} [D_1] \\ [D_2] \\ \vdots \\ [D_N] \end{pmatrix} = \begin{pmatrix} [F_1] \\ [F_2] \\ \vdots \\ [F_N] \end{pmatrix} \tag{4}$$

in which $[K_{ij}]$ is a 6×6 sub-matrix, and $[F_i]$ a 6×1 sub-vector. $[K_{ii}]$ only relates to the state of Block i, and $[K_{ij}]_{i\neq j}$ is defined by the contact and connection constraint between Blocks i and j. The components of $[K_{ij}]$ and $[F_i]$ are derived according to the minimization of potential energy Π:

$$\begin{aligned} [K_{ij}] &= \sum_{m=1}^{M} [K_{ij}]_m; \ \ with\ k_{rs}^{ij} = \frac{\partial^2 \Pi_m}{\partial d_{ri}\, \partial d_{sj}}, \ r, s = 1 \sim 6 \\ [F_i] &= \sum_{m=1}^{M} [F_i]_m; \ \ with\ f_r^i = -\frac{\partial \Pi_m(0)}{\partial d_{ri}}, \ r, s = 1 \sim 6 \end{aligned} \tag{5}$$

in which M is the total number of energy sources, and 0 refers to the beginning of a time step. Normally, strain energy and internal energy are regarded as positive potential energy, whiles external work as negative. All potential energy sources can be divided into *non-contact* terms which are irrelevant to block contacts, and the *contact* terms. Table 2 summarizes the resultant $[K_{ij}]$ and $[F_i]$ of various energy sources in *DDA*.

2.3 COMPUTATION FLOWCHART

Figure 5 depicts the flowchart of *DDA* computation. The input data include block geometry and control points, material properties (block and joints), and loadings. Within each step computation, *DDA* conducts: 1) contact search; 2) computation of non-contact terms; 3) open-close iterations; 4) checking for the maximum displacement; 5) updating of block coordinates, stresses, and velocities. The step computation is continued until the last step.

The open-close iterations are an important breakthrough in *DDA*, which compute contact terms, solve the global equations $[K][D]=[F]$, identify new contact states, and check for the convergence of solution. The main purpose of this scheme is to seek the right contact states at the end of every time step, under the contact constraints of no penetration and no tension. There are three types of contact states (*MO*): 1) opened (*MO=0*); 2) sliding (*MO=1*); 3)

locked ($MO=2$). The converging criterion is that in the two successive iterations, the identified contact states of all contacts have no change, i.e.

$$\sum_{i=1}^{N_2}(MO_i^j - MO_i^{j-1}) = 0 \ \ for\ Iteration\ j\ and\ N_2\ contacts \tag{6}$$

Table 2. Summary of the resultant $[K_{ij}]$ and $[F_i]$ in *DDA*

Energy source	Energy type and expression	Sub-matrix $[K_{ij}]$,$[F_i]$
Block deformation	Strain energy $\frac{1}{2}\iint[\varepsilon]^T[E][\varepsilon]dxdyw_z$	$[K_{ii}]= S_0^i[EE]w_z$
Block initial stress	Internal energy $\iint[\varepsilon]^T[\Sigma_0^i]dxdyw_z$	$[F_i]= S_0^i[\Sigma_0^i]w_z$
Block inertia force	External work $\rho_i\iint(u\ \ v)\ (u''\ \ v'')^T dxdyw_z$	$[K_{ii}]=2\rho_i[TT]_i/\Delta^2\ w_z$ $[F_i]=2\rho_i[V_0^i][TT]_i/\Delta\ w_z$
Block mass body force	External work $-\rho_i\iint(u\ \ v)\ (b_x\ \ b_y)^T dxdyw_z$	$[F_i]=2\rho_i S_0^i w_z[b]$
Block point load	External work $-(u\ \ v)\ (p_x\ \ p_y)w_z$	$[F_i]=[T_i]^T_{(x,y)}[p]w_z$
Block 1D displacement constraint	Strain energy $\frac{1}{2}k(\delta_0-[D]^T[C])^2w_z$	$[K_{ii}]=k[C][C]^Tw_z$; $[F_i]=-k\delta_0[C]w_z$
Block 2D displacement constraint	Strain energy $\frac{1}{2}k(\delta_x^2+\delta_y^2)w_z$	$[K_{ii}]=k[T_i]^T[T_i]w_z$; $[F_i]=-k[T_i]^T[d]w_z$
Block bolting constraint	Strain energy $\frac{1}{2}k(\delta_0+dl)^2w_z$ $=k(\delta_0+[D_j]^T[G_j]-[D_i]^T[E_i])^2w_z$	$[K_{ii}]=k[E_i][E_i]^Tw_z$; $[K_{jj}]=k[G_j][G_j]^Tw_z$; $[K_{ij}]=-k[E_i][G_j]^Tw_z$; $[K_{ji}]=-k[G_j][E_i]^Tw_z$; $[F_i]=k\delta_0[E_i]w_z$; $[F_j]=-k\delta_0[G_j]w_z$
Block rotation constraint	Strain energy $\frac{1}{2}kr^2(\theta_0-\gamma_0)^2w_z$	$k_{ii}^{33} = kr^2w_z$; $f_i^3 = kr^2\theta_0w_z$
Block pin-connection constraint	Strain energy $\frac{1}{2}k(\delta_x^2+\delta_y^2)w_z$	$[K_{ii}]=k[T_i]^T[T_i]w_z$; $[K_{jj}]=k[T_j]^T[T_j]w_z$; $[K_{ij}]=-k[T_i]^T[T_j]w_z$; $[K_{ji}]=-k[T_j]^T[T_i]w_z$; $[F_i]=-k[T_i]^T[d]w_z$; $[F_j]=k[T_j]^T[d]w_z$
Block mass damping	External work $c_m\rho_i\iint(u\ \ v)\ (u'\ \ v')^T dxdyw_z$	$[F_i]=-c_m\rho_i[TT]_i[V_0^i]w_z$
Normal contact spring	Strain energy $\frac{1}{2}k_n(d_0+[D_i]^T[P_i^N]+[D_j]^T[Q_j^N])^2w_z$	$[K_{ii}]=k_n[P_i^N][P_i^N]^Tw_z$; $[K_{jj}]=k_n[Q_j^N][Q_j^N]^Tw_z$; $[K_{ij}]=k_n[P_i^N][Q_j^N]^Tw_z$; $[K_{ji}]=k_n[Q_j^N][P_i^N]^Tw_z$; $[F_i]=-k_nd_0[P_i^N]w_z$; $[F_j]=-k_nd_0[Q_j^N]w_z$
Shear contact spring	Strain energy $\frac{1}{2}k_n(s_0+[D_i]^T[P_i^S]+[D_j]^T[Q_j^S])^2w_z$	$[K_{ii}]=k_s[P_i^S][P_i^S]^Tw_z$; $[K_{jj}]=k_s[Q_j^S][Q_j^S]^Tw_z$; $[K_{ij}]=k_s[P_i^S][Q_j^S]^Tw_z$; $[K_{ji}]=k_s[Q_j^S][P_i^S]^Tw_z$; $[F_i]=-k_ss_0[P_i^S]w_z$; $[F_j]=-k_ss_0[Q_j^S]w_z$
Contact sliding	External work $-(\mu f_n+C)$ $(-[D_i]^T[P_i^F]+[D_j]^T[Q_j^F])\psi w_z$	$[F_i]=-(\mu f_n+C)[P_i^F]\psi w_z$; $[F_j]=(\mu f_n+C)[Q_j^F]\psi w_z$

*Definitions of the relevant terms can be found in [7,9,10].

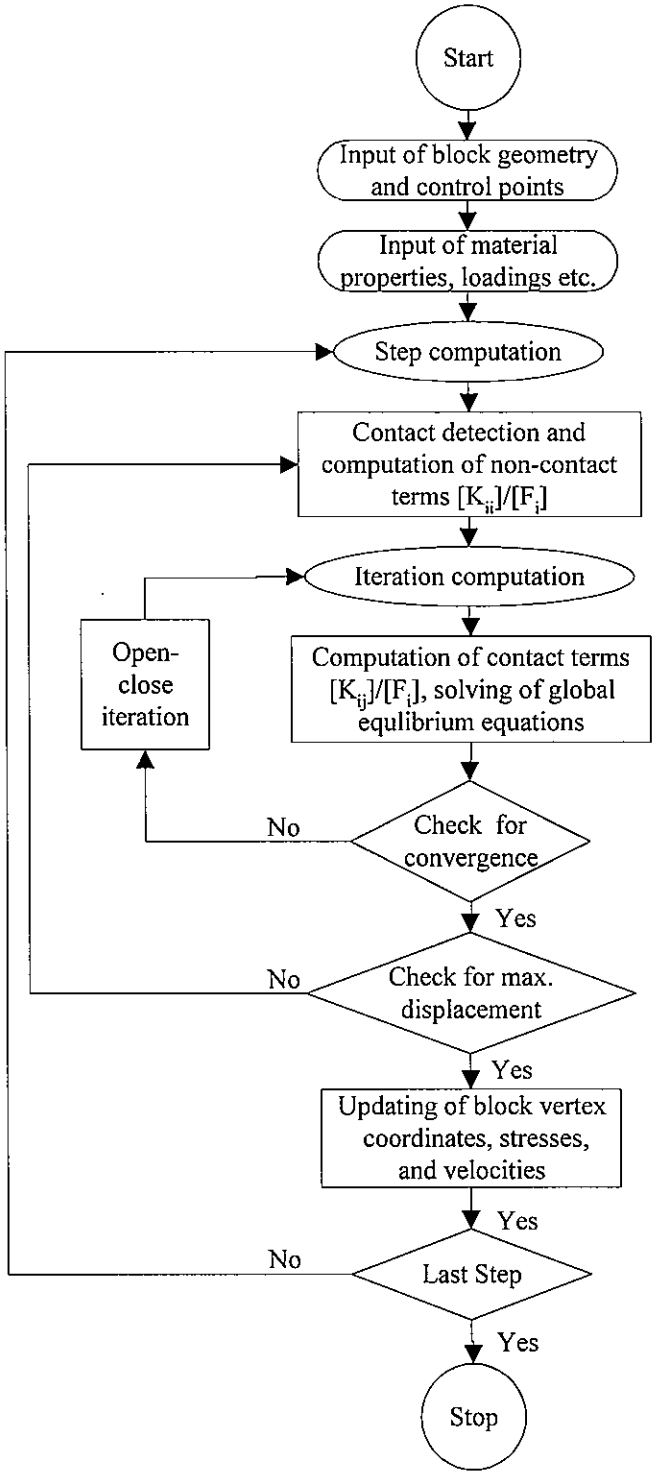

Figure 5. Flowchart of *DDA* computation

2.5 RECENT DEVELOPMENTS

As *DDA* draws more attention in the international society of computational mechanics, its developments has been in great progress recently. Table 3 provides a partial list of current developments on *DDA*. This table divides these developments into six groups: 1) solid block itself; 2) block contacts and joints; 3) various constraints; 4) insight study; 5) engineering

applications; 6) manifold method. Most of them can be found in the proceedings of *ICADD1* and *IFDDA1*.

In the front of the research objective of this paper, the prototype of *DDA* is not ready to do the simulation of fracture propagation yet, because its first-order displacement function can not capture the stress concentration within a DDA block. If a higher-order displacement function [14,15,17] is used, only the fragmentation across a block instantly can be simulated. If each *DDA* block is refined by finite elements [11,13], fracturing simulation then requires an excellent remeshing program and the ability of transferring block parameters between pre- and post-fracture. Lin etc. [20,36] added the concept of fracture mechanics to deal with cracking direction, but doing this requires a crack tip as a *priori*. The artificial joint concept proposed by the author [12] provides another alternative, which was the choice in the paper.

Table 3. Partial list of recent developments in DDA

Main Group	Sub-group	Contributors
DDA blocks	Refined stress field	Shyu [11], Ke [12], Chang [13], Koo etc. [14,15], Ma [16], Lin & Lee [17]
	Material non-linearity	Chang [13], Ohnishi etc. [18]
	Fragmentation	Lee [19], Lin etc. [20]
	Fracture propagation	Ke [10,12], Lin etc. [20]
	Circular particles	Lin [21], Ke [9], Ohnishi & Miki [22]
	3D *DDA* blocks	Shi [23]
	Coupled-flow in blocks	-
Block contacts/joints	Varying shear strength	Shi [24], Ke [12]
	Joint dilatancy	Thapa [25]
	Non-linearity	-
	Lagrange's contact constraint	Lin etc. [20], Hilbert etc. [26]
Various constraints	Displ. constraints	Ke [9,12], Ohnishi etc. [18]
	Force constraints	Ke & Bray [9]
Insight studies	Time integration	Ke [12]
	Rotation effect	Yeung [27], Ke [12,28], MacLaughlin & Sitar [29]
	Simplex integration	Shi [30]
Engineering Applications	Rock slopes	Yeung [27], Ke etc. [31], Chen & Lin[32]
	Underground openings	Ke [12], Chang [13], Yeung etc. [33], Chen etc. [34]
	Rock foundation	Yeung [27], Chang [13]
	Granular media	Lin [21], Ke [9], Ohnishi & Miki [22]
	Composite materials	Shyu [11], Ke [35]
	Fracturing simulation	Ke [10,12], Lin etc. [36]
	Impact	Ma [16], Cai etc. [37]
	Rock joint flow	-
	Viscous fluid flow	-
	Solid-fluid interaction	Ke & Tang [38]
	Commercialization	Chen etc. [39]
Manifold method	Complex material domains	Shi [40]

- : new area without contributor.

3 DDA COMBINED WITH ARTIFICIAL JOINT CONCEPT

This section describes the combination of *DDA* with the *artificial joint concept*, which enables *DDA* to simulate fracture propagation, as well as the required modifications in the original *DDA* code and the corresponding verifications. Before these, the micro-texture of a solid, which is closely related to the above concept, is addressed first as follows.

3.1 MICRO-TEXTURE OF SOLIDS

In a micro scale, solid is not continuous at all, and it is an assemblage of many tiny elements. In general, solid has two kinds of micro-textures: 1) *crystalline* texture; 2) *clastic* texture (see Figure 6 [41]). The elements composing the former texture are crystals, between which are pretty tight edge-to-edge contacts due to perfect interlocking, resulting in a very low porosity. Figure 6a depicts the sketch of a *gabbro* thin section. Those for the clastic texture are discrete particles, between which are usually point contacts with visible pores. Figure 6b shows the sketch of a *orthoquartzite* thin section.

No matter which texture a solid belongs to, the interfaces between elements are usually weaker and softer than the solid elements. As a result, when subjected to loading, these interfaces will deform more or break before the elements do. If some fissures pre-exists within the elements, they behave just like the element interfaces. Accordingly, all these micro-textures and their mechanical properties affect the macro-behavior of a solid, and they provide a different way to connect with fracturing simulation.

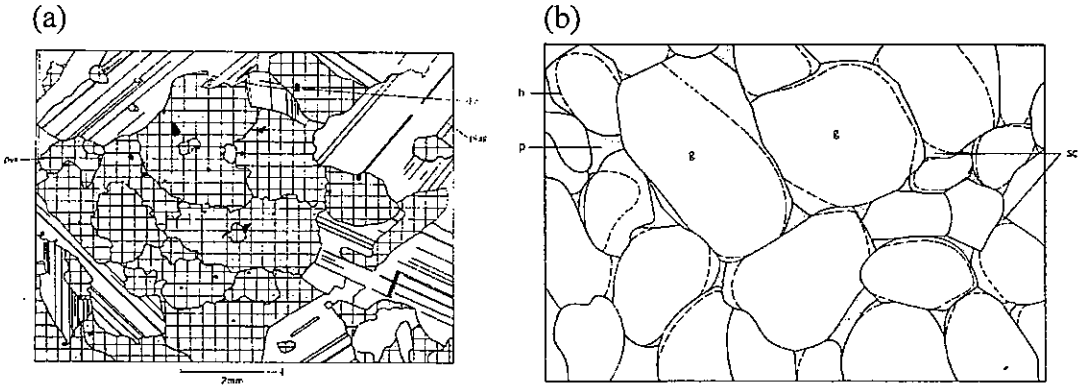

Figure 6. Micro-texture of a solid: a) crystalline; b) clastic [41]

3.2 ARTIFICIAL JOINT CONCEPT

The *artificial joint concept* was proposed by the author in 1993 [12]. This concept include two parts: 1) *cutting*, which adds artificial joints of a certain type into a *DDA* block and creates a system of *sub-blocks*; 2) *patching*, which glues these sub-blocks together according to some given strength of artificial joints. Figure 7 provides an illustrative example, in which the left-side figure represents a complex block domain containing some internal cracks, and the right-side one depicts the resultant system of 26 sub-blocks cut by two orthogonal artificial joint sets.

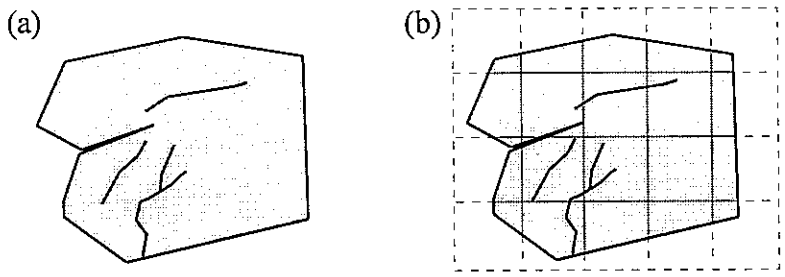

Figure 7. A complex block domain: a) prototype; b) refined by artificial joints

If the given strength of artificial joints is infinitely strong, a refined stress field within a DDA block can be obtained, because of each sub-block having its own stress state. On the other hand, if the artificial joints are assigned with the strength of the micro-interfaces in solid, they become pre-defined cracking paths within the *DDA* block. That is whenever the contact stress along an interface between two adjacent sub-blocks exceeds a limit, this contact interface fails and lose its cementing strength, followed by the stress redistribution and the propagation of cracking to the other interface. The energy loss due to fracturing is automatically modeled by the release of strain energy of contact springs in DDA. More importantly, if the pattern and strength of artificial joints are both similar to those of micro-interfaces in solid, the results of DDA simulation is expected to approach the real behavior.

3.3 REQUIRED MODIFICATIONS IN DDA CODE

3.3.1 Establishment of micro-texture

If precise scanners and digitized processors are available, then it is easy to attain the digitized micro-texture along a certain section of a solid, which can be in turn regarded as the geometry input for *DDA* simulation. Otherwise for a known homogeneous solid, artificial joint generator for regular meshes can be used. Five mesh generators have been completed for this purpose, and included in the code *KDC*. *KDC* can create joint meshes containing rectangular, right-angle triangular, parallelogram, equal-angle triangular and hexagonal sub-blocks (Figure 8), and can automatically delete the joint segments outside the selected block domains.

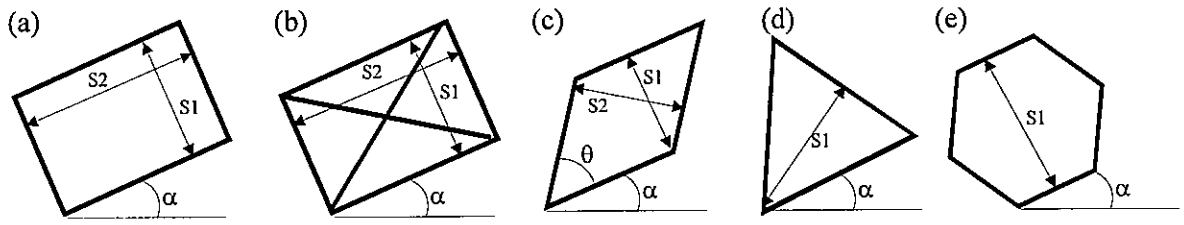

Figure 8. Regular artificial joint meshes of Type: a) *A*; b) *B*; c) *C*; d) *D*; e) *E*

3.3.2 Treatment of joints having cementing strength

3.3.2.1 Search for edge-to-edge contacts

Because the prototype of *DDA* code is unable to handle the joints having cementing joints (also called *incipient joints* [41], those joints having cohesion c and tensile strength T_0), fracturing simulation requires adding this feature into the code. It is known that cementing

strength only appears along the edge-to-edge contacts, and in the *DDA* analysis, an edge-to-edge contact is composed of two point contacts (or called a *contact pair*)

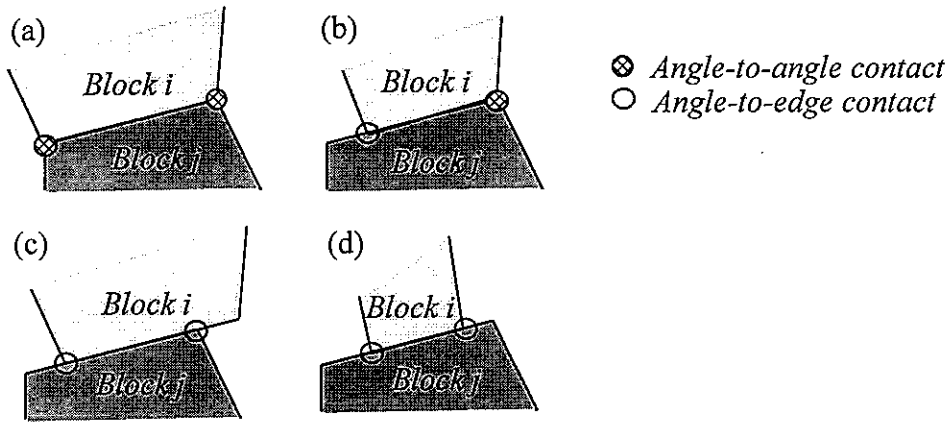

Figure 9. Four possible contact pairs: a) two *A-A* contacts; b) one *A-A* and one *A-E* contacts; c) two *A-E* contacts on the opposed sides; d) two *A-E* contacts on the same side

There are four geometrically possible contact pairs (Figure 9), which are: 1) two *A-A* contacts; 2) one *A-A* and one *A-E* contacts; 3) two *A-E* contacts on the opposed sides; 4) two *A-E* contacts on the same side. At the start of each step, after identifying all possible point contacts, these contact pairs are then sought in order to determine their contact length L and the corresponding cementing strength (cL and T_0L). Based on the *equally-sharing* principle, such a cementing strength is halfly assigned to its individual point contacts.

3.3.2.2 Modified failure criteria at point contacts

In the prototype of *DDA* code, the failure behavior at each point contact obeys the *Mohr-Coulomb*'s rule with zero cohesion, as shown in Figure 10a. It is noted in this figure that the x- and y-axes represent the total contact forces N and T (but not σ and τ). Figure 10b depicts the failure criteria for cementing point contacts, which is called the *Mohr-Coulomb*'s rule plus a *tensile cutoff*, as used in rock mechanics. Now each cementing point contact can resists a certain amount of tensile force, i.e., it can be in a tensile contact state ($MO=-2$). Whenever any point contact of a cementing contact pair fails under tension or shearing, the whole contact pair is judged to be failed, losing its cementing strength and becoming purely frictional (referring Figure 10a). According to the above, the original *DDA* code was modified and named *KDFO*, which is subjected to the following verifications.

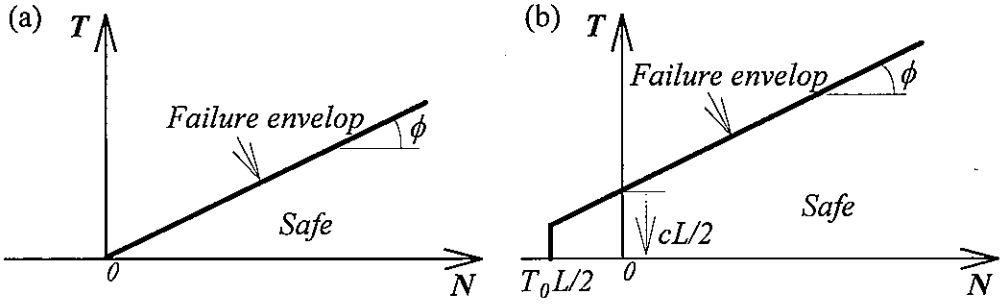

Figure 10. Failure criteria for a point contact: a) purely frictional; b) cementing

3.3.2.3 Verification of *KDFO* for cohesive joints

Figure 11 shows a rigid rectangular block ($H=1/\sqrt{2}\ m$, $L=\sqrt{2}\ m$, $\rho = 2600kg/m^3$) sitting on an incline of $\beta = 45°$. The interface between the block and incline is known to have a ϕ of $30°$, and two values of c are given in Table 4. Gravity turns on at $t \geq 0sec$. The other parameters used in *KDFO* are normal contact stiffness $k_n = 10^{12}N/m$, timestep $\Delta = 0.01sec$, block elastic modulus $E = 10^{20}Pa$, and *Poisson's ratio* $\nu = 0.2$.

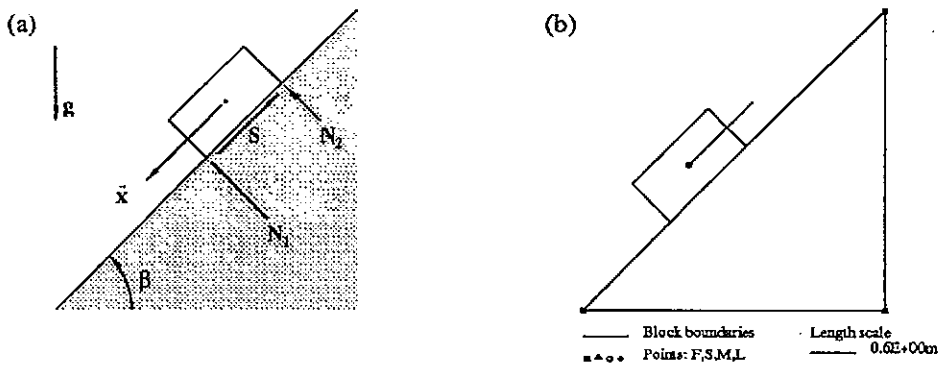

Figure 11. Verification example of *KDFO* for cohesive joints: a) original geometry; b) displaced geometry at $t=1sec$, $\phi=0°$ and $c=0$

According to the limiting equilibrium method (*LEM*), the corresponding theoretical solutions can be obtained and summarized below.

1) when the block is idle (i.e., $W\sin\beta < W\cos\beta\tan\phi + cL$, W is the block weight)

$$\begin{aligned} \ddot{x} &= 0 \\ S &= W\sin\beta \\ N_1 &= \frac{1}{2}\left(\cos\beta + \frac{H}{L}\sin\beta\right)W \\ N_2 &= \frac{1}{2}\left(\cos\beta - \frac{H}{L}\sin\beta\right)W \end{aligned} \tag{6}$$

2) when the block is sliding (i.e., $W\sin\beta \geq W\cos\beta\tan\phi + cL$)

$$\begin{aligned} \ddot{x} &= \frac{W(\sin\beta - \cos\beta\tan\phi) - cL}{M} \\ S &= W\cos\beta\tan\phi \\ N_1 &= \frac{1}{2}\left\{\cos\beta\left(1 + \frac{H}{L}\tan\phi\right)W + \frac{H}{L}cL\right\} \\ N_2 &= \frac{1}{2}\left\{\cos\beta\left(1 - \frac{H}{L}\tan\phi\right)W - \frac{H}{L}cL\right\} \end{aligned} \tag{7}$$

Table 4 compares the theoretical solutions and the computation results of *KDFO* at $t = 1sec$. It can be seen that the differences between them are negligible, indicating the validity of *KDFO* for treating cohesive joints. Figure 11b depicts the block geometry computed by *KDFO* at $t=1sec$, $\phi=0°$ and $c=0$.

Table 4. Verification example of *KDFO* for cohesive joints: one block on an incline

	LEM's solutions				*KDFO* results @ $t=1sec$			
c (Pa)	$\ddot{x}/g$	N_1/W	N_2/W	S/W	$\ddot{x}/g$	N_1/W	N_2/W	S/W
10000	0	$\frac{3}{4\sqrt{2}}$	$\frac{1}{4\sqrt{2}}$	$\frac{1}{\sqrt{2}}$	5×10^{-8}	0.5303	0.1768	0.7071
1000	0.24341	0.46948	0.23763	0.46369	0.24340	0.46950	0.23760	0.46370

3.3.2.4 Verification of *KDFO* for incipient joints

Figure 12 depicts a $0.1\times0.2m$ jointed rock specimen ($E = 2\times10^{10}Pa$, $\nu = 0.2$) subjected to uniaxial tension in the horizontal direction. The central dotted line in this figure represents a cementing joint ($\phi = 30°$, $c = 500Pa$, $T_0 = 100Pa$), and the shaded blocks in the both sides are the two rigid loading plates ($E = 10^{20}Pa$, $\nu = 0.2$). The interfaces between the rock blocks and loading plates are infinitely strong, and P equals to the half of the total horizontal tensile force. The other parameters used in *KDFO* are $k_n = 10^8 N/m$ and $\Delta = 0.00001sec$.

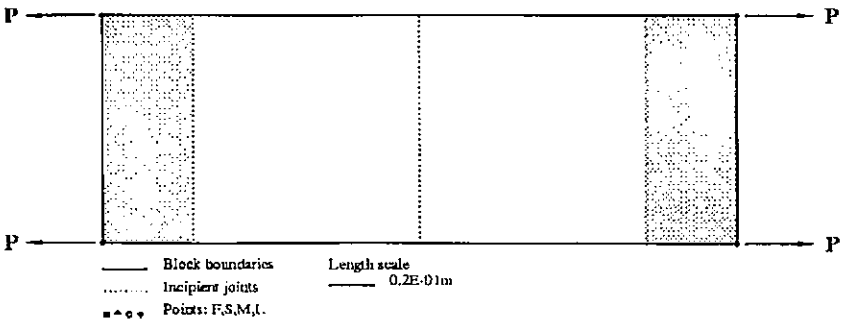

Figure 12. Verification example of KDFO for incipient joints: uniaxial tensile testing

When P equals to a constant of $5N$, the *KDFO* result indicates that the central cementing joint breaks at $t = 0.00061sec$. If it assumes that the rock specimen is also rigid and the loads Ps are directly applied to its ends (Figure 13), then the theoretical solution yields $t_e = (\pi/4)\sqrt{m/k} = 0.00057sec$ in which the total tensile resistance across the central joint just equals to $2P$. It is noted that this computed t_e is very close to $0.00061sec$ obtained by *KDFO*.

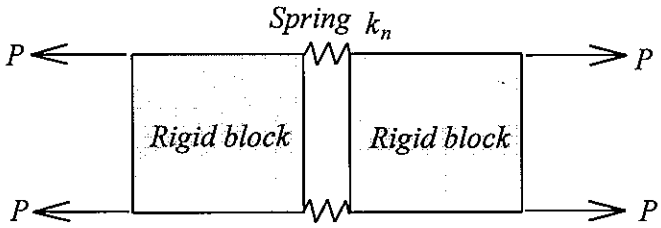

Figure 13. Uniaxial tensile testing of two rigid blocks connected by springs

Now if P increases constantly with time, i.e. $P = \alpha t$, then the *KDFO* code can monitor the cracking of the central joint and determine the value of P_f upon joint failure, which is subsequently used to compute the macro-tensile strength of this jointed rock T_0^* (= $2P_f$/specimen width). Table 5 summarizes the computation results of *KDFO* code for different values of α. It can be seen that the higher the loading rate α is, the higher the

obtained strength, as observed in common loading tests. From this table, it can be concluded that $T_0^* = T_0 + \alpha\Delta$/specimen width. Also, it is found that when $\alpha \leq 100N/sec$, the obtained T_0^* is very close to the originally given tensile strength of the joint ($T_0=100Pa$). This value of α ($=100N/sec$) will be used in the uniaxial tensile testing of the next section.

Table 5. Verification example of *KDFO* for incipient joints: uniaxial tensile testing

α (N/sec)	20	50	100	200	500	1000	2000	5000	8000
t_f^* (sec)	0.2501	0.1001	0.0501	0.0251	0.0101	0.0052	0.0026	0.0011	0.0010
P_f (N)	5.001	5.0025	5.005	5.01	5.025	5.05	5.1	5.25	7.6
T_0^* (Pa)	100.02	100.05	100.1	100.2	100.5	103	102	105	152

4 NUMERICAL SIMULATION OF CRACKING IN TENSILE COLUMN

In this section, the *KDFO* code is used to simulate the fracturing behavior of a cemented rock subjected to uniaxial tension, with focus upon the influences of the artificial joint type and its orientation, which represent the micro-texture of the rock..

4.1 SIMULATION LAYOUT

4.1.1 Specimen size and force boundary

The layout of such a uniaxial tensile testing is similar to that in Figure 12, in which the rock specimen is still $0.1 \times 0.2m$ in size, at the two ends connected with two loading plates, and the two pairs of horizontal tensile forces P are acting at the outer corners of these loading plates. Here, a constant loading rate was used, i.e., $P = \alpha t$, and α was selected to be $100N/sec$. The only difference is that the micro-texture of the rock specimen is defined by the different artificial joint meshes described as follows.

4.1.2 Micro-texture of rock specimen

Figure 14 depicts the seven cases of artificial joint meshes (dotted lines) used to cut the rock specimen, in any of which the rock specimen becomes an assemblage of sub-blocks almost having the same area, but with different shapes and orientations. These sub-blocks are then patched together by assigning a certain amount of cementing strength.

CASES A00, A30, and *A45* in Figure 14 are manufactured by Type *A* artificial joint mesh but at the different orientations ($\alpha = 0, 30, 45°$). They mainly contain $2 \times 2cm^2$ square sub-blocks, except along the outer boundaries of the rock specimen, and these three cases possess *50, 68,* and *68* sub-blocks, respectively. On the other hand, *CASE B00, B30,* and *B45* are made of Type *B* artificial joint mesh, but also at the different orientations ($\alpha = 0, 30, 45°$). They mainly contain $3.608cm^2$ equal-angle triangular sub-blocks, except along the outer boundaries of the rock specimen, and these three cases possess *60, 72,* and *64* sub-blocks, respectively. *CASE C00* is made of Type *E* artificial joint mesh, mainly consisting of $3.464cm^2$ hexagonal sub-blocks. The total number of sub-blocks for this case is *66*.

The cementing strengths assigned to the artificial joints are a ϕ of $30°$, c of $500Pa$, and T_0 of $100Pa$. The other parameters used in *KDFO* are $k_n = 10^8 N/m$ and $\Delta = 0.0002sec$. The computer used is a *Pentium-120 PC*. The *CPU* time for the run of each case varies from *0.5* to *12 hrs*, depending upon the total number of contacts and the frequency of changing contact states during computation.

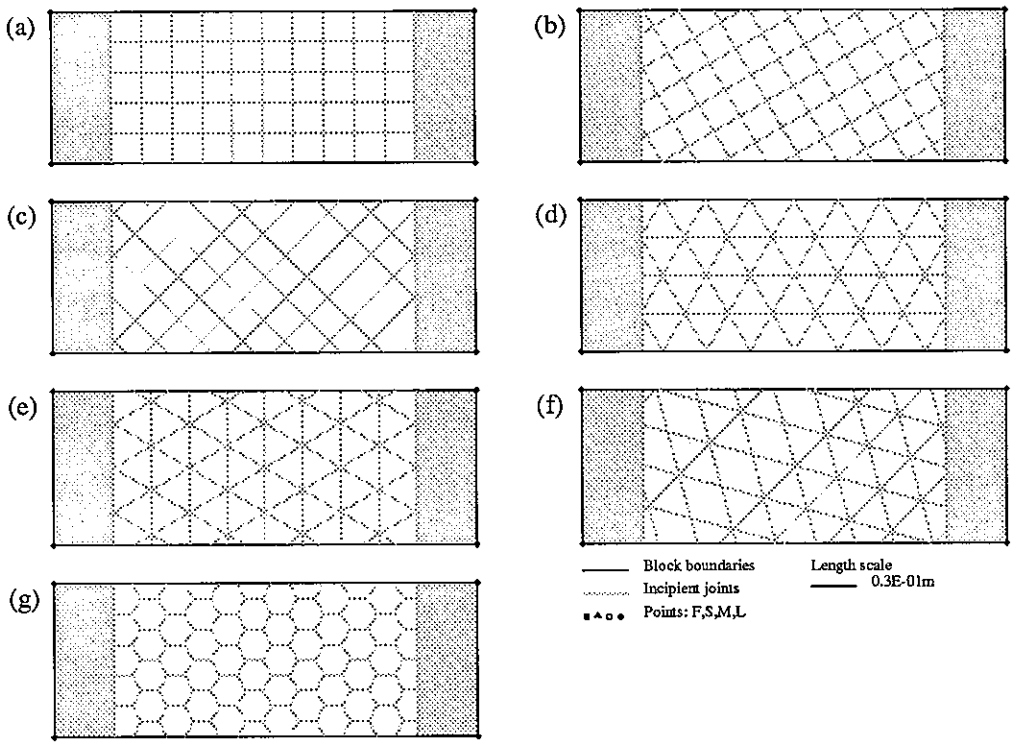

Figure 14. Artificial joint meshes used in tensile columns: a) *A00*; b) *A30*; c) *A45*; d) *B00*; e) *B30*; f) *B45*; g) *C00*

4.2 SIMULATION RESULTS AND DISCUSSIONS

4.2.1 Macro-behavior of cracking simulation

Like the verification example for incipient joints, here the *KDFO* code can also "monitor" the total survival number of cementing contact pairs as well as the formation of major faults (those cutting across the specimen), such that it can subsequently compute the failure load P_f and the macro-tensile strength of the specimen T_0^*. Note when the first major fault or conjugate faults appear, the specimen is actually cut into separate pieces, i.e., the specimen is discontinuous along the tensile direction and can not take any tensile load at all. Due to the inertia effect or stress disturbance after the formation of the first major fault, the second or other major faults might occur.

Table 6 summarizes the simulation results of *KDFO* computation. It can be seen from this table that only *CASE A00* yields $T_0^* \sim 100Pa$ because of one artificial joint set orthogonal to the loading direction, whiles the rest cases yield $T_0^* < 100Pa$ (between *60* and *80Pa*) because their artificial joints are inclined to the loading direction and some failure mode is controlled by shearing. Detailed discussions on cracking patterns will be addressed in the following sub-sections.

Table 6. Fracturing simulation results of *KDFO* computation for uniaxial tension

CASE	Sub-blocks	Size (cm^2)	no.	t_1 *(sec)*	P_f *(N)*	T_0^* *(Pa)*	t_2 *(sec)*	t_3 *(sec)*
A00	Square	*4.00*	*50*	*0.0502*	*5.01*	*100.2*	*0.0502*	*0.0502*
A30	Square	*4.00*	*68*	*0.0366*	*3.65*	*73.0*	*0.0366*	-
A45	Square	*4.00*	*68*	*0.0309*	*3.08*	*61.6*	*0.0552*	-
B00	Equal-angle triangular	*3.61*	*60*	*0.0364*	*3.63*	*72.6*	-	-
B30	Equal-angle triangular	*3.61*	*72*	*0.0376*	*3.75*	*75.0*	-	-
B45	Equal-angle triangular	*3.61*	*64*	*0.0312*	*3.11*	*62.2*	*0.0836*	-
C00	Hexagonal	*3.46*	*66*	*0.0397*	*3.96*	*79.12*	*0.0585*	-

*t_1, t_2, t_3 are the occurring times of the first (pair), second (pair), and the third (pair) major fractures.
- nil.

4.2.2 Fracturing patterns of *CASE A00, A30* and *A45*

Figure 15 depicts the deformed geometries and principal stress fields of *CASE A00* just before and after major faults forming, and at $t = 0.1sec$. In these figures, those artificial joints which have changed from *dotted* lines to *solid* lines, are failed and have lost their origially given cementing strength (c, T_0). The principal stress trajectory is plotted at the centroid of each sub-block, in which solid lines represent *compression*, dotted lines *tension*, and the line length the *magnitude*. Although the original geometry and loading for this case are truly symmetric, the stress field along the loading direction just before fracturing reveals a little disturbance (Figure 15a). Figure 15b shows that the specimen instantly broke into ten pieces at $t = 0.0502sec$. Figure 15c exhibits that at $t = 0.1sec$, the eight broken blocks in the middle became stress-free, and the other two blocks connected with applied loads were still under stress due to the inertia effect.

Figure 16 depicts the deformed geometries and principal stress fields of *CASE A30* just before and after a pair of major faults forming and at $t = 0.1sec$. Figure 16a exhibits that at $t = 0.0364sec$, a pair of major faults gradually eroded the cross section of the specimen, and only a pair of small cementing joint segments survived, resisting the whole tensile loading. Figure 16b shows that that $t = 0.0366sec$, a pair of major faults completely formed, cutting the specimen into three sub-block clusters, and the stress field revealed a little chaos probably due to the sudden energy release by faulting. Figure 16c exhibits that at $t = 0.1sec$, the middle sub-block cluster became almost stress-free, and the flying-away others connected with loading plates were still under stress due to the inertia effect.

Figure 17 depicts the deformed geometries and principal stress fields of *CASE A45* just before and after the first major fault forming, and just after the second. Although the original geometry and loading for this case are also symmetric, the simulation results become totally non-symmetric probably due to the accumulated round-off error of the computer. Figure 16a exhibits that at $t = 0.0304sec$, the first major fault gradually ate out the cross section of the specimen, and only a small cementing joint segment survived, taking the whole tensile loading. Figure 17b shows that that $t = 0.0309sec$, the first major fault completely formed, cutting the specimen into two sub-block clusters with different sizes. Figure 17c exhibits that that $t = 0.0522sec$, the second major fault formed near the right interface with the loading plate, cutting the whole specimen into three sub-block clusters.

Referring to Table 6, the value of T_0^* obtained from *CASE A00* is the highest, and pretty close to the originally given joint tensile strength (*100Pa*). This is because one artificial joint set for this case is orthogonal to the loading direction, and all fracturing is caused by tensile failure. *CASES A30* and *A45* yield $T_0^*=73$ and *61.6Pa*, respectively. Because their artificial joints are inclined to the loading direction, the shear strength (ϕ, c) of the artificial joints also participate in the fracturing process. Given the square sub-blocks, material properties and loading, it can be locally concluded that at the joint orientation $\alpha = 0°$, the specimen yields the highest macro-tensile strength T_0^*, and as α approaches $45°$, the specimen gives the lowest one.

4.2.3 Fracturing patterns of *CASE B00, B30* and *B45*

Figure 18 depicts the deformed geometries and principal stress fields of *CASE B00* just before and after a pair of major faults forming, and at $t = 0.1sec$. Figure 18a exhibits that at $t = 0.0364sec$, a pair of major faults gradually eroded the cross section of the specimen, and only a small cementing joint segment survived, taking the whole tensile loading. Figure 18b shows that that $t = 0.0366sec$, a pair of major faults completely formed, cutting the specimen into three sub-block clusters, and the stress field revealed a little chaos probably due to the sudden energy release by faulting. Figure 18c exhibits that at $t = 0.1sec$, the middle sub-block cluster became almost stress-free and idle, and the two flying-away ones connected with loading plates were still under stress due to the inertia effect.

Figure 19 depicts the deformed geometries and principal stress fields of *CASE B30* just before and after a pair of major faults forming, and at $t = 0.05sec$. Because in this case one artificial joint set is orthogonal to the loading direction, fracturing mainly develops along this joint direction. Figure 19a exhibits that at $t = 0.0372sec$, a pair of major faults gradually eroded the cross section of the specimen, and only three small cementing joint segments survived, taking the whole tensile loading. Figure 19b shows that that $t = 0.0376sec$, a pair of major faults completely formed, cutting the specimen into three sub-block clusters, and the stress field revealed a little chaos probably due to the sudden energy release by faulting. Figure 19c exhibits that at $t = 0.05sec$, the middle sub-block cluster became almost stress-free and idle, and the two flying-away ones connected with loading plates were still under stress due to the inertia effect.

Figure 20 depicts the deformed geometries and principal stress fields of *CASE B45* just before and after a pair of major faults forming, and just after the second. Because in this case one artificial joint set is deeply inclined (~75°) to the loading direction, fracturing almost develops along this joint direction. Figure 20a exhibits that at $t = 0.0311sec$, a pair of major faults gradually eroded the cross section of the specimen, and only a pair of small cementing joint segments survived, taking the whole tensile loading. Figure 20b shows that that $t = 0.0312sec$, a pair of major faults completely formed, cutting the specimen into three sub-block clusters, and the stress field revealed a little chaos probably due to the sudden energy release by faulting. Figure 20c exhibits that at $t = 0.084sec$, the second pair of major faults formed near the two interfaces with the loading plates, cutting the whole specimen into five sub-block clusters. At this moment, the middle sub-block cluster became almost stress-free and idle, and the clusters connected with loading plates were still under stress due to the inertia effect.

Referring to Table 6, *CASES B00, B30* and B*45* yield $T_0^*=72.6$, 75.0 and $62.2Pa$, respectively, all of which are smaller than the originally given joint tensile strength (*100Pa*). This is because most of the artificial joints for these cases are inclined to the loading direction, the shear strength (ϕ, c) of the artificial joints also participate in the fracturing process. Given the equal-angle triangular sub-blocks, material properties and loading, it is not possible for

these cases to conclude the relation between T_0^* and joint orientation α. However, since *CASE B30* contains one artificial joint set orthogonal to the loading direction, it yields the highest value of T_0^*.

4.2.4 Fracturing pattern of *CASE C00*

Figure 21 depicts the deformed geometries and principal stress fields of *CASE C00* just before and after the first major fault forming, and just after the second. Because the original geometry and loading for this case are not symmetric, the simulation results are not symmetric, either. Figure 21a exhibits that at $t = 0.0395sec$, fracturing initiated near the right interface with the loading plate. Figure 21b shows that that $t = 0.0397sec$, the first major fault completely formed, cutting the specimen into two sub-block clusters with different sizes, and the stress field of all sub-blocks was still in a smooth transition. Figure 21c exhibits that that $t = 0.059sec$, the second major fault formed near the left interface with the loading plate, cutting the whole specimen into three sub-block clusters. Referring to Table 6, *CASE C00* yields $T_0^*=79.12Pa$, which is still smaller than the originally given joint tensile strength ($100Pa$). This is the same because the artificial joints for this case are inclined to the loading direction, the shear strength (ϕ, c) of the artificial joints also participate in the fracturing process.

4.2.5 Summary and discussions

The main goal of this section is under uniaxial tension to study the influences of different regular artificial joint meshes and their orientations on the fracturing behavior. Based on the above simulation results, it ends up with the following briefs:

1) the micro-texture of a solid like the shape of crystals or sub-blocks (defined by artificial joints) and their arrangement corresponding to the loading direction (defined by artificial joint orientation) both affect the macro-behavior of the solid subjected to uniaxial tension;
2) the above macro-behavior include the formation sequence and spatial distribution of major faults, failure mode of fracturing (tensile or shearing), and the computed macro-tensile strength T_0^*;
3) under the given specimen size, material properties and loading, the difference in T_0^* caused by the type and orientation of artificial joint mesh is about *40%*; for Type *A* artificial joints, the maximum of appears T_0^* at $\alpha = 0°$, and the minimum occurs as α approaches *45°*; for Type *B* artificial joints, no good trend exists;
4) because of the inertia effect or stress disturbance after the first major fault forming, the second or more major faults might occur within the specimen;
5) although the original geometry and loading for some case are pretty symmetric, the simulation results might become totally non-symmetric probably due to the accumulated round-off error of the computer.

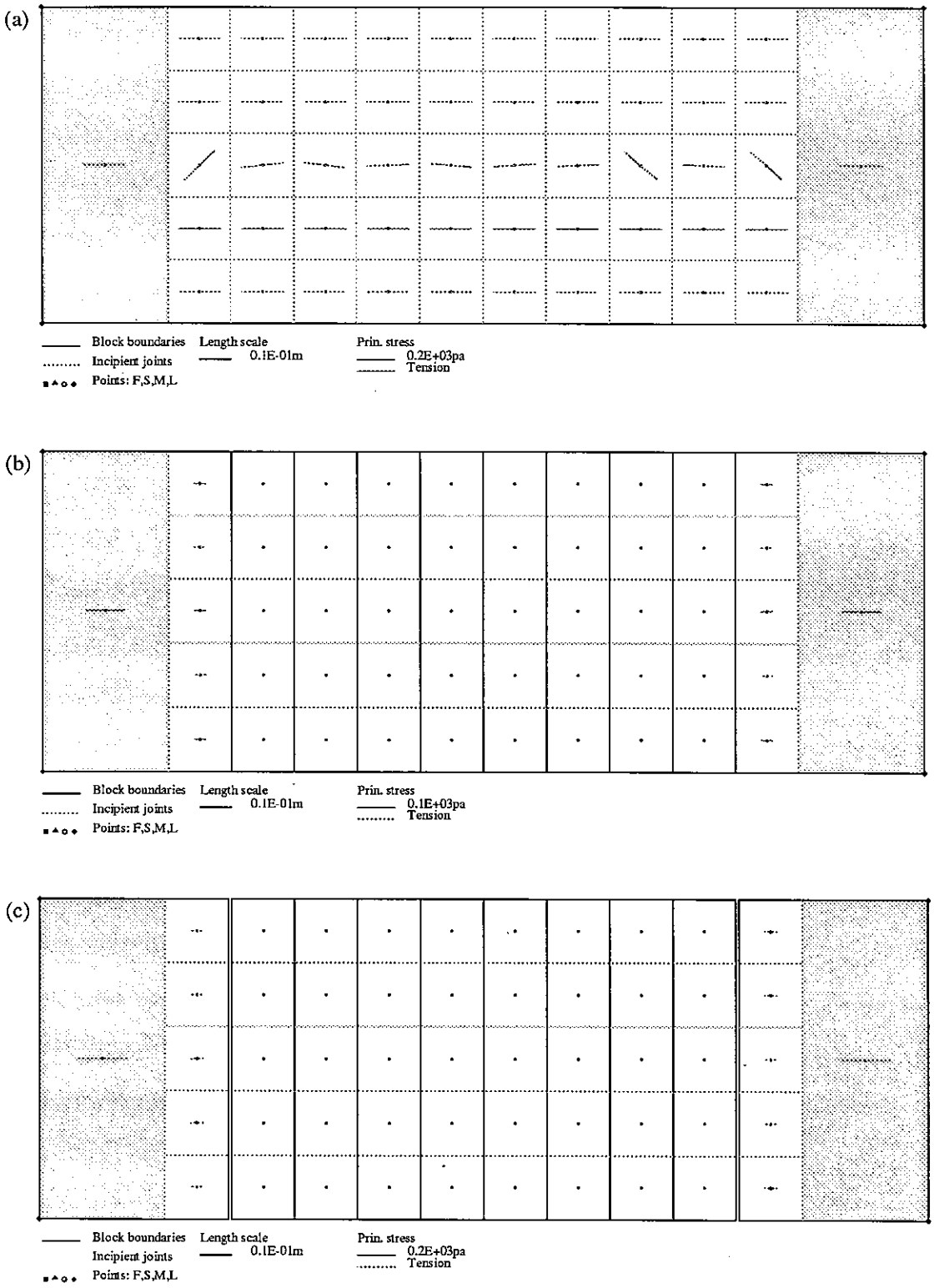

Figure 15. Fracturing pattern of *Case A00*, deformed geometries and principal stress fields at: a) $t = 0.05$; b) $t = 0.0502$; c) $t = 0.1sec$

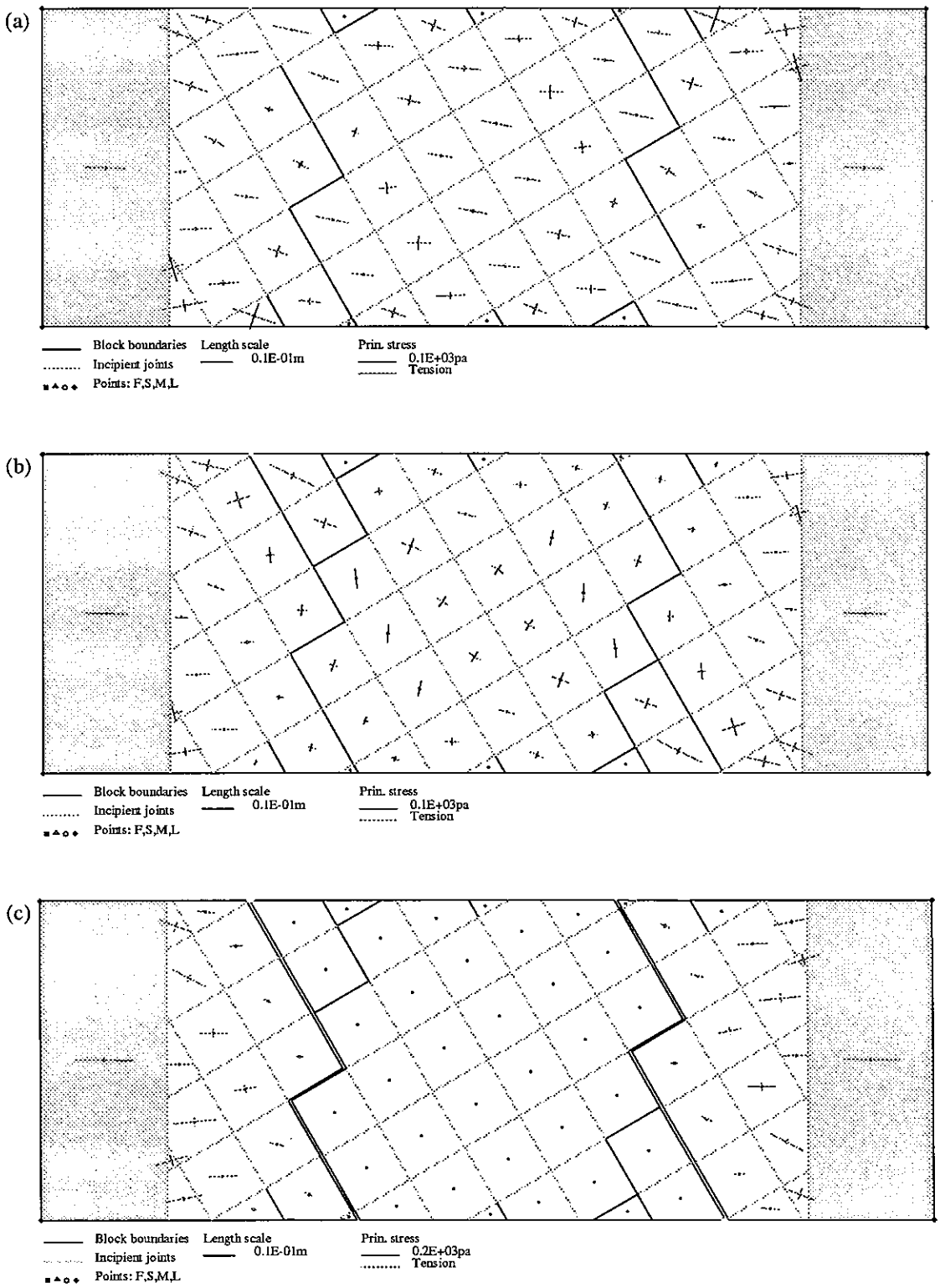

Figure 16. Fracturing pattern of *Case A30*, deformed geometries and principal stress fields at: a) $t = 0.0364$; b) $t = 0.0366$; c) $t = 0.1sec$

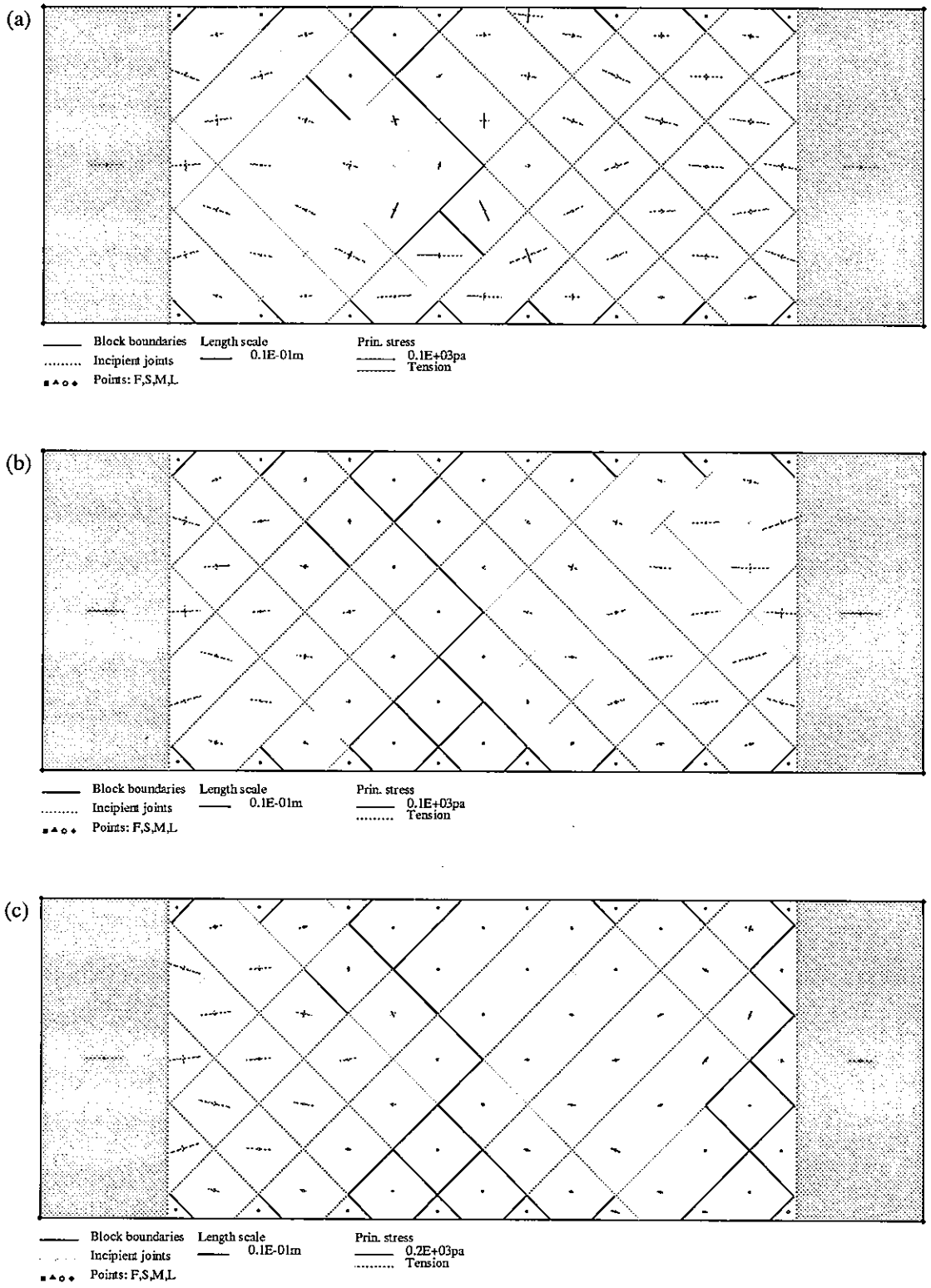

Figure 17. Fracturing pattern of *Case A45*, deformed geometries and principal stress fields at: a) $t = 0.0304$; b) $t = 0.0309$; c) $t = 0.0552sec$

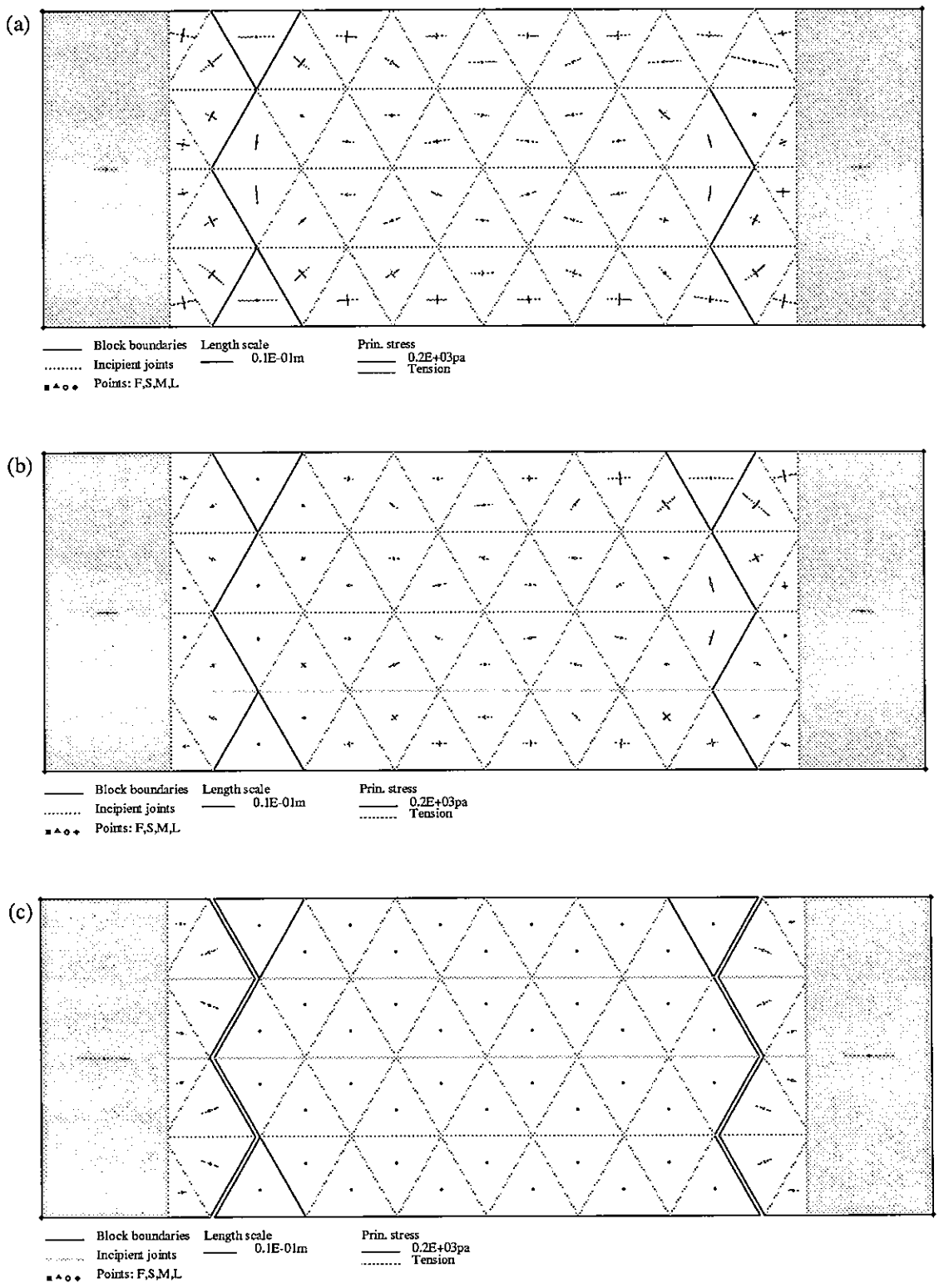

Figure 18. Fracturing pattern of *Case B00*, deformed geometries and principal stress fields at: a) $t = 0.0364$; b) $t = 0.0366$; c) $t = 0.1sec$

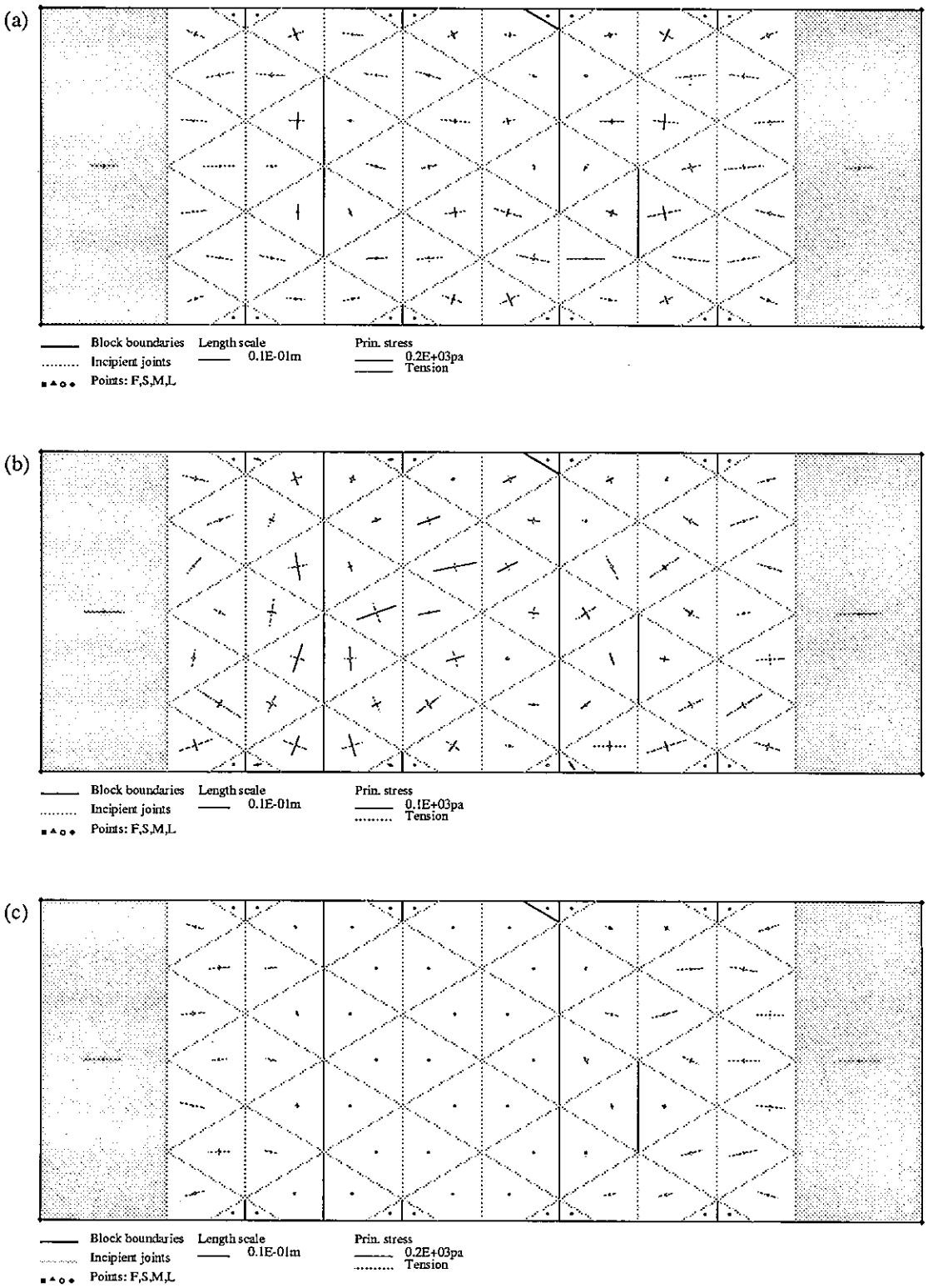

Figure 19. Fracturing pattern of *Case B30*, deformed geometries and principal stress fields at: a) $t = 0.0372$; b) $t = 0.0376$; c) $t = 0.05sec$

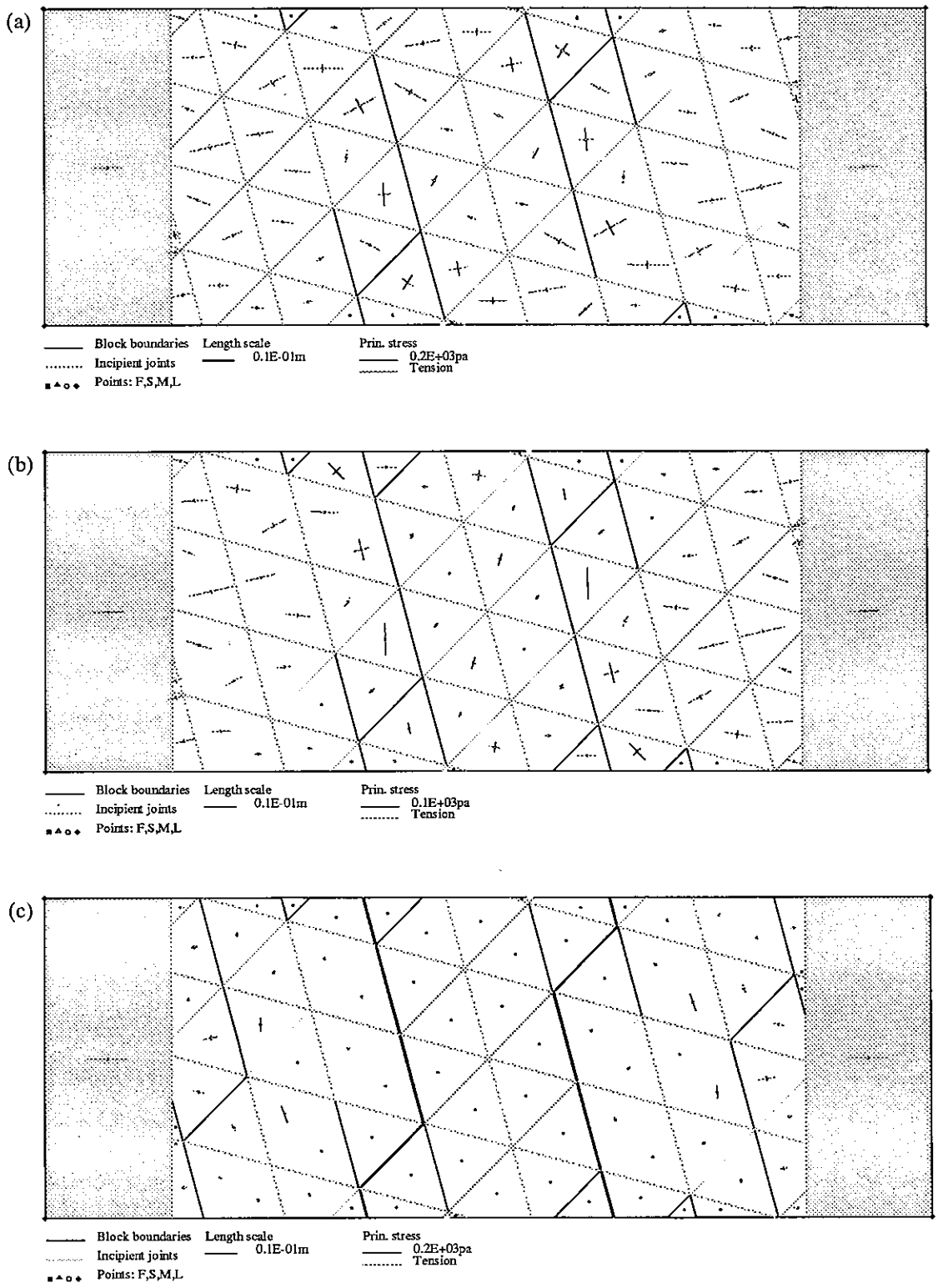

Figure 20. Fracturing pattern of *Case B45*, deformed geometries and principal stress fields at: a) $t = 0.0311$; b) $t = 0.0312$; c) $t = 0.084sec$

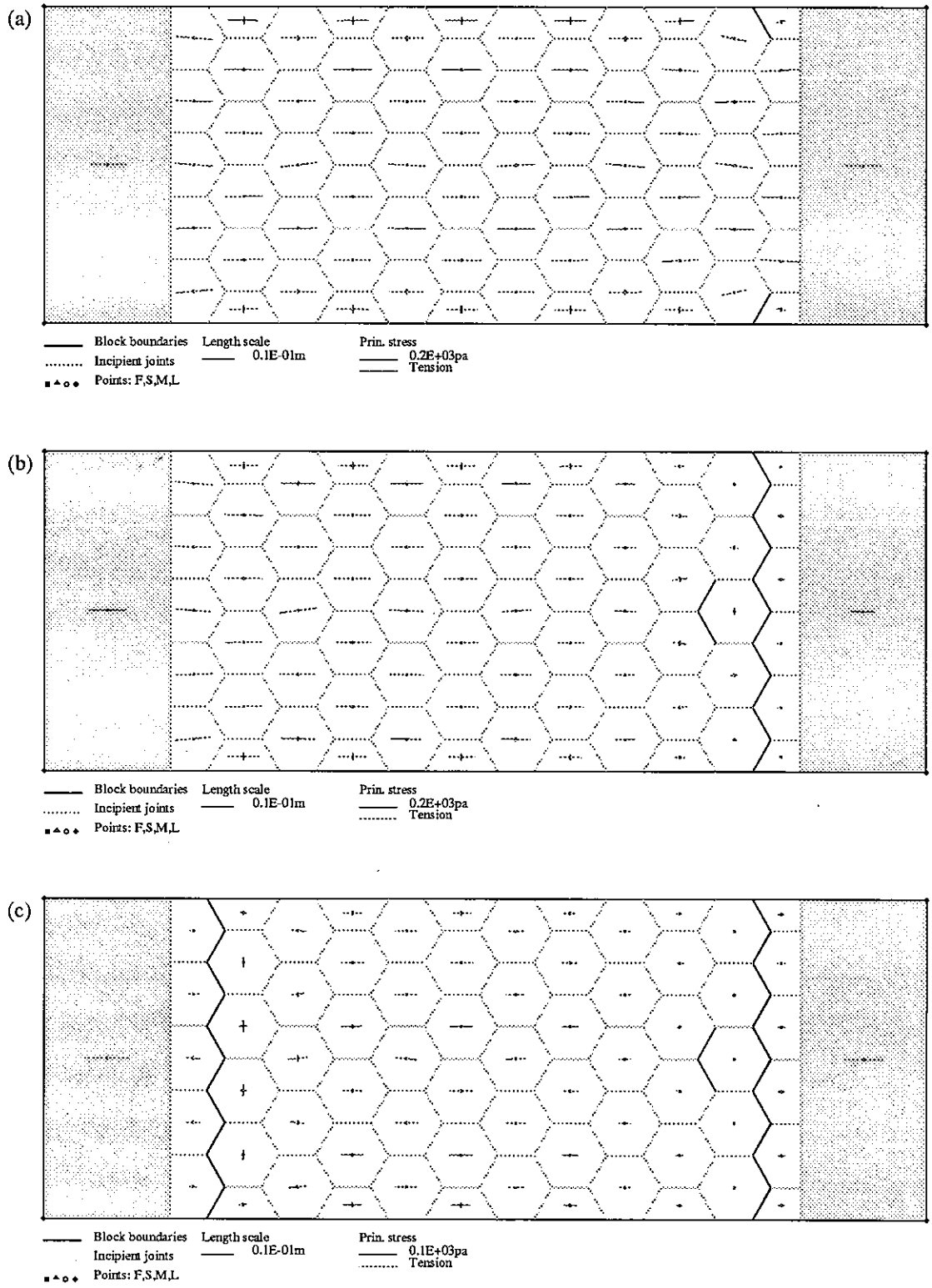

Figure 21. Fracturing pattern of *Case C00*, deformed geometries and principal stress fields at: a) $t = 0.0395$; b) $t = 0.0397$; c) $t = 0.059sec$

5 APPLICABLE EXAMPLE: A MILITARY SHELTER SUBJECTED TO IMPACT

As mentioned in the first section, the subject of fracture propagation has been extensively applied to the various fields of civil materials, mechanical media, electronic materials, and military industry. An attempt in this section is made to utilize the *KDFO* code to simulate the impact behavior of a simplified military shelter. The initial objective of this example is to establish the relationships between the impact-resistance of a shelter and the following factors like the geometry and material properties of a shelter, connection of a shelter and ground, the geometry/material properties/approaching velocity of a warhead, etc. However, considering the time constraint, only one set of input parameters was examined as follows. Thus the purpose of this section would be to merely illustrate the capability of *KDFO* in dealing with impact/failure problems.

Figure 22a shows an imaginary arched military shelter (about $12m \times 4m$ *in size*, $E = 2\times10^{10}Pa$, $\nu = 0.2$), the middle of which is subjected to the impact of an approaching rigid warhead ($E = 10^{20}Pa$, $\nu = 0.2$, $V=100m/sec$) at $t = 0sec$. This shelter is composed of 80 sub-blocks (cut by Type *A* artificial joints: $\phi = 40°$, $c = 500Pa$, $T_0 = 100Pa$). The foundation block is fixed at its four corner points, and the interface between the shelter and foundation has a ϕ of $30°$. The other parameters used in *KDFO* are $k_n = 10^{10}N/m$ and $\Delta = 0.0002sec$.

The computation results of *KDFO* code indicated that the first crack of the shelter initiated just beneath the impact point at $t \approx 0.000005sec$, and the shelter became totally collapsed without no cementing joint survived at $t \approx 0.00244sec$. Figure 22bcd depicts the deformed geometries and principal stress fields of the shelter during impact. It can be seen from Figure 22b that the top roof of the shelter started to fracture at $t = 0.0002sec$, and the two sub-blocks just adjacent to the warhead were under high stress concentration (if given some failure criterion, these two should fail). Figure 22c shows at $t = 0.001sec$ that a dense stress wave propagated into the two wings of the shelter, leading to more cracking. At $t = 0.01sec$, most of the shelter broke into discrete pieces with huge discontinuous deformation, and the target protected by the shelter would be destroyed soon after the warhead penetrated (Figure 22d). In order to protect the target form destruction under the same impact energy, possible solutions are to increase the interface strength or to enlarge/reshape the shelter.

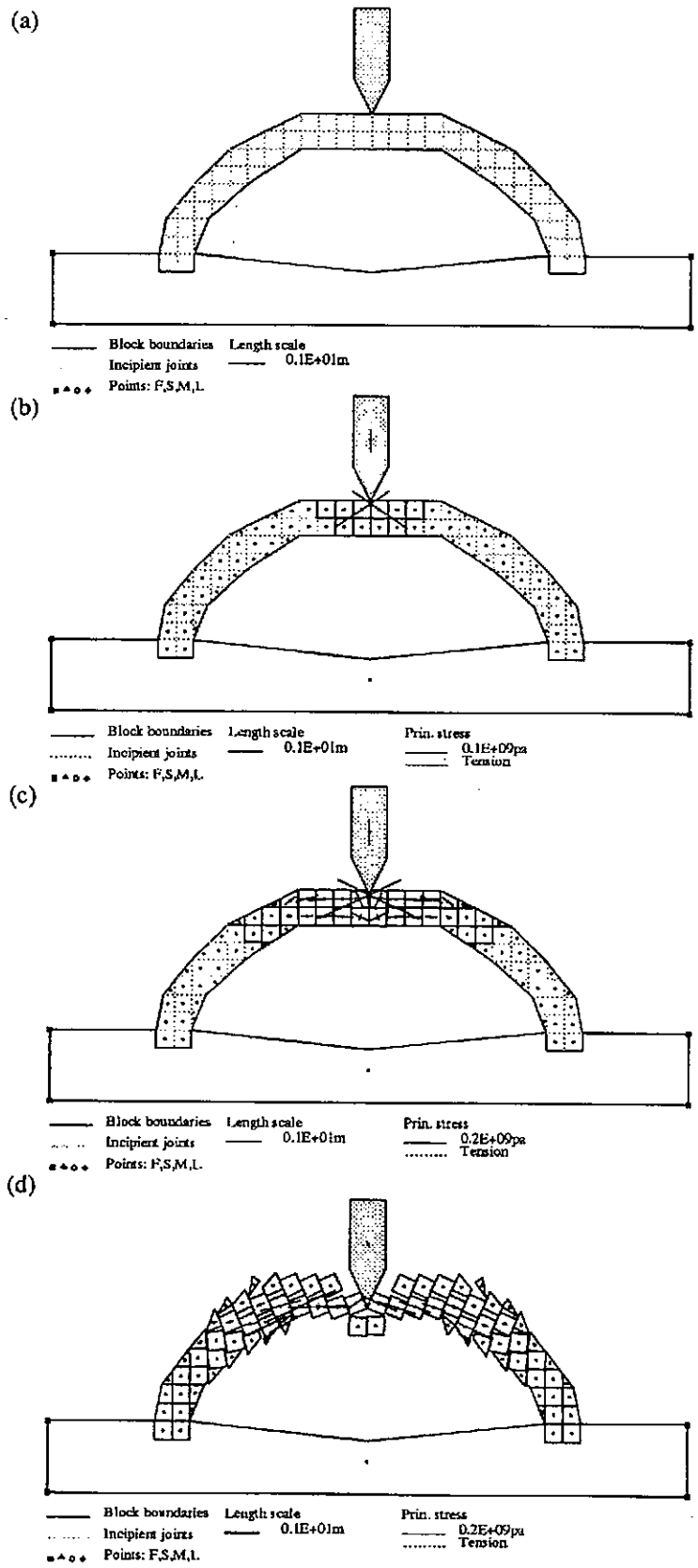

Figure 22. Impact-fracturing simulation of a military shelter, deformed geometries and principal stress fields at: a) $t = 0$; b) $t = 0.0002$; c) $t = 0.001$; d) $t = 0.01sec$

6 CONCLUDING REMARKS

This paper briefly compared several analyses for fracturing simulation, and introduced the artificial joint concept to enable *DDA* for this purpose as well as the associated modifications in *DDA* code. From the fracturing simulation under uniaxial tension, it is found that the loading rate and the micro-texture of the rock both affected the fracturing behavior, in terms of the formation sequence and spatial distribution of major faults, failure mode of cracks, and the obtained macro-tensile strength T_0^*. The contributions of other factors like different cementing strength, loading mode, and the density of artificial joint mesh are left in the future for research. The fracturing example of a military shelter illustrated the capability of *KDFO* for impact problems.

There still is a distance between the fracturing analysis with the artificial joint-based DDA and the practical use. The author suggests the following tasks for the future developments regarding this subject:

1) how to combine precise scanners and digitized processor for automatically providing the input geometry of micro-texture of a solid section;
2) how to rationally measure the interface strength of the micro-texture in solid which is subsequently input as that of the artificial joints;
3) including higher-order (*2* or *3*) displacement function and non-linear material laws into *DDA* code to more precisely capture the deformational behavior of sub-blocks;
4) allowing the fragmentation of each sub-block according to a certain breakage criteria to cover the case that sub-blocks are weaker than interfaces, and to relax the limitation of cracking directions pre-defined by the given artificial joints;
5) adopting a more efficient equation solver or parallel processing to increase computation speed.

7 ACKNOWLEDGMENTS

Financial support was partially provided by the National Science Council of R.O.C., under the grant NSC-85-2211-E-033-001. The author is deeply indebted to Dr. Gen-hua Shi and Prof. Richard E. Goodman of University of California at Berkeley for their continuous encouragement.

REFERENCES

1. Rice, J. R., "Mathematical analysis in the mechanics of fracture", *Fracture and Advanced Treatise*, H. Liabowitz ed., Vol. 2: 191-311 (1985).
2. Zhong, Z., *Finite Element Procedures for Contact-Impact Problems*, Oxford, UK: Oxford University Press (1993).
3. Schlange, E. & Van Mier, J.G.M., "Fracture simulation in concrete and rock using a random lattice," *Proc. 8th Intl. Conf. Computer Methods & Advances in Geomech.*, Vol. 2 (1994).
4. Cundall, P. A. and Hart, R. D. (1989), "Numerical modeling of discontinua, " *Proc. First Conf. Discrete Element Methods*, Golden, Colorado, G. G. W. Mustoe, M. Henriksen and H-P Huttelmaier, eds., 17p.
5. Cundall, P. A., "A Computer model for simulating progressive, large scale movements in blocky rock systems," *Proc. Intl. Symp. on Rock Fracture*, Nancy, France, II-8 (1971).

6. Munjiza, A., Owen, D.R.J. & Huang, G. J., "Modeling aspects of discrete/finite element technology," *Proc. 1st Intl. Conf. on Analysis of discontinuous Deformation*, J. C. Lin, C.-Y. Wang & J. Sheng, eds, Chungli, Taiwan: 164-186 (1995).
7. Shi, Gen-Hua, *Discontinuous Deformation Analysis - A New Numerical Model for the Statics and Dynamics of Block Systems*, Ph.D. Dissertation, Department of Civil Engineering, U.C. Berkeley (1988).
8. Shi, Gen-Hua and Goodman, R. E., "Discontinuous deformation analysis," *Proc. 25th U.S. Symp. Rock Mech.*, Evanston, Ill., USA (1984).
9. Ke, T.-C. and Bray, J., "Modeling of particulate media using discontinuous deformation analysis," *J. Engrg. Mechanics, ASCE*, Vol.121, No.11: 1234-1243 (1995).
10. Ke, T.-C. Discontinuous Numerical Simulation of Fracture Propagation, NSC Project Report: 85-2211-E-033-001, Chungli, Taiwan: 76p (1997). (in Chinese)
11. Shyu, K.-K., *Nodal-based Discontinuous Deformation Analysis*, Ph.D Dissertation, Department of Civil Engineering, University of California at Berkeley (1993).
12. Ke, T.-C, *Simulated Testing of Two-Dimensional Heterogeneous and Discontinuous Rock Masses Using Discontinuous Deformation Analysis*, Ph.D Dissertation, Department of Civil Engineering, University of California at Berkeley (1993).
13. Chang, T.-C., *Nonlinear Dynamic Discontinuous Deformation Analysis with Finite Element Meshed Block Systems*, Ph.D Dissertation, Department of Civil Engineering, University of California at Berkeley (1994).
14. Koo, C.-Y., Chern, J.-C. and Chen, S., "The development of the second-order displacement function for discontinuous deformation analysis", *Proc. 6th Conf. Geotechnical Engrg. in Taiwan*: 665-674 (1995).
15. Koo, C.-Y. and Chern, J.-C., "The development of DDA with the third-order displacement function", *Proc. 1st Intl.Forum on DDA*, M. Reza Salami and Don Banks, eds., Berkeley, CA: 342-349 (1996).
16. Ma, M., "Single field formulation of manifold method", *Proc. Working Forum on the Manifold Method of Material Analysis*, Jenner, CA: 39-60 (1995).
17. Lin, J.-S. and Lee, D.-H., "Manifold method using polynomial basis functions of any-order," *Proc. 1st Intl. Forum on DDA*, Berkeley, CA, USA: 365-372 (1996).
18. Ohnishi, Y., Tanaka, M. and Sasaki, T., "Modification of the DDA for elasto-plastic analysis with illustrative generic problems, " *Proc. 35th U.S. Symp. on Rock Mechanics*, Lake Tahoe, CA: 45-50 (1995).
19. Lee, J., *Unpublished DDA program to simulate the cracking of intact blocks according to a prescribed maximum tensile strain rate*, University of California at Berkeley (1990).
20. Lin, C.-T., Amadei, B. and Sture, S. and Jung, J., "Using an augmented Lagrangian method and block fracturing in the DDA method, " *Proc. 8th Intl. Conf. Computer Methods and Advances in Geomech.*, Morgantown, W. Virginia, Vol.1: 837-842 (1994).
21. Lin, H.-C., *Discontinuous Deformation Analyses of Block and Granule Systems*, Master Thesis, Department of Civil Engineering, National Central University, Chungli, Taiwan (1993).
22. Ohnishi, Y. and Miki, S., "Development of Circular and Elliptic Disc Elements for DDA," *Proc. 1st Intl. Forum on DDA*, Berkeley, CA, USA: 44-51 (1996).
23. Shi, Gen-hua, *Personal communication* (1995).
24. Shi, Gen-hua, *User Manual of DDA* ('1994 Version).
25. Thapa, B., "Joint shear displacement-dilation analysis using in-situ opposing profiles, " *Proc. 35th U.S. Symp. on Rock Mechanics*, Lake Tahoe, CA: 51-56 (1995).
26. Hilbert, L. B., Yi, W., Cook, N. G. W., Cai, Y. and Liang, G.-P., "A new discontinuous finite element method for interaction of many deformable bodies in geomechanics, " *Proc.*

8th Intl. Conf. Computer Methods and Advances in Geomech., Morgantown, W. Virginia, Vol.1: 831-836 (1994).
27. Yeung, M., *Application of Shi's Discontinuous Deformation Analysis to Rock Slope*, Ph.D Dissertation, Department of Civil Engineering, University of California at Berkeley (1991).
28. Ke, T.-C., "Modification of DDA with respect to rigid-body rotation," *Proc. 1st Intl. Conf. on Analysis of discontinuous Deformation*, J. C. Lin, C.-Y. Wang & J. Sheng, eds, Chungli, Taiwan: 260-273 (1995).
29. MacLaughlin, M. M. and Sitar, N., "Rigid-body rotations in DDA," *Proc. 1st Intl. Forum on DDA*, Berkeley, CA, USA: 620-636 (1996).
30. Shi, Gen-hua, "Modeling dynamic rock failure by discontinuous deformation analysis with simplex integration," *Proc. 1st North American Rock Mech. Symp.*, Austin, TX, USA: 591-598 (1995).
31. Ke, T.-C., Thapa, B. and Goodman, R. E., "Stability analysis of a penstock slope," *Proc. 1st North American Rock Mech. Symp.*, Austin, TX: 1109-1116 (1994).
32. Chen, S. and Lin, J.-S., "Application of DDA to evaluation and solution of slope stability," *Proc. '94 Rock Engrg. Symp. in Taiwan*: 269-277 (1994).
33. Yeung, M., Klein, S. J. and Ma, M., "Application of the discontinuous deformation analysis to the evaluation of rock reinforcement for tunnel stabilization," *Proc. 1st North American Rock Mech. Symp.*, Austin, TX: 607-614 (1994).
34. Chen, S., Chern, J. C. & Koo, C. Y., "Study on the performance of tunnel near slope by DDA," *Proc. 1st Intl. Conf. on Analysis of discontinuous Deformation*, J. C. Lin, C.-Y. Wang & J. Sheng, eds, Chung-Li, Taiwan: 109-123 (1995).
35. Ke, T.-C., "Application of DDA to block-in-matrix materials," *Proc. 35th U.S. Symp. on Rock Mech.*, Lake Tahoe, CA: 33-38 (1995).
36. Lin, T., Amadei, B., Ouyang S. & Huang, C., "Development of fracturing algorithms for jointed rock masses with DDA," *Proc. 1st Intl. Conf. on Analysis of discontinuous Deformation*, J. C. Lin, C.-Y. Wang & J. Sheng, eds, Chungli, Taiwan: 64-90 (1995).
37. Cai, Y., Liang, G.-P., Shi, Gen-hua and Cook, N. G. W., "Studying an impact problem by using LDDA method", *Proc. 1st Intl.Forum on DDA*, M. Reza Salami and Don Banks, eds., Berkeley, CA: 288-294 (1996).
38. Ke, T.-C. and Tang, J.-H., "Modeling of solid-fluid interactions using the manifold method," *Proc. 2nd North American Rock Mech. Symp.*, Montreal, Quebec, Canada: 1815-1822 (1996).
39. Chen, G., Miki, S. and Ohnishi, Y., "Practical improvements on DDA ", *Proc. 1st Intl.Forum on DDA*, M. Reza Salami and Don Banks, eds., Berkeley, CA: 302-309 (1996).
40. Shi, G.-H., "Modeling rock joints and blocks by manifold method," *Proc. 32rd U.S. Rock Mechanics Symp.*, Santa Fe, New Mexico: 639-648 (1992).
41. Goodman, R. E., *Engineering Geology - Rock in Engineering Construction*, 1st edn., John Wiley & Sons, Inc., New York: 412p (1993).

MODELING OF PROGRESSIVE FRACTURE IN JOINTED ROCK BY DDA METHOD

C. Y. Koo[1] and J. C. Chern[2]

Geotechnical Research Center, Sinotech Engineering Consultants, Inc., Taipei, Taiwan

ABSTRACT: This paper presents a new approach for modeling the progressive fracture in jointed rock mass. The block fracturing algorithm developed enables the simulation of progressive failure process of jointed rock mass under loading. Two modes of block fracturing, i.e., tensile splitting and shearing, were considered. The Mohr-Coulomb failure criterion with cohesion, friction and tensile parameters was used to develop the fracturing algorithm of solid block. Illustrative applications demonstrate that the new approach can not only simulate the rock progressive failure, but also provide a useful tool to evaluate the deformation and strength parameters of jointed rock mass for practical engineering purpose.

1. INTRODUCTION

Investigation on the stability of rock engineering problems such as tunnel, cavern, high slope and foundation has been of significant interest for geotechnical engineers. In many rock engineering problems, the rock masses encountered are often discontinuous media containing numerous discontinuity planes such as fissures, joints, shears and even faults. The stability of rock mass around cavern, slope or foundation is usually associated with the sliding of these discontinuities, the propagation of these planes or the fracture of rock blocks. However, in analyzing an engineering problem, it is impractical to incorporate all of these weak planes into the model. An equivalent rock mass property has to be used. Therefore, it is important to investigate the influences of discontinuity planes on the deformation and strength properties of jointed rock mass.

Because of the computational complexity in analyzing the behavior of jointed rock mass, it is almost impossible to solve the problems by analytical approach with the exception of rock mass with simple, regular pattern of joints. Hence, numerical approach may be a better alternative. Numerical methods based on continuum approach, such as finite element method(FEM), often adopts special elements, for instance, joint element or thin-layer element to simulate the discontinuity. For the problems with small displacement, good simulation results can be obtained. However, for the problems with large displacement along joints, block splitting or block fracturing, it is usually very difficult to simulate these behavior by using continuum approach. It is even more difficult to simulate the failure of discontinuous medium due to progressive extension of discontinuity planes or fracture of rock blocks. In this respect, the Discontinuous Deformation Analysis(DDA) based on the discontinuum approach originally developed by Gen-hua Shi may be more suitable for simulating the behavior of these discontinuous media.

---

[1]Geotechnical Engineer
[2]Manager

Though Lin(1995) was the first who develops the block fracturing algorithm for DDA method, his work used linear displacement function or constant stress formulation for blocks. This paper presents the block fracturing algorithm based on DDA method and proposes the incorporation of block fracturing algorithm into DDA with third order displacement function. This enables the simulation of progressive failure behaviour and the evaluation of deformation and strength characteristics of jointed rock mass. Two modes of block fracturing, i.e., tensile splitting and shearing, were considered. The Mohr-Coulomb failure criterion with cohesion, friction and tensile parameters was used to develop the fracturing algorithm of solid block. During the process of loading, the initiation and progress of block fracturing can be calculated. Several examples of validation study were conducted and applications presented.

2. MODELING OF JOINTED ROCK MASS

Since the pioneering work on jointed rock by Goodman, Taylor and Brekke(1968), joint element was widely used to simulate the discontinuity in numerical analysis. Later, Desai and Zaman(1984), Pande and Sharma(1979) introduced the concept of thin-layer element. Therefore, the behaviour of joint slide and shear can be simulated by appropriate elasto-plastic constitutive model. However, due to the limitations of continuum approach, both joint element and thin-layer element can only calculate the small displacement along joints. Cundall(1971) adopted force method with the explicit scheme to develop the Distinct Element Method(DEM) based on discontinuum approach. DEM can simulate the large displacement problem with block contact, rotate, slide and movement. However, due to the limitation of explicit scheme, the time step must reduce to very small for numerical convergency by using DEM. The DDA method first developed by Gen-hua Shi in 1988 also based on discontinuum approach, but adopted the displacement method with the implicit scheme. This makes the DDA method more similar to the widely used FEM. Therefore, it can be easily accepted and used by research workers.

As we know, the engineering rock is heterogeneous and quite often discontinuous. In some situations, the performance of rock mass is dominated by the properties of pervasive discontinuities, especially in jointed rock mass. Hence, the modeling capability of discontinuities is important for numerical simulation of jointed rock mass. Due to the unique complete block kinematics in DDA method, DDA can deal with the complicated interaction between discrete blocks separated by discontinuities under ensured equilibrium conditions. It treats blocks as distinct elements, and each of these distinct elements can contact, slide and rotate with other blocks. Accordingly, with the block kinematics, DDA is more easily to capture the behavior of jointed rock mass. However, cracks are often appeared in rock block associated with discontinuities during the construction of rock engineering. It is more practical if the fracturing mechanics is considered in DDA method. By this reason, this paper develops the fracturing algorithm for DDA, the implementation of the fracture algorithm to the DDA code and its application to simulate the progressive failure of jointed rock mass. The following section presents the formulation of the fracturing algorithm.

3. BLOCK FRACTURE ALGORITHM FOR DDA

Modes of Fracture

In general, rock fracture in an ideally linear elastic brittle material can be possibly caused by three basic kinds of stresses, i.e., normal stress, shear stress and out-of-plane shear stress,

or the combinations of them. Different loading configurations lead to the three basic distinct fracture modes. These fracture modes can be demonstrated by Figures 1(a) to (c). Figure 1(a) shows the opening mode caused by normal stress. Figure 1(b) shows the shearing mode caused by shear stress. Figure 1(c) shows the tearing mode caused by out-of-plane shear stress. If we consider all of these three fracture modes into DDA method, the fracture behavior of linear elastic brittle material may be conducted. However, only two in-plane fracture modes, i.e., mode 1 and mode 2, are considered in the current two-dimensional theory of DDA method.

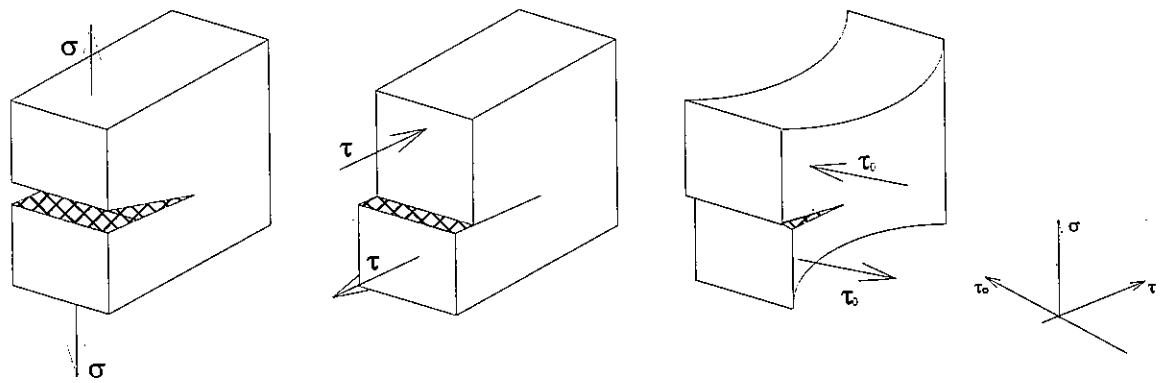

(a) Mode 1: $\tau=\tau_0=0$ opening mode (b) Mode 2: $\sigma=\tau_0=0$ shearing mode (c) Mode 3: $\tau=\sigma=0$ tearing mode Co-ordinate system

Figure 1 Fracture modes of rock material

Calculation of Principle Stresses in Each Block

To investigate the possibility of block fracturing, the principle stresses of each block should be calculated first. The linear elastic deformation is used in current DDA version, and the elastic stresses can be obtained by the following relations:

$$\begin{bmatrix} \sigma_x \\ \sigma_y \\ \tau_{xy} \end{bmatrix} = \frac{E}{1-v^2} \begin{bmatrix} 1 & v & 0 \\ v & 1 & 0 \\ 0 & 0 & \frac{1-v}{2} \end{bmatrix} \begin{bmatrix} \varepsilon_x \\ \varepsilon_y \\ r_{xy} \end{bmatrix}$$

If the first order displacement function is adopted, the strain of each block can be expressed as follows:

$$\begin{bmatrix} \varepsilon_x \\ \varepsilon_x \\ r_{xy} \end{bmatrix} = \begin{bmatrix} \frac{\partial u}{\partial x} \\ \frac{\partial v}{\partial y} \\ \frac{\partial u}{\partial y} + \frac{\partial v}{\partial x} \end{bmatrix} = [B_i]_{3\times 6}[D_i]_{6\times 1} \quad ; \qquad [B_i] = \begin{bmatrix} 0 & 0 & 0 \\ 0 & 0 & 0 \\ 0 & 0 & 0 \\ 1 & 0 & 0 \\ 0 & 1 & 0 \\ 0 & 0 & 1 \end{bmatrix}$$

$$[D_i] = [u \quad v \quad r_0 \quad \varepsilon_x \quad \varepsilon_y \quad r_{xy}]$$

Also, if the third order displacement function is adopted, the strain of each block can be expressed as follows:

$$\begin{bmatrix} \varepsilon_x \\ \varepsilon_x \\ r_{xy} \end{bmatrix} = \begin{bmatrix} \dfrac{\partial u}{\partial x} \\ \dfrac{\partial v}{\partial y} \\ \dfrac{\partial u}{\partial y} + \dfrac{\partial v}{\partial x} \end{bmatrix} = [B_i]_{3\times 20}[D_i]_{20\times 1} = \begin{bmatrix} B_{i1} \\ B_{i2} \\ B_{i3} \\ B_{i4} \end{bmatrix} [D_i]$$

$$[B_{i1}] = \begin{bmatrix} 0 & 0 & 0 \\ 0 & 0 & 0 \\ 1 & 0 & 0 \\ 0 & 0 & 1 \\ 0 & 0 & 1 \end{bmatrix} ; \quad [B_{i2}] = \begin{bmatrix} 0 & 1 & 0 \\ 2x & 0 & 0 \\ 0 & 0 & 2x \\ y & 0 & x \\ 0 & x & y \end{bmatrix} ; [B_{i3}] = \begin{bmatrix} 0 & 0 & 2y \\ 0 & 2y & 0 \\ 3x^2 & 0 & 0 \\ 0 & 0 & 3x^2 \\ 2xy & 0 & x^2 \end{bmatrix} ; [B_{i4}] = \begin{bmatrix} 0 & x^2 & 2xy \\ y^2 & 0 & 2xy \\ 0 & 2xy & y^2 \\ 0 & 0 & 3y^2 \\ 0 & 3y^2 & 0 \end{bmatrix}$$

$$[D_i] = [d_1, d_2, d_3, \ldots, d_{20}]_{1x20},$$

where $d_1, d_2, d_3, \ldots, d_{20}$ are coefficients of third order displacement function.

The block principle stresses of each block can be calculated by the following formula.

$$\sigma_1 = \frac{\sigma_x + \sigma_y}{2} + \sqrt{\tau_{xy}^2 + \frac{1}{4}(\sigma_x - \sigma_y)^2}$$

$$\sigma_3 = \frac{\sigma_x + \sigma_y}{2} - \sqrt{\tau_{xy}^2 + \frac{1}{4}(\sigma_x - \sigma_y)^2}$$

where σ_1 is maximum principle stress and σ_3 is minimum principle stress.

Mohr-Coulomb Failure Criterion

The Mohr-Coulomb criterion of three parameter, cohesion, friction and tensile strength (S_0, ϕ, T_0) as shown in Figure 2 are used to develop the fracturing algorithm. Figure 3 shows the stress state of Mohr-Coulomb circle when the principle stresses meet the failure envelop.

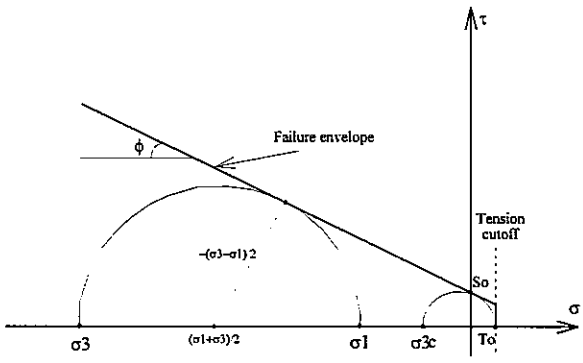

Figure 2 Mohr-Coulomb failure circle with tensile strength

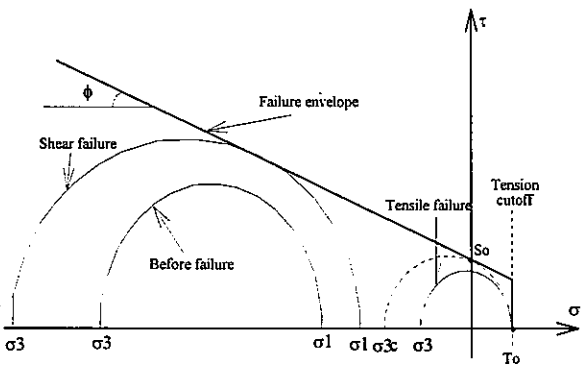

Figure 3 Demonstration of block principle stress meets Mohr-Coulomb failure envelop

Based on Mohr-Coulomb theory, σ_3 can be obtained, and expressed as follows.

$$\sigma_3 = -C_0 + \sigma_1 Tan^2(\frac{\pi}{4} + \frac{\phi}{2})$$

where $\sigma 3c$ are defined by

$$\sigma 3c = -C_0 + T_0 Tan^2(\frac{\pi}{4} + \frac{\phi}{2})$$

$$C_0 = 2S_0 Tan(\frac{\pi}{4} + \frac{\phi}{2})$$

C_0 is the rock strength without confining stress. σ_3 is the minor principle stress when fail and $\sigma 3c$ is the minor principle stress when block meets both the tensile failure and shear failure criteria.

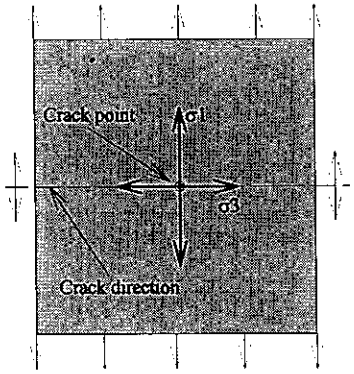

Figure 4 Cracking direction of tensile failure

1> Criteria of Block Tensile Failure:

According the Mohr-Coulomb theory, the criteria of tensile fracture can be expressed as follows:

$$\sigma_1 \geq T_0 \quad \text{if} \quad \sigma_1 > \sigma_3 > 0$$

$$\sigma_1 \geq T_0 \quad \text{if} \quad \sigma_1 > 0 > \sigma_3 > \sigma_{3c}$$

Tensile fracture occurred when the principle stresses of block meet one of the tensile failure criteria. The direction of crack line is parallel to the minor principle stress as shown in Figure 4.

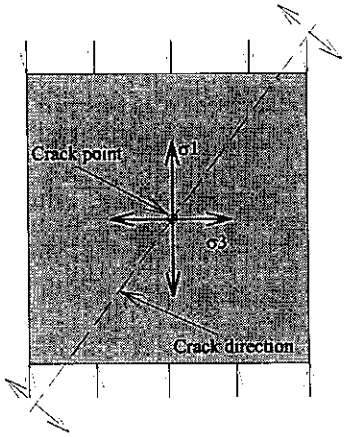

Figure 5(a) Cracking direction of shear failure

2> Criteria of Block Shear Failure:

The criteria of shear fracture can be expressed as follows:

$$\sigma_3 \geq -C_0 + \sigma_1 \text{Tan}^2(\frac{\pi}{4} + \frac{\phi}{2}) \quad \text{if} \quad \sigma_1 > 0 > \sigma_{3c} > \sigma_3$$

$$\sigma_3 \geq -C_0 + \sigma_1 \text{Tan}^2(\frac{\pi}{4} + \frac{\phi}{2}) \quad \text{if} \quad 0 > \sigma_1 > \sigma_3$$

Shear fracture occurs when the principle stresses of block meet one of the shear failure criteria. The direction of crack line is $\alpha + (45^0 + \phi/2)$ or $\alpha - (45^0 + \phi/2)$ to the direction of major principle stress as shown in Figures 5(a) and (b), where α is the angle between the direction of major principle stress and horizontal axis as shown in Figure 5(c), and can be obtained by the following formula.

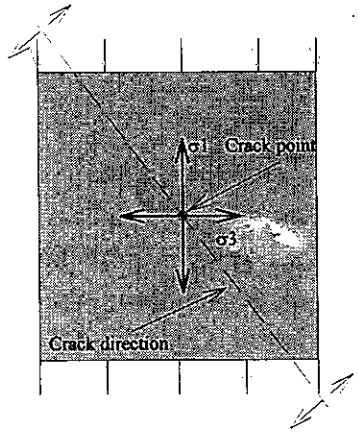

Figure 5(b) The other cracking direction of shear failure

$$\alpha = Cot^{-1}(\frac{\tau_{xy}}{\sigma_1 - \sigma_x})$$

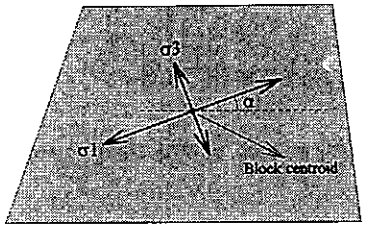

Figure 5(c) Direction of α angle

Fracture Propagation throughout the Block

Fracture will occur if block principle stresses meet the Mohr-Coulomb Failure Criterion. According to the tensile or shear fracture mode described in the above

section, the crack line with different direction and path which depends on the failure mode will be generated. The following section introduces how to compute the crack line within the block.

1> Tensile cracking

Tensile cracking occurred when block principle stress meets tensile failure criteria. The direction of tensile crack line is shown in Figure 6(a). After cracking, the solid block is divided into two sub-blocks. The crack line passes through the block centroid, and its slope is parallel to the direction of minor principle stress. If the third order displacement function is adopted, the crack line will pass through the measuring point that first meets the failure criteria within the block, and its slope is also parallel to the direction of minor principle stress. The tensile crack line can be expressed as the following equation.

$$y = Cot\alpha \cdot x + (y_c - Cot\alpha \cdot x_c)$$

x_c, y_c are defined as the coordinates of block centroid. In 3rd order DDA case, x_c, y_c are defined as the coordinates of the measuring point which meets the tensile failure criteria in block. The direction of major principle stress is parallel to the following equation.

$$y = Tan\alpha \cdot x + (y_c - Tan\alpha \cdot x_c)$$

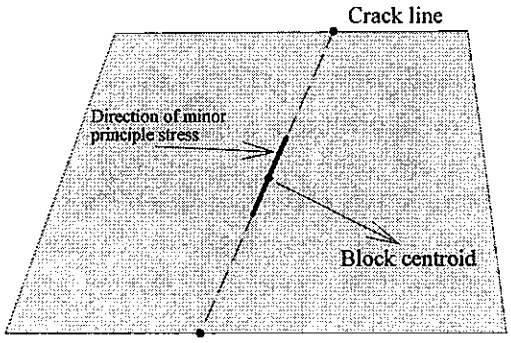

Figure 6(a) Direction of tensile crack line

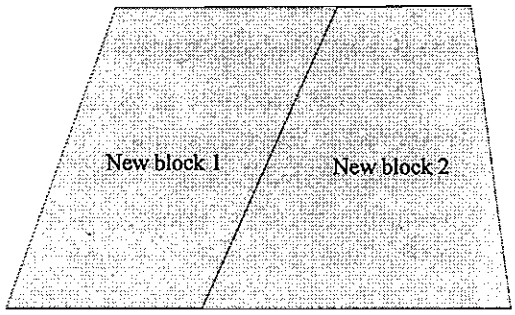

Figure 6(b) New blocks are generated after tensile fracture occurred

2> Shear cracking

Shear cracking occurred when block principle stress meets shear failure criteria. The direction of shear crack line is shown in Figure 7(a). After cracking, the solid block is divided into two sub-blocks. The crack line passes through the block centroid, and its slope is inclined at $\alpha \pm (\pi/4 + \phi/2)$ of the direction of minor principle stress. If the third order displacement function is used, the crack line will pass through the measuring point that first meets the failure criteria within the block, and its slope is also inclined at $\alpha \pm (\pi/4 + \phi/2)$ of the direction of minor principle stress. The shear crack line can be expressed as the following equation.

$$y = Cot(\alpha + \frac{\pi}{4} + \frac{\phi}{2}) \cdot x + (y_c - Cot(\alpha + \frac{\pi}{4} + \frac{\phi}{2}) \cdot x_c)$$

or

$$y = Cot(\alpha - \frac{\pi}{4} - \frac{\phi}{2}) \cdot x + (y_c - Cot(\alpha - \frac{\pi}{4} - \frac{\phi}{2}) \cdot x_c)$$

x_c, y_c are defined as the coordinates of block centroid. In 3rd order DDA case, x_c, y_c are defined as the coordinates of the measuring point which meets the shear failure criteria in block. The definition of α angle is the same as tensile cracking case described above.

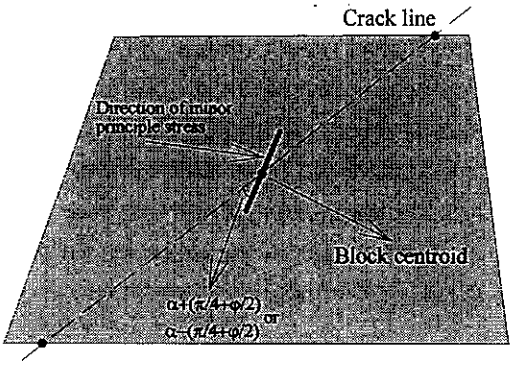

Figure 7(a) Direction of shear crack line

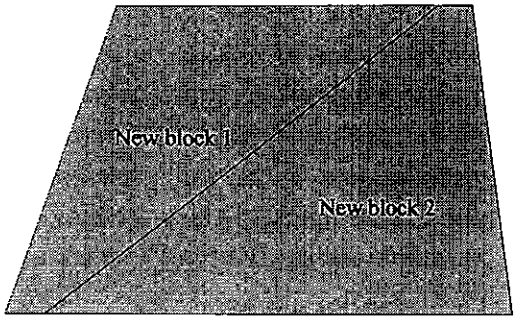

Figure 7(b) New blocks are generated after shear fracture occurred

4. VALIDATIONS OF BLOCK FRACTURE ALGORITHM

Based on the original DDA code, the new code with block fracture algorithm named Fra_DDA was developed. To verify the block fracture algorithm, several validation studies were carried out in this section.

Example 1: Uniaxial Compression Test

The first example is to verify the shear fracture algorithm and the strength of rock sample with exact solution. A rock sample of 7.3 cm wide and 15 cm high without confining pressure under strain controlled load at its upper plate was used. The Mohr-Coulomb material parameters assumed for rock sample are friction angle = 30^0, cohesion = 40 kg/cm^2 and tensile strength = 10.5 kg/cm^2, and joint parameters are friction angle = 30^0, cohesion = 0 and tensile strength = 0. Figure 8(a) shows the original configuration and Figures 8 (b) and (c) show the computed results after fracturing.

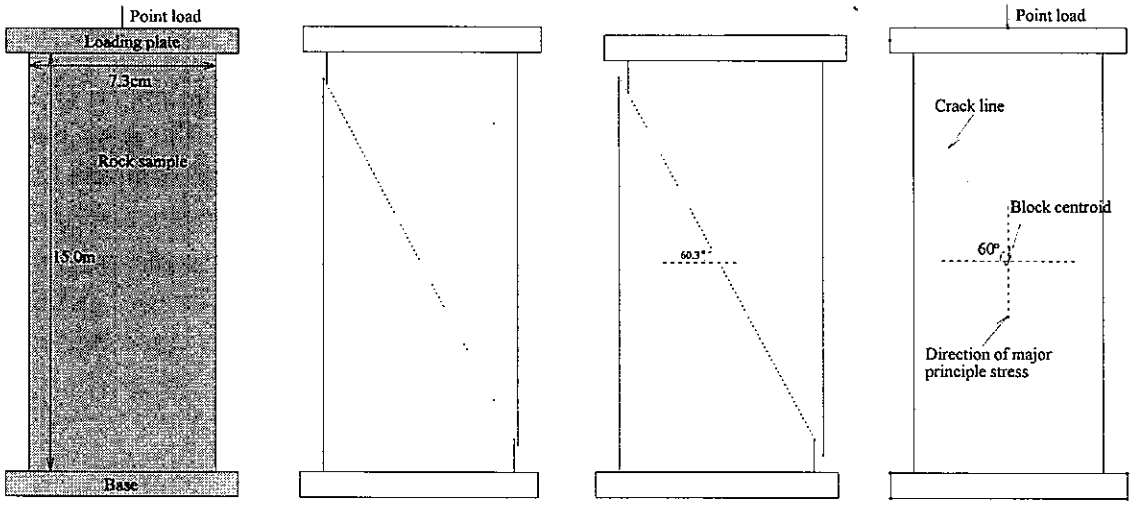

(a) Original configuration (b) after 1800 time steps of calculation (c) after 3600 time steps of calculation (d) Theoretical results

Figure 8 Numerical simulation of uniaxial compression test

Comparing the final result of Figure 8(c) with theoretical result shown in Figure 8(d), the computed shear fracture plane is almost the same as the theoretical shear fracture plane. Meanwhile, the peak compression strength of 140.5 kg/cm^2 can also be obtained from stress and strain curve shown in Figure 10. Comparing the computed peak compression strength with the exact solution of 138.56 kg/cm^2 obtained by the formula $C_0 = 2S_0 Tan(\pi/4 + \phi/2)$, it may be seen that good agreement in results can be obtained. Based on these comparisons, the shear fracture algorithm of block is judged to be valid.

Example 2: Uniaxial Tensile Test

The second example is to verify the tensile fracture algorithm using uniaxial tensile test. The configuration of rock sample is the same as the example 1. Figure 9(a) shows the original configuration and Figures 9(b) and (c) show the computed results after fracturing. Comparing the final result of Figure 9(c) with the theoretical result, the computed tensile fracture plane is the same as the theoretical tensile fracture plane which is parallel to the minor principle stress. Meanwhile, the peak tensile strength of 20.5 kg/cm^2 can also be obtained from stress and strain curve as shown in Figure 10. Comparing the computed peak tensile strength with the assumed tensile strength of 20 kg/cm^2, it may be seen that good agreement in results can be obtained. Based on these comparisons, the tensile fracture algorithm of block is judged to be valid.

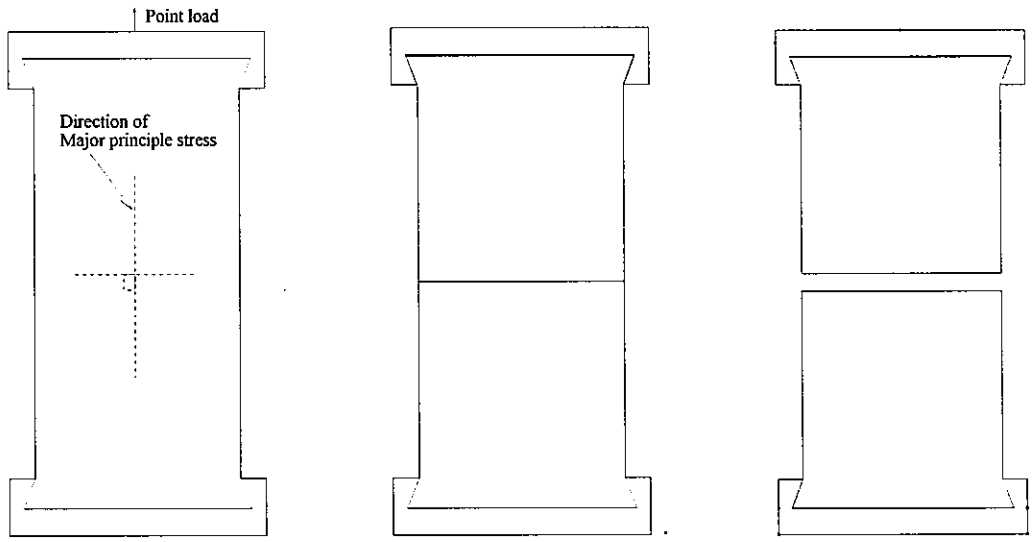

(a) Original configuration (b) after 900 time steps of calculation (c) after 2700 time steps of calculation

Figure 9 Numerical simulation of uniaxial tensile test

5. APPLICATION EXAMPLES

Simulation of Loading Behavior of Rock Sample with Single Joint

Because of the existence of bedding or joint plane with different inclinations, the rock samples show different stress-strain and strength behavior under loading. The following examples demonstrate the capability of Fra_DDA program to simulate the stress-strain relation and progressive fracture of rock. Samples (1)-(5) in Table 1 show the rock samples with no joint or with one joint of different orientations. All of the rock samples in Table 1 are

of the same size of 7.3 cm wide and 15 cm high under confining pressure of 23.6 kg/cm^2. Strain controlled loading was applied at the upper plate of the rock sample. The material parameters of all rock samples are assumed to be the same with friction angle = 30^0, cohesion = 40 kg/cm^2 and tensile strength = 20.5 kg/cm^2; and joint parameters are friction angle = 30^0, and no cohesion and tensile strength assumed. The computed results including rock strength, failure mode and stress-strain curve are also summarized in Table 1.

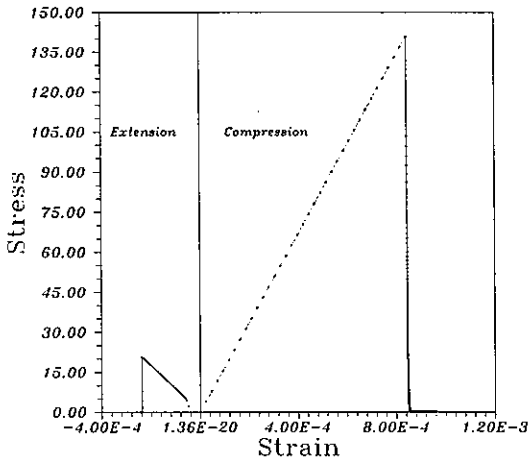

Figure 10 Stress and strain curve of intact sample under compression and tension

Table 1 Numerical simulation of Jointed rock by Fra_DDA

	Rock sample	Description	Rock strength	Failure type	Failure mode
(1)	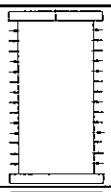	Intact rock Confining pressure: 23.6 kg/cm^2	Peak strength: 245 kg/cm^2 Residual: 85 kg/cm^2	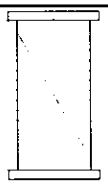	Shear fracture
(2)	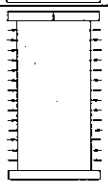	Intact rock with a single 60^0 inclined discontinuity Confining pressure: 23.6 kg/cm^2	Peak strength: 85 kg/cm^2	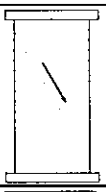	Slide
(3)	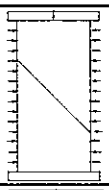	Intact rock with a single 45^0 inclined discontinuity Confining pressure: 23.6 kg/cm^2	Peak strength: 160 kg/cm^2	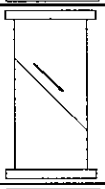	Slide
(4)	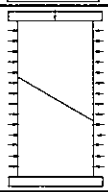	Intact rock with a single 30^0 inclined discontinuity Confining pressure: 23.6 kg/cm^2	Peak strength: 215 kg/cm^2		Combined slide and Shear fracture
(5)	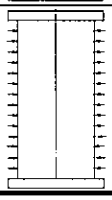	Intact rock with a single 90^0 inclined discontinuity Confining pressure: 23.6 kg/cm^2	Peak strength: 225 kg/cm^2		Shear fracture

	Stress-strain curve
(1)	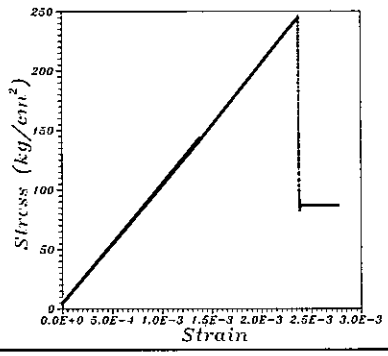
(2)	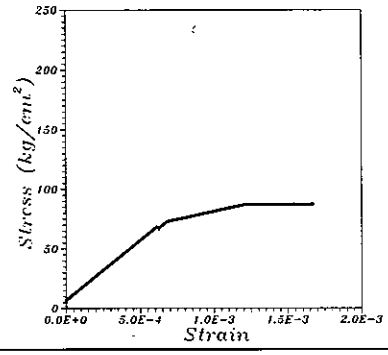
(3)	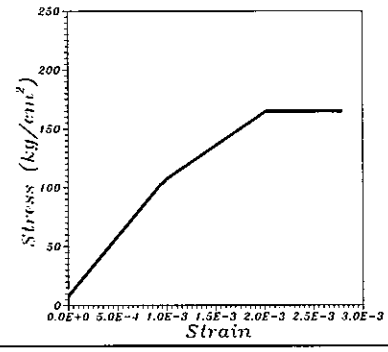
(4)	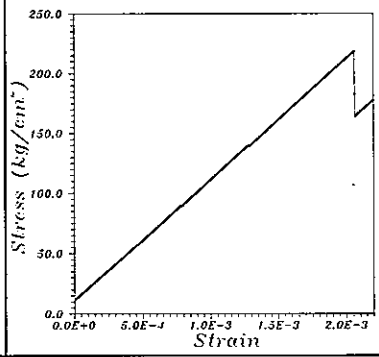
(5)	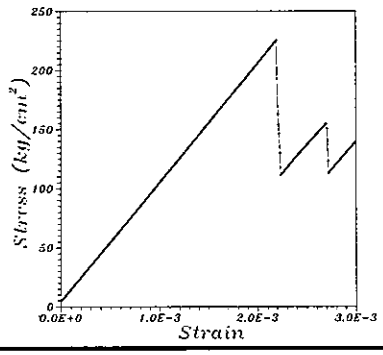

Table 1 Cont.

For the intact rock sample, rock remains linear elastic before reaching the peak strength of 245 kg/cm^2. After loading exceeding the peak shear strength, fracture occurred in rock sample with failure mode and stress-strain curve shown in Table 1. From the result obtained, after cracking, the shear strength of rock sample reduced to 85 kg/cm^2. It can be concluded that the residual is only came from joint friction. For the cases of Samples (2) and (3) with the joint inclinations are 60^0 and 45^0, rock failure is in slide mode. If the joint is 30^0 inclined(sample 4), mixed mode combined shear and slide modes is occured. If the joint is 90^0 inclined(Sample 5), shear fracture is occured. The computed results and failure modes shown in Table 1 demonstrate that Fra_DDA provides a new and easier approach than laboratory test to simulate the anisotropic behavior of jointed rock.

Simulations of Loading Behavior of Rock Sample with Multiple Joints

The following examples demonstrate the numerical uniaxial compression test on multiple jointed rock mass by using Fra_DDA program. Two rock samples of 7.3 cm wide and 15 cm high shown in Figures 11(a) and 12(a) with inclined joint sets at 22.5^0 and 45^0 respectively, were used. Strain controlled loading was applied at the upper plate of rock sample. The strength parameters of rock material are : friction angle = 33.6^0, cohesion = 20 kg/cm^2 and tensile strength = 10.5 kg/cm^2; and joint parameters are friction angle = 30^0, and no cohesion and tensile strength assumed.

Figures 11(b) and (c) show the computed results of progressive failure process of the sample with joint sets inclined at 22.5^0. From the results obtained, shear fracture occurred at the right corner of the rock sample and small displacements along joints are observed. Therefore, it can be concluded that the failure mode of the rock sample can be attributed to mixed mode. In this case, additional works were made that the crack line can consecutively propagate from its neighboring crack point.

Figures 12(b) and (c) show the computed results of sample with joint sets inclined at 45^0. From the results obtained, only sliding displacements occurred. Similar to the rock sample with single joint inclined at 45^0 described earlier, both of them showed sliding failure mode.

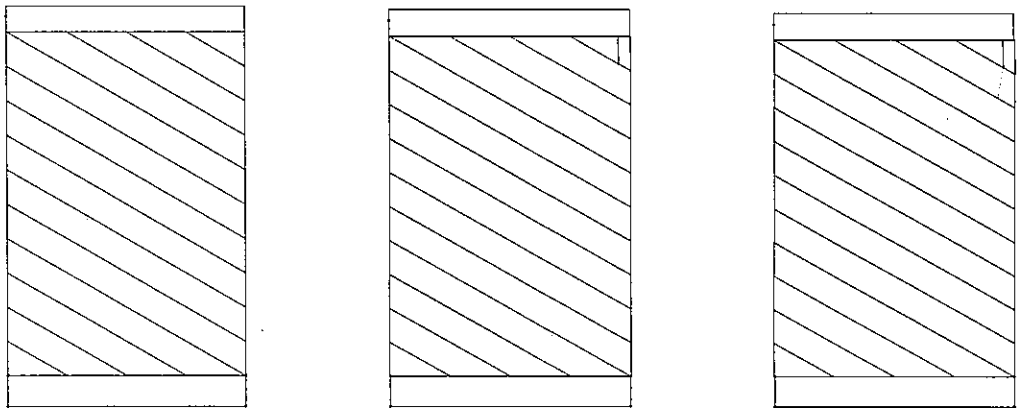

(a) Original configuration (b) Cracking occurred at the right corner of rock sample during calculation (c) Final computed result by Fra_DDA

Figure 11 Numerical simulation of uniaxial compression test on sample with multiple joints inclined at 22.5^0

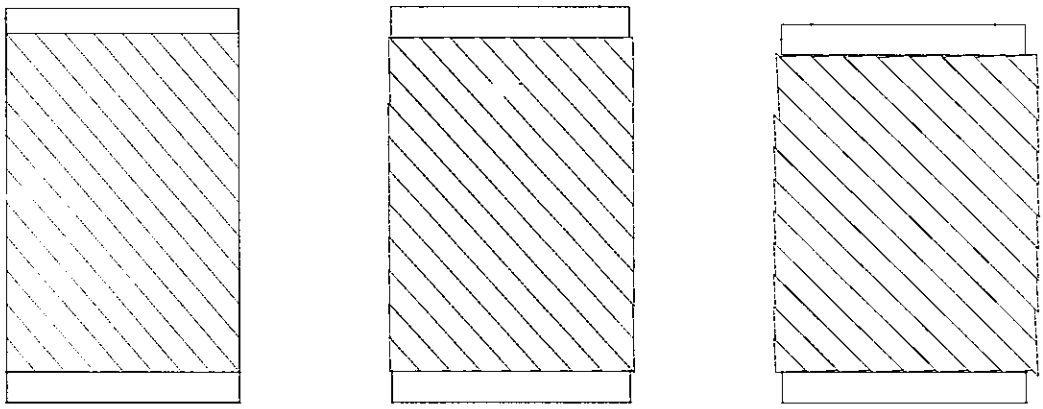

(a) Original configuration (b) Slide failure along pre-exist joints occurred during calculation (c) Final results show the slide mode of failure

Figure 12 Numerical simulation of uniaxial compression test on sample with multiple joints inclined at 45^0

As another illustration on the application of Fra_DDA, the comparison of numerical simulations obtained by Fra_DDA and laboratory physical model test results on samples with two crossing joint sets are presented. The rock samples with two symmetric crossing joint sets inclined at 30^0 and 45^0 are shown in Figures 13(a) and 14(a). The configurations of these two rock samples are the same except their inclinations of joint sets. Rock samples are 12.5 cm wide and 30 cm high without confining pressure, and strain controlled loading applies at the upper plate of each of the sample. The material parameters of rock blocks are: friction angle = 30^0, cohesion = 9.3 kg/cm^2 and tensile strength = 10.5 kg/cm^2; and joint parameters are friction angle = 31.2^0, and no cohesion and tensile strength assumed.

In the first case with joint sets inclined at 30^0, the mixed failure mode combined shear and slide failure occurred. Figures 13(b)(c) show the progressive failure process simulated by Fra_DDA. The peak strength obtained from the stress-strain curve of the rock sample is 28 kg/cm^2 shown in Figure 13(d) which agrees well with the peak strength of 26.9 kg/cm^2 by the physical model test. Comparing the stress-strain curves shown in Figures 13(d) and (e), it can be seen that the tendency is very similar. The only disagreement in results computed by Fra_DDA with those of the physical model test are the stiffer stress-strain curve obtained. This probably can be attributed to the simple constitutive models of joint and block employed in DDA method whereas in physical model test plastic deformation or even the imperfection of sample may result in softer stress-strain curve.

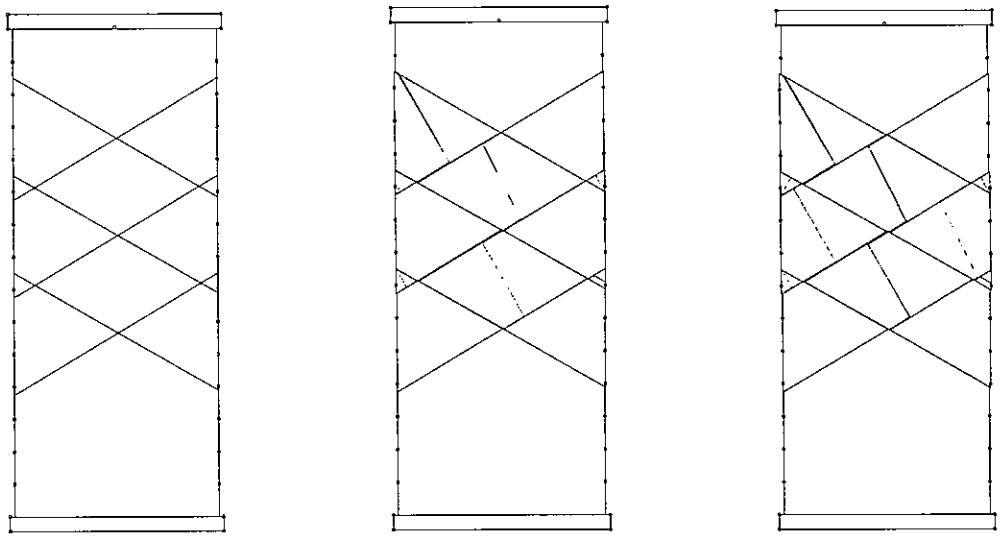

(a) Original configuration (b) Cracking occurred during calculation (c) Final results show the mixed mode of failure

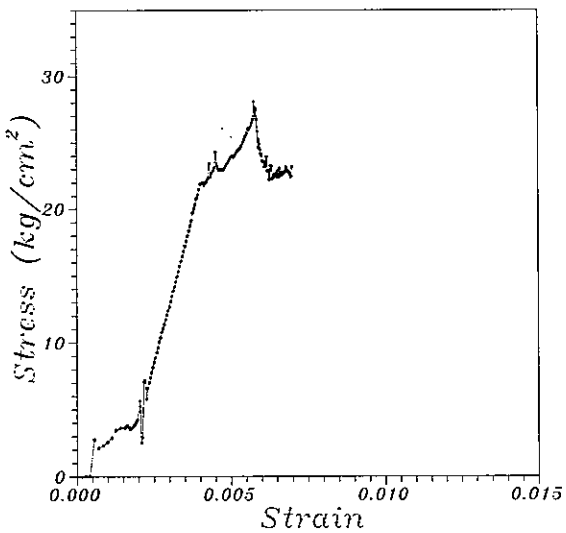

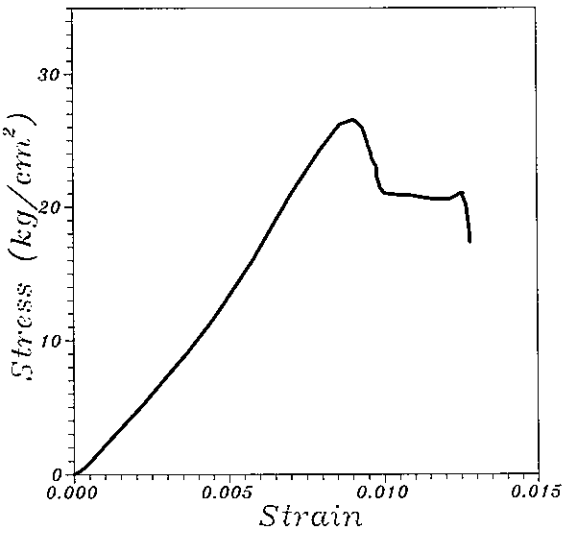

(d) Stress-strain curve computed by Fra_DDA (e) Stress-strain curve of physical model test

Figure 13 Numerical simulation of uniaxial compression test on sample with two crossing joint sets inclined at 30^0

In the second case with joint sets inclined at 45^0, the sliding mode occurred. Figures 14(b)(c) show the progressive failure process simulated by Fra_DDA. The peak strength of

this rock sample is 1 kg/cm^2 as shown in Figure 14(d). The very small peak strength obtained is in agreement with theoretical value since it is in unstable condition when the joint inclination is higher than the friction angle. However, the physical model test showed higher strength.

In summary, from the results of two illustrative examples described above, Fra_DDA can capture two important failure behavior of jointed rock, that is block fracturing and block sliding along joints which is difficult to assess analytically or experimentally. With the simple block and joint models in the current version, rather good simulation in the behavior of jointed rock can be obtained. With further improvement in joint and block models, DDA could be a useful tool for engineering purpose.

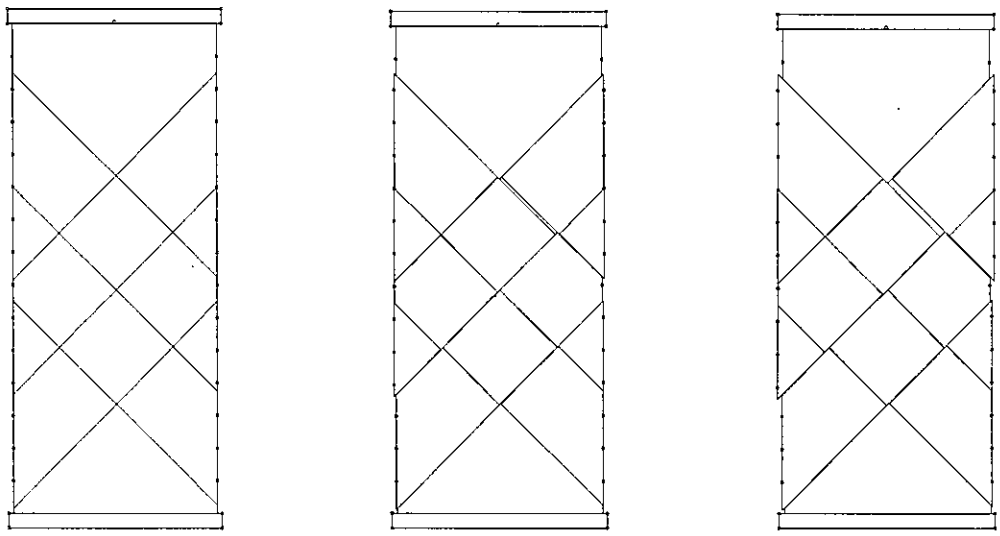

(a) Original configuration (b) Sliding occurred during calculation (c) Final results show the slide mode of failure

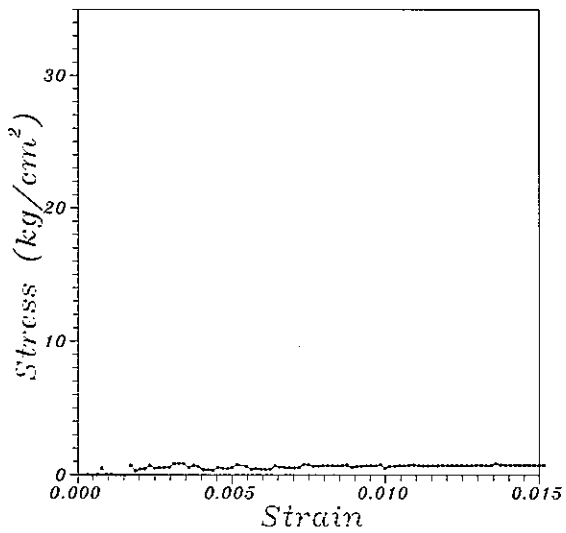

(d) Stress-strain curve computed by Fra_DDA

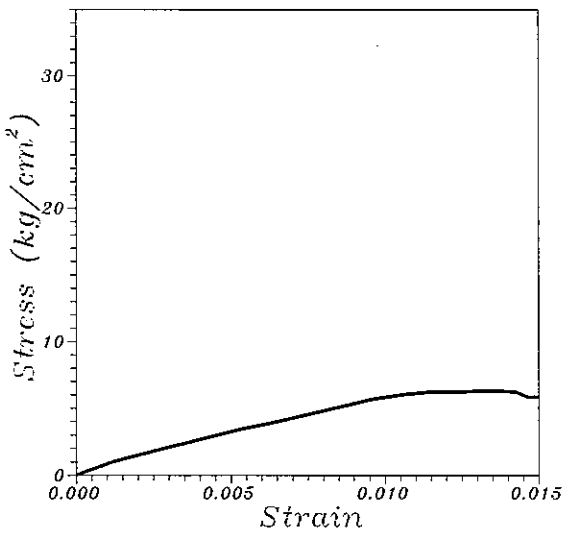

(e) Stress-strain curve of physical model test

Figure 14 Numerical simulation of uniaxial compression test on sample with two crossing joint sets inclined at 45^0

6. CONCLUSIONS

A new approach which incorporates the block fracture algorithm into DDA method for the modeling of progressive failure in jointed rock mass is presented in this paper. This method proposed intends to model the macro behavior of brittle material such as jointed rock mass for which no rational method of estimation is available at present. Progressive failure of the material was modeled by sliding of joint plane, fracturing of rock block due to shear and splitting of rock block due to tension. The complete formulation of block fracture algorithm for DDA was developed and the method of this algorithm combined into third order DDA was also proposed. Based on the formulation, a new code named Fra_DDA has been developed. Verified examples show that Fra_DDA is valid for the problem of jointed rock. From the results obtained by illustrative applications, Fra_DDA can capture the major features of loading behavior of jointed rock including failure mode and stress-strain relation. An improved modeling capability than other methods based on continuum concept such as FEM or analytical solution is obvious. By improving the joint and block models with nonlinear constitutive laws, it is believed that Fra_DDA can be a useful tool to evaluate the strength and deformation characteristics of jointed rock mass for practical engineering purpose.

ACKNOWLEDGMENTS

The authors wish to thank Dr. John-ho Chia for his helpful discussions on the behavior of rock joints and Dr. Shue-yeong Chi for his valuable suggestions. Acknowledgment is also extended to Sinotech Engineering Consultants, Inc. for funding this research project.

REFERENCES

Barry N. Whittaker, Raghu N. Singh and Gexin Sun, (1992) *Rock Fracture Mechanics Principle, Design and Application,* Elsevier Scientific Publishing Company, Amsterdam.

Cundall, P. A. (1971), "A computer model for simulating Progressive, Large Scale Movements in Blocky Rock Systems," Proceedings Symposium, International Society of Rock Mechanics, Nancy 2, No. 7.

Desai, C.S. Zaman, M.M., Lightner, J.G. and Siriwardane, H.J., (1984) "Thin-layer Element for Interfaces and Joints", Int. J. Num. Anal. Mech. Geomech. 8, pp19-43.

Goodman, R. E. (1980), *Introduction to Rock Mechanics*, Wiley, New York.

Goodman, R.E., Taylor, R.L. and Brekke, T.L., (1968) "A Model for Mechanics of Jointed Rock", J. Soil Mech. and Found. Div., A.S.C.E. 94, pp637-659.

Huang, T. H., (1994) "A Study on Deformability of Rock Masses Under Multiaxial Stress Conditions" Report to the Sinotech Foundation for Research and Development of Engineering Sciences and Technologies, Report No. : SFRDEST R-95-RM-01-1 Taipei. Taiwan. (in Chinese).

J. C. Chern, C. Y. Koo and S. Chen,(1995) "Development of Second Order Displacement Function for DDA and Manifold Method", Working Forum on the Manifold Method of Material Analysis, pp183~202, Vicksburg .

Ke, Te-chih (1993), "Simulated Testing of Two Dimensional Heterogeneous and Discontinuous Rock Masses Using Discontinuous Deformation Analysis," Ph.D. Thesis, Dept. of Civil Engineering, University of California, Berkeley.

Koo, C. Y., and Chern, J. C. ,(1996) "The Development of DDA with Third Order Displacement Function", Proceedings of the first International Forum on Discontinuous

Deformation Analysis and Simulation of Discontinuous Media., pp. 342-350, Berkeley California, U.S.A.

Lin, C. T., (1995) "Extensions to the Discontinuous Deformation Analysis for Joint Rock Masses and Other Blocky Systems" Ph.D. Dissertation, University of Colorado, Boulder.

Shi, G. H. (1988), "Discontinuous Deformation Analysis: A New Numerical Model for the Statics and Dynamics of Block Systems," Ph.D. Thesis, Dept. of Civil Engineering, University of California, Berkeley.

Shi, G. H. (1996), "Manifold Method", Proceedings of the first International Forum on Discontinuous Deformation Analysis and Simulation of Discontinuous Media., pp. 52-205, Berkeley California, U.S.A.

"The Application of Discontinuous Deformation Analysis in Rock Mechanics" Report to the Research Foundation of Sinotech Engineering Consultants, Inc., Taipei. Taiwan (1995). (in Chinese)

Viscosity Coefficient of the Rockfall Simulation

Masato SHINJI, Hiroyuki OHNO
OYO Corporation, Rock Engineering Department, Omiya, Japan.
Yasunori OTSUKA
OYO Corporation, Kansai Branch Office, Suita, Japan.
Guichen MA
OYO Corporation, Rock Engineering Department, Omiya, Japan.

ABSTRACT: Rockfall simulation considering viscosity in discontinuous deformation analyses has been developed and applied in various sites upon designing rockfall prevention works. A detailed examination is required to estimate the energy occurred with rockfall for design of the rockfall prevention work, and it is known that this energy is affected by viscosity coefficient. Further, this viscosity coefficient has a physical value that is different from equivalent friction coefficient or restitution coefficient of a slope, and thus, varies according to the condition of a slope. However, there still is no definite way to establish this viscosity coefficient, and it is determined accordingly at the site.

In this paper, the authors attempted to study the correlation between viscosity coefficient and equivalent friction coefficient, and to examine the variation of viscosity coefficient according to different slope conditions.

As a result, it was possible to define a relationship between slope condition (effects of talus deposits, trees, etc.) and viscosity coefficient. It was found that viscosity coefficient changed within the range of 0.05～0.30tf*sec/m^4 according to respective slope conditions.

1. INTRODUCTION

At the steep slope adjacent to roads or railways, there is high dangerousness of occurring the rockfall size larger than a human head. Conventionally in Japan, we have taken measures to prevent rockfall due to a generalized method called the "Rockfall Countermeasure Manual(*Rakuseki Taisaku Binran*)". These guidelines were based on the assumption that the rockfall was no larger than a human head (diameter: approximately 30cm). However, in actual cases of rockfalls, the large boulders measuring several meters in diameter is occurred. It is important that we properly estimate the shock load (the external force which acts on prevention constructions), when rockfall prevention works are designed. However, the rockfall speed is not estimated practically and properly with the guidelines of this Manual, if there is a rockfall that is larger than the sizes defined in the

Manual. Thus, currently, it is still difficult to compute specific external forces in the respective sites.

Recently, the rockfall simulation considering viscosity in discontinuous deformation analysis has been developed, for the design of rockfall prevention works at various sites[1)2)]. Rockfall energy becomes an important issue upon designing the rockfall prevention work, and this energy is known to be affected by viscosity coefficient of the slope. Further, this viscosity coefficient has a physical value that is different from the equivalent friction coefficient or the restitution coefficient of the slope, and thus, tends to vary according to the condition of the slope. However, there still is no definite way to establish this viscosity coefficient, and it is determined accordingly at the site. To apply this method in various sites, there is a need to establish proper viscosity coefficients according to slope conditions.

In this paper, the authors studied the correlation between viscosity coefficient and equivalent friction coefficient, and examined the variation of viscosity coefficient according to different slope conditions.

2. DISCONTINUOUS DEFORMATION ANALYSIS CONSIDERING VISCOSITY

The equation of motion considering viscosity is defined as follows as seen in Figure 1, in the system of particle.

$$m\frac{dv}{dt} = mg\sin\theta - \mu_d vV \qquad \text{Eq. (1)}$$

Where; θ: Slope gradient (degree), m: Mass of rockfall(ton),
v: Velocity of rockfall(m/sec), V: Volume of rockfall(m^3),
g: Gravitational acceleration (9.8m/sec^2), μ_d: Viscosity coefficient (tf*sec/m^4)

Discontinuous deformation analysis (DDA) was developed by Shi & Goodman, and it is useful to numerically analyze dynamic behavior of mutual blocks of discontinuous rock media. In this study, the authors utilize the DDA method improved to simulate rockfall by Onishi and Yamamukai[3)].

Rockfall experimentation conducted up to now, assumed that the mean rockfall speed would be a constant velocity[4)] about of 19m/sec, due to energy loss and air resistance when falling down the slope, if the fall height of the falling block is

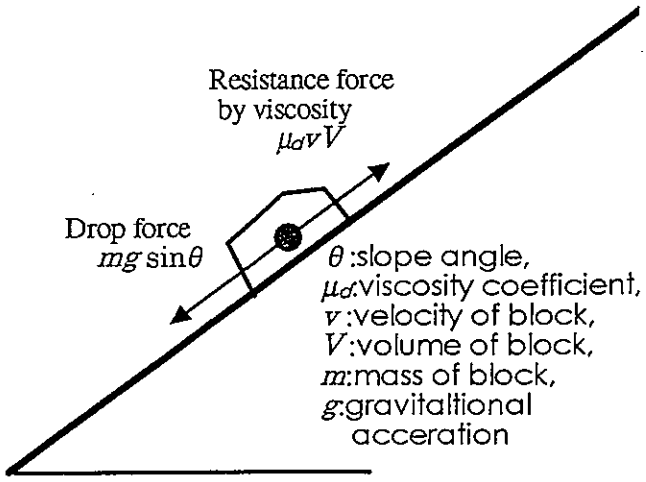

Fig. 1 The concept of resistance force for rockfall simulation.

higher than 50 m. In the rockfall simulation using DDA to analyze resistance force such as energy loss and air resistance when the block goes down a slope, we utilize the viscous force to represent those effects. In specific, as indicated in Equation (1), the resistance force corresponds to the volume and falling speed of block. For this reason, we assumed the following equation as viscous force.

$$\begin{pmatrix} f_x \\ f_y \end{pmatrix} = \frac{\mu_d}{\Delta t}\begin{pmatrix} u \\ v \end{pmatrix}$$

Where; f_x, f_y: Viscous force per unit volume (tf/m^3), Δt : Time step (sec),
u, v: Increment of displacement (m)

The potential energy accumulated with viscous force resistance can be expressed with the following equation.

$$\Pi_v = \int_s (u \quad v)\begin{pmatrix} f_x \\ f_y \end{pmatrix} ds$$

Where; s: Area of rock mass block (m^2)

It is possible to analyze the effects of viscous by differentiating the displacement variables of potential energy and applying them in the conventional DDA formulation.

3. CHARACTERISTICS OF OBJECTIVE AREA

There are a total of 8 sites, $A \sim H$ areas for review of this study. Figure 2 illustrates the cross section of representative slopes at each objective area. The slope condition and rockfall condition of respective area are summarized as follows.

Table 1 The result of analyzed viscosity coefficient at each objective area.

Area	Slope condition				Fallen rock		Analyzed viscosity coefficient (tf·sec/m^4)
	Geological condition	Trees	Fall height	Average gradient	Form of rock	Density of rock	
A	Talus deposits	Not exit	115m	51°	Angular	2.5 tf/m^3	0.10~0.15
B	Talus deposits	Exit	180m	45°	Angular	2.6 tf/m^3	0.20~0.25
C	Talus deposits	Abundance	170m	36°	Angular	2.5 tf/m^3	0.25
D	Talus deposits	Abundance	45m	43°	Angular	1.8 tf/m^3	0.25~0.30
E	Bare rocks	Not exit	40m	70°	Angular	2.7 tf/m^3	0.05~0.10
F	Bare rocks	Not exit	50m	85°	Angular	2.5 tf/m^3	0.05
G	Talus deposits	A few	50m	40°	Angular	2.5 tf/m^3	0.15
H	Talus deposits	Exit	50m	55°	Angular	2.4 tf/m^3	0.25~0.30

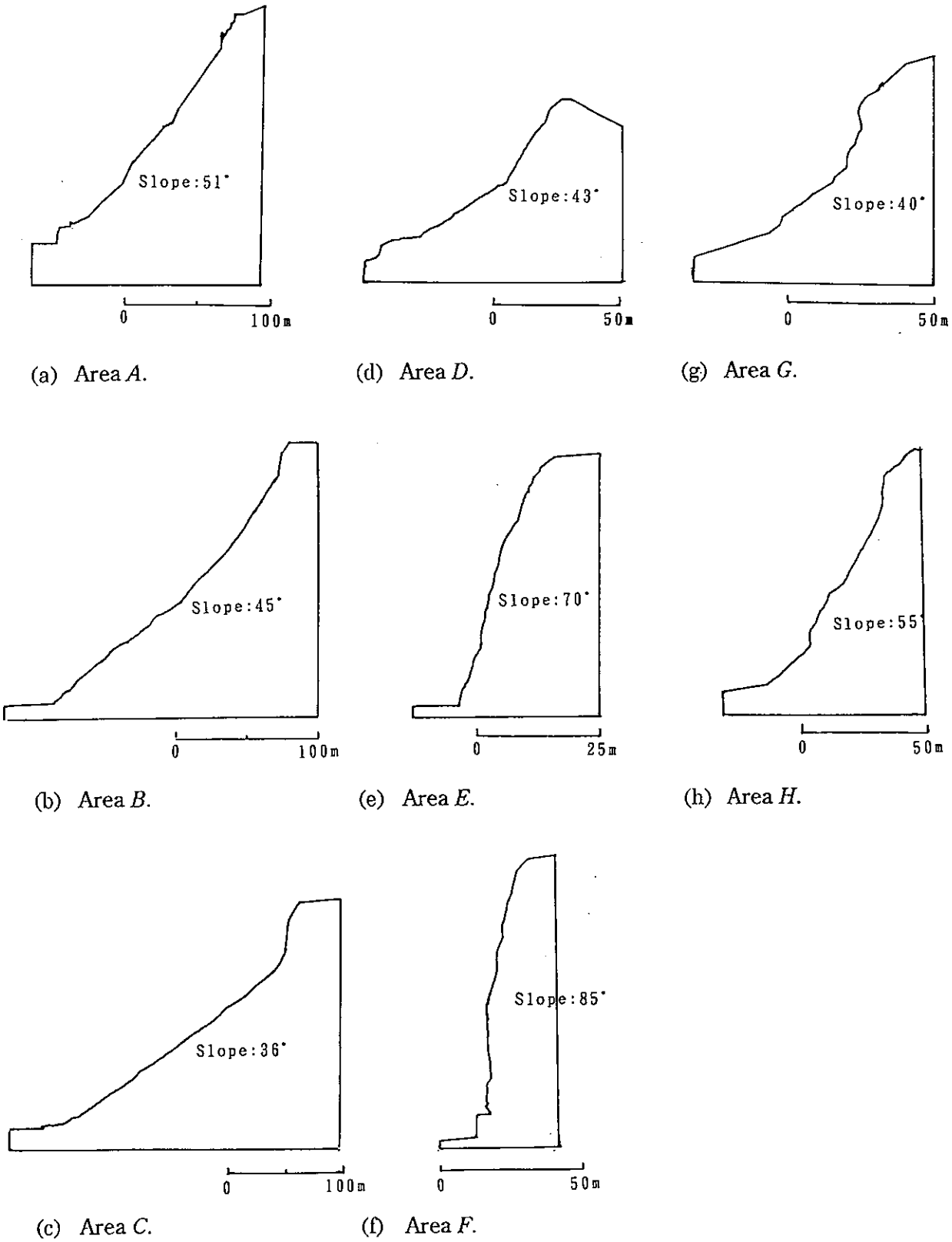

Fig. 2 The typical cross section of each objective area.

Area *A* has a mean slope of approximately 51 degrees angle, with much talus deposits but limited tree growth. Fallen rocks are angular shape with a fall height of about 115 m.

Area *B* has an average slope gradient of about 45 degrees, with some talus deposits and arboreal growth. Fallen rocks are angular shape with a fall height of about 180 m.

Area *C* has an average slope gradient of about 36 degrees, with some talus deposits and abundance of arboreal growth, with the catch walls in several places. Rockfalls are angular shape with a fall height of about 170 m.

At Area *D*, there is a slope of approximately 43 degrees angle, that is a talus deposits with abundance of arbores. The rocks which fell from about 45 meters high take the angular form.

At Area *E*, there is a steep slope with a mean angle of approximately 70 degrees. The angular rocks fall down the bare slope where a little grass grows, from about 40 meters high.

Area *F* is a steep slope with a mean angle of approximately 85 degrees, with not much plant growth on the slope exposed rock. Rockfalls are angular shape with a fall height of about 50 m.

The slope at Area *G* has an average gradient of about 40 degrees, with some talus deposits and a few arbores. Rockfalls are angular form with a fall height of about 50 m.

The slope at Area *H* has an average gradient of about 55 degrees, with some talus deposits and arboreal growth. The angular rocks fell from about 50 meters high.

4. ANALYSIS RESULTS AND DISCUSSION

4.1. ANALYSIS METHOD AND RESULTS

To seek the viscosity coefficient according to respective slope condition we employed a inverse analysis method, in which the viscosity coefficient was computed to conform actual rockfall condition. This procedure was conducted as shown in Figure 3. Further, only one cross section was computed when there weren't multiple cross sections for the

Table 2 The viscosity coefficient of each slope condition.

Slope condition			Viscosity coefficient	Slope class*
Geological condition	Trees	Form of rock		
Bare rocks	Not exit	Spherical	——	A
Bare rocks	Not exit	Angular	0.05~0.10	B
Talus deposits	Not exit	Angular	0.10~0.20	C
Talus deposits	Exit	Angular	0.20~0.30	D

*) The "Slope class" is classified by the "Rockfall Countermeasure Manual"

objective area.

The viscosity coefficient attained as a result of the analysis is shown in Table 1.

As it is apparent, the range of viscosity coefficient tended to change between 0.05~0.30tf*sec/m^4 due to different slope conditions (talus deposits or arboreal growth, etc.). The viscosity coefficient was larger when there was more talus deposits and arboreal growth, and tended to drop when ground surface was limited to plant growth on the slope of bare rocks.

Table 2 illustrates the correlation that summarizes these tendencies. It was not possible to review the A-rank slopes defined in the slope category of the Rockfall Countermeasure Manual, since there was no data available, however, based on the changes in viscosity coefficients of B~D-rank slope categories, it is assumed that the A-rank coefficient is less than 0.05tf*sec/m^4.

4.2. CORRELATION WITH EQUIVALENT FRICTION COEFFICIENT

In this section, we examine the correlation between equivalent friction coefficient defined in the Rockfall Countermeasure Manual and viscosity coefficient utilized in this study.

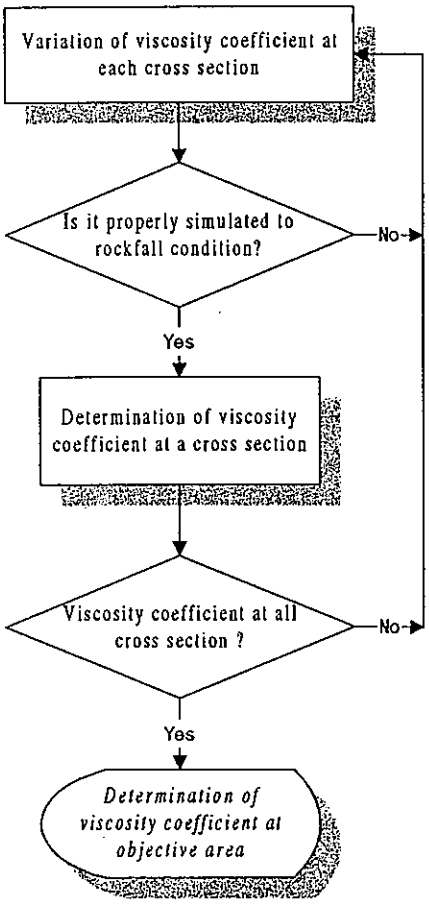

Fig. 3 Flow chart of the estimation of viscosity coefficient by the rockfall simulation.

The following equations are assumed using the equation (1) that considers viscosity, when;

Time t = 0, velocity of rockfall v = 0, fall distance s = 0

$$v = \frac{mg\sin\theta}{\mu_d V}\left[1-\exp\left(-\frac{\mu_d V}{m}t\right)\right]$$

$$s = \frac{m^2 g\sin\theta}{\mu_d{}^2 V^2}\left[1-\exp\left(-\frac{\mu_d V}{m}t\right)\right]+\frac{mg\sin\theta}{\mu_d V}t$$

When using the equation considering equivalent friction coefficient, the equation of motion is defined as;

$$m\frac{dv}{dt} = mg\sin\theta - \mu_r mg\cos\theta \qquad \text{Eq.(2)}$$

Where; μ_r: Equivalent friction coefficient

The following equations are assumed, when;

Time t = 0, velocity of rockfall v = 0, fall distance s = 0

$$v = g(\sin\theta - \mu_r\cos\theta)t$$

$$s = \frac{1}{2} g(\sin\theta - \mu_r \cos\theta)t^2$$

Based on the above, the following equation is assumed for the correlation between equivalent friction coefficient and viscosity coefficient;

$$\mu_r mg\cos\theta = \mu_d vV$$

$$v = \alpha\sqrt{2gH}$$

Here; α: Residual coefficient (coefficient remained rockfall speed),
H: Fall height (m)

$$\mu_r = \tan\theta(1-\alpha^2) \qquad \text{Eq. (3)}$$

$$\mu_d = \frac{\rho g(1-\alpha^2)\sin\theta}{\alpha\sqrt{2gH}} = \frac{\rho g\cos\theta}{\alpha\sqrt{2gH}}\mu_r \qquad \text{Eq. (4)}$$

Based on the above equation, the correlation between equivalent friction coefficient and viscosity coefficient is assumed for a function of fall height H. Therefore, it is not the case that one viscosity coefficient is determined for a certain equivalent friction coefficient.

The equation of motion that considers viscosity coefficient is a formula that expresses resistance force of air, grass and trees. Therefore, it is an equation of motion of the rock that falls through air, instead of sliding on a slope.

On the other hand, the equation of motion that considers equivalent friction coefficient is a formula that expresses resistance of the rock when it slides down a slope. Thus, it is different from an equation of motion used for rocks falling through the air.

Rocks can fall through air, slide down a slope, roll down a slope or even bump down a slope, in actually these phenomena complexly act to rockfall. Therefore, a formula that considers all these phenomena would be most suitable for accurate computations. However, it is difficult to create such equation of motion. Equations for viscosity coefficients and equivalent friction coefficient both assumed that falling rock is simple phenomenon.

Since these two equations of motion are differ in the assumptions of resistance force of the falling rock, it is extremely impossible to find simple correlation between equivalent friction coefficient and viscosity coefficient. Further, the differences in such assumption makes it apparent that the correlation between viscosity coefficient and equivalent friction coefficient can only be expressed as function of fall height H.

The correlation between equivalent friction coefficient and viscosity coefficient using equation (4) is shown in Figure 4. The value which is calculated from data indicated on the Rockfall Countermeasure Manual, is illustrated in this figure.

Further, we sought the equivalent friction coefficient of each location for review, using this equation. As illustrated in Table 3, the correlation between equivalent friction coefficient by Rockfall Countermeasure Manual, and equivalent friction coefficient sought

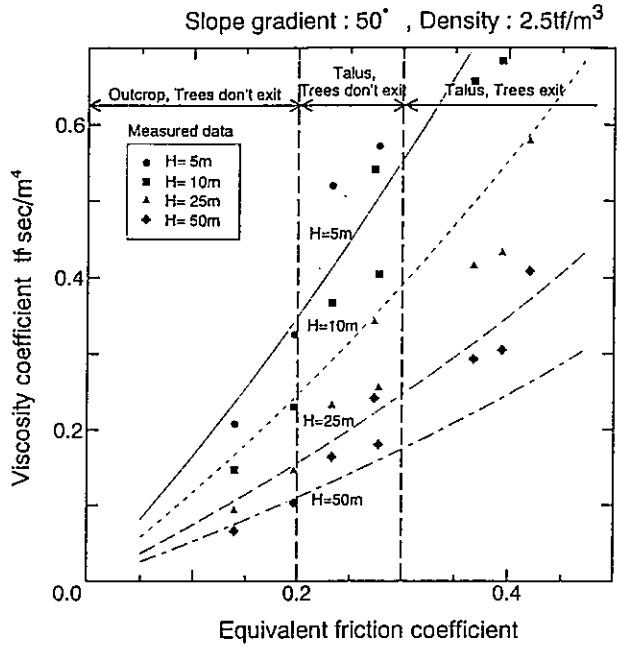

Fig. 4 The correlation between the equivalent friction coefficient and the viscosity coefficient.

Table 3 The comparison between the viscosity coefficient and the equivalent friction coefficient.

Area	Condition		Slope class	Residual coefficient	Equivalent friction coefficient
	Geological	Trees			0.1 0.2 0.3 0.4 0.5 0.6 0.7
A	Talus deposits	Not exit	C	0.85	
B	Talus deposits	Exit	D	0.75	
C	Talus deposits	Abundance	D	0.75	
D	Talus deposits	Abundance	D	0.75	
E	Bare rocks	Not exit	B	0.95	
F	Bare rocks	Not exit	B	0.95	1.11
G	Talus deposits	A few	C	0.85	
H	Talus deposits	Exit	D	0.75	

——— : Range of equivalent friction coefficient by the Rockfall Countermeasure Manual,

○ : Design value of the Rockfall Countermeasure Manual,

□ : Equivalent friction coefficient calculated by the residual coefficient and gradient,

.... : Range of equivalent friction coefficient calculated by the viscosity coefficient.

*) The residual coefficient is assumed by the slope class of Manual.

from equation (4), shows almost same value, other than for Area *F*. It is also possible to seek the equivalent friction coefficient from the residual coefficient and slope gradient. Equation (3) was used to seek for the equivalent friction coefficient indicated with a rectangle symbol in the Table.

The slope of Area *F* was almost perpendicular. As it is apparent from equation (4), there is a $\cos\theta$ in denominator. This means the equivalent friction coefficient calculated from viscosity coefficient will become an extremely large value as the slope becomes more perpendicular. Due to similar reasons, the equivalent friction coefficient of Area *E* calculated from viscosity coefficient will also become a slightly large value. The equivalent friction coefficient defined in equation (2) is based on the assumption that the rock slides down the slope, and targets a slope of less than 60 degrees angle. Therefore, it is impossible to use the equivalent friction coefficient for such steep slopes that are almost perpendicular.

5. CONCLUSIONS

In this paper, we examined the variation in viscosity coefficient according to different slope conditions. The conclusions were as follows:

1) Viscosity coefficient tended to change within a range of $0.05 \sim 0.30 tf*sec/m^4$ according to slope conditions. It was larger when there were trees and talus deposits, and tended to be smaller when ground surface was limited to plant growth or bare rocks.
2) As a result of comparative studies with equivalent friction coefficient of the Rockfall Countermeasure Manual, it was found that viscosity coefficient was not different from equivalent friction coefficient. However, there is a limit to the application of friction coefficient for steep slopes, because equivalent friction coefficient is assumed to be the value for a mean slope angle of less than 60 degrees.

Currently an entire slope is assumed to have one viscosity coefficient. However, in practical slopes, there are both bare part and talus part at the entire slope, and different resistance forces are generated at respective points. For this reason, there is a need for some process that groups the slope into the several layers, which have respectively different viscosity coefficients.

As indicated in Yoshida's method, the issue of rockfall is a field that requires a statistical approach. There is a great possibility that the behavior of the rockfall may vary due to small changes of the starting point of the rockfall, or the effect of rolling on the slope. Simply speaking, it is thought that there is a butterfly effect of the chaos.

Future studies need to solve these problems, with the analysis that appropriately conforms to the conditions of the site.

ACKNOWLEDGMENTS

The authors gratefully acknowledge the cooperation of this study by Professor Y.SASAKI, Hiroshima University, Department of Civil and Environment Engineering.

REFERENCES

1) H. SEKI, K. SASAHARA, Y. ITO, R. YOSHINAKA & M. SHINJI (1995): An application of Discontinuous Deformation Analysis for a Design of Rock Prevention Work, Proc. of the 26th Symposium of Rock Mechanics, pp.391～395.

2) H. OHNO, M. TAKAHASHI, Y. SONE & M. SHINJI(1996): The Analysis of Rockfall Mechanism, Proc. the Thirty-first Japan National Conference on Geometrical Engineering, pp. 1477～1480.

3) K. YAMAMUKAI(1994): Rockfall Simulation of Slope using Discontinuous Deformation Analysis and Studies on Applications, Master Thesis of Kyoto University.

4) Z. MIKAMI (1984): Rockfall Prevention and Protection Engineering Methods, Rikou-tosho.

Dynamic Deformation and Stress Field Analysis of Fault

Xiaoli Deng

School of Geo-science and Surveying Engineering, Wuhan Technical University of Surveying and Mapping
39 Luoyu Road, Wuhan, China, 430070

Abstract

Fault deformation surveying is a kind of dynamic geodesy made on the fault areas where there is strong information of crustal movement. It is one of the observational methods used in China for monitoring fault deformation and studying precursory anomaly of earthquakes.

In this paper, the time series analysis (TSA) is applied to data processing of fault deformation observation. Based on the studies of characteristics of fault movement, a dynamic deformation model is proposed by using a combination of grey theory and time series analysis. In the model, the fault deformation is divided into a regular part and a stochastic part.

Because the time series analysis cannot always correctly explain the deformation mechanism of fault movement, a method for analysis of fault stress field based on the discontinuous deformation analysis (DDA) is presented. A fault is considered as a fault block system, and can be divided into blocks in the analysis along, but not limited to, the natural discontinuities. The displacement parameters and the stress field of fault block system can be compute using the discontinuous deformation analysis. Through comparison of the displacement parameters obtained respectively by the TSA and the DDA, the stress field is achieved.

1. Introduction

Fault is a plane where rock breaks and strong deformation happens. Fault has the characteristic of lower intensity and easy deformation as compared with the complete rock. Earthquakes, especially shallow earthquakes, closely relate to fault movement. The results of geodetic deformation surveying show that fault zone is the most significant crustal deformation zone. With the action of tectonic stress, three types fault movement may happen. The first type is a quick displacement, such as earthquake movement. The second type is long-term slide without earthquake. The last one is the slide between the first and second ones. In addition, some seasonal movement can also happen on fault zone, which is related to temperature, raining, and underground water, and just occur in shallow crust.

To determine the current intensity of deformation at the fault zone and its characteristic and process, deformation monitoring is carried out by using baseline measurement and leveling, which crosses or nears the fault. The length of measuring

line that crosses the fault is from several meters to several kilometers. The observing cycle is one or two months. Leveling determines the changes of height of the two benchmarks situated at different side of the fault. Baseline measurement determines the changes of distance between two baseline marks situated at different side of the fault. According to the changes of height and distance, the relative displacement and moving velocity can be computed. This monitoring of fault movement has following features:

1. The deformation surveying that carried out on the strong deformation zone may obtain information of fault movement that is the cause of crustal motion. The information may also be relative to dynamics process of earthquake, including precursor of earthquake.
2. The data from deformation surveying having the contribution of many factors are strongly disturbed. The results contain many dynamic factors of environment, including tectonic or non-tectonic, seismic or non-seismic factors.
3. It is a typical dynamic surveying. Observation results are generally presented as time series, and it may have some relationship with tectonics, mechanics and information.

The processing of the observation data at the fault zone aims at: (1)Obtaining the information of current tectonic movement , and of the processes of development and occurrence of earthquakes, such as information of precursory deformation anomaly, of slip during the occurrence of earthquake, and of adjustment after earthquake. (2)According to the information obtained, the possible earthquake, including its time, location, and magnitude, may be predicted.

If we take the fault zone as a system, its input information is very complex and the relationships between input and output is very fuzziness. In this paper, time series analysis is applied to the data processing of fault deformation. An equivalent system based on fault output information is established. The precursory deformation anomaly is recognized by analyzing the system. The last point, also the most important, is that we attempt to apply the discontinuous deformation analysis (DDA) to the fault system, for having a better understanding about the mechanical properties of development and occurrence of earthquakes.

2.Dynamic deformation analysis of fault movement

2.1 Theory of time series analysis

Time series analysis applies mainly to modeling and predicting for stable time series. For a normal, stable, and zero average time series $\{X_t\}$ $(t = 1,2,\ldots,N)$, if the value X_t is related not only to values $X_{t-1}, X_{t-2}, \ldots, X_{t-n}$, but also to disturbances $a_{t-1}, a_{t-2}, \ldots, a_{t-m}$, according to the concept of multiple regression analysis, dynamic model can be described as

$$X_t = \sum_{i=1}^{n} \varphi_i X_{t-i} - \sum_{j=1}^{m} \theta_j a_{t-j} + a_t \qquad (1)$$

where $a_t \sim NID(0,\sigma_a^2)$, that is, a_t satisfies independent normal distribution, which the average equals to zero and the variance is σ_a^2 .

Equation (1) is called n order autoregressive and m order moving average model denoted with $ARMA(n,m)$. Where $\varphi_i (i = 1,2,\ldots,n)$ are the autoregressive parameters; $\theta_j (j = 1,2,\ldots,m)$ are the moving average parameters. Particularly, with $\theta_j = 0$, equation (1) become a n order autoregressive model denoted with $AR(n)$; with $\varphi_i = 0$, equation (1) become a m order moving average model $MA(m)$.

Equation (1) is a kind of parameter model. The main task of the time series analysis is to determine these parameters. It would also contain test and process of data, choice and test of model, and optimization of parameter.

2.2 Predicting method of $ARMA$ model

Let $\hat{X}_t(l)$ is the predicting result at step l, the forecasting formula based on the minimum variance of the error of the predicted value is

$$\hat{X}_t(l) = \begin{cases} \sum_{i=1}^{n} \varphi_i X_{t+l-i} - \sum_{j=1}^{m} \theta_j a_{t+l-j} & l = 1 \\ \sum_{i=1}^{l} \varphi_i \hat{X}_t(l-i) + \sum_{i=l}^{n} \varphi_i X_{t+l-i} - \sum_{j=1}^{m} \theta_j a_{t+l-j} & 1 < l \le m \\ \sum_{i=1}^{l-1} \varphi_i \hat{X}_t(l-i) + \sum_{i=l}^{n} \varphi_i X_{t+l-i} & m < l \le n \\ \sum_{i=1}^{n} \varphi_i \hat{X}_t(l-i) & l > n \end{cases} \tag{2}$$

2.3 Hybrid time series model of fault movement

Fault is influenced by tectonic stress and dynamic factors surrounding it. The output result of fault system is a non-stable time series. A $ARMA$ model mentioned above can not be directly built for it. To deal with it, the deformation of a fault system is divided into a regular part and a stochastic part. First, we fit a curve for the regular part. Second, we build a $ARMA$ model for the stochastic part. Therefore the total deformation of a fault system can be written as

$$X_t = d_t + \varepsilon_t \tag{3}$$

where d_t is the regular part of fault deformation, ε_t is the stable and stochastic part of fault deformation. d_t can described as

$$d_t = (-aX_1 + u)e^{-at} + \sum_{k=1}^{q} e^{\gamma_k t}(A_k \cos\frac{2\pi}{T_k}t + B_k \sin\frac{2\pi}{T_k}t) \tag{4}$$

where a, u, A_k, B_k, γ_k $(k = 1,2,\ldots,q)$ are parameters. Equation (4) has two terms. The first one is exponent trend, and the another one is periodic trend.

In equation (4), exponent trend term is a $GM(1,1)$ model based on theory of grey system. For the original data series $\{X_t\}$, perform an accumulated generating operation, denoted with AGO:

$$X_t^{(1)} = \sum_{i=1}^{t} X_i \qquad (t = 1,2,\ldots,N) \tag{5}$$

One gets a new data series $\{X_t^{(1)}\}$. It corresponds to the differential equation:

$$\frac{dX^{(1)}}{dt} + aX^{(1)} = u \tag{6}$$

where a and u are grey parameters. Equation (6) is called $GM(1,1)$. The answer of $GM(1,1)$ is

$$X_{t+1}^{(1)} = (X_1 - \frac{u}{a})e^{-at} + \frac{u}{a} \tag{7}$$

where X_1 is the first data in $\{X_t\}$. Equation (7) is the formula of grey prediction. Perform the inverse of AGO for $X_{t+1}^{(1)}$:

$$X_{t+1}^{(0)} = X_{t+1}^{(1)} - X_t^{(1)} \tag{8}$$

In the original data, the value at step $t+1$ is predicted from the previous ones using the formula:

$$X_{t+1} = (-aX_1 + u)e^{-at} \tag{9}$$

Grey modeling demands non-stochastic data series and is usually used to analyze regular trend. Equation (9) represents a trend of exponent increase or decrease. It can accurately describe long-term changes of fault movement.

The second term in equation (4) describes the periodic variation of amplitude. It may be used to represented the environmental effects, which have obviously periodic changes based on seasons, such as raining, temperature, underground water, etc.

From (1), (3), and (4), we can obtain a hybrid model of a fault system:

$$\begin{aligned} X_t = (-aX_1 + u)e^{-at} + \sum_{k=1}^{q} e^{\gamma_k t}(A_k \cos\frac{2\pi}{T_k}t + B_k \sin\frac{2\pi}{T_k}t) \\ + \sum_{i=1}^{n} \varphi_i \varepsilon_{t-i} - \sum_{j=1}^{m} \theta_j a_{t-j} + a_t \end{aligned} \tag{10}$$

where T_k is the k-th period.

2.4 Method for recognizing the precursor deformation of fault

The recognization of anomalous deformation of a fault has two aspects. One is to identify the anomalous changes of the fault in the past. The other is to recognize the anomalous changes of the fault related to the development and occurrence of a forthcoming earthquake. As much information of the fault system is contained in the signal variance σ_x^2 and the residual variance σ_a^2 , the recognizer may be directly built:

$$\begin{aligned} \sigma_X^2 &= \frac{1}{N}\sum_{t=1}^{N}[X_t - \mu_X]^2 \\ \sigma_a^2 &= \frac{1}{N-n}\sum_{t=n+1}^{N}\left[X_t - \sum_{i=1}^{n}\varphi_i X_{t-i} + \sum_{j=1}^{m}\theta_j a_{t-j}\right]^2 \end{aligned} \tag{11}$$

where μ_X is the average of $\{X_t\}$.

3. Stress field analysis of fault

Much research showed that the anomalous deformation of fault could be considered as one of the precursor of strong and large earthquakes. The time series analysis is

usually used in analyzing the data gathered through deformation monitoring. As the model of the time series analysis was based on the output $\{X_t\}$ of fault system, it focuses mainly on deformation measurement data. Hence it only does some geometrical analysis. To correctly explain the deformation mechanisms and study the mechanical properties of fault, the above techniques of deformation analysis must be further developed.

The discontinuous deformation analysis (DDA) is widely used in geotechnical engineering. It can closely describe the real mechanical properties of the motion of block system. The discontinuous deformation analysis(DDA) could be applied to the tectonic stress field analysis of fault in two ways. (1)A single fault can be divided into mutually acting blocks forming a block system. The blocks are separated between each other along the natural discontinuities of a fault or any other arbitrary boundaries convenient for the analysis. Based on the theoretical relationship between the force and displacement for the fault block system, by adjusting the force on the boundaries, so that the displacement obtained from the discontinuous deformation analysis coincide with the one from the time series analysis, the stress field of the fault can be determined. (2)A relatively larger region including several faults can also be considered a block system in a manner similar to a single fault. Using the observation results in the region or on the fault zones provided by different kinds of deformation surveying, such as GPS surveying, leveling, and baseline measurement, we can study the discontinuous deformation of the fault system and the tectonical stress field in the region. We will limit our detailed discuss in the first aspect in this paper.

3.1 Motion equation of fault block system

We only discuss the horizontal deformation of a single fault, and assume the media has the isotropic linear elastic rheological property. The displacement (u,v) for any point (x,y) in the block can be described by six variables. It can be written(Shi,1993)

$$\begin{pmatrix} u \\ v \end{pmatrix} = \begin{pmatrix} t_{11} & t_{12} & t_{13} & t_{14} & t_{15} & t_{16} \\ t_{21} & t_{22} & t_{23} & t_{24} & t_{25} & t_{26} \end{pmatrix} \begin{pmatrix} u_0 \\ v_0 \\ r_0 \\ \varepsilon_x \\ \varepsilon_y \\ \varepsilon_{xy} \end{pmatrix}_i \tag{12}$$

or

$$\begin{pmatrix} u \\ v \end{pmatrix} = T_i D_i \tag{13}$$

where subscript i represent the i -th block. u_0, v_0 represent respectively translations along the X, Y directions of a rectangular coordinate frame in an inertia space; r_0 is the rotation angle about point (x_0, y_0); $\varepsilon = (\varepsilon_x \ \varepsilon_y \ \varepsilon_{xy})^{\mathrm{T}}$ is the strain vector.

The motion of the block system is constrained by the fact that no crack and mutual invasion between blocks. According to this condition and the principle of minimum potential energy in elasticity, we can simplify the equation of motion to a system of linear equation:

$$\begin{pmatrix} K_{11} & K_{12} & \cdots & K_{1n} \\ K_{21} & K_{22} & \cdots & K_{2n} \\ \vdots & \vdots & \cdots & \vdots \\ K_{n1} & K_{n2} & \cdots & K_{nn} \end{pmatrix} \begin{pmatrix} D_1 \\ D_2 \\ \vdots \\ D_n \end{pmatrix} = \begin{pmatrix} F_1 \\ F_2 \\ \vdots \\ F_n \end{pmatrix} \tag{14}$$

or

$$KD = F \tag{15}$$

where K_{ij} in matrix K is a submatrix of 6×6 order; D_{ij} and F_{ij} are submatrix 6×1 . D_i represents the deformation variables of the i -th block; F_i is the sum of body force, external forces and inertia force applied on the i -th block . Submatrix K_{ii} is related to the material properties of the i -th block, and K_{ij} $(i \neq j)$ is determined by the contacting condition of the i -th and the j -th blocks.

3.2 Computation of the stress field of fault block system

From the data of crossing fault leveling and baseline measurement, the relative horizontal displacement of two sides can be obtained using the time series analysis. Let's denote this displacement by D_0 . It is the really happened displacement. The stress field corresponding to it is the real stress field. However this stress can not be obtained by the time series analysis. We have to compute it using the discontinuous deformation analysis. The discontinuous deformation analysis method gives the displacement corresponding to certain known boundary forces. Let's use D to denote the displacement obtained from the DDA. Evidently, what we should do is to alter the boundary forces till $|D - D_0|$ arriving at a given small value (Fig.1). The stress in this

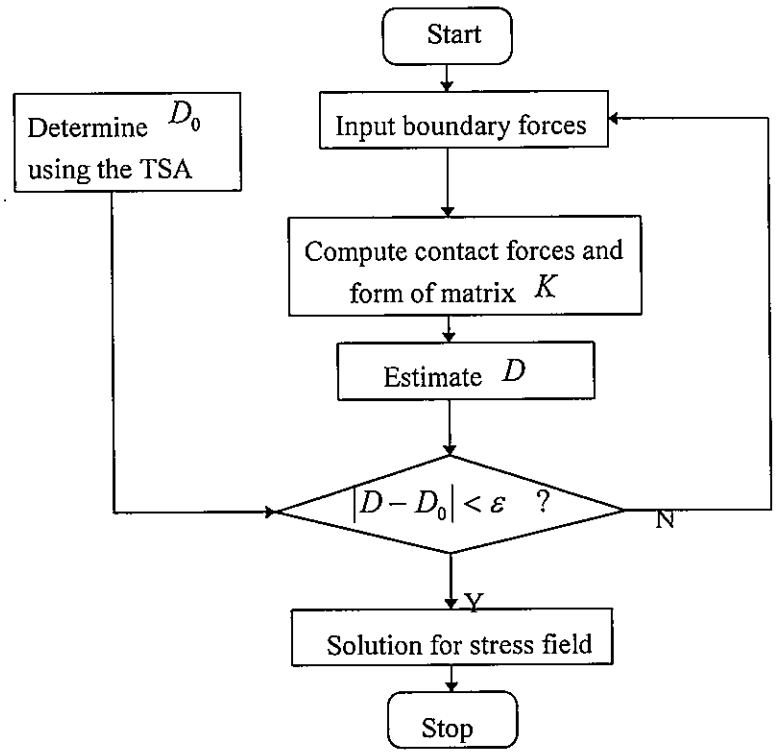

Figure 1. Flowchart of stress field analysis of the fault block system

situation is then what we are searching for. In this manner, we can simulate the stress before, in the moment, and after earthquakes, and analysis the variation of the stress field .

4. Conclusions

A dynamic hybrid model based on the method of time series analysis has been presented, in which the non-stochastic part is accurately described by a function, and ARMA model is established for the residual series.
We have discussed the possibility and method of applying the discontinuous deformation analysis for studying the relationship between the stress field and the displacement of fault block system. Detailed process has been proposed for using this method to a single fault.

Acknowledgments

The author wishes to thank Dr. Chen Guang-qi and Dr. Guo Jun-yi for useful discussions with them.

References

1. Ke, T.-C. and Bray.J.(1995), Modeling of particulate media using discontinuous deformation analysis, Journal of Engineering Mechanics, Vol.121, No.11. pp 1234-1243
2. Ren, D.-Y. and Ding, X.-L.(1996), Dynamic deformation analysis of open pit slopes, Proceedings of the 8th FIG international symposium on deformation measurements, pp 157-163
3. Shi, G.-H.(1993), A new method of discontinuous deformation analysis for block system, Science Publication, China, 243 pp
4. Yang, S.-Z. and WU, Y.(1992), Time series analysis in engineering application, Science publication, China, 802 pp

Tunnel Engineering Applications Using Discontinuous Deformation Analysis with Finite Element Mesh

Kuokai Shyu,[1] Chiao-Tung Chang[2] and M. Reza Salami[1]

[1]North Carolina A&T State University, Greensboro, NC 27411, USA
[2]Numerical Manifold Development, 18645 E. Gale Ave., #200, Industry, CA 91748, USA

ABSTRACT: Tunnel or rock engineering usually involves issues of discontinuity as a result of the complex geometry. In tunnel excavation one must consider the consequence of the interactions of discontinuous geological formations and the initial stresses built-in by the overburden or the tectonic squeezing movements over the years. Dynamic rock burst and subsequent closing of the tunnel immediately following excavation sometimes occurs at a tunnel construction site. Conventional continuum numerical models have difficulty in predicting or simulating these types of catastrophic response. A numerical model that couples a finite element mesh with each block of two-dimensional discontinuous deformation analysis has been developed to overcome the complexity of the computations. Numerical simulations are performed to qualitatively analyze the response to tunnel excavation by the underlying geological formations of (nearly) horizontal and vertical joint sets of shale rocks due to preexisting initial stresses in the rocks.

1. INTRODUCTION

It is common, indeed, that conventional continuum numerical models can not satisfactorily solve or fit the requirements of the reality, such as the discontinuity. Complex geometry and discontinuity are truly the major difficulties for the computational world, so as to the numerical modeling of rock engineering and tunnel engineering—the block system. Throughout the history, mathematicians developed a lot of wonderful theories and mechanics for the continuum—a beam. Great efforts have been made on discontinuities as the enhancements of continuum mechanics, though, current modern numerical models based on solid mechanics are still interested in one beam (or one solid), and that leaving discontinuity the uneasy subject for mathematicians and numerical people to study.

Material volume, such as the geological formation of discontinuous joints, may contain multi-block and/or multi-beam system. The interactions among the blocks (beams) are complicated, far more than people can imagine. A block system kinematics is generally necessary for a numerical model to describe the movements of the blocks and the interactions along the block boundaries. Until recently, when Shi [1] proposed "discontinuous deformation analysis (DDA)," which included a complete block system kinematics to obtain large displacement and deformation solutions for discrete multi-body system, engineers and researchers began fascinated by its technical breakthrough for discontinuity.

The major advances of DDA include "open-closed iteration" and "inertia matrix." Open-closed iteration is the algorithm to find the correct contact states of the multi-block system and to satisfy the convergence criteria of no-tension and no-penetration conditions at any contact position. An accurately-integrated inertia matrix controls the stability of open-closed iteration, and it also makes DDA a dynamic model, of which the solutions of large displacement and deformation are the accumulations of the small increment from each time step.

DDA chooses the complete first order polynomial as displacement function for a two-dimensional block, no matter how irregular the shape of the block is. However, the stress field and the deformation ability of the DDA block are restricted. In order to refine stress field and to enhance deformation ability of the block, finite element meshes are incorporated into DDA blocks [2,3]. Some other improvements to the deformation ability of the blocks have also been done [4–6].

Since the introduction of DDA, it has been used extensively in rock engineering and tunnel engineering, in which rock slope stability, tunnel excavation, and dynamic rock burst have been successfully simulated and investigated (e.g., Shi [7], Ohnishi *et al.* [8], Chen *et al.* [9], Tsai [10], Chang *et al.* [11], Dong *et al.* [12], Pei & Lu [13], and Shyu & Salami [14]). In this paper, the response of tunnel excavation under the geological formation of shale rocks due to preexisting initial stresses in the rocks are studied by use of discontinuous deformation analysis with four-node isoparametric finite element mesh. The major joint set will be either horizontal or vertical (or nearly). The purposes of doing this are to qualitatively analyze the critical cases and to simulate the system of multi-laminated beam—a classical numerical subject in computational mechanics. The approximation of initial stresses in the rocks are either calculated by overburden pressure (regions of recent sedimentation) or by the tectonic squeezing movements over the years (horizontal stress is nearly three times the vertical initial stress).

2. NUMERICAL SIMULATIONS

In this Section, the responses of an underground circular tunnel after excavation are investigated. This tunnel is assumed to be in a region of shale geological formations. The major joint set will be either horizontal or vertical (or nearly). The joint spacing is set to be 1 m. The centroid of the tunnel is 358 m under ground level, and the diameter of the tunnel is 15 m. The area of block system analyzed is 100 m by 100 m. Young's modulus and Poisson's ratio for shale rock are 10000 MPa and 0.28. Unit mass for shale rock is 0.0023 Mkg/m^3, and the joint friction angle is 20°. Throughout all the following simulations, elastic plane strain and dynamic calculations are performed. Time step is 2000, and time interval is 0.0005 s. The initial stresses are assigned at the Gauss points of each element, and are approximated as follows. Initial vertical stress

$$\sigma_{yy}^0 = -\gamma h \tag{1}$$

where γ is the unit weight, and h is the overburden depth. Initial horizontal stress

$$\sigma_{xx}^0 = \frac{\nu}{1-\nu}\sigma_{yy}^0 \tag{2}$$

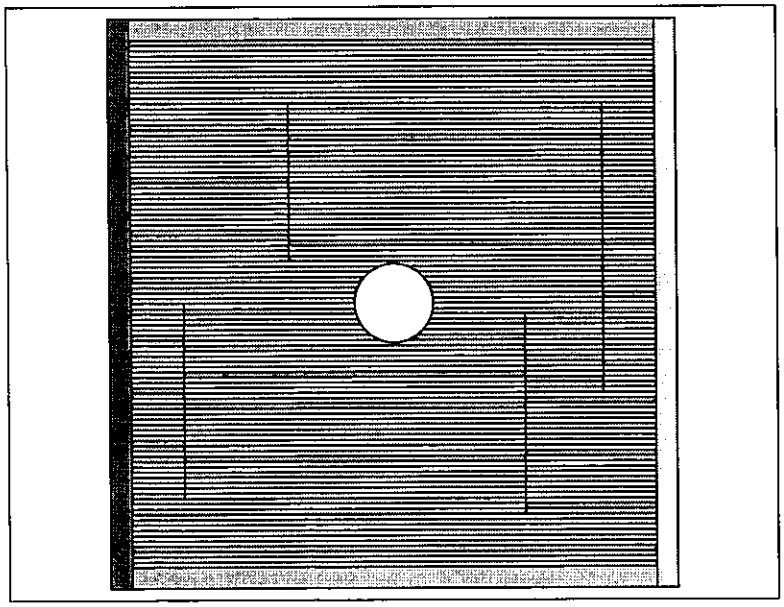

Figure 1. Tunnel in horizontal shale rocks.

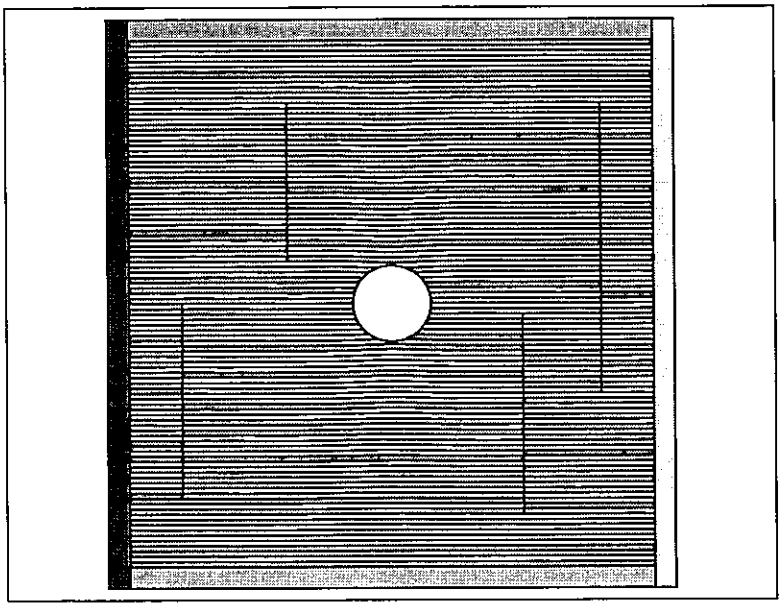

Figure 2. Tunnel in horizontal shale rocks, step 200.

for recent sedimentation geological formations and ν is the Poisson's ratio, or

$$\sigma_{xx}^{0} = 3\sigma_{yy}^{0} \tag{3}$$

for initial horizontal stress caused by the tectonic squeezing movements over the years.

2.1 Horizontal Joint Set

The first case is to study the excavation of a circular tunnel at the region of horizontally jointed shales. Figure 1 shows the mesh of the block system containing horizontally discontinuous shale beams with finite element mesh in each shale (the element mesh is not

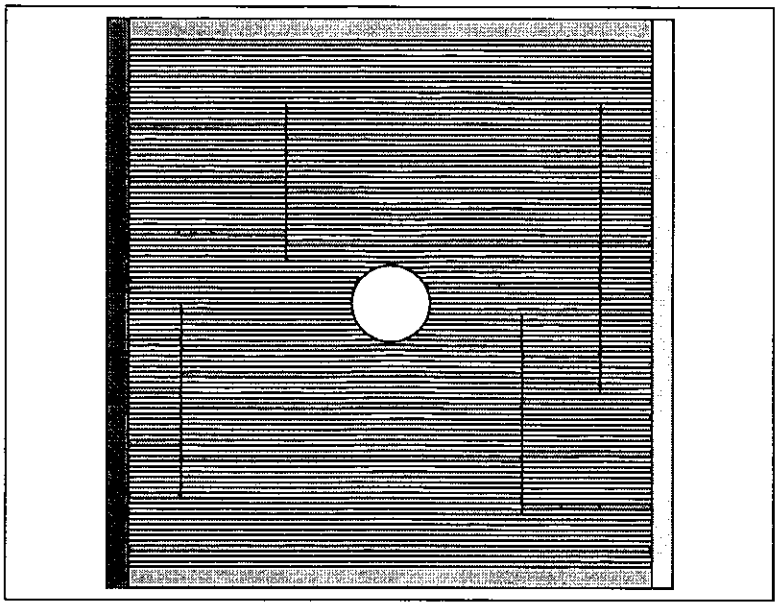

Figure 3. Tunnel in horizontal shale rocks, step 1000.

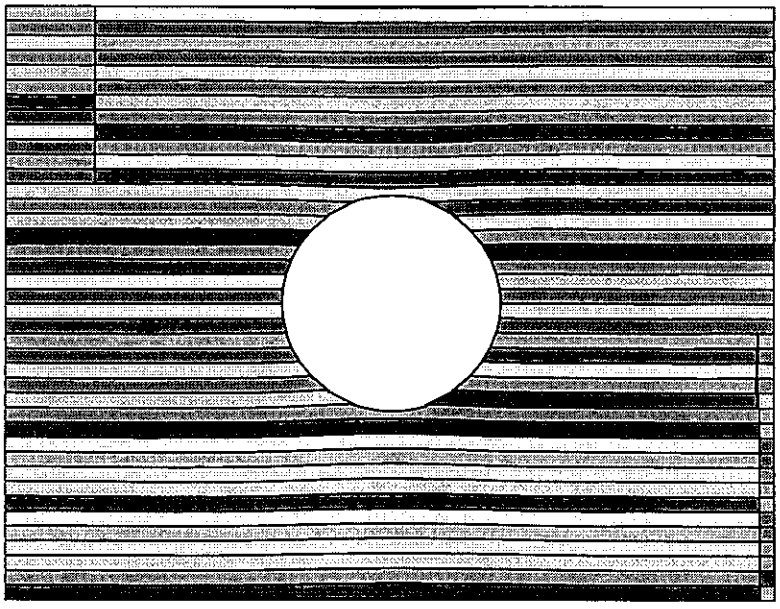

Figure 4. Tunnel in horizontal shale rocks, step 2000.

shown). Only few vertical joints exist and are away the tunnel. The purpose of this arrangement is to numerically study the behavior of multi-laminated beam system and to qualitatively analyze the response of the tunnel after excavation. The initial stresses are first calculated using (1) and (2). Figure 2 illustrates the computation at step 200. The effect of flexure burst of the shales immediately starts on both top and bottom of the tunnel in the process of dynamic computation. It demonstrates the possibility of computing multi-laminated beam system using proposed numerical model. Figure 3 shows the result after step 1000. At this stage, the displacements and deformations around the tunnel are smaller than those at step 200. The bouncing effect caused by dynamic elastic energy of the shales may explain this phenomenon. The final result of step 2000 is presented in Figure 4.

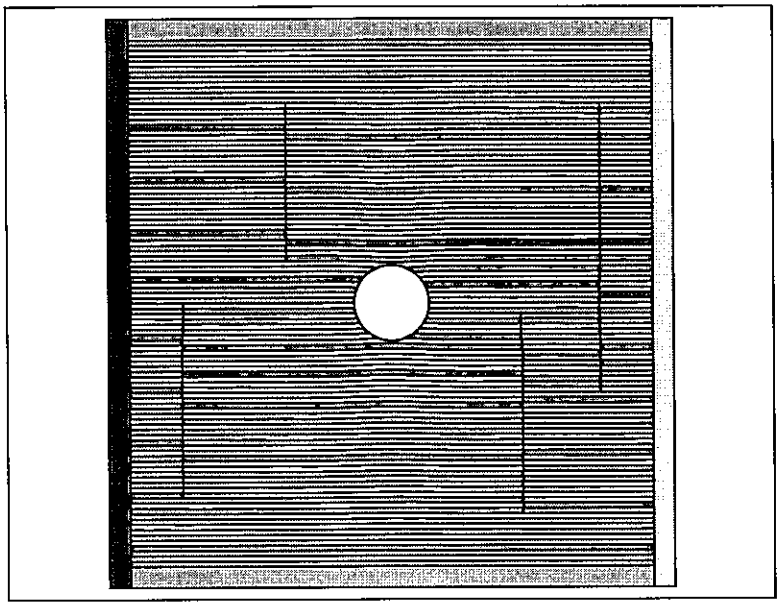

Figure 5. Tunnel in horizontal shale rocks, higher horizontal initial stress, step 200.

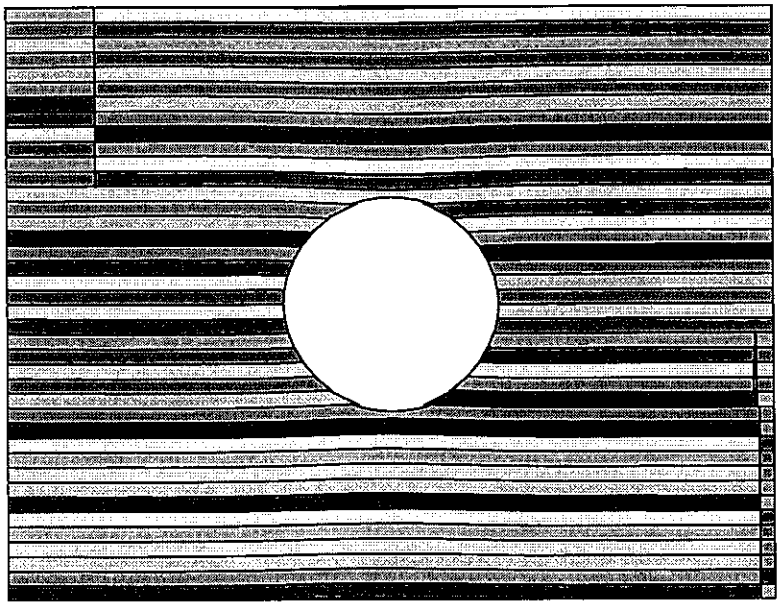

Figure 6. Tunnel in horizontal shale rocks, higher horizontal initial stress, step 2000.

Next, the block system is analyzed under higher initial horizontal stress by using (3). Figures 5 and 6 show the same degree of flexure burst at both top and bottom of the tunnel. This is probably due to the reason that long, continuous shale rocks are modeled around the tunnel without any vertical joint intersected. However, the effect of closing the tunnel is more significant than that of the previous case.

From the above computations, the area of disturbance is most likely around the excavation site. If further assuming that the shale rocks around the excavation may fail and break to pieces due to dynamic flexure burst, the situation can be totally different.

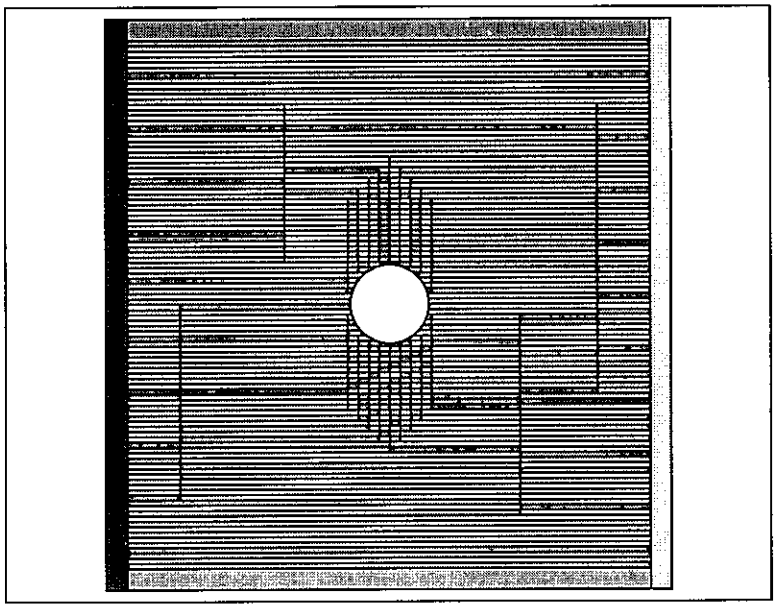

Figure 7. Tunnel in horizontal shale rocks with possible failure zone.

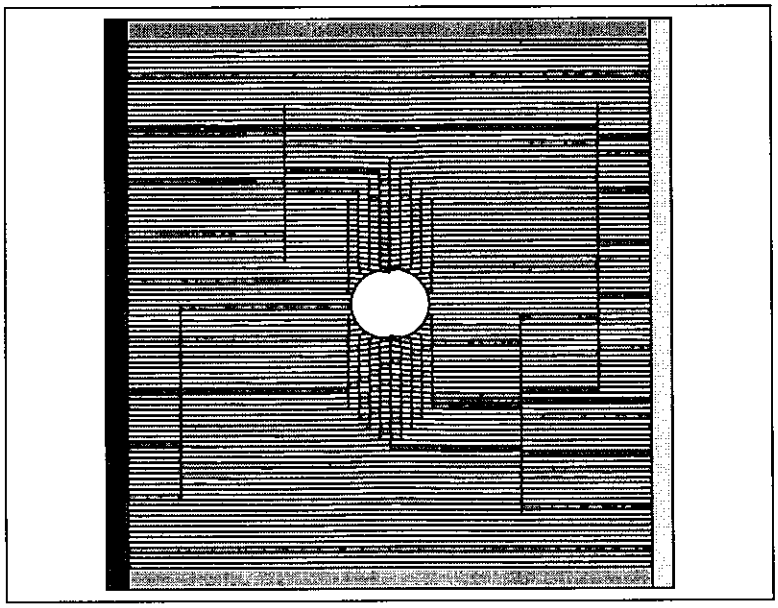

Figure 8. Tunnel in horizontal shale rocks with possible failure zone, step 200.

Figure 7 illustrates the block system with failure zone around the tunnel and the horizontal initial stresses are calculated by (2). After step 200, rocks at both top and bottom of the tunnel are tending to pop out and fall into tunnel. This phenomenon may happen because the vertical initial stress is higher than horizontal's. The vertical initial stress will cause the blocks in the failure zone to push in the direction toward the tunnel, whenever the horizontal initial stress is not strong enough to hold the blocks of the failure zone in position. Also, the effect of closing of the tunnel is readily to happen. Figure 8 demonstrates the above investigation.

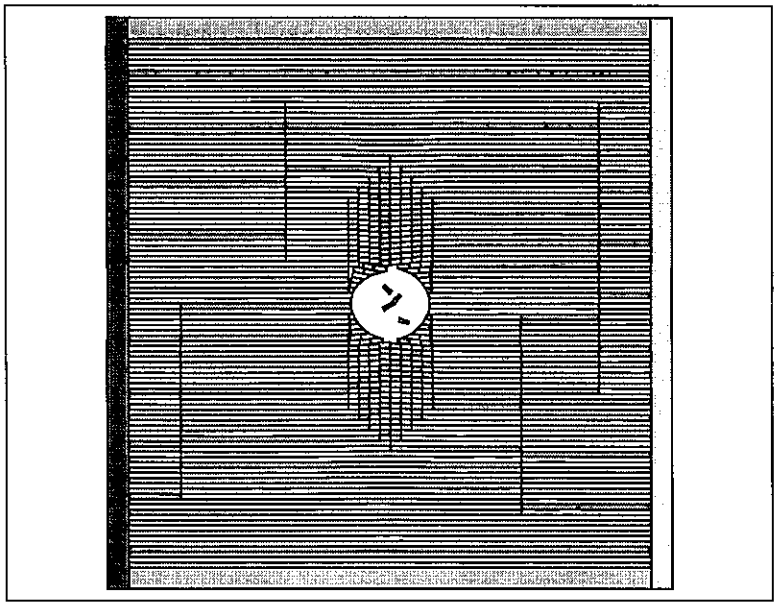

Figure 9. Tunnel in horizontal shale rocks with possible failure zone, step 800.

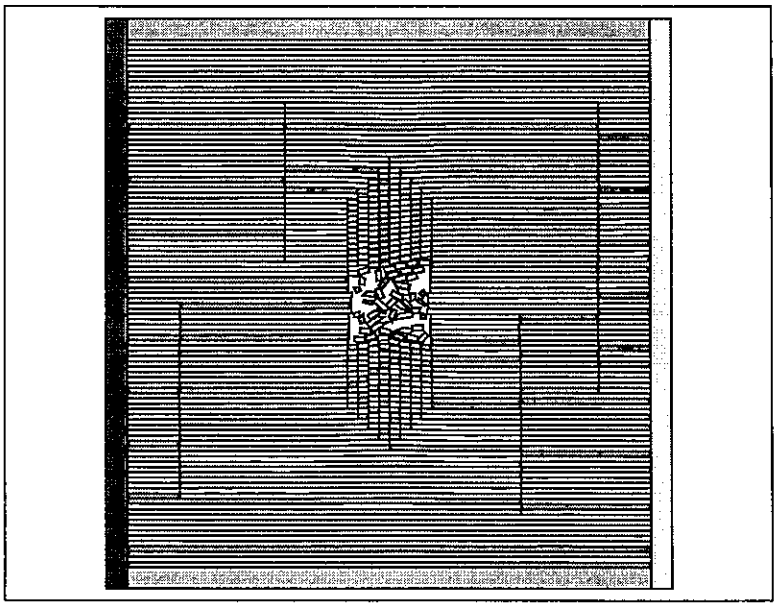

Figure 10. Tunnel in horizontal shale rocks with possible failure zone, step 2000.

At step 400, the blocks at both top and bottom of the tunnel are beginning to pop out and fall into tunnel (the figure is not shown). Using dynamic calculation, the pop-out blocks from the bottom of the tunnel will fly in the air, and will possibly collide with those from the top. Figure 9 shows the result of step 800. It also shows that the initiation of the failure of the top vaults. At step 1200, the failure of the bottom arches significantly progresses (not shown). At step 1600, more blocks from the top fall in, and at step 1800, loose blocks from the bottom also join in. Figure 10 displays the final result of step 2000. The tunnel is closed and filled with loose blocks from the failure zone.

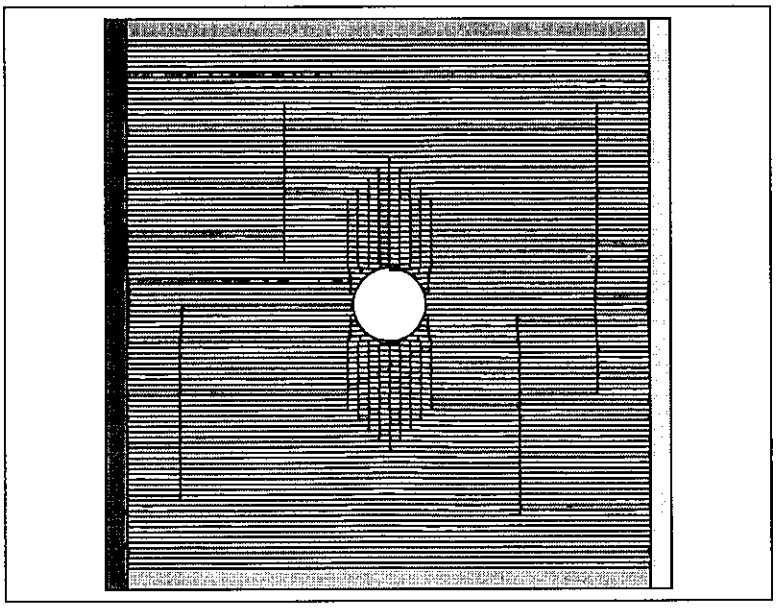

Figure 11. Tunnel in horizontal shale rocks with possible failure zone, higher horizontal initial stress, step 600.

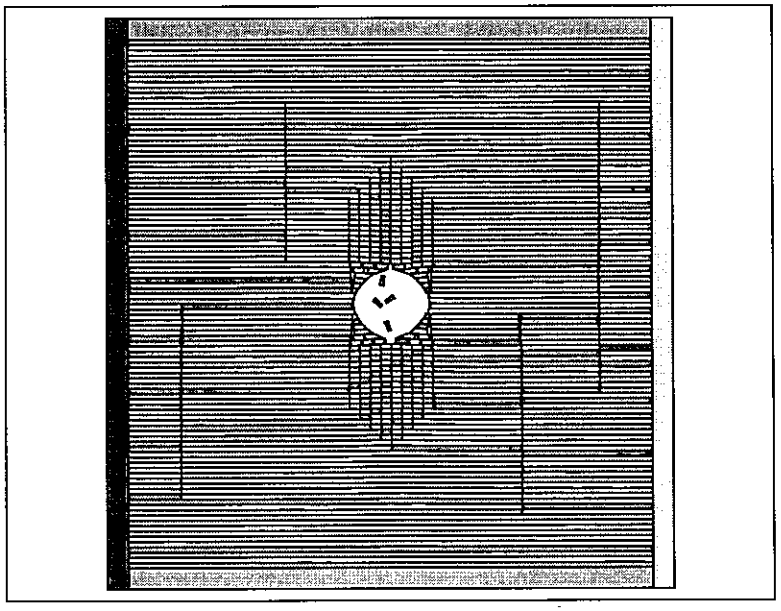

Figure 12. Tunnel in horizontal shale rocks with possible failure zone, higher horizontal initial stress, step 1400.

As a comparison, higher horizontal initial stresses calculated by (3) are applied to the above block system. Due to higher horizontal stress, the blocks at both top and bottom of the tunnel can be held steady in position while facing the pushing force from vertical initial stress. At steps 200 and 400 (not shown), there are no blocks popping out from the failure zone, while the tunnel keep squeezing in. At step 600, the initiation of the popping of the blocks at top begins. Figure 11 illustrates the effect. Figure 12 shows the result at step 1400. At this moment, only few blocks are flying inside the tunnel. This accounts for the reason that higher horizontal stress will hold the blocks in position longer.

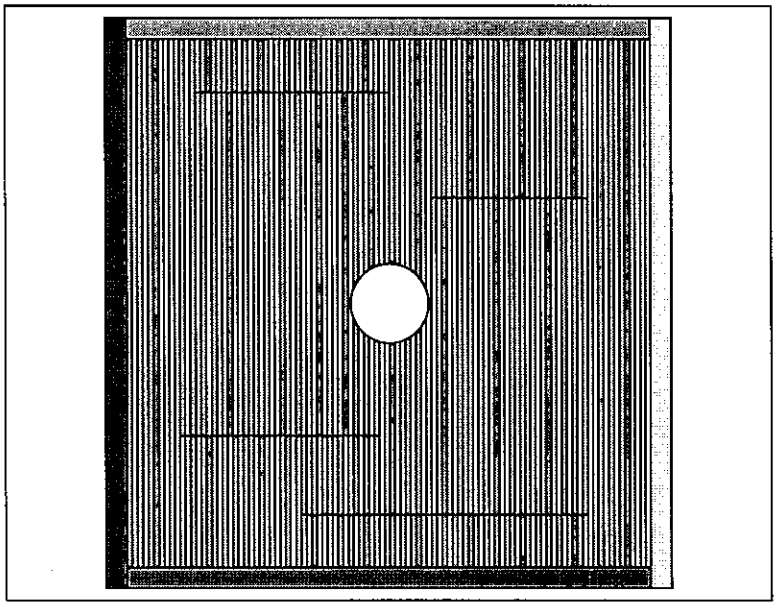

Figure 13. Tunnel in vertical shale rocks, lower horizontal initial stress.

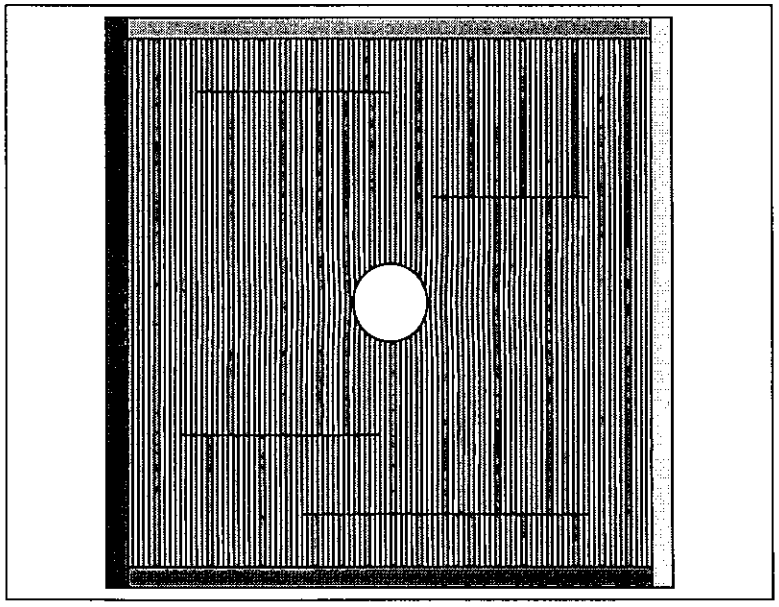

Figure 14. Tunnel in vertical shale rocks, lower horizontal initial stress, step 200.

2.2 Vertical Joint Set

Similar to the horizontal joint set case, a circular tunnel is assumed to be in the region of vertically jointed shales. Horizontal and vertical joint sets are probably the critical cases for tunnel engineering, either less or more. Figure 13 shows the block system mesh of the shales. Again, only few horizontal joints are arranged. Lower horizontal initial stress is used by (2). Figure 14 demonstrates the result after step 200. Using dynamic procedure, the effect of flexure burst of the shales at both right and left sides of the tunnel immediately initiates, as happened in the horizontal joint set case.

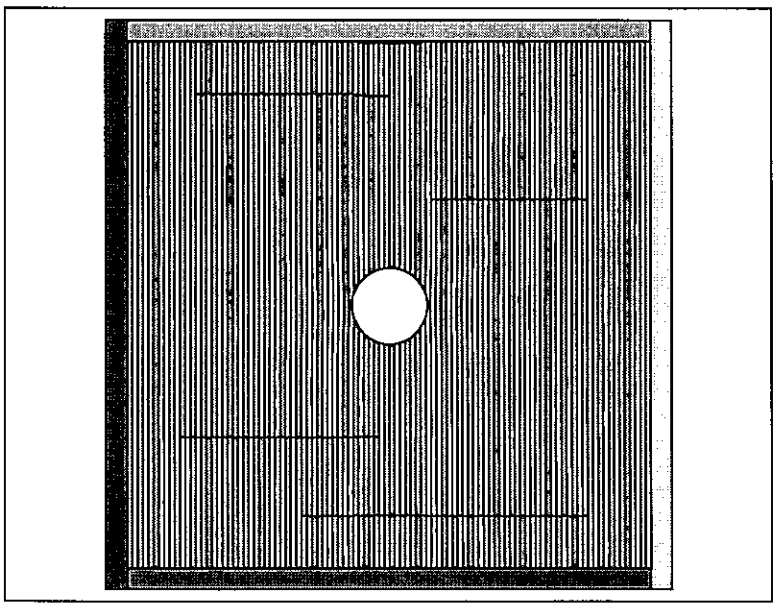

Figure 15. Tunnel in vertical shale rocks, lower horizontal initial stress, step 1000.

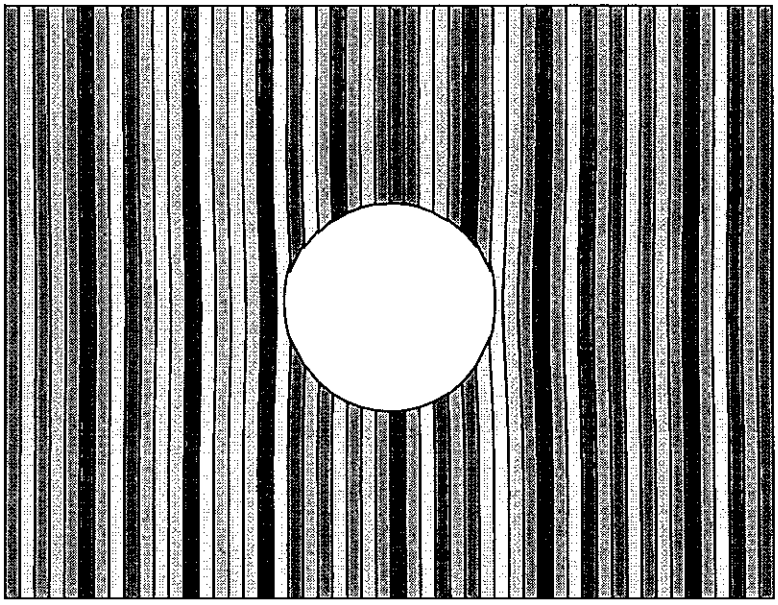

Figure 16. Tunnel in vertical shale rocks, lower horizontal initial stress, step 2000.

It should be pointed out that, in the vertical joint set case, vertical initial stress may act as the driving force to accelerate the buckling of the shale column, whenever the horizontal disturbance exists. Secondly, the sliding of the shale rocks may speed up the closing of the tunnel as well, whenever the horizontal initial stress is not high enough to squeeze the vertical column and keep them from sliding down. Figure 15 illustrates the result after step 1000, in which the effect of bouncing back and forth of the columns may occur. And Figure 16 reveals the final result after step 2000, in which the closing of the tunnel can be mostly due to the sliding of the vertical shales right above the tunnel.

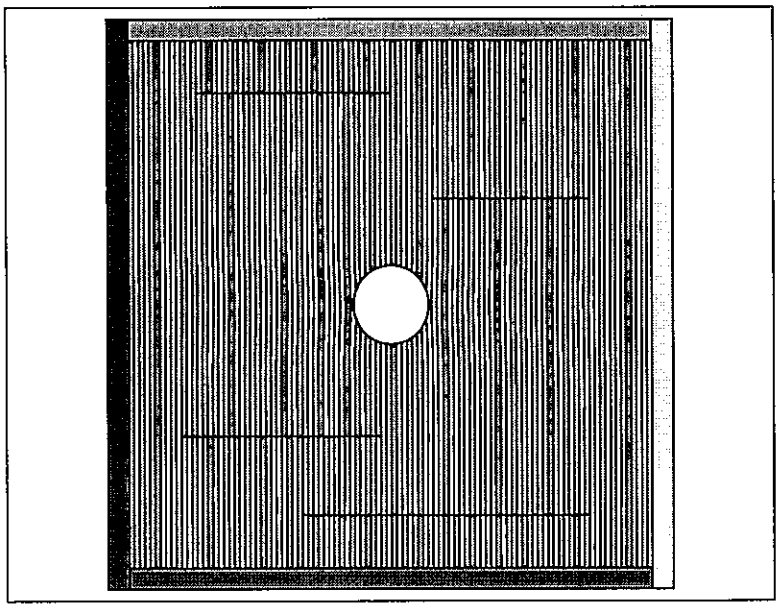

Figure 17. Tunnel in vertical shale rocks, higher horizontal initial stress, step 200.

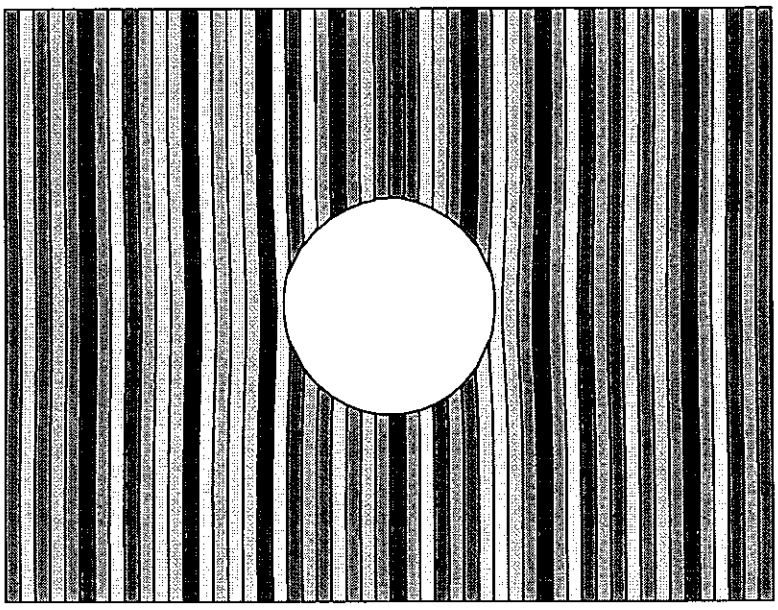

Figure 18. Tunnel in vertical shale rocks, higher horizontal initial stress, step 2000.

Next, the block system is calculated under higher initial horizontal stress by using (3). Figure 17 shows the same degree of flexure burst at both right and left sides of the tunnel at step 200. Figure 18 demonstrates the result after step 2000. It also shows that the simulation has the effect of closing the tunnel by the sliding down of the vertical shales above the tunnel. However, the degree of the sliding is less than that of previous case. This may occur when the horizontal initial stress is much higher in this case than that of previous one. The result will be that it actually squeezes the vertical column and increases the magnitude of the friction force.

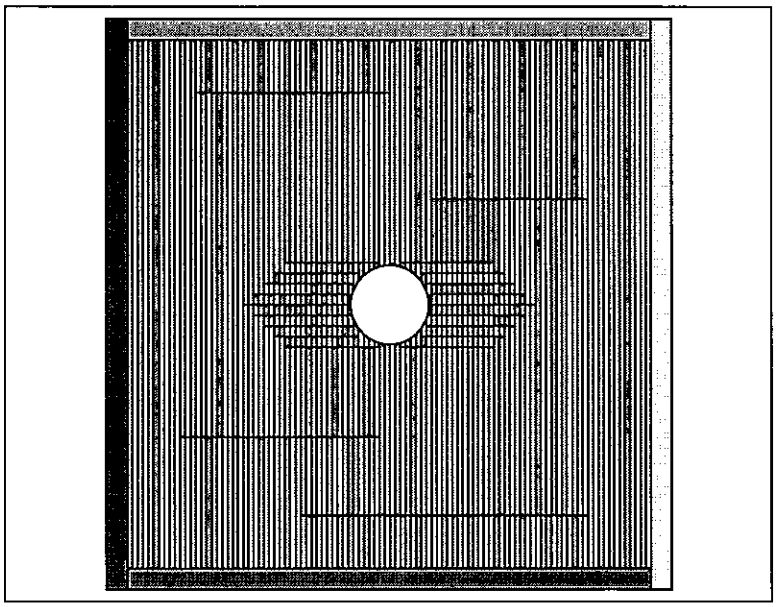

Figure 19. Tunnel in vertical shale rocks with possible failure zone.

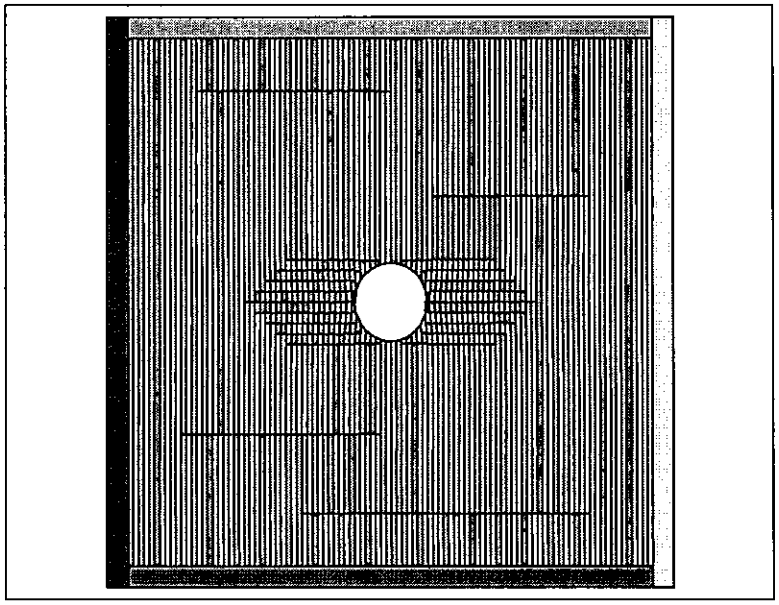

Figure 20. Tunnel in vertical shale rocks with possible failure zone, step 200.

If, however, the dynamic flexure burst and buckling of the vertical columns in the vicinity of the tunnel will cause the shales to fail and break to pieces, the result may be significantly different. Figure 19 illustrates the block system with possible failure zone (horizontal joints) around the tunnel and the horizontal initial stresses are calculated by (2). This numerical arrangement of the failure zone will only present the qualitative analysis of failure mode around the area of excavation. Figure 20 shows the simulation after step 200. It shows that the initiation of the buckling or failure of columns is progressing, where the horizontal disturbance is readily acting against the columns.

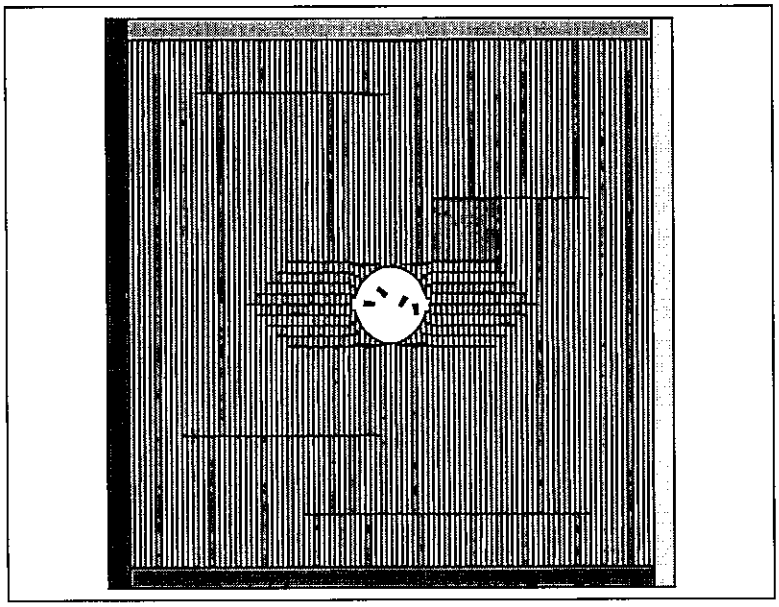

Figure 21. Tunnel in vertical shale rocks with possible failure zone, step 800.

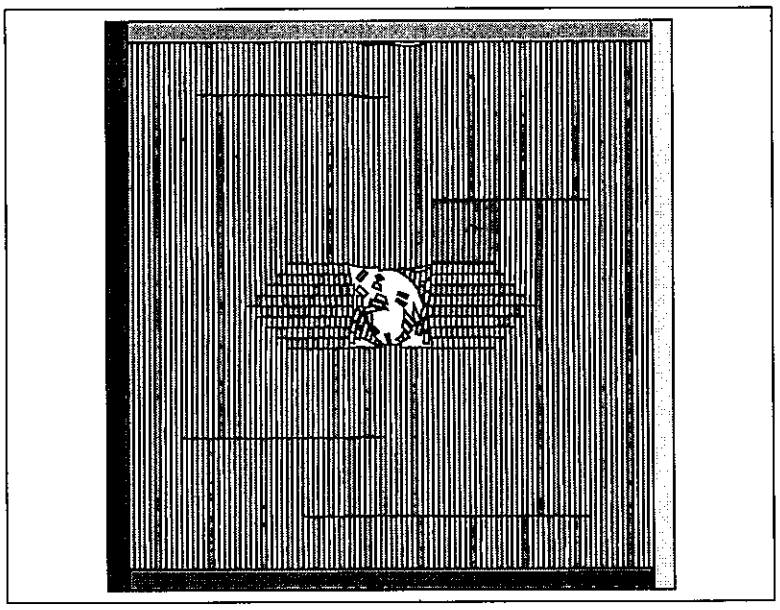

Figure 22. Tunnel in vertical shale rocks with possible failure zone, step 2000.

After the computation of step 400, the blocks at both right and left sides of the tunnel are starting to pop out and fly into the tunnel (not shown). Figure 21 displays the result after step 800. The blocks keep flying and the side walls have the tendency to fail as well. And the columns right above the tunnel are sliding down causing the possibility of closing the tunnel. At step 1600, the side walls start to collapse (not shown). Figure 22 reveals the final result of computation after step 2000. Using dynamic procedure, this failure sequence will only take place within one second. If the computation continues, the excavation area will definitely be closed and filled with the loose blocks.

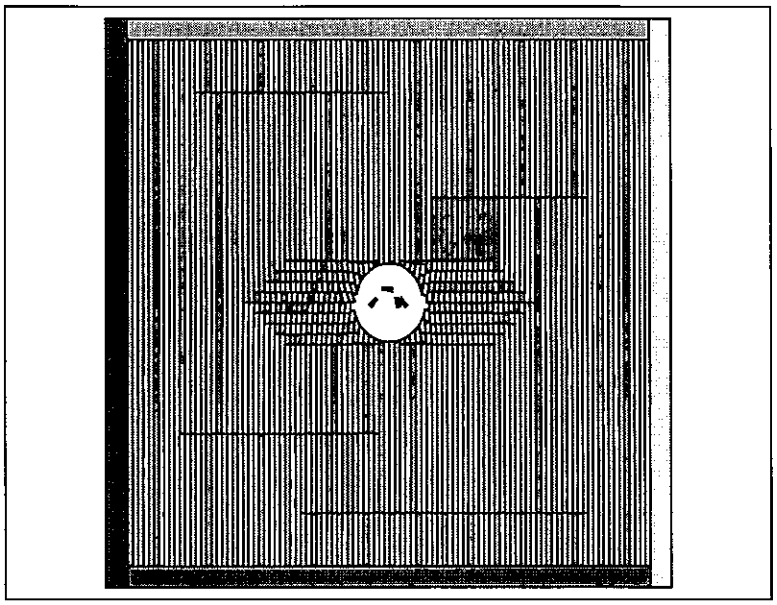

Figure 23. Tunnel in vertical shale rocks with possible failure zone, higher horizontal initial stress, step 600.

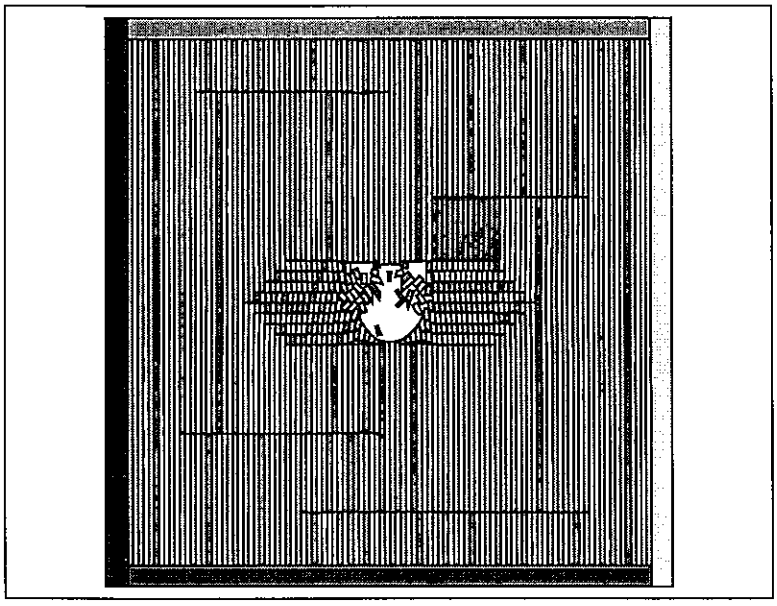

Figure 24. Tunnel in vertical shale rocks with possible failure zone, higher horizontal initial stress, step 1400.

The following simulation is to incorporate higher horizontal initial stress to the above block system. Due to high horizontal stress, the blocks at both sides of the tunnel pop out immediately at step 200 (not shown). This is different from the case of horizontal joint set because the high horizontal stress will push the blocks out and cause the effect of buckling of the vertical columns. Figure 23 demonstrates the result at step 600. Compared with the case of lower horizontal stress, the degree of closing the tunnel is more significant. Figure 24 shows the computed result at step 1400. The side walls have already collapsed. At step 2000, the damage of the tunnel is more severe than that of lower horizontal initial stress.

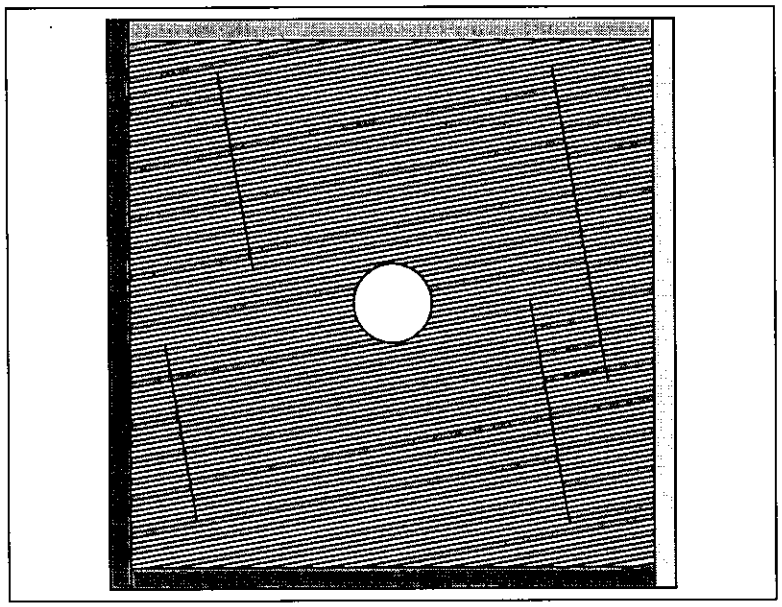

Figure 25. Tunnel in nearly horizontal shale rocks, higher horizontal initial stress.

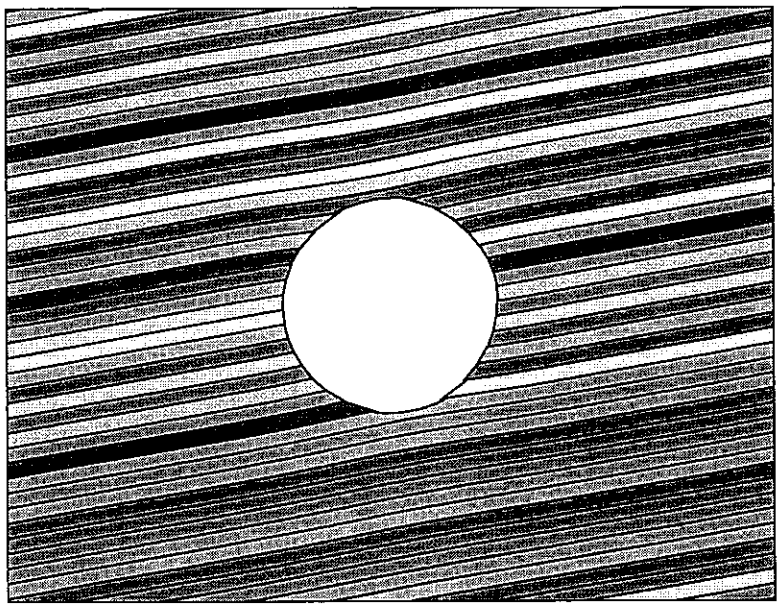

Figure 26. Tunnel in nearly horizontal shale rocks, higher horizontal initial stress, step 2000.

2.3 Nearly Horizontal Joint Set

As complementary analyses to the cases of horizontal and vertical joint sets, joint set directions are offset by a small amount (say, 10°). The higher horizontal initial stress is used only for the following simulations. This is to provide the parameter study of the tunnel analysis, if the slanted joint set will act significantly differently. Figure 25 illustrates the block system with shale rocks of nearly horizontal joint set. Figure 26 displays the computation after step 2000, in which the result is similar to that of horizontal joint set case. Though, the sliding effect of the long beams happened in this case may speed up the closing of the tunnel.

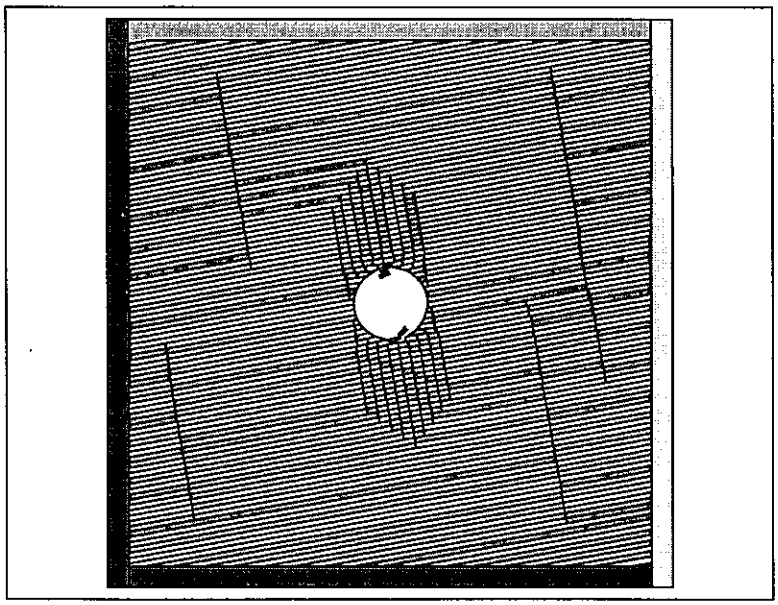

Figure 27. Tunnel in nearly horizontal shale rocks with possible failure zone, higher horizontal initial stress, step 600.

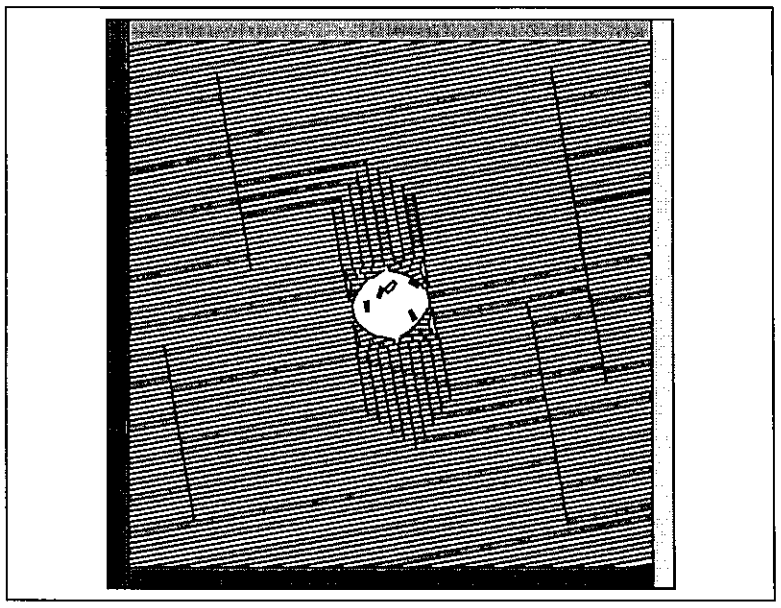

Figure 28. Tunnel in nearly horizontal shale rocks with possible failure zone, higher horizontal initial stress, step 1600.

Next, at step 600, Figure 27 shows the result of the tunnel with a possible failure zone around it. When at step 200 (not shown), the blocks at both top and bottom of the tunnel are starting to pop out. This phenomenon is truly different from that of horizontal joint set. And at step 400, blocks have already popped out and fell into the tunnel. Probably, with the higher horizontal stress to hold blocks in position in horizontal joint set case, slanted joint set may produce uneven squeezing, and thus one of the blocks slips out first. At step 1400, the result is similar to previous one with one more block in the air. Figure 28 reveals the computation result at step 1600.

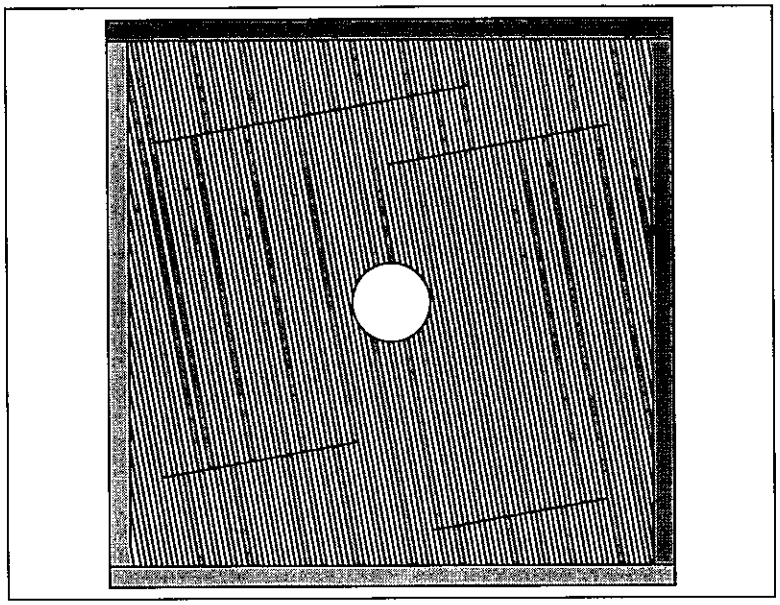

Figure 29. Tunnel in nearly vertical shale rocks, higher horizontal initial stress.

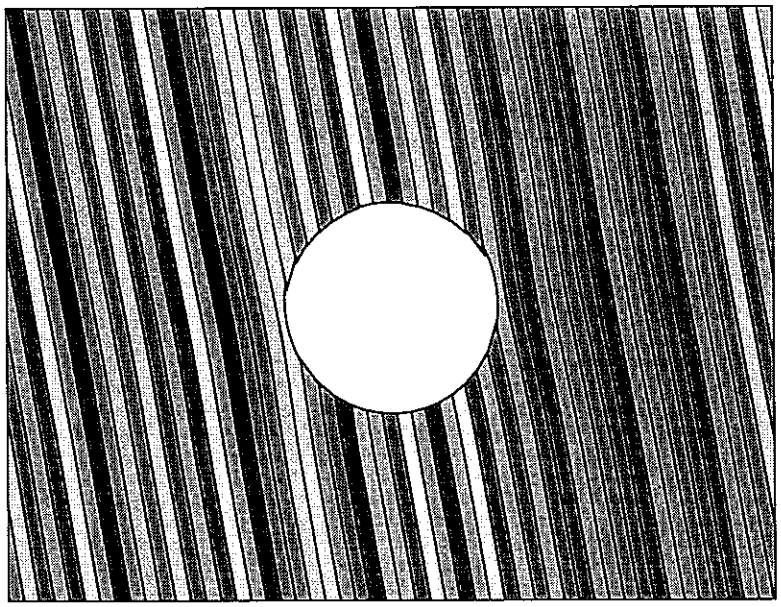

Figure 30. Tunnel in nearly vertical shale rocks, higher horizontal initial stress, step 2000.

2.4 Nearly Vertical Joint Set

Figure 29 illustrates the block system with shale rocks of nearly vertical joint set with slightly slanted angle of 10° from vertical. With higher horizontal initial stress, the dynamic flexure burst can onset quickly. The sliding of the columns above the tunnel can also be observed (note that the friction angle of the joint set is 20°). The vertical initial stress may become the driving force to buckle the columns when the horizontal initial stress exists to disturb the stability. Figure 30 displays the computation after step 2000, in which the result is similar to that of vertical joint set case. The effect of closing of the tunnel can be directly computed.

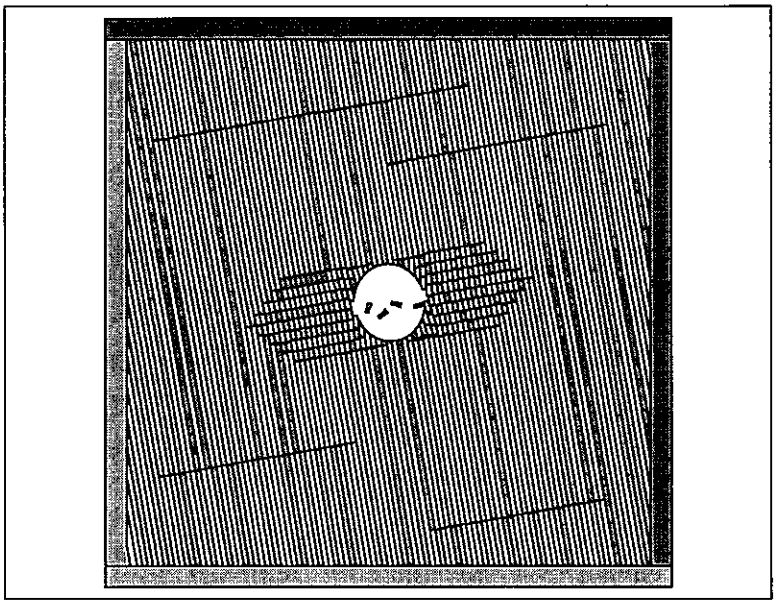

Figure 31. Tunnel in nearly vertical shale rocks with possible failure zone, higher horizontal initial stress, step 600.

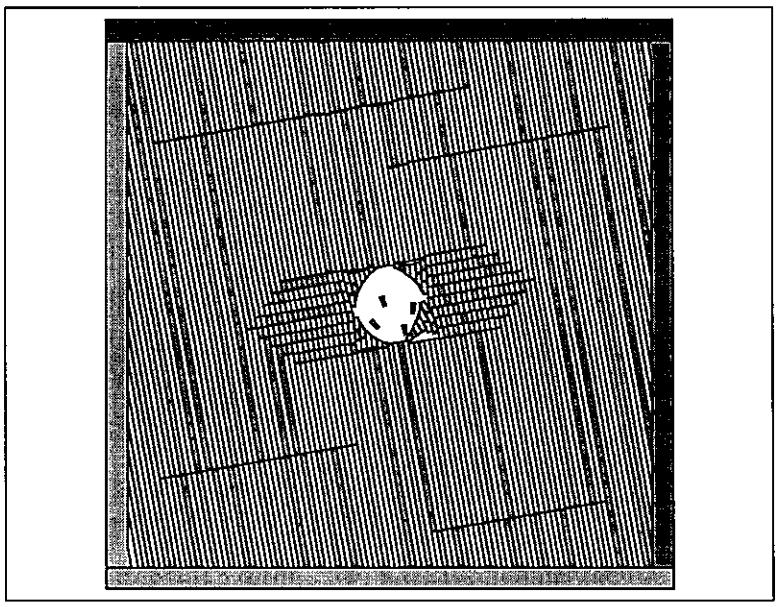

Figure 32. Tunnel in nearly vertical shale rocks with possible failure zone, higher horizontal initial stress, step 1400.

Similar to the case of vertical joint set, high horizontal initial stress will cause the blocks at the side walls to buckle and begin popping out at step 200 (not shown). At step 600, Figure 31 shows the result of the tunnel in nearly vertical joint set shale rocks with a possible failure zone around it. At this time, the right side of the tunnel seems more likely to fail quickly than the left side. Slanted vertical joint set may produce uneven response for each side of the walls. Figure 32 illustrates the computed result after step 1400. Again, the response at the right side wall is more severe and quicker. At the time of step 2000, the right side wall has already collapsed while the left side wall remains partially stable.

3. CONCLUSIONS

Dealing with tunnel or rock engineering applications one must face the reality of discontinuity. Discontinuity may produce complex, dynamic physical interactions of massive moving bodies by its nature, for example, sliding, colliding, and dynamic rock burst, etc. Thus, it is also true that experienced engineers, geologists and numerical analysts may have hard time facing discontinuity. The introduction of discontinuous deformation analysis provides a way for engineers and scientists to overcome challenges of mother nature and computational impasse.

Tunnel excavation by the underlying geological formations of (nearly) horizontal and vertical joint sets of shale rocks is numerically analyzed by use of discontinuous deformation analysis with a finite element mesh inside each block. The phenomenon of dynamic rock burst and flexure burst is predicted and simulated due to built-in initial stresses in the rocks. The response of the tunnel right after excavation is qualitatively analyzed by different cases of joint set. The investigation of a classical numerical subject—system of multi-laminated beam—is possibly solved by the proposed numerical model.

REFERENCES

1. Shi, G.-H., Discontinuous deformation analysis—a new numerical model for the statics and dynamics of block systems, *Ph.D. Dissertation,* University of California, Berkeley, California, May 1988.
2. Shyu, K., Nodal-based discontinuous deformation analysis, *Ph.D. Dissertation,* University of California, Berkeley, California, December 1993.
3. Chang, C.-T., Nonlinear dynamic discontinuous deformation analysis with finite element meshed block system, *Ph.D. Dissertation,* University of California, Berkeley, California, May 1994.
4. Ke, T.-C., Simulated testing of two dimensional heterogeneous and discontinuous rock masses using discontinuous deformation analysis, *Ph.D. Dissertation,* University of California, Berkeley, California, December 1993.
5. Lin, J.-S. and Lee, D.-H., Manifold method using polynomial basis functions of any order, *Proc. 1st Int. Forum Discon. Defor. Analy.,* M. R. Salami and D. Banks eds., 365–372, Berkeley, California, 12–14 June 1996.
6. Koo, C.-Y. and Chern, J.-C., The development of DDA with third order displacement function, *Proc. 1st Int. Forum Discon. Defor. Analy.,* M. R. Salami and D. Banks eds., 342–349, Berkeley, California, 12–14 June 1996.
7. Shi, G.-H., Simplex Integration for manifold method and discontinuous deformation analysis, *Proc. 1st Int. Conf. Analy. Discon. Defor.,* J. C. Li, C.-Y. Wang and J. Sheng eds., 1–25, Chungli, Taiwan, December 21–23 1995.
8. Ohnishi, Y., Chen, G.-Q. and Miki, S., Recent development of DDA in rock mechanics, *Proc. 1st Int. Conf. Analy. Discon. Defor.,* J. C. Li, C.-Y. Wang and J. Sheng eds., 26–47, Chungli, Taiwan, December 21–23 1995.
9. Chen, S., Chern, J.-C. and Koo, C.-Y., Study on the performance of tunnel near slope by DDA, *Proc. 1st Int. Conf. Analy. Discon. Defor.,* J. C. Li, C.-Y. Wang and J. Sheng eds., 109–123, Chungli, Taiwan, December 21–23 1995.

10. Tsai, F. C., Estimation of rock mass disturbance around a repository drift using the DDA method, *Proc. Work. Forum Manifold Meth. Mater. Analy.*, **1**, 87–104, Jenner, California, October 4–6 1995.
11. Chang, C.-T., Monteiro, P. J. M. and Shyu, K., Dynamic analyses of large underground caverns using nonlinear discontinuous deformation analysis with finite element meshed block system, *Int. J. Numer. Analy. Meth. Geomech.*, In Press.
12. Dong, X.-C., Wu, A.-Q. and Ren, F., A preliminary application of discontinuous deformation analysis (DDA) to the Three Gorges Project on Yangtze River, China, *Proc. 1st Int. Forum Discon. Defor. Analy.*, M. R. Salami and D. Banks eds., 310–317, Berkeley, California, June 12–14 1996.
13. Pei, J.-M. and Lu, Z.-H., An application of DDA to a jointed rock slope, *Proc. 1st Int. Forum Discon. Defor. Analy.*, M. R. Salami and D. Banks eds., 395–400, Berkeley, California, June 12–14 1996.
14. Shyu, K. and Salami, M. R., Stability of Bartlett Dam, *Proc. 1st Int. Forum Discon. Defor. Analy.*, M. R. Salami and D. Banks eds., 440–445, Berkeley, California, June 12–14 1996.

SOIL SLOPE STABILITY ANALYSIS USING DDA

Jeen-Shang Lin and Shiou Chen

Department of Civil and Environmental Engineering
University of Pittsburgh, Pittsburgh, PA 15261, USA

ABSTRACT

This study employs DDA in conducting the slope stability analysis of soils. Issues regarding how to obtain the factor of safety and how to estimate consequences of failure are addressed. The meaning of the critical failure surface is examined in terms of the slope displacement. A two-stage procedure is also presented for general application.

INTRODUCTION

Despite many of its shortcomings, the limiting equilibrium method is very much "the" method used in practice for evaluating the stability of slopes today. The problems associated with this method are well recognized[1]. Inability to provide an estimate of failure consequences is also a serious drawback. This study demonstrates how DDA can be applied to assess soil slope stability and resolve many of the issues that can not be properly answered by the limiting equilibrium methods.

This study addresses first the issue of computing the factor of safety. Conventionally, the safety margin of a slope is expressed in terms of a factor of safety, or FS, defined as follows,

$$FS = \frac{\sum \tau_f}{\sum \tau}$$

where, τ_f is the available shear strength, and τ the shear stress along the slip surface. The minimum FS obtained among all the potential slip surfaces is used as the FS of the slope, and the corresponding slip surface is considered the most critical slip surface for design. In this procedure soils are considered rigid since no deformation of the soil is incorporated.

To be compatible with the limiting equilibrium method, static analyses are carried out using rigid blocks for determining FS. Each rigid block has three degrees of freedom: two transnational and one rotational. Using seven blocks generally provides enough degrees of freedom for accurately modeling the soil above a slip surface. Using rigid blocks also reduces the computation cost.

In DDA, the forces between blocks are transmitted via contacts. To facilitate contact detection and thus reduces the number of iteration, Huang and Ma[4] suggested that the block corners be trimmed. This is incorporated into the current analysis. A typical slope model in a

DDA analysis is depicted in Fig. 1.

In the past, two approaches have been devised to compute FS of slopes using DDA. For instance, Yeung and Goodman[6] developed a scheme by focusing on the movement of a control point. Their efforts mainly lie in determining how low the strength reduction can be tolerated before the control point moves dramatically. From this reduction, they then determined the factor of safety. This type of approach is useful when the failure plane is not known in advance. When many blocks are involved, this approach may not have a good resolution. This is illustrated in Fig. 2 for which an accurate determination of FS turns out to be difficult. Huang and Ma[4], on the other hand, simply used the results from the first time step from a dynamic analysis. By using the shear stress and strength from contact points, they give FS of one for unstable slopes--which makes it difficult to compare with the FS from conventional study.

There are two ways that can be used in finding FS that is in consistent with the conventional definitions. One is to use the static analysis with elasto-plastic contact springs, together with a secant stiffness approach[4]. The other is to adopt a dynamic approach together with the adoption of the D'Alembert's principle. Either approach gives two sets of FS, one for global FS, the other individual block FS. The first approach, however, requires iteration, FS generally converges within about 10 iterations as demonstrated in Fig. 3. Fig. 3 further shows how FS converges with iteration: blocks with FS less than one gradually transmit their unbalanced forces to neighbors and eventually converge to a stable FS as iteration proceeds.

This study also finds out that a FS so determined will satisfy the following two criteria,

(1) For a stable slope, which has a global FS of greater than one, the minimum individual block FS is one. For if an individual block fails, it would transmit unbalanced forces to other stable blocks. As a result, no block should have a FS less than one.

(2)For an unstable slope, the global FS should equal to the FS of each individual block. For if a slope is unstable, the redistribution of the unbalanced force will continue until it reaches a uniform FS for all blocks.

Figs. 4 (a) and 4(b) are typical results from this study for a circular slip surface and they satisfy the above criteria. Also shown in these figures are the FS on the block interfaces. It is interesting to note that when a block fails all its edges reach the same degree of strength mobilization, and its FS on the base and on the side are the same. This is not so for stable blocks, and they may have different side and base FS.

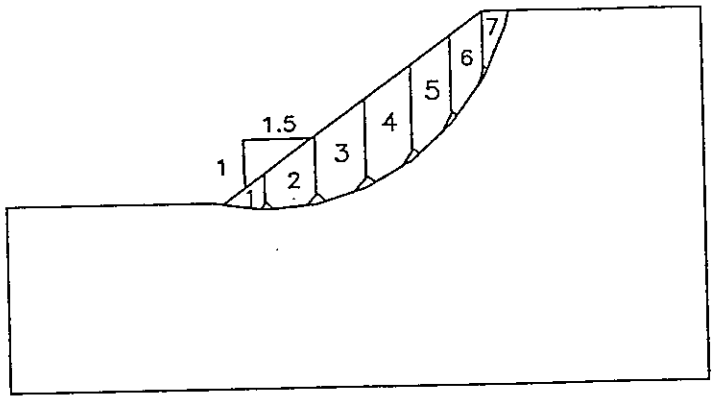

Figure 1 Typical setup for a slope under investigation for this study

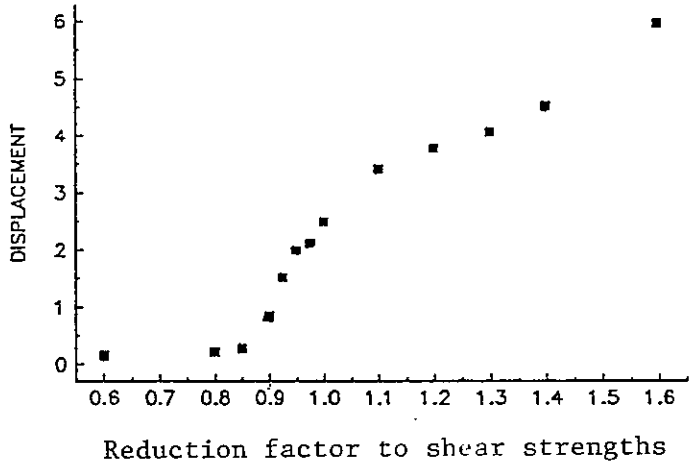

Figure 2 Using target movement as a guide may give enough resolution for determining FS

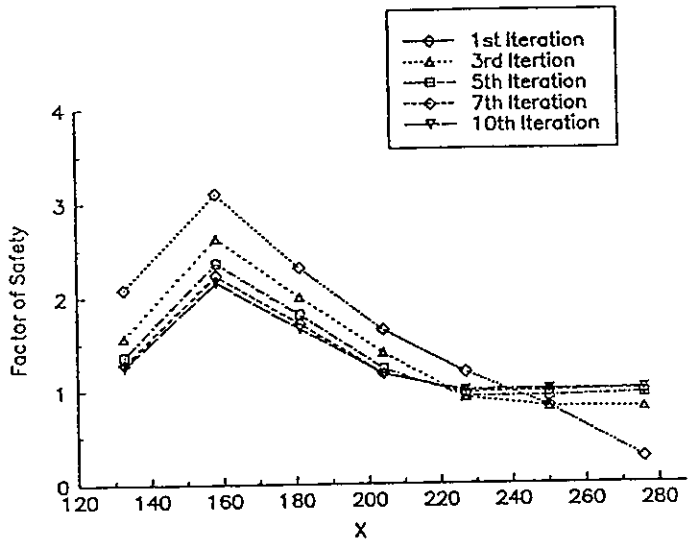

Figure 3 Static FS stabilizes with iteration

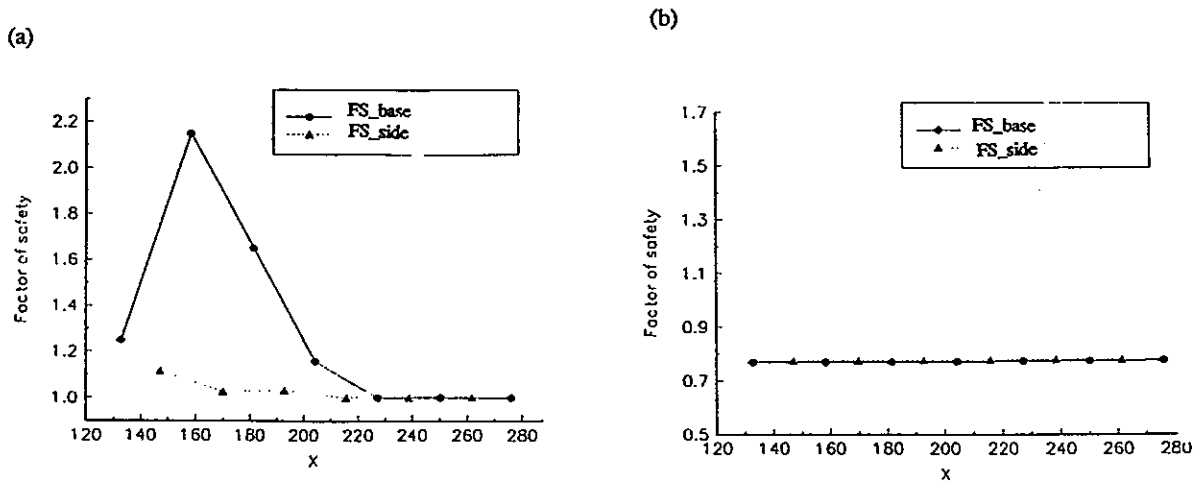

Figure 4 Distribution of individual block FS (a) stable slopes (b) unstable slopes

THE MOST CRITICAL SLIP SURFACE

In the past, a slope stability analysis can only obtain FS and it is therefore natural that the slip surface with the smallest FS is considered the most critical. But, is it?

"Most critical" in itself is a relative description and has no meaning until it is placed within a proper context. It is argued here that the most critical slip surface should be the one that may incur the severest damage. Unfortunately, damage caused by a slope failure is often site specific. This study suggests that for a general application a damage be defined in terms of the crest movement, or in terms of the volume of the displaced soil. For a homogeneous slope, these two definitions give almost identical most critical slip surface.

A homogeneous soil slope which is deliberately made unstable by using a very low shear strength is studied here. For this example problem, the crest movements are plotted against FS for various unstable slip surfaces in Fig. 5. It is interesting to note that how much scatter in the crest movement there is in this plot for a given FS. The slip surface that is associated with the largest slope movement is depicted in Fig. 6(a). In contrast, the slip surface that is associated with the minimum FS is plotted in Fig. 6(b). There are several slip surfaces that all give the same minimum FS, the one that is associated with the largest crest movement is plotted here. It is clear that the slip surface associated with the minimum FS is not the most critical, neither does it give the largest crest movement, nor does it involve the largest volume of displaced soil.

CONCLUSIONS: A TWO-STAGE PROCEDURE

In using DDA, not only the factor of safety can be found, but also the slope displacement can be computed. If the FS is greater than one, the slope displacement is negligible. On the other hand, if the FS is less than one, the system is not in equilibrium. From Newton's second law the unbalanced forced will result in a slope downward acceleration. As soils move they may encounter a different base gradient which may alter the forces acting on them, and a slope may reach a new equilibrium position after some movements.

Thus, this study proposes that a DDA slope stability be conducted in two stages. In stage one, the static FS is computed. If a slope has a global FS close to or less than one, a second stage using a dynamic analysis is initiated. Soils are allowed to deform for this part of the analysis, which is a better modeling of the real scenario. Using a linear displacement field within a block, each deformable block is modeled with six degrees of freedom in this study.

REFERENCES

1. Whitman, R.V. and Bailey, W.A., "Use of Computers for Slope Stability Analysis." J. of the Soil Mech. and Found. Div., ASCE, Vol. 93, No.4 (1967), pp. 475-498.
2. Shi, G. W., Block System Modeling by Discontinuous Deformation Analysis,

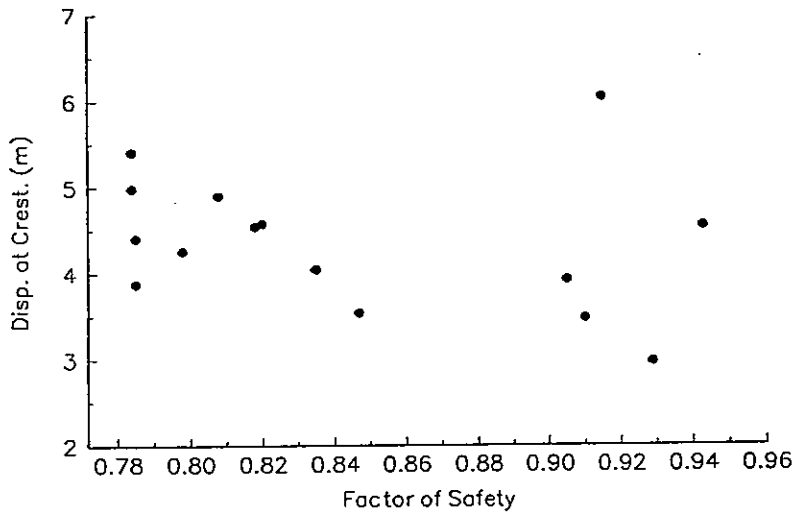

Figure 5 Maximum crest movement

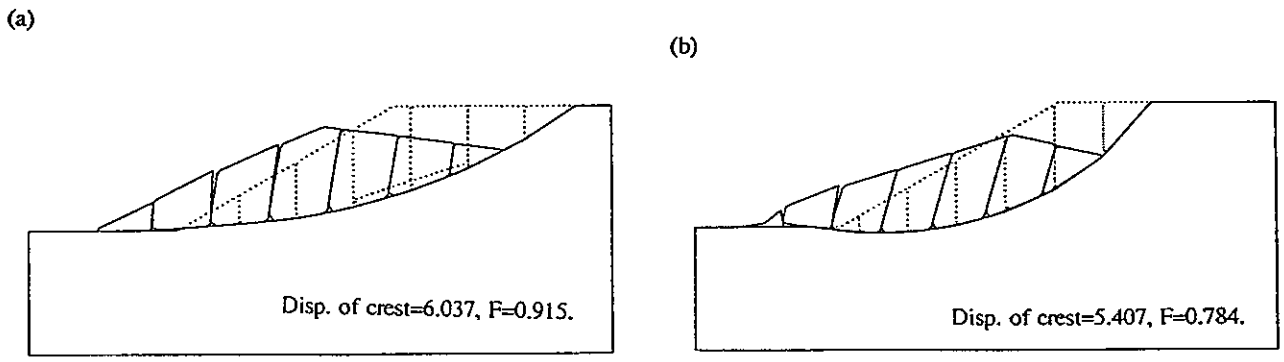

Figure 6 Critical slip surfaces corresponding respectively to (a) minimum FS (b) maximum crest movement

Computational Mechanics Publication, Southsampton, UK, 1993.

3. Huang, An-Bin and Ma, Max Y., (1992). " Discontinuous Deformation Slope Stability Analysis." Stability and Performance of Slopes and Embankments II, Geotechnical Special Publication No. 31, ASCE, pp. 479-490.
4. Chang, C.S., "Discrete Element Method for Slope Stability Analysis." Journal of Geotechnical Engineering, ASCE, Vol. 118, No. 12 (1992)., pp. 1889-1905.
5. Yeung, M.R. and Goodman, R.E., (1992). " Use of Shi's Discontinuous Deformation Analysis on Rock Slope Problems," Stability and Performance of Slopes and Embankments II, Geot. Special Publication No. 31, ASCE, pp. 461-478.
6. CAGE, G-CASE Task Group on slope stability, User's guide: UTEXAS2 SLOPE STABILITY PACKAGE. (U.S. Army Engineer Waterways Experiment Station, 1989).

LARGE DISPLACEMENT AND FINITE STRAIN DDA: AN IMPLEMENTATION AND PHYSICAL VERIFICATION

J.-S. LIN, R. AL-ZAHRANI, A. MUNJIZA[1], and D. H. LEE[2]

Department of Civil and Environmental Engineering, University of Pittsburgh, USA
[1]Department of Engineering, QMW, University of London, U.K.
[2]Department of Civil Engineering, National Cheng-Kung University, Taiwan, ROC

ABSTRACT

This paper implements a general procedure that accounts for large strain and finite rotation for the continuous and discontinuous analysis. The various issues of implementation are discussed first. The framework of the implementation is also presented. The implementation is then verified through physical tests in which the deformation of the objects involved reaches up to fifty per cent.

INTRODUCTION

Problems related to interaction of discrete objects often involve large displacements and finite strains In the original DDA formulation, Shi adopted a first order polynomial basis function for displacement,

$$\begin{bmatrix} u \\ v \end{bmatrix} = \begin{bmatrix} a_0 + a_1 x + a_2 y \\ b_0 + b_1 x + b_2 y \end{bmatrix} \qquad (1)$$

Shi further expressed u and v as a function of rigid body motion and the small straining of an element as,

$$\begin{bmatrix} u \\ v \end{bmatrix} = \begin{bmatrix} 1 & 0 & -(y-y_o) & (x-x_o) & 0 & (y-y_o) \\ 0 & 1 & (x-x_o) & 0 & (y-y_o) & (x-x_o) \end{bmatrix} \begin{bmatrix} u_o \\ v_o \\ \theta_o \\ e_{xx} \\ e_{yy} \\ e_{xy} \end{bmatrix} \quad (2)$$

where, x_o and y_o are the coordinates of the centroid, u_o, v_o, and θ_o are the rigid body movements, where e_{ij} represents infinitesimal strain tensor. This formulation works well if the assumption of small displacement and small strain are satisfied. But a serious problem arises if this formulation is used in the cases where a large displacement or a finite deformation is expected.

This problem has been addressed by (Lin and Lee, 1996) through the use of polar decomposition. It clearly showed that a pure rotation in Eq. (2) actually introduces a stretching which is not accounted for by the six independent variables. In other words, the independent variables of Eq. (2) are not adequate. Thus, to avoid accumulating a large error an alternate formulation using coefficients of the polynomials as the independent variables are necessary.

For a general polynomial basis function, a local approximation to the displacement field in DDA can be written as

$$\begin{aligned} u &= \sum_{i=0}^{N} \sum_{j=0}^{M} a_{i+j} \quad X^i Y^j \\ v &= \sum_{i=0}^{N} \sum_{j=0}^{M} b_{i+j} \quad X^i Y^j \end{aligned} \quad (3)$$

in which the coefficients a and b are the independent variables. A framework has been developed for computer generating code associated with any order of a polynomial bass function of any order (Lin and Lee, 1996). It is well known, however, that higher order polynomial functions tend to oscillate and are of limited use, therefore, an implementation based only upon a complete second order polynomial is presented in this study.

It is also important that the strain and stress measures used have to be indifferent to the frame of reference. In other words, they should be objective. Depending upon the constitutive relationships to be used, different stress and its energy conjugate strain measure can be employed. For the nature of the problem to be analyzed, updated Lagrange approach is adopted. We will base this discussion using the second Piola-Kirchhoff stress tensor and the Green-Lagrange strain tensor. Other stress and strain

measures can easily be adapted from the current results.

The Green-Lagrange strain tensor, ϵ_{ij}, is defined as

$$\varepsilon_{ij} = \frac{1}{2}\left(\frac{\partial u_i}{\partial X_j} + \frac{\partial u_j}{\partial X_i} + \frac{\partial u_k}{\partial X_i}\frac{\partial u_k}{\partial X_j}\right) \qquad (4)$$

it can be expressed as a sum of the linear infinitesimal component, eij, and a nonlinear component, η_{ij} as

$$\varepsilon_{ij} = e_{ij} + \eta_{ij} \qquad (5)$$

The second Piola-Kirchhoff stress tensor, S_{ij}, based upon the undeformed

$$\sigma_{ij} = \frac{\rho_d}{\rho_u}\frac{\partial x_i}{\partial X_m} S_{mn} \frac{\partial x_j}{\partial X_n} \qquad (6)$$

configuration can be related to Cauchy stress, σ_{ij}, of the deformed state by where ρ_d and ρ_u represent the mass density in the deformed and undeformed configurations, respectively. The ρ_d/ρ_u ratio equals the determinant $1/|F|$.

FRAMEWORK OF THE FORMULATION

This formulation presented in this study is derived using the virtual work principle. A linearization procedure of Bathe(1982) was employed.

(1) For a plane strain problem, taking into account the symmetric nature of the strain tensor, the strain- displacement relationship is written in the following form

$$[\varepsilon] = [B][a] + \frac{1}{2}[A][G][a] \qquad (7)$$

Let DOF be the number of the terms in the basis function (which is 12 in this study), then [B] is a 3 by 2DOF matrix which represents a conventional linear strain-displacement relationship, [A] is a 3 by 4 matrix which contains the derivatives of [u], [G] is a 4 by 2DOF matrix in which [G][a] give

$$([G][a])^T = [\frac{\partial u}{\partial X} \quad \frac{\partial u}{\partial Y} \quad \frac{\partial v}{\partial X} \quad \frac{\partial v}{\partial Y}] \qquad (8)$$

while ½ [A][G][a] together gives the nonlinear strain component [η].

(2) At any time step, the stress to be found is first formulated in terms of the second Piola-Kirchhoff stress tensor, S^n_{ij} as

$$S^n_{ij} = S_{ij} + \Delta S_{ij} \qquad (9)$$

where S_{ij} is the existing stress which equals Cauchy stress,σ_{ij}. The incremental virtual work of the system under body forces, f_i^B, line loads, f_i^L, and point loads, F_i , can be written as,

$$\sum \int S^n_{ij} \delta \varepsilon_{ij} \; dV = \sum \int f_i^B \delta u_i dV + \sum \int f_i^L \delta u_i dl + \sum F_i \delta u_i \quad (10)$$

Substituting Eq. (9) into (10) and linearizing the expression, while introducing other terms such as inertia , one may obtain a set of simultaneous equations of the following form

$$([K_L] + [K_{NL}] + [K])[a] = [P] \qquad (11)$$

where,

$$[K_L] = \sum \int [B]^T [C][B] \; dV \qquad (12)$$

$$[K_{NL}] = \sum \int S_{ij} d\eta_{ij} dV = \sum \int [G]^T [S][G] dV \quad (13)$$

$$[P] = -\sum \int [B]^T [\sigma] dV + \sum \int f_i^B [X] dV + \sum \int f_i^L [X] dl + \sum F_i [X] \quad (14)$$

[K] stands for all other contribution to the stiffness matrix. The exact integration for [K], $[K_L]$ and most of [P] can all readily be carried out, but not so for $[K_{NL}]$ nor for the initial stress force vector. The matrix [S] and the vector [σ] both contain various terms of S_{ij} which are functions of x and y. It is generally not possible to obtain the S_{ij} versus x, and y relationship explicitly because the principal stress axes keep changing as an object deforms.

To circumvent this problem the following solution is employed: First, a number of stress sampling points are selected that more or less uniformly cover an object. This is equivalent to introduce a stress layer on each discrete element. The stresses at these points are computed and updated at each time step. Before computing $[K_{NL}]$, a least square fit through these sampling points for each stress component is carried out for each object. This gives a polynomial approximation to the existing stress field. With this information, the exact integration of $[K_{NL}]$ can be obtained. This study uses a bi-linear least square fit. One may examine the goodness of the fit and decides if a higher order polynomial fit is required.

(3) After [a] is solved, the strains and Δs_{ij} are computed, and S^n_{ij} are found. The application of Eq. (6) gives the Cauchy stress. The geometry is then updated. The analysis continues on to the next time step.

(4) For the contact interaction, the boundary of an object is approximated as piecewise-linear.

PHYSICAL VERIFICATION

To verify the implementation of this study, physical tests were conducted on rings made out of elastic polymer foam. The outer diameter of the ring was subjected to a compression that causes a deformation up to 50% of its original length. Each ring is modeled as an individual element with a hole. The present implementation allows for incorporation of multiple holes to an element.

The test results for one ring under compression are summarized in Fig. 1. The various deformation configurations from the computed results are depicted in Fig. 2. The deformation of an ongoing test involving 5 rings is depicted in Fig. 3.

It is concluded that the test results provide a reasonable verification of the framework presented. This framework has also been successfully implemented in manifold method (Lin, 1997).

ACKNOWLEDGEMENTS

The second author would like to thank the government of Saudi Arabia for the support of his graduate study at the University of Pittsburgh.

REFERENCES

1. Bathe, K. J., Finite Element Procedures in Engineering Analysis, Prentice-Hall, 1982.
2. Lin, J-S and Lee, D-H, "Manifold Method Using Polynomial Basis Function of Any Order," Proceeding, International Forum on DDA, Berkeley, 1996.
3. Shi, G. W., Block System Modeling by Discontinuous Deformation Analysis, Computational Mechanics Publication, Southampton, UK, 1993.
4. Lin, J-S, "Manifold Method for Geotechnical Analysis," submitted to ASCE, Journal

of Geotechnical Engineering, 1997.

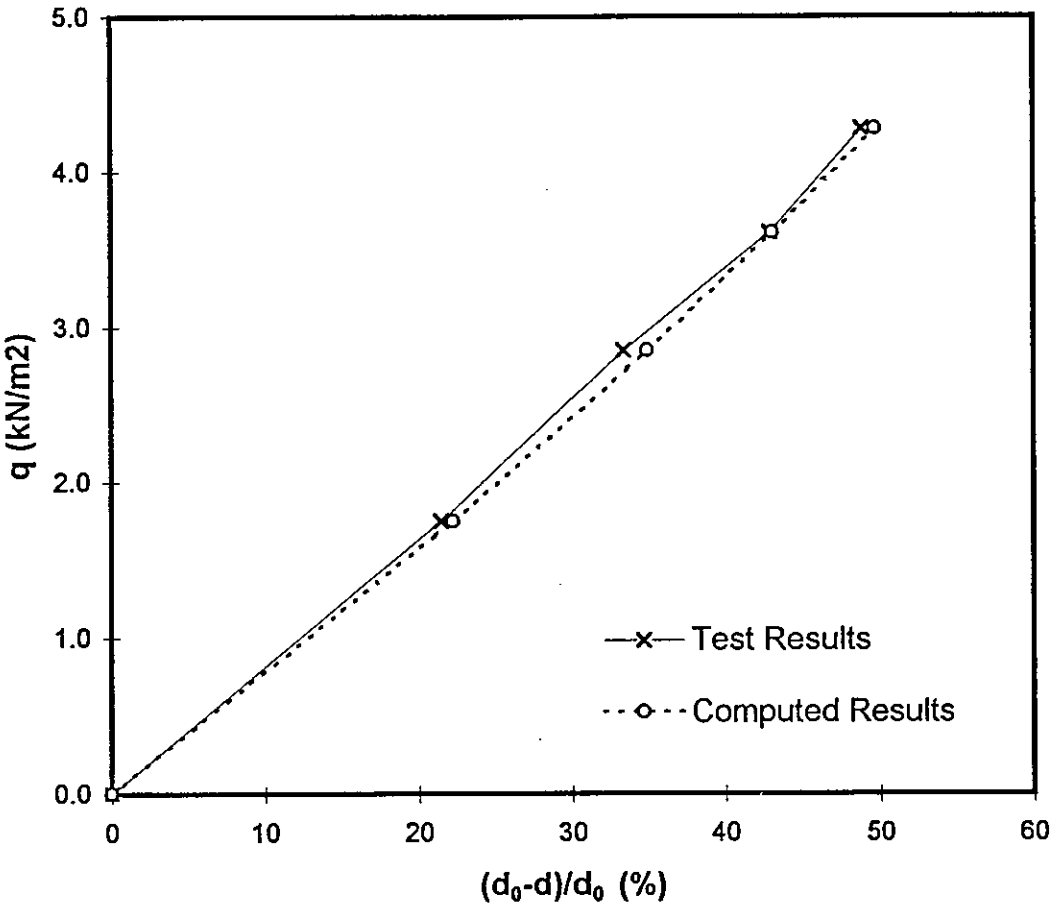

Figure 1 Comparisons of the computed results versus the laboratory measurements for one ring under compression.

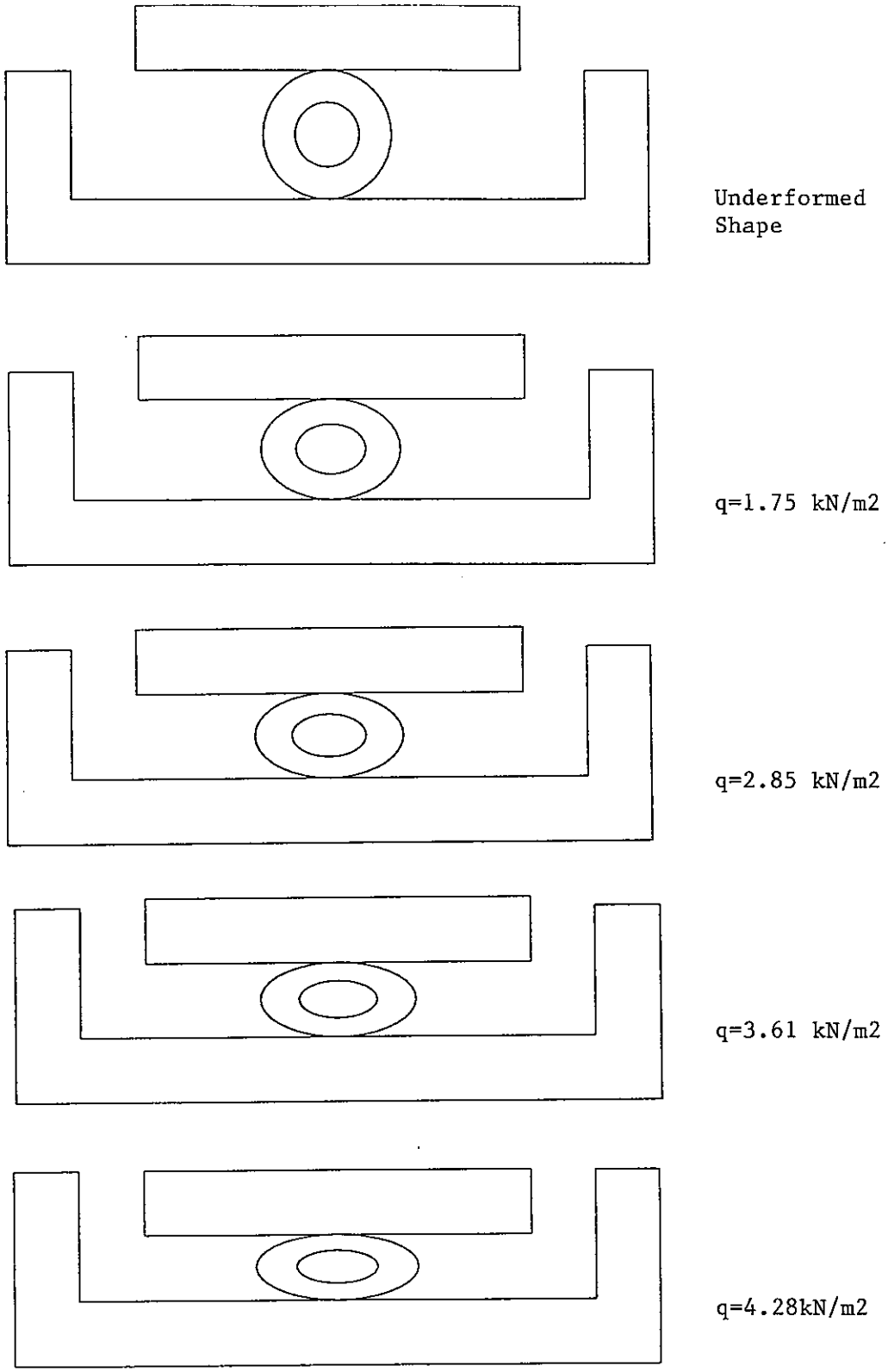

Figure 2 The deformation corresponding to the various stages of loading in Fig. 1.

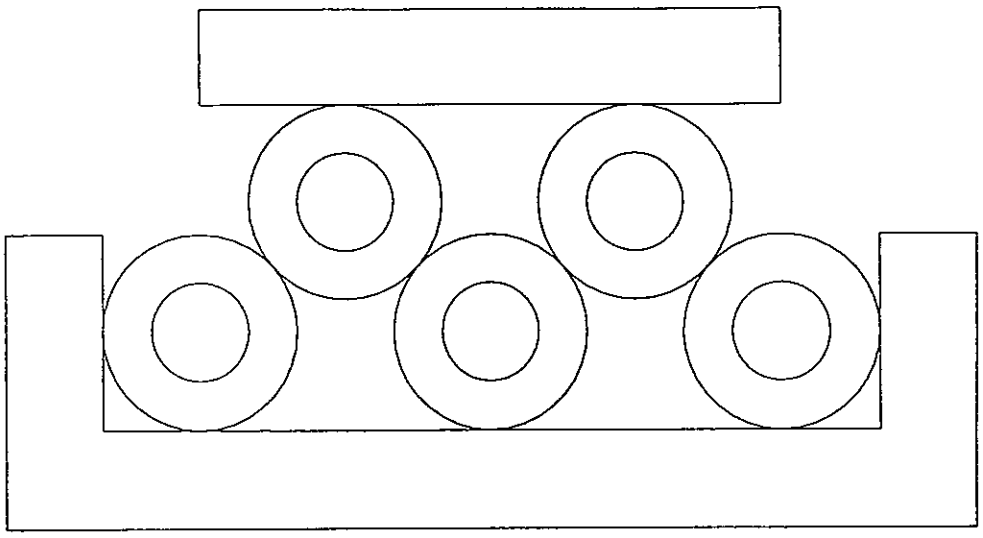

(a) Undedormed Configuration

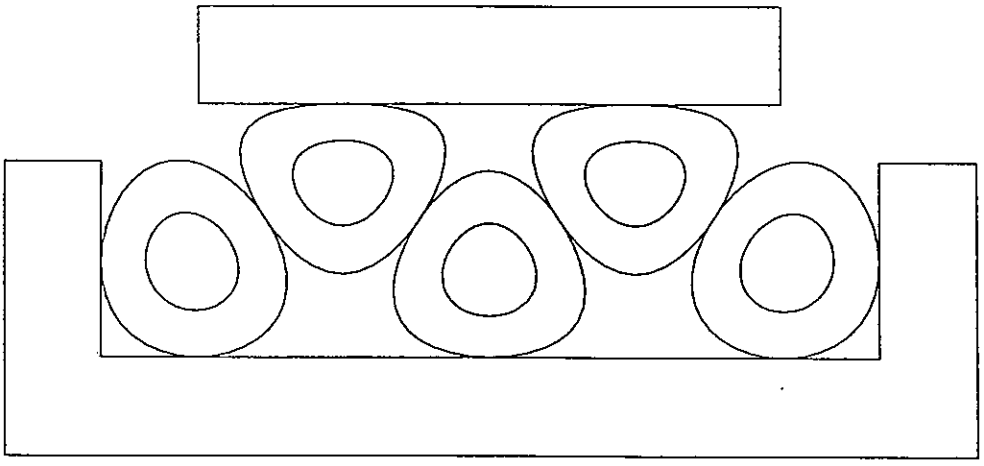

(b) Configuration after some compression

Figure 3 Preliminary results showing deformation of five rings under compression.

DDA APPLIED TO DEFORMATION ANALYSIS OF COARSE GRANULAR MATERIALS (BALLAST)

TATSUYA ISHIKAWA

East Japan Railway Company, Tokyo, Japan,

E-mail:t_ishi@ra2.so-net.or.jp

YUZO OHNISHI

Kyoto University, Kyoto, Japan

AKIRA NAMURA

Railway Technical Research Institute, Tokyo, Japan

ABSTRACT

In order to investigate railway track deterioration in detail, the application of DDA to the cyclic plastic deformation of coarse granular materials was discussed with simulating monotonic loading and cyclic loading triaxial tests of ballast. As a result, it was shown that DDA is to some extent an effective method to analyze the behavior of ballast. But it was revealed in DDA that there were some defects of handling the frictional contact mechanism.

Keywords: *coarse granular material, angularity, friction angle, triaxial test, railway*

INTRODUCTION

At ballasted railway track, the phenomenon that irregularity of rail level due to train passage gets worse, that is what we call "track deterioration" or "growth of track irregularity", is frequently observed. In general, the dominant factor of track deterioration is supposed to be the plastic deformation of "railroad ballast", ballasted track composed of crushed stone (ballast), which is caused by repeated train passages. Since such a phenomenon influences the safety of train operation, it is very important to understand and clarify the cyclic plastic deformation characteristics of ballast.

Cyclic loading tests with a full-scale track and laboratory triaxial tests of ballast samples had been performed[1][2]. The cyclic plastic deformation of railroad ballast, strength and deformation property of ballast have been discussed based on these test results. However a triaxial test result can not directly interpret a full-scale track test result and the both results are not well related in reality. In this case the analytical and numerical study is effective to explain the relation between the former and the latter.

In this paper, the application of the discrete analysis to the cyclic plastic deformation of coarse granular materials was discussed by simulating monotonic loading and cyclic loading triaxial tests of ballast with DDA (Discontinuous Deformation Analysis[3][4]) in order to investigate track deterioration in detail.

OUTLINE OF SIMULATION

Fig. 1 (a) describes generally the analysis model for simulating triaxial tests of ballast. Fig. 1 (b) shows the block element mesh before loading, where the ballast specimen consists of about 300 elastic polygon elements.

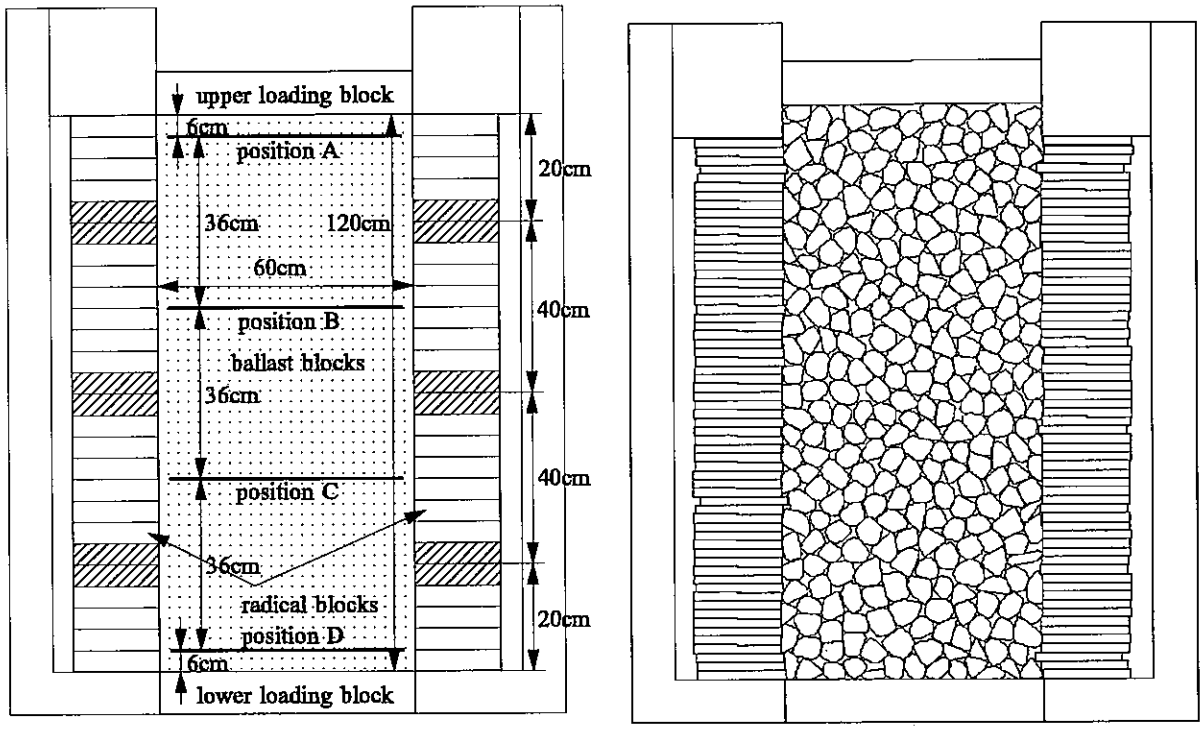

(a) analysis model (b) before loading

Figure 1. Triaxial test

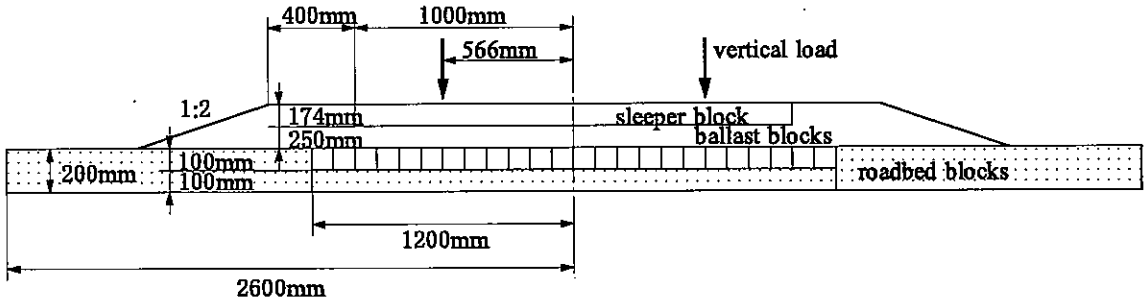

(a) analysis model

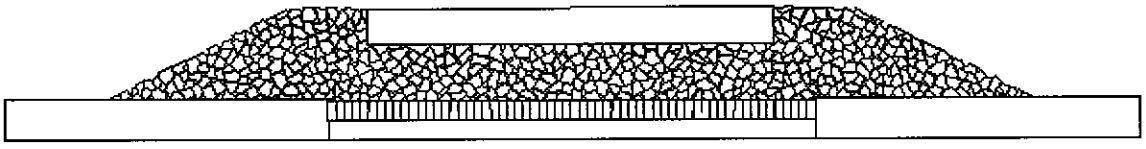

(b) before loading

Figure 2. Full-scale track test

Fig. 2(a) shows the size, dimension and boundary condition of analysis model (cross section) for simulating cyclic loading tests of a full-scale track. Fig. 2(b) shows the typical element mesh before loading, where the railroad ballast consists of about 500 elastic polygon elements. Each element (block) is separated by its boundaries and blocks are divided by the method of Voronoi tessellation[5].

Three analysis models are used in the triaxial test simulation, which is divided by Voronoi tessellation with the number of divisions equal to 300, 400, 500. (Fig. 3 shows the grain size distribution of analysis model and Table 1 shows the features of each analysis model in comparison with experimental results.) The package of blocks was made by falling blocks into a box by free fall from a certain height. Table 2 shows the material properties of the blocks and the joint properties of these analysis models.

The results of triaxial test simulation are mainly discussed in this paper, using models as shown in Fig. 1 and Fig. 2. The triaxial test simulation were performed as follows; At first the isotropic consolidation was done at different confining pressure (σ_3) equal to 19.6kPa, 39.6kPa, 58.9kPa. Subsequently monotonic loading (ML) tests were performed, controlling axial stress ratio at the rate of (σ_1/σ_3= 1)/sec (being simply converted to axial strain (ε_1) rate equal to about 0.30%/sec) at each σ_3.

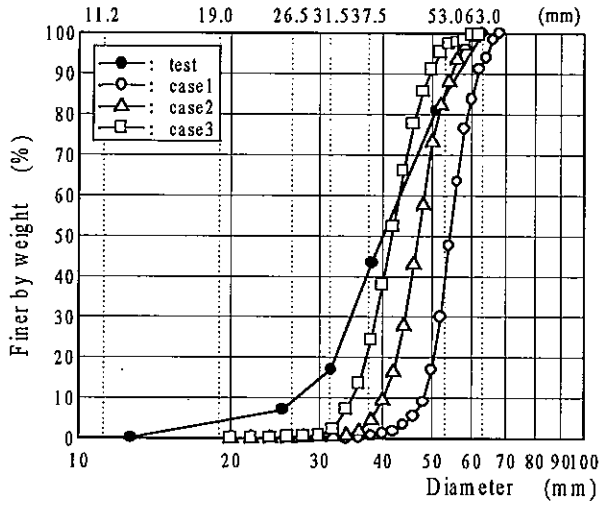

Figure 3. Grain size distribution

Table 1. Features of analysis model

component		case1	case 2	case 3	tests
number of ballast blocks		296	389	489	——
uniformity	U_c	1.15	1.20	1.23	1.70
mean grain size	D_{50}	5.4mm	4.6mm	4.2mm	4.1mm
porosity	n	15.8 %	16.5 %	15.9 %	38.2 %
mean co-ordination number	$\overline{N}$	4.82	4.35	4.56	——

Table 2. Material and joint properties

component	ballast blocks	loadingblocks	radical blocks
unit mass γ	2.77t/m^3	1.00t/m^3	1.00t/m^3
Young's modulus E	20.0GPa	1000.0GPa	0.1GPa
Poisson's ratio ν	0.1	0.1	0.1
cohesion of surface C	0	0	0
friction angle ϕ_u	50 or 55°	0	0

Table 3. Analysis condition

(a) monotonic loading

No.	model	σ_3	ϕ_u	q_{max}
AML-11a	case1	19.6kPa	50°	126.8kPa
AML-11b	case1	19.6kPa	55°	135.1kPa
AML-12a	case1	39.2kPa	50°	225.5kPa
AML-12b	case1	39.2kPa	55°	282.2kPa
AML-13a	case1	58.9kPa	50°	319.5kPa
AML-13b	case1	58.9kPa	55°	397.3kPa
AML-21b	case2	19.6kPa	55°	121.5kPa
AML-22a	case2	39.2kPa	50°	260.0kPa
AML-22b	case2	39.2kPa	55°	261.6kPa
AML-23b	case2	58.9kPa	55°	335.6kPa
AML-31b	case3	19.6kPa	55°	44.0kPa
AML-32a	case3	39.2kPa	50°	203.1kPa
AML-32b	case3	39.2kPa	55°	210.7kPa
AML-33b	case3	58.9kPa	55°	346.8kPa

(b) cyclic loading

No.	model	σ_3	ϕ_u	$(\sigma_1/\sigma_3)_{max}$
ACL-11b	case1	19.6kPa	55°	5.0
ACL-12b	case1	39.2kPa	55°	5.0
ACL-13b	case1	58.9kPa	55°	4.0
ACL-14b	case1	58.9kPa	55°	5.0
ACL-15b	case1	58.9kPa	55°	6.0

Cyclic loading (CL) tests at a constant σ_3 were performed after isotropic consolidation. Axial sinusoidal cyclic deviatoric load ($q = \sigma_1 - \sigma_3$) was applied to the specimen at a load of frequency (f) of 0.1Hz with an axial stress range of the principal stress ratio (σ_1/σ_3) equal to 1 - 6. Table 3 shows the analysis condition together with the test condition.

DEFECTS OF DDA

Shape of blocks

The circular disc element is often used to calculate the behavior of granular materials by using discontinuous analysis. But it is known that analysis results are strongly influenced by the shape and assemblage of blocks. It is reported that the internal friction angle ϕ of the DEM (Distinct Element Method) simulated specimen with circular disc elements wouldn't become larger than 20°, even if the block friction angle ϕ_u on the contact surface of each block is larger than 45° [6].

In our experiment the internal friction angle of the actual ballast derived from triaxial tests is

55°[2]. At the beginning it is easily expected that there will be a strong question about the reliability of the DDA simulation results where ballast is treated as circular disc element. Herein, polygon elements generated by Voronoi tessellation were employed to simulate triaxial tests of ballast by DDA. In order to discuss the influence of the shape of blocks on the analysis results, the result of DDA with polygon elements was compared with the one of DDA with circular disc elements[7].

Using circular disc elements (Fig. 4), a loading block at the top went on moving downwards during the process of isotropic consolidation with the condition described in Table 3 as the vertical displacement of the loading block at the top increased in proportion to the analysis time. The simulation with circular elements was performed until the analysis time reached at about 9.0 seconds. The loading block at the top did not stop falling. So we considered that the simulation didn't converge.

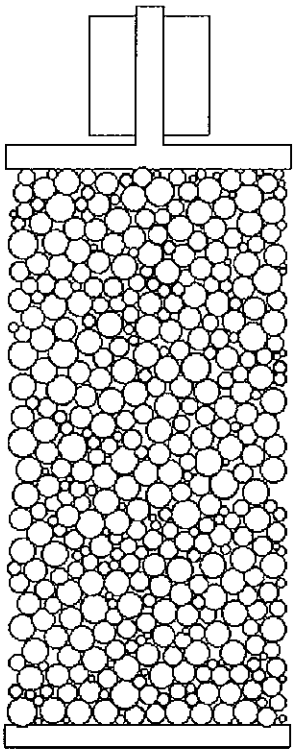

Figure 4. Circular disc model (before loading)

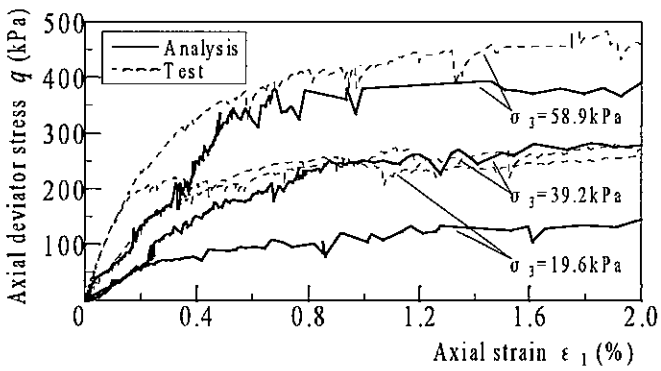

(a) effect of confining pressure

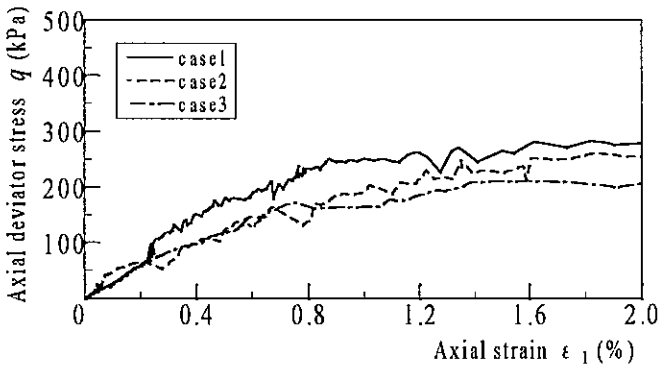

(b) three analysis models

Figure 5. Stress-strain relation (with polygon elements)

Whereas using polygon elements, the simulation converges as Fig. 5 during both the isotropic consolidation and the subsequent deviatoric loading. Fig. 5(a) shows the comparison of stress-strain relation at each confining pressure between test results and analysis results using polygon elements. Fig. 5(b) shows the stress-strain relations of three analysis models in which difference is the number of blocks.

Seeing Fig. 5, the results of DDA are similar to the results of triaxial tests in the curve form of

the stress-strain relation. But the peak stress level of the analysis is low in comparison with the stress level of experiments. This trend increases as the number of divisions increases, though the relation of analysis between axial strain (ε_1) and radial strain (ε_3) agrees with the relation of tests as shown in Fig. 6.

We presume that the reason why the analysis with circular disc elements didn't converge whereas the analysis with polygon elements converged under the same analysis condition, will be explained by the following two reasons:

(1) the confining pressure was loaded in an instant from state of the constraint of analysis in the case of using circular disc elements, though the confining pressure was loaded step by step when using polygon elements. The deformation of blocks at the high loading speed is larger than the one at the slow loading speed in the simulation of DDA.

(2) the angularity (the index of sharpness) of blocks has a considerable influence on the deformation of the assemblage of blocks[8]. These results show that DDA with polygon elements divided by Voronoi tessellation is an proper method to analyze the deformation of coarse granular materials which have large friction angle such as ballast.

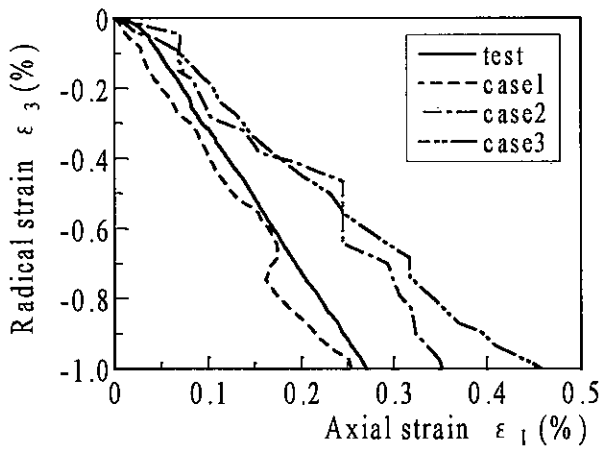

Figure 6. Axial strain-radical strain relation (with polygon elements)

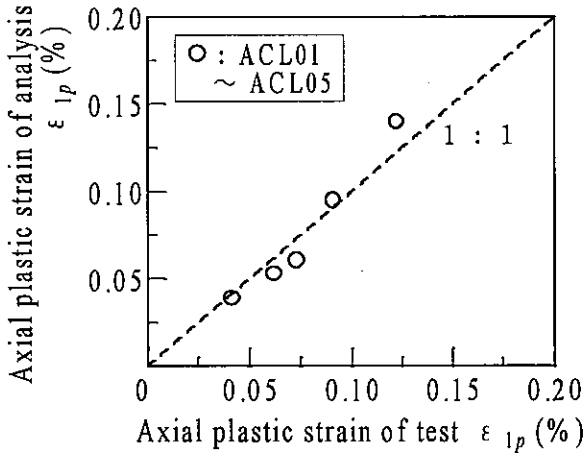

Figure 7. Comparison of plastic strain at first cycle (with polygon elements)

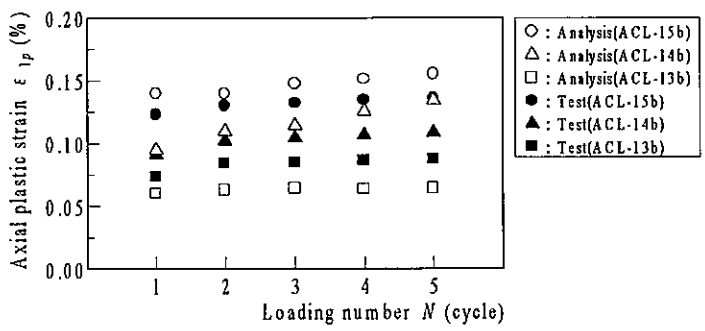

Figure 8. Increment of plastic strain with CL (with polygon elements)

Fig. 7 shows the comparison in the plastic strain generated at the first cyclic loading between

test results and analysis results. The plastic strain at the first cycle generated by DDA is nearly as large as the experiment. Also, the amount of the plastic strain became almost the same as test result in subsequent loading (Fig. 8). These results show that DDA can simulate the cyclic plastic deformation of ballast without setting any particular constitutive relation except the frictional law.

Contact properties

From the preceding results, it is concluded that DDA can simulate the particle movement of ballast under cyclic loading to some extent, which causes a plastic deformation of the coarse granular materials. But it was also recognized that consideration of the shape of blocks would not well simulate the stress-strain relation. So herein, the influence of the block to block contact properties in the analysis is discussed by simulating triaxial tests by DDA changing the value of friction angle ϕ_u. Fig. 9 shows the comparison of stress-strain relation between test results and analysis results with polygon elements in the case of ϕ_u = 50° and 55°. It is commonly said that using circular disc elements the difference in the friction angle has little influence on the stress-strain relation of analysis[6]. However Fig. 9 shows that the stress level at the same strain tends to decrease as the friction angle decreases. This means that it is possible to evaluate the influence of the friction angle between blocks in the case of analysis with the element which characterize the angularity such as polygon element. DDA with polygon elements is more practical than the one with circular disc elements to analyze the deformation of the coarse granular materials.

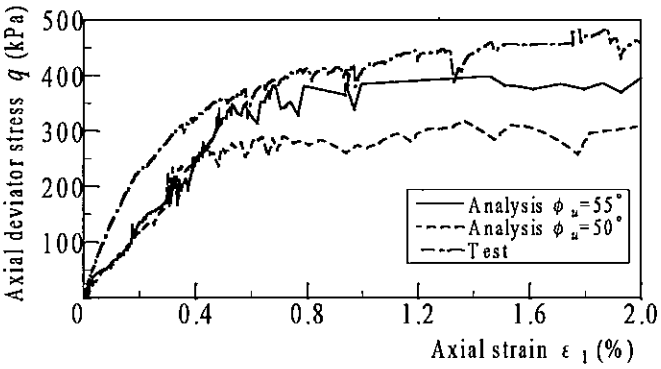

Figure 9. Influence of friction angle (with polygon elements)

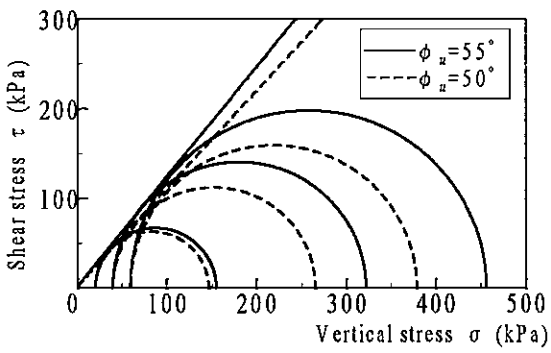

Figure 10. Mohr's stress circles and failure lines

Fig. 10 shows Mohr stress circles for ϕ_u = 50° and 55° derived from the analysis results of monotonic loading at the confining stresses of σ_3 = 19.6kPa, 39.6kPa, 58.9kPa, and the failure lines for ϕ_u = 50° and 55° derived from Mohr stress circles. Fig. 10 indicates that the angle of the failure line for ϕ_u = 55°, that is the internal friction angle ϕ, is about 51° and the one for ϕ_u = 50° is about 47°.

The internal friction angle for the specimen decreases nearly as much as the difference of the friction angle. This result explains the hypothesis that it is commonly said that the internal friction angle ϕ is the sum of the friction angle ϕ_u and the angle influenced by dilatancy and inter-locking

[9]. However the internal friction angle derived from analysis results is less than the block friction angle of analysis condition contrary to test results. This response indicates that DDA has some defects about the contact mechanism influenced by dilatancy and inter-locking, otherwise the determination of the friction angle has some defects in analyzing the deformation of the coarse granular materials. In fact, as the surface of ballast is very rough, it is expected that the angularity of ballast would considerably be higher than the particle of sand. So we may underestimate the influence of the angularity though we can't reveal that considering the angularity is interpreted as either the improvement of the contact mechanism or the increment of the friction angle. It is necessary to study more about this defect of DDA as well as the influence of the shape of blocks.

Convergence in DDA calculation

In this section, the defects about the convergence of analysis solution discerned in a series of analyses are discussed together with the measures to be taken for overcoming these defects. The following items are pointed out:

(1) DDA employed with rigid circular disc elements to calculate the triaxial test did not converge as mentioned in foregoing sentences. With using rigid circular disc elements, the allowable penetration which is the allowable distance to penetrate each other at the contact between two blocks, was increased step by step. But it didn't give a good solution. We presume that these responses will be explained by being unable to treat the plane contact as face to face contact on account of rigid circular disc elements, because it is commonly said that the moment of rotation transmitted at face to face contact has such a considerable influence on the results of the discontinuous analysis as the internal friction angle increases[10]. Whereas using polygon elements, the plane contact did not take into account in this analysis. This feature may bring on the analysis results that the internal friction angle was less than the block friction angle as mentioned in foregoing sentences.

(2) Axial stress and axial strain are plotted against analysis time (T) in Fig. 11. Fig. 11(a) shows that there are some parts where the axial stress fluctuation strongly, though the T- ε_1 relationship is piecewise smooth as shown in Fig. 11(b). This phenomenon is an example of analysis results that indicated very slow convergence among a series of analyses performed this time. In order to overcome these shortcomings for convergence, various measures by changing the analysis condition were taken as follows:

a) Change of the ratio of normal penalty stiffness to tangent penalty stiffness

When the ratio of normal penalty stiffness to tangent penalty stiffness decreases, the convergence of analysis results is improved.

b) Approaching of Young's modulus of blocks to the one of original rocks

As the result that the triaxial tests were simulated by DDA assuming the equivalent deformation modulus derived from the stress-strain relation of the triaxial test or Young's modulus of original rocks as Young's modulus of blocks, it was denoted that the convergence of analysis results was improved when Young's modulus of blocks approached the one of original rocks.

c) Decreasing the allowable distance of penetration

When the allowable distance of penetration decreases in connection with the block size, the convergence of analysis results is improved.

These responses indicate that balancing between the stiffness of penalty and the allowable distance of penetration is especially significant to improve the convergence of analysis solution.

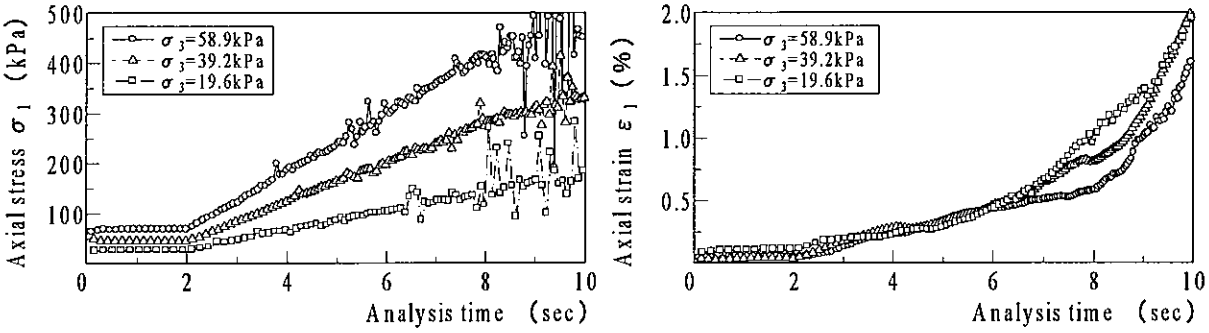

(a) axial stress-time relation (b) axial strain-time relation

Figure 11. Change of Stress and strain along time (with polygon elements)

CONCLUSIONS

In this paper, the application of DDA to the cyclic plastic deformation of coarse granular materials was discussed by simulating monotonic loading and cyclic loading triaxial tests of ballast. As a result, it is shown that DDA is to some extent an effective method to analyze the behavior of coarse granular materials. But in terms of both the convergence of the analysis and the internal friction angle less than the block friction angle of the gravel surface, it is revealed that there are some defects in the analysis method. When the deformation of coarse granular materials which have large friction angle such as ballast is simulated by DDA in particular, we may have to improve the contact mechanism of DDA because the analysis results of DDA depends strongly on the frictional contact property of the block surface. Therefore, the investigation of both the friction angle of the block surface and the stiffness of penalty is important in applying DDA to the practical problems as well as the investigation of the shape of blocks, and further studying the defects described in this paper in detail, it is believed that DDA will be able to analyze practical problems with better accuracy.

ACKNOWLEDGMENT

The authors would like to thank Prof. Masashi Kamon and Prof. Qousai Chen of Kyoto University for many invaluable discussions and suggestions.

REFERENCES

1. Ishikawa, T. and Namura, A. : Cyclic Deformation Characteristics of Railroad Ballast in Full-Scale Tests, *Proc. of JSCE*, 512/IV-27, pp.47-59, 1995.

2. Sunaga, M., Ishikawa, T. and Namura, A. : The Present Designing and Maintenance of Railroad Ballast in Ballasted Track, *Soils and Foundations*, Vol.43 No.2, pp.10-14, 1995.
3. Shi, G.H. and Goodman, R.E. : Discontinuous Deformation Analysis and its Application to Rock Mechanics Problems, *Proc. of 25th U.S.Symp. on Rock Mech.*, pp.269-277, 1984.
4. Shi,G.H. and Goodman, R.E. : Two Dimensional Discontinuous Analysis, *Int.J.Num.Anal.Methods Geomech. 9*, pp.541-556, 1985.
5. Ohnishi,Y. and Kono, M. : Distinct Element Analysis of Jointed Rock Mass Modelled by Voronoi Tessellation, *Proc. of JSCE*, 376/Ⅲ-6, pp.231-239, 1986.
6. Sawada, S., Pradhan, B.S., Toki, K. and Yamashita, N. : Effects of Element Shape and Initial Density on the Distinct Element Analyses, *Proc. of Symp. on failure of ground and strain localization*, pp.163-170, 1994.
7. Ohnishi, Y. and Miki, S. : Development of Circular and Elliptic Disc Element for DDA, *Proc. of The First International Forum on Discontinuous Deformation Analysis(DDA) and Simulations of Discontinuous Media*, pp.44-51, 1996.
8. Matsushima, T. and Konagai, K. : Simple Shear Simulation of Granular Assemblage using Distinct Regular-Polygon-Element Method, *SEISAN-KENKYU*, Vol.48 No.7, 1996.
9. Technical Committee on Mechanics of Granular Materials : *Mechanics of Granular Materials*, pp.115-116, The Japanese Society of Soil Mechanics and Foundation Engineering, 1993.
10. Iwashita,K., Matsuura, K. and Oda, M. : Distinct Element Method with The Effect of Moment Transfer at The Contact Points, *Proc. of JSCE*, 529/Ⅲ-33, pp.145-154, 1995.

Geological Survey for DDA and its Application to a Large Rock Cavern

Hiroshi CHIKAHISA[1], Kaoru KOBAYASHI[1], Kazunobu MATSUMOTO[1], Masayuki TSUTSUI[1] and Yuzo OHNISHI[2]

[1]Tobishima Corporation, Tokyo 102, Japan
[2]Kyoto University, Kyoto 606-01, Japan

ABSTRACT: The Takayama Festival Float Art Museum consists of dome shape exhibition hall of 40.5m in diameter and tunnel type art gallery of 70m length, which is the first underground museum utilizing a large-scale rock cavern in Japan. In the design stage, it is important to examine the behavior of discontinuities of rock masses on discussing the stability of a large cavern.

Survey and analysis described in this paper was executed to examine the behavior of discontinuities of rock masses surrounding a large cavern after excavation. The analysis method used is the DDA. Geometric properties consisting of directions, pitches and length of discontinuities were surveyed in a geological survey tunnel and boreholes. In-situ shearing tests were executed to examine mechanical properties of rock masses, and laboratory shearing tests were executed to gain mechanical properties of discontinuities.

From the results of DDA, the behavior of rock masses surrounding a large cavern during excavation is examined.

1. INTRODUCTION

There are a number of elegant examples of the use of rock caverns for public spaces and architectural structures in Northern Europe[1],[2],[3]. The structures are rarer in Japan where rock caverns have been used for petroleum storage, tunnels for underground passages and utilities and the reuse of abandoned mines. The Takayama Festival Float Art Museum[4] having underground exhibition hall, shown in Figure 1, is the first experience in Japan.

Usually in Japan, plan and design of buildings for the public must confirm to the Building Standards Law. And the underground art museum required the approval of the Minister of Construction as an exceptional structure of the law, because the safety of the underground museum, which is the first construction in Japan, cannot be confirmed within the law. A

comprehensive assessment was made from the standpoint of hazard prevention and structural safety[5] in the Committee organized in the Building Center of Japan in commission of the Minister of Construction.

This paper describes how the underground opening was surveyed and designed for structural safety mainly concerning discontinuities in the rock masses to determine the behavior surrounding the cavern.

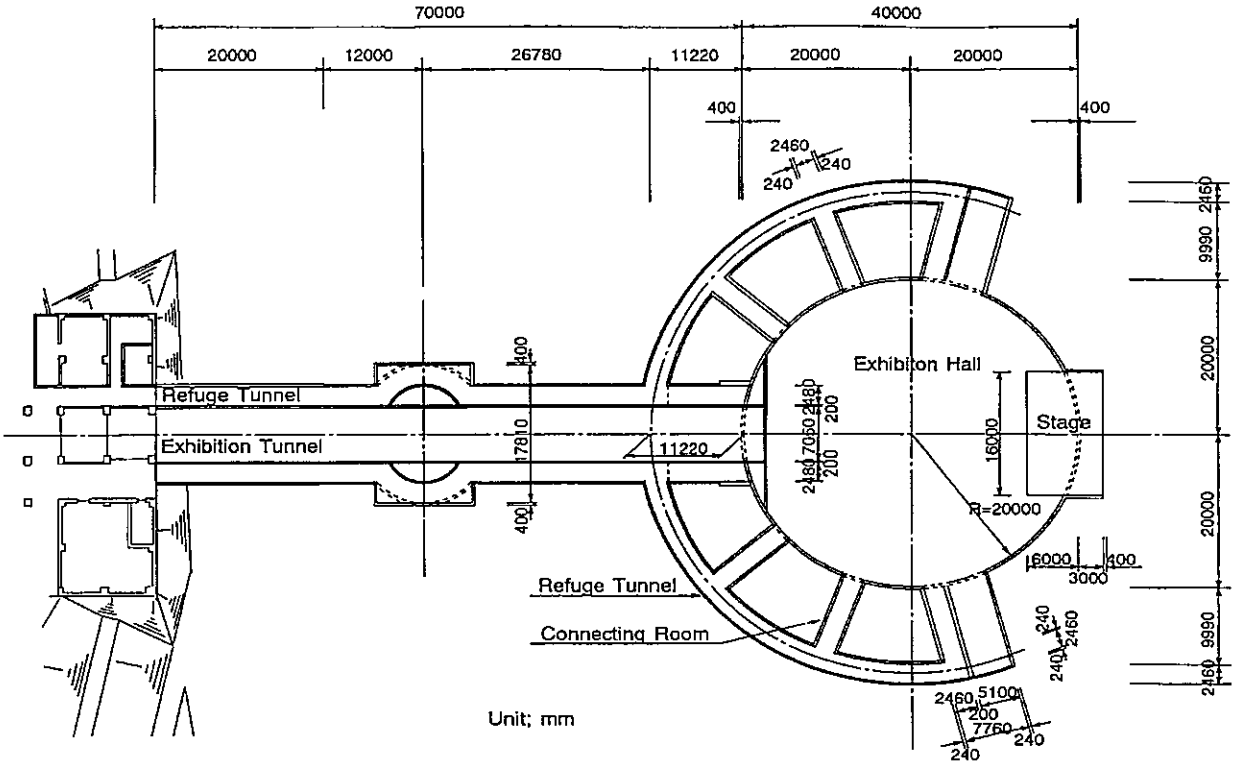

Figure 1. Plan of the Takayama Festival Float Art Museum

2. GEOLOGICAL SURVEY

2.1 *Outline*

The site is located on the north-west slope of a ridge, 720 m in elevation between Sunorikawa River and Ayatagawa River originating from Mt. Genjidake, to the south-west of the Takayama Basin in Gifu Prefecture in Japan. The ground around the site is comprised of surface soil, cohesive soil of colluvial sediment, and pyroclastic flow-derived welded tuft among igneous rock, so-called Nohi rhyolite of the late Cretaceous to Paleogene period. The Atotsugawa Fault lies about 25km to the north of the site and stretches northeast to southwest; about 40 km to the south, the Adera Fault extends northwest to southeast[6].

In order to survey the ground properties necessary for the design and construction, a horizontal geological survey tunnel 4m in width, 4m in height, and 80m in length was excavated towards the crown portion of the exhibition hall, and geological survey borings were conducted at five

points shown in Figure 2.

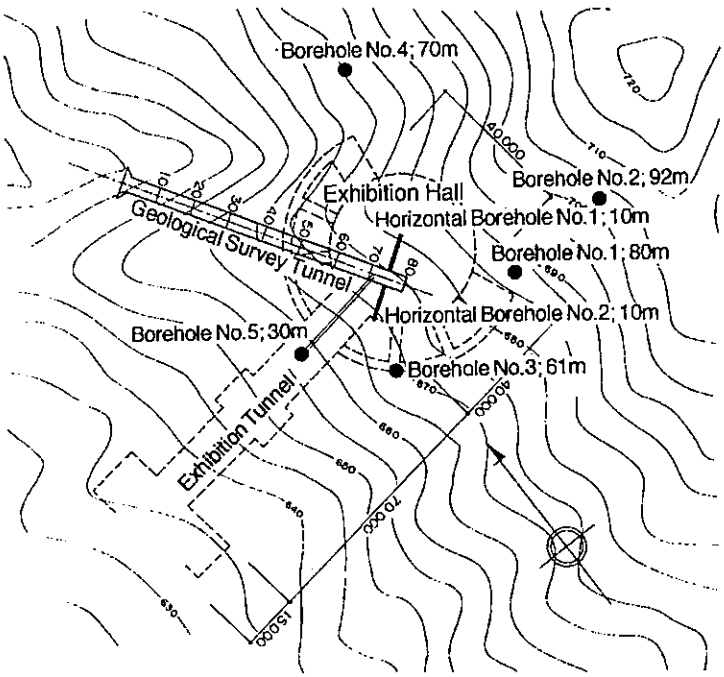

Figure 2. Location of the Geological Survey Tunnel and Boreholes

2.2 *Surveys and Tests of Discontinuities*

Surveys and tests were performed using the boreholes and a geological survey tunnel to determine the distribution and geometrical characteristics of discontinuities with regard to the items shown in Table 1. The results of these surveys and tests are described below.

Table 1. Items of surveys and tests on discontinuities

Item	Location	Estimated item
Borehole scanning	Borehole No.1 and No.2, Horizontal boreholes	Orientation and spacing of discontinuities
Observation of the geological survey tunnel	Geological survey tunnel	Orientation, spacing and length of discontinuities
In-situ rock shear test	Geological survey tunnel	Residual strength of rock mass
Laboratory rock shear test	No.5 boring core, Blocks with joint filled clay	Shearing strength of discontinuities
X-ray examination	Clay in joint	Clay mineral

1) Geometrical characteristics of discontinuities

The full data of the discontinuities from the geological survey tunnel, No.1 and No.2 boreholes, and the horizontal boreholes, as well as the results of cluster division are shown in the lower hemispherical isometric projection in Figure 3[7]. In this figure, the first group corresponds to low-angle faults, the second group to the Atotsugawa Fault system, and the third group to the Adera Fault system. Representing the points of maximum density of the representative values of directionality for the various groups on the cluster projection gives the results shown in Table 2. For reference, the directional distribution coefficient K for the case of the Fisher distribution and the standard deviation[8] are also shown in the figure.

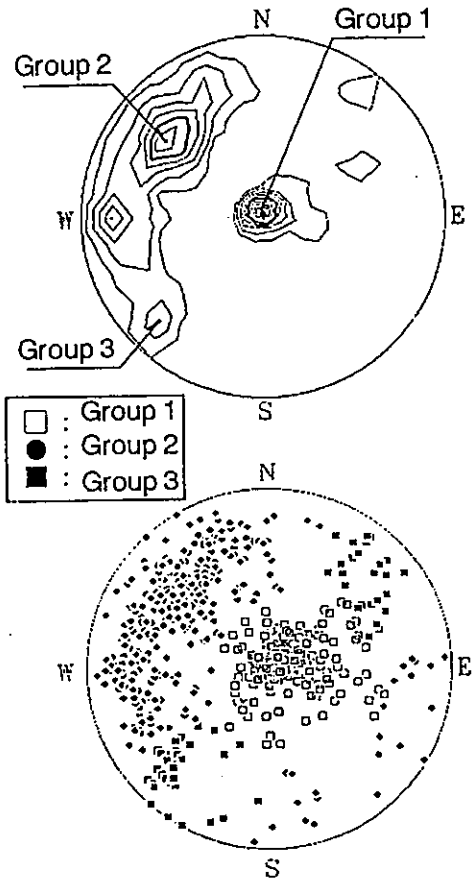

Figure 3. Cluster division in the lower hemispherical isometric projection

Table 2. Orientation of discontinuities

Group	Number of data	Dip angle (degree)	Dip direction (degree)	Variance coefficient of orientation (K)	Standard deviation (σ)
1	197	15	230	11.94	0.289
2	232	68	128	4.20	0.488
3	62	77	45	1.46	0.828

With regard to the spacing of discontinuities, data was used that would not result in deviation for the various directional groups. That is to say, for group 1 data from vertical boreholes 1 and 2

were used, for group 2 data from the side wall of the geological survey tunnel was used, and for group 3 data of horizontal boreholes taken from the geological survey tunnel was used. The distribution of semi-trace length from the point of intersection to a measurable end point was investigated for discontinuities intersecting a 0.5m high scan line using data of the geological survey tunnel for each directional group as shown in Figure 4. The cases where the end point was not evident from the geological survey tunnel for groups 2 and 3 were omitted from the data, a uniform distribution was assumed, and the length of the discontinuities evaluated according to the method of Priest et al[9]. The length and the spacing of C_H class rock at the location of the underground opening for each directional group can be seen in Table 3.

Projecting the geometric characteristics evaluated above onto the longitudinal axis of the geological survey tunnel gives the result shown in Figure 5.

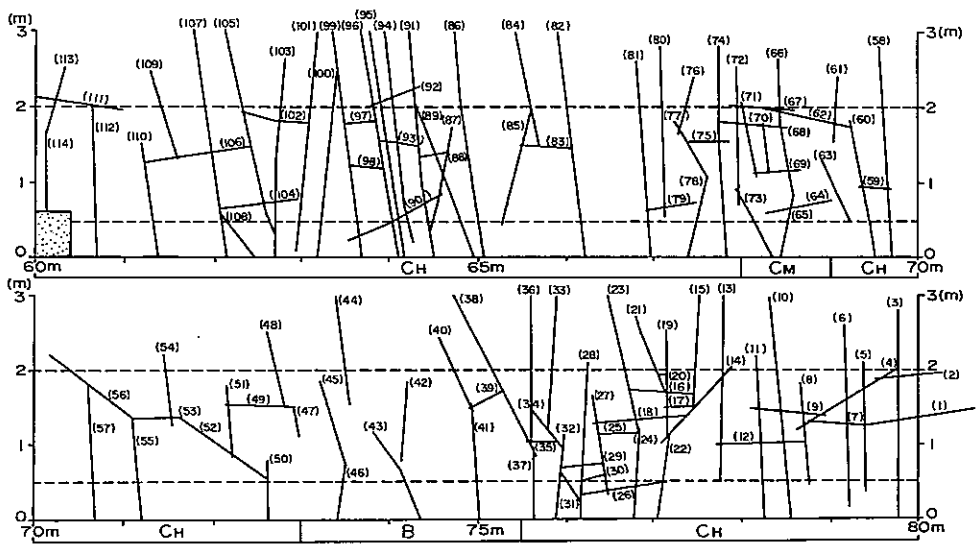

Figure 4. A sketch of discontinuities at side wall of the geological survey tunnel

Table 3. Spacing and length of discontinuities in C_H class rock masses

Group	Spacing and its standard deviation (m)	Estimated length (m)
1	3.2(1.78)	2.1
2	2.1(0.17)	13.7
3	2.4(1.23)	7.4

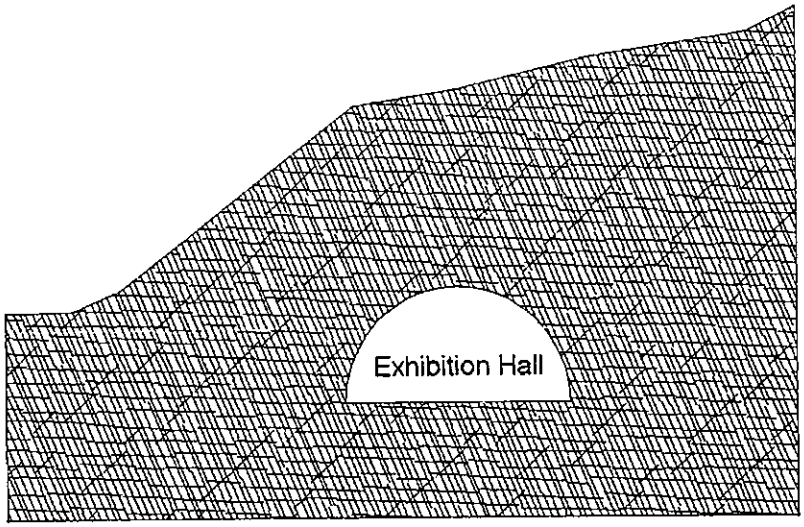

Figure 5. Distribution of discontinuities estimated from in-situ surveys (Parallel to the longitudinal axis of the geological survey tunnel)

2) Mechanical properties of the discontinuities

The shear strength of each type of discontinuity was obtained from the following three direct shear tests:

a) In-situ rock shear tests at the geological survey tunnel.
b) Laboratory rock shear tests of discontinuities of No.5 boring core.
c) Laboratory rock shear tests of blocks with discontinuity filled clay.

In the case of a), the residual strength was evaluated as the general shear strength of discontinuities surrounding the rock cavern. In the case of b), the strength of discontinuities stress relieved by excavation or weathered by water, and the case of c), carried out for three positions where discontinuities filled clay had been confirmed, i.e., the shear strength of weak discontinuities. The results of the shear tests of the various discontinuities are shown in Table 4.

Table 4. Share strength of discontinuities in C_H class rock masses

	Friction angle (degree)	Cohesion (MPa)	Condition of discontinuities
In-situ shear test	56	2.20	General discontinuity
Laboratory shear test			
No.5 boring core	35	0.107	Weathered discontinuity
Blocks with joint filled clay	20	0.015	Weak discontinuity

2.3 *Selection of Maximum Velocity on the Ground*

The maximum velocity of earthquake motion on the seismic bedrock was determined by studying the data from past earthquakes[10] and estimating the influence of the Adera and

Atotsugawa Faults, which are close to the rock cavern. Amplification factors near the surface deduced from ground response analysis and existing design practices were taken into consideration to determine the maximum velocity on the surface (Table 5).

Table 5. Maximum velocity on the ground surface in the dynamic stress-deformation analysis

(Unit; kine)

Level	Velocity on the bedrock	Amplification factor	Velocity on the ground surface	Remarks
Level 1	10	1.9	25	Effects of middle-scale middle-distance earthquakes
Level 2	25		50	Effects of the Atotsugawa Fault

3. DDA ANALYSIS MODEL

The 2-dimensional analytical model described in Figure 6 was used to predict the behavior of rock masses surrounding the underground opening, based on the survey of the C_H class rock masses. As the analytical section runs parallel to the Adera Fault system that is the third group, the block model consists of discontinuities of the low-angle system and the Atotsugawa Fault system.

For the analysis, as shown in Table 6, a total of four cases were considered. Three cases under normal conditions were studied for the differences in discontinuity shear strength with stress relieved by excavation as the loading condition. And the other one case for loading due to earthquake inertia forces resulting from seismic activity corresponding to a level 2 earthquake. For the direction of seismic loading in case 4, the force was left to right for the horizontal direction shown in the analysis model of Figure 6, and applied downwards in the vertical direction. The time interval for each step was $\Delta t = 0.2$ second for the normal loading cases and $\Delta t = 0.5$ second for the earthquake loading case. The number of steps was 500. For the physical properties of the blocks, the weight per unit volume was taken as $\gamma = 2.6$ ton/m^3, modulus of elasticity E = 5,470 MPa, and Poisson's ratio $\nu = 0.27$. With regard to the initial stresses, the AE method was used. As a result, the vertical stress was taken to be approximately equal to the self-weight of the overburden ($\sigma_V = \gamma H$), and the horizontal stress half that value ($\sigma_H = 0.5\sigma_V$). For each case, a total of 13 fixed points were set.

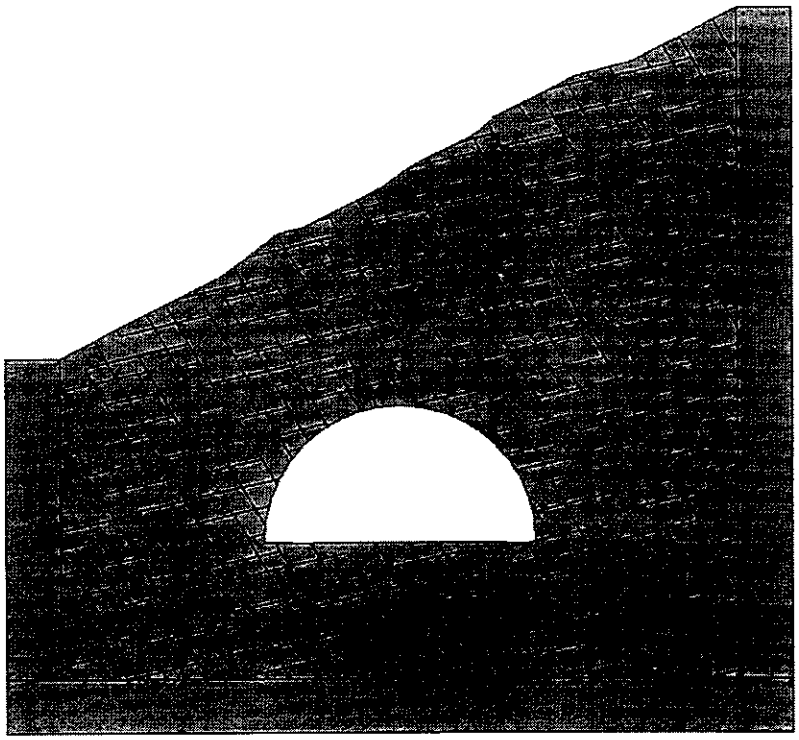

Figure 6. DDA block model

Table 6. Cases and each condition of DDA

Case	Shear strength of discontinuity		Condition of stress and load	Time step (sec.)	Number of step
	Friction angle (degree)	Cohesion (MPa)			
1	56	2.20	Initial stress	0.2	500
2	35	0.107	Initial stress	0.2	500
3	20	0.015	Initial stress	0.2	500
4	56	2.20	Initial stress and inertia force Seismic intensity is 0.65 (horizontal) and 0.33 (vertical)	0.05	500

4. RESULTS OF DDA

The block displacement and deformation results obtained by analysis for each case is shown in Figure 7. Principal stress of case 3 is shown in Figure 8.

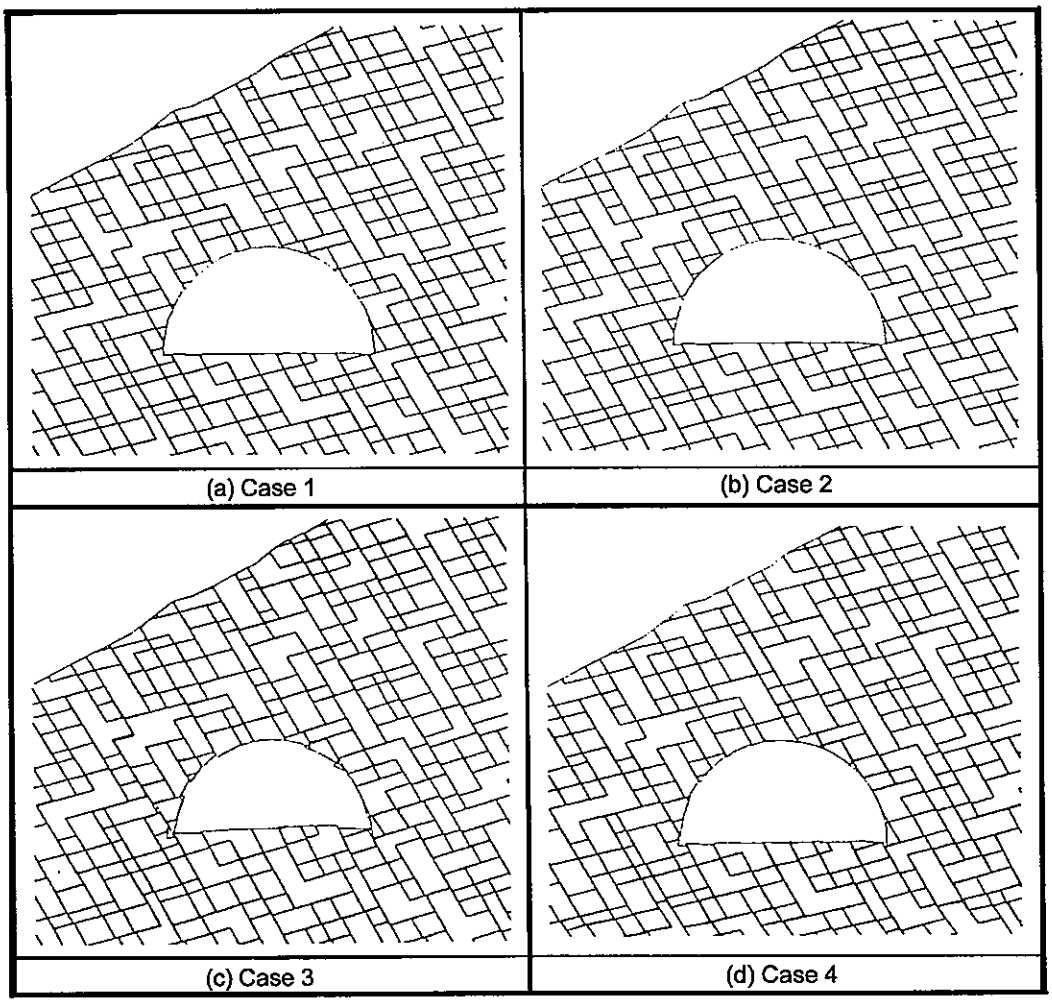

Figure 7. Results of DDA (Displacement and deformation of the blocks of C_H class)

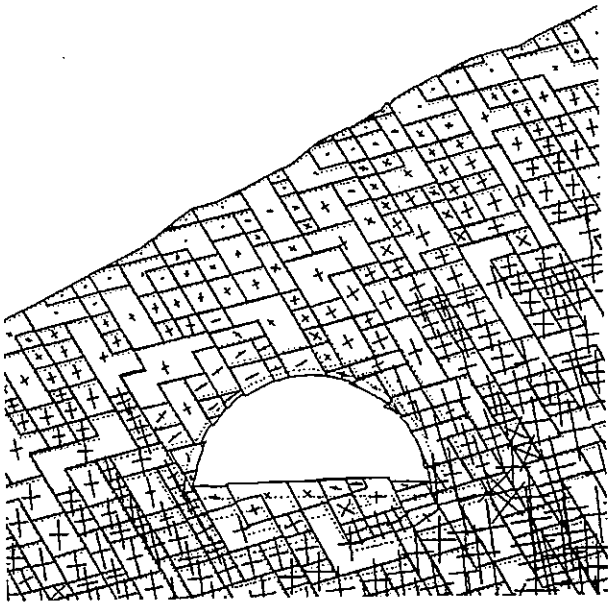

Figure 8. Principal stresses of case 3

4.1 *Comparison by a Property of Discontinuities*

For case 1 (ϕ = 56 deg., c = 2.2 MPa), the maximum displacement occurring at the base was 3.5mm and block dropping during excavation would not be anticipated. For this case, the results are the same as those obtained by FEM analysis.

For case 2 (ϕ = 35 deg., c = 0.107 MPa), the friction angle of discontinuities loosened due to excavation or weathering is near the basic friction angle. The maximum displacement being 16.4mm, dropping of one upper right block could be considered possible.

For case 3 (ϕ = 20 deg., c = 0.15 MPa), the evaluation of the shear strength of all the discontinuities in the model was performed on the assumption that the discontinuity was a weak surface filled clay. The breaking out and dropping of upper blocks and pushing out of blocks in the left wall were clearly evident. Furthermore, the opening of the discontinuity advanced about 5.7m from the excavation surface. The maximum displacement was 540mm indicating considerable deformation behavior.

4.2 *In Case during Earthquake*

For case 4, in case during earthquake, the analysis was performed to examine the failure of the rock cavern with shallow overburden during earthquake in which tensile failure was considered to occur as the result of opening of the discontinuities contained by the rock mass. The result of analyses using the value of shear strength of the low-angle fault system discontinuities obtained from in-situ shear tests showed that tensile stress occurred in the upper left two blocks only, and a maximum displacement of 40mm resulted in the upper left portion.

5. CONCLUSIONS

In this paper, the evaluation of input parameters and the behavior of rock masses with discontinuities were studied using DDA analysis for the construction of a large-scale underground opening. From the results, in particular the following conclusions can be drawn:

1) Even in the case of a large underground opening with shallow overburden, in a relatively stiff rock mass, if the shape of the space is such that the stress flow in the tangential direction is easily maintained, deformation behavior due to excavation will be small.
2) In the progressive opening of a discontinuity, the existence of a weak discontinuity is a major contributing factor.

For this analysis model, as typical values were used without taking into account the unevenness of such things as the distribution of discontinuities, it is necessary that additional consideration be given during management of the construction phase.

There are few cases of analysis involving complex 3-dimensional distributions of discontinuities for the case of large underground openings. Therefore, it is planned to carry out

research by gathering data during the construction of this rock cavern in order to confirm the applicability of the analysis methods.

ACKNOWLEDGMENT

The authors are deeply indebted to Dr. Gen-Hua Shi, for providing DDA source code and his valuable comments at this construction site in Takayama. Thanks are also due to Mr. Kinta Nakada for funding this project and making every effort to realize it. In addition, we also thank Mr. Yutaka Hosoe for his careful preparations at the construction site.

REFERENCES

1. Laine, O., et al. 1986. "Rock Engineering in Finland" Finnish Tunneling Association.
2. Saari, K., et al. 1988. "The Rock Engineering Alternative" Finnish Tunneling Association.
3. Barton, N., Tunbridge, L., et al. 1991. "Design Studies for Norway's Olympic Cavern" *Tunnels & Tunneling*, 22-25.
4. Nakada, K., Chikahisa, H., Kobayashi, K. and Sakurai, S. 1996. "The Plan and Survey of an Underground Art Museum in Japan, Using Large-Scale Rock Cavern" *Tunnelling and Underground Space Technology* **11**(4), 431-443.
5. Chikahisa, H., Kobayashi, K., Matsumoto, K., Nakahara, H. and Tsutsui, M. 1995. "Planning and Design of Underground Rock Cavern with Shallow Overburden (in Japanese)" *The Proceedings of the Symposium on Underground Space (JSCE)* **1**, 7-16.
6. The Research Group for Active Faults of Japan. 1991. "Active faults in Japan: Sheet Maps and Inventories (in Japanese)" University of Tokyo Press.
7. Yoshinaka, R., Yoshida, J. and Fujita, T. 1987. "Three-dimensional Statistical Approach to Joint Orientation Data and its Application to Block Theory" *Proceedings of the 7th Japan Symposium on Rock Mechanics*.
8. Mantab, M. A., Bolstad, D. D., Alldredge, J. R. and Shanley, R. J. "Analysis of Fracture Orientation for Input to Structural Models of Discontinuous Rock" 1972. U.S. Bureau of Mines, Report of Investigation 7669.
9. Priest, S. D. and Hudson, J. A. 1981. "Estimation of Discontinuity Spacing and Trace Length Using Scanline" *Int. J. Rock Mech. Min. Sci. & Geomech. Abstr.* **18**, 183-197.
10. Sugiyama, T. 1990. "A Map of Expected Maximum Acceleration in Chubu Area (in Japanese)" *Reports of Structural Studies* **411**, 19-27.

Manifold Method And Its Applications To Engineering

Weiyuan Zhou, Qiang Yang and Xiaodong Kou
Dept. of Hydraulic Eng., Tsinghua University, Beijing, PR China

ABSTRACT: The manifold method is an approximate method for solving differential equations defined in a domain with arbitrary shapes. It is applicable to any boundary value problems with moving least square interpolants. This method requires only nodal data. No element connectivity is needed. Lagrangian multipliers are used to ensure the essential boundary conditions in smooth mathematics states. Weighted orthogonal basis functions are constructed so that the requirement for solving equations at each quadrature point is eliminated. In this paper, the manifold method is described. The newly developed "manifold method", based on finite cover systems, has the potential to meet more engineering requirements. Dr. Gen-hua Shi (1991) proposed this method. In his paper "numerical manifold Method", the term "manifold" is defined as a generalization of the differential manifold which is the main subject of differential geometry, topology, differential topology and modern algebra of mathematics. The difference of the manifold and the traditional differential manifold is the following: the global functions of the differential manifold are highly differentiable and entirely defined irrelevant with the covers; the defined global functions of the manifold are based on covers and only piecewise differentiable, mostly discontinuous on the contact interfaces. Manifolds connect many individual folded domains together to cover the entire material domains. The basic theory of the manifold method is expressed and explained in this paper.

1 INTRODUCTION

In geotechnique engineering, it has become clear that in numerical analysis, mesh generation is a far more time-consuming and expensive task than assembly and solution of the finite element equations. It requires a lot of time for preparation of data. Three dimensional meshing is still an extremely burdensome task and the conversion of solid models to finite element data is time-consuming and often introduces numerous ambiguities.
Nayrole *et al.* (1992) have recently introduced a very interesting and promising method which they call the diffuse element method. In this method, only a mesh of nodes and a boundary description is needed to developed the Galerkin Equations. The interpolating functions are polynomials which are fit to the nodal values by least-square approximation. The finite element mesh is totally unnecessary in this method.
In the domain of composite materials, the corresponding integral representation of the solution of the boundary-value problem is proximate with the account of interpolants of the derivatives of some orders which is defined within a cover.

Numerical examples makes it clear that by manifold method stress concentrations and stress intensity factors at discontinuities could be computed very conveniently. For crack propagation and coalescence of fissures, it is very advantageous to compute their behaviours without remeshment around crack tips.
The manifold method was developed with element-free method to cope with coupled problems involving discontinua and continua. It may be widely used in solving geotechnique problems which generally imply discontinuous joints in rock materials such as, slope slides, foundation stability and underground engineering.

2 MANIFOLD STRUCTURE AND COVERS ON POLYGON DOMAINS

Set M forms a differential manifold structure if defining M a set of limited and countable charts. A point in set M corresponds a chart in the domain. In Euclidean space, $q = q(q_1, q_2, \cdots, q_n)$, there exists a one-to-one mapping $f : W \to U$, subset $W \subset U$. Set M in U domain, so the map function is a open set as shown in Fig. 1(a).
• There exist manifold structure and map in sphere surface $S^2(x, y, z) : x^2 + y^2 + z^2 = 1$. For example, two stereographic projections $(U_i, f_i, i = 1, 2)$, as shown in Fig. 1(b),

$$\begin{aligned} W_1 &= S^2 - (N), \qquad & U_1 &= R_1^2 \\ W_2 &= S^2 - (S), \qquad & U_2 &= R_2^2 \end{aligned} \tag{1}$$

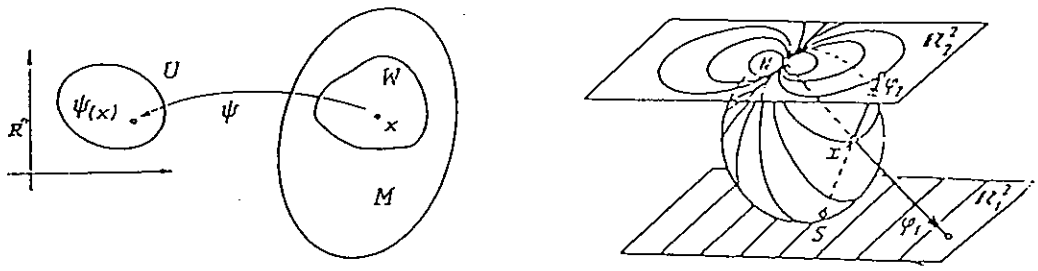

(a) (b)

Figure 1: Map of manifold

The manifold method is adopted to find the approximate solution of a boundary value problem. At first, overlapped covers are set up in the polygon domain K. Interpolating functions are to be established, which satisfy the boundary values. For each cover, an approximate solution which may be certain elementary functions is established. As shown in Fig. 2, P_j, $j = 1, 2, \cdots, n_b$ are the vertices of the polygon K; P_q, $q = n_b + 1, \cdots, l$ are middle points of its sides in the polygon; P_m, $m = l + 1, \cdots, M$ are inner points of K where $n_b < l < M$.
An approximate solution is found by the manifold method for a polygon domain. The cover for K polygon is referred to countable covers which exhibit sectors, circular disks or semicircular disks.
Shape functions in covered domains could be used to express the mathematical solutions in the domain. They may be some basic functions fitted to special boundaries or derivatives along the interfaces between neighbor domains. As shown in Fig. 2, these expressions form the base of boundary solutions when using the manifold method.

3 DISCRETE COORDINATE FUNCTIONS DEFINED IN COVERED DOMAINS

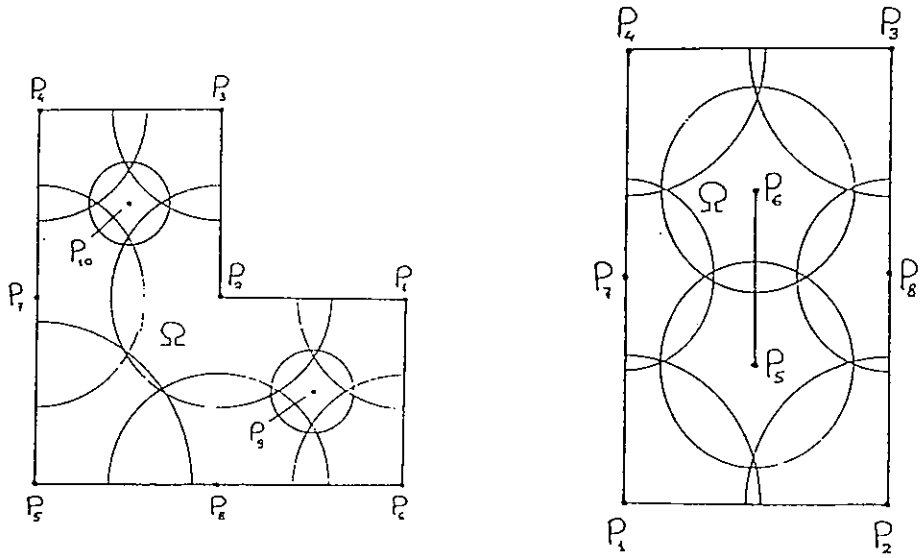

Figure 2: A multifold covering of the polygon K

It is different with F.E.M for implementation of manifold method to establish shape functions which are found by the way given below:
On assuming that u denotes the function within a cover, their values on fitted pointed are u_i, $i = 1, 2, \cdots n$. The function $u_k(x)$ is the approximate function of u,

$$u_k(x) = \sum_{i=1}^{n} \lambda(x) u_i \tag{2}$$

Covers are established over polygon K, which require a shape function. The shape function is found by the weighted residual method. The above mentioned shape function is expressed by piecewise continuous functions, which will lead to the structure stiffness matrix after the shape functions are set up.
In a cover, any number of points may be assumed to be fitted points for the solution in the domain. The value for the fitted points are given below:

$$u_i = u(x_i) \qquad i = 1, 2, \cdots n. \tag{3}$$

and their approximate solutions are

$$u_k = \sum_{i=1}^{n} \lambda_i(x) u_i \qquad i = 1, 2, \cdots n. \tag{4}$$

which may be expressed in terms of multi-variable polynomial, triangular polynomials, Legendre or Chilisheve polynomials.
In order to find u_k, a basic function $\Phi = \{\Phi_1, \Phi_2, \cdots, \Phi_m\}^T$ is defined in cover C, and then

$$u_k = \sum_{j=1}^{m} \Phi_j(x) a_j = \Phi^T(x) \mathbf{a} \tag{5}$$

where $\mathbf{a} = \{a_1, a_2, \cdots, a_m\}^T$ is one set of unknown parameters. At each nodal points in the domain,

$$u_k(x_i) = \sum_{j=1}^{m} \Phi_j(x_i) a_j \tag{6}$$

By moving least square method, $u_k(x_i)$ could be found for weighted function $W(x_i)$

$$\min \int_c W(x_i)[u_k(x_i) - u_i]^2 dc = \min \int_c W(x_i)[\Phi^T(x_i)\mathbf{a} - u_i]^2 dc \tag{7}$$

The derivative of Eqn. 7 with respect to a leads to

$$\begin{aligned} &2W(x_i)[\Phi^T(x_i)\mathbf{a} - u(x_i)]\phi(x_i) = 0 \\ &W\Phi^T\mathbf{a}\Phi = Wu\Phi \\ &W\Phi^T\Phi\mathbf{a} = W\Phi u \end{aligned} \tag{8}$$

If set

$$S = W\Phi^T\Phi, \qquad T = W\Phi \tag{9}$$

then

$$S\mathbf{a} = Tu \Longrightarrow \mathbf{a} = S^{-1}Tu \tag{10}$$

and

$$u_k = \Phi^T S^{-1} T u = \lambda u \tag{11}$$

The shape function λ are expressed as

$$\lambda = \Phi^T S^{-1} T \tag{12}$$

and

$$\lambda_{,i}^T = \Phi_{,i}^T S^{-1} + \Phi^T(S^{-1}T_{,i}) = \Phi_{,i}^T S^{-1} T + \Phi^T(S_{,i}^{-1}T) + \Phi^T(S^{-1}T_{,i}) \tag{13}$$

By means of shape functions, the unknowns u can be obtained consequently.

4 GALERKIN METHOD IN SOLUTION OF BOUNDARY PROBLEMS

In domain K, its boundary problem based on the manifold method concept which is described above are easily solved by various numerical methods. Here Galerkin method is applied. Based on variational principles, the equation to be solved is:

$$Lu = f \qquad n \in k \tag{14}$$

According to the Galerkin method,

$$(Lu_0 - f, \Phi_i) = 0, \quad i = 1, 2, \cdots, n \tag{15}$$

The solution of eqn. (15) is equivalent to that of eqn. (14). Within the cover C, linear functions are adopted as

$$u_h = \sum_{l=1}^{k} \Phi_l u_l \tag{16}$$

It is clear u_h denote those unknowns to be solved linear equation. Eqn. (15) become

$$\sum_{l=1}^{k}(L\Phi_l, \Phi_k)u_l = (f, \Phi_k) \qquad k = 1, 2, \cdots, n \tag{17}$$

This formula gives weak form solutions, and they are obtained from each cover domains. It is shown as Fig. 3.

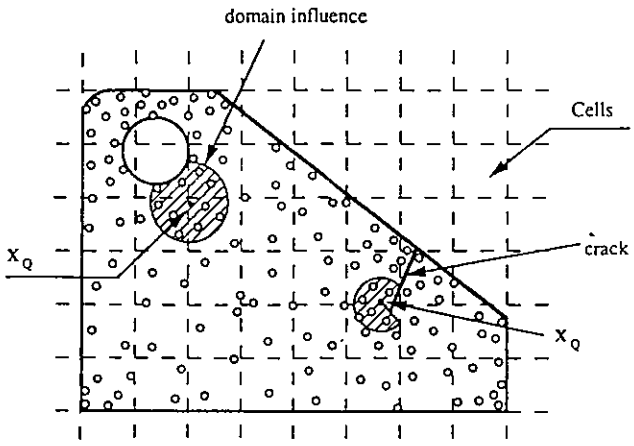

Figure 3: Covers for quadrature of structure

5 GEOTECHNIQUE ENGINEERING APPLICATIONS

In a domain Ω, a boundary value problem can be defined as

$$\begin{aligned} \nabla\boldsymbol{\sigma} + \mathbf{b} &= 0 \\ \boldsymbol{\sigma}\cdot\mathbf{n} &= \bar{\mathbf{t}} \quad \text{on stress boundary} \quad \Gamma_t \\ \mathbf{u} &= \bar{\mathbf{u}} \quad \text{on displacement boundary} \quad \Gamma_u \end{aligned} \tag{18}$$

In the domain Ω, the quadrature variational equation is

$$\int_\Omega \delta(\nabla V^T) : \boldsymbol{\sigma} d\Omega = \int_\Omega \delta V^T \cdot \mathbf{b} d\Omega + \int_{\Gamma_t} \delta V^T \cdot \bar{\mathbf{t}} d\Gamma + \int_{\Gamma_u} \delta\lambda^T \cdot (\mathbf{u} - \bar{\mathbf{u}}) d\Gamma + \int_{\Gamma_u} \delta V^T \cdot \lambda d\Gamma \tag{19}$$

where λ is introduced as Lagrangian multipliers. By using eqn. (16), the stiffness matrix is obtained as

$$\begin{aligned} K_{ij} &= \int_\Omega B_i^T D B_j d\Omega - \int_{\Gamma_u} \Phi_i S N D B_j d\Gamma - \int \Gamma_u B_i^T D^T N^T S \Phi_j d\Gamma \\ f_i &= \int_{\Gamma_t} \Phi_i F d\Gamma + \int_\Omega \Phi_i b d\Omega + \int_{\Gamma_u} B_i^t D^T N^T S \bar{\mathbf{u}} d\Gamma \end{aligned} \tag{20}$$

where

$$B_i = \begin{bmatrix} \Phi_{i,x} & 0 \\ 0 & \Phi_{i,y} \\ \Phi_{i,y} & \Phi_{i,x} \end{bmatrix} \qquad N = \begin{bmatrix} n_x & 0 & n_y \\ 0 & n_y & n_x \end{bmatrix} \qquad S = \begin{bmatrix} S_x & 0 \\ 0 & S_y \end{bmatrix} \tag{21}$$

where

$$S_x = \begin{cases} 1, & u_x \quad \text{prescribed on} \quad \Gamma_u \\ 0, & u_x \quad \text{unknown on} \quad \Gamma_u \end{cases} \qquad S_y = \begin{cases} 1, & u_y \quad \text{prescribed on} \quad \Gamma_u \\ 0, & u_y \quad \text{unknown on} \quad \Gamma_u \end{cases} \tag{22}$$

A test example is a cantilever beam. From the elasticity theory, the exact solution is

$$\begin{aligned} u_x &= \frac{P}{6EJ}(y - \frac{d}{2})[(6l - 3x)x + (2 + \nu)(y^2 - 2Dy)] \\ u_y &= \frac{P}{6EJ}[3\nu(y^2 - 2Dy + \frac{D^2}{2})(l - x) + \frac{1}{4}(4 + 5\nu)D^2x + 3(l - \frac{x}{3})x^2] \end{aligned} \tag{23}$$

where

$$J = \frac{D^3}{12} \tag{24}$$

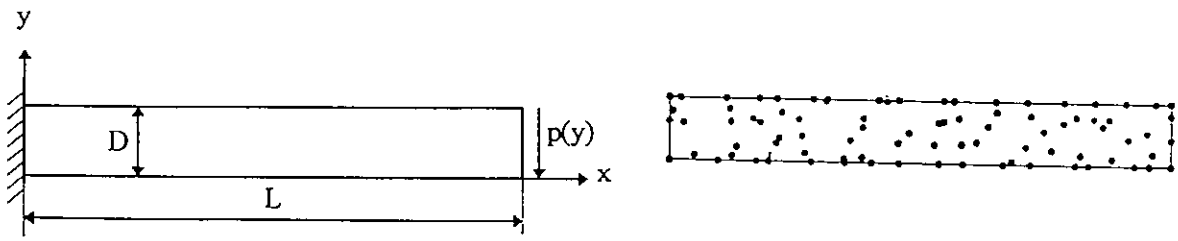

Figure 4: Description of the beam problem and nodal points

The configuration of the manifold method calculation is shown in Fig. 4 where $E = 3 \times 10^7$, $D = 1$, $L = 8$. The comparison of the manifold method, the finite element method and the elasticity theory is shown in Table 1. The result has illustrated that the manifold method has higher accuracy than that of the finite element method and can even reach high accuracy when the material is near incompressible state.

method	$\nu = 0.25$	$\nu = 0.4999$
manifold method	0.999	0.999
F.E.M.	0.607	0.029

Table 1: Ratio of deflection $W^{\text{num}}/W^{\text{exact}}$

Another test example is about a semi-infinite body subjected to a concentrated force. Here only a plane problem is considered with a simplified model, see Fig. 5(a). As shown in Fig. 5(c), it is quite evident that the result of the element free method (EFM) is much closer to the exact solution than that of the finite element method (FEM).
Here shown the stability analysis of the ship lock at Three Gorges Project in China on the Yangtse River. It is a five-stage lock with steep banks in two sides. A water head of 160m is applied on the dam after reservoir water impounding. The ship lock is going to be excavated in three years. As shown in Fig. 7, a layout of the ship lock and profile are presented. In the lock site, granite rocks with joints and faults have been found. A lot of research had been done about the stability of the lock. In the paper, manifold method is used to analyze the slope behaviour and its stability. It is clear that no elements data are required. Only nodal point data are provided. The slope stability factor contour obtained by the manifold method are presented in Fig. 6

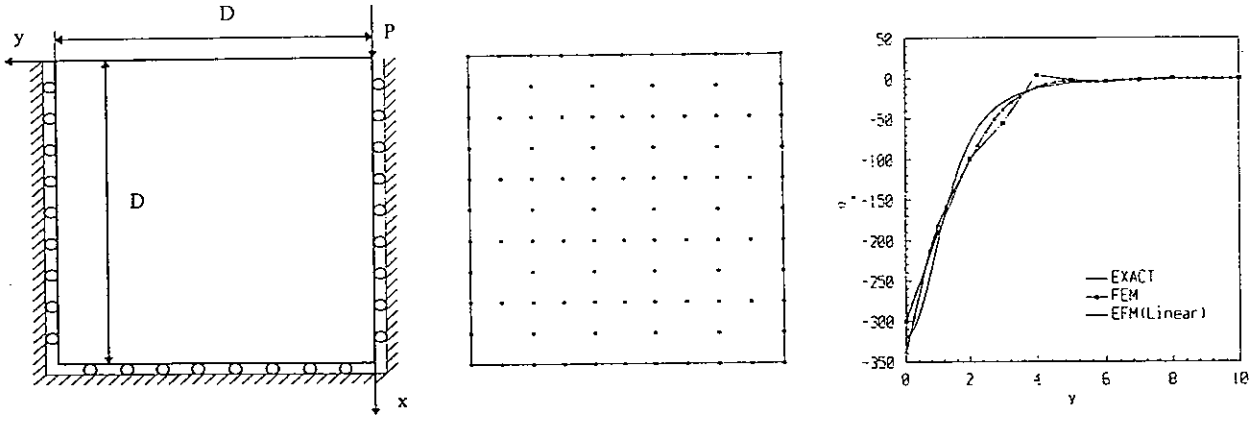

(a) (b) (b)

Figure 5: A plane semi-infinite problem (a) simplified model; (b) node distribution; (c) normal stress σ_x distribution at $x = 2$

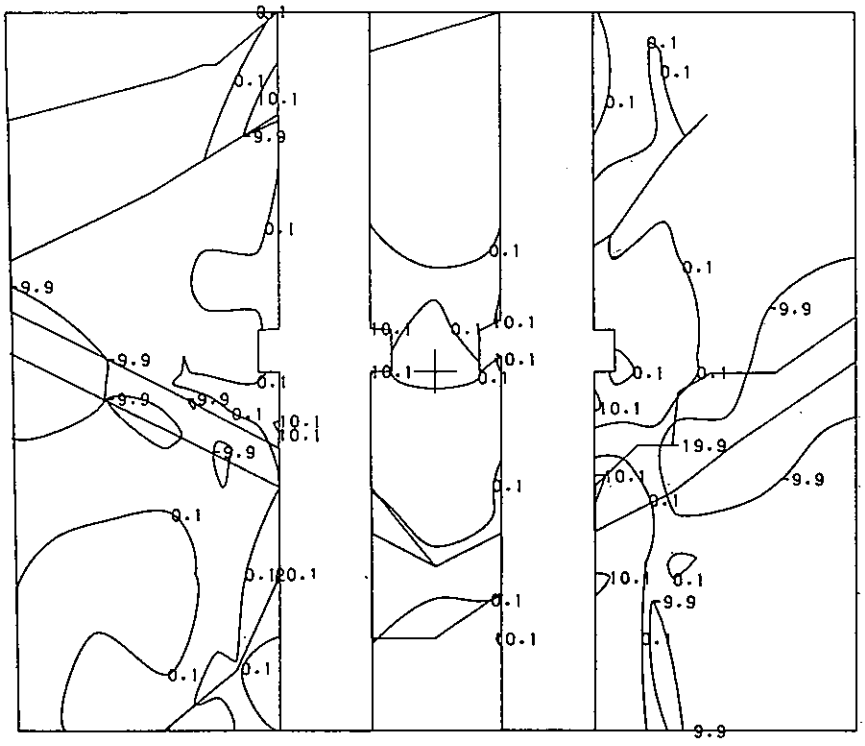

Figure 6: Point safety factor distribution of Three Gorges ship lock on the horizontal cross section at ∇ 150.00

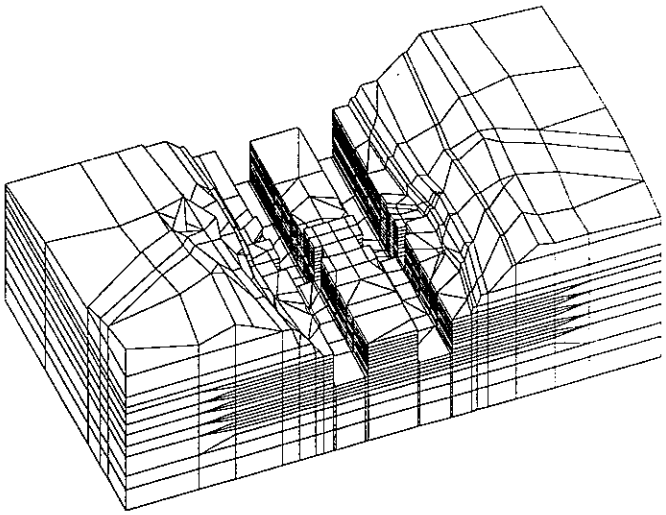

Figure 7: Layout of the Three Gorges ship lock

6 CONCLUSION

The starting point of the manifold method and element-free method is to simplify the analysis procedure and use coarse integration. The test example shows that such ways don't decrease the accuracy of the numerical result.
Since the interpolants in the method is for all domain, the smoothing step in F.E.M postprocessing procedure can be omitted.
The manifold method and element-free method has great potential for geotechnique engineering problem because the mesh generation becomes totally unnecessary in the method.

ACKNOWLEDGMENTS: The research work reported here is supported by National Science Foundation and Chengdu Hydroelectric Design Institute. The work of Yang Ruoqiong, Yan Gongri, Xiao Hongtian and Wang Zhiren is appreciated greatly.

REFERENCES

Belyschko, T., Lu, Y. Y. and Gu L. (1994). Element-free Galerkin Methods. *Int. J. for Num. Methods in Eng.* **37**, 329-256.

Lin, Dezhang, Mo, Haihong, (1994). Manifold method of material analysis. R.M.I., The Univ. of Oklahoma.

Lu, Y. Y., Belyschko, T. and Gu L. (1994). A new implementation of the element free Galerkin Method. *Compu. Methods Appl. Mech. Enggr.* **113**, 397-414.

Nayrole, B., Touzot, G. and Villon, P. (1992). Generating the finite element method: diffuse approximation and diffuse elements. *Comput. Mech.* **10**, 307-318.

Shi, Genhua (1991). Manifold Method of Material Analysis. *Transaction of the Ninth Army Conference*, on Applied Mathematics and Computing. 51-76. Minneapolish Minnesoda.

Shi, Genhua (1992). Manifold Method Fractured and Jointed Rock Masses. Lake Tahoe, California.

Crack Propagation and Thermal Fracture Analysis by Manifold Method

Guo-Xin Zhang, Yasuhito Sugiura and Hiroo Hasegawa

I.N.A. Corporation ,Tokyo 112 Japan

ABSTRACT

Manifold method is used to simulate crack initiation and propagation and thermal fracture problem. By supposing that cracks can only initiate and propagate along the edge of mathematical mesh and failure criterion follows three parameters Mohr-coulomb's low, and by adding thermal load item ,the original manifold method proposed by Shi is extended. The modified version of manifold method program can be used to simulate crack propagation problems both static and dynamic. And can also be used to analysis thermal fracture problems which can be often seen in engineering structures. Some numerical examples showing the application of the modified manifold method are presented .

INTRODUCTION

Manifold method is a new numerical method which provides a unified framework for solving problems dealing with both continuous and discontinuous media, since it first introduced by Shi [1][2] , the concept and potential use of it has drawn a great attention from international researchers in engineering fields. The most innovative features of manifold method are the concept of cover and the use of two set of meshes. The covers overlap each other and form the displacement and stress in the whole region. The two set of meshes are physical meshes and mathematical meshes . The physical meshes describe the physical domain include boundary and discontinuities of problem to be solved and define the integration area, the mathematical meshes is used to build covers and has to be larger enough to cover every point of the physical mesh. The concept of covers and the use of two sets of meshes make manifold method can be viewed as the combination of finite element method and DDA ,so it has the advantages both FEM and DDA : can solve continuous , discontinuous ,contact, large scale deformation and movement problems like DDA and can get fine stress distribution like FEM. These powerful abilities of manifold method make it possible to simulate crack initiation and propagation problems.

Recently, there are two kinds of techniques have been developed in dealing with fracture problems by DDA and manifold method. One is so called "artificial joint-based" method introduced by Ke [3][4]. In this method ,the block domain is divided into sub-blocks by imaginary boundaries and these imaginary boundaries are called "artificial joint". Strengths are assigned to the artificial joints so that the original block is still a solid one. If

the stress state on an artificial joint satisfies Mohr-Coulomb's low ,the artificial joint cracks and becomes a real boundary. Another technique was developed by AMADEI et al [5][6] . In this method, intact block is also divided into sub-blocks and the continuity is preserved along the sub-block contacts. A crack has been pre-initiated and can propagate not along the edges of sub-blocks but through the sub-block in front of the crack tip. Both methods use Mohr-Coulomb's low as the failure criterion.

In this paper, crack initiation and propagation problem is also studied by manifold method. In dealing with fracture of structure, no sub-blocks are divided ,but it is supposed that cracks can only initiate and propagate along the edge of mathematical meshes. And thermal load is also added to Shi's original manifold method to simulate thermal fracture problems. Some numerical examples are given to show the validity of the new extension of manifold method.

CRACK MODOLING

In this paper, it is supposed that cracks can only initiate and propagate along the edge of mathematical meshes (or elements) .

In manifold method, mathematical meshes and physical meshes divide the physical domain with discontinuities into elements, and every element is covered by three covers. For examples, in Fig.1 physical meshes (solid line) and mathematical meshes (dot line) divide the block with one joint c-d into 7 elements. Because the cover associated with node 5 is divided into two by physical meshes, there are 8 covers : 1,2,3,4,5_1,5_2,6,7. Element ① is covered by covers 1,4,3; element ② is covered by 1,2,4;.....;element ⑥ is covered by covers 4,5_1,7; element ⑦ is covered by 4,5_2,7. If the adjacent edge of two adjacent elements is a physical joint, displacement here is discontinuous, but if the adjacent edge is not a physical joint but the edge of mathematical meshes, displacement compatibility on this edge should be satisfied and the compatibility is ensured by the fact that the adjacent two elements are covered by two same covers. In Fig .1 ,both element ① and ④ are covered by covers 3 and 4,so that the displacement on edge a-b is continuous.

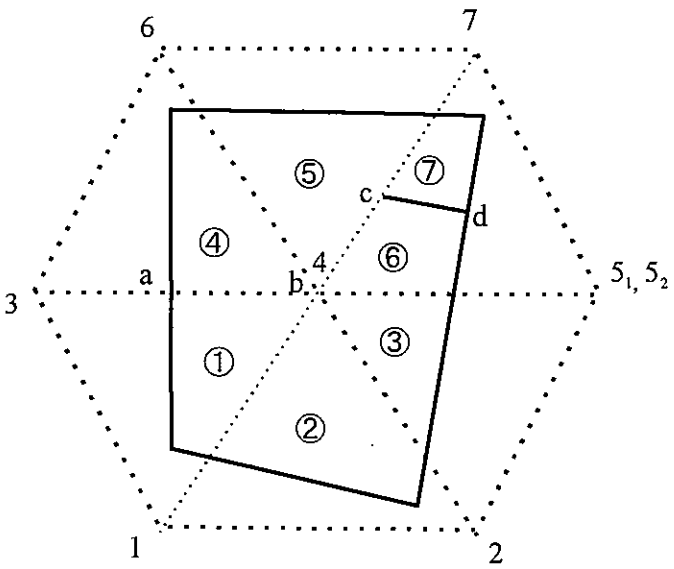

Fig. 1

But in the covers that cover elements ⑥ ,⑦ ,because there is only one same cover 4,the displacement on edge c-d is not compatible and c-d is a physical joint. So that ,if two same covers cover two adjacent elements, the adjacent edge of these two elements is a edge of mathematical meshes; but if only one or no same cover among the covers that cover two adjacent elements, the adjacent edge of these two elements is a physical joint.

Based on the properties mention above, the joint propagation along the edges of mathematical meshes can be simulated. After a edge cracked, the new joint should be add into the physical meshes, but there are two cases in reforming the mathematical meshes: if the new joint broken the original cover into two, a new cover should be added into the cover system and the mathematical meshes should be reformed; but if the new joint did not brake any cover, nothing is needed to be done to the cover system and mathematical meshes. The concept of path-connectedness [7] can be used to decide whether a new joint brake a cover or not: if a cover is still path-connected after a edge cracked, the original cover is still one cover; if a cover is not path-connected after a edge cracked ,the cover is divided into two by the edge. For example, Fig. 2 shows a physical domain a-b-c-d with a physical joint e-f. Cover associated with node 4 covers the polygon of 1-2-5-7-6-3; cover associated with node 7 covers the polygon of 4-5-8-10-9-6. The existing of joint e-f has no influence to the connectedness of these two covers. If edge e-7 cracked , cover associated with node 7 is still path-connected because any pair of points can be connected by a path in it, but cover connected with node 4 is divided into two because any point in triangle e-f-7 can not be connected with a point in polygon of 1-2-5-f-7-6-3 outside the triangle of e-t-7 by a path in polygon of 1-2-5-f-7-6-3, so that cover associated with node 4 is divided into two by the new joint e-7 and new cover associated with node 4 should be added to covers system and the mathematical meshes should be reformed.

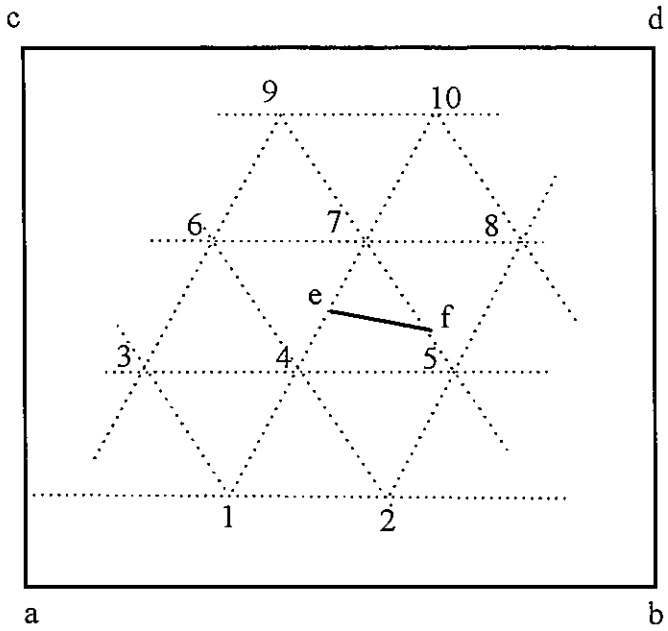

Fig. 2

The fracture criterion selected here is a Mohr-Coulomb's low with three parameters. Take σ'_y indicates the normal stress and τ'_{xy} indicates the shearing stress on a edge ,the fracture criterion is as bellow:

$$\begin{array}{lll} \sigma'_y = T_0 & & \textit{Tensile failure} \\ \left|\tau'_{xy}\right| = C & 0 < \sigma'_y < T_0 & \textit{Shearing failure} \\ \left|\tau'_{xy}\right| = C - \sigma'_y \tan\phi & \sigma'_y < 0 & \textit{Shearing failure} \end{array} \quad (1)$$

where : T_0 represents the tension strength of material, C represents cohesion, ϕ is the friction angle.

The stresses on every edges are the maximum stresses of two adjacent elements, and the stresses are transformed from global coordinate system to local coordinate system. For crack tip, if the stresses on all edges connected with crack tip do not satisfy the fracture criterion, the average stresses of all the elements surrounding the crack tip are used to judge if the crack propagates.

Analyzing procedures are different between dynamic and static problems. For dynamic problem, in every step of calculation, all the edges that satisfy the failure criterion above crack. But for static problem, because the results have no relation with time and calculation steps , the load are divided into several loading steps, in every loading step, many steps of calculation are performed , in every calculation step ,permitting only one edge with the maximum failure potential cracks, calculation continues until there is no new crack.

In the present research, no energy loss is considered during fracturing. In order to ensure the energy conservation, the new cover is enforced to have the same velocity and coordinate with the original one.

THERMAL LOADING MATRIX FOR COVER

Cracks always happen in massive concrete structures and rock mass, and thermally-induced stress can greatly influence the crack initiation and propagation(G.X Zhang et al[8][9], Frank.C. Tsai [10]).In the simulation of crack initiation and propagation of structure, thermal loading should be taken into consideration .

Under the linear expansion low, the immediate mechanical response of element e caused by temperature change is a variation of strains as blow:

$$\{\varepsilon_0\}_e = \alpha \Delta T_e \begin{Bmatrix} 1 \\ 1 \\ 0 \end{Bmatrix} \quad (2)$$

where $\{\varepsilon_0\}_e$ is the incremental of strain , α is the coefficient of linear expansion, ΔT_e is temperature change. The potential energy of element e caused by thermal expansion (2) is

$$\Pi_e = -\iint_e \{\sigma\}^T \{\varepsilon_0\}_e dxdy = -\{\delta\}_e^T \iint_e [B_e]^T [D]\{\varepsilon_0\}_e dxdy = -S_e \{\delta\}_e^T [B_e]^T [D]\{\varepsilon_0\}_e \qquad (3)$$

where S_e is the area of element e; $\{\delta\}_e^T$ is displacement incremental of element e; $[B]_e$ is strain matrix; $[D]$ is elastic matrix.

There for , the thermal loading matrix is

$$\{F\}_e^t = S_e \alpha \Delta T_e [B]_e^T [D] \begin{Bmatrix} 1 \\ 1 \\ 0 \end{Bmatrix} \qquad (4)$$

EXAMPLES

Block With Crack Loaded by Point Load

This example simulates the crack propagation in a block of 2×2m with a crack of 1 meter long loaded by vertical load and horizontal load. The material properties and calculation conditions are given in Table 1.

Fig. 3 depicts the principal stress field and crack propagation of cracked block loaded by vertical load P=100 t. Load P is divided into 10 steps , in every loading step 10 t of vertical load is loaded. At the first loading step, the stress in block is not large enough to let new crack initiates or the exiting crack propagates, but at the second loading step, the stress at the tip of exiting crack satisfies the Mohr-Coulomb's low , the crack begin to propagate (Fig.3 (b)). In every calculating step , the crack propagates through one edge of element, in six calculation steps of loading step two, the crack penetrates the block (Fig. 3 (c) (d)). Because the load P is still exerted on the block after the crack penetrates the block, new crack initiates near the point of load.

Table 1 Material Properties and Calculation Conditions

Elastic Modulus	19600 MPa
Poisson's Ratio	0.24
Unit Mass	2400kg/m³
Tension Strength T_0	0.98 MPa
Cohesion C	2.94 MPa
Friction Angle ϕ	30 degree
Calculation Mode	Static
Penalty	50000000 t/m

Fig. 4 shows the principal stress field and crack propagation of cracked block loaded by horizontal load H=100 t. The material properties and analysis conditions are same with the example above (see Table 1). Load H is also divided into 10 steps.

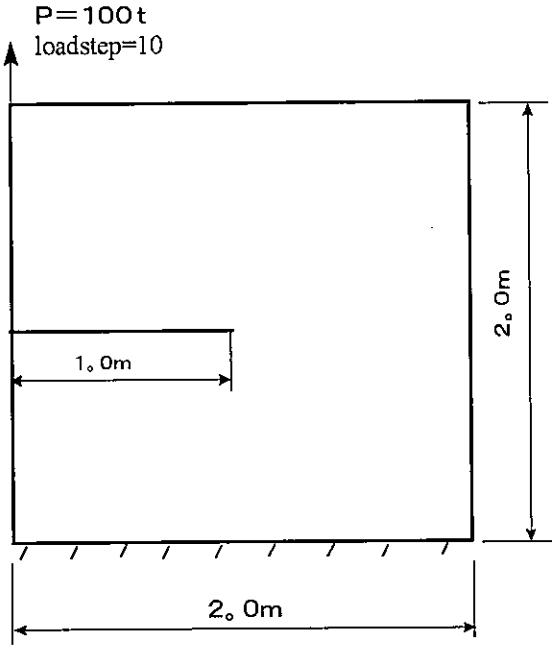

(a)

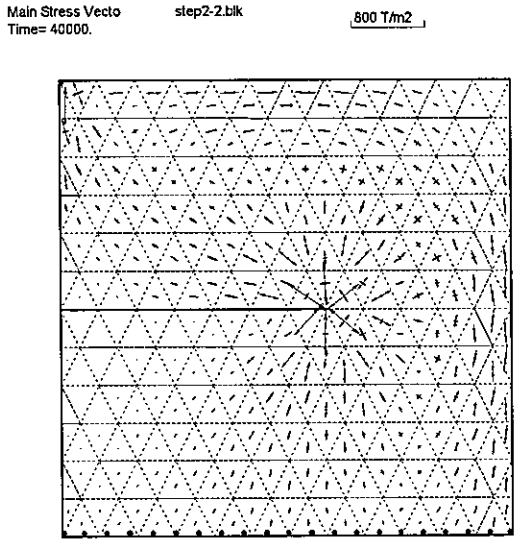

(b)

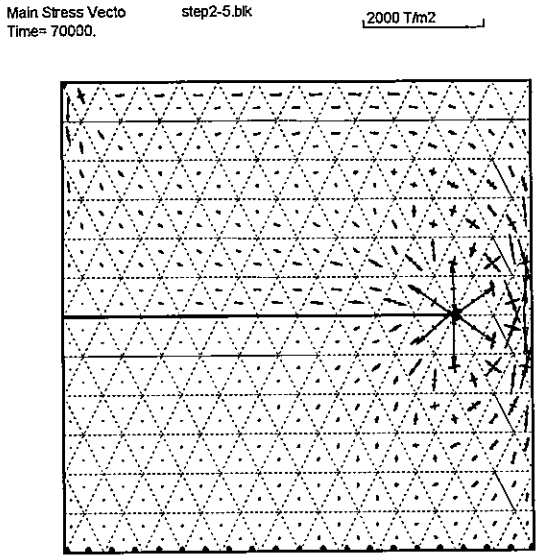

(c)

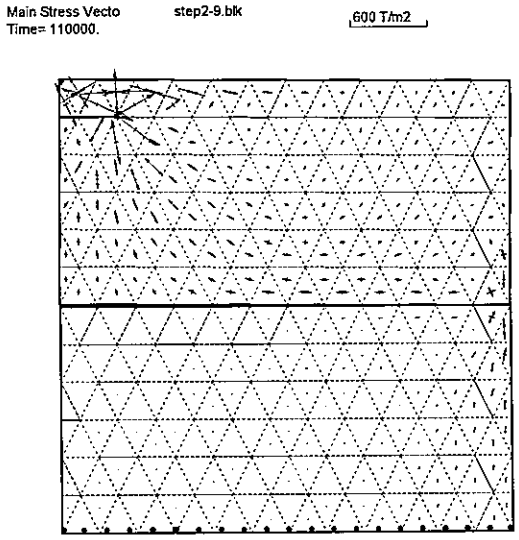

(d)

Fib. 3 (a) Block With Crack Loaded by Vertical Load P=100 t, Total Loadstep=10
(b) Crack Propagation and Principal Stress at Loadstep=2, Calculation step=2
(c) Crack Propagation and Principal Stress at Loadstep=2, Calculation step=5
(d) Crack Propagation and Principal Stress at Loadstep=2, Calculation step=9

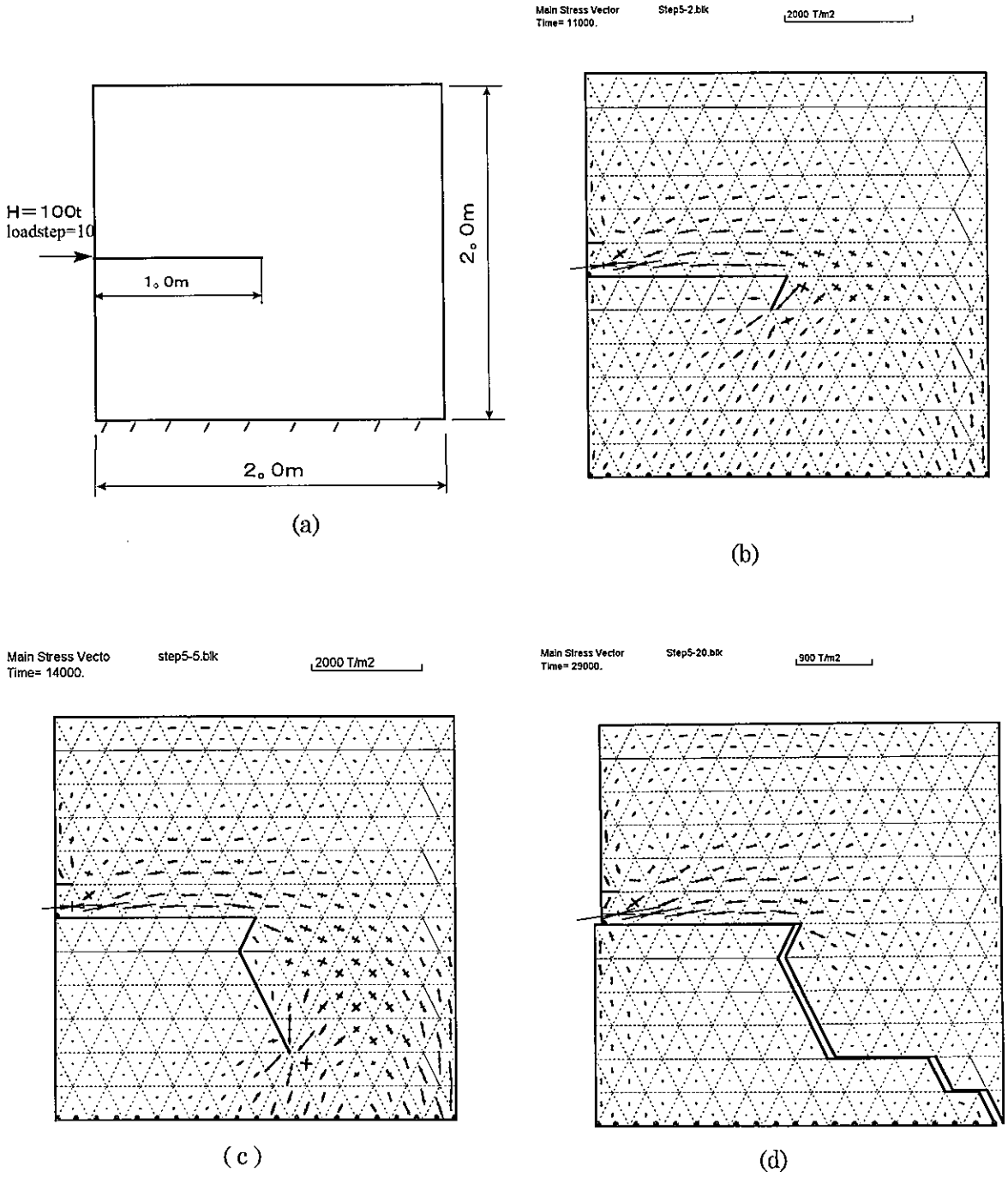

Fib. 4 (a) Block With Crack Loaded by Horizontal Load P=100 t, Total Loadstep=10
(b) Crack Propagation and Principal Stress at Loadstep=5,Calculation step=2
(c) Crack Propagation and Principal Stress at Loadstep=5,Calculation step=5
(d) Crack Propagation and Principal Stress at Loadstep=5,Calculation tsep=20

Because the stress concentration near the load point , new crack firstly initiates along the edge of element near the load at forth loading step. At fifth loading step, the old crack begin to propagates from the crack tip (Fig. 4 (b)), and in ten calculation steps the total block is broken. The displacement after twenty calculation steps in fifth loading step can be seen in Fig. 4 (d).

In this example, although the load H is parallel with the crack, but the crack also propagates in first mode, that is , the failure of edge is not caused by shear stress but tension stress.

Failure of Three Points Bending Beam.

Fig. 5 depicts a beam loaded by a vertical load P=50t at the central point of upper surface. The Young's modulus and Poisson's ratio of the beam are 19600 MPa and 0.2, respectively. The unit weight of material is 2.0 t/m³. The other parameters and analysis conditions are the same with that used in the example above and the 'static' mode is also used in this example. Load P is divided into ten loading steps. The principal stress ,displacement and crack propagation of some calculation steps at loading step 2 and 3 are shown in Fig. 6.

From Fig. 6 (a) it can be seen that, there are stress concentrations near two restrain points and loading point. The maximum tension stress occurs at the middle part of lower surface of the beam , the stresses are almost the same with the results got by means of structure mechanics. At third loading step, the maximum tension stress reach the failure criterion and new crack initiates at the middle of lower surface of the beam and the crack propagates until the beam ruptures (Fig.6 (b) (c) (d)). The results show that at the given condition, the bearing capacity of the beam is less than 30 ton.

If the load is continually applied on the beam, the broken blocks will move. A example of moved blocks is shown in Fig.6 (e).

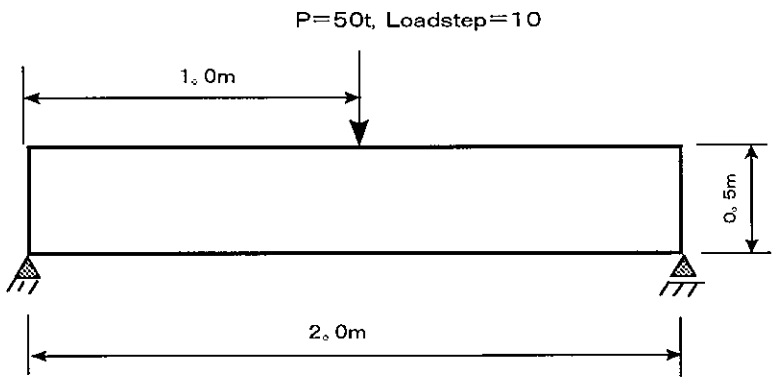

Fig. 5 Three Points Bending Beam

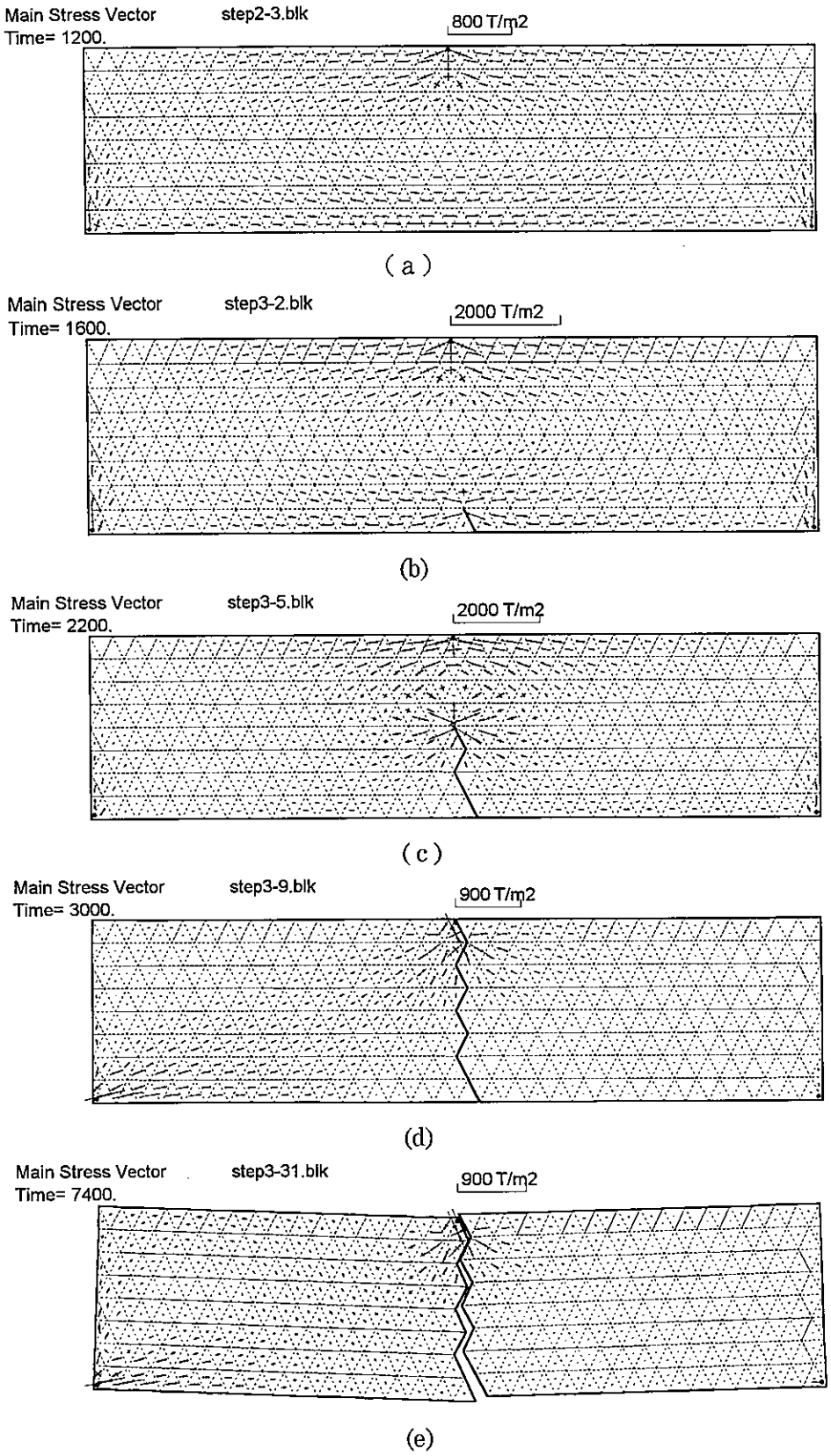

Fig. 6 Principal stress and crack propagation process at (a) loading step 2 calculation step 2, (b) loading step 3 calculation step 2, (c) loading step 3 calculation step 5, (d) loading step 3 calculation step 9, (e) loading step 3 calculation step 31,

Thermal Cracks of Concrete Block

Fig. 7 depicts two layers of concrete of 20 meters long and 9 meters high. The lower layer is old concrete, the upper layer is new concrete. Suppose when placing the new concrete, the temperature both old concrete and new concrete is 20℃. After the new concrete is placed, the surrounding temperature keeps 20℃ for 8 days, from the beginning of ninth day, the surrounding temperature drops 20 ℃ in two days, i.e. , the surrounding temperature becomes 0℃ after 10 days of new concrete is placed. The two side face and the lower surface of concrete is considered as isothermal, the heat transfers with surrounding only from upper surface of concrete. It is supposed that the hydration heat totally came out during first eight days, that is, no new hydration heat generates from ninth day and the adiabatic temperature arising of new concrete is 30℃. The temperature fields are calculated by FEM. The temperature field at the beginning of ninth day is shown in Fig. 8.

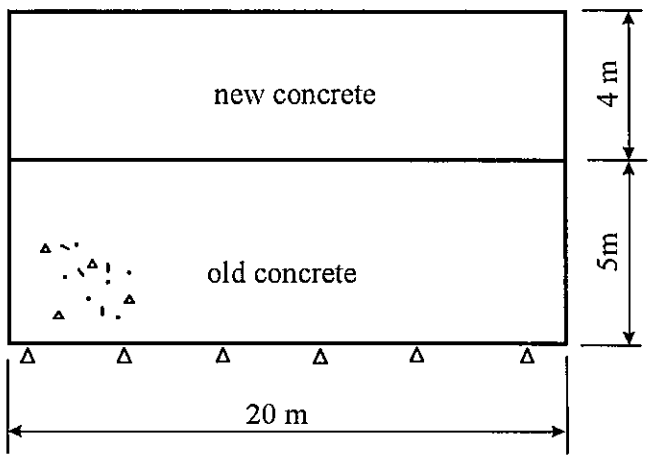

Fig. 7

Table 2 Material Properties and Calculation Conditions

		Old concrete	New Concrete
Elastic Modulus		19600 MPa	4900 MPa
Poisson's Ratio		0.2	0.2
Body force	fx	0.0	0.0
	fy	-2400kg/m³	-2400kg/m³
Unit Mass		2400kg/m³	2400kg/m³
Linear Expansion		0.00001 /℃	0.00001 /℃
Tension Strength T_0		0.98 MPa	0.49 MPa
Cohesion C		2.94 MPa	1.96 MPa
Friction Angle ϕ		30 degree	30 degree
Calculation Mode		Static	Static
Penalty		50000000 t/m	50000000 t/m

The numerical analysis by manifold method begins from ninth day after the new concrete is placed . The initial stress is supposed to be zero, and the Young's modulus is supposed to keep constant. The parameters and conditions used in analysis are shown in Table 2.

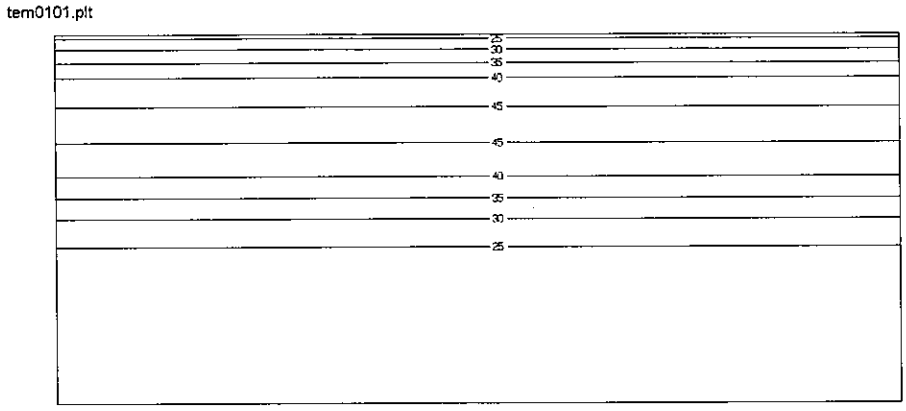

Fig. 8 Initial Temperature Field for Thermal Fracture Analysis

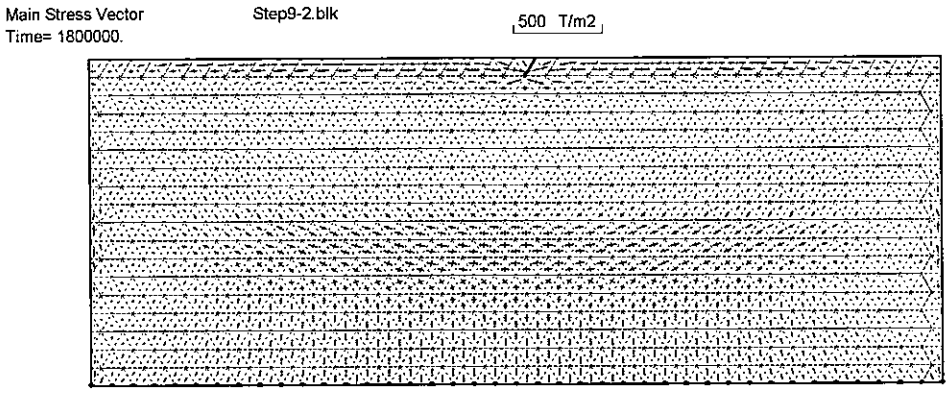

(a)

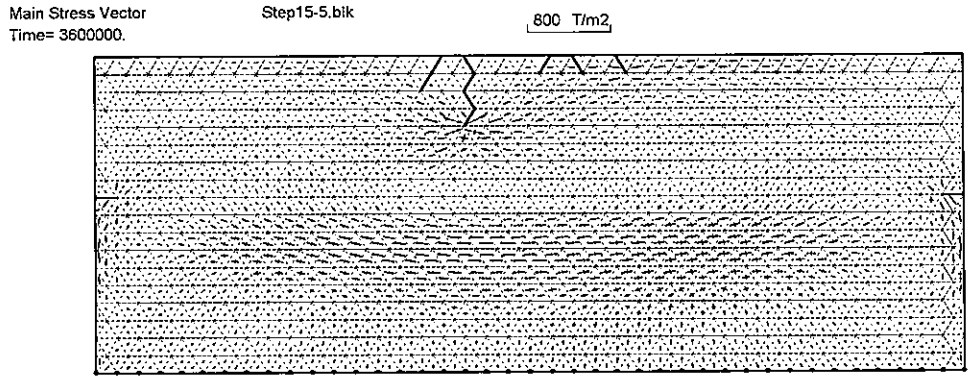

(b)

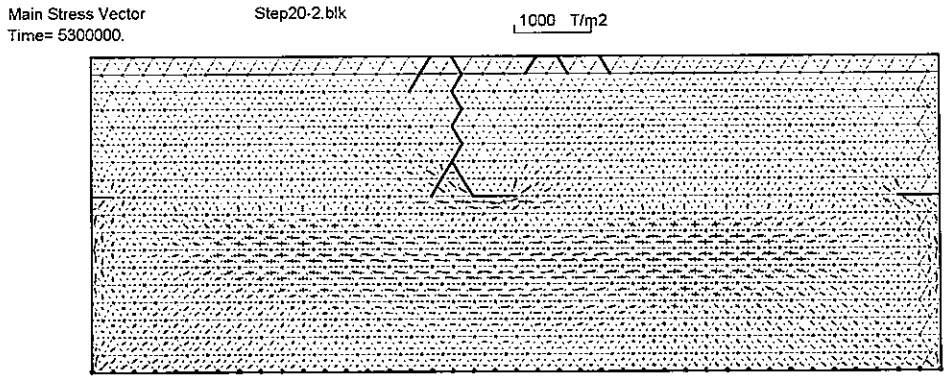

(c)

Fig. 9 Stress Field and Cracks after (a) 4 days (b) 14 days

(c) 30 days of Temperature Drops

Form the results and Fig. 9 it can be seen that, the stresses in old concrete in the first twenty days are almost compression because the self gravity and the temperature arising of it. Tension stress occurs near the upper surface of new concrete and the interface of new concrete and old concrete, and along with the temperature drops of new concrete , the area and the value of tension stress become larger and larger. At forth day after temperature drops, the first crack occurs at the middle of the upper surface of new concrete. After the occurrence of crack, only the tension stress in a limited area near the crack decreased , the stresses far from the crack are still in a larger level, so that there five cracks initiated on the upper surface of new concrete.

Along with the temperature drops , one crack propagates into the concrete but it stops when it reaches the interface of new concrete and old concrete, that because the strength of old concrete is larger and the tension stress is smaller. Cracks also occur along the interface at two side.

Thermal Fracture of Concrete Frame

Another example is given here to show the application of thermal fracture analysis by manifold method. Fig. 10 shows a concrete frame of 10×10m fixed at two feet loaded by self gravity and temperature shock. The parameters of material and calculation conditions are same with that of the old concrete listed in Table 2. The initial temperature of the frame is 20℃. From time=0, the temperature of inner side of the frame drops to 0℃ in one day, the outside of the frame is considered as isothermal. The principal stress and cracks of the frame at some steps are given in Fig.10.

From the results and Fig.10 it can be seen that, at the beginning of temperature drops, self gravity plays an important part in the stress distribution, the stress in the two columns is mainly pressure and in lower side of upper beam is tension. Because the two upper corners cause stress concentration, crack firstly initiates there at the end of the first day after the temperature dropped. Thermal shock causes great temperature gradient and tensile stress in the inner side of frame, so that many surface cracks initiate on the inner side of frame, but only some cracks in lower-central part of the beam propagate into the concrete (see Fig. 10 (b) and at last, one crack penetrates the beam(see Fig. 10 (c)).

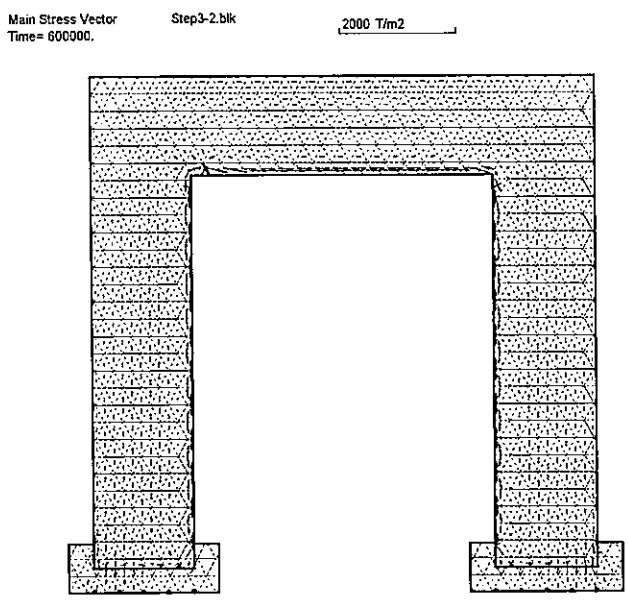

Fig.10 (a)

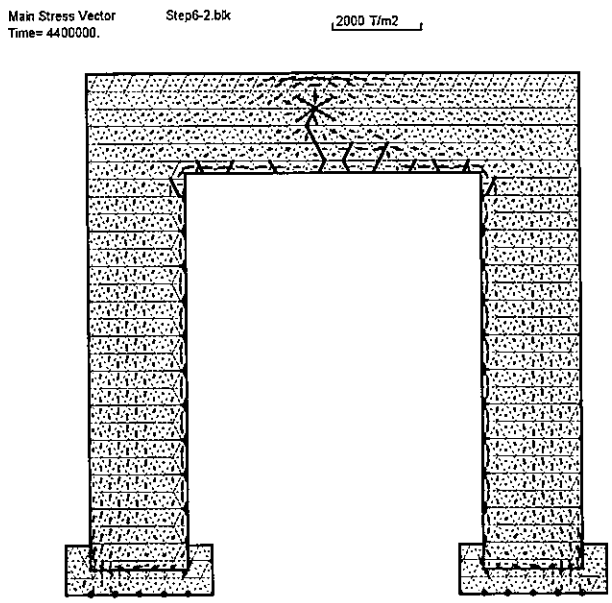

Fig. 10 (b)

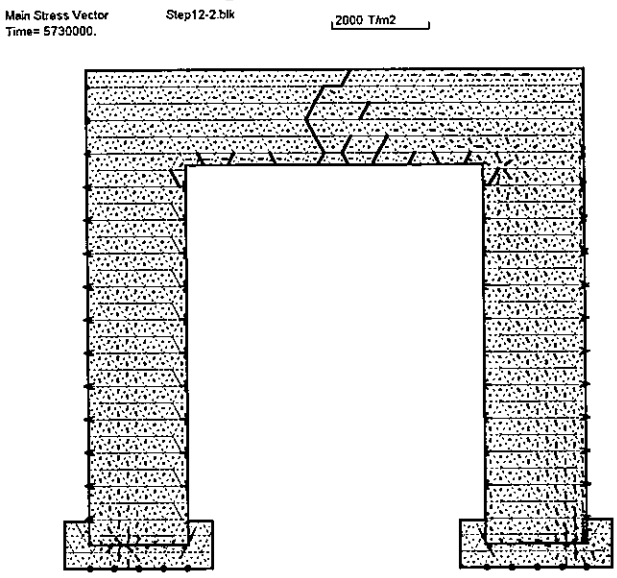

Fig.10 (c)

Fig.10 The principal stress and cracks of concrete frame loaded by self gravity and thermal shock at

(a) The end if the first day after temperature dropped
(b) The fourth day after temperature dropped
(c) The seventeenth day after temperature dropped

A flying object hitting an arch

As an examples to show the application of modified manifold method to dynamic problem, the failing process of an imaginary arch hit by a flying object is simulated.

Fig.11 a shows the analysis modal, the thick lines are boundary and physical joints, the thin lines are the edge of mathematical mesh and these are potential cracks, the bottom of structure is fixed. The material of arch and abutments is same, but the strength of abutments is assigned a extremely high value so that cracks can only initiate and propagate in arch. The material properties and calculation conditions are listed in Table 3.

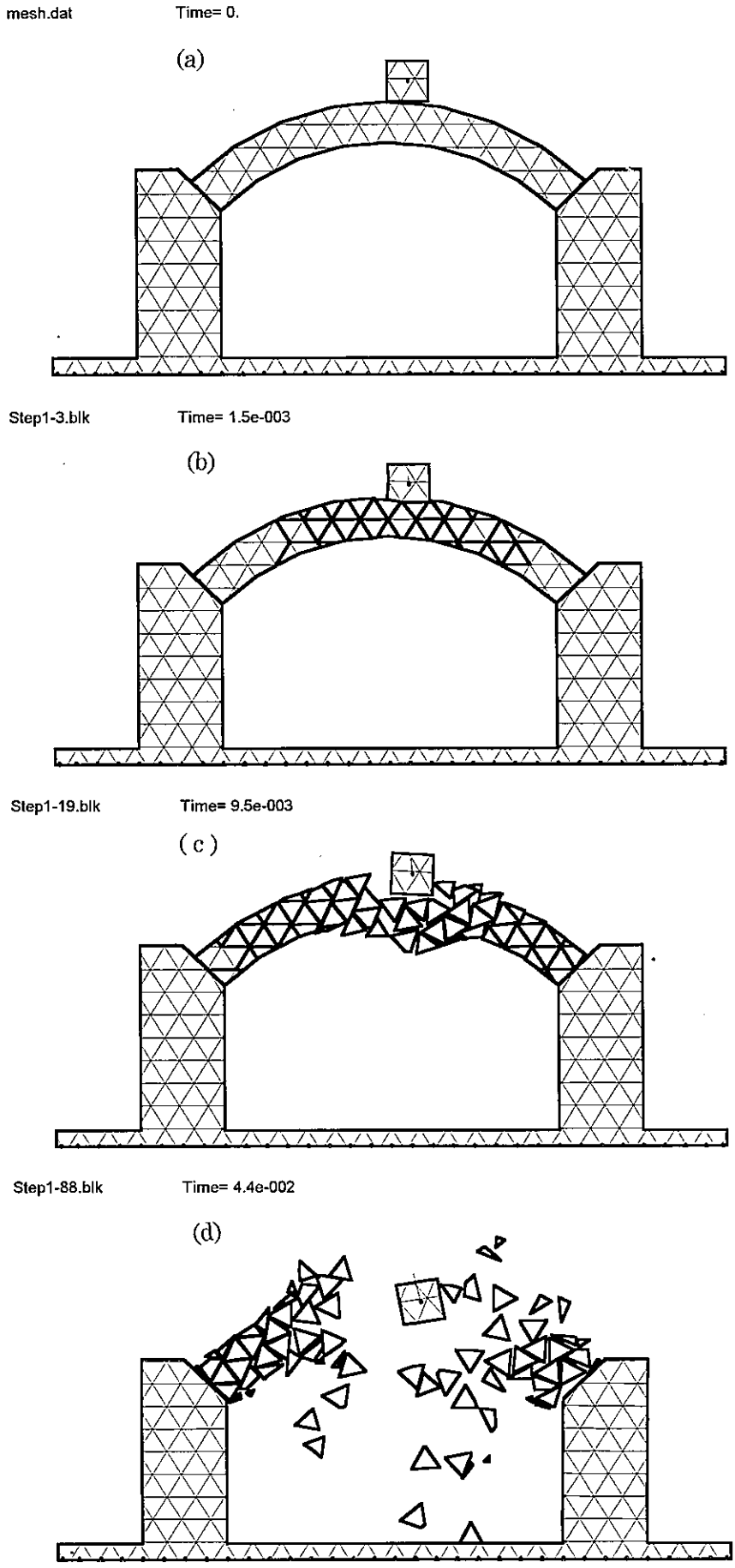

Fig. 11 Cracking of arch at t= : (a) 0; (b) 0.0015;(c) 0.0095;(d) 0.044 sec

The velocity of the flying block is $v_x = 0, v_y = -140 m/\sec$.

Table 3 Material Properties and Calculation Conditions

	Abutment	Arch
Elastic Modulus	1960 MPa	1960 MPa
Poisson's Ratio	0.24	0.24
Unit Mass	2400kg/m³	2400kg/m³
Tension Strength To	9800 MPa	0.01 MPa
Cohesion C	29400 MPa	0.03 MPa
Friction Angle ϕ	30 degree	10 degree
Calculation Mode	dynamic	dynamic
Penalty	10000000 t/m	10000000 t/m

Fig. 11b~ Fig. 11d show some of the deformed geometry of the arch. At the beginning of the block hit the arch, many cracks initiate near the percussion point and rapidly propagate to the two abutments, at time t=0.0095 sec ,almost all the edges failed, and in a very shot time the arch collapsed into many blocks, some blocks reach the bottom at t=0.44 sec.

CONCLUSION

The use of two sets of meshes made manifold method possible to solve crack initiation and propagation problems. In this paper, by supposing that cracks can only initiate and propagate along the edge of mathematical meshes, an extension that can analyze fracture problems is added to Shi's original manifold method program. And by adding the thermal load term, the modified version can be used to simulate the crack initiation and propagation caused by mechanical load and temperature change. The given examples show that, manifold method can get the fine stress distribution and can simulate the crack propagation very well.

But because linear displacement functions are used in this study, the precision of stress distribution, especially near the tip of cracks, is not high enough to catch the crack extension precisely. Further study is needed to promote the precision of analysis and to combine the fracture mechanics with manifold method in the simulation of crack extension.

ACKNOWLEDGMENTS

The author deeply appreciates Dr. Gen-hua Shi and Professor Yuzo Ohnishi for providing the original source code of manifold method and many valuable suggestions, and for leading the author to the wonderful world of manifold method.

REFFERENCES

1. Shi, G.H. "Modeling of Rock Joints and Blocks by Manifold Method", *Proceedings of the 32rd U.S. Symposium on Rock Mechanics, Santa Fe, New Mexico,(1992), 639-648.*
2. Shi GenHua. "Manifold Method", *Proceedings of the First International Forum on Discontinuous Deformation Analysis (DDA) and Simulations of Discontinuous Media, Berkeley, California, USA,(1996). 52-204.*
3. Te-chin Ke. "Artificial Joint-Based Manifold Method", *Working Forum on the Manifold Method of Material Analysis, Jenner, California, USA,(1995), Vol1. 21-37.*
4. Te-chin Ke. "Artificial Joint-Based DDA", *Proceedings of the First International Forum on Discontinuous Deformation Analysis (DDA) and Simulations of Discontinuous Media, Berkeley, California, USA,(1996).326-333.*
5. Bernard Amadei, Chihsen Lin and Jerry Dwyer. "Recent Extensions to DDA Method". *Proceedings of the First International Forum on Discontinuous Deformation Analysis (DDA) and Simulations of Discontinuous Media, Berkeley, California, USA,(1996).1-30.*
6. C.T. Lin and B. Amadei. "Application of DDA Augmented Lagrangian Method and Fracturing Algorithms in the Manifold Method". *Working Forum on the Manifold Method of Material Analysis, Jenner, California, USA,(1995).*
7. Jeen-Shang Lin. "Continuous and Discontinuous Analysis Using the Manifold Method". *Working Forum on the Manifold Method of Material Analysis, Jenner, California, USA,(1995). Vol1. 1-20.*
8. G.X. Zhang and G.T. Liu. "Thermally Stressed Multiple System in Steady State". *Theoret. Fracture Mech., 17,69-81(1992).*
9. G.X. Zhang and G.T. Liu. "Harmonic Thermal Fracture of Multiple Crack System and The Stability of Cracks in RCC Arch Dam". *Eng. Fracture Mech. Vol. 54, No. 5, 653-656(1996).*
10. Frank C. Tsai. "Estimation of Rock Mass Disturbance Around a Repository Drift Using the DDA Method". *Working Forum on the Manifold Method of Material Analysis, Jenner, California, USA(1995), Vol.1,87-104.*

CRACK PROPAGATION USING MANIFOLD METHOD

Yaw-Jeng Chiou, Ren-Jow Tsay, and Wai-Lin Chuang

Department of Civil Engineering, National Cheng Kung University,
Tainan, Taiwan 701, R. O. C.

ABSTRACT: The predication of crack propagation is studied by using the manifold method. A local mesh refinement scheme and auto remeshing are proposed to extend the manifold method. The model is first verified by comparing the numerical stress intensity factor with the benchmark solution and the result shows satisfactory accuracy. The stationary growing crack problems are then investigated. The manifold method is thus proved to be an attractive new numerical technique for fracture mechanic analysis.

INTRODCUTION

The prediction of crack propagation has been one of the important topics to researchers. Because of its mathematical singularity and the moving boundary characteristics, most of the researchers solved it numerically. However, there are few methods available today that can model the arbitrary crack propagation efficiently.

Many researchers applied the finite element method with remeshing to study the crack propagation and its stress analysis [1-3]. Nevertheless, the application of finite element method with remeshing to study the crack growth problem is not an easy task and is usually very time consuming. The refined mesh by the finite element method stays with the crack; thus the mesh numbers increase sequentially. Furthermore, it is almost impossible to automatically remesh finite elements about an arbitrarily growing crack. Alternatively, some researchers applied the boundary element method to investigate the problem [4]. The boundary element method possesses some advantages over the finite element method in that it avoids a large part of remeshing, and that its required effort is consequently much less than that of the finite element method. However, since the boundary element method requires a Green's function to solve the governing equations, the scope of problems which it can treat is quite limited. The presence of crack causes substantial difficulties and some specialized techniques, such as domain subdivision and hypersingular methods, must be used. Recently, Belytschko *et al.* adopted the moving least square interpolation concept to develop the element-free Galerkin method [5]. This method is essentially similar to the diffuse element method introduced by Nayroles *et al.* [6]. It can also be considered as the generality of the finite element method. In the element-free Galerkin method, only a group of nodes and a boundary description, but not the element meshes, are needed to construct the discrete equations. Consequently, on the investigation of crack propagation, the burdens for the finite element method with remeshing are avoided. Belytschko *et al.* [7, 8], and Lu *et al.* [9] by using the element-free Galerkin method successfully calculated the stress intensity factor and predicted the crack propagation.

The numerical methods mention above are established on the basis of continuous media. Therefore, the analysis of discontinuous structure by these methods is usually not an easy task. Recently, Shi [10, 11] proposed the manifold method in which the finite covers theory in mathematics is introduced to develop the approximation theory of unknown functions. This method provides a unified framework for solving problems dealing with both

continuums and jointed materials. It retains most of the attractive features of discontinuous deformation analysis (DDA) [12], and can be considered as the generalized finite element method and discontinuous deformation analysis. One of the most innovative features of the method is that it employs both physical mesh and mathematical mesh to form the physical problem. The physical mesh is dictated by the physical boundary of a problem, while the mathematical mesh by the computational consideration. These two meshes are inter-related through the application of weighting functions. The manifold method has been adopted and modified by some researchers [13-19]. In addition, it is interesting to note that the manifold method possesses some characteristics similar to those of the element free Galerkin method, though in the element free Galerkin method the multi-body dynamic interaction mechanism has not yet been included in the analysis procedures.

The manifold method is applied in this study to investigate the crack propagation. A local mesh refinement scheme and auto remeshing are proposed to extend the manifold method. The numerical model is first verified by comparing the numerical stress intensity factor with the benchmark solution. The stationary growing crack problems are then investigated, and the stress distributions are presented.

FUNDAMENTALS OF THE MANIFOLD METHOD

1. The physical mesh and the mathematical mesh

The manifold method [10, 11] provides a unified framework for solving problems dealing with both continuums and jointed materials. It employs both physical mesh and mathematical mesh to form the physical cover. The physical mesh is a unique portrait of the physical domain of a problem and defines the integration fields. It includes the boundary of the material volume, joints, blocks and the interfaces of different materials zones. The mathematical mesh defines the fine or rough approximations. The mathematical mesh can be a mesh of some regular pattern, or a combination of some arbitrary figures. This mesh is chosen according to the problem geometry, solution accuracy requirements, and the physical property zoning. It is used for building covers and has to be large enough to cover every point of the physical mesh.

Fig. 1 shows the schematic illustration of the physical mesh and mathematical mesh. A structure containing a cavity and a crack defines the physical mesh. The triangular mesh is arbitrary selected as the mathematical mesh. The superposition of these two meshes gives a covered manifold of the problem. It is important to note that the manifold method does not require a mathematical mesh to conform to the physical boundary of a problem.

2. The basic formulation

For the manifold method, the cover displacement functions are independently defined on individual physical covers. Local displacement functions can be connected to form a global displacement function on the whole material volume. In the case of two dimensional manifold computation, the cover displacement functions $u_i(x, y)$ and $v_i(x, y)$ are defined on physical cover U_i. The global displacement functions $u(x,y)$ and $\upsilon(x,y)$ on the whole physical cover system are defined from the cover displacement functions as follows.

$$u(x,y) = \sum_{i=1}^{n} \omega_i(x,y) u_i(x,y)$$

$$\upsilon(x,y) = \sum_{i=1}^{n} \omega_i(x,y) \upsilon_i(x,y) \qquad (1)$$

where $\omega_i(x,y)$ are weight functions,

$$\omega_i(x,y) \geq 0, (x,y) \in U_i$$
$$\omega_i(x,y) = 0, (x,y) \notin U_i$$

with $$\sum_{(x,y)\in U_i} \omega_i(x,y) = 1$$

For a triangular mathematical mesh, the basic triangle bounded by three nodes, say 1, 2, and 3, the assumption of a linear displacement field leads to the following linear equations.

$$u(x,y) = a_1 + a_2 x + a_3 y$$
$$v(x,y) = b_1 + b_2 x + b_3 y \tag{2}$$

where a_i and b_i are constant. These constant coefficients are determined by evaluating the displacements at all three nodes, and then expressing the coefficients as a function of nodal displacement. Substituting the determined coefficients into Eq. (2) yields the linear displacement field as follows.

$$\begin{bmatrix} u(x,y) \\ v(x,y) \end{bmatrix} = \begin{bmatrix} f_1(x,y) & 0 & f_2(x,y) & 0 & f_3(x,y) & 0 \\ 0 & f_1(x,y) & 0 & f_2(x,y) & 0 & f_3(x,y) \end{bmatrix} \begin{bmatrix} u_1 \\ v_1 \\ u_2 \\ v_2 \\ u_3 \\ v_3 \end{bmatrix} \tag{3a}$$

or

$$\begin{bmatrix} u(x,y) \\ v(x,y) \end{bmatrix} = [T_e(x,y)][D_e] \tag{3b}$$

where

$$[f_1(x,y) \quad f_2(x,y) \quad f_3(x,y)] = [1 \quad x \quad y] \begin{bmatrix} f_{11} & f_{12} & f_{13} \\ f_{21} & f_{22} & f_{23} \\ f_{31} & f_{32} & f_{33} \end{bmatrix}$$

$$\begin{bmatrix} f_{11} & f_{12} & f_{13} \\ f_{21} & f_{22} & f_{23} \\ f_{31} & f_{32} & f_{33} \end{bmatrix} = \frac{1}{\Delta} \begin{bmatrix} x_2y_3 - x_3y_2 & x_3y_1 - x_1y_3 & x_1y_2 - x_2y_1 \\ y_2 - y_3 & y_3 - y_1 & y_1 - y_2 \\ x_3 - x_2 & x_1 - x_3 & x_2 - x_1 \end{bmatrix}$$

and

$$\Delta = \begin{vmatrix} 1 & x_1 & y_1 \\ 1 & x_2 & y_2 \\ 1 & x_3 & y_3 \end{vmatrix}$$

Thus, in the finite element, the cover functions are the constant functions u_i and v_i over the whole cover, while the weight functions $w_i(x, y)$ are the shape functions $f_i(x, y)$.

The equilibrium function for a system of n physical covers can be derived by applying the minimum potential energy principle and expressed as

$$\begin{bmatrix} \mathbf{K}_{11} & \mathbf{K}_{12} & \mathbf{K}_{13} & .. & \mathbf{K}_{1n} \\ \mathbf{K}_{21} & \mathbf{K}_{22} & \mathbf{K}_{23} & .. & \mathbf{K}_{2n} \\ \mathbf{K}_{31} & \mathbf{K}_{32} & \mathbf{K}_{33} & .. & \mathbf{K}_{3n} \\ .. & .. & .. & .. & .. \\ \mathbf{K}_{n1} & \mathbf{K}_{n2} & \mathbf{K}_{n3} & .. & \mathbf{K}_{nn} \end{bmatrix} \begin{bmatrix} \mathbf{D}_1 \\ \mathbf{D}_2 \\ \mathbf{D}_3 \\ .. \\ \mathbf{D}_n \end{bmatrix} = \begin{bmatrix} \mathbf{F}_1 \\ \mathbf{F}_2 \\ \mathbf{F}_3 \\ .. \\ \mathbf{F}_n \end{bmatrix} \tag{4}$$

where $\mathbf{K}_{ij}$ is a 2×2 submatrix, $\mathbf{K}_{ii}$ depends on the material properties of cover i, $\mathbf{K}_{ij}$ ($i \neq j$) is defined by the overlapping or contact between cover i and cover j; $\mathbf{D}_i$ and $\mathbf{F}_i$ are 2×1

submatrices, $\mathbf{D}_i$ represents the displacement variables of physical cover i, and $\mathbf{F}_i$ is the loading on cover i distributed to the displacement variables.

On the investigation of discontinuous behaviour, the block interactions are modelled according to the block kinematics in DDA [12]. A penalty formulation is adopted to restrain the block penetration, and the Mohr-Coulomb's law and a shear spring are used to model the sliding of block.

IMPLEMENTATION OF CRACK PROPAGATION PREDICATION

The maximum circumferential stress theory [20] is adopted to determine the direction of crack growth measured from the current crack line θ.

$$K_I \sin\theta + K_{II}(3\cos\theta - 1) = 0 \tag{5}$$

where K_I and K_{II} are the stress intensity factors of mode I and mode II, respectively. The stress intensity factors are determined by the crack opening displacement method [21].

$$K_I = \sqrt{\frac{\pi}{2r}}\frac{E\cdot\delta_1}{2(1-v^2)} \tag{6}$$

$$K_{II} = \sqrt{\frac{\pi}{2r}}\frac{E\cdot\delta_2}{2(1-v^2)} \tag{7}$$

where E is Young's modulus, δ_1 and δ_2 are the deformation normal to and along crack face as depicted in Fig. 2, v is Poisson's ratio, and r is the distance from the crack tip to the measure point.

The adaptive covers approximation in which the number of cover functions is free to be adopted or abandoned is proposed to construct the auto remeshing in the manifold method. Since the crack induced discontinuous behaviour can be modelled by the discontinuous deformation analysis [12], the former refined mesh is thus abandoned when the crack grows to the newer one. The required mesh refinement region is accompanied the crack tip. Consequently, the proposed method can highly reduce the required computer storage and successfully enhance the computation efficiency. The radius of the required mesh refinement region R is determined by the users. It is chosen to be 10% to 20% of the maximum dimension of the structure in this study. The triangular mesh is used, and the refining of the triangular mesh is constructed according to its relative position. The mesh containing the crack tip is refined by connecting the crack tip and vertexes, while the other neighbouring meshes are refined by connecting its centre and vertexes. Fig. 3 shows the representative mesh refinement around the crack tip.

NUMERICAL RESULTS AND DISCUSSION

1. The infinite plate with a hole

Referring to Fig. 4, an infinite plate with a central circle hole subjected to a unidirectional tensile load is investigated. The $80m \times 80m$ plate with a hole of radius 2m subjected to uniform load 5t/m is considered in this study. The Young's modulus is chosen to be E=1000 t/m^2, Poisson's ratio $v = 0.24$, and stiffness of contact spring k = 50000 t/m. The distribution of stress ratio σ_x / S along y axis and comparison with the exact solution [22] are presented in Fig. 5. It is found that the results obtained by the manifold method agree well with the exact solution. However, because the constant stress element can not accurately catch the stress at the edge of the hole, the discrepancy exists for the stress concentration. It can be improved by refining the element mesh.

2. The cantilever beam with edge crack

Fig. 6 shows a cantilever beam with edge crack subjected to a pair of symmetric load P. The analytical stress intensity factor of this beam [23] is

$$K_I = \frac{P}{th^2}[2\sqrt{3}(\frac{a}{h}+0.64)] \tag{8}$$

where a is crack depth, t is beam width, and h is half height of the beam.

In this study, the Young's modulus is chosen to be E=100000 kg/cm^2, Poisson's ratio $\nu = 0.3$, the stiffness of normal and shear springs $k_n = k_s = 5000000$ kg/cm, and P=5000 kg. The stress intensity factor calculated by the manifold method and comparison with the analytical results are presented in Fig. 7. One can see that the stress intensity factor shows satisfactory agreement. The crack propagation after seven steps is given in Fig. 8. Fig. 9 shows the distribution of maximum principal stress. It is obviously found the stress concentrates around the crack tip.

3. The finite plate with edge crack

Fig. 10 shows a finite plate with edge crack subjected to a unidirectional tensile load. The analytical stress intensity factor of this plate [24] is

$$K_I = \{1.99 - 0.41\frac{a}{W} + 18.7(\frac{a}{W})^2 - 38.48(\frac{a}{W})^3 + 53.85(\frac{a}{W})^4\}S\sqrt{a} \tag{9}$$

where W is width of plate, a is crack depth, and S is the unidirectional tensile load.

A $2cm \times 1cm$ $(H = 1cm, w = 1cm)$ plate with edge crack subjected to unidirectional tensile load 1kg/cm is investigated. The Young's modulus is taken as E=100000 kg/cm^2, Poisson's ratio $\nu = 0.3$, and contact spring stiffness $k_n = k_s = 5000000$ kg/cm. The comparison of stress intensity factor is shown in Fig. 11. It is found that the stress intensity factor calculated by the manifold method agrees well with that by element free Galerkin method [8] and analytical result. The crack propagation after seven steps is given in Fig. 12. The maximum principal stress distribution is presented in Fig. 13. One can also see the stress concentrates around the crack tip.

CONCLUSIONS

A modified manifold method is proposed to study the crack propagation prediction. The proposed method is successively verified by comparing the numerical results with the benchmark solution. This method can highly reduce the required computer storage and enhance the computation efficiency. The manifold method is thus proved to be an attractive new numerical method for fracture mechanic analysis and crack propagation predication.

ACKNOWLEDGMENT

This study is supported by the National Science Council of Republic of China under grant NSC86-2621-P-006-027. The computer program developed for this study benefits from adapting some codes from the DDA program written by Dr. G. H. Shi.

REFERENCES

1. Bittencourt T. N., P. A. Waarzynek, A. R. Ingraffea and J. L. Sousa, Quasi-automatic simulattion of crack propagation for 2D LEFM problems. *Engng Fracture Mech.*, 1996, **55**, 321-334.
2. Lim I. L., I. W. Johnston and S. K. Choi, A finite element code for fracture propagation

analysis within elasto-plastic continuum. *Engng Fracture Mech.*, 1996, **53**, 193-211.
3. Shephard, M. S., N. A. B. Yehia, G. S. Burd and T. J. Weidner, Computational strategies for nonlinear and fracture mechanics problems, automatic crack propagation tracking. *Comput. Struct.*, 1985, **20**, 211-223.
4. Chai, G., K. Zhang, and D. Wu, Stress intensity factors for semi-elliptical surface cracks in plates and cylindrical pressure vessels using the hybrid boundary element method. *Engng Fracture Mech.*, 1995, **52**, 1035-1054.
5. Belytschko, T., Y. Y. Lu, and L. Gu, Element-free Galerkin methods. *Int. J. Numer. Meth. Engng.*, 1994, **37**, 229-256.
6. Nayroles, B., G. Touzot, and P. Villon, Generalizing the finite element method: diffuse approximation and diffuse elements. *Comput. Mech.*, 1992, **10**, 307-318.
7. Belytschko, T., Y. Y. Lu, L. Gu, and M. Tabbara, Element-free Galerkin methods for static and dynamic fracture. *Int. J. Solids Struct.*, 1995, **32**, 2547-2570.
8. Belytschko, T., Y. Y. Lu, and L. Gu, Crack propagation by element-free Galerkin methods. *Engng Fracture Mech.*, 1995, **51**, 295-315.
9. Lu, Y. Y., T. Belytschko, and M. Tabbara, Element-free Galerkin method for wave propagation and dynamic fracture. *Comput. Meth. Application Mechanical Engng*, 1995, **126**, 131-153.
10. Shi, G. H., Manifold method of material analysis. *Transactions of the Ninth Army Conference on Applied Mathematics and Computing*, Minneapolis, Minnesoda, U. S. A., 1991, pp. 51-76.
11. Shi, G. H., Numerical manifold method. *Working Forum on the Manifold Method of Material Analysis*, California, U. S. A., 1995, Vol.2, pp. 1-180.
12. Shi, G. H., *Discontinuous deformation analysis: a new numerical method for the static and dynamics of block systems.* Ph. D. Dissertation, Department of Civil Engineering, University of California, Berkeley U. S. A., 1988.
13. Chang, C. T. and P. J. M. Monteiro, Nonlinear entrance level manifold method. *Working Forum on the Manifold Method of Material Analysis*, California, U. S. A., 1995, Vol.1, pp. 127-146.
14. Chen, G., S. Miki, and Y. Ohnishi, Automatic creation of mathematical meshes in manifold method of material analysis. *Working Forum on the Manifold Method of Material Analysis*, California, U. S. A., 1995, Vol.1, pp. 105-126.
15. Ke, T. C., Artifical joint-based on manifold method. *Working Forum on the Manifold Method of Material Analysis*, California, U. S. A., 1995, Vol.1, pp. 21-38.
16. Lin, D. and H. Mo, Manifold method of material analysis. *Working Forum on the Manifold Method of Material Analysis*, California, U. S. A., 1995, Vol.1, pp. 147-164.
17. Lin, J. S., Continuous and discontinuous analysis using the manifold method. *Working Forum on the Manifold Method of Material Analysis*, California, U. S. A., 1995, Vol.1, pp. 1-20.
18. Shyu, K. and M. R. Salami, Manifold method with four-node isoparametric finite element method. *Working Forum on the Manifold Method of Material Analysis*, California, U. S. A., 1995, Vol.1, pp. 165-182.
19. Wang, C. Y., J. Sheng, M. H. Chen, and C. C. Chuang, Approximation theories for the manifold method. *Working Forum on the Manifold Method of Material Analysis*, California, U. S. A., 1995, Vol. 1, pp. 61-86.
20. Erdogan, F. and S. C. Sih, On the crack extension in plates under plane loading and transverse shear. ASME, *J. basic Engng.*, 1963, **85**, 519-525.
21. Lim, I. L. and I. W. Johnston, On stress intensity factor computation from the quarter-point element displacements. Commun. Appl. Numer. Meth., 1992, **8**, 291-300.

22. Timoshenko, S. P. and J. N. Goodier, *Theory of Elasticity*, 3rd Ed., McGraw-Hill Book Co., Inc., New York, 1970.
23. Murakami, Y., *Stress Intensity Factors Handbook (Vol. 1)*, Pergamon Books Ltd., Great Britain, 1987.
24. Broek, D., *Elementary Fracture Mechanics*, 4th Ed., Martinus Nijhoff, Dordrecht, 1986.

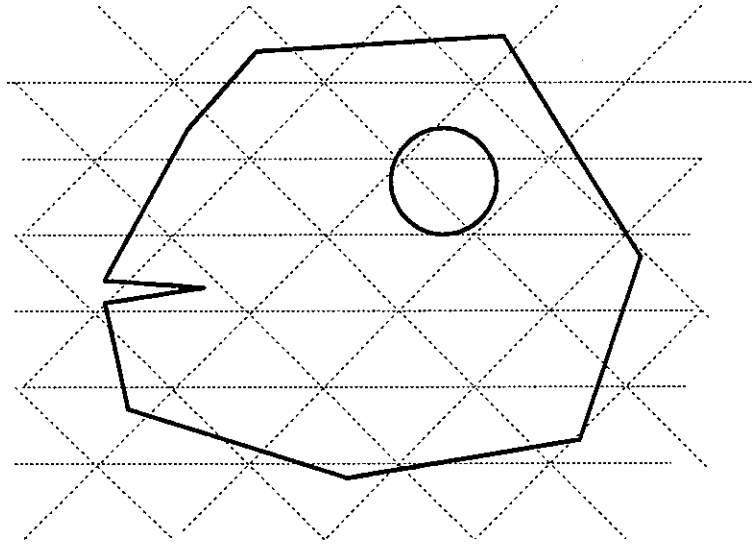

Fig. 1 The physical mesh and the mathematical mesh in manifold method

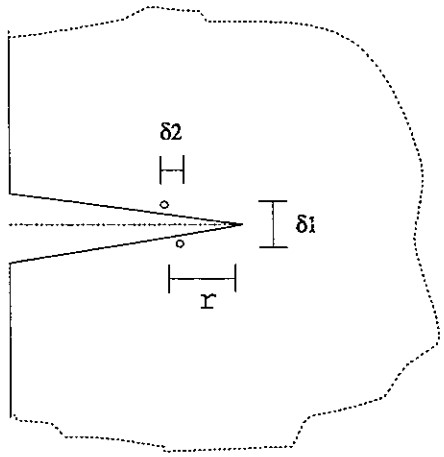

Fig. 2 The crack opening displacement and measure point

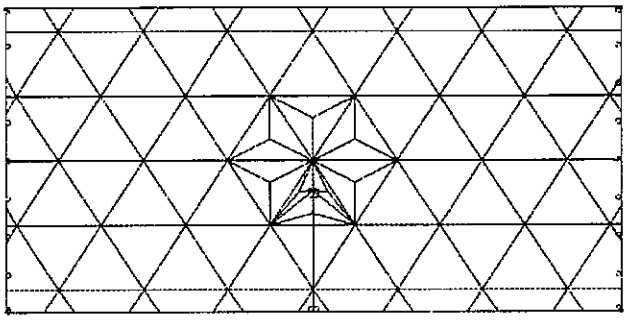

Fig. 3 Mesh refinement at the crack tip

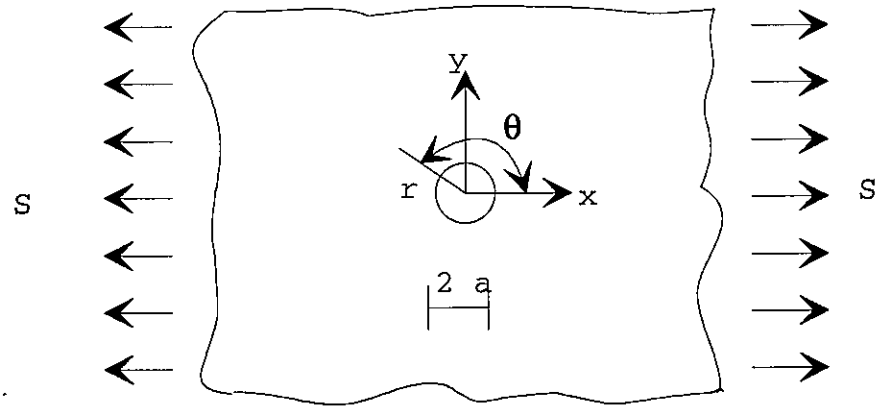

Fig. 4 The infinite plate with a circle hole

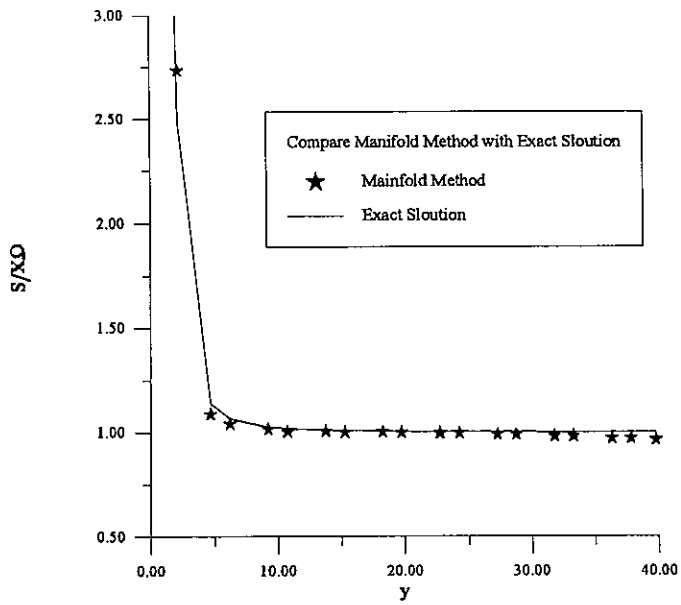

Fig. 5 Comparison between the exact solution and manifold solution results for stress σ_x

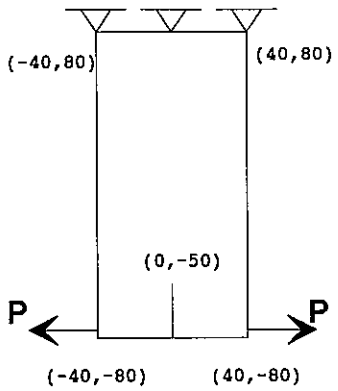

Fig. 6 Cantilever beam with edge crack

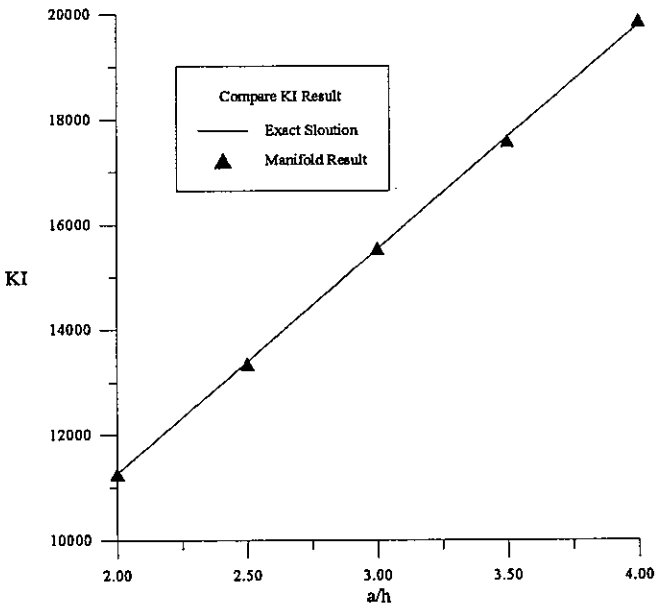

Fig. 7 Comparison of stress intensity factor

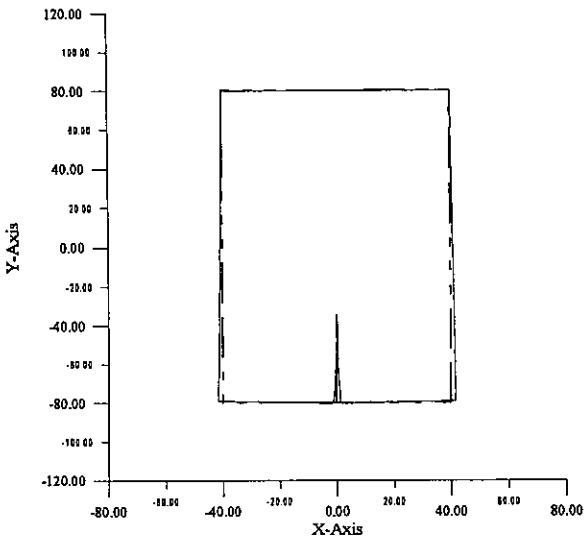

Fig. 8 Crack propagation after seven steps

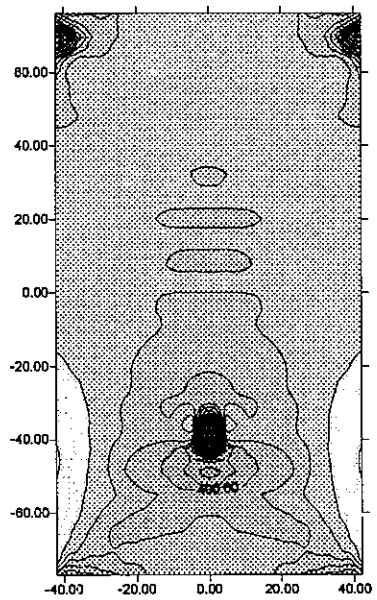

Fig. 9 The distribution of maximum principal stress

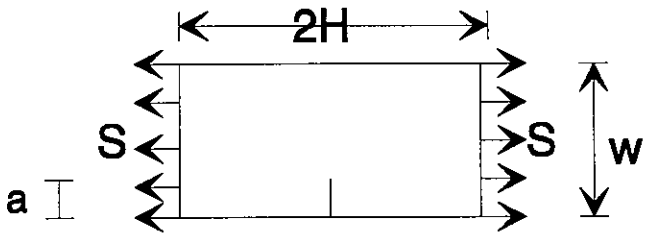

Fig. 10 Plate with edge crack

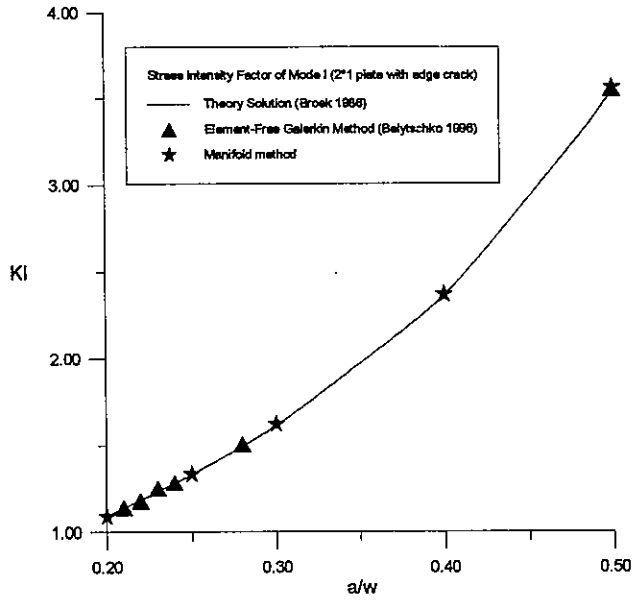

Fig. 11 Comparison of stress intensity factor

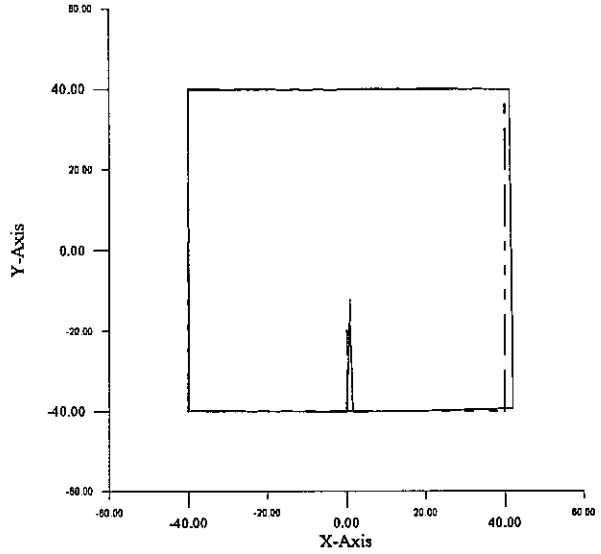

Fig. 12 Crack propagation after seven steps

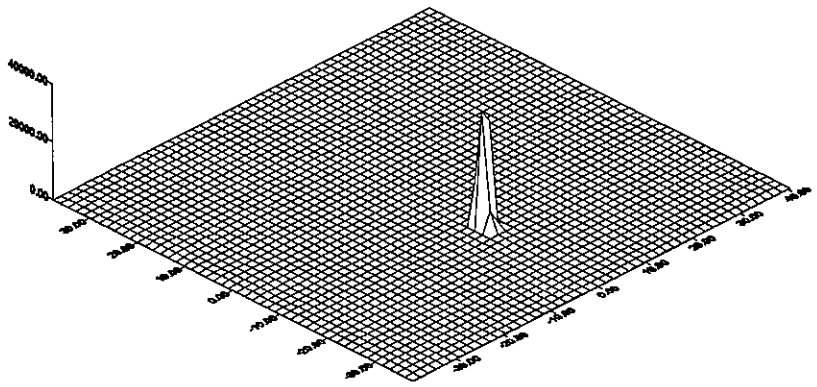

Fig. 13 The distribution of maximum principal stress

Elastic - Plastic Analysis of Jointed Rock Models by Manifold Method

Takeshi Sasaki, Seiji Morikawa, Daisuke Ishii
Intelligent Systems Department, Kajima Corporation,
2-7 Motoakasaka 1-Chome, Minato-ku, Tokyo, 107, Japan
Yuzo Ohnishi
School of Civil Engineering, Kyoto University
Yoshida Honcho, Sakyo-ku, Kyoto, 606-01, Japan

ABSTRACT: In large-scale rock structures with the discontinuous planes existing in a rock mass, the behavior of deformation and stress distribution along structure are strongly influenced by the pattern of the discontinuous planes. However, in general, the jointed rock mass is assumed to be more partially and doubtfully connected than completely discontinuous. Hence, the authors presented the elastic-plastic analysis of a discontinuous model of jointed rock mass based on combined Manifold method which was developed by G. H. Shi(1991).

The authors adapted Drucker-Prager's elastic-plastic yield criterion, Jaumann co-rotational derivative for objectivity of stresses for rotation, a rock bolting element and improved numerical instability caused by very small elements generated from auto mesh algorithm in original Manifold method(Shi).

Since, the presented methods are applied an underground excavated cavern of quasi static models and a collision between rock masses in dynamic problems. The applicability of the presented methods is examined and the results are obtained to agree qualitatively with the physical phenomenon. Further development will be carried out in the future on friction characteristics of actual discontinuous plane of rock mass.

1 INTRODUCTION

There are two types of discontinuous planes existence in the rock mass at the same time. One is a clearly isolated as faults and the other is more doubtfully connected as joints and cracks. In the circumstances, the former problems are handled by the use of DDA proposed by Shi(1989). DDA[1] assumes constant strain in a block, therefore it does not express the stress concentration in a block where a block size is relatively large in comparison with analytical area. Manifold method, divided by FEM elements in DDA blocks, deals with both the discontinuous models like DDA and the continuous models like FEM at the same time. This paper outlines the Manifold method and describes the applicability for rock mechanics problems considering the elastic-plastic constitutive law and a rock bolting element.

2 OUTLINE OF THE THEORY(G.H.Shi,1991)

In the Manifold method [2],[3], the finite covers which define the displacements are overlapped on the material blocks which contain discontinuous planes in an analytical area, as shown in Fig.1. The finite covers are shape functions, which are disconnected on the two sides of the discontinuous planes. The equilibrium equation is solved dynamically with contact problem by Penalty method.

The function of the finite covers is expressed by Eq.(1).

$$F(x,y)=\sum_{i=1}^{n} w_i(x,y)\, f_i(x,y) \tag{1}$$

where,

$w_i(x, y)$: weight function, $f_i(x, y)$: displacement shape function, x, y : generalized coordinates.

The weight function is given the following characteristics when if the mathematical mesh and the physical mesh are overlapped, the weight function has a certain value.

$$w_i(x, y) \geq 0 \quad (x, y) \in U_i \tag{2}$$

And the non-overlapping area is zero in Eq.(3).

$$w_i(x, y) = 0 \quad (x, y) \notin U_i \tag{3}$$

Total value of the weight function in the overlapped area is 1.

$$\sum_{(x,y)\in U_j} w_j(x, y) = 1 \tag{4}$$

In the case of FEM the physical region and the mathematical region coincide and DDA is a special case in which one block has one cover. Hence, Manifold method is a generalized method covering both FEM and DDA[4]. Significance of Eq.(3) is to deal with mathematical meshes independently on the shape of physical blocks.

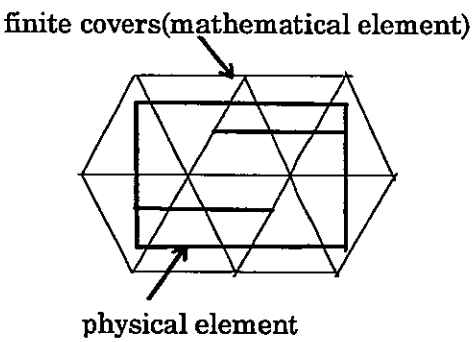

Fig.-1 Finite covers on joints

(1) Displacement shape function of elements

In the case of a triangle element, the constant strain is assumed as shown in Eq.(5), as in the case of FEM .

$$u = a_1 + a_2 x + a_3 y \quad , \quad v = b_1 + b_2 x + b_3 y \tag{5}$$

where, u : displacement of x direction, v : displacement of y direction.

The nodal displacement of x, y directions in a triangular element is expressed by Eq.(6).

$$\{D_i\} = \{ u_1\ v_1\ u_2\ v_2\ u_3\ v_3 \} \tag{6}$$

The displacement of an arbitrary point in an element is expressed by Eq.(7).

$$\begin{Bmatrix} u \\ v \end{Bmatrix} = \begin{bmatrix} f_1 & 0 & f_2 & 0 & f_3 & 0 \\ 0 & f_1 & 0 & f_2 & 0 & f_3 \end{bmatrix} \{D_i\} = [T_i]\{D_i\} \tag{7}$$

where,

$$\begin{Bmatrix} f_1 \\ f_2 \\ f_3 \end{Bmatrix}^T = \begin{Bmatrix} 1 \\ x \\ y \end{Bmatrix}^T \begin{bmatrix} f_{11} & f_{12} & f_{13} \\ f_{21} & f_{22} & f_{23} \\ f_{31} & f_{32} & f_{33} \end{bmatrix} \tag{8}$$

$$\begin{bmatrix} f_{11} & f_{12} & f_{13} \\ f_{21} & f_{22} & f_{23} \\ f_{31} & f_{32} & f_{33} \end{bmatrix} = \begin{bmatrix} 1 & x_1 & y_1 \\ 1 & x_2 & y_2 \\ 1 & x_3 & y_3 \end{bmatrix}^{-1} \tag{9}$$

(2) Stiffness matrix of elements

The stiffness matrix of an element is calculated by the principle of minimum potential energy as shown in Eq.(10).

$$[k_{rs}]_{ii} = \frac{\partial^2 \Pi_e}{\partial d_{ri} \partial d_{si}} = \frac{S^e}{2} \frac{\partial^2}{\partial d_{ri} \partial d_{si}} \{D_i\}^T [E] \{D_i\} = S^e [B_r]^T [E] [B_s] \qquad \mathrm{r,s} = 1,2,3 \tag{10}$$

where, S^e: area of physical element, $[E]$: stress-strain constitutive law, $[B_s]$: strain matrix of an element.

Hence, the integration of elements is applied in each physical block. Differing from the normal FEM, Manifold method is applied the additional conditions of Eq.(2) and Eq.(3) in the elemental integration.

(3) Contact matrices of elements

The contact conditions at the boundaries of discontinuous planes are judged by Eq.(7), as shown in Fig. 2. In this case, the square penetrating energy on a contact point between two elements is converged toward zero by Penalty method.

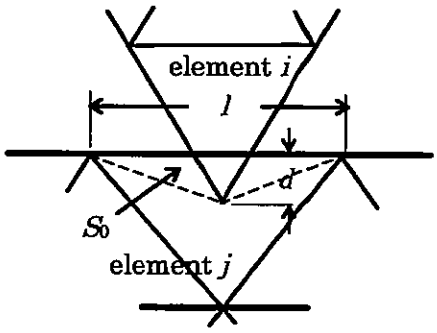

Fig. - 2 Penetration of physical blocks

The strain energy of the contact spring by penetration between elements i and j in Fig.2 is evaluated by Eq.(11), where d is expressed by Eq.(12) with the coordinate functions $\{H\}$ and$\{G\}$, and the unknowns $\{D_i\}$ and $\{D_j\}$ of elemental nodes.

$$\Pi_P = \frac{P}{2} d^2 \tag{11}$$

$$d = (\frac{S_0}{l} + \{H\}^T \{D_i\} + \{G\}^T \{D_j\})^2 \tag{12}$$

$$[k_{rs}]_{ii} = \frac{\partial^2 \Pi_P}{\partial d_{ri} \partial d_{si}} = \frac{P}{2} \frac{\partial^2}{\partial d_{ri} \partial d_{si}} \{D_i\}^T \{H\}^T \{H\} \{D_i\}$$

$$= P\{H\}^T \{H\} = [k_{\lambda P}]_{ii}$$

$$[k_{rs}]_{ij} = -P\{H\}^T \{H\}^T = [k_{\lambda P}]_{ij}$$

$$[k_{rs}]_{ji} = -P\{G\}^T \{H\}^T = [k_{\lambda P}]_{ji}$$

$$[k_{rs}]_{jj} = P\{G\}^T \{G\}^T = [k_{\lambda P}]_{jj} \tag{13}$$

$$\{f_r\}_i = -\frac{\partial \Pi_P}{\partial d_{ri}} = -\frac{PS_0}{2}\frac{\partial}{\partial d_{ri}}\{H\}^T\{D_i\}$$
$$= -\frac{PS_0}{2}\{H\} = \{F_{\lambda P}\}_i$$
$$\{f_r\}_j = -\frac{\partial \Pi_K}{\partial d_{rj}} = \frac{PS_0}{2}\frac{\partial}{\partial d_{rj}}\{G\}^T\{D_i\}$$
$$= \frac{PS_0}{2}\{G\} = \{F_{\lambda P}\}_j \tag{14}$$

where,

P : Penalty coefficient, S_0 : penetrating area of physical elements, $\{H\},\{G\}$: function of nodal coordinates x_i, y_i.

Eq. (13) and (14) are superposed on global equilibrium equations.

(4) Stiffness matrices of rock bolts

Fig. 3 shows that two arbitrary points (x_i, y_i) and (x_j, y_j) in elements i and j are connected by a rock bolt. Let u_i, v_i, u_j, v_j, each be displacements of the points i and j in x and y directions respectively and the deformation of the rock bolt is given by Eq.(15).

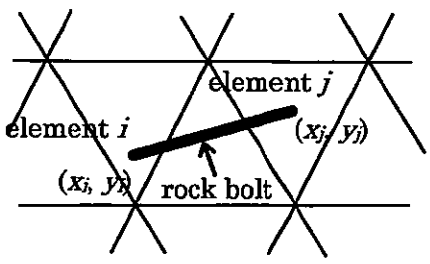

Fig. - 3 Modeling of a rock bolt

$$dl=(1/l)[(u_i, v_i)\{l_x, l_y\}^T - (u_j, v_j)\{l_x, l_y\}^T \tag{15}$$
$$l = \sqrt{(x_i - x_j)^2 + (y_i - y_j)^2} \tag{16}$$
$$l_x = (1/l)(x_i - x_j) \quad , \quad l_y=(1/l)(y_i - y_j) \tag{17}$$

where,

l : the length of the rock bolt, l_x, l_y : the direction cosines.

Let S_b be the stiffness of the rock bolt, the stress of the rock bolt is defined by Eq.(18).

$$f = -S_b(dl/l) \tag{18}$$

The strain energy of the rock bolt is given by Eq.(19).

$$\Pi_R = -(1/2)fdl=(S_b/2l)dl^2=(S_b/2l)\{D_i\}^T\{E_i\}\{E_i\}^T\{D_i\}$$
$$-(S_b/l)\{D_i\}^T\{E_i\}\{G_j\}^T\{D_j\}+(S_b/2l)\{D_j\}^T\{G_j\}\{G_j\}^T\{D_j\} \tag{19}$$

where,

$\{E_i\}^T=[T_i]^T\{l_x, l_y\}^T$, $\{G_j\}^T=[T_j]^T\{l_x, l_y\}^T$

By minimizing the potential energy of Eq.(19), the stiffness matrix of the rock bolt is given by Eq.(20)~(23).

$$[k_{rs}]_{ii} = \frac{\partial^2 \Pi_R}{\partial d_{ri}\partial d_{si}} = \frac{S_b}{2l}\frac{\partial^2}{\partial d_{ri}\partial d_{si}}\{D_i\}^T\{E_i\}^T\{E_i\}\{D_i\}$$
$$= (S_b / l)\{E_i\}^T\{E_i\} = [K_{\lambda R}]_{ii} \tag{20}$$

$$[k_{rs}]_{ij} = \frac{\partial^2 \Pi_R}{\partial d_{ri}\,\partial d_{sj}} = \frac{S_b}{2l}\frac{\partial^2}{\partial d_{ri}\,\partial d_{sj}}\{D_i\}^T\{E_i\}^T\{G_j\}\{D_j\}$$
$$= (S_b / l)\{E_i\}^T\{G_j\} = [K_{\lambda R}]_{ij} \tag{21}$$

$$[k_{rs}]_{ji} = \frac{\partial^2 \Pi_R}{\partial d_{rj}\,\partial d_{si}} = \frac{S_b}{2l}\frac{\partial^2}{\partial d_{rj}\,\partial d_{si}}\{D_j\}^T\{G_j\}^T\{E_i\}\{D_i\}$$
$$= (S_b / l)\{G_j\}^T\{E_i\} = [K_{\lambda R}]_{ji} \tag{22}$$

$$[k_{rs}]_{jj} = \frac{\partial^2 \Pi_R}{\partial d_{rj}\,\partial d_{sj}} = \frac{S_b}{2l}\frac{\partial^2}{\partial d_{rj}\,\partial d_{sj}}\{D_j\}^T\{G_j\}^T\{G_j\}\{D_j\}$$
$$= (S_b / l)\{G_j\}^T\{G_j\} = [K_{\lambda R}]_{jj} \tag{23}$$

(5) Friction condition of block surfaces and Penalty method

Fig. 4 shows the concept of the criteria of Penalty method for block penetration by Sasaki et al. (1994). Shi (1989) applied the Penalty method to both the normal penetration and the shear component. In this criteria, if the shear stress is smaller than the fiction strength, no block stress conditions are caused due to the non-slip condition (locking) being applied to the block.

Hence, the authors introduced the shear stiffness K_s just for the shear component instead of the Penalty term and the Penalty method is applied only to the normal component by using the Penalty coefficient S_1.

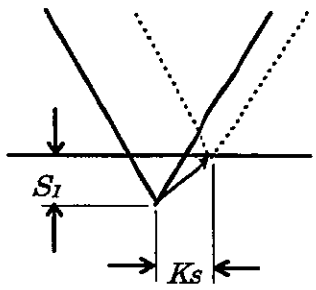

Fig. - 4 Criteria of the Penalty method

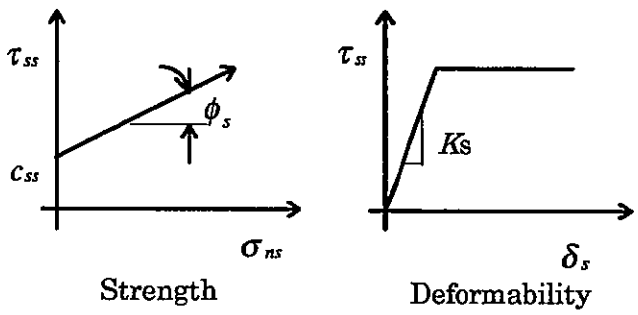

Fig. - 5 Friction condition of element faces

Fig.5 shows Mohr-Coulomb's friction conditions of a block face. The criteria of the friction conditions of a block face is given by Eq. (24) and (25).

$$\tau_{ss} < \sigma_{ns}\tan\phi_s + c_{ss}\text{, shear spring constant} = K_s \tag{24}$$

$$\tau_{ss} \geq \sigma_{ns}\tan\phi_s + c_{ss}\text{ , shear spring constant} = 0 \tag{25}$$

where,
τ_{ss} : the shear stress of a block face, σ_{ns} : the normal stress of a block face, c_{ss} : the cohesion of a block face, ϕ_s : the fiction angle of a block face, K_s : the shear stiffness of a block face.

(6) Elastic - plastic constitutive law of elements

The authors introduced the elastic-plastic constitutive law based on Drucker-Prager's yield criteria for an element shown in Fig.6. The yield function is expressed by Eq.(26). Eo and H' are Elastic and Work hardening coefficient respectively in Fig.6.

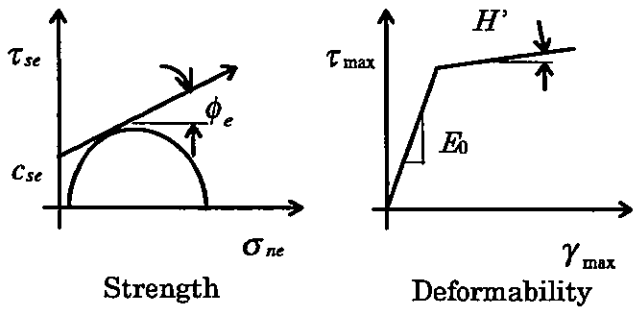

Fig.-6 Strength and deformability of elements

$$F = \alpha J_1 + \sqrt{J_2} - \bar{\sigma} / \sqrt{3} = 0 \tag{26}$$

$$J_1 = \sigma_{ii} \ , \ J_2 = S_{ij} S_{ij} \tag{27}$$

$$\alpha = \sqrt{\frac{\sin^2 \phi_e}{3(3+\sin^2 \phi_e)}} \ , \ \bar{\sigma} = c_e\{3(1-2\alpha^2)\} \tag{28}$$

where,
σ_{ii}: $\sigma_1 + \sigma_2 + \sigma_3$: the principal stresses, S_{ij} : the deviatoric stresses, J_1, J_2 : the first and second invariants of deviatoric stresses, c_e: the cohesion of an element, ϕ_e : the friction angle of an element.

(7) Global governing equations and time integration

The equation of motion for dynamic problems is given by Eq.(29).

$$M \ddot{u}^{t+\Delta t} + C \dot{u}^{t+\Delta t} + K u^{t+\Delta t} = R^{t+\Delta t} \tag{29}$$

where,
M : the inertia force matrix, C : the viscosity matrix, K : the global stiffness matrix, R : the external force vector, $\ddot{u}$: the acceleration of nodes, $\dot{u}$: the velocity of nodes, u : the displacement of nodes, t : time, Δt : time increment.
The global governing equation (29) is solved at each small time step of incremental forward differential equations. Rearranging Eq.(29) by displacement increment Δu,

$$\tilde{K} \cdot \Delta u = \tilde{F} \tag{30}$$

$$\tilde{K} = \frac{2}{\Delta t^2} M + \frac{2}{\Delta t} C + K \tag{31}$$

$$\tilde{F} = \frac{2}{\Delta t} M \cdot \dot{u} + \Delta F \tag{32}$$

where, Δu : the increment displacement. The total displacement vector $\Delta u^{t+\Delta t}$ is given by Eq.(33).

$$u^{t+\Delta t} = \sum \Delta u^i \tag{33}$$

where, Δu^i : the incremental displacement at time step i.
The iteration method is necessary when solving the penetration in the case that d is not smaller than a certain

value.

The coordinates of elements are updated at each time step in Up-dated Lagrangian formation. The stress increment with element rotation Δr_0 at each time step is represented by Jaumann's co-rotational differential, hence, the objectivity of the stress is fulfilled. Then the stresses before and after the rotation are superposed by Eq.(34) and (35).

$$\dot{\sigma}_{ij} = \Delta\sigma_{ij} + \sigma_{ik}\Delta W_{kj} + \sigma_{jk}\Delta W_{ki} \tag{34}$$

The total stress is expressed by Eq.(35).

$$\sigma_{ij}^{t+\Delta t} = \sigma_{ij}^{t} + \dot{\sigma}_{ij}\Delta t \tag{35}$$

where, $\dot{\sigma}_{ij}$: the stress rate tensor, $\Delta\sigma_{ij}$: the stress increment tensor, ΔW_{ij} : the rigid rotation increment tensor.

This manipulation is important, for instance, in the case of the large spin motion on toppling analysis of slope and the elastic-plastic analysis in which a block has the different principal axis of strain at each step in particular.

3 NUMERICAL MODELS AND RESULTS

Fig.7 shows the dual cavern model with six discontinuous planes. Here, in order to express the roller conditions along boundaries, the dummy elements are attached. The dimensions of two caverns are assumed height =18m and width =12m respectively. The material properties of rock mass, the elastic modulus E_0=1GPa, Poisson's ratio ν =0.25, cohesion c_{se}=0.5MPa, the internal friction angle ϕ_e =40° and the work hardening coefficient H'=10MPa are assumed respectively. The characteristics of discontinuous planes, the friction angel of surface ϕ_s =10° , shear stiffness K_s=10MPa, Penalty coefficient of perpendicular direction P=100GPa are assumed respectively. The initial stresses is assumed 1MPa of the hydrostatic conditions at the caverns. Total number of elements and nodes are 2231 and 1487 respectively. Fig.7 shows the principal stress and the plastic regions at the 20 steps in time increment 0.1sec of the quasi static condition without rock bolts. The plastic regions are distributed along discontinuous planes near the caverns. Fig.8 shows the result with rock bolts as same conditions as Fig.7 above described. The stiffness of rock bolt is assumed S_b=2MN of the truss elements shown in Fig.8.

In comparison with Fig.7 and Fig.8, the effectiveness of the rock bolts is evidenced in the plastic regions in Fig.8, which are larger than in Fig.7 at the left side of each caverns along the discontinuous planes.

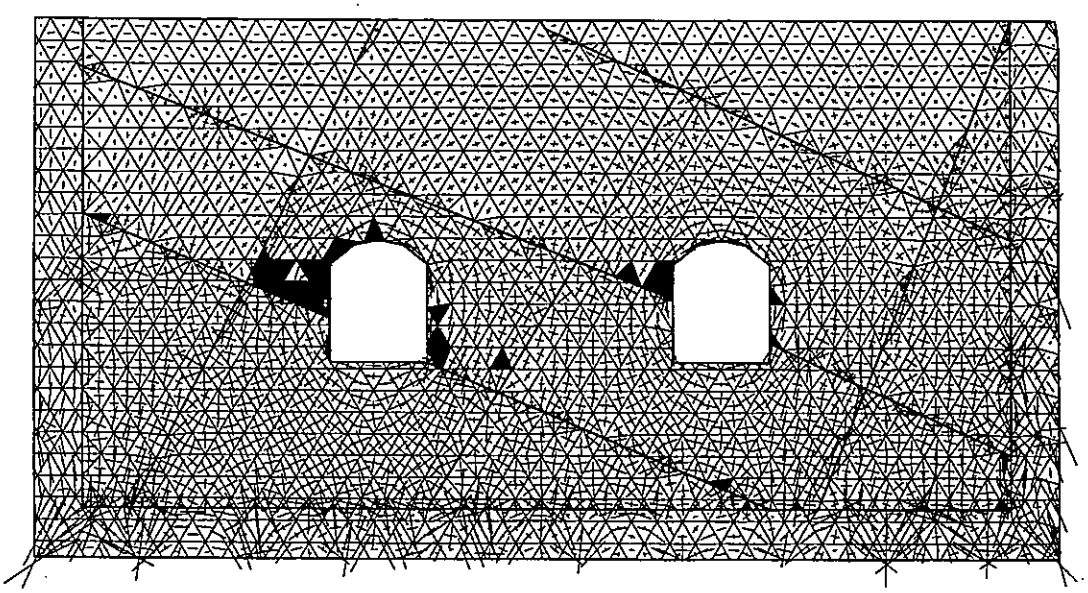

Fig. - 7 Plastic regions of the dual cavern model

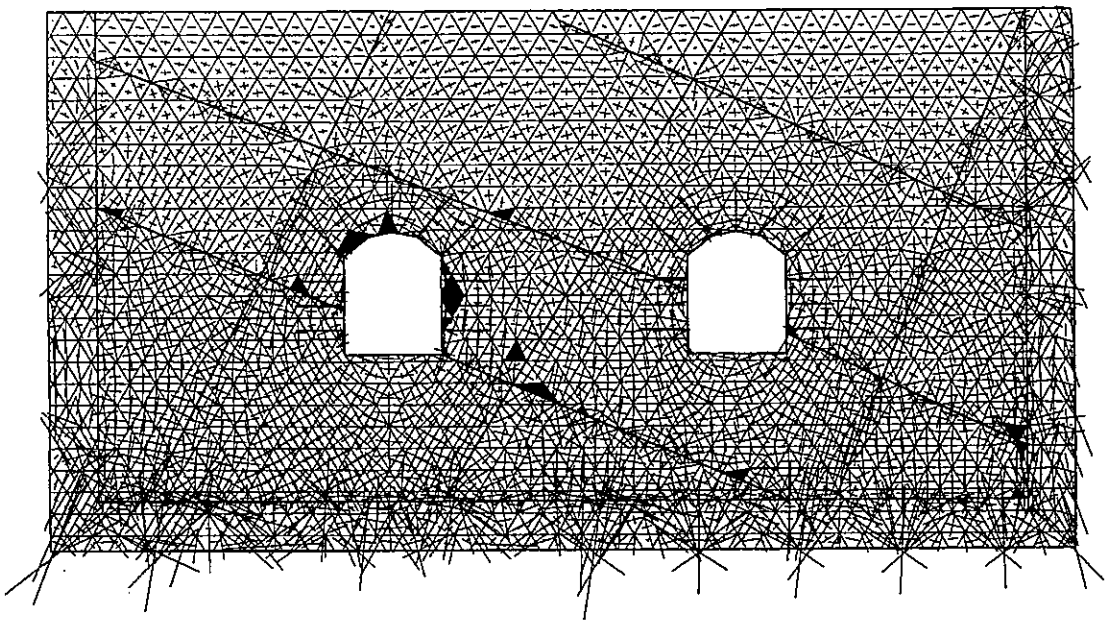

Fig. - 8 Plastic regions of the dual cavern model with rock bolts

4 CONCLUSIONS

The authors examined the applicability of Manifold method for the rock mechanics problems by using the dual cavern model with discontinuous planes in the elastic-plastic analysis with rock bolts. The results showed the distribution of the plastic regions along the part of the upper side of a pair of discontinuous planes near the caverns. These results agree with the physical phenomenon of the characteristics in rock mechanics. The effects of rock bolts is indicated obviously for the plastic area but less for the deformation. The advantages of Manifold method is that the mathematical mesh is independent of the physical mesh. Therefore, the studies for the result on mesh dependency, especially in the case of the elastic-plastic analysis, is can be easily repeated.

ACKNOWLEDGMENT

The authors would like to acknowledge to Dr. G. H. Shi for many informative discussions.

REFERENCES

1)Shi, G. H. : Block system modeling by Discontinuous Deformation Analysis, Univ. of California, Berkeley, Dept. of Civil Eng. August, 1989.

2)Shi, G. H. : Manifold method of material analysis, Trans. 9th Army Conf. on Appl. Math. and Comp., Rep. No. 92-1. U.S. Army Res. Office,1991.

3)Shi, G. H. : Modeling rock joints and blocks by Manifold method, Proc. 33rd U.S. Symp. on Rock Mech., A.A. Balkema, pp.639-648, 1992.

4)Sasaki, T., Ishii, D., Ohnishi, Y., Yoshinaka, R. : Stability analysis of rock foundations by discontinuous deformation analysis, 8th ISRM Tokyo Congress, Technical Session of rock foundation, pp.337～342, 1995.

5)Sasaki, T., Ohnishi, Y. : Manifold method and its application to rock mechanics problems, Proc. 1st Conf. of the Japan Society for Comp. Eng. and Science, pp.901～904, 1996.

Utilization of Finite Covers in the Manifold Method for Accuracy Control

Hideomi Ohtsubo, Katsuyuki Suzuki, Kenjiro Terada, and Katsuyoshi Nakanishi

Department of Naval Architecture and Ocean Enging., The University of Tokyo, Bunkyo-ku, Tokyo 113, Japan

ABSTRACT: The remarkable features of the Manifold Method are utilized to develop a new analysis tool for CAD embedded CAE systems. Renaming the method specialized for MDA the finite cover method, we examine its applicability and the ability of controlling the approximation levels for structural analyses. By using finite number of mathematical covers of square shape and of the same size, the overlap of which constitutes a continuous approximation region, we look at this new idea as a basis for the development of one of the mesh-free methods.

1. INTRODUCTION

Manifold Method (MM)[1],[2] is known to be a newly developed analysis tool and has several remarkable features from a practical point of view. By distinguishing the domain for defining approximation functions and the physical one, the MM has a significant features such that (1) both continuous and discontinuous deformation/motion can be dealt with simultaneously. That is the reason why the MM is said to be a generalized method that unifies both Discontinuous Deformation Analysis (DDA)[3] method and Finite Element Method (FEM). In addition, since finite number of mathematical domains, called covers, is introduced for defining the approximation functions, regardless of the geometry of the structures, it is possible (2) to analyze an arbitrary domain, and (3) to require there with desired accuracy.

Although the first feature mentioned in the above has been mainly emphasized in the literature[2], less attention have been paid to the last two. This fact is probably due to the fact that the MM was originally developed for the deformation/motion analysis of rock masses in geotechnical engineering field by Ohnishi et al.[2] and that therefore most of the reports utilizing the MM has been limited to such a research area that requires continuous deformation with discontinuous motion. Since the features (2) and (3) are suitable particularly for the CAD/CAE system designed for MDA (Mechanical Design Automation), the MM could be a key technique for our future analysis environment. In this context, let us call this distinguished analysis tool as finite cover method (FCM) especially when aiming at the integration of design and analysis. We shall show in this paper that the FCM has a capability of accuracy control by introducing various approximation function on finite covers. It is also emphasized that the MM can be a kind of a mesh-free analysis tool and would play a central role in the CAD/CAE-integrated system by combining with the multi-voxel based FEM[4].

2. FINITE COVER APPROACH BY MANIFOLD METHOD[1]

(1) Mathematical Finite Covers

The FEM takes a process of discretizing the physical space into the finite number of "elements", approximating the unknown functions (e.g., displacement, stress, etc.) by defining simple interpolating functions over each element, and combing all the equations into a system of equations based on the element connectivity information. On the other hand, although the FCM also discretize both the physical and function spaces, it distinguishes the mathematical domain, called the "mathematical cover", into which the approximation functions are introduced from the physical domain where the governing equations are given in the weak form. The finite number of mathematical covers are located over the physical domain so that neighboring covers are overlapped each other and each of their edges coincides with the next cover, see Fig.1. The stiffness matrix is constructed for all the overlapped regions (each of them is called an element) and combined for equating the finite dimensional system of governing equations.

Fig.2(a) shows that mathematical covers are located over the whole body of the geometrical information of discontinuity. By defining multiple set of overlapped regions, i.e., elements, on the discontinuities, the FCM can deal with its discontinuous deformation or motion, see Fig.2(b). Note here that, although we can introduce any shape, the shape of covers used in this paper are chosen to be a square or cubic so that the multiple voxel-based analysis can be combined in the future.

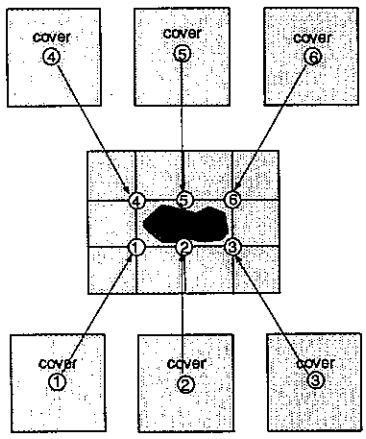

Fig.1 Concept of finitely covering

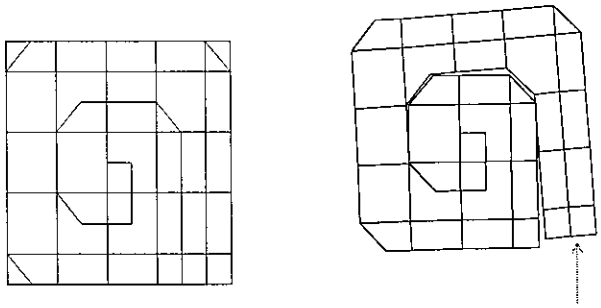

(a) Physical body covered by FCM mesh (b) Deformed configuration

Fig.2 Typical example of FCM analysis

(2) Element Stiffness Matrix[5]

In order to approximate the displacement field, we introduce the following two kinds of functions to the i-th cover:

$f_i(x, y)$: (displacement) cover function

$w_i(x, y)$: weight function

where the former can be defined for each cover arbitrarily. Also, the latter function is defined over U_i as follows:

$$w_i(x,y) \geq 0 \quad (x,y) \in U_i \tag{1}$$

$$w_i(x,y) = 0 \quad (x,y) \notin U_i \tag{2}$$

where U_i is the common region of mathematical and physical domains, and the summation of them must be a unity such that

$$\sum_{x,y \in U_i} w_i(x,y) = 1 \tag{3}$$

Note that, in the case of FEM, the condition (2) is not necessary since the mathematical domain and the physical one coincides while the DDA identifies the mathematical cover with a physical block.

Thus, after the cover functions plus the weight functions are defined on each cover, the actual displacement function can be approximated as the weighted sum of them, e.g., for the displacement in the x-direction, we have

$$u\ (x,y) = \sum_{i=1}^{k} f_i(x,y) w_i(x,y) \cdot \tag{4}$$

where k is the number of covers used for interpolation and i indicates the cover number. While any cover function can be introduced onto the mathematical cover, the continuity of the displacement field on each element are postulated according to the weight functions.

If we define $s_{1,i}$ as a constant, each cover has just one degree of freedom for one component of displacement:

$$f_i(x,y) = a_{1,i}\, s_{1,i} \tag{5}$$

Also, the higher order approximation is achieved by introducing corresponding polynomials together with unknown coefficients for each cover function, e.g., for a linear and a quadratic functions, we respectively have

$$f_i(x,y) = a_{1,i}\, s_{1,i} + a_{2,i}\, s_{2,i}(x,y) + a_{3,i}\, s_{3,i}(x,y) \tag{6}$$

$$f_i(x,y) = a_{1,i}\, s_{1,i} + a_{2,i}\, s_{2,i}(x,y) + a_{3,i}\, s_{3,i}(x,y) + a_{4,i}\, s_{4,i}(x,y) + a_{5,i}\, s_{5,i}(x,y) \tag{7}$$

It should be noted that the totality of the approximation functions has a hierarchical structure of cover functions. If we defines the (displacement) cover functions in the x and y-directions as,

$$f_i(x,y)=a_{1,i}\,s_{1,i}+a_{2,i}\,s_{2,i}(x,y)+..+a_{m,i}\,s_{m,i}(x,y) \tag{8}$$

$$g_i(x,y)=b_{1,i}\,s_{1,i}+b_{2,i}\,s_{2,i}(x,y)+..b_{m,i}\,s_{m,i}(x,y) \tag{9}$$

on a mathematical cover, U_i, the unknown displacement fields are approximated as

$$u\ (x,y)=\sum_{i=1}^{k} f_i(x,y)w_i(x,y)=\sum_{i=1}^{k}(a_{1,i}\Phi_{1,i}+a_{2,i}\Phi_{2,i}+\ldots+a_{m,i}\Phi_{m,i}) \tag{10}$$

$$v\ (x,y)=\sum_{i=1}^{k} g_i(x,y)w_i(x,y)=\sum_{i=1}^{k}(b_{1,i}\Phi_{1,i}+b_{2,i}\Phi_{2,i}+\ldots+b_{m,i}\Phi_{m,i}) \tag{11}$$

where we have defined $\Phi_{j,i}=s_{j,i}\,w_i$. In matrix representation, we have

$$\begin{Bmatrix} u \\ v \end{Bmatrix}=\left[\begin{array}{cc:c} \Phi_{1,1}\cdots\Phi_{m,1} & 0 & \cdots \\ 0 & \Phi_{1,1}\cdots\Phi_{m,1} & \cdots \end{array}\right]\left[a_{1,1}\ \cdots\ a_{m,1}\ \vdots\ b_{1,1}\ \cdots\ b_{m,1}\ \ |\cdots|\cdots|\cdots\right]^T \tag{12}$$

$$=[N_1\ \ N_2\ \ \cdots\ \ N_k][A_1\ \ A_2\ \ \cdots\ \ A_k]^T$$

Substituting this form into the governing equations of weak form for each element, the stiffness matrix and the generalized force vector so that the system of equations are constructed according to the connectivity information of finite covers.

Although the cover used here is a square type, the weight functions in it is the same as the bilinear shape functions of an finite element when we identify the overlapped region as an element. Also, the polynomials are used for the cover function although there is any limitation provided that they construct a linearly independent set within a cover. In the numerical analysis in the following sections, we shall use the piecewise constant , linear and quadratic functions, the latter two of which are illustrated in Fig.3.

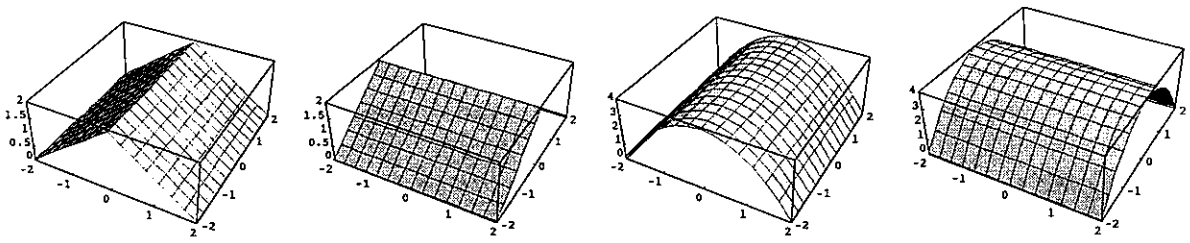

$s_{2,i}(x,y)$ $s_{3,i}(x,y)$ $s_{4,i}(x,y)$ $s_{5,i}(x,y)$

(xy axes are labeled with local coordinates whose origin is located at the center of each cover)

(a) Linear functions (b) Quadratic functions

Fig.3 Cover displacement functions

(3) Boundary conditions

Let $u(x, y)$ and $v(x, y)$ be displacement function in the x- and y-directions, respectively defined by Eqn. (10) and (11). Here we present how to treat the boundary conditions in implementing the FCM computer program.

The displacement boundary condition must be applied to the actual boundary. However, since unknown coefficients have not been introduced on the actual boundary, the constraints must be provided by the penalty terms. For example, if the displacement $(\bar{u},\ \bar{v})$ is given on the boundary, Γ_u, the penalty potential can be represented by

$$\Pi_u=\frac{1}{2}\int_{\Gamma_u}\{u(x,y)-\bar{u},\ v(x,y)-\bar{v}\}\begin{bmatrix} p_x & 0 \\ 0 & p_y \end{bmatrix}\begin{Bmatrix} u(x,y)-\bar{u} \\ v(x,y)-\bar{v} \end{Bmatrix}d\Gamma \tag{13}$$

where p_x and p_y are the penalty parameters.

Similarly, when the tractions, t_x and t_y, are applied on Γ_t, the potential energy due to the external surface force is evaluated as follows:

$$\Pi_t=-\int_{\Gamma_t}\{u(x,y),v(x,y)\}\begin{Bmatrix} t_x \\ t_y \end{Bmatrix}d\Gamma \tag{14}$$

3. NUMERICAL EXAMPLES

(1) Pressurized thick circular tube

We here just emphasize the modeling and analysis capability of the FCM (or equivalently MM) by carrying out a simple numerical analysis of static, plane strain linear elasticity problems. The structure, its geometry information and the boundary conditions are given in Fig.4 and the material is assumed be a standard steel of Young's modulus: 284 GPa and Poisson's ratio: 0.32. Note here that the MM or FCM mesh does not need to fit to the physical boundary. Fig.5 shows the von-Mises stress distribution evaluated at the center of each element. However, commercial pre-postprocessors available for FEA cannot incorporate the idea of covering, the FCM mesh must have been converted to FEM mesh artificially made to export the results to it. In this context, the combination of the multiple-voxel modeling technique with the FCM seems very promising since it can provide the geometry and the results by voxel picture elements (voxels), see Fig. 6 for the concept.

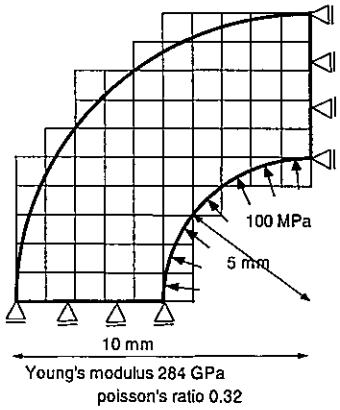

Fig.4 Thick circular tube

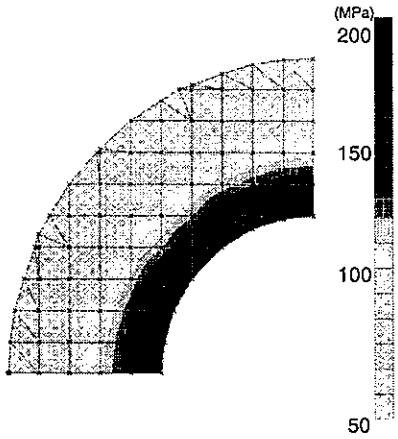

Fig.5 von Mises stress distribution

(2) Degrees of Approximation and its influence on the solution accuracy

In order to investigate the capability of higher order approximation, we here utilize the cover functions introduced in Section 2. Let us consider the two cases of different approximation levels by using different polynomial cover functions. The first case adopts constant cover functions which, together with weight functions, provide the same approximation scheme as the FEM using bilinear shape functions. The second case utilize two kinds of quadratic cover functions, both of which are given in Fig.3(b), together with linear (Fig.3(a)) and constant ones.

Fig.8 shows the y-component of normalized stress along line AB specified in Fig.7 for each case. As can be seen from the figure, the first case, which is the same as bilinear approximation in FEM, reveals discontinuity of stress value at each central position, which corresponds to a node in FEM, of edge of mathematical covers used in the FCM mesh. Although the lower approximation seems to provide relatively large error especially on the element boundaries, it is found that the use of higher order cover functions, namely the second case, would overcome such a discrepancy. The fact can also be recognized by the values of intensity factor at Point B, that is, the second case provides the value higher than 3.0 while the first case cannot accommodate a high gradient of stress field.

It is also possible to locate any cover functions of different approximation levels from place to place. Fig. 9 shows the two possible choices for higher approximation and let us call them case a and b. Here the region to be approximated using linear cover functions are highlighted and the remaining portion is approximated by constant cover function only. For both cases, the stress concentration factors evaluated at point B specified in Fig.7 are 3.410 and 3.409, respectively. For the purpose of comparison, the values 2.593 and 3.412 have been obtained for the case that only constant cover function are used in all the covers and the case using quadratic ones for the whole domain. This implies that the FCM can afford to control the accuracy of analyses by selecting appropriate order of cover function and by locating the higher order covers over possible error-

accumulating regions. In addition, if we utilize the special functions such as wavelets as cover functions, the singularity nature of the solution might be captured with relatively little effort.

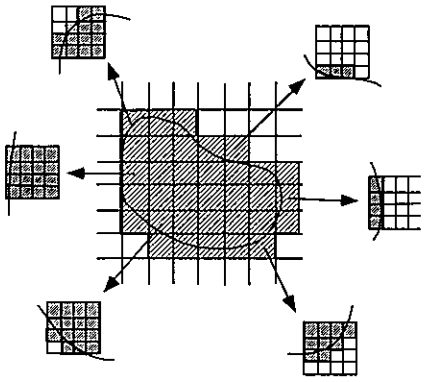

Fig.6 Concept of voxel-based modeling

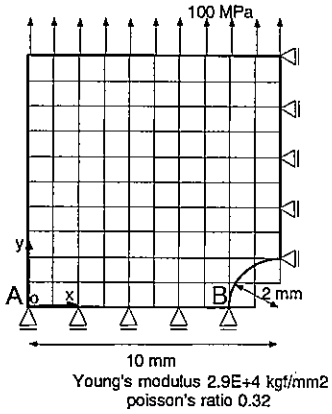

Fig.7 Infinite plate with a circular hole

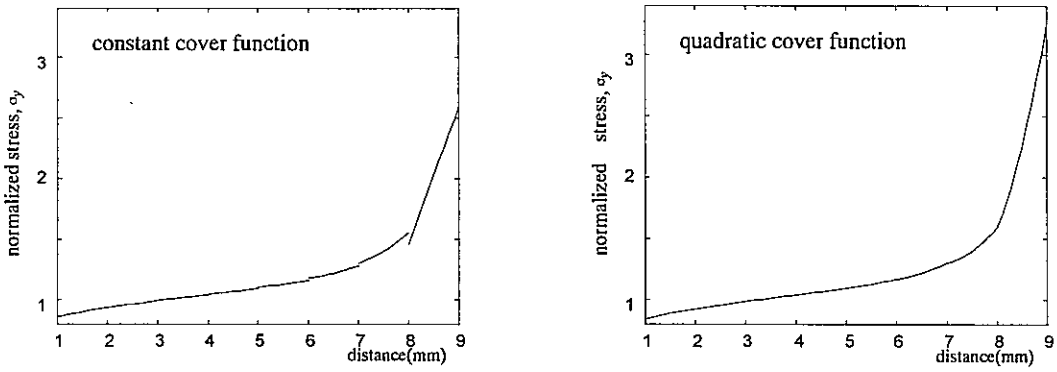

(a) case 1: constant cover function only (b) case 2: with quadratic cover function

Fig.8 Comparison of stress values for the cases of different approximation levels

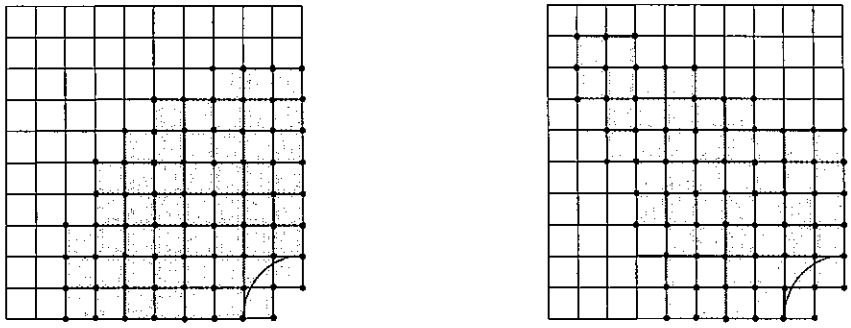

(a) case a (b) case b

Fig.9 Locally-located finite covers of higher order approximation

4. CONCLUSIONS

We have reconsidered and examined the capability of the Manifold Method (MM), which has been applied to rock mechanical problems involving discontinuous deformation/motion, within the framework of Computer-Aided Engineering (CAE) use. Together with the affinity with DDA and FEM, its preferable features such as the flexibility for accuracy control and the simplicity of modeling prompted us to call the MM as the finite cover method (FCM).

As the first attempt to introduce the FCM concept to CAD/CAE-dominated engineering field, the capability of accuracy control, which is one of the major requirement to practical analysis tools, are justified by simple numerical examples. It was found that the introduction of different approximation levels of cover functions illustrated the applicability of adaptive method such as p-method for FEM. Also, the extension to a mesh-free technique incorporated with the nature of FCM has been anticipated by utilizing the same size of square shape of mathematical covers. The development in this paper and the ongoing our research would provide a good insight into a way to evolve computational mechanics.

REFERENCES

1) Shi, G. H. : Manifold Method of material analysis, Transactions of the 9th Army Conference on Applied Mathematics and Computing, Report No. 92-1. U.S. Army Research Office, 1991.

2) Ohnishi, Y : Study of applicability of the Manifold Method to rock engineering, Proceedings of workshop for the Applications of Advanced Computational Science and Technology in Construction Engineering, Group for Advanced Computational Science and Technology, 1996, pp.1-8 (in Japanese).

3) Shi, G. H. : Block system modeling by Discontinuous Deformation Analysis, Univ. of California, Berkeley, Dept. of Civil Eng. August, 1989

4) Ohtsubo, H., Suzuki, K., Terada, K. and Yonesato, N. : Analysis method for solid structures using multiple voxel information, Proceedings of Computation Engineering and Sciences, Vol.2, No.2, pp. 395-398, 1997 (in Japanese).

5) Nakanishi, K. : Study on the finite cover method, Bachelor thesis, The University of Tokyo, 1997 (in Japanese).

Static Contact Problems of Discrete Systems Solved by the Diffuse Element Method

Ming-Hong Chen, Chung-Yue Wang and Jopan Sheng

Department of Civil Engineering,
National Central University, Chung-Li, 32054, Taiwan, R.O.C.

Keywords: Diffuse Element, Discontinuous, Contact, Lagrange Multiplier, Collocation

ABSTRACT

In this paper, a new numerical method called "Diffuse Element Discontinuous Deformation Analysis (DEDDA)" is presented to perform the multi-body contact analysis of a discrete system. The Diffuse Element can define an arbitrary point within the analysis domain as a reference point, and the area surrounding the reference point is defined as an "influence zone". The approximation function of an influence zone is determined by weighted least squares fitting of calculated nodal displacement values within the zone. Once the approximation function is determined, the derivatives of physical quantities at the corresponding reference point are obtained. The Diffuse Element Method can be considered as an extension of the Finite Element Method. The major difference between them is the requirement of connectivity condition of element nodal points in FEM is no longer necessary in the Diffuse Element Method. In the Diffuse Element Method, each influence zone contains different amount of nodes, and nodes within each influence zone could be added or extracted at any time as the analyst desired. This feature makes it is more suitable to do the problems with stress concentration effects or with dynamic fracturing process.

To conquer difficulties admitted in applying conventional penalty spring method to the contact analysis. The Augmented Lagrange Multiplier method is adopted into the formulation of this newly proposed discontinuous deformation analysis method.

Through it the contact force is attained through iteration and the initially selected penalty number does not affect the result of predicted contact force. Numerical results demonstrate that this DEDDA method performs the contact analysis of discrete system very well.

1. INTRODUCTION

It is difficult to analyze discontinuous problems by continuous numerical models. Since the DDA method was first introduced by Shi in 1988, engineers may have a new tool to attack the discontinuous problems in geo-mechanics [1]. However, the constant strain field description of the deformation of each DDA block is sometimes too coarse to represent the real stress distribution within a block of irregular geometry. For improving the displacement approximation function used in each block, sub-block [5, 9] (or called artificial joint [4]) and attaching FEM mesh to block [3, 8, 10] were then developed. The concept of former is dividing an entire block into many " sub-blocks, and these sub-blocks are connected by penalty springs with very high stiffness. These penalty springs keep all the sub-blocks moving together during the analysis, and satisfy the compatibility requirement of continuum materials. Combination of the DDA and the FEM provides a possible solution to gain a better result through using more nodes or with higher order shape functions. This improved DDA method is also called nodal-based discontinuous deformation analysis (NBDDA), and can be treated as a simplification of the Manifold Method recently developed by Shi [2].

The Diffuse Element Method was first introduced by Nayroles etc. in 1992 [6]. The algorithm and structure of this method are very similar to FEM and the Manifold method, the analyzed domain is discretized by some nodal points and getting the global equilibrium from local analysis. Only a set of distributed nodes and a boundary description is needed in the Diffuse Element Method. While the conventional FEM mesh used to build the approximation function is unnecessary in this method. The connectivity of nodes to element in FEM is not required any more. Through the weighted least square fitting of nodal values within an influence zone, a more precise result can be obtained as reported by references [7]. The diffusion of the connectivity of nodal points has the

capability of constructing the local approximation more flexible and based on more data surrounding the reference point. This concept is somewhat like the usage of independent physical mesh and independent mathematical mesh in the Manifold method. The relations and similarities between the Diffuse Element Method and the Manifold had been discussed elsewhere by the authors [11].

The main goal of the long term research of the authors is to develop a more effective computational method which can simulate the dynamic behavior of a solid body from a continuous medium to a discontinuous one with cracks, damage or fragmentation.. etc. in one complete simulation process. The adaptive, fracturing algorithms, accurate and flexible approximation theories, contact detection and analysis techniques, nonlinear deformation theories and the time integration schemes all are the items have to be included into the above prediction model. In this paper, the diffuse element method, collocation time integration scheme and the Lagrange multiplier contact theory are used to form a new computation model to solve the dynamic contact problems of discrete system.

2. FORMULATION

2.1 Basic Theories of the Diffuse Element Method

There are two major features of the Diffuse Element Method. One is the local weighted least squares fitting and the other is the no explicit elements. In the diffuse approximation method, around any arbitrarily chosen reference point "$\bar{x}$" in the domain, $n^{\bar{x}}$ nearest nodes can be selected, then the displacement function is locally approximated by a set of well known base functions $\langle p(x) \rangle$:

$$u^{\bar{x}}(x) = \langle p(x) \rangle \left\{ a^{\bar{x}} \right\} = \sum_{j=1}^{m} p_j(x) a_j^{\bar{x}} \tag{1}$$

where $\langle p(x) \rangle$ is a vector of "m" independent base functions, most often polynomial terms, for example $[p(x)]^T = [1, x, y, x^2, xy, y^2]^T$, and $\left\{ a^{\bar{x}} \right\}$ is a vector of "m" approximation

coefficients. The total weighted least square error between the approximate value $u^{\bar{x}}(x)$ expressed by Eq.(1) and the analytical value $u(x)$ can be expressed as

$$J^{\bar{x}}\left(a^{\bar{x}}\right)=\sum_{i=1}^{n} w^{\bar{x}}(x_i)\left(u_i-u^{\bar{x}}(x_i)\right)^2 \tag{2}$$

where $w^{\bar{x}}(x_i)$ is the weighting of error at each node, and "n" is the numbers of nodes selected surrounding "$\bar{x}$". Substituting Eq. (1) into Eq. (2) leads to

$$\begin{aligned} J^{\bar{x}}\left(a^{\bar{x}}\right)&=\sum_{i=1}^{n} w^{\bar{x}}(x_i)\left(u_i-\langle p(x_i)\rangle\left\{a^{\bar{x}}\right\}\right)^2 \\ &=\left(\{u_i\}-[P_n]\left\{a^{\bar{x}}\right\}\right)^T[W]\left(\{u_i\}-[P_n]\left\{a^{\bar{x}}\right\}\right) \quad j=1,m \end{aligned} \tag{3}$$

As the coordinates of nodes are known, the stationary of $J^{\bar{x}}\left(a^{\bar{x}}\right)$ means

$$[P_n]^T[W][P_n]\left\{a^{\bar{x}}\right\}-[P_n]^T[W]\{u_i\}=0 \tag{4}$$

let

$$\left[A^{\bar{x}}\right]=[P_n]^T[W][P_n]=\sum_{i=1}^{n} w^{\bar{x}}(x_i)\{p(x_i)\}\langle p(x_i)\rangle$$

$$\left[B^{\bar{x}}\right]=[P_n]^T[W]=\sum_{i=1}^{n} w^{\bar{x}}(x_i)\left[0\cdots\{p(x_i)\}\cdots 0\right]$$

then Eq. (4) can be reformed as

$$\left[A^{\bar{x}}\right]\left\{a^{\bar{x}}\right\}=\left[B^{\bar{x}}\right]\{u_i\} \tag{5}$$

From Eq.(5) and Eq.(1), we may have

$$u^{\bar{x}}(x)=\langle p(x)\rangle\{a^{\bar{x}}\}=\langle p(x)\rangle\left[A^{\bar{x}}\right]^{-1}\left[B^{\bar{x}}\right]\{u_i\}=\langle N^{\bar{x}}(x)\rangle\{u_i\}$$
$$\langle N^{\bar{x}}(x)\rangle=\langle p(x)\rangle\left[A^{\bar{x}}\right]^{-1}\left[B^{\bar{x}}\right] \tag{6}$$

The element number of shape function matrix $\langle N^{\bar{x}}(x)\rangle$ is equal to the number of nodes within influence zone used in Eq. (6). In other words, the shape function is a one dimension matrix of $(1\times n)$. Due to the introduction of weighting function into the formulation, the shape function in Eq. (6) could no longer be polynomials, even we select polynomial terms as base function. According to above derivations, there may be variable number of nodes around each reference point "$\bar{x}$", and it also may be with different approximate coefficient number. It is obvious that this type of approximation theory breaks the connectivity requirement between nodes and approximation coefficients in FEM. It should be noted in Eq. (6), the number of nodes chosen around a reference point must be more than or at least equal to the number of shape function terms, to avoid $\left[A^{\bar{x}}\right]$ being a singular matrix. When the number $n^{\bar{x}}$ is larger than the number "m" of approximation coefficients, it is possible to get the coefficient values due to least square fitting.

The derivative $\left(\frac{\partial u}{\partial x}\right)_{\bar{x}}$ of a function $u(x)$ at point "$\bar{x}$" is obtained by differentiating $\langle p(x)\rangle$ with respect to x either from Eq. (1), or form Eq. (6) as

$$\left(\frac{\partial u}{\partial x}\right)_{\bar{x}}=\left\langle\left(\frac{\partial p}{\partial x}\right)_{\bar{x}}\right\rangle\{a^{\bar{x}}\}=\left\langle\frac{\partial N^{\bar{x}}}{\partial x}\right\rangle\{u_i\}$$
$$\left\langle\frac{\partial N^{\bar{x}}}{\partial x}\right\rangle=\left\langle\frac{\partial p}{\partial x}\right\rangle\left[A^{\bar{x}}\right]^{-1}\left[B^{\bar{x}}\right] \tag{7}$$

where

$\{u_i\}$ is the vector formed by the nodal values inside the influence zone.

$\{a^{\bar{x}}\}$ is considered as a constant vector in the influence zone.

2.2 Comparison Between the Diffuse Element Method and the FEM

According to the basic theories presented in the previous section, one can realize that the Diffuse Element Method replace the interpolation function valid on an element in FEM by a local weighted least squares fitting, in a small neighborhood of a point "$\bar{x}$". The number of interpolation functions used in FEM must match the number of nodes that construct an element. While the Diffuse Element Method defines a "influence zone" to construct the interpolation function from nodes surrounding the reference point "$\bar{x}$" without specific nodes-element connectivity. Since the distribution of nodes in each influence zone centered at a reference point "$\bar{x}$" is arbitrary and the size of the influence zone can be defined by the analyst. The number of nodes could vary with respect to different reference point "$\bar{x}$". Therefore, the final format of shape functions is not uniform in whole domain, even only one type of base function is used.

In FEM, the weighting function $w^{\bar{x}}(x_i)$ used in Eq. (2) is usually set to be unit over the whole element to represent the error on each node with same importance. But in the Diffuse Element Method the weighting function on each node decreases in magnitude with longer distance from reference point and it reduces to be zero as a node locates outside the influence zone. The choice of weighting function is arbitrary as long as it is positive and continuous together with its derivatives up to the desired degree. An exponential weighting function of the following form is considered in this paper:

$$w_i\left(d_i^2\right)=\begin{cases}\dfrac{e^{-(d_i/c)^2}-e^{-(d_{mi}/c)^2}}{\left(1-e^{-(d_{mi}/c)^2}\right)}, & d_i \le d_{mi}\\ 0, & d_i > d_{mi}\end{cases} \tag{8}$$

where d_i is the distance from node x_i to reference point $\bar{x}$. The d_{mi} determines the domain of influence zone of $\bar{x}$, and c is the longest distance between each two nodes inside the zone. Based on this weighting function, the first order derivative of exponential weighting function is continuous in the influence zone.

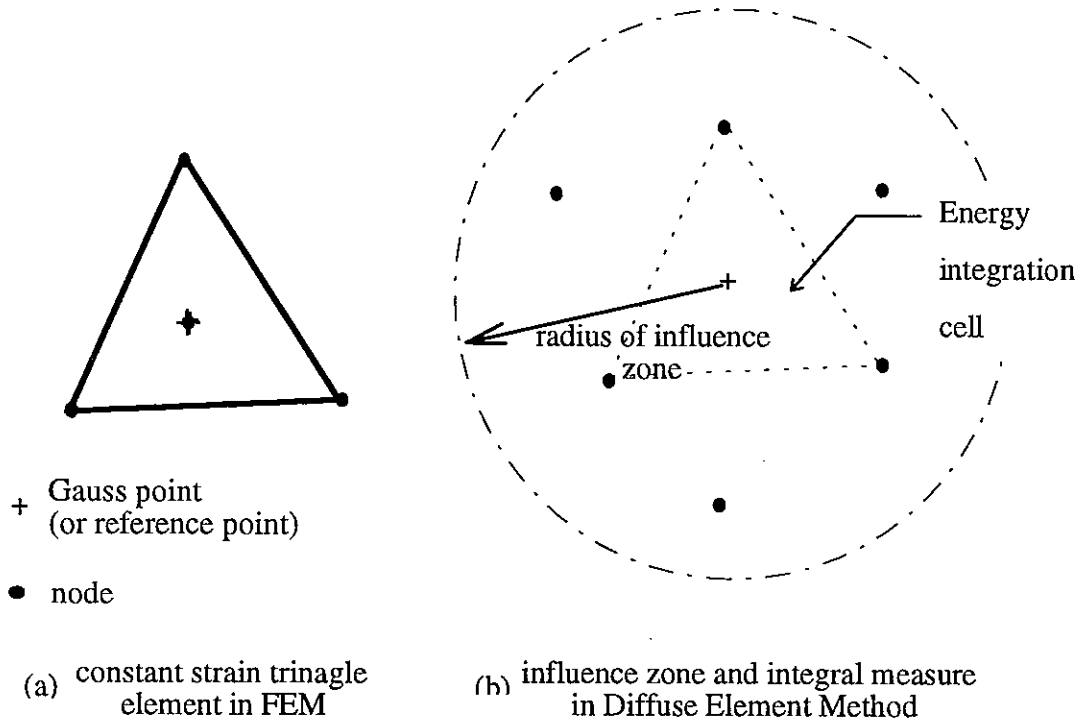

Fig. 1 Comparison between the element defined in the FEM and the Diffuse Element Method

Another difference between the FEM and the Diffuse Element Method is the application of Gauss quadrature rule. In FEM, the integration of strain energy over a triangle element can be obtained by multiplying the stress and strain valued at the quadrature points with corresponding integration weighting coefficients and element area as shown in Fig. 1. The application of quadrature rules in Diffuse Element Method is very similar to FEM except that stress and strain values of the quadrature point are determined by values of all the nodes contained in the influence zone centered by the quadrature point as shown in the Fig. 1. The more nodes to be included in deriving the stress and strain values at reference point the better result is generally obtained. Diffuse Element Method offers a way to arrange the nodal point distribution and density very adaptively depending on the practical necessity. In order to calculate the total strain energy of the whole deformable body, a mesh for applying quadrature rule is required. This mesh is different from a FEM mesh which is used both to construct the approximation function and to calculate the strain energy, but can be free to be refined or

split as required by some physical problems without concerning the connectivity of nodes. The range bounded by dashed lines in Fig. 1 is a integral measurement cell. It can be easily accomplished by the mesh generation techniques in FEM. The shape of the integration cell can be any shape as it has suitable quadrature rule. This integration cell mesh satisfies the requirements of non-overlapping and non-separating condition and the sum of all element's area is equal to the total area of domain. However, its vertices do not need to be a nodal point.

3. CONTACT ANALYSIS

3.1 Contact Detection

The success of the discontinuous deformation analysis of any discrete system strongly depends on the scheme of contact analysis, which includes the contact detection, impenetrability condition, load transfer mechanism and associated data structure among different bodies. In the computational contact analysis, block boundaries are discretized and connected by nodes. In general, there are three types of contact condition admitted: "vertex to vertex", "edge to edge" and "vertex to edge". All the three types can be decomposed into "vertex to edge" type contact. During the contact analysis of any two bodies, a 3-node contact pair is formed that contains a vertex point of a block, and two nodes of a edge on the boundary of the other block to be penetrated. In each 3-node contact detection pair, the contact forces are treated as nodal forces and shape functions are unnecessary during the analysis.

Assume d_n is the normal penetration of entering vertex P_1 enters penetrated edge $\overline{P_2P_3}$ (shown in Fig. 2) , then penetration depth in normal direction of the edge can be determined as

$$d_n=\frac{1}{l}\begin{vmatrix}1 & x_1+u_1 & y_1+v_1\\ 1 & x_2+u_2 & y_2+v_2\\ 1 & x_3+u_3 & y_3+v_3\end{vmatrix}$$
$$\approx\frac{1}{l}\left(S_0+\begin{Bmatrix}y_2-y_3 & x_3-x_2\end{Bmatrix}\begin{Bmatrix}u_1\\ v_1\end{Bmatrix}+\begin{Bmatrix}y_3-y_1 & x_1-x_3\end{Bmatrix}\begin{Bmatrix}u_2\\ v_2\end{Bmatrix}+\begin{Bmatrix}y_1-y_2 & x_2-x_1\end{Bmatrix}\begin{Bmatrix}u_3\\ v_3\end{Bmatrix}\right) \tag{9}$$

let

$$l = \overline{P_2P_3} = \sqrt{(x_2 - x_3)^2 + (y_2 - y_3)^2}$$

$$[H]_{1\times 2} = \langle y_2 - y_3 \quad x_3 - x_2 \rangle / l$$

$$[G1]_{1\times 2} = \langle y_3 - y_1 \quad x_1 - x_3 \rangle / l$$

$$[G2]_{1\times 2} = \langle y_1 - y_2 \quad x_2 - x_1 \rangle / l$$

$$S_0 = \begin{vmatrix} 1 & x_1 & y_1 \\ 1 & x_2 & y_2 \\ 1 & x_3 & y_3 \end{vmatrix} \tag{10}$$

substitute Eq. (10) into Eq. (9), and d_n is rewritten as

$$d_n = [H]\begin{Bmatrix} u_1 \\ v_1 \end{Bmatrix} + [G1]\begin{Bmatrix} u_2 \\ v_2 \end{Bmatrix} + [G2]\begin{Bmatrix} u_3 \\ v_3 \end{Bmatrix} + S_0/l \tag{11}$$

and the potential energy caused by normal contact spring is

$$\begin{aligned} \pi_{kn} = pd_n^2/2 &= \tfrac{p}{2}\left([H]\begin{Bmatrix} u_1 \\ v_1 \end{Bmatrix} + [G1]\begin{Bmatrix} u_2 \\ v_2 \end{Bmatrix} + [G2]\begin{Bmatrix} u_3 \\ v_3 \end{Bmatrix} + S_0/l\right)^2 \\ &= \tfrac{p}{2}(\{D_1\}^T[H]^T[H]\{D_1\} + \{D_2\}^T[G1]^T[G1]\{D_2\} \\ &+ \{D_3\}^T[G2]^T[G2]\{D_3\} + (S_0/l)^2 + 2\{D_1\}^T[H]^T[G1]\{D_2\} \\ &+ 2\{D_1\}^T[H]^T[G2]\{D_3\} + 2\{D_2\}^T[G1]^T[G2]\{D_3\} \\ &+ (2S_0/l)[H]\{D_1\} + (2S_0/l)[G1]\{D_2\} + (2S_0/l)[G2]\{D_3\}) \end{aligned} \tag{12}$$

form Eq. (12) the system stiffness matrix and force vector should be modified as:

$$
\begin{aligned}
&p[H]^T[H] \rightarrow [K_{11}] \\
&p[G1]^T[G1] \rightarrow [K_{22}] \\
&p[G2]^T[G2] \rightarrow [K_{33}] \\
&p[H]^T[G1] \rightarrow [K_{12}] \\
&p[G1]^T[H] \rightarrow [K_{21}] \\
&p[H]^T[G2] \rightarrow [K_{13}] \\
&p[G2]^T[H] \rightarrow [K_{31}] \\
&p[G1]^T[G2] \rightarrow [K_{23}] \\
&p[G2]^T[G1] \rightarrow [K_{32}] \\
&-(2pS_0/l)[H] \rightarrow \{F_1\} \\
&-(2pS_0/l)[G1] \rightarrow \{F_2\} \\
&-(2pS_0/l)[G2] \rightarrow \{F_3\}
\end{aligned}
\tag{13}
$$

In the above equation, each subscript mean the corresponding local nodal number to the stiffness and load matrix of the global system.

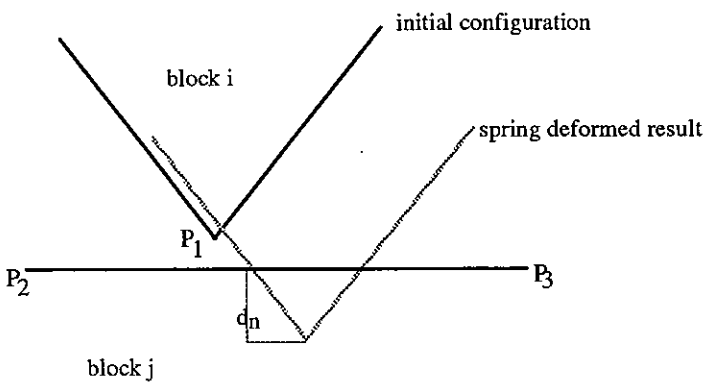

Fig. 2 The deformation of the normal contact spring

3.2 Augmented Lagrange Multiplier Method

Usually, the contact force is calculated by the penalty contact spring method, but it is difficult to reach a balance point between the spring stiffness and the condition of numerical calculation. Usually, the usage of softer spring will cause a serious penetration, while the stiffer spring result to ill matrix condition although the penetration depth may

be reduced. A possible solution of escaping this puzzle of penalty spring stiffness selection is to use the augmented Lagrange multiplier method.

In the augmented Lagrange multiplier, the real contact force is denoted as $\bar{\lambda}$. Within any time step, an arbitrary softer spring stiffness is used as an initial value to obtain a trial contact force λ^0. This λ^0 value is added to the load vector of the governing equations of current time step for the next iteration. Since the initial spring stiffness used here is very soft, then the penetration depth associated with λ^0 will be relatively deep. Theoretically speaking, the deformation of the contact spring is approaching to zero when the impenetrability condition is satisfied. After changing the force vector of system and resolving the governing equations again, contact spring between blocks will still deform because λ^0 is less than $\bar{\lambda}$, then we obtain another contact force λ^1. Through this iteration, the spring force increment ($\lambda^1 - \lambda^0$) will be less than first trial contact force (λ^0). Since the initial force vector of current time step had been added with λ^0 to resist some inertial force and loading, therefore the penetration depth obtained from this iteration is getting less. The difference between λ^k and $\bar{\lambda}$ must be monotonically decreasing as the iteration number "k" increase. The iterations for contact force within this time step will be terminated when the error is converged within some predefined small tolerance value ε.

The iterative formula of contact force calculation is:

$$\lambda_{n,m}^{k+1} = \lambda_{n,m}^{k} + p^k d_{n,m} \tag{14}$$

where n implies normal contact, m is the node number of contact point, k and $k+1$ are iteration number, p^k is the initial spring stiffness and d_n is the deformation of normal contact spring. We can express the potential derived from normal contact spring as

$$\begin{aligned} \pi_{\lambda_{n,m}} &= -\lambda_{n,m} \cdot d_n \\ &= -\lambda_{n,m} \cdot \left((S_0/l) + [H]\{D_1\} + [G1]\{D_2\} + [G2]\{D_3\} \right) \end{aligned} \tag{15}$$

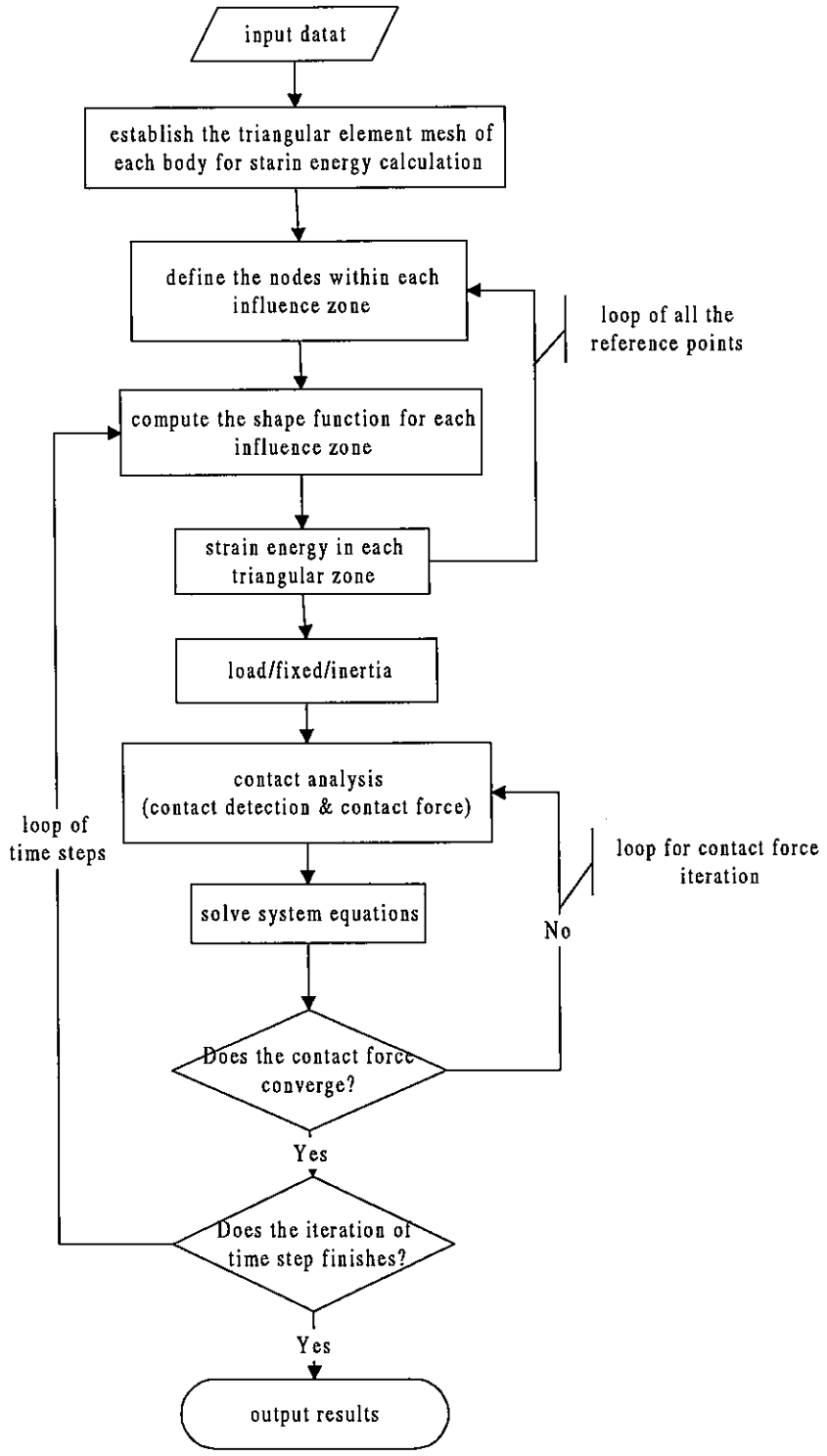

Fig. 3 The flow chart of Diffuse Element Discontinuous Deformation Analysis Method

and the system force vector should be added with

$$\lambda_{n,m}[H] \rightarrow \{F_1\}$$
$$\lambda_{n,m}[G1] \rightarrow \{F_2\}$$
$$\lambda_{n,m}[G2] \rightarrow \{F_3\} \tag{16}$$

The norm of all normal contact forces existed within a time step is evaluated after each iteration. The norm of kth iteration is

$$\left\|\lambda_n^k\right\| = \sqrt{\left(\lambda_{n,1}^k\right)^2 + \left(\lambda_{n,2}^k\right)^2 + \cdots + \left(\lambda_{n,m}^k\right)^2} \tag{17}$$

The iteration procedure stops when

$$\frac{\left\|\left\|\lambda_n^{k+1}\right\| - \left\|\lambda_n^k\right\|\right\|}{\left\|\lambda_n^k\right\|} \leq \varepsilon \tag{18}$$

ε is a reasonable tolerance. Only the force vector updates itself in each iteration, the system stiffness matrix is kept the same as the one at the beginning of the time step during the whole contact force iterative process.

Fig. 3 shows the flow chart of this newly proposed "Diffuse Element Discontinuous Deformation Analysis (DEDDA)" method. Since the number of nodes contained by each reference zone is a variant, the derivation of shape function is following a sequence of the reference points to be evaluated. Both the boundary and loading conditions are related to the reference point where the condition located, therefore the correct reference point should be picked and then the corresponding shape function is determined. Based on the outputs of nodal displacements the strains and stresses can be figured out by Eq. (7).

The iteration loop for contact force calculation in the flow chart of DEDDA method (see Fig. 3) is more complicated than other units of the chart. Fig. 4 shows the flow chart of the "Contact Analysis" block unit in the Fig. 3. The details of each block unit in the Fig. 4 are explained as following:

(A). $\lambda_n^0 = -d_n^0 \cdot p_n^0$, $\lambda_s^0 = d_s^0 \cdot p_s^0$

(B). Normal contact points separate when $d_n^{k+1} > 0$

If the value

$$\Delta\lambda_n = \left(\lambda_n^{k+1} - \lambda_n^k\right) < \lambda_n^k / 10$$

then the calculated contact force is acceptable. Next step is to adjust the stiffness value of normal contact spring as

$$p_n^{k+1} = \sqrt{p_n^k}$$

Shear contact points reverse when $d_s^{k+1} \cdot \lambda_s^k < 0$,

If the following value

$$\Delta\lambda_s = \left|\lambda_s^{k+1} - \lambda_s^k\right| < \lambda_s^k / 10$$

then the calculated contact force is acceptable. Next step is to adjust the stiffness value of shear contact spring as

$$p_s^{k+1} = \sqrt{p_s^k}$$

(C). $\lambda_n^{k+1} = \lambda_n^k$, $\lambda_s^{k+1} = \lambda_s^k$

(D). $\lambda_n^{k+1} = -d_n^{k+1} \cdot p_n^k + \lambda_n^k$

$$p_n^{k+1} = -\lambda_n^{k+1} / d_n^{k+1}$$

$$\lambda_s^{k+1} = -d_s^{k+1} \cdot p_s^k + \lambda_s^k$$

$$p_s^{k+1} = \lambda_s^{k+1} / d_s^{k+1}$$

(E). $\dfrac{\left\|\left\|\lambda_n^{k+1}\right\| - \left\|\lambda_n^k\right\|\right\|}{\left\|\lambda_n^k\right\|} < \varepsilon$, $\dfrac{\left\|\left\|\lambda_s^{k+1}\right\| - \left\|\lambda_s^k\right\|\right\|}{\left\|\lambda_s^k\right\|} < \varepsilon$

It is worth noting in part (D) that the contact force is updated by adding a force increment, which is equal to the multiplication of penetration and spring stiffness, and the spring stiffness is also updated by dividing penetration into contact force. Following this procedure the value of contact spring stiffness is adjusted based on some criteria during the contact force iteration. It is found that this newly proposed algorithm is much more convenient than the conventional penalty method which sticks to a fixed input stiffness value.

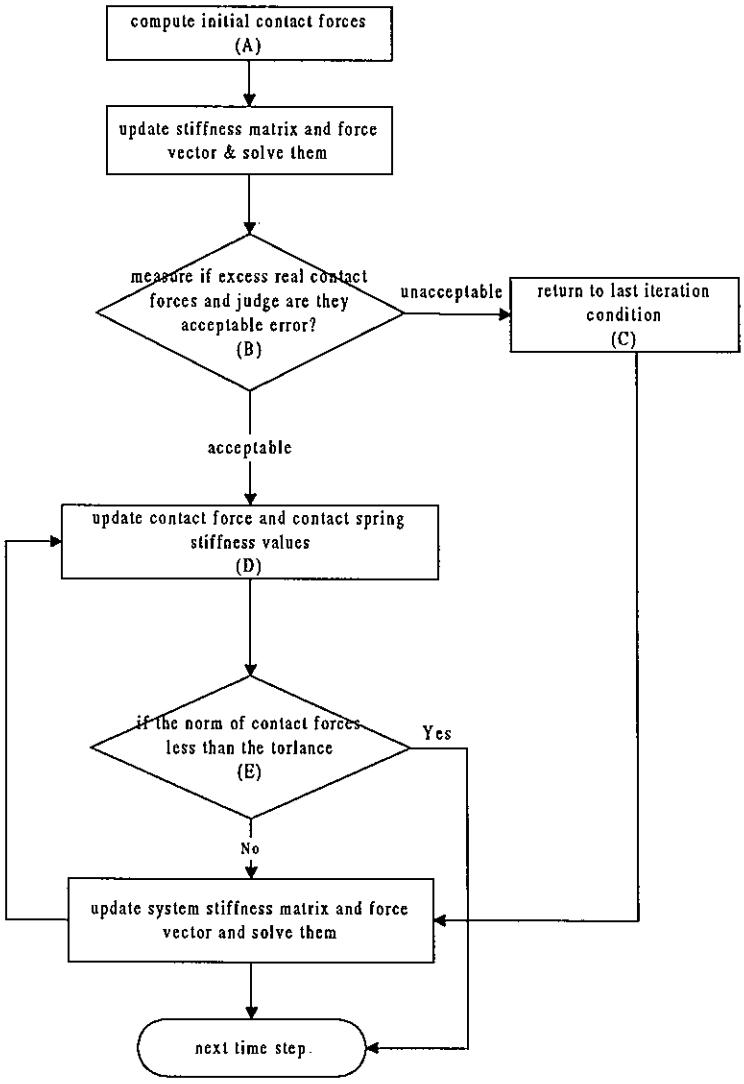

Fig. 4 The flow chart of the Augmented Lagrange multiplier method

4. NUMERICAL EXAMPLES

A computer code is developed according to the theory of the DEDDA method. Two examples are made to demonstrate the capability and accuracy of this newly proposed method. It is noted that the computer code is a dynamic formulation. The static analyses can be conducted by using a numerical damping technique. This technique sets the initial velocity of each point obtained from previous time step equal to zero to damped out the inertial effect. Then the system of dynamic equations are reduced to a static system.

Example 1:

The deflection effect of a cantilever beam under a point load at free end (see Fig. 5) is simulated by FEM and Diffuse Element Method. Both 3-node and 4-node finite elements are used for the study. The mesh for the energy integration cell of the DEDDA method is the same as the finite element mesh. Simulation results are listed in Table 1. It can be seen from the Table 1 that with the same number of nodes the DEDDA method can get very well results even just using linear polynomial function.
are very high.

Table 1 Comparison of Beam Analysis Results by the FEM and the Diffuse Element Method

nodes number	FEM 3 node element	FEM 4 node element	DEDDA Method
15	0.161	0.313	0.261
27	0.266	0.439	0.492
51	0.316	0.488	0.482
analytical solution		0.519	

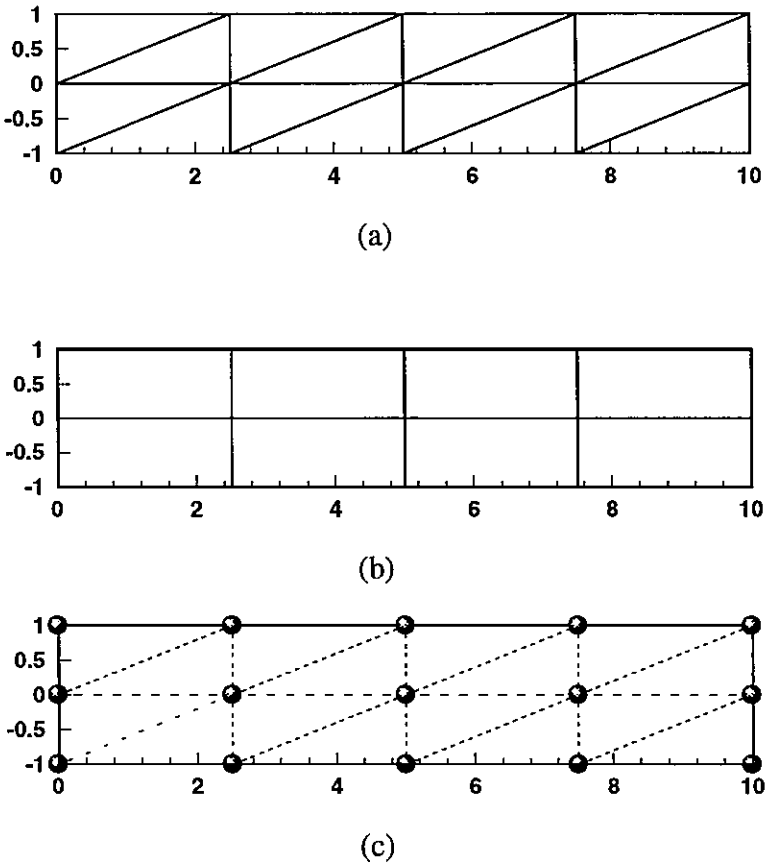

Fig. 5 Numerical model of cantilever beam under end load,(a)triangular FEM mesh, (b) 4-node FEM mesh, (c) DEDDA mesh with triangular integration cell

Example 2:

A numerical model with two blocks in contact is shown in Fig. 6. The contact pressure between these two blocks is analyzed by the modified Lagrange multiplier method. The loading **P** is 50000N and a tiny initial contact spring stiffness value 1 N/m is given. The contact pressure distribution is shown in the Fig. 7. There are stress concentration effects around the block corners as expected and the integration of the contact pressure is equilibrium with the loading **P**. Very small penetration depth is calculated after applying the modified Lagrange multiplier method. This implies both the degree of satisfaction of the impenetrability condition and the accuracy of calculated contact force

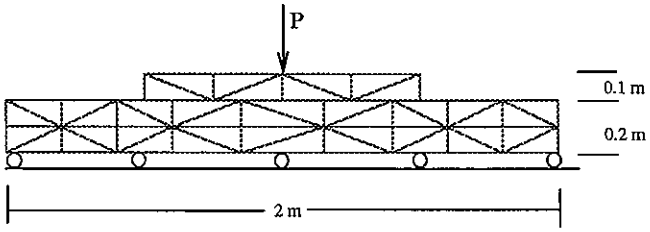

Fig. 6 A numerical model of two deformable bodies in contact

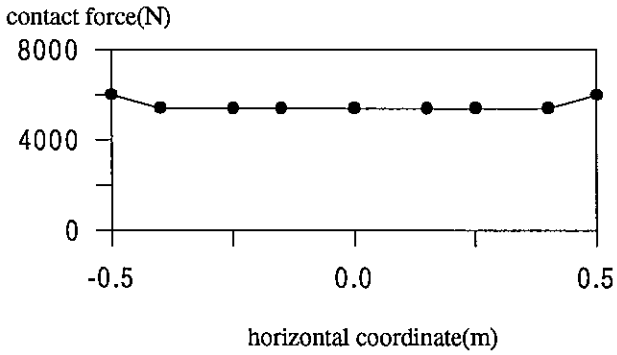

Fig. 7 Contact force distribution of example 2

5. CONCLUSIONS

A new computational method called "Diffuse Element Discontinuous Deformation Analysis" is presented in this paper. The combination of the Diffuse Element theory with a modified augmented Lagrange multiplier method makes this new formulation be capable of conducting the contact analysis among multi-body discrete system. The modified Lagrange multiplier method is very efficient and accurate to calculate the contact force. Compared with conventional penalty method, this new Lagrange multiplier method avoids the difficulty of selecting a suitable penalty value for contact spring and can approach the true contact force through an spring stiffness self-adjusting algorithm.

REFERENCES

1. Shi Gen-Hua (1988), " *Discontinuous Deformation Analysis : A New Numerical Model for the Statics and Dynamics of Block Systems,*" Ph. D. Thesis, Department of Civil Eng., University of California, Berkeley.
2. Shi Gen-Hua (1991), " Manifold Method of Material Analysis " , *Proc. Ninth Army Conference on Applied Mathematics and Computing*, Minneapolis, Minnesota, U. S. A.
3. Shyu Kuokai (1993), " *Nodal-based Discontinuous Deformation Analysis* " , Ph. D. Thesis, Department of Civil Eng., University of California, Berkeley.
4. Ke, T. C. (1993), " *Simulated Testing of 2D Heterogeneous and Discontinuous Rock Masses Using Discontinuous Deformation Analysis* " , Ph. D. Thesis, Department of Civil Eng., University of California, Berkeley.
5. Lin, C. T. (1995), " *Extensions to the Discontinuous Deformation Analysis for Jointed Rock Masses and Other Blocky Systems* " ,Ph. D. Thesis, University of Colorado, Boulder,.
6. Nayroles, B., G. Touzot and P. Villon (1992), " Generalizing the Finite Element Method: Diffuse Approximation and Diffuse Elements " , *Computational Mechanics*, Vol. 10, pp. 307-318.
7. Belytschko T., Lu, Y. Y. and Gu L. (1994), " Element-Free Galerkin Methods " , *International Journal for Numerical Methods in Engineering*, Vol. 37, pp. 229-256.
8. Yang Sun-Ting (1994), "*A Manifold Method for the Continuous and Discontinuous Deformation Analysis of Solids*", Master Thesis, Department of Civil Eng., National Central University, Chungli, Taiwan, R. O. C. (Chinese)
9. Sun, Pau-Tau(1995), "A Modified Discontinuous Deformation Analysis (DDA) Method in Solid Mechanics ", Master Thesis, Department of Civil

Eng., National Central University, Chungli, Taiwan, R. O. C. (Chinese)

10. Chen, Ming-Chih (1996) ， " A 2D Discontinuous Deformation Analysis by Mixed DDA & Finite Element Method " ， Master Thesis, Department of Civil Eng., National Central University, Chungli, Taiwan, R. O. C. (Chinese)

11. Wang, Chung-Yue; Jopan Sheng; M. H. Chen and C. C. Chuang, (1995), " Approximation Theories for the Manifold Method " , Working Forum on the Manifold Method of Material Analysis, U. S. Army Corps. of Engineers, Vol. I, pp. 61-86.

Analysis of Loose Earth Pressure in Trap Door Test by the Distinct Element Method

Takeshi ASANO, Masao NISHIMURA, Hitoshi MASUI, Shigeru KAMEDA

Technical Research Institute, Okumura Corporation, 387 Ohsuna, Tsukuba-shi, JAPAN.

1. Introduction

Recent development of construction technologies has allowed shield tunnels with various sectional shapes to be produced. The earth pressure that acts on such a shield tunnel will depend on the sectional shape, and may differ from the pressure acting on a single circular shield tunnel. In the conventional design method, it is assumed that the vertical pressure acting on a shield tunnel exerted by a covering of fine sand of 1 to 2 times larger in thickness than the diameter of the shield tunnel is Terzaghi's loose earth pressure. However, it is questionable whether Terzaghi's formula may be extended for determining earth pressure for all types of shield tunnels, which have different sectional shapes. In this study, we conducted trap door tests and tunnel tests to assess the effects of sectional shape on earth pressure acting on shield tunnels and investigated the applicability of Terzaghi's loose earth pressure by comparing the test results. We also conducted the distinct element method (DEM) to analyze the generation mechanisms of earth pressure.

2. Outline of experiment

The soil chambers used for the experiment are illustrated in Fig.1 and Fig.2. An overall view and the load cells on the twin trap doors are shown in Photos 1 and 2, respectively. The soil chambers were installed at their lower center either with twin trap doors or with a rectangular section tunnel formed by a upper plate and two side walls. The inner size of

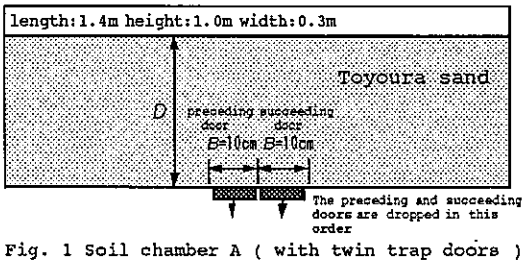

Fig. 1 Soil chamber A (with twin trap doors)

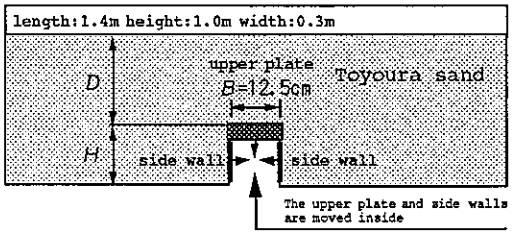

Fig. 2 Soil chamber B
(with a upper plate and side walls)

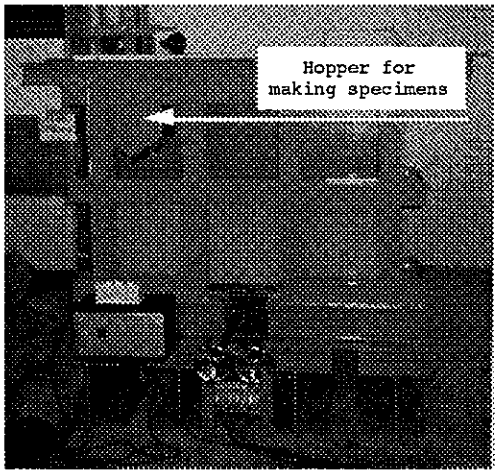

Photo 1 Overview of the soil chamber

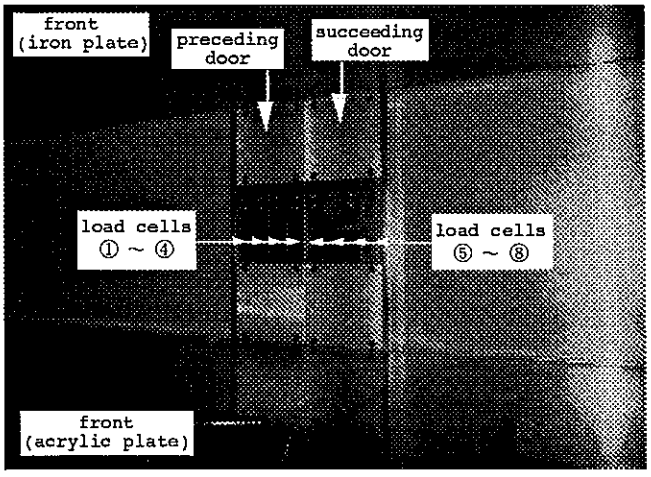

Photo 2 Load cells (within twin trap doors)

the chambers was 140 cm in length, 30 cm in width, and 100 cm in height. The front and bottom surfaces of the chambers were acrylic plates of 4 cm in thickness, and the side and rear surfaces were iron plates. The ground material was Toyoura sand, which had been adjusted to a relative density of 77% (unit volume mass γ = 1.57 g/cm^3) with a mobile hopper by the air-pluviation method. After constructing the ground model, the left door (the preceding door) of the twin trap doors was dropped 2.0 mm, and then the right door (the succeeding door) was dropped 5.0 mm. For the chamber with a tunnel, the upper plate was dropped 2.0 mm, then the side walls were moved 2.0 ~ 3.0 mm. In another trial, the side walls were moved 2.0 mm first, then the upper plate was dropped 2.0 ~ 3.0 mm. The displacements of and earth pressures on the trap doors, upper plate, and side walls were measured. Earth pressures were measured with load cells installed within the trap doors, upper plate, and side walls. Four cells were installed in each trap door (Photo. 2). Thirteen cells in total were installed in the surfaces of the tunnel, i.e. five in the upper plate and eight in the right side wall. Test cases are listed in Table 1. The parameters of the experiment with trap doors (CASE0) were the ratio of earth covering (D) to the width of a trap door (B). Four tests were conducted with parameters D/B = 1, 2, 4, and 6. For tests on the tunnel with side walls, the height of the side wall (H) was either 15 cm (CASE1) or 25 cm (CASE2). The parameters were D/B = 2 and 4 in CASE1, and D/B = 2, 3, and 4 in CASE2. For each case, two types of tests were conducted by either dropping the upper plate first or moving the side walls first.

Table 1 Test cases

CASE0 (H=0cm)	-D -2D -4D -6D	
CASE1 (H=15cm)	-2Du -4Du	-2Ds -4Ds
CASE2 (H=25cm)	-2Du -3Du -4Du	-2Ds -3Ds -4Ds

Note1: In CASE2-2Du, D/B=2, and the upper plate was moved first

Note2: In CASE2-4Ds, D/B=4, and the side walls were moved first

3. Test results

3.1 Trap door tests (CASE0)

The relationships between trap door displacement and earth pressure for CASE0-2D and 4D (D= 20 and 40 cm) are shown in Fig. 3 and Fig.4, respectively. Each pressure value is the mean of measurements by load cells in a door and was normalized with the initial earth pressure. The horizontal axis represents the sum of the displacements of the preceding and succeeding doors, and 0.0 ~ 2.0 mm corresponds to the drop of the preceding door, and 2.0 ~ 7.0 mm shows the drop of the succeeding door.

As the preceding door dropped, the earth pressure on the preceding door suddenly fell off and then became constant. The constant pressure value , when normalized with the initial earth pressure, was smaller for a larger D/B ratio. The earth pressure on the succeeding door rose suddenly and then became constant. The rise of earth

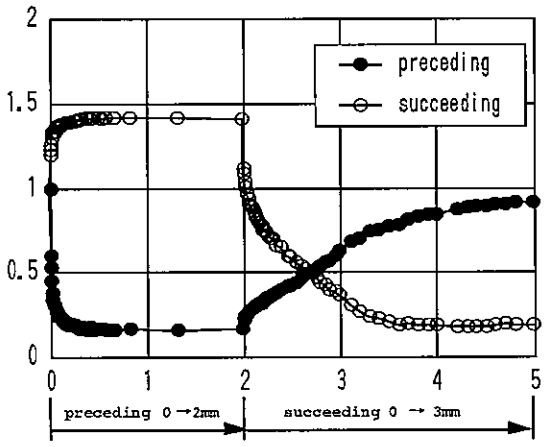

Displacement of trap doors (mm)

Fig.3 Change in earth pressure (CASE0-2D)

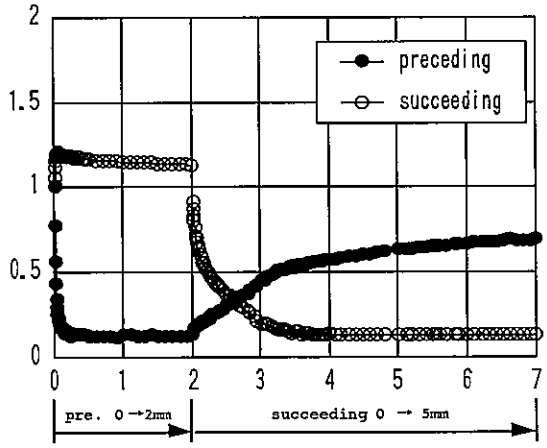

Displacement of trap doors (mm)

Fig.4 Change in earth pressure (CASE0-4D)

pressure on the succeeding door depended on the depth of earth covering. For D > 40 cm, earth pressure marked a sudden rise forming a peak and then gradually decreased until it became constant. For D < 20 cm, on the other hand, earth pressure increased rapidly without forming a peak until it became constant.

As the succeeding door dropped, the earth pressure on the succeeding door decreased, and the pressure on the preceding door, which was stationary at that time, increased. The drop of earth pressure on the succeeding door was slower than the fall of the pressure on the preceding door, which was observed during the drop of the preceding door.

3.2 Tunnel tests (CASE1, CASE2)

The relationships between the displacements of the upper plate and side walls and earth pressure for CASE2-2Du and 2Ds (H = 25 cm and D = 25 cm) are shown in Fig. 5 and Fig. 6, respectively. Each pressure value is the mean of measurements by load cells in the upper plate or the right side wall, which was normalized with the initial earth pressure. The horizontal axis represents the sum of the displacements of the upper plate and side walls. For the test in which the upper plate was moved first, 0.0 ~ 2.0 mm corresponds to the movement of the upper plate, and 2.0 ~ 5.0 mm corresponds to the movements of the side walls. For the test in which the side walls were moved first, 0.0 ~ 2.0 mm corresponds to the movements of the side walls, and 2.0 ~ 5.0 mm is the drop of the upper plate.

When the upper plate was moved first, the earth pressure on the upper plate decreased until it became constant. The drop was gentler than the drop in the trap door tests. When the side walls were subsequently moved, the earth pressure on the upper plate gradually increased. The rise at the central section of the upper plate was large, and the pressure was larger than the initial earth pressure when the side walls were moved 1.0 ~ 3.0 mm. On the other hand, the pressure acting on the side walls decreased suddenly and became constant when the side walls were moved 0.3 mm.

When the side walls were moved first, the pressure acting on the upper plate rose suddenly but slightly. The earth pressure on the side walls decreased rapidly and became constant when the side walls were moved about 0.3 mm, as in the case when the upper plate was dropped first. When the upper plate was subsequently moved, the pressure on the upper plate gradually decreased, and it became constant when the upper plate was moved 3.0 mm. The pressure on the side walls increased very gradually and did not become constant even when the upper plate was moved more than 3.0 mm.

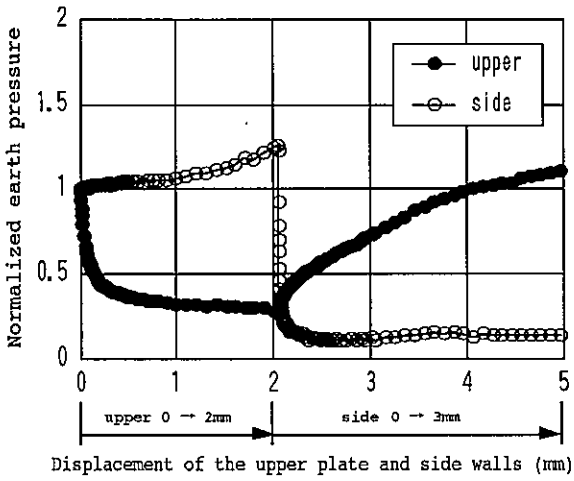

Fig.5 Change in earth pressure (CASE2-2Du)

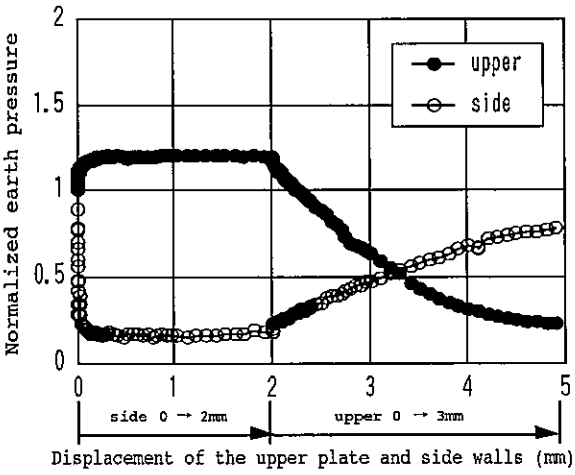

Fig.6 Change in earth pressure (CASE2-2Ds)

3.3 Comparison with Terzaghi's loose earth pressure

The mean earth pressures on the trap doors and the upper plate and Terzaghi's

loose earth pressure are shown in Fig. 7(a) and 7(b). The horizontal axes represent D/B, and the vertical axes represent the normalized earth pressures acting on the trap doors or upper plate. For each trap door test (CASE0), two values are plotted, which are the values for 1) only the preceding door was dropped 2.0 mm, and 2) both two doors were dropped 2.0 mm. The values after the succeeding door dropped 2.0 mm (the preceding door had already been dropped 2.0 mm) are the mean of the earth pressures acting on the preceding and succeeding doors. For tests on tunnels with side walls (CASE1 and 2), two values are plotted, which are the values for 1) the upper plate was moved 2.0 mm,and 2) the side walls were moved 2.0 mm. In Fig. 7 it is shown that the earth pressures immediately after the drop of the preceding trap door or the upper plate correlate well with Terzaghi's loose earth pressure regardless of the existence of side walls or the order of movement of the upper plate and side walls. On the other hand, the mean earth pressure on the preceding and succeeding trap doors immediately after the succeeding door was dropped 2.0 mm was larger than Terzaghi's loose earth pressure. Although the final door width was equal, the mean earth pressure acting on the doors was different when both doors were simultaneously dropped and when they were moved in succession. The rise of earth pressure acting on the upper plate by the movement of side walls depended on the order of movement of the upper plate and side walls. When the earth pressure on the upper plate was already the loose earth pressure (when the upper plate had already dropped), the rise of earth pressure on the upper plate by the movement of side walls was large. In the tests on tunnels with side walls, the final earth pressure acting on the upper plate was very different depending on the order of their movement.

4. Analysis by the DEM

The DEM was conducted on trap door tests and tunnel tests. This section discusses the analyses on CASE0-2D, CASE2-2Du, and CASE2-2Ds and compares the analytical results with the aforementioned test results. The initial element array is shown in Fig. 8. The element radii were 0.4 cm, 0.5 cm , and 0.6 cm, respectively. Their normal spring constants k_n were calculated with the two-dimensional cylinder-contact theory. The tangent spring constants were k_s = 0.25 k_n, increment of time Δt = 1.0 x 10^{-5} second, the friction angles between elements and between an element and either a trap door, upper plate, or side wall were all 40.1° , and the damping coefficient was the critical damping coefficient.

4.1 Relationship between earth pressure and displacement

The analyzed relationships between mean earth pressures and displacements of trap doors, upper plate, and side walls were compared with experimental results.

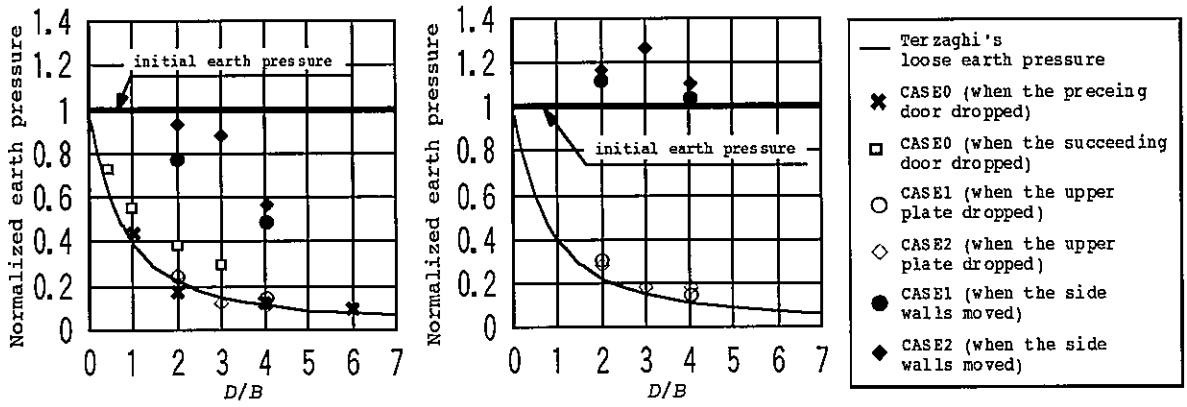

(a) Twin trap doors and upper plate moved first (b) Side walls moved first

Fig.7 Earth pressure acting on trap doors or upper plate

All earth pressure values were normalized with the initial earth pressure as in Fig. 5 and Fig. 6. The value of displacement in each experiment is the sum of displacements of the preceding and succeeding trap doors, or of the upper plate and side walls.

(a) CASE0-2D

The change of earth pressure acting on the preceding and succeeding trap doors is shown in Fig. 9. The figure shows that the analysis precisely reproduced the change of earth pressure on the trap doors.

(b) CASE2-2Du

The change of earth pressure acting on the upper plate and side walls is shown in Fig. 10. The figure shows that the analysis quite precisely reproduced the change of earth pressure on the upper plate and side walls by the drop of the upper plate. For the change of earth pressure by the movement of side walls, the analysis could not reproduce the rapid drop of earth pressure on the side walls, but derived a value almost equal to the experimental result for the pressure on the side walls after the pressure finished dropping and became constant. However, the rise of earth pressure on the upper plate by the movement of the side walls was much smaller than the experimental value.

(c) CASE2-2Ds

The change of earth pressure acting on the upper plate and side walls is shown in Fig. 11. As in CASE2-2Du, the reduction of the earth pressure acting on the side walls by the movement of the walls was not as rapid as in the experiment, but the pressure after it became constant was almost equal to the experimental value. In the experiment, the earth pressure on the upper plate became constant immediately after the side walls were moved. On the other hand, the analysis showed a gradual increase of earth pressure, which finally became almost constant at a wall displacement of 2.0 mm. The increase of earth pressure acting on the upper plate from the initial pressure value was larger in the analysis than in the experiment. The increase of earth pressure acting on the side walls by the drop of the upper plate was also smaller in the analysis than in the experiment. Although the reduction curve

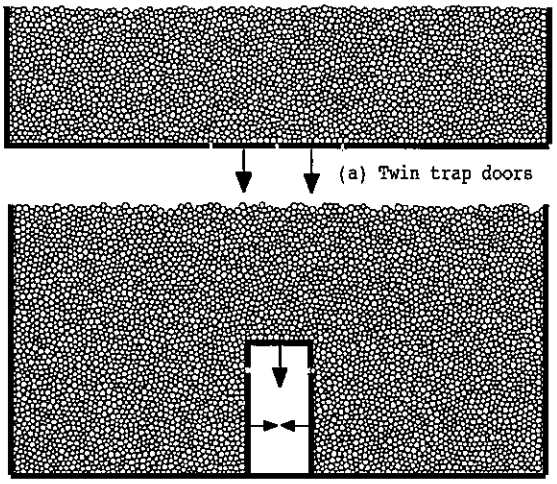

(b) Tunnel with side walls

Fig.8 Initial element array

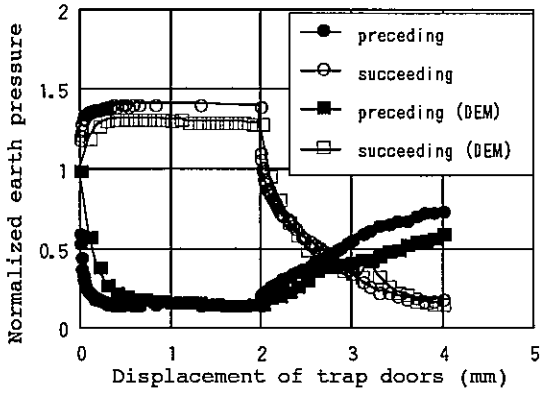

Fig.9 Change in earth pressure (CASE0-2D)

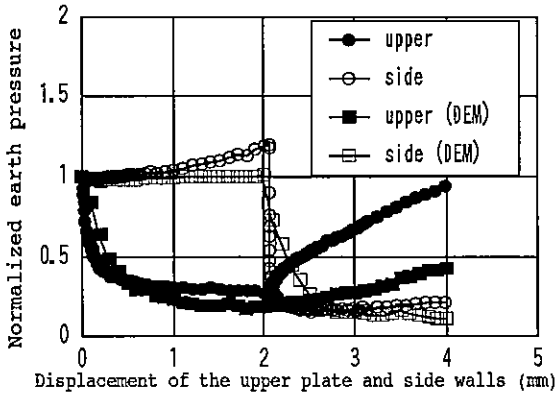

Fig.10 Change in earth pressure (CASE2-2Du)

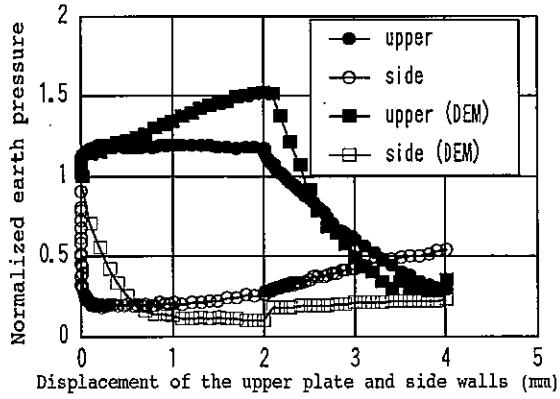

Fig.11 Change in earth pressure (CASE2-2Ds)

of earth pressure acting on the upper plate by the drop of the plate was slightly different, the analysis well reproduced the experiments.

4.2 Contact forces between elements

The distribution of contact forces between elements determined by the DEM is shown. The intensity of the forces is expressed by the thickness of the segment that connects the centers of the elements. Sections in which forces were smaller than 0.18N in intensity (the initial vertical earth pressure that corresponds to a soil covering of $D/2$ in Fig. 8) are not shown in the figures to elucidate the regions of small contact forces.

(a) CASE0-2D

The distribution of contact forces between elements when the preceding trap door was moved 2.0 mm is shown in Fig. 12. A region of small contact force was generated above the preceding door, which was surrounded by an arch of large contact forces. Fig. 13 shows the force distribution when both the preceding and succeeding doors were moved 2.0 mm. A small arch that stands over both edges of the succeeding door and a large arch that stands on the left edge of the preceding door and the right edge of the succeeding door are shown. As shown in Fig. 9, the rise of earth pressure acting on the preceding door by the drop of the succeeding door was small, and did not exceed the initial pressure value. The formation of these double arches is likely to be the cause of such a small increase. The distribution of element displacement which was generated while the preceding door was displaced from 0.0 to 0.1 mm and from 1.9 to 2.0 mm is shown in Fig. 14 and Fig. 15, respectively. As shown in the figures, there was a gradual reduction of element displacement from the elements adjacent to the trap doors to the elements near the ground surface, which continued until the earth pressure on the trap doors became constant. When the earth pressure on the trap door became constant, the displacement of the elements near the doors was relatively larger than the displacement in other regions. These elements of large displacements are low in inter-element contact forces, but are not totally isolated from the surrounding elements but are mutually affected, and, as a consequence, keep the earth pressure on the trap doors constant.

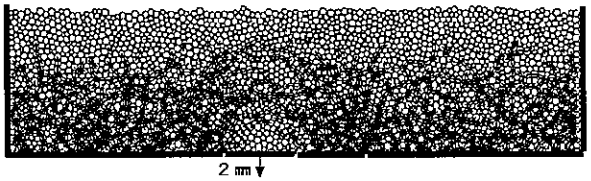

Fig.12 Contact force : CASE0-2D
(Displacement of the preceding door:2.0mm)

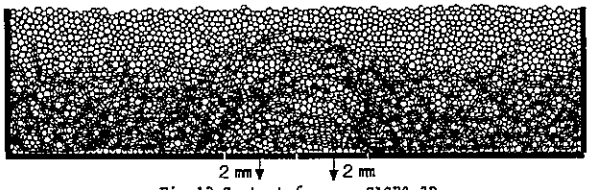

Fig.13 Contact force : CASE0-2D
(Displacements of the preceding and succeeding doors:2.0mm)

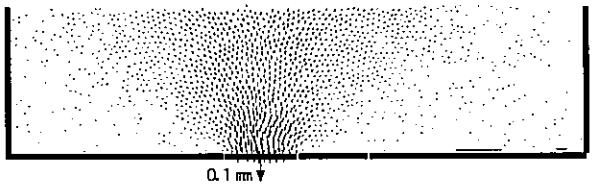

Fig.14 Element displacement vector : CASE0-2D
(Displacement of the preceding door:0.0 → 0.1mm)

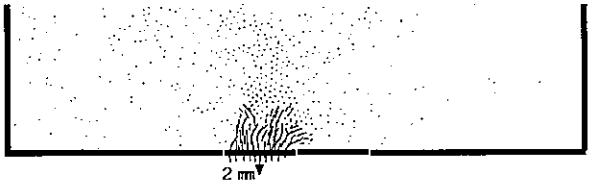

Fig.15 Element displacement vector : CASE0-2D
(Displacement of the preceding door:1.9 → 2.0mm)

(b) CASE2-2Du

The distribution of contact forces between elements when the upper plate was dropped 2.0 mm is shown in Fig. 16. As in the trap doors, an arch was created above the upper plate. No effect of the side walls is shown. Fig. 17 is the distribution of element displacement when the upper plate was displaced from 1.9 mm to 2.0 mm. The displacement near the upper plate was relatively large. The configuration of this region was almost identical to the analysis for twin trap doors (Fig. 15), and the figure showed no

effect of the presence of side walls. Fig. 18 is the distribution of contact forces between elements when the upper plate and side walls were all moved 2.0 mm. The forces near the side walls were significantly reduced by the movement of the side walls but the reduction in the peripheral regions was small. The arch that had been created during the drop of the upper plate was maintained by the force transmission between the sides of the upper plate and the chamber base. It is likely to be the cause of an increase in the pressure on the upper plate by the movement of the side walls being smaller than the experimental observation. Fig. 19 shows the distribution of element displacement generated when the side walls were displaced from 0.0 to 2.0 mm. The figure shows that there was no significant displacement of elements near the sides of the upper plate and that the arch above the upper plate was kept.

(c) CASE2-2Ds

The distribution of contact forces between elements when the side walls were moved 2.0 mm is shown in Fig. 20. The contact force of the elements near the side walls was small. This region of small contact force is almost identical to the region observed when the side walls were moved in CASE 2-2Du (Fig. 18). The earth pressure acting on the side walls was also similar to CASE 2-2Du. Fig. 21 shows the distribution of element displacement when the side walls were moved from 0.0 to 2.0 mm. The element displacement distribution was also similar to the distribution in CASE2-2Du except that the increase of earth pressure acting on the upper plate by the movement of the side walls was larger than in CASE2-2Du because, unlike CASE2-2Du, no arch was formed before the movement of the side walls. The contact forces between elements when the upper plate was dropped 2.0 mm are shown in Fig. 22, and the element displacement distribution generated when the upper plate was dropped from 1.9 to 2.0 mm is shown in Fig. 23. The figures show large contact forces near the side walls and small values above the upper plate, but this tendency is not as clear as in Fig. 16 (CASE2-2Du, when the upper plate was dropped). The region of large element displacements in Fig. 23 is more wide than that in Fig. 15 (twin trap doors) or that in Fig. 17 (upper plate moved before side walls), which is likely to be due to the earth at the sides of the upper plate being loosened by the movement of the side walls.

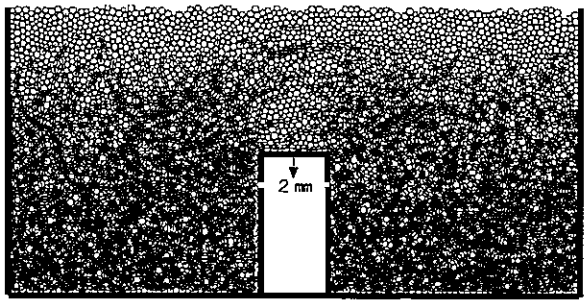

Fig.16 Contact force : CASE2-Du
(Displacement of the upper plate:2.0mm)

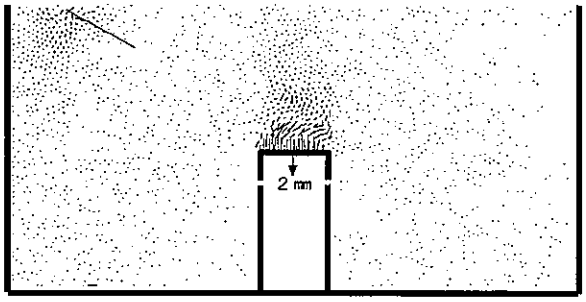

Fig.17 Element displacement vector : CASE2-2Du
(Displacement of the upper plate:1.9 → 2.0mm)

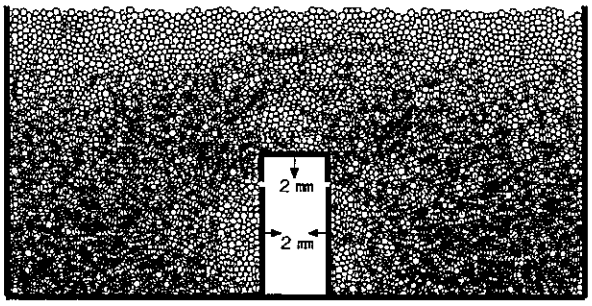

Fig.18 Contact force : CASE2-2Du
(Displacements of the upper plate and the side walls:2.0mm)

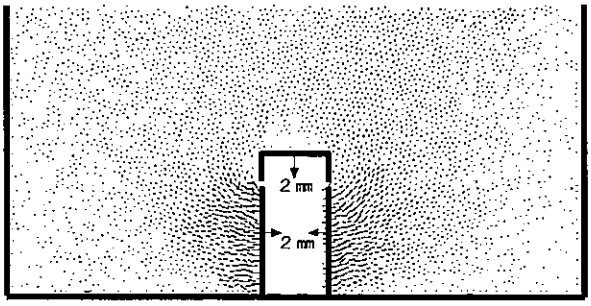

Fig.19 Element displacement vector : CASE2-2Du
(Displacements of the side walls:0.0 → 2.0mm)

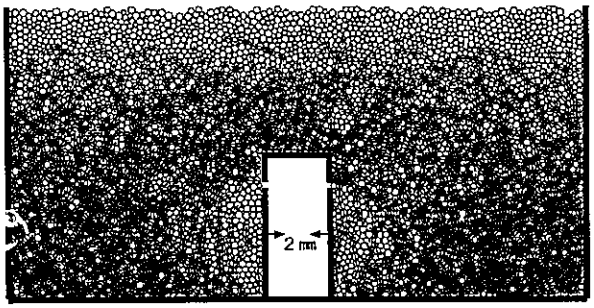

Fig.20 Contact forces : CASE2-Ds
(Displacements of the side walls:2.0mm)

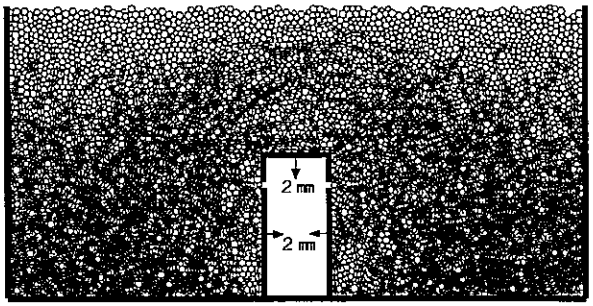

Fig.22 Contact forces : CASE2-2Ds
(Displacements of the upper plate and the side walls:2.0mm)

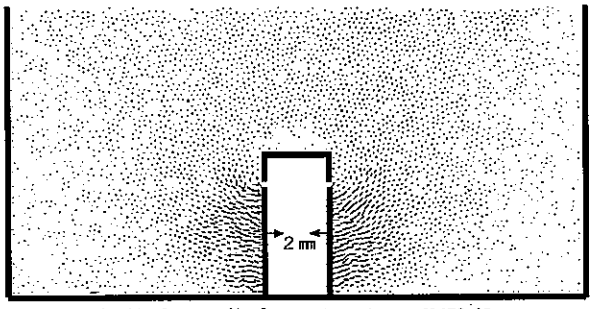

Fig.21 Element displacement vector : CASE2-2Ds
(Displacements of the side walls:0.0 → 2.0mm)

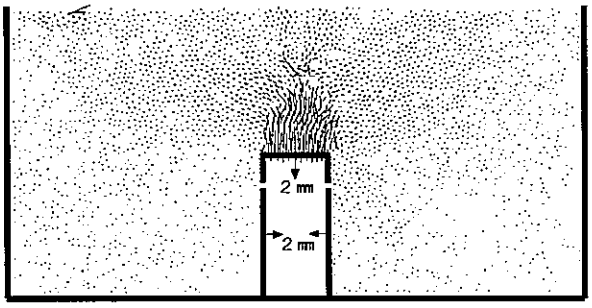

Fig.23 Element displacement vector : CASE2-2Ds
(Displacement of the upper plate:1.9 → 2.0mm)

5. Conclusion

A trap door test device was used to understand the effects of sectional shape on earth pressure acting on shield tunnels, and compared the test results with Terzaghi's loose earth pressure. Moreover the DEM was used to analyze the changes of ground displacement distribution and contact force distribution of elements, and to investigate the generation mechanisms of earth pressure.

The following results were obtained: 1) The vertical earth pressure of sandy soil on a single trap door can be adequately calculated from Terzaghi's loose earth pressure. 2) The earth pressure on twin trap doors cannot be calculated by Terzaghi's formula. The mean earth pressure on twin trap doors is larger than Terzaghi's loose earth pressure. 3) The earth pressure on a upper plate with side walls is significantly affected by the order of movement of the upper plate and side walls. Earth pressures may be very different even though the final displacements of the upper plate and side walls are the same. 4) For a tunnel with side walls, the vertical earth pressure on the upper plate can be adequately obtained from Terzaghi's loose earth pressure when only the upper plate drops and the side walls stay still. In these cases, the side walls have almost no effect on the vertical earth pressure. 5) For a tunnel with side walls, the vertical earth pressure on the upper plate, which is similar to Terzaghi's loose earth pressure when only the upper plate is dropped, is larger than Terzaghi's loose earth pressure when the side walls are subsequently moved. The excess was larger for higher side walls. 6) The earth pressure on twin trap doors can be precisely reproduced by the DEM. The formation of arch action can be easily reproduced with contact forces between elements or element displacement distribution. 7) The earth pressure on the upper plate while moving the upper plate and the earth pressure on side walls while moving the side walls can be reproduced with the DEM. However, the earth pressure on side walls while moving the upper plate, or the earth pressure on the upper plate while moving the side walls may be different for experimental and analytical results. Since the DEM can precisely reproduce the experimental results of twin trap doors, this difference may be attributable to inadequate assumptions regarding the friction angles between the side walls and elements, which are now under investigation.

NUMERICAL STUDY ON SUPPORT EFFECTS OF CABLE BOLT IN DISCONTINUOUS ROCK MASS

Hideo KINASHI & Satoru AMANO
OBAYASHI Corporation, Tokyo, Japan

ABSTRACT : This paper will describe a numerical study on the support mechanism and the reinforcement effect of cable bolt installed in discontinuous rock mass. The cable bolt is fully bonded and non-pretensioned reinforcement method, which has been mainly used in mines making effective use of the flexibility. Firstly, the mechanical behavior of the cable bolt will be demonstrated based on the result of a simple simulation concerning a tunnel excavation in both continuous and discontinuous rock mass. Secondly, the result of numerical experiments to evaluate the reinforcement effect of the cable bolt will be described. The reinforcement effect of the cable bolt will be compared with that of the rock anchor, which is installed with pretension. The result of the numerical experiments indicated that the reinforcement effect of the two methods were nearly equivalent, although the support mechanism of the methods are quite different.

1. INTRODUCTION

Recently, underground caverns such as underground hydraulic-power house or energy storage facility, tend to be large and to be constructed deeply. In these underground caverns, the important subject is to secure the mechanical stability and to reduce the construction cost.

One of the most important factors to affect the stability of the cavern is the presence of the joints in a rock mass. According to the recent result of field measurements conducted in a underground hydraulic-power house (Akagi et al. 1995), it is pointed out that joints have a great influence on the mechanical and hydraulic behavior of the rock mass.

A private underground research laboratory was constructed by Obayashi Corporation in Kamioka Mine to study various issues related to the design and construction of underground caverns in discontinuous rock mass. The field experiments were executed with five-year plan starting from 1991 (Tamai et al. 1994). The authors have already reported the site investigation results concerning the joint system of the Kamioka experiment site (Amano et al. 1995a), and the numerical simulation result of a drift excavation considering the mechanical and geometrical properties of joints (Kinashi et al. 1995a). In the numerical simulation, a Distinct Element Method (Cundall 1980) was applied, and the rock mass was modeled with rock blocks divided by joints. The result of the numerical simulation indicated that the joint deformation and convergence observed in the field were satisfactorily simulated.

In this study, numerical experiments were carried out to estimate the stability of the large-scale underground cavern in discontinuous rock mass. In large-scale underground caverns such as underground hydraulic-power house, rock anchor has been commonly used as one of the main supports. Rock anchor is a rock reinforcement method which is installed with pretension. On the other hand, the authors have been studying the applicability of the cable bolt which is fully bonded and non-pretensioned rock reinforcement in order to reduce construction period and cost. In the following, the result of numerical experiments will be described concerning the reinforcement effect of the cable bolt and the rock anchor.

2. SUPPORT MECHANISM OF CABLE BOLT

Basically, the same material is used in both the cable bolt and the rock anchor. The difference between both reinforcement methods exists in the presence of pretension and the bonding process. Figure 1 shows the concept of support mechanism of both reinforcement methods. In the case of the cable bolt, the grouting material and the cable strand are installed after the borehole is drilled in the rock mass (Figure 1-a). When the cavern is excavated and displacement occurs in the rock mass, the axial force arises in the cable bolt and the cable bolt exhibits the reinforcement effect. Since joints are generally more deformable than rock matrix, larger axial force on the cable bolt is found at the location of intersection with joints. On the other hand, in the case of rock anchor, the cable strand is installed after the borehole is drilled, and the end of the cable strand is bonded with grouting material. Then, the pretension force is applied on the cable strand. As a result, deformation of joints is restrained by this pretension force.

To simulate the support mechanism of the cable bolt and the rock anchor as shown in Figure 1, they are modeled using the Cable Element incorporated in UDEC (Universal Distinct Element Cord, Itasca Consulting Group 1996) as shown in Figure 2. Since the cable bolt is fully bonded, multiple nodes are set on the cable bolt. The spring which represents the axial stiffness of the cable bolt is also set between each node. The spring and the slider, which represent the stiffness and the strength of grouting material, respectively, are set so as to connect each node with the rock mass element. On the other hand, in the case of rock anchor, nodes are set only both ends of the cable strand. The pretension force is given between the two nodes.

In the following, mechanical behavior of the cable bolt will be described through a simple simulation using the Cable Element. Figure 3 shows the model geometry used in the simulation for both continuous and discontinuous rock mass. Figure 4 shows the mechanical behavior of the cable bolt obtained from the simulation. As shown in Figure 4(a), in the case of continuous rock

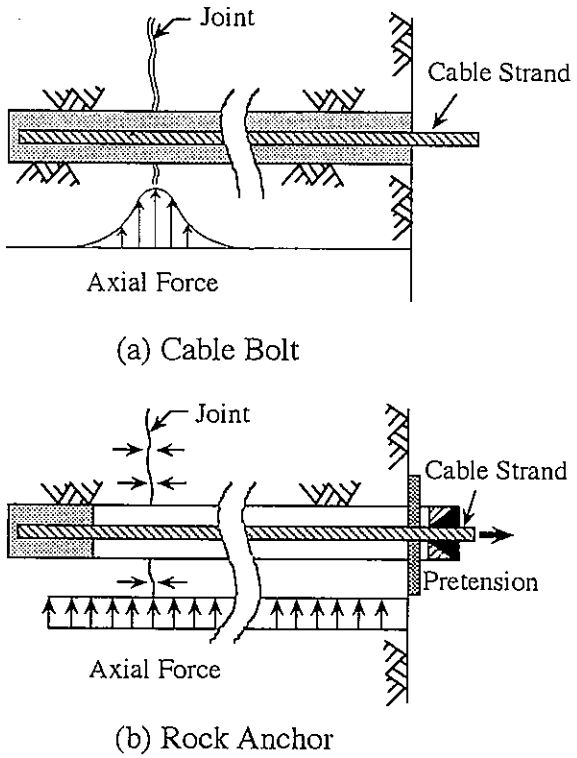

Figure 1. Concept of support mechanism

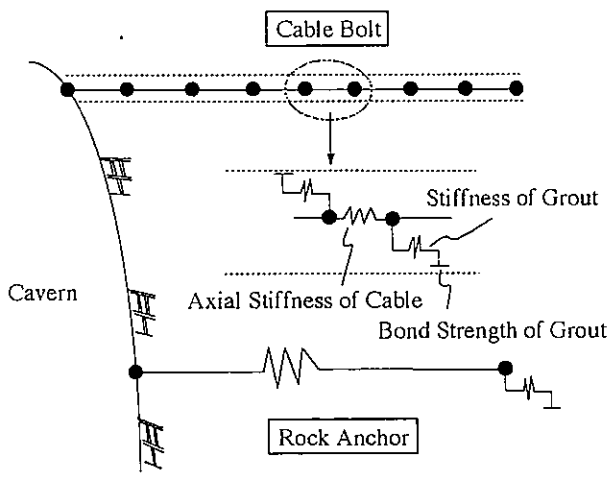

Figure 2. Modeling of cable bolt and rock anchor

mass, the peak point of axial force, the neutral point where there is no relative displacement between rock mass and the cable bolt, and the reverse point where the shear force is equal to zero, coincide with each other. That is to say, the shear force induced between the excavation surface and the neutral point acts to pull out the cable bolt, and the shear force induced in deeper side from the neutral point acts to fix the cable bolt in the rock mass. As shown in Figure 4(b), in the case of discontinuous rock mass, the peak point of axial force is located at the intersection point with joint. This peak axial force is induced corresponding to joint displacement, and expected to restrain the joint displacement by this axial force. In the same way as the case of continuous

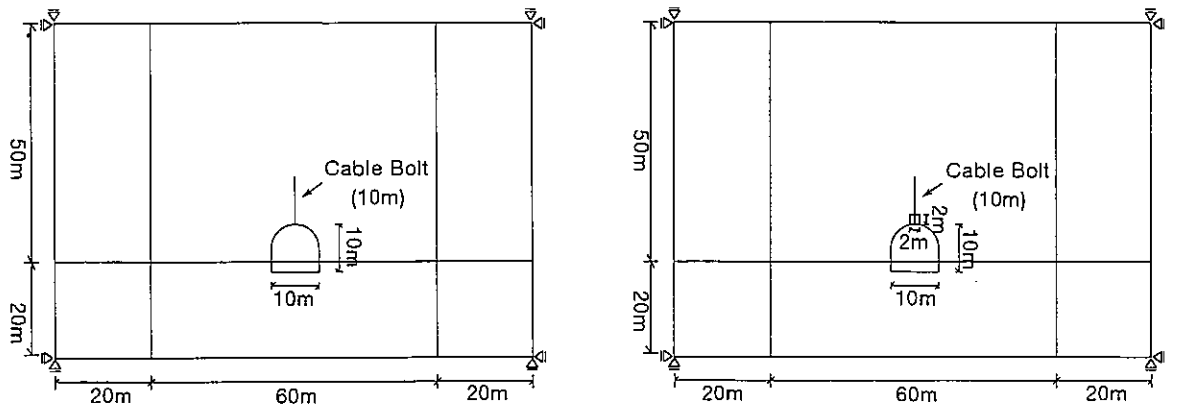

(a) Continuous rock mass (b) Discontinuous rock mass

Figure 3. Model geometry for simple simultion

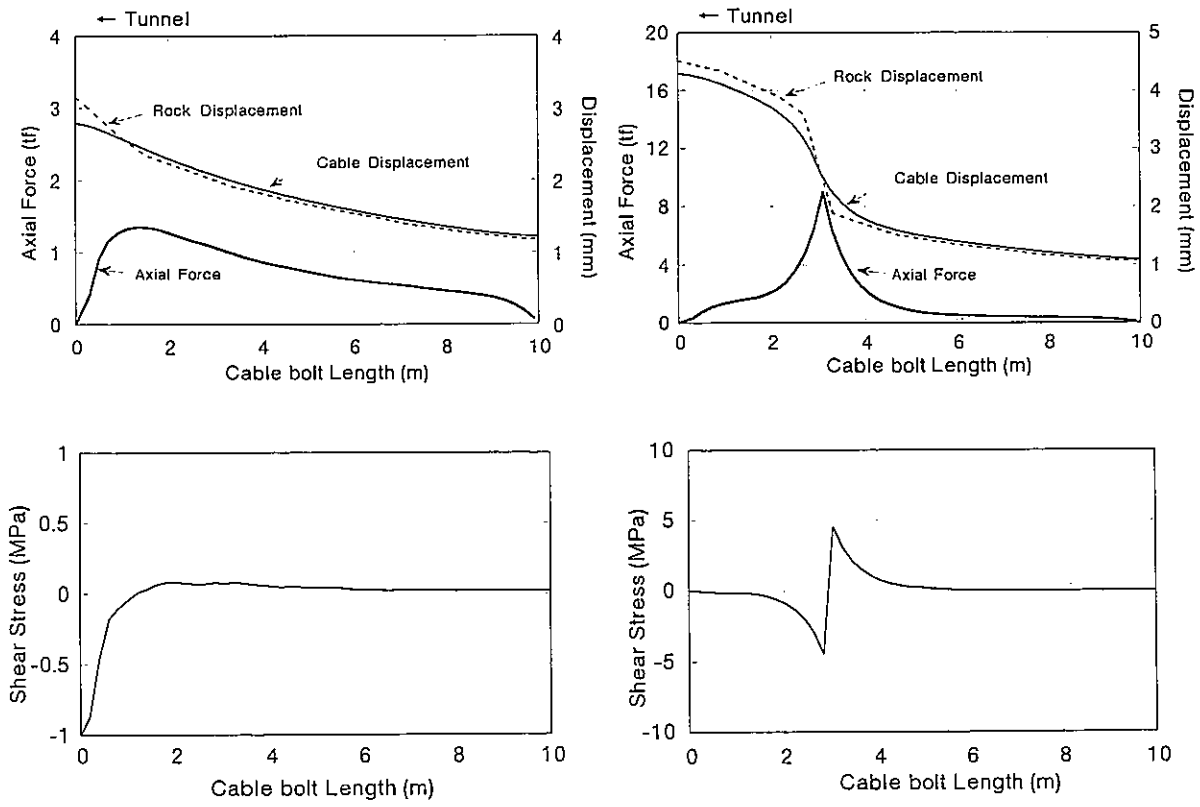

(a) Continuous rock mass (b) Discontinuous rock mass

Figure 4. Mechanical behavuor of cable bolt

rock mass, the peak point of axial force, the neutral point, and the reverse point of shear force coincide with each other.

As indicated in the result of the simulation mentioned above, the interaction between the rock mass and the cable bolt though the grouting material can be considered by the Cable Element. It enables us to simulate the reinforcement effect of the cable bolt in conformity with the actual field behavior. Since UDEC adopts the finite difference approach with successive approximation, axial force is calculated at every time-step from the relative displacement between the rock mass and the cable bolt. The algorithm generally used in finite element method would not be suitable to incorporate the concept of the relative displacement between the rock mass and the cable bolt.

3. PROCEDURE OF NUMERICAL EXPERIMENTS

In order to consider the mechanical and geometrical properties of joints, UDEC was used in the numerical simulation.

Modeling of joint geometry is based on the field investigation conducted in the Kamioka experiment site. Joint geometry which affects on the rock mass behavior is frequency, orientation and size. Procedure and assumptions which are employed to construct the model in this study are as follows.

1) Joints are represented as traces on the two dimensional plane. The geometry of traces is described by the location of the center point, the dip angle, and the trace length. Each center point of the joint is generated based on the mean spacing, which is assumed as 10m in this study.
2) Joint orientation is generated stochastically according to the results of in-situ joint survey at the Kamioka experiment site. Based on the observed distribution of the dip angle, each dip angle is generated using random numbers.
3) Each trace length is assumed as 20 m, which is roughly equal to the width of the cavern.
4) A discrete block model is constructed by managing end points and intersection points of the traces so that the joint trace map can be used in the numerical simulation. Figure 5 shows the discrete block model constructed according to the procedure mentioned above. Each block is subdivided into triangular finite difference elements and is treated as elastic material.

The pretension force is given between the two nodes. The pretension force of each rock anchor is supposed to be 90 tf. However, actually applied pretension force in the numerical simulation was 60tf on the upper 4 stages and 30 tf on the lower 7 stages, considering the installation pitch of the rock anchor in the depth direction, because the numerical simulation is performed under two dimensional plane strain condition.

Three cases of numerical simulation were carried out in this study. Those are the cases of

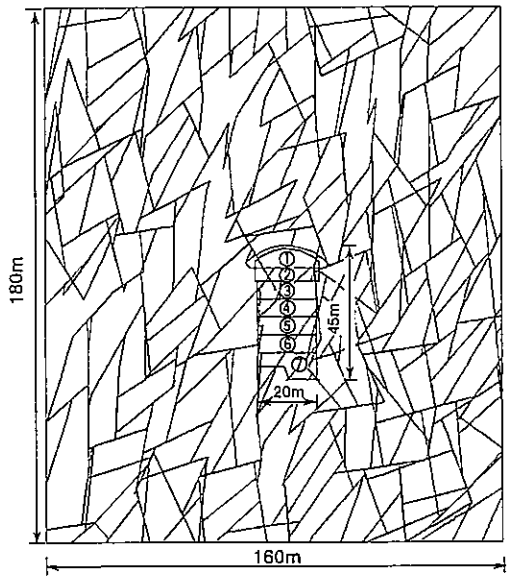

Figure 5. Discrete block model

using the cable bolt, the rock anchor, and no reinforcement. In the three cases, shotcrete was considered, but rock bolt and final lining concrete were not considered.

The numerical simulation was executed at 8 steps, including the initial stress analysis and excavation of top heading and benches. Excavation steps are shown in Figure 5.

The elastic modulus and Poisson' s ratio of the rock matrix were determined from the results of the borehole dilatometer test and unconfined compression test, respectively. The properties of the rock matrix are summarized in Table 1.

Mechanical properties of joint were determined from direct shear test using jointed samples collected in the Kamioka experiment site. Input parameters used in Barton & Bandis joint model (Barton & Bandis 1990) were obtained as shown in Table 2.

To estimate the bond properties of the cable bolt, in-situ pullout tests were carried out (Tsuchihara et al. 1995), and input parameters of the cable element were determined as shown in Table 3. In this study, it is supposed that 4 cable strand (ϕ 17.8 mm) will be installed in a borehore. Roof arch concrete and shotcrete were also considered in the numerical simulation. Table 4 indicates their input parameters.

The initial stresses in the rock mass were determined from the result of in-situ stress measurement by means of the conical-ended borehole technique conducted in the Kamioka experiment site (Sakaguchi 1994). Table 5 shows the initial stress components used in the numerical simulation.

4. RESULTS OF NUMERICAL SIMULATION

4.1 Axial Force on Cable Bolt and Rock Anchor

Figure 6 (a) and (b) show the distribution of the axial force on the cable bolt and the rock anchor. As shown in Figure 6 (a), the axial force on the

Table 1. Parameters of rock matrix

Density	2.600 kg/m ^{3}
Elastic modulus : E	10,000 MPa
Poisson's ratio : ν	0.25
Cohesion : c	3 MPa
Friction angle : ϕ	46 deg.

Table 2. Parameters of joint

Normal stiffness : K_n	10.2 MPa
Shear stiffness : Ks	2.2 MPa
Joint compressive strength : JCS	51.0 MPa
Joint roughness coefficient : JRC	9.4
Residual friction angle : ϕ r	27 deg.

Table 3. Parameters of cable element

CABLE STRAND :	
Density	6,083 kg/m^3
Young's modulus	190,000 MPa
Tensile strength	1,550 kN
Failure strain	0.035
Compressive strength	1,550 kN
GROUT :	
Shear stiffness	180 MN/m/m
Bond strength	600 kN/m

Table 4. Parameters of roof concrete and shotcrete

ROOF CONCRETE :	
Density	2,200 kg/m^3
Elastic modulus	19,600 MPa
Poisson's ratio	0.2
SHOTCRETE :	
Density	2,200 kg/m^3
Elastic modulus	17,000 MPa
Poisson's ratio	0.2

Table 5. Initial stress components

σ xx	σ zz	τ zx
2.14 MPa	4.13 MPa	0.77 MPa

cable bolt has the peak value at the intersection points with joints, and the axial force arises through grouting material in proportion to the relative displacement between the rock mass and the cable bolt. This type of the axial force distribution is a characteristic feature of the cable bolt as fully bonded reinforcement.

As shown in figure 6 (b), the axial force on the rock anchor has uniform value along the cable strand, whose value is equal to the sum of the initial pretension force and additional load caused by the excavation.

4.2 Joint Displacement

Figure 7 shows the joint shear displacement comparing with the three cases. In Figure 7, thickness of the line along each joint indicates the magnitude of joint shear displacement. As indicated in Figure 7, the maximum value of the joint shear displacement is 28.2mm, 29.0mm, and 37.5mm, respectively. The maximum value of the joint opening is 2.5 mm, 2.2mm, and 34.4mm, respectively. The result of numerical simulation clearly indicates that the joint displacement is restrained by the

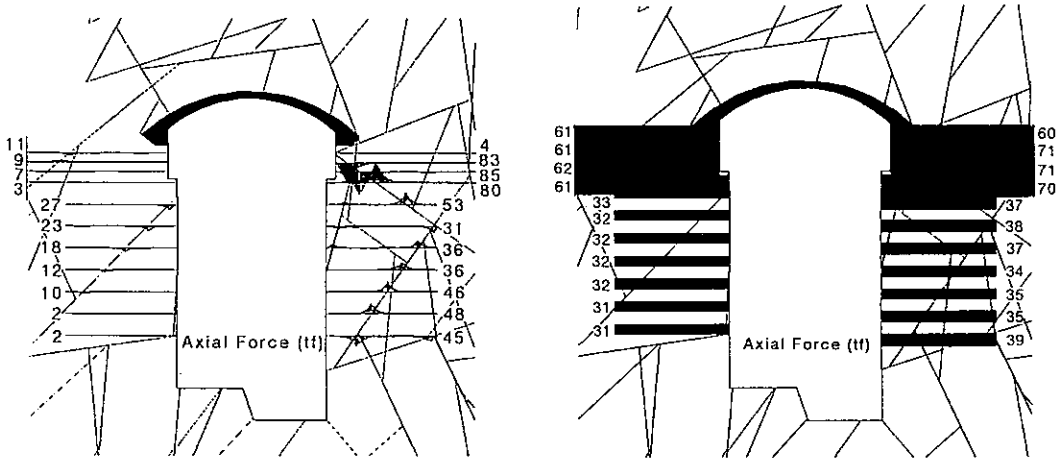

(a) Cable bolt (b) Rock anchor

Figure 6. Axial force of cable bolt and rock anchor

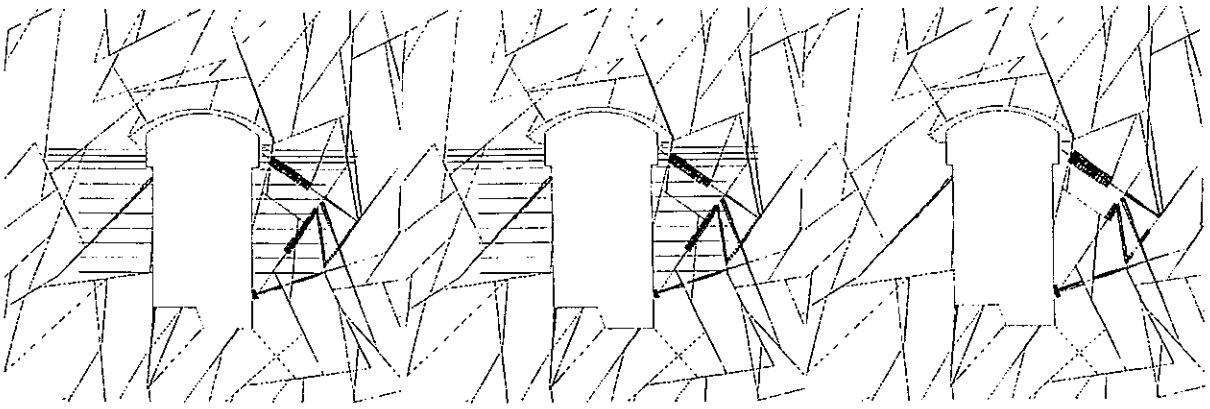

(a) Cable bolt (max. 28.2 mm) (b) Rock anchor (max. 29.0 mm) (c) No reinforcement (max. 37.5 mm)

Figure 7. Shear displacement of joint

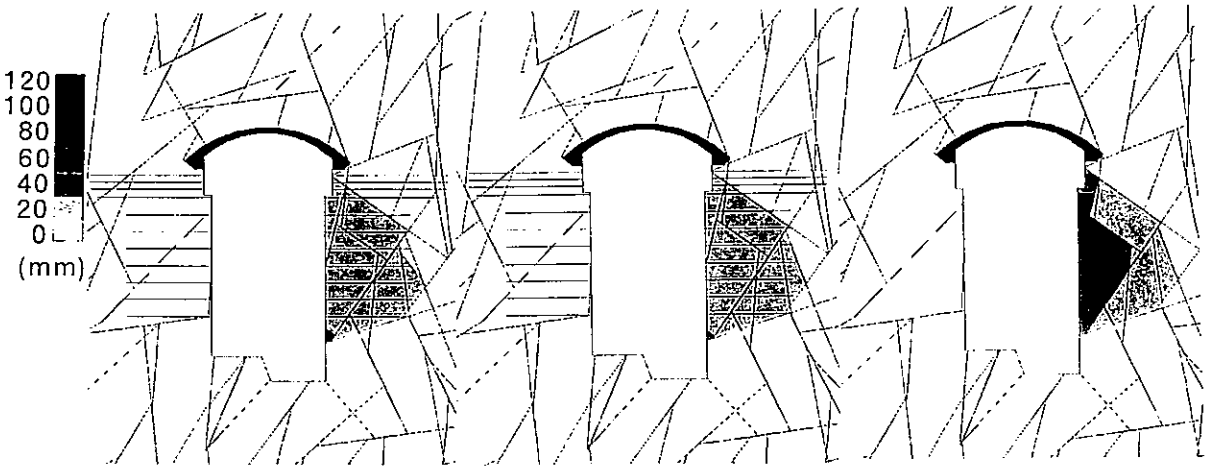

(a) Cable bolt (max. 41.4 mm) (b) Rock anchor (max. 40.8 mm) (c) No reinforcement (max. 124.3 mm)

Figure 8. Contour map of Horizontal displacement

cable bolt or the rock anchor. The reinforcement effect is remarkable in the region of the right side of the cavern, because the orientation of the joint is unstably inclined in the region of the right side of the cavern.

4.3 Rock Mass Displacement

Figure 8 shows the contour map of the horizontal displacement around the cavern. In the case of no reinforcement, displacement at the right side of the cavern is fairly larger than those of the cases of using the cable bolt or the rock anchor. On the other hand, the horizontal displacement at the left side of the cavern is nearly equal in three cases. As indicated in Figure 8, the maximum horizontal displacement is 41.4mm, 40.8mm, and 124.3mm, respectively. The reinforcement effect of the cable bolt can be said nearly equal to that of the rock anchor in terms of the restrain of the horizontal displacement.

5. CONCLUSIONS

It was demonstrated that the mechanical behavior of the cable bolt in continuous and discontinuous rock mass can be effectively simulated using the Cable Element incorporated in UDEC. Since the Cable Element can consider the interaction between the rock mass and the cable bolt though the grouting material, it is suitable for simulating the reinforcement effect of the cable bolt in conformity with the actual field behavior.

The result of numerical experiments indicates that the reinforcement effect of the cable bolt and the rock anchor is almost equivalent under the assumed condition in this study, although the support mechanism of both reinforcement methods are clearly different. In the case of the cable bolt, the joint displacement is restrained by the axial force of the cable bolt induced by the joint displacement. In the case of rock anchor, the displacement of the rock mass is reduced because

the pretension force actively gives the confining pressure to increase the shear resistance of the joint surface. Though the pretension is more effective in some instances, it is expected that the reinforcement effect of the cable bolt and the rock anchor is almost equivalent in accordance with the result of the numerical simulation.

REFERENCES

Akagi T., H. Horii, T. Tanaka, T. Yamabe, Y. Uchida : Investigation, test and measurement of discontinuous rock mass, Proc. of 26th. Sympo. of Rock Mech., Committee on Rock Mech., Japan Society of Civil Engineers, pp. 574-583, 1995 (in Japanese)

Amano S. & H. Shirahata : Discrimination of conductive fractures based on the information from geological investigations, Proc. of 26th. Sympo. of Rock Mech., Committee on Rock Mech., Japan Society of Civil Engineers, pp. 126-130, 1995a (in Japanese)

Amano S., H. Kinashi & T. Tanaka : Numerical experiments on support effect of cable bolts in fractured rock mass, Proc. of 5th. Tunnel Engineering, Japan Society of Civil Engineers, pp. 155-160, 1995b (in Japanese)

Barton N. & S. Bandis : Review of predictive capabilities of JRC-JCS model in engineering practice, Proc. of Int. Sympo. on Rock Joints, pp.603-610,1990

Cundall P.A. : UDEC - A generalized distinct element program for modelling jointed rock, Report PCAR-1-80, European Research Office, U.S Army, Contact DAJA37-79-C-0548, 1980

Itasca Consulting Group, Inc.: UDEC(Universal Distinct Element Code) Version 3.0 User's Manual, 1996.

Kinashi H., H. Shirahata, K. Nagahisa, T. Tamano & T. Tanaka: Estimation of joint characteristics based on joint survey and application of DEM analysis to the discontinuous rock mass, Proc. of 26th. Sympo. of Rock Mech., Committee on Rock Mech., Japan Society of Civil Engineers, pp. 126-130, 1995a (in Japanese)

Kinashi H., S. Amano & T. Tanaka : Stochastic modelling of rock joint system and numerical experiments on stability of underground openings, Proc. of 26th. Sympo. of Rock Mech., Committee on Rock Mech., Japan Society of Civil Engineers, pp. 16-20, 1995b (in Japanese)

Sakaguchi K., K. Sugawara, K. Nagahisa & T. Kaneda: Application of conical ended borehole technique to inhomogenious rock and consideration, Proc. of 9th. Japan Sympo. on rock Mech., pp.229-234, 1994 (in Japanese)

Tamai A., T. Mikami & K. Akiyoshi : Study on three-dimensional mechanical behaviors by tunnel excavation in discontinuous rock mass, Proc. of 9th. Japan Sympo. on rock Mech., pp.605-610, 1994 (in Japanese)

Tsuchihara H., T. Ninomiya, M. Inoue & K. Nagahisa : Application test of cable bolts to in-situ rock mass, Proc. of 5th. Tunnel Engineering, Japan Society of Civil Engineers, pp. 149-154, 1995 (in Japanese)

A static model of granular materials in a bin using Distinct Element Analysis

Jun Yoshida
Izumi Research Institute, Shimizu Corporation, Tokyo, Japan

ABSTRACT : When granular materials in a bin are modeled by Distinct Element Method, the arrangement of particles in a bin or hopper has very large effect to their behavior. In this study, the methods of modeling, which realize the regular and irregular arrangements in two dimensional DEM, are proposed. According to the comparison between DEM and Janssen's equation which is widely used in a structural design of silos, the validity of the model is indicated. In addition to two dimensional analysis, three dimensional simulation is demonstrated.

Keywords : Distinct Element Method, Granular Material, Bin, Static Pressure, Particle Arrangement

1. Introduction

When granular materials in a bin are modeled by Distinct Element Method (DEM), the effect of the initial arrangement of particles is sometimes ignored or not considered. However, the arrangement of particles in a bin or hopper has very large effect to their behavior.

DEM was originally proposed by Cundall (1971), and its application was extended to granular materials by Cundall et al.(1979). The applications to a silo or hopper were demonstrated by Campbell (1986), Kiyama et al.(1983), Yoshida (1993) and so on. In these papers, a lot of models were examined to show the capability of DEM and to analyze the behavior of particles, but most of them were two dimensional one, and there has scarcely been a detail discussion on the method how to arrange the particles initially. In this study, the arrangement of particles is investigated from a view point of representing the static pressure distribution in a bin. The next section shows the regular arrangement of particles on two dimensional model. Then, the irregular or random arrangement is discussed. In order to verify the results of DEM, the distributions of its static pressure are compared to the Janssen's equation which is commonly used in a design of silos. Finally, the example of three dimensional DEM is shown and also compared to the Janssen's.

2. Particles arranged regularly

2.1 Method of arranging

In this study, the arrangement is basically placed in two categories, regular and irregular. The regular arrangement means that there are equal horizontal distances between particles, and they are alternately placed in vertical direction (see Fig.1(a)). In the DEM simulation, to attain the static equilibrium needs some repetitions just like the dynamic calculation. If the whole particles are initially arranged, they are moved simultaneously with gravity, and settled after several steps. The example which is composed of a bin of 30cm-wide and 70cm-high with 2000 particles is shown in Fig.1(a). The lines between particles and wall represent the contact forces. Most of them at the side wall tend to upward from the wall, but those of the upper part show different tendency. This means that a negative friction is occurred near the top of the layer. To consider the practical

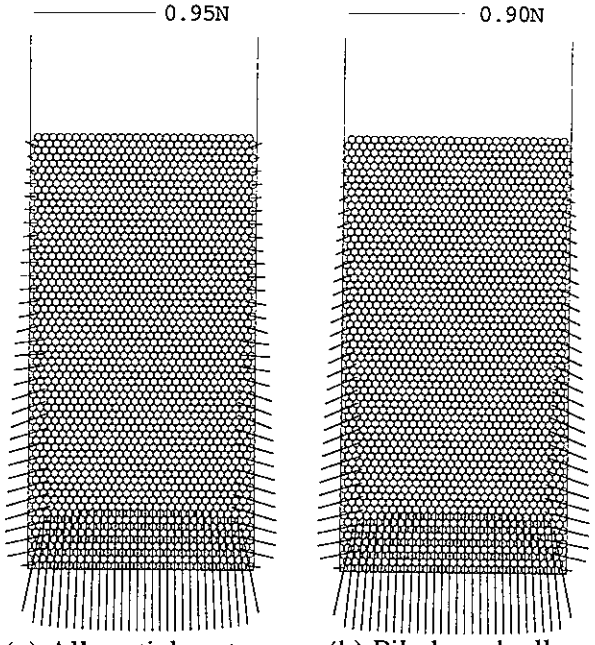

(a) All particles at once (b) Piled gradually

Fig.1 Difference of modeling order

bin, the particles are arranged orderly from the bottom, and the friction on the wall must be positive. Therefore, this example can not express the equilibrium state properly. Then, in the next model, the particles are gradually layered from the bottom. Actually, a row of particles are set on the bottom at first, and their movement is calculated until their velocity is converged. After the convergence, the second row is set on the first. So far, the layer of particles are created. Fig.1(b) shows one of the examples. The contact forces show the resemblance with (a), but are more reasonable than those in (a). From this comparison, it is said that the regular arrangement is seemingly simple, but when the initial state would be properly created, the method of arranging is important.

2.2 Static pressure

Static pressures in a bin are represented by

Table 1 Material properties

Parameters	Unit	Value
Particle density	kg/m^3	2.0×10^3
Normal (Shear) stiffness	N/m	100.0(20)
Damping coefficient	s	3.0×10^{-3}
Friction coefficient (Wall)		0.70(0.50)
Diameter of particle	mm	10.0

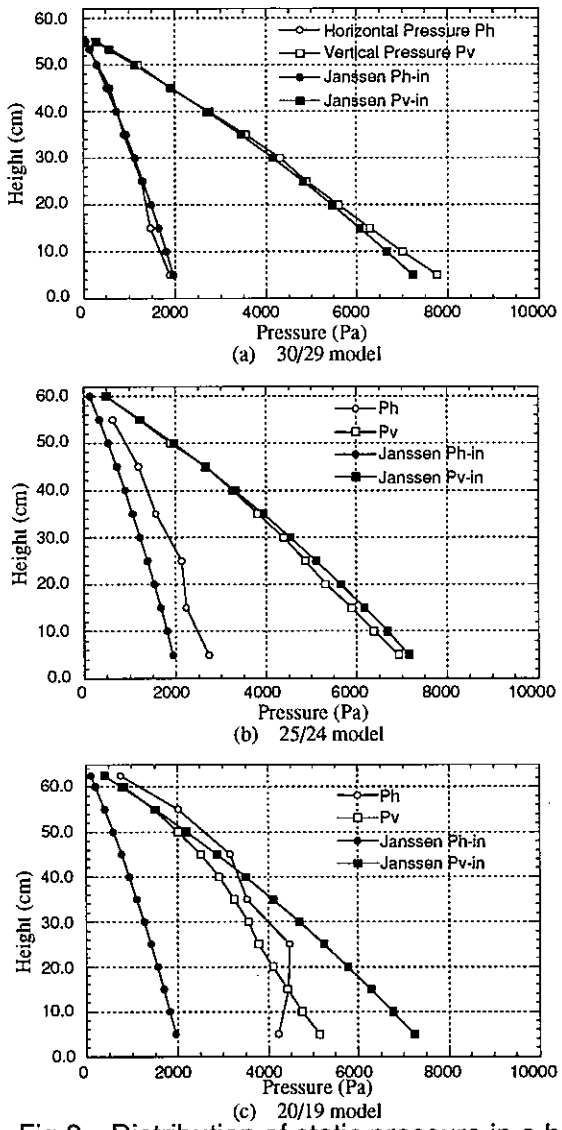

Fig.2 Distribution of static pressure in a bin Janssen's calculated with input parameter

Janssen's equation and in the design of a silo the pressure distribution calculated by Janssen's is widely accepted as a static load. In this session the pressure distribution obtained by the regular arrangement is compared to Janssen's. In the DEM simulation, the contact force between particles is directly obtained, but the pressure or stress is not. Therefore, the pressure in the layer is calculated as a volumetric average of the contact forces.

Fig.2 shows the pressure distribution in a bin. In Fig.2(a), the result of DEM shows similar distribution to Janssen's, but there is big difference in Fig.2(c). The figure (a) shows the results of 30/29 particles each row, (b) shows those of 25/24 and (c) shows those of 20/19. The difference of the arrangement natu-

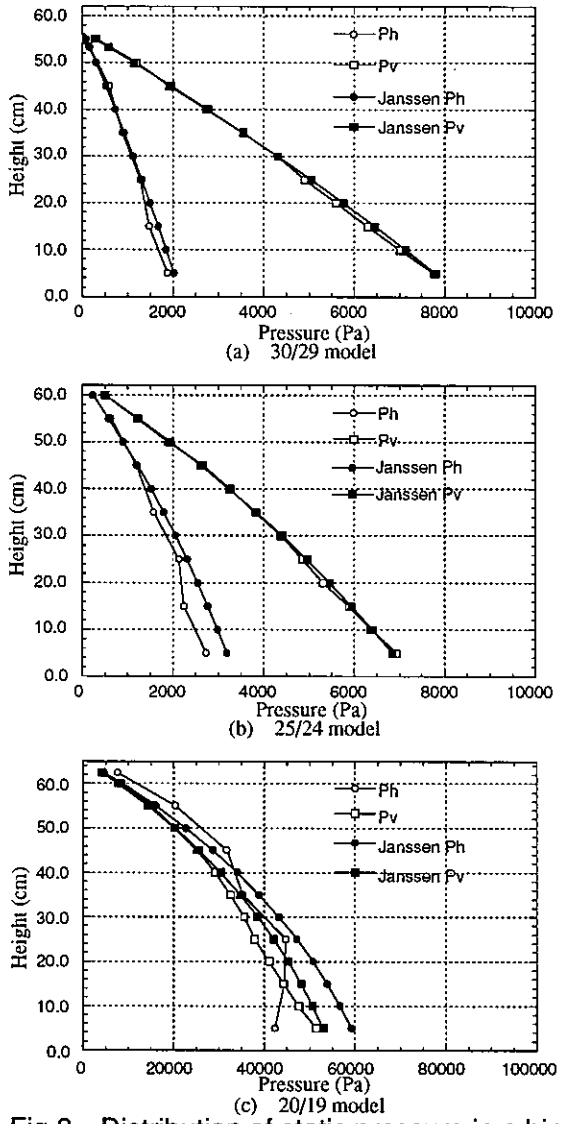

Fig.3 Distribution of static pressure in a bin Janssen's calculated with DEM result

rally gives the different distribution. In Fig.2, the distribution of Janssen's is calculated with the parameters which reflect the input of DEM, i.e. friction coefficient (see Table 1). The difference between DEM and Janssen's seems to come from this assumption. Then, the parameters are calculated from the results of DEM, and compared to the Janssen's distribution again in Fig.3. The distributions show similarity on an average. This means that it is necessary to use the practical value other than the input in order to obtain the valid distribution. However, in Fig.3(c) the shape of the curve has some difference, and this comes from the fact that the original assumption of Janssen's equation does not hold good.

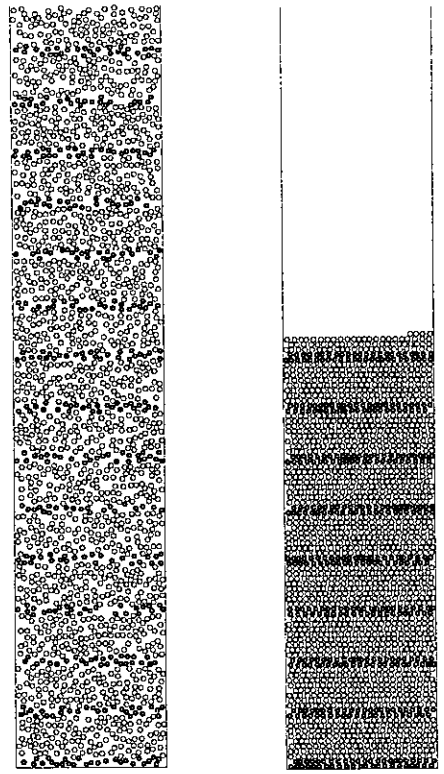

(a) Example of (1) (b) Example of (2)
Fig.4 Modeling method

3. Irregular arrangement of particles

3.1 Modeling method

The regular arrangement is quite easy to understand because of its regularity. To make an irregular model has some difficulties with randomness. When we would like to make an irregular arrangement, there are three methods how to place the particles.

(1) The center of a particle is set at random in the limited space, and if its area crosses the other particles which were already placed, it is eliminated. This modeling guarantees the randomness, but the void ratio in the initial state is too large to calculate the equilibrium. (see Fig.4(a))s

(2) The center of a particle is set at random on the bottom at first, and the rows are gradually piled up with the equal vertical distance to the size of a particle. This modeling loses some randomness, but can obtain the equilibrium effectively. (see Fig.4(b))

(3) Particles are set regularly at first, and some particles are removed at random. This method is very easy to realize, but

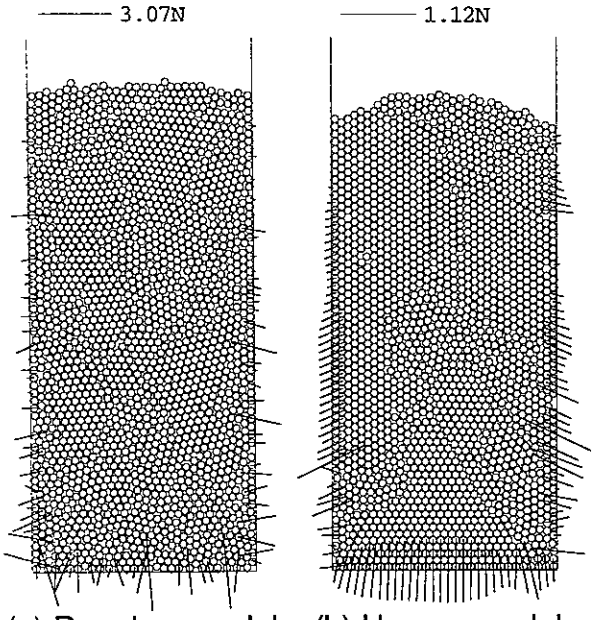

(a) Ramdom model (b) Hopper model

Fig.5 Irregular arrangement of particles

there is a problem mentioned in the previous section, and also the randomness is not secured.

In this study, the (2) is selected to simulate the irregular arrangement.

3.2 Static Pressure

Two types of arrangement is established. One is called the Random model which is followed the scheme mentioned above. The other is called the Hopper model. First, the particles are placed in a hopper which is defined at the top of a bin. Next, its orifice is opened, and the particles are fed to the bin. The results of the both models after convergence are shown in Fig.5. The Random model shows randomness successfully, but in the Hopper model there exists a part of regularity. Therefore, it is difficult to make a random model which is created by feeding, especially in two dimensional simulation.

The pressure distributions of these models are shown in Fig.6. The results of DEM are equivalent to the Janssen's distribution. Consequently, DEM can show the reasonable results in the case of irregular arrangement. However, as mentioned above, there is a limitation in two dimensional analysis.

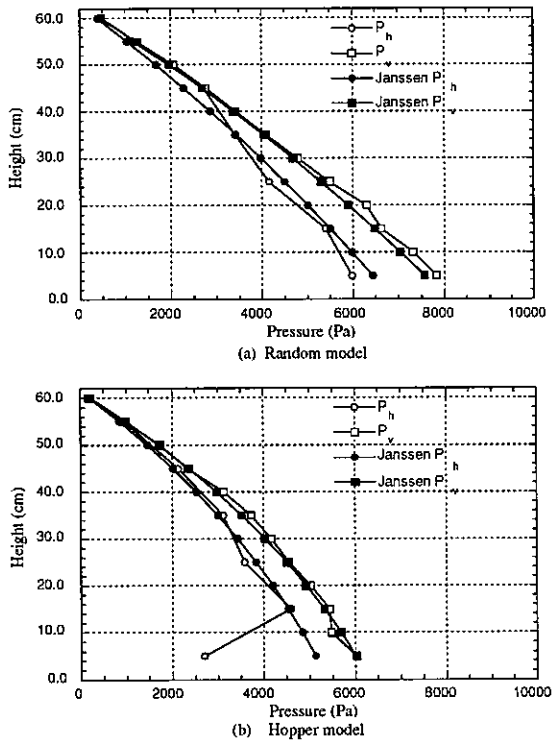

Fig.6 Distribution of static pressure in a bin Janssen's calculated with Dem results

4. Discussions

4.1 Modeling method

In the case of the regular arrangement, it's better to make layers gradually from the bottom. However, the Random model is not influenced by the order of piling up. This fact shows that because in the regular arrangement the space between particles is small, the stiffness or deformation factor has an influence from the beginning and causes a negative friction. On the contrary, in the Random model, there is much space than the regular one, so the deformation between particles has less effect than the movement of a particle itself. Therefore, the difference

Table 2 Parameters from DEM results

MODEL Name	Contact Angle(deg)	Porosity (%)	Coord. Number
30/29	59.6	10.52	4.80
25/24	52.7	19.52	4.00
20/19	40.0	20.57	3.99
Random	47.3	18.59	4.12
Hopper	49.2	14.68	3.57

of the method is mixed up.
Fundamentally, the particles must be gradually piled up from the bottom in a silo problem, but it is sometimes possible to place the particles at once like the Random model. This problem is not so important in two dimensional DEM, but 3-D DEM sometimes needs very time consuming calculation to pile up the particles.

4.2 Effect of particle arrangement

While five types of arrangement are examined, the distributions of the DEM results are completely different. Among the regular arrangements, the horizontal distance between particles causes the increase of the horizontal pressure. So, this means the contact angle between particles is an important factor in order to quantify the effect of the particle arrangement. However, the angle can be easily grasped in the regular arrangement, but it's very difficult in the irregular one. Other than the contact angle, the porosity and coordination number seem to be important factors. Table 2 shows their value of each model. From this table, it's difficult to see the specific relation. However, it seems to indicate the larger horizontal pressure according to the larger porosity. To tell the truth, in the regular arrangement, the coordination number must be clear, but it contains some numerical error.

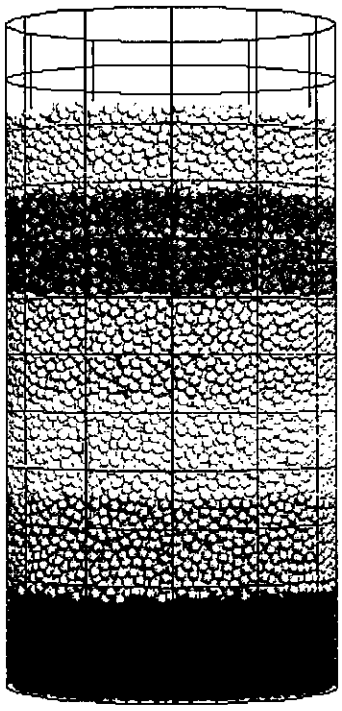

Fig.7 Appearance of 3-D model

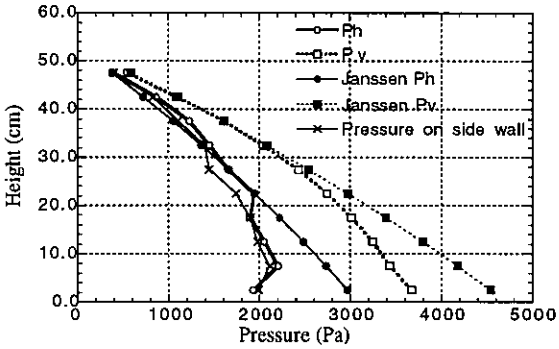

Fig.8 Static pressure in 3-D model

5. Example of 3-D model

To deal with the granular material, the problem is essentially three dimensional, but in spite of the recent progress of the computer, three dimensional calculation of DEM is limited in the number of elements. However, it is possible to simulate more than 50,000 particles now. Then, the example of 3-D model is shown here. The total number of particles in a cylindrical bin are 40,000, and the size of the bin is 30cm-diameter and 60cm-high. The material properties are the same as two dimensional model. The way of modeling is also like two dimensional one. 5000 particles per each step are generated at random, and they are gradually piled up. The appearance of the 3-D model is shown in Fig. 7. Compared to the two dimensional model the particles look like more crowded, but in fact the porosity of this result is 43.0% and that of two dimensional Random model is 18.6%. The porosity of 2- and 3-D is originally different from 21.6% to 47.6% which is calculated from the ratio of circle/square and sphere/cubic. Therefore, there is not much difference in porosity.
The pressure distributions are shown in Fig.8. The shape of the curbs, which are described by DEM and Janssen's equation, are not so different, but they are gradually apart to the bottom. The difference between Janssen's and DEM comes from the assumption of Janssen's, and this tendency is fore-

seen from the result of two dimensional model. In Fig.8, Janssen's distribution gives larger loads than the DEM result, so the problem is not severe from the view point of the structural design. Then, there seems to be a possibility to make the structural design more reasonable.

6. Conclusions

Initial modeling of DEM is a very important factor in granular problems. Its effects on static pressures are examined using two dimensional DEM. The several modeling methods are proposed to simulate a silo problem, and the regular and irregular arrangements are reasonably realized. The static pressures obtained from DEM results indicate the similar distribution to the Janssen's equation. However, to calculate the Janssen's pressure, the parameters must be determined from the DEM result, and if the assumptions of Janssen's are invalid, the distribution curbs of DEM and Janssen's show difference.

The static pressure is largely influenced by the arrangement of particles, and this effect seems to relate to the contact angle, porosity and coordination number.

In this paper, the effect of arrangement is examined, but the static pressure practically depends on so many parameters which influence to , i.e. friction, size of particle, size distribution, etc. Furthermore, a present study treats only static problems, but in a silo design, the dynamic behavior during discharge or earthquake is more important than static. A basic study on dynamic pressure is shown by Yoshida (1993), but in order to understand a complicated behavior in dynamic state a lot of experiments and simulations are necessary.

References

1) Cundall, P.A. : The measurement and analysis of accelerations in rock slopes, Ph.D. Thesis, Imperial College, London (1971)
2) Cundall, P.A. & O.D.L. Strack : A discrete numerical model for granular assemblies, Geotechnique, 37, 47 (1979)
3) Campbell, C.S. : Computer simulation of rapid granular flows, Proc. 10th U.S.N.C. of Appli. Mech., ASME, 327 (1986)
4) Kiyama, H. & H. Fujimura : Application of Cundall's discrete block method to gravity flow analysis of rock-like granular material, Proc. of JSCE, 333, 137 (1983)
5) Yoshida, J. : Study of static pressure of granular materials in a silo using the distinct element method, KONA, 11, 215 (1993)
6) Yoshida, J. : An analytical study of pulsation phenomena of granular materials in silos during discharge, J. of Soc. Powder Tech. Japan, 30, 166, (1993)

Combined Finite/Discrete Element Method - Improved Contact Solutions

A.MUNJIZA, G.J.HUANG, J.S.LIN[1]
Department of Engineering, QMW, University of London, U.K.
[1]*Department of Civil and Environmental Engineering, University of Pittsburgh, U.S.A.*

SUMMARY

Combined finite/discrete element method involves large number of (solid) bodies, each discretised into finite elements. The bodies interact through mechanical contact at points where boundaries touch and both the accuracy and the robustness of the combined finite/discrete element method greatly depend on contact algorithms employed.

Recent developments at QMW are summarised in this paper. These include a solution strategy based on discretisation of the assumed potential contact field together with considerably improved contact detection. The most important features of these recent developments include relatively easy implementation for bodies of general shape and size, preservation of energy and momentum balance and reduced CPU time and memory requirements. Contact detection related improvements include a contact detection algorithm with total detection time proportional to N (total number of separate bodies).

1. INTRODUCTION

Discrete element methods[1,2,3,5] are characterised by systems comprising a large number of separate (distinct) bodies often called discrete elements. Discrete elements are usually free to move in space and time and thus interact with each other, while discrete element-like static formulations are often termed Discontinuous Deformation Analysis or DDA[4].

In discrete element methods, each discrete element is considered as a separate body that interacts with neighbouring elements. Routine discrete element problems may involve million of interacting discrete elements and in this context fast and efficient contact algorithms are necessary. In other words the effective solution of large scale discrete element problems relies upon robust contact detection and contact interaction algorithms being employed.

This is also the case for the combined finite - discrete element method[5], where each discrete element is discretised into finite elements, while the distribution of individual discrete elements, shape of individual discrete elements and the total number of discrete elements all change in time.

In recent years there has been a significant progress made at QMW regarding both contact detection and contact interaction between bodies. A summary of these improvements is presented in this paper without going into the algorithmic details of the contact procedures employed.

2. CONTACT INTERACTION

One of the key issues in the developement of numerical methods for a large class of problems is the treatment of general contact impact, i.e. the enforcement of the constraint that no point in the space is occupied by more then one body at the same time.

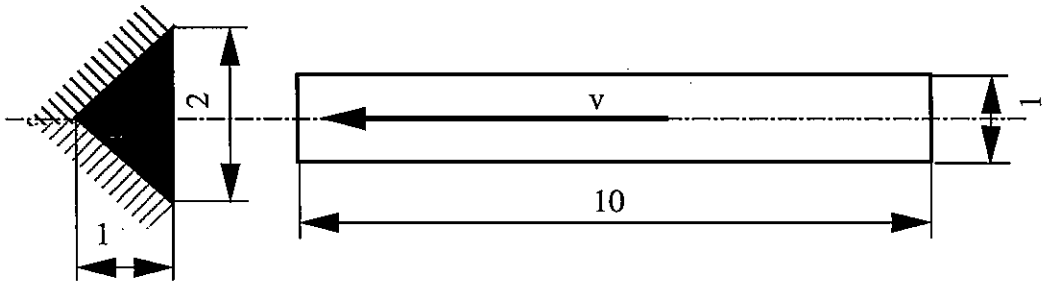

Figure 1. Bar shaped heap impact problem

Traditionally contact algorithms consider contact at discrete points and are usually designed to handle only a selected class of contact situations. For instance, one of the classic assumptions in conjunction with the penalty method is the assumption of small penetration. However, such an assumption is not always valid. In large systems a situation where a small active force is balanced by a relatively large passive force can arise, while in some cases even small penetration can lead to a significant increase of the energy of the system[5].

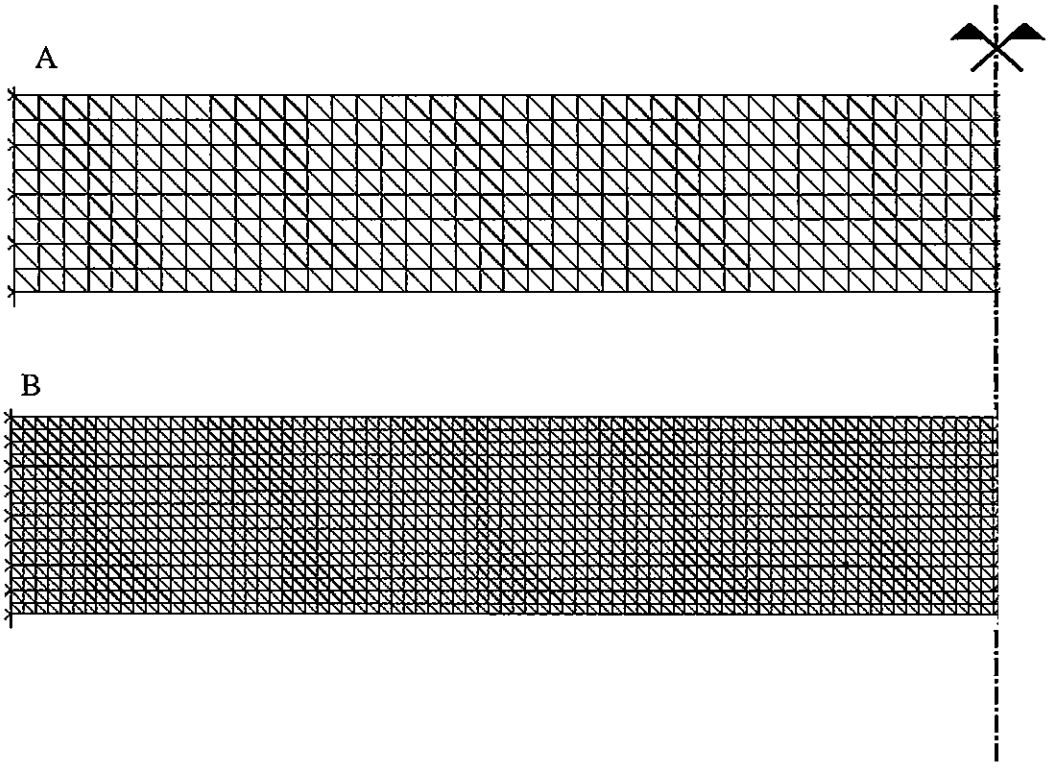

Figure 2. Configurations of bar shaped heaps

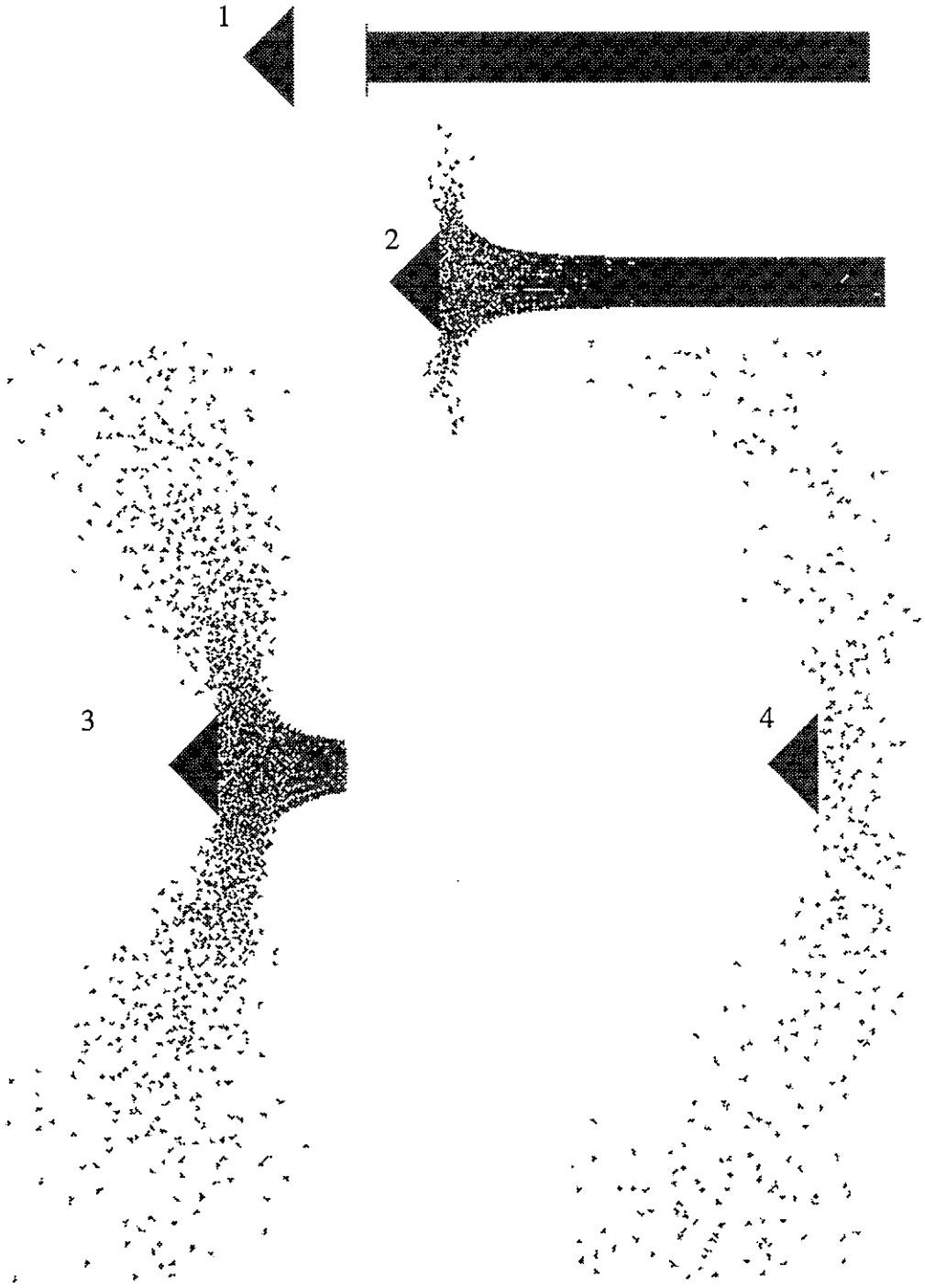

Figure 3. Motion sequence for heap "A"

Recently at QMW a general contact algorithm with contact kinematics suited for systems comprising very large number of interacting bodies was developed. It is out of the scope of this paper to discuss the details of the proposed algorithm. The main features of the algorithm are as follows:

1. Energy and momentum balances are preserved for small, medium and large penetration.
2. Only the in-core database for contact-free analysis is necessary.

3. Realistic distribution of contact forces is obtained
4. Detection of boundary surfaces is not necessary.
5. Both sequential and vectorised/parallel implementations are possible.

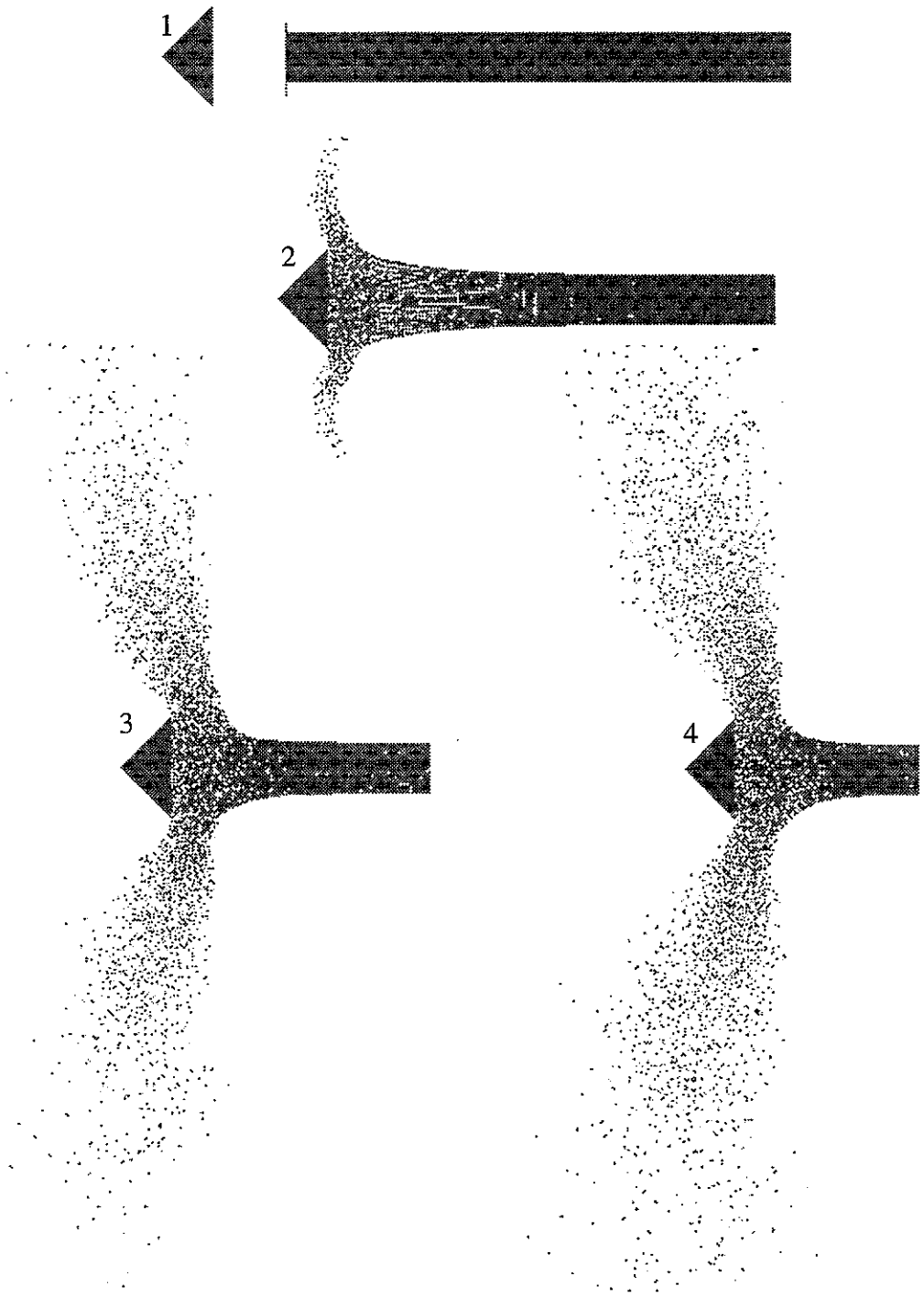

Figure 4. Motion sequence for heap "B"

A practical application of the algorithm is shown in Figure 1. A bar-shaped heap of rigid bodies is impacted against a rigid triangular obstacle. Two heaps are considered, Figure 2.

The motion sequence for each heap is shown in Figures 3 and 4, while the energy balance is shown in Figure 5, which shows actual preservation of energy balance after release of all contacts.

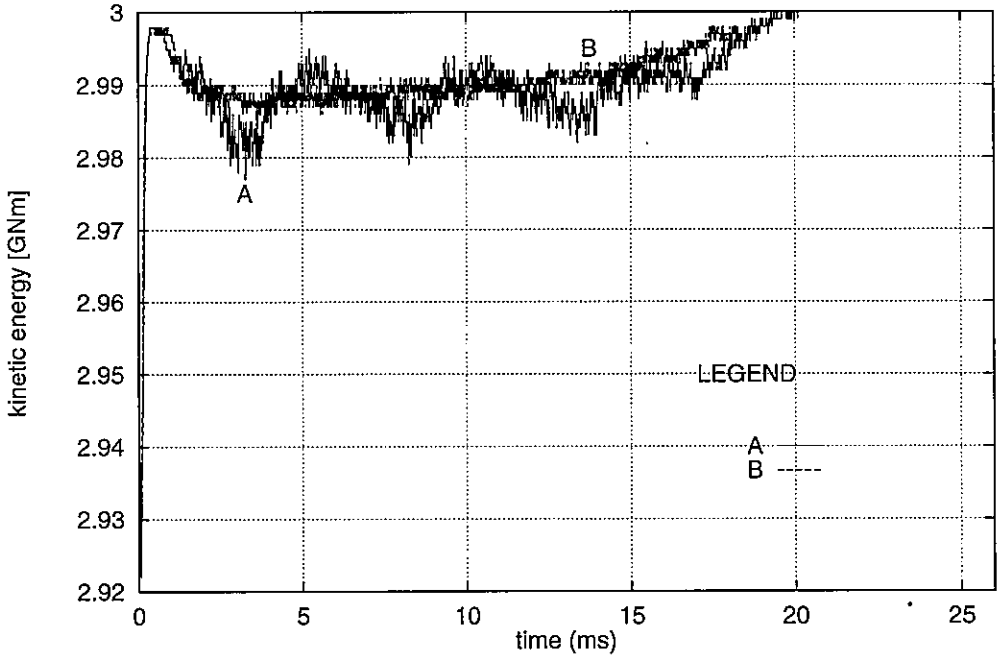

Figure 5. Total kinetic energy of all fragments of the bar shaped heap

3. CONTACT DETECTION

Conventional contact algorithms for finite element analysis usually have the simplest contact detection procedures implemented, while in discrete element methods a fast and efficient contact detection algorithm is needed. In general the optimal contact detection algorithm is dependent upon the problem to be solved. Two situations can be identified, *dense packing* and *loose packing*, Figure 6. Both loose and dense packing are for instance present in transient dynamics problems where individual bodies may move significantly, Figure 7.

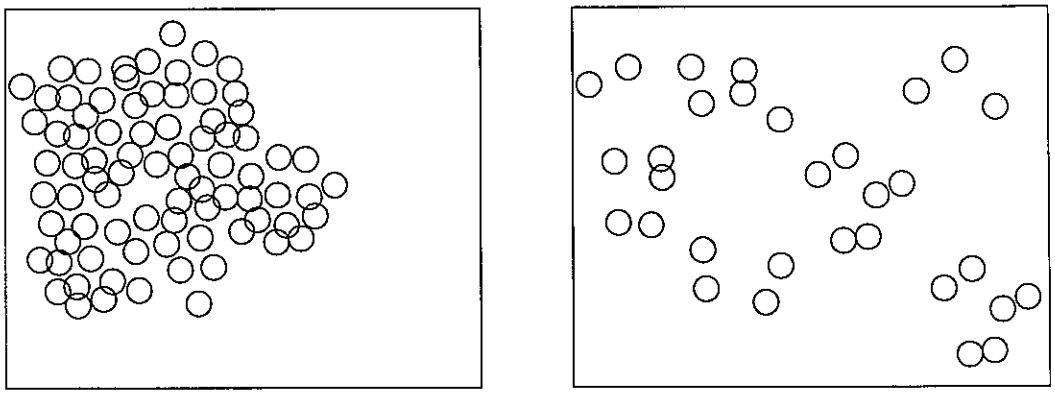

(a) (b)

Figure 6. (a) dense and (b) loose packing

Most of the contact detection algorithms reported in recent years can be classified as body based search or space based search and are usually designed for either loose or dense packing, while some can handle quasi-static problems only. Real problems where contact detection is a big issue are transient dynamics problems where packing can be changing in time from loose to dense and vice-versa. Thus an algorithm that could handle both loose and dense packing would be of great advantage. Among such algorithms is the BSD contact detection algorithm used in RG code (a first combined finite discrete element code)[5]. This algorithm has CPU time proportional to $Nln(N)$, where N is the total number of objects. The memory requirements are proportional to $NlnB$, where B is the space size.

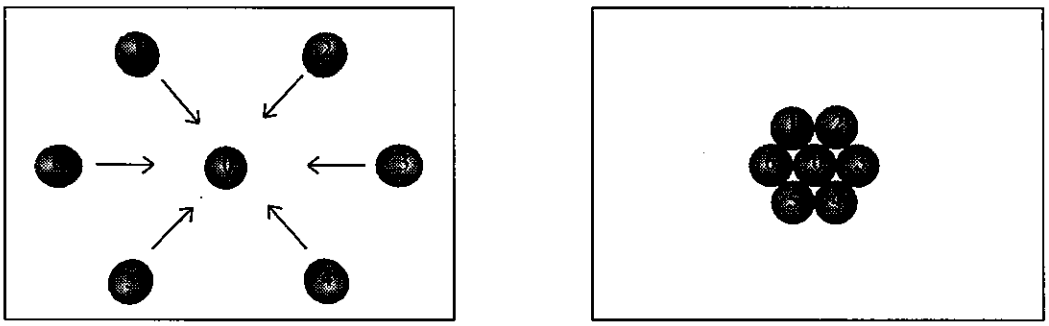

Figure 7. Typical dynamic problem

Discrete element analysis may involve extensive CPU requirements. Parallel and distributed processing offers exciting opportunities in this direction. In spite of ever improving CPU and RAM performance of hardware, there will always be scope for designing better algorithms. In this context, a contact detection algorithm that satisfies the following criteria has been developed at QMW recently:

1. CPU requirements measured in terms of total CPU time needed to detect all contacting pairs is proportional to the total number of objects N.

$$T = c_t N$$

2. Total RAM requirements are

$$M = c_s B + c_n N$$

   where c_t c_n and c_s are constants.
3. CPU time is independent of packing.

The proposed algorithm is termed NBS, where N stands for "No", B stands for "Binary" and S stands for "Search". In other words, the NBS algorithm does not involve any binary search, which makes it more efficient both in terms of CPU time and memory requirements when compared with binary based search strategies.

It is out of scope of this paper to go into details of the proposed algorithm. The performance of the algorithm is illustrated through a numerical example. The example shown in Figure 8 involves a jet of 0.5 million round bodies sprayed against rigid target. The problem consumed less than 30Mb of RAM space. An Indy (32Mb RAM) workstation has been employed for simulation, which confirms that both the memory and CPU requirements of the NBS contact detection algorithm are minimal.

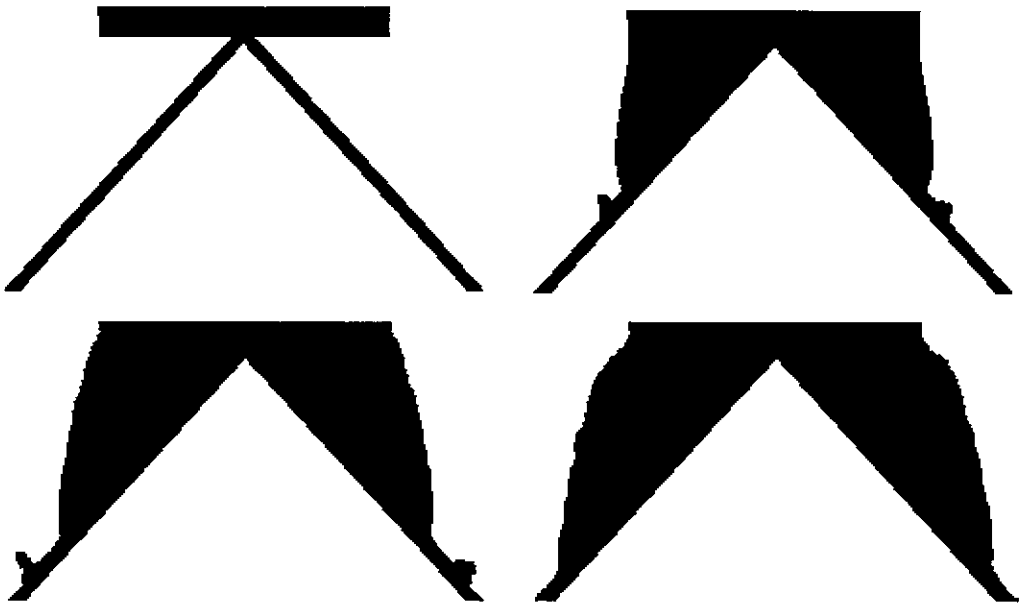

Figure 8. A problem comprising 0.5 million circular discs

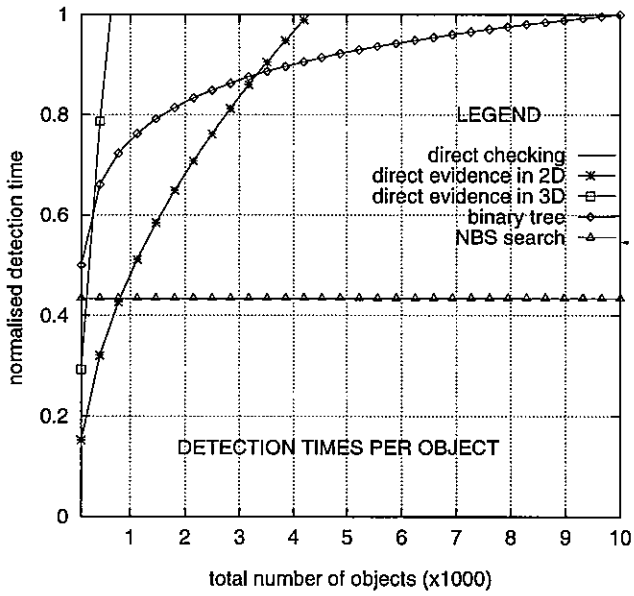

Figure 9. Comparison of contact detection algorithms
(total detection time per element)

In fact memory requirements of the algorithm are insignificant and do not change significantly with considerable change in packing density. On the other hand, the relationship between the total detection time and the total number of discrete elements comprising the problem is linear, the result confirmed by both theoretical investigations and numerical experiments. The total detection time for the algorithm does not depend on packing density. In this context, the NBS contact detection algorithm has better performance than binary search based algorithms as shown in Figure 9, where the theoretical total detection time T divided by the total number of discrete elements N, i.e. the detection time per discrete

element $t = T/N$, for different classes of algorithms is shown. The advantage of the NBS contact detection algorithm with t being constant in respect to the size of the problem, is self evident.

3. CONCLUSION

Some recent developments centered on the algorithmic aspects of the combined finite/discrete element method are summarised in this paper. Although the current developments include a wide range of problems, basic features of novel algorithms concerning contact only are summarised in this paper.

These include a novel (NBS) contact detection algorithm for discrete systems of bodies of general packing. The performance of the algorithm in terms of both memory and CPU time is superior to binary based searches.

In addition a discretised interaction algorithm for bodies of general shape and size comprising exact preservation of energy balance irrespective of the size of penetration is illustrated through numerical examples shown.

Both algorithms greatly contribute to the general improvement of the existing combined finite-discrete element code.

REFERENCES

1. P.A.Cundall, 'A computer model for simulating progressive large-scale movements in blocky rock systems', *Proc. Int. Symp. on Rock Fracture*, Nancy, France, II-8, (1971)
2. J.R.Williams, 'Contact analysis of large numbers of interacting bodies using discrete modal methods for simulating material failure on the microscopic scale' *Eng.Comput.*, 5, 198-209, (1988)
3. M.Oldenberg, L.Nilsson, 'A position code algorithm for contact searching', *Int. j. numer. methods. eng.*, 37, 359-386 (1994)
4. S.Gen-Hua,R.E.Goodman, 'Discontinuous deformation analysis - a new method for computing stress, strain and sliding of block systems' *Key Questions in Mechanics*, Balkema, Rotterdam, 381-393, (1988).
5. A.Munjiza,D.R.J.Owen,N.Bićanić, 'A Combined finite-discrete element method in transient dynamics of fracturing solids', *Int. J. Engineering Computations*, 12, 145-174, (1995)

Size effect analysis of plain concrete beams by using RBSM

H. Kitoh[1], N. Takeuchi[2], M. Ueda[3], H. Higuchi[4], A. Kambayashi[3] and M. Tomida[5]

1) Osaka City University, Osaka 558, Japan, 2) Meisei University, Tokyo 191, Japan
3) Takenaka Co., Chiba 270-13, Japan, 4) Abe-Kogyo Co., Gifu 500, Japan
5) Ishikawa National College of Tech., Ishikawa 929-03, Japan

ABSTRACT : Based on the experimental evidence of solids under the ultimate state of loading, KAWAI proposed a family of new discrete models (Rigid Bodies-Spring Models : RBSM) in 1977. These models consist of rigid bodies and two types of connecting springs, one of which resists dilatational deformation, while the other resists shear deformation. Therefore, RBSM can easily express cracking and slippage to give an indication of a failure of concrete structures. However, RBSM had one drawback : that was, the mesh division used affects the collapse pattern obtained. Therefore, the authors applied Voronoi elements for analysis using RBSM. In this paper, the collapse analyses of plain concrete beams under bending, using RBSM with Voronoi tessellation to an universal mesh division, are presented. The applicability of the method to the size effect analysis of concrete structures is also discussed.

1. INTRODUCTION

RBSM is a numerical analysis method developed as a limit analysis of structures, in which the total structure is idealized as an assemblage of rigid body elements connected by two kinds of distributed springs[1]. This idealization can lead the comprehensive expression of discontinuous phenomenon due to cracking and slippage that significantly affects a failure of concrete structures[2][3]. However, the RBSM solution on failure modes tends to be controlled by its element division, because the strain energy is evaluated along its element boundaries. When the essential failure cannot be included in the mesh division, then the over-estimated solution on collapse loads is obtained[4]. Further, the method requires skill because cracking patterns depend upon the uncertainty in the distribution of the material strength.

Voronoi tessellation was introduced into the element division of RBSM to numerically examine the constitutive relation of materials by TOI et al.[5] The tessellation is directly adopted as element of RBSM that can accept arbitrary polygonal elements. However, it was difficult to make the mesh division of the polygons manually, because they are formed to equalize every territory of their reference points[6]. Thus, the authors developed a computer aided system to automatically form the tessellation, using computer-generated, pseudo-random numbers as their reference points[7].

In this study, the geometry of Voronoi element division by the developed system is examined, and the applicability of RBSM with the Voronoi elements to the discrete limit analysis of plain concrete beams is also discussed including the size effect on strength of the beams. The beams to be analyzed are subjected to pure bending, in which the distribution of the material strength affects the initiation and the propagation of cracking.

2. BRIEF DESCRIPTION OF A TWO DIMENSIONAL RBSM

For brief introduction of a two dimensional RBSM, we considered two rigid triangular elements as shown in *Figure* 1. Of course, an arbitrary polygon or circle can be used instead of a triangular element. They are assumed to be in equilibrium with external loads and reaction forces of the spring system which are distributed over the contact surface of two adjacent bodies.

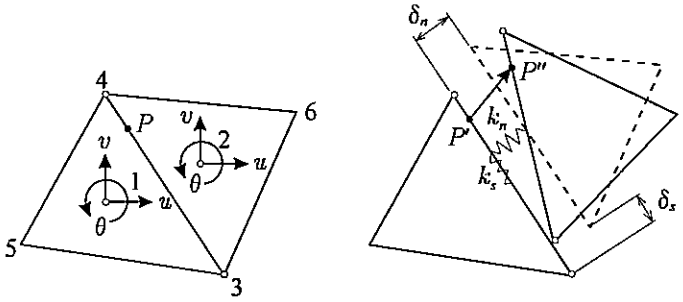

Figure 1. Two dimensional rigid triangular elements

The rigid displacement field is assumed in each element in terms of the displacement (u,v,θ) of the centroid as shown in *Figure* 1. More precisely horizontal and vertical displacements U, V at the arbitrary point P can be given by the following equations :

$$U = Q \cdot u \tag{1}$$

$$U = \lfloor U_{\mathrm{I}}, V_{\mathrm{I}}; U_{\mathrm{II}}, V_{\mathrm{II}} \rfloor^T \qquad u_i = \lfloor u_1, v_1, \theta_1; u_2, v_2, \theta_2 \rfloor^T \qquad Q = \left(\begin{array}{cc:c:cc:c} 1 & 0 & -(y-y_1) & 0 & 0 & 0 \\ 0 & 1 & (x-x_1) & 0 & 0 & 0 \\ \hdashline 0 & 0 & 0 & 1 & 0 & -(y-y_2) \\ 0 & 0 & 0 & 0 & 1 & (x-x_2) \end{array}\right)$$

where subscript I, II or 1, 2 indicate element number 1 or 2, respectively. (x_1, y_1) and (x_2, y_2) are the coordinate values of the centroid for each element.

The relation of the displacement between the global coordinate system and the local coordinate system along the side $\overline{34}$ of the triangular element is derived by the following matrix equation :

$$\overline{U} = R \cdot U \tag{2}$$

$$\overline{U} = \lfloor \overline{U}_{\mathrm{I}}, \overline{V}_{\mathrm{I}}; \overline{U}_{\mathrm{II}}, \overline{V}_{\mathrm{II}} \rfloor^T \qquad R = \left(\begin{array}{cc:cc} l_1 & m_1 & 0 & 0 \\ l_2 & m_2 & 0 & 0 \\ \hdashline 0 & 0 & l_1 & m_1 \\ 0 & 0 & l_2 & m_2 \end{array}\right) \qquad \begin{array}{l} l_1 = \cos(\overline{x}, x) = y_{43}/l_{34} \\ l_2 = \cos(\overline{x}, y) = x_{43}/l_{34} \\ m_1 = \cos(\overline{y}, x) = x_{34}/l_{34} \\ m_2 = \cos(\overline{y}, y) = y_{43}/l_{34} \end{array}$$

where l_{34} is the length of side $\overline{34}$, $x_{ij} = x_i - x_j$, the superscript (-) indicates the local coordinate system and $\boldsymbol{R}$ is a coordinate transformation matrix.

Using these displacements (U,V) with the local coordinate system, the relative displacement vector $\boldsymbol{\delta}$ of the point P can be derived as follows :

$$\boldsymbol{\delta} = M \cdot \overline{U} \tag{3}$$

$$\boldsymbol{\delta} = \lfloor \delta_n, \delta_s \rfloor^T \qquad M = \left(\begin{array}{cc:cc} -1 & 0 & 1 & 0 \\ 0 & -1 & 0 & 1 \end{array}\right)$$

Therefore, substituting eq.(1) and eq.(2) into eq.(3), the following relation with the rigid displacement field is easily obtained :

$$\boldsymbol{\delta} = M \cdot R \cdot Q \cdot u = B \cdot u \qquad (B = M \cdot R \cdot Q) \tag{4}$$

$$B = \left(\begin{array}{c:c:c:c:c:c} -l_1 & -m_1 & l_1(y-y_1) - m_1(x-x_1) & l_1 & m_1 & -l_1(y-y_2) + m_1(x-x_2) \\ \hdashline -l_2 & -m_2 & l_2(y-y_1) - m_2(x-x_1) & l_2 & m_2 & -l_2(y-y_2) + m_2(x-x_2) \end{array}\right)$$

The spring constants k_n and k_s which resist normal and tangential forces respectively on the

contact surface between element I and element II can be determined systematically by using the finite difference equation for strain components as follows :

$$\boldsymbol{\varepsilon}=\begin{pmatrix}\varepsilon_n\\ \gamma_s\end{pmatrix}=\frac{1}{h_1+h_2}\begin{pmatrix}\delta_n\\ \delta_s\end{pmatrix}=\frac{1}{h}\boldsymbol{\delta} \qquad (5)$$

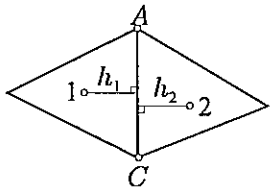

Figure 2. Definition of the projected length

where $h = h_1+h_2$ is the projected length of a vector connecting centroids along the line perpendicular to AC, as shown in *Figure* 2.

On the contact surface $\overline{AC}$ shown in *Figure* 2, the normal and tangential stresses σ_n, τ_s are assumed to satisfy the following equations :

$$\sigma_n=\frac{(1-\nu)E}{(1-2\nu)(1+\nu)}\varepsilon_n \quad , \quad \tau_s=\frac{E}{(1+\nu)}\gamma_s \qquad (6)$$

Substituting eq.(5) into eq.(6), the following relation can be obtained :

$$\left.\begin{aligned}\sigma_n&=\frac{(1-\nu)E}{(1-2\nu)(1+\nu)}\cdot\frac{\delta_n}{h_1+h_2}\\ \tau_s&=\frac{E}{(1+\nu)}\cdot\frac{\delta_s}{h_1+h_2}\end{aligned}\right\} \qquad (7)$$

On the other hand, from the definition of the spring constants, the following relations are obtained :

$$\sigma_n=k_n\cdot\delta_n \quad , \quad \tau_s=k_s\cdot\delta_s \qquad (8)$$

Therefore, comparing equations (7) and (8), expressions for k_n and k_s can be derived as follows:

$$\left.\begin{aligned}k_n&=\frac{(1-\nu)E}{(1-2\nu)(1+\nu)(h_1+h_2)}\\ k_s&=\frac{E}{(1+\nu)(h_1+h_2)}\end{aligned}\right\} \qquad (9)$$

From eq. (9) the stress-relative displacement relation is derived by the following matrix equation :

$$\boldsymbol{\sigma}=\boldsymbol{D}\cdot\boldsymbol{\delta} \qquad (10)$$

$$\boldsymbol{\sigma}=\lfloor\sigma_n,\tau_s\rfloor^T \qquad \boldsymbol{D}=\begin{pmatrix}k_n & 0\\ 0 & k_s\end{pmatrix}$$

$$\boldsymbol{\delta}=\lfloor\delta_n,\delta_s\rfloor^T$$

Based on the above preliminaries, the strain energy expression of the in-plane element V can be obtained as the following matrix equation :

$$V=\frac{1}{2}\int_{l_{34}}\boldsymbol{\delta}^T\cdot\boldsymbol{D}\cdot\boldsymbol{\delta}\,\mathrm{ds}=\frac{1}{2}\boldsymbol{u}^T\int_{l_{34}}\left(\boldsymbol{B}^T\cdot\boldsymbol{D}\cdot\boldsymbol{B}\right)\mathrm{ds}\cdot\boldsymbol{u} \qquad (11)$$

Applying Castigliano's theorem to eq.(11) the following stiffness equation can be derived :

$$\frac{\partial V}{\partial \boldsymbol{u}}=\boldsymbol{K}\cdot\boldsymbol{u}=\boldsymbol{P} \qquad (12)$$

where K is a (6×6) symmetric matrix and P is a nodal load vector defined by the following equation :

$$P = \lfloor X_1, Y_1, M_1; X_2, Y_2, M_2 \rfloor^T \tag{13}$$

3 . GENERATION OF VORONOI TESSELLATION

Voronoi tessellation can be formed by connecting the circumcentres of the Delaunay triangle network as shown in *Figure* 3, in which the reference points are used as the apexes of the triangle. The geometry of the polygons is consistent with RBSM formulation, in which strain is evaluated by a finite different scheme with the interval of the length between the centroids of the neighbor elements, because the lines between the centroids of the neighbor polygons cross their boundary lines perpendicularly.

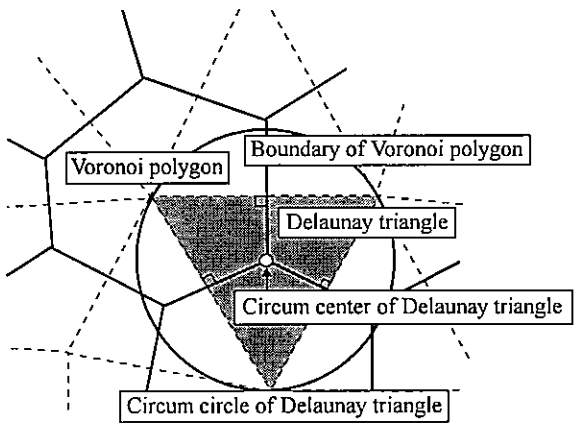

Figure 3. Voronoi tessellations and Delaunay triangles

Figure 4 shows an example of the polygons formed with 1000 reference points of random numbers according to the linear congruence method[8], in which small polygons due to the characteristics of pseudo-random numbers can be seen.

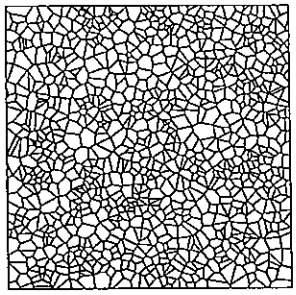

Figure 4. Example of mesh division

The evaluation on element size is required for nonlinear analysis of concrete structures where the close relationship between crack opening width and fracture energy has been recognized. Therefore, the frequency of the element area was examined as an index of element size.

In *Figure* 5, the horizontal axis indicates the ratio of an element area A to a mean element area in the percentage of the frequencies. This figure is an example for 1000 reference points of random numbers and their similar tendencies. It shows that the maximum frequency occurred at less than 1 of A/A_{mean}, when the number of the points increased. *Figure* 6 shows the distribution of the apexes of an element and it can be shown that the major shape was a hexagon, which is generally regarded as stable in nature.

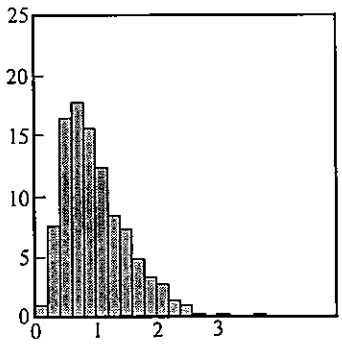

Figure 5. Frequency distribution of element area

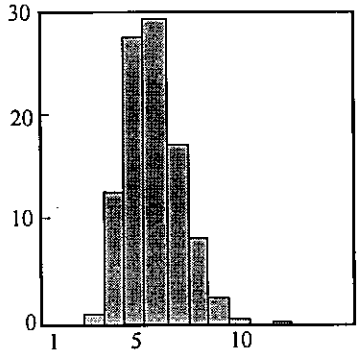

Figure 6. Frequency distribution of number of apexes

Figure 7 shows the distribution of the lengths and the directions of the element boundaries in *Figure* 5 in the polar coordinate system, which is an example of when the initial values of the generation were set at 17 and 31.

Figure 8 shows another example of when they were set 1 and 4. *Figure* 7 shows a uniform distribution, while in *Figure* 8, obvious orientation to 135 degrees can be found. Thus, attention should be paid to such orientation due to pseudo random numbers.

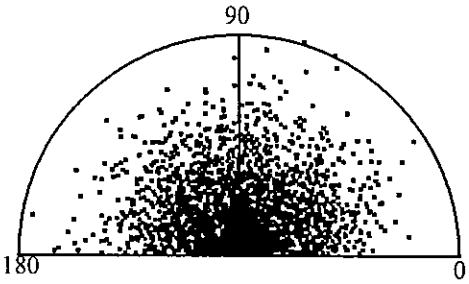

Figure 7. Distribution of the lengths and the directions of the element boundary (non-directional)

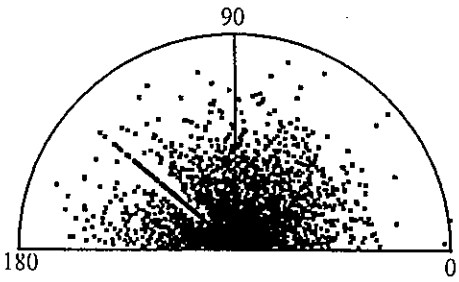

Figure 8. Distribution of the lengths and the directions of the element boundary (directional)

4. CONSTITUTIVE LAW OF CONCRETE

The broken line on *Figure* 9 shows the uniaxial stress-strain curve of the concrete. In the numerical calculations, this curved line is approximated according to the trilinear solid line. In this paper, F_c being the compressive strength, the first yield level $F_{c1} = 0.5F_c$, the second yield level $F_{c2} = 0.95F_c$, and the reduction ratio of the stiffness $\beta = 0.5$. After the second yielding at $\varepsilon_{cu}(0.3\%)$, F_{c2} is maintained until collapse. Beyond this point, until reaching $2\varepsilon_{cu}$, the stress decreases with a corresponding increase in the strain, and it stays finally at $0.2F_c$. The tension-softening effect is thereby taken into consideration. The tensile stress is released going along the cubic equation of strain. However, in this study, the linear function connecting with (F_t, ε_{cr}) and $(0,n\varepsilon_{cr})$, is introduced and n = 40, 20 or 10 are used, considering size effect.

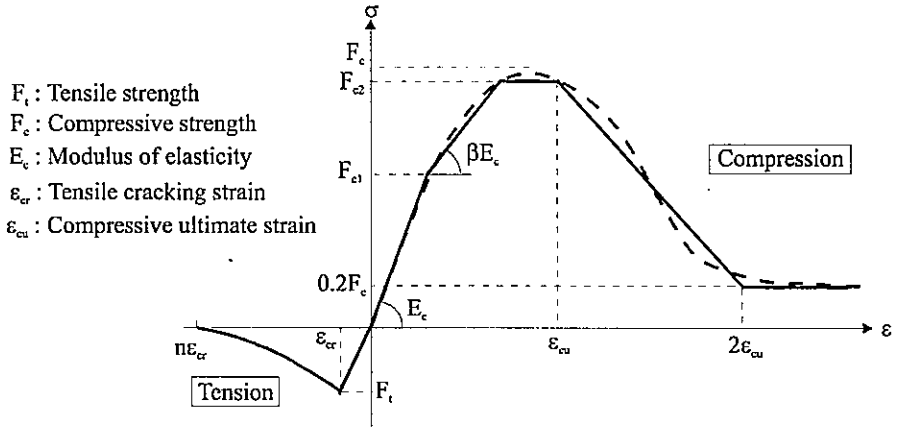

Figure 9. Stress-strain relationship for concrete

The shearing slippage surface is defined by Mohr-Coulomb's criterion, and after yielding, the associated flow rule is employed, and moves on the surface. Based on the supposition above, *Figure* 10 shows the yield and collapse surface of concrete using RBSM. The state 0 shows elasticity, the surface 1 is cracking, the state 2 is the condition where the residual stresses become zero, in *Figure* 9, that is a state of tension on the left side from $n\varepsilon_{cr}$. The state 3 shows first yield, the surface 4 shows

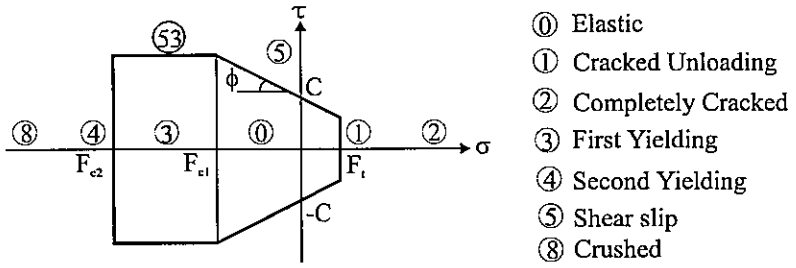

Figure 10. Yield and collapse surface for concrete

second yield, and the state 8 is the normal strain having the condition reached at the strain limit ε_{cu} of *Figure* 9. The surface 5 shows shear slipping. After this state, in the case where first yield compression of the state 3 has occurred, the state follows the stage in the surface 53.

5. NONLINEAR ANALYSIS ALGORITHM

In concrete structures, shapes change as cracking develops, and then stress is released on the cracking surface. The released stress or load leads to a decline of convergence of solutions near and at the ultimate stage of loading. To overcome this condition, we proposed an algorithm for material nonlinear analysis [3][10], in which r_{min} method[9] was modified to add the released force to the remaining load while counting the applied load, and to simultaneously take account of the slip, cracking and compressive failure.

However, the algorithm is to be originally applied to an incremental load method. This method is inadequate to simulate the crack propagation in detail, because the failure of plain concrete beams under bending is brittle. The algorithm can also be applied to an incremental displacement method if the incremental displacement is taken as external force. Thus, the following nonlinear analysis was carried out according to an incremental displacement method.

6. ANALYSIS OF PLAIN CONCRETE BEAMS

Using RBSM with Voronoi elements, the analyses of the plain concrete beams as shown in *Figure* 11 were carried out to examine the size effect. Three beams with different heights were analyzed. Specimen No.1, No.2 and No.3 had 5cm, 10cm and 20cm heights respectively. Further, two cases of element divisions were used. One had almost the same elemental area for each specimen, and the other had the same number of elements.

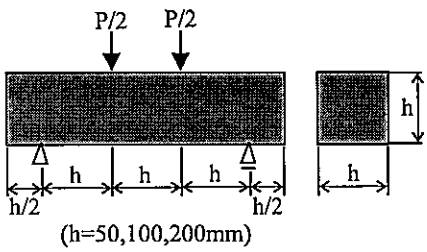

Figure 11. Analyzing model of plain concrete beam

6.1 Numerical example with same areas of Voronoi elements

The element divisions for all specimens were made to have almost the same average areas, about $1cm^2$, and number of elements were about 200, 800 and 3200 respectively, for No.1, No.2 and No.3. Moreover, another element division for all specimens were also prepared with the different initial values of the random number for element generation. *Figure* 12 is an example of element divisions.

Table 1 shows the material constants used. Those values and the critical tensile strain of 20 ε_{cr} in strain softening curve evaluated by

Table 1. Material property constants of concrete

Compressive strength	(F_c)	34.3 MPa
Tensile strength	(F_t)	2.9 MPa
Cohesive strength	(C)	4.7 MPa
Angle of friction	(f)	37.0 deg.
Modulus of elasticity	(E_c)	27.5 GPa
Poison's ratio	(n)	0.2

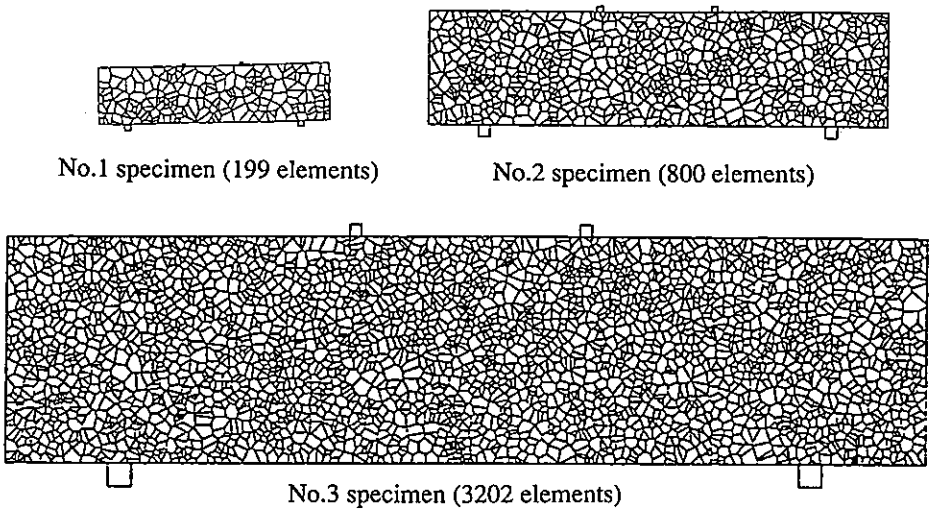

Figure 12. Voronoi elements of a plain concrete beam (same average area)

fracture energy were commonly used for all specimens.

An example of crack propagation is shown in *Figure* 13, in which several initial cracks were observed in and around pure bending regions, and then they grew gradually, and consequently, a

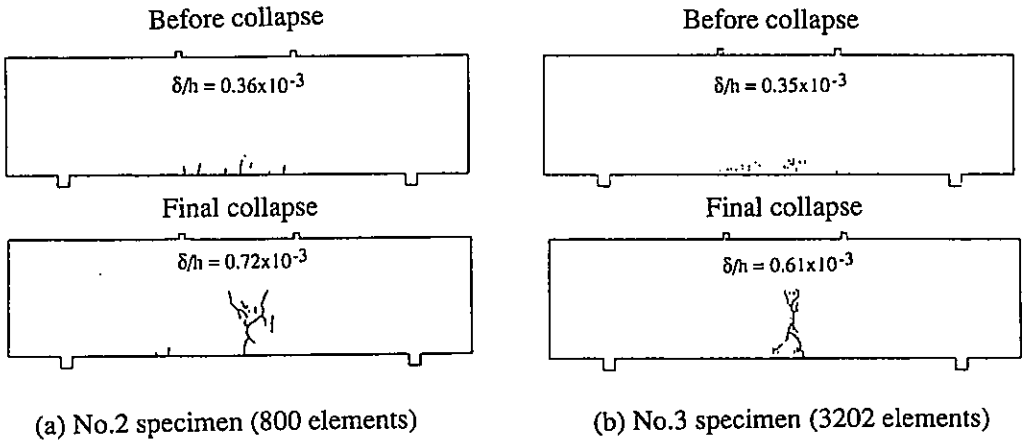

Figure 13. Crack patterns of plain concrete beam (same average area)

major crack in tension was formed which caused the structural collapse.

The load carrying capacities and the relations between applied load and displacement are shown in Table 2 and *Figure* 14, respectively.

In these examples where an identical strain softening curve was used, the solutions of these specimens with different heights, both on the crack propagation and the normalized strength, were somewhat different. When the specimen size was longer, the $P/(h^2Ft)$ value decreased as shown in *Figure* 17. This shows the size effect.

Table 2. Maximum load (with the same area)

Specimen	Number of elements	Max. Load (kN)	$P/(h^2F_t)$
No.1	199	3.74	0.50
	200	4.19	0.56
No.2	800	13.8	0.48
	798	14.1	0.49
No.3	3202	51.6	0.45
	3198	49.3	0.42

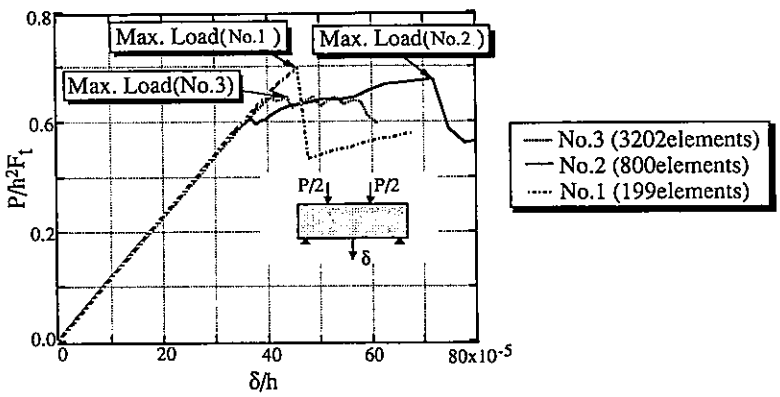

Figure 14. Load-Displacement relation (same element area)

6.2 Numerical example with the same number of Voronoi elements

To analyze the specimens with the same number of elements, the element division for No.2 was made as shown in *Figure* 15. In the case of No.3 specimen, the critical tensile strain in the strain-softening curve was set at $10\varepsilon_{cr}$, and in case of No.1 it was set at $40\varepsilon_{cr}$. Other constants were the same as Table 1.

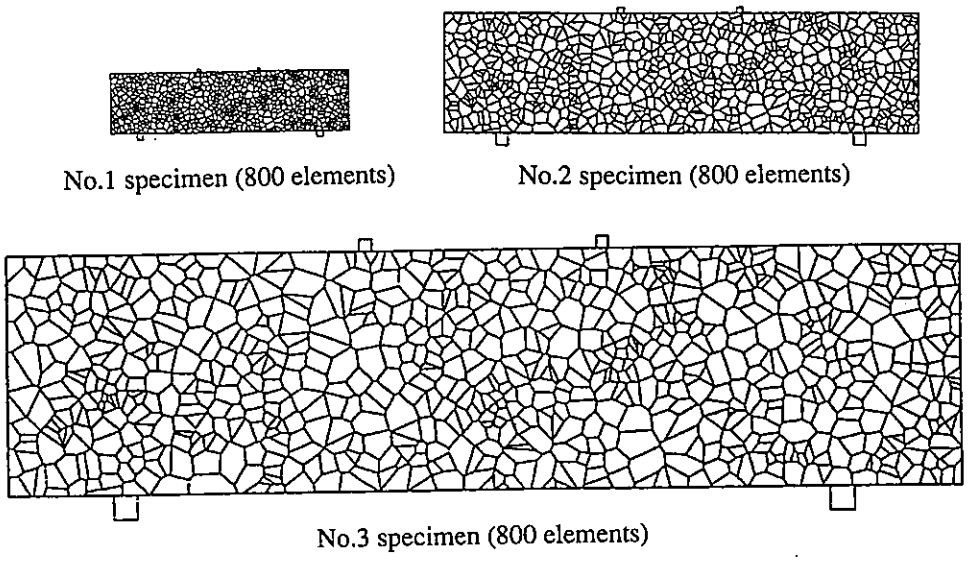

Figure 15. Voronoi elements of plain concrete beam (same number of elements)

Figure 16 shows the crack propagation for specimen No.2, and the load carrying capacities are also listed in Table 3. The differences on the former between two specimens was slight, while that of the latter was enough to show the size effect, which was probably caused by that of the strain-softening curve in tension.

The numerical results obtained in this section are plotted in *Figure* 17, in which the vertical and the horizontal axis are bending strength and beam height, respectively, and

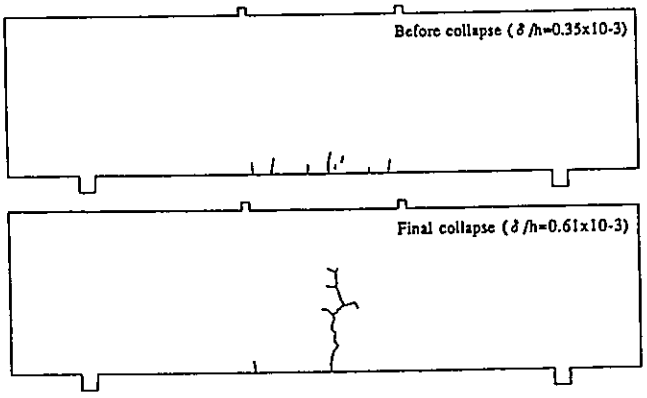

Figure 16. Crack patterns of plain concrete beams (the same number of element)

Table 3. Maximum load (with same number of elements)

Number of elements	Specimen	Max. Load (kN)	$P/(h^2F_t)$
800	No.1	4.3	0.57
	No.2	13.8	0.48
	No.3	44.7	0.39
798	No.1	4.4	0.58
	No.2	14.1	0.49
	No.3	43.3	0.37

the lines also show the experimental results. This figure shows that the degradation of the strength for a higher specimen due to size effect was observed numerically.

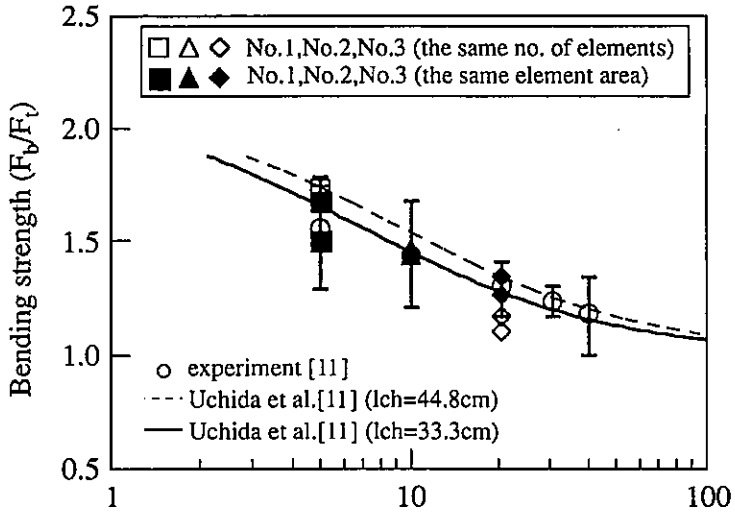

Figure 17. The height of beam-bending strength relationship

7. CONCLUSIONS

The collapse analysis of plain concrete beams has been carried out by using RBSM with an automatic mesh generating system of Voronoi polygons. The conclusions obtained are as follows:

1) The validity of RBSM with Voronoi elements has been verified for the nonlinear analysis of concrete structures up to failure including discontinuous phenomenon due to cracking, even if the failure mode could not be presumed.
2) The size effect of concrete structures could be considered when the strain-softening curve under tension was defined by fracture energy.

The size effect has been generally recognized to be caused by the reasons that follow:

1) Concrete is not homogenous and there is a probability of how the strength and the defect will be distributed.
2) Shrinkage varies with the size of the concrete member.

It should be required to examine concrete from a microscopic viewpoint, to see if the size effect can be observed numerically when the defect and the strength are distributed according to a probability along the boundaries of Voronoi elements.

REFERENCES

[1]Kawai,T. : New element models in discrete structural analysis, J. of the Society of Naval Architects of Japan, No.141,pp187-193,1977

[2]Kawai,T. et al. : Discrete limit analysis of reinforced concrete structures (1-3), SEISAN-KENKYU, Monthly J. of Institute of Industrial Science, Univ. of Tokyo, Vol.38,No.4-6,1986(in Japanese)

[3]Kawai,T. et al. : Application of a discrete limit analysis to reinforced concrete shear panels, Proc. 2nd World Congress on Computational Mechanics, August 27-31,1990,Stuttgart,FRG,pp862-865.1990

[4]Takeuchi,N. and Kawai,T. : On the error evaluation of the solutions obtained by the new discrete limit analysis,Proc. of 15th Symposium on Matrix method, pp77-82,1981(in Japanese)

[5]Toi.Y. et al. : Mesoscopic simulation of microcracking behaviors of brittle polycrystalline materials,SEISAN-KENKYU, Monthly J. of Institute of Industrial Science, Univ. of Tokyo, Vol.42,No.7,pp444-447,1990(in Japanese)

[6]Iri,M.(Supervision) : Computational geometry and geographical information process, Kyoritsu Pub.,1993(in Japanese)

[7]Takeuchi,N et al. : On the automatic mesh generation for RBSM by using Voronoi tessellation, Proc. of the JSCE 48th annual meeting, Part I,pp1430-1431,1993(in Japanese)

[8]Fushimi,M. : Random numbers, Univ. of Tokyo Press, Tokyo, 1989(in Japanese)

[9]Yamada, Y. et al. : Plastic stress-strain matrix and its application for the solution of elasto-plastic problems by a finite element method, Int. J. of Mechnical Science, Vol.10,pp343-354,1968

[10]Takeuchi,N. and Kawai,T. : A discrete limit analysis of granular materials including effects of the solid contact, US-Japan seminar, MICROMECHANICS OF GRANULAR MATERIAL, October 26-30, SENDAI, ZAO, pp116-125(1987)

[11]Uchida,Y et al. : Application of fracture mechanics to size effect on flexural strength of concrete, Proc. of JSCE,No.442,pp101-107,1992(in Japanese)

Development of discrete limit analysis and its application to the solid mechanics

N.TAKEUCHI[1)] and T.KAWAI[2)]

1) Meisei University, Tokyo 191 JAPAN
2) Science University of Tokyo, Tokyo 162 JAPAN

ABSTRACT : In order to break through bottleneck of finite element nonlinear analysis in solid mechanics, Prof. Kawai proposed a family of new simplified element basing on the experimental evidence of solids under the ultimate state of loading in 1977[1]. Since then a series of verification studies have been made in steel structures successfully.

However in case of foundation structures as well as concrete structures, influence of crack initiation due to tensile loading often can not be neglected. In view of this, TAKEUCHI developed a new algorithm of inelastic analysis in 1987[2]. It is applicable to analyze the coupled failure of solids due to slippage and tensile cracking.

In this paper, the theoretical basis of this algorithm is described first, and then applicability of the discrete limit analysis for the solid mechanics are also discussed.

1. Brief description of RBSM

For brief introduction of a three dimensional RBSM, we considered two rigid bodies as shown in *Figure* 1. Of course, an arbitrary polyhedron or polygon can be used. They are assumed to be in equilibrium with external loads and reaction forces of the spring system which are distributed over the contact surface of two adjacent bodies.

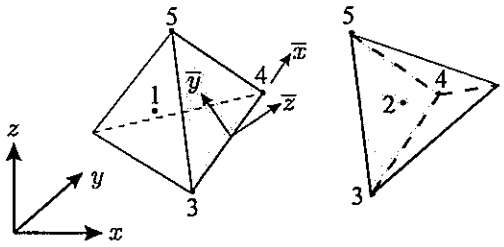

Figure 1. Three dimensional rigid element

The rigid displacement field is assumed in each element in terms of the displacement u_i of the centroid. More precisely displacements U_i at the arbitrary point P can be given by the following equations :

$$U_i = Q_i \cdot u_i \tag{1}$$

$$U_i = (U_i\, V_i\, W_i)^t\,,\ \ u_i = (u_i\, v_i\, w_i\, \theta_i\, \phi_i\, \chi_i)^t\,,\ \ Q_i = \begin{bmatrix} 1 & 0 & 0 & 0 & (z-z_i) & -(y-y_i) \\ 0 & 1 & 0 & -(z-z_i) & 0 & (x-x_i) \\ 0 & 0 & 1 & (y-y_i) & -(x-x_i) & 0 \end{bmatrix}$$

where subscript i indicate element number.$(x_i\, y_i\, z_i)$ are the coordinate values of the centroid for each element.

The relation of the displacement between the global coordinate system and the local coordinate system along the contact surface is derived by the following matrix equation :

$$\bar{U}_i = R \cdot U_i \tag{2}$$

$$\bar{U}_i = (\bar{U}_i\, \bar{V}_i\, \bar{W}_i)^t\,,\ \ R = \begin{bmatrix} l_1 & m_1 & n_1 \\ l_2 & m_2 & n_2 \\ l_3 & m_3 & n_3 \end{bmatrix}$$

where the superscript (-) indicates the local coordinate system and R is a coordinate transformation matrix.

Using this displacement $\bar{U}$ with the local coordinate system, the relative displacement vector δ of

the point P can be derived as follows :

$$\delta = \sum_{i=1}^{2} M_i \cdot \bar{U}_i \tag{3}$$

$$\delta = (\delta_{s\bar{x}}\, \delta_{s\bar{y}}\, \delta_n)^t\,,\ M_1 = \begin{bmatrix} -1 & 0 & 0 \\ 0 & -1 & 0 \\ 0 & 0 & -1 \end{bmatrix},\ M_2 = \begin{bmatrix} 1 & 0 & 0 \\ 0 & 1 & 0 \\ 0 & 0 & 1 \end{bmatrix}$$

Therefore, substituting eq.(1) and eq.(2) into eq.(3), the following relation with the rigid displacement field is easily obtained :

$$\delta = \sum_{i=1}^{2} M_i \cdot R \cdot Q_i \cdot u_i = \sum_{i=1}^{2} B_i \cdot u_i \qquad (B_i = M_i \cdot R \cdot Q_i) \tag{4}$$

The stress-relative displacement relation is assumed by the following matrix equation :

$$\sigma = D \cdot \delta \tag{5}$$

$$\sigma = (\tau_{s\bar{x}}\, \tau_{s\bar{y}}\, \sigma_n)^t\,,\ D = \begin{bmatrix} k_{s\bar{x}} & 0 & 0 \\ 0 & k_{s\bar{y}} & 0 \\ 0 & 0 & k_n \end{bmatrix},\ k_n = \frac{(1-\nu)E}{(1+\nu)(1-2\nu)h},\ k_{s\bar{x}} = k_{s\bar{y}} = \frac{E}{(1+\nu)h}$$

where k_n and $k_{s\bar{x}}$, $k_{s\bar{y}}$ are the spring constants which resist normal and tangential forces respectively on the contact surface between element 1 and element 2. $(h = h_1 + h_2)$ is the projected length of a vector connecting centroids along the contact surface.

On the other hand, strain components are determined by using the finite difference equation as follows :

$$\varepsilon = \frac{1}{h}\delta \tag{6}$$

Based on the above preliminaries, the strain energy expression of the in-plane element V can be obtained as the following matrix equation :

$$V = \frac{1}{2}\int_A (\delta^t \cdot \delta)\, dA = \frac{1}{2} u \int_A B^t D B dA u \tag{7}$$

Applying Castigliano's theorem to eq.(7) the following stiffness equation can be derived :

$$\frac{\partial V}{\partial \sigma} = K \cdot u = P \tag{8}$$

where K is a (6×6) symmetric matrix and P is a nodal load vector

2. Constitutive law for the discrete limit analysis

In the RBSM, the authors considered that reaction stresses are not tensor but vector, and consequently Coulomb's condition may be the most realistic constitutive law for such a discrete system representing granular materials. As is well known, Coulomb's condition can be represented by two straight lines which relate the normal stress σ_n and the shearing stress τ_s . The yield condition of soil-like materials can be modified as shown in *Figure* 2.

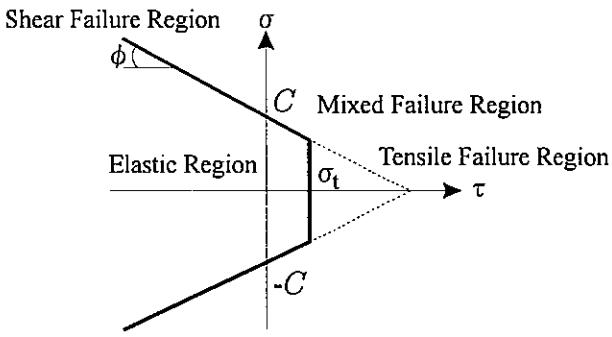

Figure 2. Modified Coulomb's condition where the tensile failure is considered

If σ_n reaches σ_t, σ cannot become greater than this value and therefore the relation

between normal stress and strain can be shown as in *Figure 3(a)*. This is the state of tensile yielding. In the case of granular materials like soils, it is commonly observed that s is relieved as soon as it reaches σ_t as shown in *Figure 3(b)*. In this paper a new algorithm is proposed by assuming the spring characteristic as shown in *Figure 3(b)* under tensile failure.

On the other hand, for determination of spring constants in shear failure, the ordinary plastic flow rule is adopted. It is assumed that plastic yielding will occur if stresses in these spring systems satisfy the following condition :

$$f(\sigma) = 0 \tag{9}$$

where $f(\sigma)$ is the yield function in the flow theory of plasticity.

Based on the associated flow rule in which yield function f is equal to plastic potential Q, the relation between stress increments $\Delta\boldsymbol{\sigma}$ and strain increment $\Delta\boldsymbol{\varepsilon}$ can be finally obtained in the following form :

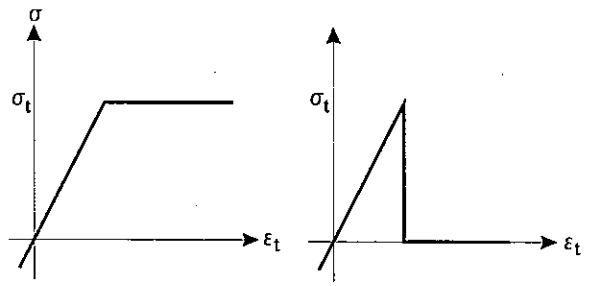

(a)tensile yielding (b)tensile fracture

Figure 3. Modified Coulomb's condition where the tensile failure is considered

$$\Delta\sigma = \left[k^{(e)} - \frac{k^{(e)}\frac{\partial f}{\partial \sigma}\Delta\varepsilon}{\frac{\partial f}{\partial \sigma}k^{(e)}\frac{\partial f}{\partial \sigma}}\right]\Delta\varepsilon \tag{10}$$

where D is the spring matrix and superscript (e) indicates the status of elasticity. Therefore, the plastic spring matrix can be obtained as follows :

$$k_{ij}^{(p)} = k_i^{(e)}\delta_{ij} - \frac{1}{\sum k_i^{(e)}\bar{f}_i^2}\bar{f}_i\bar{f}_j k_i^{(e)}k_j^{(e)} \qquad \left(f_i = \frac{\partial f}{\partial \sigma_i}\right) \tag{11}$$

where $k_{ij}^{(e)}$ is the elastic spring constant and $k_i^{(e)}$ is the diagonal term of the spring matrix.

3. A proposed algorithm for nonlinear analysis

A new algorithm is proposed by applying the incremental load procedure developed by Yamada et al[3] for the nonlinear problem of soil foundations whose failure condition is described in the preceding section. In this method (Rmin method), the rate of load increment to yield the most heavily stressed element can be calculated by stress distribution and load increment at the present stage as shown in *Figure 4*.

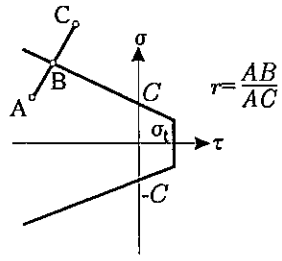

Figure 4. Rate of load increment in the case of shear failure

In this figure, point A represents the stress condition at the previous step, while point C signifies the stress state at the present step. However, the stress equilibrium actually cannot be maintained at the point C and the load increment should be stopped at point B on the failure curve. In this condition the required rate of load increment r can be calculated. Once the stress point lies on the failure curve, it may move according to the plastic flow rule until the unloading occurs.

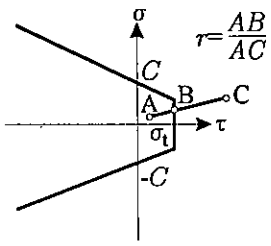

Figure 5. Rate of load increment in the case of tensile failure

A similar calculation must be made for tensile failure as shown in *Figure 5*. Point B represents the tensile strength in this figure. When the stresses exceed the tensile strength, the stresses should be reduced to the level corresponding to point B using this rate of stress increment. And then stress (σ_t) must be relieved in that element as shown in *Figure* 3(b). Following this operation, both normal and shear springs should be cut to prevent the stress transfer through a common boundary until recontact of

these elements occurs.

All of the possible rate of load increments corresponding to the failure patterns should be calculated in all of the elements, and the minimum rate of load increment must be determined at each step.

The stress relaxation is usually followed by tensile failure. If the load incremental method is applied to the stress relaxation process exactly, endless calculation should be repeated corresponding to the tensile failure which may occur continuously. Therefore, a supplement of the iterative operation as shown in *Figure* 6 is to be considered at the present loading step.

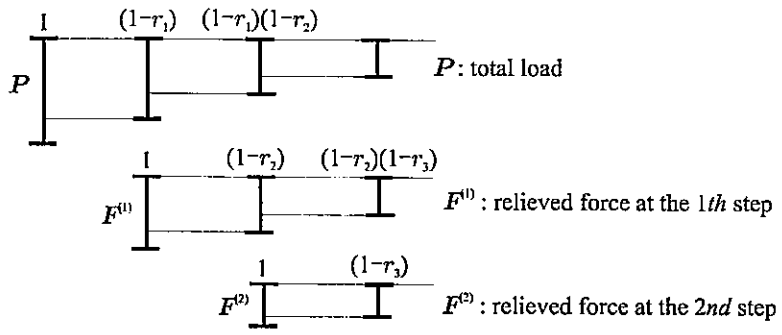

Figure 6. Concept of the rate of load increment

The load $P^{(i+1)}$ at the $(i+1)$th step can be calculated by using the load $P^{(i)}$ and the rate of load increment r_i at the present step (i) as follows :

$$P^{(i+1)} = (1 - r_i)P^{(i)} \tag{12}$$

Therefore, in the case of shear failure, residual load $P^{(n)}$ at the nth step can be obtained by using initial load P as follows :

$$P^{(n)} = \prod_{i=0}^{n-1} [(1 - r_i)]\, P \qquad (r_o = 0) \tag{13}$$

On the other hand, if crack initiation will cause stress relaxation, relieved forces are taken into account in eq.(13) as follows :

$$P^{(n)} = \prod_{i=0}^{n-1} [(1 - r_i)]\, P + \sum_{k=1}^{n} \left(\prod_{i=k}^{n} [(1 - r_i)]\, F^{(k-1)} \right) \tag{14}$$

where $F^{(k)}$ is the relieved force at the kth step.

Here r_{TOTAL} implies the cumulative rate of load increment and it can be defined as follows :

$$r_{TOTAL} = \sum_{k=1}^{n} \left(\prod_{i=0}^{k-1} [(1 - r_i)] \right) r_k \tag{15}$$

The calculation must be repeated until $r_{TOTAL} = 1$ in each stage of loading.

The rate of load increment specified before calculation may change due to stress relaxation caused by crack initiation. Therefore in this case the concept of r_{TOTAL} may not be correct, but the process of progressive failure may be observed. If $r_{TOTAL} = 1$ is realized, however, the iteration must be stopped and the result of calculation may be considered reliable.

4. Application to the solid mechanics

(1) Soil and rock mechanics

As a numerical example, the behavior of an anchor block in the soil foundation subjected to a horizontal force is studied. As shown in *Figure* 7(a) tensile stress may be induced in the rear vertical wall of a given block and a cavity may be produced due to tensile cracking as shown in *Figure* 7(b).

(a) before deformation (b)after deformation

Figure 7. Anchor block subjected to horizontal force

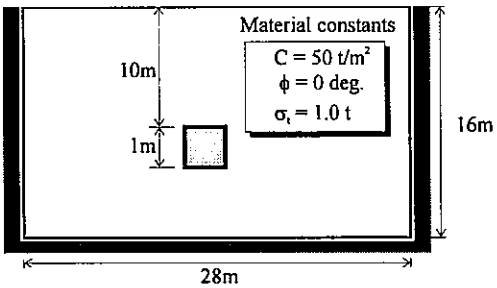

Figure 8. Numerical model

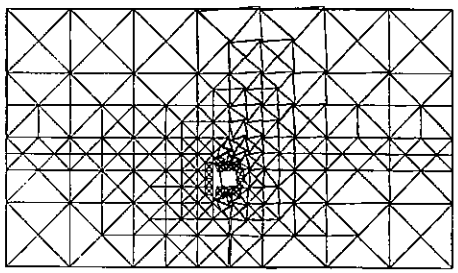

Figure 9. Displacement mode

Figure 8 shows the numerical model. The displacement mode are shown in *Figure 9*. From this figure, separation of the soil on the rear wall of the block and rise of the displacement field near the front wall can be seen. It can be concluded that this new algorithm can present realistic solution.

Finally the load-displacement relationship is given in *Figure 10*. It can be seen from this figure that the displacement corresponding to the latter solution is larger than that of the former, while the load carrying capacity is smaller.

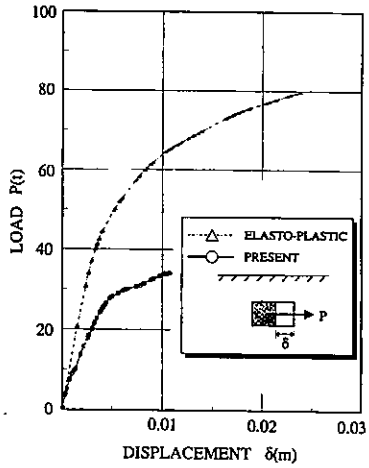

Figure 10. Load-displacement curve

(2) Concrete structure

As the next example, the behavior of an anchor bolt in the concrete block subjected to a pull-out load is studied. *Figure* 11 shows the experimental and numerical model.

Figure 12 show the patterns of tensile crack development. The left hand side is experimental result and the other side is proposed numerical result. From this figure, present method may predict relatively good crack patterns.

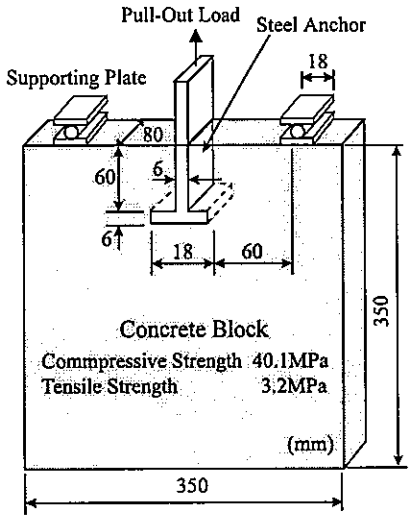

Figure 11. Numerical model

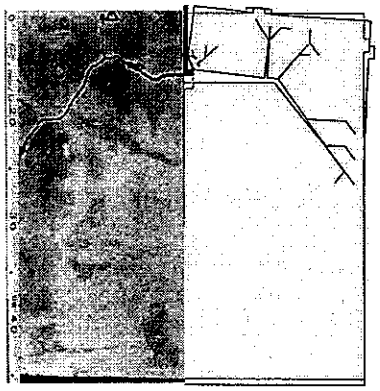

(a)experimental (b) numerical

Figure 12. Failure pattern

(3)Timber beam

As the next example, the behavior of timber beam with a rectangular notch subjected to bending is studied. *Figure* 13 shows the experimental and numerical model. The beams used in this experiment are American pine.

Figure 14 show the experimental result. The experimental results indicated that tensile cracking grew from the corners the notch along woody fiber. *Figure* 15 shows the numerical result. In this case of numerical analysis, a large tensile stress depending on the depth of the notch was computed at the

corner of the notch and the initial cracking load is related to depth of the notch.

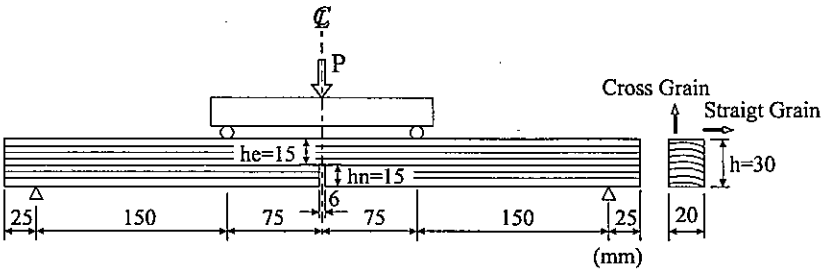

Figure 13. Experimental and numerical model for timber beam

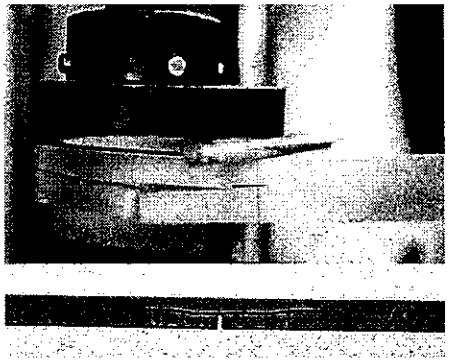

Figure 14. Experimental result

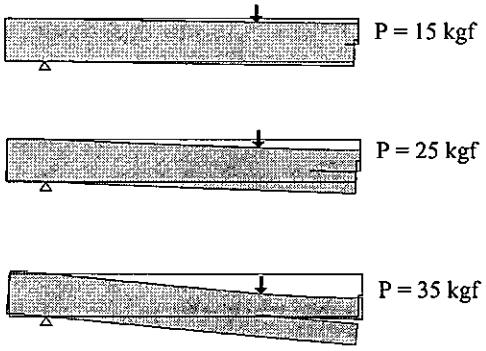

Figure 15. Numerical result

(4) Temporomandibular joint

As the last example, the behavior of the temporomandibular joint including effects of the masticatory muscle is studied[4]. The chewing motion is performed by the muscles of mastication which function with proper balance. *Figure* 16 show the muscles of mastication. The occlusion force generated by this motion greatly affect the load exerted on temporomandibular joint. As upward force is considered to be exerted on the entire mandible when the occlusion force reachs the maximum, a muscular force which hold suspend up the mandible is used as an external force in this research (*Figure* 17).

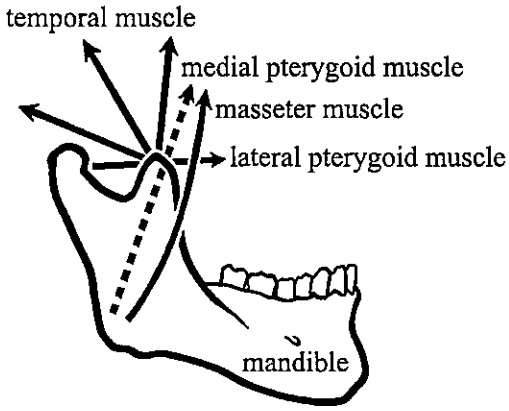

Figure 16. Masticatory muscles

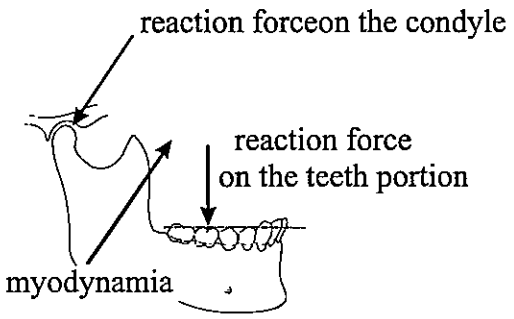

Figure 17. Equilibrium system of the mandible

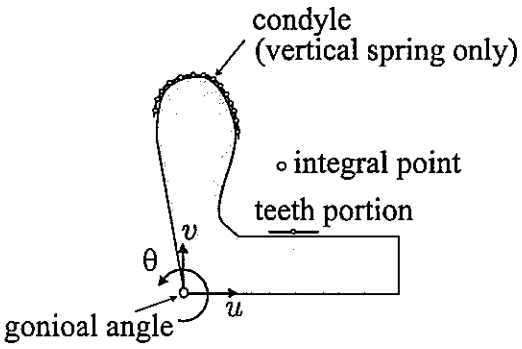

Figure 18. Numerical model

The condylar contact stress distribution is modeled based on the RBSM. On defining the model, bone fragments were considered to be rigidly fixed also after surgery so that the entire madible could

be considered as a single element (*Figure* 18). Three degrees of freedom, i.e., translation (u, v) and rotation (θ) are related to gonial angle as local reference points. Muscular forces generated by various muscles of mastication are assumed to act on this point as a single external force through conversion and aggegation.

Integral points for calculating the contact stress are defined along the contours of the uppermost face of condyle, which, together with the glenoid fossa, composed temporomandibular joint. As this portion has relatively smooth surface, a vertical spring only is fitted on each integral point, assuming that the surface bears the vertical surface force (or in other words, contact pressure) only, and does not bear the shearing force. *Figure* 19 show the assumed spring along the contours of the uppermost face of condyle.

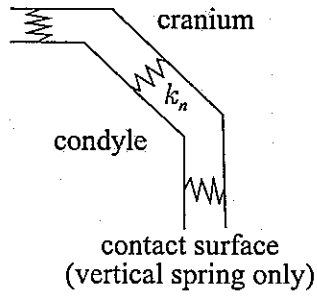

Figure 19. Spring system on the conyle

The reaction forces on the teeth are assumed and calculated to act on the molar portions, especially, on the first molar. In RBSM, because the moment reaction can be also calculated, it is possible to represent reaction forces distributed over the teeth even on one integral point. On the first molar, both vertical and shearing spring were fitted as shown in *Figure* 20.

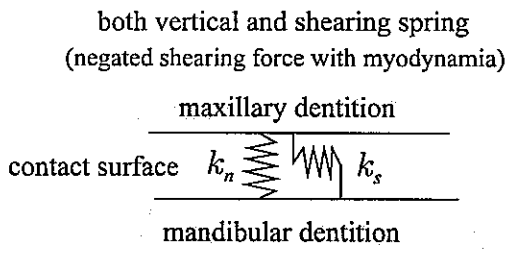

Figure 20. Spring system on the teeth

The flow of this algorithm consists two loops, i.e., the inner loop for redistributing the negative contact pressure generated in the temporomandibular joint and the outer loop for generating additional muscular force which counteracts the revirse shearing reaction force on teeth. Redistribution of negative contact pressure is calculated, according to the following procedures:

(The first step)

The contact pressure generated on integration points relative to initially given muscular force is obtained.

(The second step)

If negative contact pressure is found on some integral points, it is temporarily removed and a constraint force is added to keep the balance.

(The third step)

As this constraint force does not actually exist, a force equal to this force is added in reverse direction

The second and third steps are repeated until the negative contact pressure reduces to negligible value.

Then, the shearing reaction force exerted on teeth is detected. If the contradictory shearing reaction force is generated, a force which can counteract this reaction force us added to the muscular force, and calculation of the contact pressure exerted on the temporomandibular joint is repeated until this reaction force reduces to the negligible small value.

Figure 21 shows the numerical result for the simple model. *Figure(a)* is obtained from disregarding a shearing spring fitted on the teeth. Under this condition, the entire mandible moves forward and the contact pressure distribution is concentrated in the front of the temporomandibular joint. This condition is considered to be the one induced by occluding the upper teeth with each other. *Figure(b)* is the condition under which a frictional shearing force is produced by teeth. In this case, unreasonable reaction due to shearing is computed. *Figure(c)* is obtained when counteracting this inrealistic reaction force by means of muscular force is completed. Under this condition, direction of the reaction force on the teeth has been turned normal direction as a result of reaction force being negated by counteracting muscular force. Correspondingly, muscular force has also been corrected by repeated convergence calculations, and its direction has been changed more upward than its initial

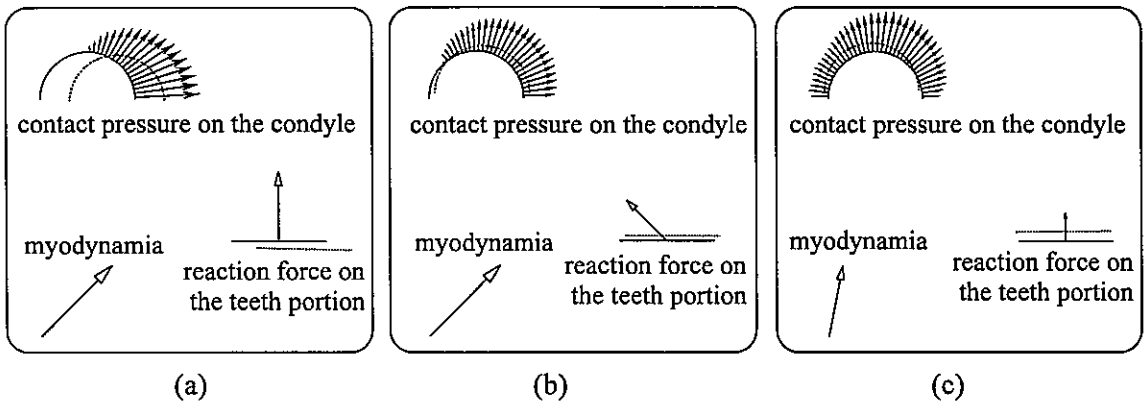

Figure 21. Numerical examples for the simple model

direction. This condition is considered to be stable because the contact pressures has been widely distributed in the entire temporomandibular joint.

Figure 22 show the numerical result for the human temporomandibular joint. This data was made by using the sectional X-ray image. The jaw deformity may be discussed by using this numerical method.

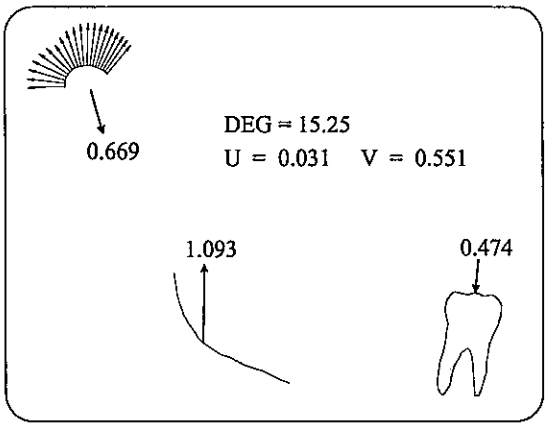

Figure 22. Numerical model for the human temporomandibular joint

5. Conclusion

A new algorithm was developed by which coupled failure due to shear and tensile loads can be treated. Although numerical examples introduced are very simple, it is believed that the present method may be useful in failure load analysis of various solid and structures.

It can be concluded that, comparing this simulation technique with the previous solution procedure, the number of 'if' sentences may increase resulting in time-consuming calculation, but a more realistic analysis can be expected.

References

[1]Kawai,T. : New element models in discrete structural analysis, *J. of the Society of Naval Architects of Japan*, No., 141, pp187-193, 1977

[2]Takeuchi,N and Kawai,T. : A discrete limit analysis of granular materials including effects of the solid contact, *US-JAPAN seminer "Micromchanics of Granular Materials", SENDAI*, pp116-125, 1987

[3]Yamada,Y., Yoshimura,N. and Sakurai,T. : Plastic stress-strain matrix and its application for the solution of elasto-plastic problems by the finite element method,*Int. J. Mechanical Science*, No.10, pp343-354, 1968

[4]Takeuchi,N., et al. : On a numerical method of contact problems for the temporomandibular joint including the effects of the masticatory muscle, *Proceedings of the 15th Simulation Technology Conference*, pp265-268 , 1996(in Japanese)

Behavior and Analysis of Deformable Continuous Media Containing Rigid Discontinuous Bodies

by

Chiang Shih[1], Yeong-Kang Wang[2], and Edwarcd C. Ting[3]

Abstract

The paper summarizes our recent effort in developing a finite element algorithm to study the behavior of a system of multiple continuous media containing bodies of distinctly different stiffness. The extreme case is that the embedded bodies are rigid.

The algorithm is based on an explicit approach which leads to a vector formulation of the finite elements. To study failure behavior of the system, extremely large deformations and elastic-plastic material models are considered. This is accomplished by introducing a convected material frame approach for the description of large deformation kinematics. Mises and Drucker-Prager models are adopted for the stiffness of continuous medium. For the embedded rigid bodies, large displacements relative to the attached deformable media are permitted. Their interfaces may be separated due to failure. Contacts between rigid bodies and between the rigid bodies and the continuous media are considered.

The current development is implemented for plane solids using four-node isoparametric elements. Numerical examples are given to illustrate the capability of the algorithm in handling fragmentation, large deformations, and structures made of a mixture of rigid and continuum elements.

[1] Research Assistant of Civil Engineering, Purdue university, West Lafayette, IN, USA

[2] Associate Professor of Civil Engineering, Chung Cheng Institute of Technology, Taiwan, ROC

[3] Professor Emeritus of Applied Mechanics, Purdue University, West Lafayette, IN, USA and Professor of Civil Engineering, National Central University, Taiwan, ROC

1. Introduction

With the help of new algorithms and computing facilities, engineers have improved their capability to predict behaviors of complicated structures. This capability gives more flexibility to the designers to create safe, functional and economical structures. Classical finite element has an enormous impact on the development of new structures. However, this approach based on variational concepts is also known to have limitations. One of the limitations is that the classical algorithms are somewhat awkward in handling complicated material behaviors and very large geometrical changes. Numerical difficulties in handling elastic-plastic irreversible behaviors, fractures, and progressive cracks are well-documented in earlier literature. Recent attempts in discrete element methods, discontinuous displacement analyses and explicit finite elements seem to provide some viable alternatives to alleviate these difficulties.

Another numerical problem which has placed considerable limitations on the applications of many algorithms is the handling of bodies with distinctly different stiffness values. The limiting case is a mixture of deformable and rigid components or a continuous medium embedded with rigid bodies. Deformations in these type of media are discontinuous and hence do not satisfy the fundamental requirements of continuum mechanics. In addition, due to the movement of rigid body, the neighboring deformable body is often subjected to very large deformations. Inelastic response, progressive cracks and separation at the interfaces should be considered in order to accurately simulate the real situations.

Our original motivation to formulate a finite element numerical procedure and to develop a corresponding computational code is to study granular soil media containing large boulders such as a boulder clay. The work is concerned with the static and transient analysis of such media where the embedded boulders may undergo large displacements, and the surrounding clay material may be subjected to large deformations. The algorithm may also find applications in studying post-failure behavior of structures, in the analysis of layered rock and soft soil media, and in the safety analysis of embedded man-made structures such as underground shelters.

Our formulation of the continuum finite element is based on a convected material frame approach to treat large geometrical changes. This approach is a modification of the traditional co-rotational formulation, commonly used to describe kinematics which include large rotations and small deformations.

In the approach, each discrete element is associated with a local coordinate system that rotates and translates with the element but does not deform. For each load or time increment, the local coordinate system assumes a new orientation and the element geometry also assumes a new shape. Thus, the element analysis includes two shape functions. One describes the displacement distribution and the other describes the geometrical shape. The corresponding strain-displacement and nodal force-stress relationships are defined in the convected local coordinates and are based on the updated geometrical shape. More importantly, if the time increment is small, the deformation increment in each element is small. Small strain theory can be used in the formulation.

Although the convected material frame approach can be applied to the traditional finite element method, it is convenient to combine it with an explicit time integration method to form an explicit analysis procedure in order to avoid the assemblage of the global stiffness matrix, which causes serious numerical difficulties when large stiffness ratio between elements exists. This resulting formulation involves only vector assemblages and vector storage if a lump mass matrix of diagonal form is assumed. Since there is no need to assemble stiffness matrices, no simultaneous equation needs to be solved as is required in the classical implicit finite element method. Therefore, by combining an explicit finite element method and a momentum equation, which governs the motion of rigid solids, the difference of material rigidity existing in the numerical calculation can be handled.

Explicit algorithms for finite element analysis have been reported in the literature during the last two decades. Belytschko and Hsieh [1973] formulated the frame elements by using the traditional co-rotational approach. Marchertas and Belytschko [1974] formulated the three dimensional plate element following a similar approach. General purpose computer codes have been widely used in industry in recent years.

Rice and Ting [1993a] have applied an approach of updated geometry to develop a plane frame analysis procedure. Rice and Ting [1993b] extended the approach of updated geometry to incorporate a similar fragmentation algorithm to study failure and fragmentation of frame structures. The concept of updated geometry is similar to the convected material frame approach.

2. Convected Material Frame Approach

The concept of convected material reference frame for displacement and strain may be illustrated in Figure 1, where the history of a body subjected to large displacement is described in four stages :

(1) the initial geometry $\underset{\sim}{X}$ at the reference time = 0,

(2) the convected material reference frame $\underset{\sim}{x}$ at time $t = n\Delta t$,

(3) the deformed body geometry $\underset{\sim}{x}'$ at time $t' = t + \Delta t = (n+1)\Delta t$, and

(4) the convected geometry $\hat{\underset{\sim}{x}}'$ at time = t'.

The convected geometry $\hat{\underset{\sim}{x}}'$ is related to the deformed body geometry $\underset{\sim}{x}'$ by a pure rotation $\underset{\sim}{Q}$.

The deformation process may be referred either to the fixed initial material reference frame $\underset{\sim}{X}$ (a standard Lagrangian description) or to the convected material reference frame $\underset{\sim}{x}$ (a convected Lagrangian description). The Cauchy stress tensor $\underset{\sim}{\sigma}$ is defined in $\underset{\sim}{X}$, or

$$d\underset{\sim}{x}' = \underset{\sim}{F}\, d\underset{\sim}{X} = \frac{\partial \underset{\sim}{x}'}{\partial \underset{\sim}{X}}\, d\underset{\sim}{X} \tag{1}$$

and

$$\underset{\sim}{\sigma} = \frac{\rho'}{\rho_0} \underset{\sim}{F}\, \underset{\sim}{S}\, \underset{\sim}{F}^T \tag{2}$$

where $\underset{\sim}{F}$ is deformation gradient tensor, ρ_0 and ρ' are the material density of the body at the states $\underset{\sim}{X}$ and $\underset{\sim}{x}'$, respectively. $\underset{\sim}{S}$ is the second Piola-Kirchhoff stress tensor.

For the incremental Cauchy stress tensor, we use the convected reference frame, or

$$d\underset{\sim}{x}' = \frac{\partial \underset{\sim}{x}'}{\partial \underset{\sim}{x}}\, d\underset{\sim}{x} = \underset{\sim}{F}'\, d\underset{\sim}{x} \tag{3}$$

and

$$\underset{\sim}{\sigma}' = \frac{\rho'}{\rho} \underset{\sim}{F}'\, \underset{\sim}{S}' \left(\underset{\sim}{F}'\right)^T \tag{4}$$

The advantage of using a convected reference frame is that for small time and small load increments where the incremental deformation is small, linear strain tensor and linear stress-strain relationships can be adopted. Although general Cauchy stress tensor still needs to be calculated, the incremental kinetic relationships may be written in the convected reference frame and the resulting equations of motion corresponding to the load increments are linear.

For the deformation process, we adopt a co-rotational formulation. That is, for each increment we approximate its kinematics as a combination of large rotation and small deformation. Thus, we define an intermediate state $\hat{x}$' such that

$$d\hat{\underset{\sim}{x}}' = \underset{\sim}{Q}\, d\underset{\sim}{x}' = \underset{\sim}{Q}\, \underset{\sim}{F}'\, d\underset{\sim}{x} \tag{5}$$

or

$$d\hat{\underset{\sim}{x}}' = \hat{\underset{\sim}{F}}' d\underset{\sim}{x} \qquad (\hat{\underset{\sim}{F}}' = \underset{\sim}{Q}\,\underset{\sim}{F}' \text{ and } \underset{\sim}{F}' = \underset{\sim}{Q}^T\,\hat{\underset{\sim}{F}}')$$

Hence, the strain tensor for deformation from $\underset{\sim}{x}$ to $\underset{\sim}{x}'$ is

$$2\underset{\sim}{E}' = \left(\underset{\sim}{F}'\right)^T \underset{\sim}{F}' - \underset{\sim}{I} = \left(\hat{\underset{\sim}{F}}'\right)^T \underset{\sim}{Q}\underset{\sim}{Q}^T \hat{\underset{\sim}{F}}' - \underset{\sim}{I}$$

$$= \left(\hat{\underset{\sim}{F}}'\right)^T \hat{\underset{\sim}{F}}' - \underset{\sim}{I} = 2\hat{\underset{\sim}{E}}' \tag{7}$$

Note that, although the total deformation in the element of the medium from $\underset{\sim}{X}$ to $\underset{\sim}{x}$ may not be small, we may take infinitesimal load increments, so that the deformation tensor from $\underset{\sim}{x}$ to $\underset{\sim}{x}'$ becomes infinitesimal, or

$$\hat{\underset{\sim}{E}}' \cong \frac{1}{2}\left(\frac{\partial \hat{\underset{\sim}{u}}}{\partial \underset{\sim}{x}} + \frac{\partial \hat{\underset{\sim}{u}}^T}{\partial \underset{\sim}{x}}\right) \tag{8}$$

where $\hat{\underset{\sim}{u}}$ is the displacement vector from $\underset{\sim}{x}$ to $\underset{\sim}{x}'$.

Furthermore, for small deformation, we may take $\rho' = \rho$. This yields

$$\underset{\sim}{\sigma}' = \underset{\sim}{F}'\underset{\sim}{S}'\left(\underset{\sim}{F}'\right)^T = \underset{\sim}{Q}^T \hat{\underset{\sim}{F}}'\underset{\sim}{S}'\left(\hat{\underset{\sim}{F}}'\right)^T \underset{\sim}{Q}$$

$$\cong \underset{\sim}{Q}^T \underset{\sim}{S}' \underset{\sim}{Q} \tag{9}$$

Or

$$\underset{\sim}{S}' \cong \underset{\sim}{Q}\,\underset{\sim}{\sigma}'\,\underset{\sim}{Q}^T \tag{10}$$

From $\underset{\sim}{x}$ to $\hat{\underset{\sim}{x}}'$, the incremental Cauchy stress is then

$$\hat{\underset{\sim}{\sigma}}' = \underset{\sim}{Q}\,\underset{\sim}{\sigma}'\,\underset{\sim}{Q}^T = \underset{\sim}{S}' \tag{11}$$

<u>Rotation Matrix for a Plane Solid Element</u>

The rigid body rotation angle of a four-node plane solid element is evaluated by the following relationships:

$$\theta^{nt} = \frac{1}{4}\left(\beta_1^{nt} + \beta_2^{nt} + \beta_3^{nt} + \beta_4^{nt}\right) \tag{12}$$

where

$$\beta_i^{nt} = \sin^{-1}\left\{\frac{1}{|l_i|\cdot|l_i'|}\left[\left(x_i^{nt} - x_c\right)\left(y_i + v_i' - y_c'\right) - \left(y_i^{nt} - y_c\right)\left(x_i + u_i' - x_c'\right)\right]\right\}$$

$$|l_i| = \sqrt{\left(x_i^{nt} - x_c\right)^2 + \left(y_i^{nt} - y_c\right)^2}$$

$$|l_i'| = \sqrt{(x_i + u_i' - x_c')^2 + (y_i + v_i' - y_c')^2}$$

$$x_c = \frac{1}{4}\left(x_1^{nt} + x_2^{nt} + x_3^{nt} + x_4^{nt}\right)$$

$$y_c = \frac{1}{4}\left(y_1^{nt} + y_2^{nt} + y_3^{nt} + y_4^{nt}\right)$$

$$x_c' = \frac{1}{4}\left(x_1 + x_2 + x_3 + x_4 + u_1' + u_2' + u_3' + u_4'\right)$$

$$y_c' = \frac{1}{4}\left(y_1 + y_2 + y_3 + y_4 + v_1' + v_2' + v_3' + v_4'\right)$$

where the nodal number $i = 1, 2, 3$, and 4.

Hence, the element rotation matrix between $\underset{\sim}{x}'$ and $\hat{\underset{\sim}{x}}'$ is

$$\underset{\sim}{Q} = \begin{bmatrix} \underset{\sim}{R} & \underset{\sim}{0} & \underset{\sim}{0} & \underset{\sim}{0} \\ \underset{\sim}{0} & \underset{\sim}{R} & \underset{\sim}{0} & \underset{\sim}{0} \\ \underset{\sim}{0} & \underset{\sim}{0} & \underset{\sim}{R} & \underset{\sim}{0} \\ \underset{\sim}{0} & \underset{\sim}{0} & \underset{\sim}{0} & \underset{\sim}{R} \end{bmatrix} \tag{13}$$

where $$\underset{\sim}{R} = \begin{bmatrix} \cos\theta^{nt} & \sin\theta^{nt} \\ -\sin\theta^{nt} & \cos\theta^{nt} \end{bmatrix}$$

(x_i, y_i) = the global coordinates of the i-th node of the element at time = 0.

(x_i^{nt}, y_i^{nt}) = the global coordinates of the i-th node of the element at time t = $n\Delta t$.
$= (x_i + u_i\ , y_i + v_i)$

(u_i, v_i) = the displacement vector, in global coordinates, of the i-th node of the element at time t = $n\Delta t$.

(u_i', v_i') = the displacement vector, in global coordinates, of the i-th node of the element at time $t' = (n+1)\Delta t$.

Kinematics for a Plane Solid

Using the rotation matrix, the convected coordinates for an element at the convected material frame $\underset{\sim}{x}$ at time t = $n\Delta t$

$$\begin{Bmatrix} \hat{\underset{\sim}{x}}^{nt} \\ \hat{\underset{\sim}{y}}^{nt} \end{Bmatrix} = \underset{\sim}{Q} \begin{Bmatrix} \underset{\sim}{x}^{nt} \\ \underset{\sim}{y}^{nt} \end{Bmatrix} \tag{14}$$

Similarly, the element deformation components of the incremental displacement vector at the convected geometry $\underset{\sim}{\hat{x}}'$ at time $t' = (n+1)\Delta t$

$$\begin{Bmatrix} \Delta \underset{\sim}{\hat{u}}^{d} \\ \Delta \underset{\sim}{\hat{v}}^{d} \end{Bmatrix} = \underset{\sim}{Q} \begin{Bmatrix} \Delta \underset{\sim}{u}^{d} \\ \Delta \underset{\sim}{v}^{d} \end{Bmatrix} \tag{15}$$

Introducing isoparametric formulation, the element incremental strains, in convected coordinates, from time $t = n\Delta t$ to $t' = (n+1)\Delta t$, are

$$\Delta \underset{\sim}{\hat{\varepsilon}} = \underset{\sim}{\hat{B}}^{nt} \, \Delta \underset{\sim}{\hat{d}} \tag{16}$$

where

$$\Delta \underset{\sim}{\hat{\varepsilon}} = \begin{Bmatrix} \Delta \underset{\sim}{\hat{\varepsilon}}_{\hat{x}} \\ \Delta \underset{\sim}{\hat{\varepsilon}}_{\hat{y}} \\ \Delta \underset{\sim}{\hat{\gamma}}_{\hat{x}\hat{y}} \end{Bmatrix}$$

$$\Delta \underset{\sim}{\hat{d}} = \left\{ \Delta \hat{d}_{1\hat{x}} \quad \Delta \hat{d}_{1\hat{y}} \quad \Delta \hat{d}_{2\hat{x}} \quad \Delta \hat{d}_{2\hat{y}} \quad \Delta \hat{d}_{3\hat{x}} \quad \Delta \hat{d}_{3\hat{y}} \quad \Delta \hat{d}_{4\hat{x}} \quad \Delta \hat{d}_{4\hat{y}} \right\}^{T}$$

$$= \left\{ \Delta \hat{u}_1^{d} \quad \Delta \hat{v}_1^{d} \quad \Delta \hat{u}_2^{d} \quad \Delta \hat{v}_2^{d} \quad \Delta \hat{u}_3^{d} \quad \Delta \hat{v}_3^{d} \quad \Delta \hat{u}_4^{d} \quad \Delta \hat{v}_4^{d} \right\}^{T}$$

$(\Delta u_i \;,\; \Delta v_i)$ = the incremental displacement vector, in global coordinates, of the i-th node of the element from time $t = n\Delta t$ to $t' = (n+1)\Delta t$.

$= (u_i' - u_i \;,\; v_i' - v_i)$

$(\Delta u_i^{d} \;,\; \Delta v_i^{d})$ = the deformation component of the incremental displacement vector, in global coordinates, of the i-th node of the element from time $t = n\Delta t$ to $t' = (n+1)\Delta t$.

Explicitly, for a four node isoparametric solid element,

$$\underset{\sim}{\hat{B}}^{nt} = \frac{1}{|J^{nt}|} \begin{bmatrix} \underset{\sim}{\hat{B}}_1^{nt} & \underset{\sim}{\hat{B}}_2^{nt} & \underset{\sim}{\hat{B}}_3^{nt} & \underset{\sim}{\hat{B}}_4^{nt} \end{bmatrix} \tag{17}$$

$$|J^{nt}| = \frac{1}{8} \left\{ \hat{x}_1^{nt} \quad \hat{x}_2^{nt} \quad \hat{x}_3^{nt} \quad \hat{x}_4^{nt} \right\} \begin{bmatrix} 0 & 1-t & t-s & s-1 \\ t-1 & 0 & s+1 & -s-t \\ s-t & -s-1 & 0 & t+1 \\ 1-s & s+t & -t-1 & 0 \end{bmatrix} \begin{Bmatrix} \hat{y}_1^{nt} \\ \hat{y}_2^{nt} \\ \hat{y}_3^{nt} \\ \hat{y}_4^{nt} \end{Bmatrix}$$

$$\underset{\sim}{\hat{B}}_i^{nt} = \begin{bmatrix} \dfrac{\partial \hat{y}^{nt}}{\partial t}\dfrac{\partial N_i}{\partial s} - \dfrac{\partial \hat{y}^{nt}}{\partial s}\dfrac{\partial N_i}{\partial t} & 0 \\ 0 & \dfrac{\partial \hat{x}^{nt}}{\partial t}\dfrac{\partial N_i}{\partial s} - \dfrac{\partial \hat{x}^{nt}}{\partial s}\dfrac{\partial N_i}{\partial t} \\ \dfrac{\partial \hat{x}^{nt}}{\partial t}\dfrac{\partial N_i}{\partial s} - \dfrac{\partial \hat{x}^{nt}}{\partial s}\dfrac{\partial N_i}{\partial t} & \dfrac{\partial \hat{y}^{nt}}{\partial t}\dfrac{\partial N_i}{\partial s} - \dfrac{\partial \hat{y}^{nt}}{\partial s}\dfrac{\partial N_i}{\partial t} \end{bmatrix}$$

where N_i are the standard shape functions.

Principle of Virtual Work and Equation of Motion

In the deformed geometry $\underset{\sim}{x}'$ at time $t' = (n+1)\Delta t$, a structural system is said to be in equilibrium when it satisfies the virtual work formulation

$$\sum_e \delta U_e = \sum_e \delta W_e \tag{18}$$

The displacements are separated into deformation and rigid body displacements from the state $\underset{\sim}{x}$ to $\hat{\underset{\sim}{x}}'$. Since the internal virtual work due to a virtual rigid body motion is zero, the internal virtual work can be expressed as

$$\sum_e \delta U_e = \sum_e \delta U_e^d = \sum_e \int_{V_e} \delta\left(\Delta \underset{\sim}{\hat{\varepsilon}}\right)^T \underset{\sim}{\hat{\sigma}}\, dV$$

where $\underset{\sim}{\hat{\sigma}}$ are the total accumulated element stresses at the deformed state $\underset{\sim}{\hat{x}}'$, which include (1) the existing element stresses $\underset{\sim}{\hat{\sigma}}^{nt}$ at the state $\underset{\sim}{x}$ and (2) the incremental stresses $\Delta \underset{\sim}{\hat{\sigma}}$ from the state $\underset{\sim}{x}$ to $\hat{\underset{\sim}{x}}'$. Or,

$$\underset{\sim}{\hat{\sigma}} = \underset{\sim}{\hat{\sigma}}^{nt} + \Delta \underset{\sim}{\hat{\sigma}} \tag{19}$$

By introducing material property tensor $\underset{\sim}{C}$,

$$\Delta \underset{\sim}{\hat{\sigma}} = \underset{\sim}{C}\, \Delta \underset{\sim}{\hat{\varepsilon}}$$

Since the deformation from $\underset{\sim}{x}$ to $\hat{\underset{\sim}{x}}'$ is infinitesimal,

$$d\hat{V} \cong dV_{nt} \quad \text{and} \quad \hat{V}_e \cong V_{nt}$$

where V_{nt} is the deformed element volume at the convected material reference frame $\underset{\sim}{x}$ at time $t = n\Delta t$. Thus,

$$\delta U_e = \delta\left(\Delta \underset{\sim}{\hat{d}}_e\right)^T \int_{V_{nt}} (\underset{\sim}{\hat{B}}^{nt})^T \underset{\sim}{\hat{\sigma}}\, dV_{nt}$$

Let $$\delta U_e = \delta\left(\Delta \hat{\underset{\sim}{d}}_e\right)^T \hat{\underset{\sim}{f}}_e^{int} ,$$

The internal nodal forces are

$$\hat{\underset{\sim}{f}}_e^{int} = \int_{V_{nt}} (\hat{\underset{\sim}{B}}^{nt})^T \, \hat{\underset{\sim}{\sigma}} \, dV_{nt} \tag{20}$$

Using the global nodal displacements $\Delta \underset{\sim}{d}_e$ through the transformation,

$$\delta U_e = \delta\left(\Delta \underset{\sim}{d}_e\right)^T \underset{\sim}{Q}^T \, \hat{\underset{\sim}{f}}_e^{int} = \delta\left(\Delta \underset{\sim}{d}_e\right)^T \underset{\sim}{f}_e^{int} \tag{21}$$

where $\underset{\sim}{f}_e^{int} = \underset{\sim}{Q}^T \hat{\underset{\sim}{f}}_e^{int}$ is the internal nodal force vector represented in the global coordinates at the convected material reference frame $\underset{\sim}{x}$ at time $t = n\Delta t$.

The element external incremental virtual work from $\underset{\sim}{x}$ to $\underset{\sim}{x}'$ reads

$$\delta W_e = \delta\left(\Delta \underset{\sim}{d}_e\right)^T \left(\underset{\sim}{f}_e^{ext} - \underset{\sim}{M}_e \, \Delta \ddot{\underset{\sim}{d}}_e\right) \tag{22}$$

and the diagonal lump mass matrix $\underset{\sim}{M}_e$ is based on the mass density ρ at the convected material reference frame $\underset{\sim}{x}$ at time $t = n\Delta t$. According to the conservation of matter for an element, the ρ value is calculated as

$$\rho = \frac{V_0}{V}\rho_0 = \frac{t_0 A_0}{t \; A}\rho_0 \tag{23}$$

where A_0, t_0, and ρ_0 are the element area, thickness and mass density at the undeformed state, respectively, and A and t is the values at the state $\underset{\sim}{x}$.

The principle of virtual work at time $t' = t + \Delta t$ is then

$$\delta\left(\Delta \underset{\sim}{d}\right)^T \left(\underset{\sim}{F}^{int} - \underset{\sim}{F}^{ext} + \underset{\sim}{M} \, \Delta \ddot{\underset{\sim}{d}}\right) = 0 \tag{24}$$

where $\underset{\sim}{F}^{ext} = \sum_e \underset{\sim}{f}_e^{ext}$, $\underset{\sim}{F}^{int} = \sum_e \underset{\sim}{f}_e^{int}$ and $\underset{\sim}{M} = \sum_e \underset{\sim}{M}_e$. Then,

$$\Delta \ddot{d}_i = \frac{1}{M_i}\left(F_i^{ext} - F_i^{int}\right), \tag{25}$$

where i is the nodal number.

Explicit Time Integration

To include a damping force, F^{dmp}, Equation (25) becomes

$$\Delta\ddot{d}_i = \frac{1}{M_i}\left(F_i^{ext} - F_i^{int} - F_i^{dmp}\right) \tag{26}$$

where $F_i^{dmp} = \alpha M \dot{d}_i$.

Using a standard central difference, the equations of motion can be written in an explicit form as

$$\Delta d_{t+\Delta t} = \left(\frac{2}{2+\alpha\Delta t}\right)\frac{\Delta t^2}{M}\left(F_t^{ext} - F_t^{int} - F_t^{dmp}\right) + \left(\frac{4}{2+\alpha\Delta t}\right)\Delta d_t - \left(\frac{2-\alpha\Delta t}{2+\alpha\Delta t}\right)\Delta d_{t-\Delta t} \tag{27}$$

where $\Delta d_{t+\Delta t}$ are increments from time $t = n\Delta t$ to $t' = (n+1)\Delta t$. The total accumulated displacements at the state $\underset{\sim}{x}'$ are

$$d_{t+\Delta t} = d_t + \Delta d_{t+\Delta t} \tag{28}$$

where d_t are the displacements at the state $\underset{\sim}{x}$ at time $t = n\Delta t$.

3. Motion of the Rigid Solids

Rigid solids represent bodies with zero deformation and zero internal stress during the entire loading process. Motion of a plane rigid solid can be characterized by only two parameters, a translation vector and a rotation. Motions of the points on the plane solid are related by their relative distances.

Translational Motion

The translational components of a rigid body motion are calculated by treating the body as a particle. The particle motion is caused by the total unbalanced force applied on the solid. The unbalanced forces may be evaluated by simply summing the global internal and external nodal forces calculated from the deformable elements, which are attached to the rigid solid. If the total unbalanced force is zero, the velocity is a constant vector. For an embedded rigid solid, it is a zero vector. There is no translational motion.

Rotational Motion

The rotation represents the relative motions of particles on the same solid. Using the mass center as the reference point, rotation may be viewed as the result of an unbalanced couple acting on the body.

For a plane motion, the rotational equation of motion has the same form as the particle motion.. Thus, the incremental force-displacement equation for time integration can be extended to the rotation part of rigid solid motion which calculates the change of angle for a time increment.

Again, we adopted a convected material frame approach, the incremental translation part of displacement, $\Delta d^{r}_{t+\Delta t}$, from time $t = n\Delta t$ to $t' = (n+1)\Delta t$, is given as

$$\Delta d^{r}_{t+\Delta t} = \left(\frac{2}{2+\alpha\Delta t}\right)\frac{\Delta t^2}{M}\left(F^{ext}_t - F^{dmp}_t\right) + \left(\frac{4}{2+\alpha\Delta t}\right)\Delta d^{r}_t - \left(\frac{2-\alpha\Delta t}{2+\alpha\Delta t}\right)\Delta d^{r}_{t-\Delta t} \quad (29)$$

The incremental rotational part of displacement, $\left(\Delta u^{\psi}, \Delta v^{\psi}\right)$, can be calculated by first evaluating the incremental change of rotational angle, $\Delta\psi$, from time $t = n\Delta t$ to $t' = (n+1)\Delta t$.

$$\Delta\psi_{t+\Delta t} = \left(\frac{2}{2+\alpha\Delta t}\right)\frac{\Delta t^2}{I_z}\left(\overline{M}^{ext}_t - \overline{M}^{dmp}_t\right) + \left(\frac{4}{2+\alpha\Delta t}\right)\Delta\psi_t - \left(\frac{2-\alpha\Delta t}{2+\alpha\Delta t}\right)\Delta\psi_{t-\Delta t} \quad (30)$$

where ψ is the change of rotational angle, I_z the mass moment of inertia of the rigid solid, and $\overline{M}^{ext}_t$ the unbalanced couple acting on the rigid solid. The unbalanced couple is calculated from the attached nodal forces about the mass center.

The corresponding incremental nodal displacements due to rotation are

$$\begin{aligned} \Delta u^{\psi} &= (x - x_c)[\cos(\Delta\psi_{t+\Delta t}) - 1] - (y - y_c)\sin(\Delta\psi_{t+\Delta t}) \\ \Delta v^{\psi} &= (x - x_c)\sin(\Delta\psi_{t+\Delta t}) + (y - y_c)[\cos(\Delta\psi_{t+\Delta t}) - 1] \end{aligned} \quad (31)$$

where (x_c, y_c) and (x, y) are the coordinates of the mass center and a point, on the rigid solid at time t, respectively.

The total accumulated displacements of the rigid solid at the state $\underset{\sim}{x}'$ are the sums of the incremental displacements. They are the vector sums of the translation and rotational components.

Interface Compatibility and Force Equilibrium

Since the rigid solid is surrounded by continuum modeled by finite elements, the tractions acting on the rigid solid are calculated from the elements at the attached nodes. If the total

nodal forces are not balanced, the unbalanced force will cause a translation of the rigid solid. If the direction of the resultant nodal force does not pass through the mass center, it generates a couple. This unbalanced couple induces a rotation. The sum of the translation and rotational displacements creates a new set of nodal displacements for the attached continuum elements, and thus a new set of nodal forces. For each time increment, we have imposed an iterative procedure to ensure force equilibrium in the rigid solids and displacement compatibility at the interfaces. In our experience, the convergence is very rapid since a small load increment is generally chosen for an explicit time integration approach. Alternatively, one may further reduce the size of load increment and treat the rigid body displacements as inputs for the subsequent increment.

4. Fragmentation and Contact

The explicit finite element formulation and the convected material frame approach for large deformation serve as the essential ingredients in the development of a fragmentation algorithm which permits the transition from a continuum to a set of discontinuous bodies. The vector formulation of the explicit algorithm allows the creation of new nodes and the handling of multi-bodies. The convected frame approach gives an accurate evaluation of the large deformation rate at the instant of transition.

In addition, a fragmentation algorithm requires a fracture criterion that governs the separation of the structure, contact algorithms to handle the collisions, and a careful bookkeeping of the storage and nodal values.

A Fragmentation Algorithm

The objective of a fragmentation algorithm is to create new nodes according to a set of fracture criteria. New surfaces are formed. We consider the algorithm in three steps: The first step is to examine the violation of failure criteria. The criteria may be in the form of stress, strain, displacement, or a hybrid formula. Empirical formulations may also be considered. For simplicity, we considered the nodal stresses which are extrapolated from the stresses at Gaussian points of elements. If the state of maximum tensile stress at a node exceeds a limiting value, the node is designated as failed.

Next, the failed node requires a check of its nodal connectivity. If the node is shared with several elements in the direction of fracture, a new node is created. On the other hand, if the

failure node is an unrestrained node, no new node will be created as if no failure had been detected.

In the third step, an expansion of the dynamic storage array and a reposition of the existing memory locations due to the creation of a new node are performed. This is equivalent to construct a new mesh for the structure. One may also call a subroutine to generate a new optimum mesh. Data needed for the subsequent calculation which may include nodal displacements, forces, masses, and internal stresses should be evaluated and stored.

Creation of New Surfaces

Creation of new nodes indicates that there will be new free surfaces. A set of criteria is required to determine the surface directions. As an illustration, we generated surfaces according to the fracture direction in consistent with the principal tensile stress failure criterion. We further restricted the new surfaces being either a horizontal plane, a vertical plane, or both. A simple stress rosette is used as the direction criterion. Each quadrant of the solid plane is divided into three sectors. According to the direction of maximum tensile stress being in one of the sectors, a horizontal plane, a vertical plane or both the vertical and horizontal plane are created.

Contact of Free Surfaces

Contact algorithm can be a critical factor to the accuracy of behavior predictions, although a precise formulation of the contact behavior is difficult. There are two major aspects in the development. First, one needs to identify the nature of contact and the positions of participating parties. Secondly, a set of contact laws is needed to model the behaviors, for example, a force-displacement relationship with geometrical and material parameters. Considerable research has been reported in the literature. Many can readily be adopted in the present algorithm.

For illustrative purposes, a contact algorithm similar to the master element-slave node concept introduced by Belytschko and Liu [1988] is proposed. We designate some of the elements in the mesh as master elements. Nodes from the remaining elements are designated as slave nodes. At the conclusion of each time increment, position of each slave node is checked to determine whether the node has penetrated into any of the master elements. If so, the penetrating node is moved back onto the element boundary and the resulting change in momentum is transferred to the corresponding nodes for the calculation of the nodal motion at the following time step.

Since the penetration of a node into an element only happens through the free surface, the master elements can then be chosen as the elements bordering the surface. Nodes on the surface are designated as the slave nodes. The rest of elements and nodes are excluded from the examination .

Once a penetration, or contact, is found, a set of projected forces are applied as input forces acting on the element nodes and the node is relocated to the element boundary.. The projected forces for the contact of two rigid solids are

$$F_p = M_p \Delta d_p / \Delta t^2 \tag{32}$$

where M_p is the mass of the penetrating node, Δd_p the penetration displacement vector, and Δt the time step. If a damping force is considered,

$$F_p' = M_p \Delta d_p / \Delta t^2 - \alpha M_p \Delta d_p / \Delta t$$

where α is the coefficient of mass damping.

5. Numerical Examples

The flowchart of an explicit finite element algorithm which has the capability of handling plane solid elements, rigid body elements, elastic-plastic behaviors, fragmentation and contact is shown in Figure 2. Based on the algorithm, a program 2DSolidR coded in Fortran is developed for PC computers. Two patch test problems are performed to verify specific portions of the algorithm, namely the fragmentation and contact routines. They are shown in Figures 3 -4. Two numerical examples are shown to illustrate the capability and accuracy of the algorithm. We use a very small number of elements to model the structures, so that all the nodal displacements and kinematics of each continuum elements can be carefully monitored and shown. The algorithm in general is very efficient and resulting code is small. All the calculations were carried out on a laptop computer in minutes.

The first patch test consists of six four-node continuum elements subjected to a rapid ramp loading. Since a soft material is assumed, wave propagates slowly through the medium and eventually the medium reaches a pseudo static condition. By assigning a limiting tensile stress at the node, the top three elements are fragmented and separated from the lower three elements. The corner elements are subjected to large deformation changes before and after the fragmentation. We note that the fragmentation process seems to be stable and the results are reasonable.

The second patch test examines the contact algorithms. We considered two continuous bodies separated by a small gap. Subjected to a uniform compression, the left corner node begins in contact with the right body and gradually portions of two bodies are in close contact. Again, the material is assumed to be soft, very large deformations are shown in both bodies. As the results shown, the contact algorithm seems to perform satisfactorily.

The first numerical example considers a structure made of six rigid elements connected by five soft deformable elements. The material property of the continuum is taken to be elastic-ideally plastic with Mises function. The middle section of the structure is subjected to ramp loading which causes large displacements as shown in Figure 5. We note that the rotation of the rigid sections severely compresses the middle element D3, and induces large shear distortions in the elements D2 and D4. Then, the bindings between the rigid elements and deformable elements are separated primarily in shear. Fragmentation occurs and the rigid elements fall off due to gravity. As the wave continues to propagate through the structure, other elements fragment as well.

Note that for the convenience of plotting, the scaling of the vertical coordinate are different in each time plot. Thus, the shapes of the elements are distorted.

The trajectories of some elements are shown in Figure 6. It is interesting to observe the deformation pattern of the middle deformable element D3. Initially, the element is squeezed by the neighboring rigid solids, then separates from them, and falls off as a free body. Due to the weight and plastic flow, the rectangular element is distorted into a triangular element. Large deformation in the elements is quite evident.

The second numerical example considers two rigid solids connected by a deformable band represented by four continuum elements, as shown in Figure 7. Elastic-ideally plastic behavior is assumed for the continuum. The top rigid solids is restricted to vertical motion and the lower solid is subjected to horizontal motion only. A very large uniform pressure, constant in time, is applied vertically. The predicted motions of all elements are plotted in Figure 8. After the initial deformation, separations occur in all the interfaces, including those between the continuum elements. As the rigid solids maintain their motions, the continuum elements continue to stretch due to ideally plastic flows. Their left edges are in contact again with the vertical solid which causes all the continuum elements to rotate. A plot of the time history of the continuum element as it flows and rotates is shown in Figure 9. Large deformation in the element may be observed. To complete the plots, time histories of the rigid solids are shown in Figure 10. We may also observe the influence of fracture and contacts on the rigid solids.

References

1. Berlytschko, T. and Hsieh, B. J., " *Non-linear transient finite element analysis with convected coordinates* ", Int. J. Numer. Meth. Eng. 7, 255-271 (1973)

2. Berlytschko, T. and Liu, W.K.," *Computational methods for impact and penetration*", Impact, Balkema, 151-164 (1988)

3. Key, S. W., " *Concept underlying finite element methods for structural analysis* ", Nuc. Eng. Design, Vol. 48, No.1, 259-268 (1978)

4. Malvern, L. E., " *Introduction to the mechanics of a continuous medium* ", Prentice-Hall Inc. (1969)

5. Marchertas, A. H. and Belytschko, T., " *Non-linear finite-element formulation for transient analysis of three-dimensional thin structures* ", Argonne National Laboratory Report ANL-8104, Illinois (1974)

6. Rice, D. L. and Ting, E. C., " *Large displacement transient analysis of flexible structures* ", Int. J. Numer. Meth. Eng., 36, 1541-1562 (1993a)

7. Rice, D. L. and Ting, E. C., " *Fragmentation algorithm for finite element failure simulation and analysis* ", Int. J. Numer. Meth. Eng., 36, 3859-3881 (1993b)

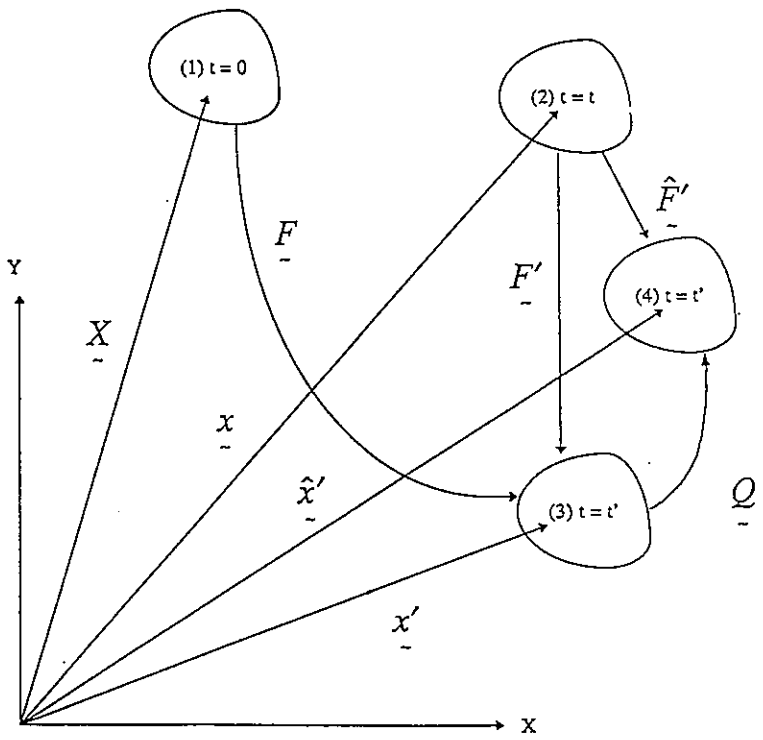

Figure 1. Convected Material Frame Approach

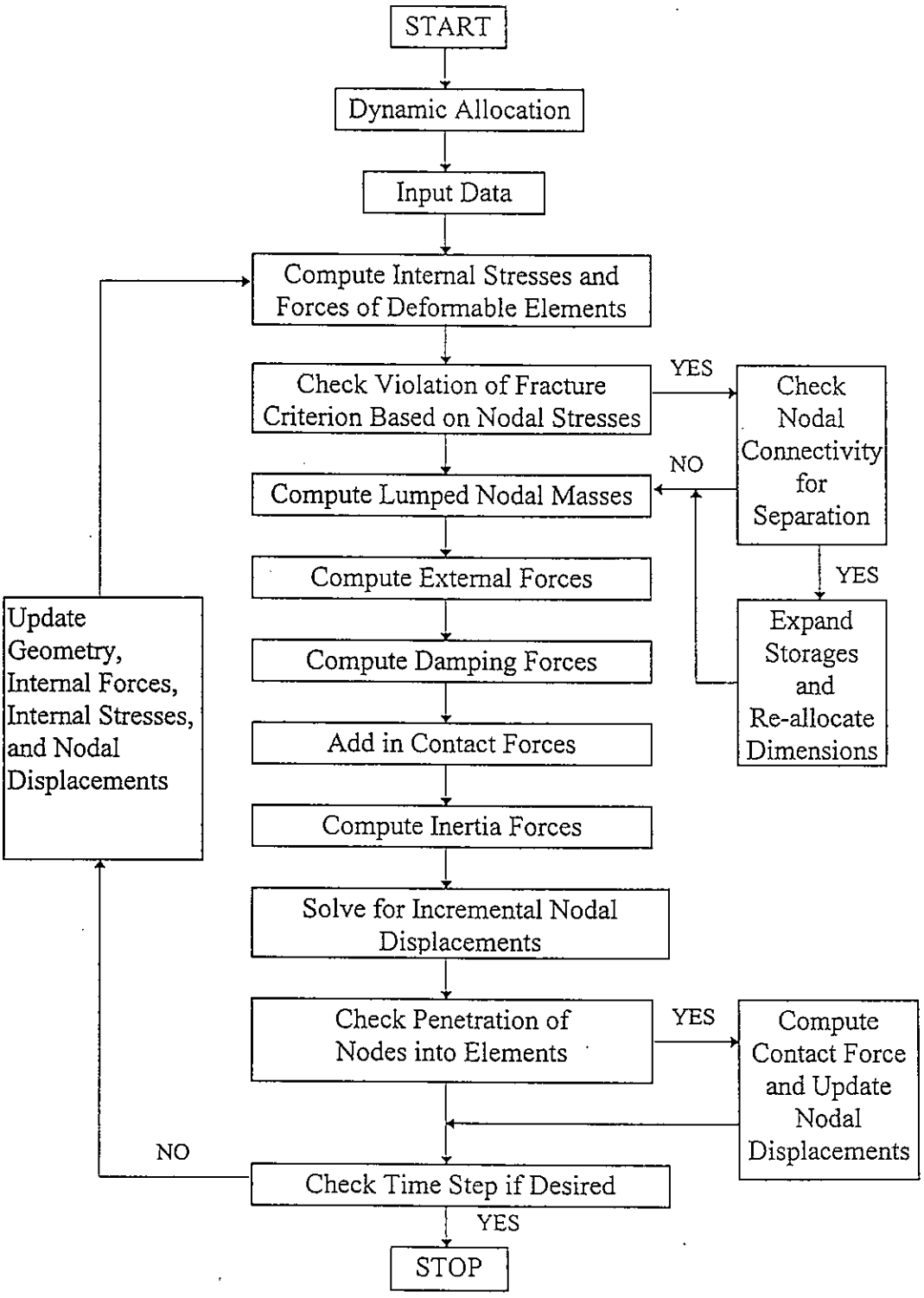

Figure 2. Flow Chart of the Algorithm

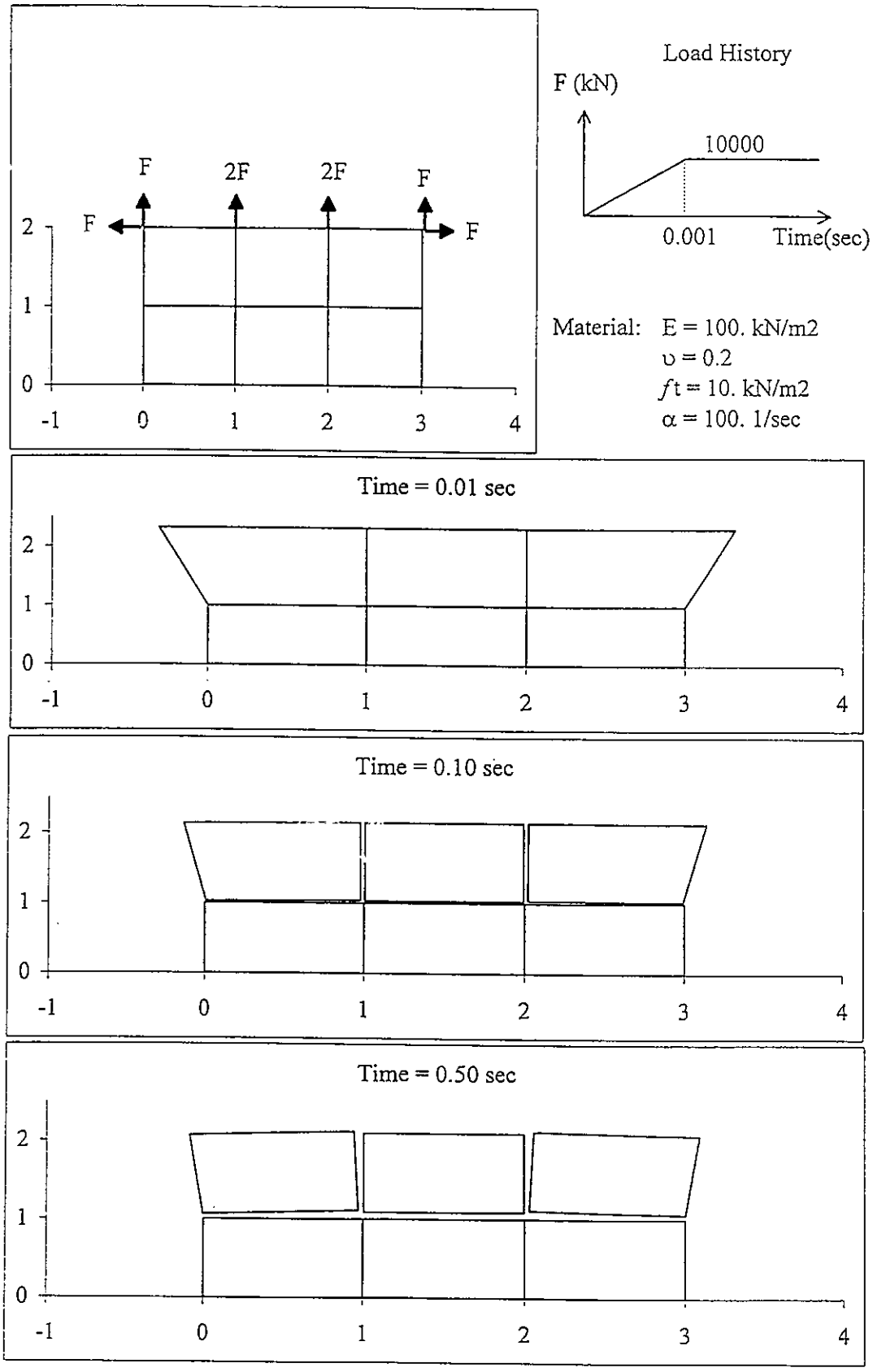

Figure 3. A Patch Test for the Fragmentation

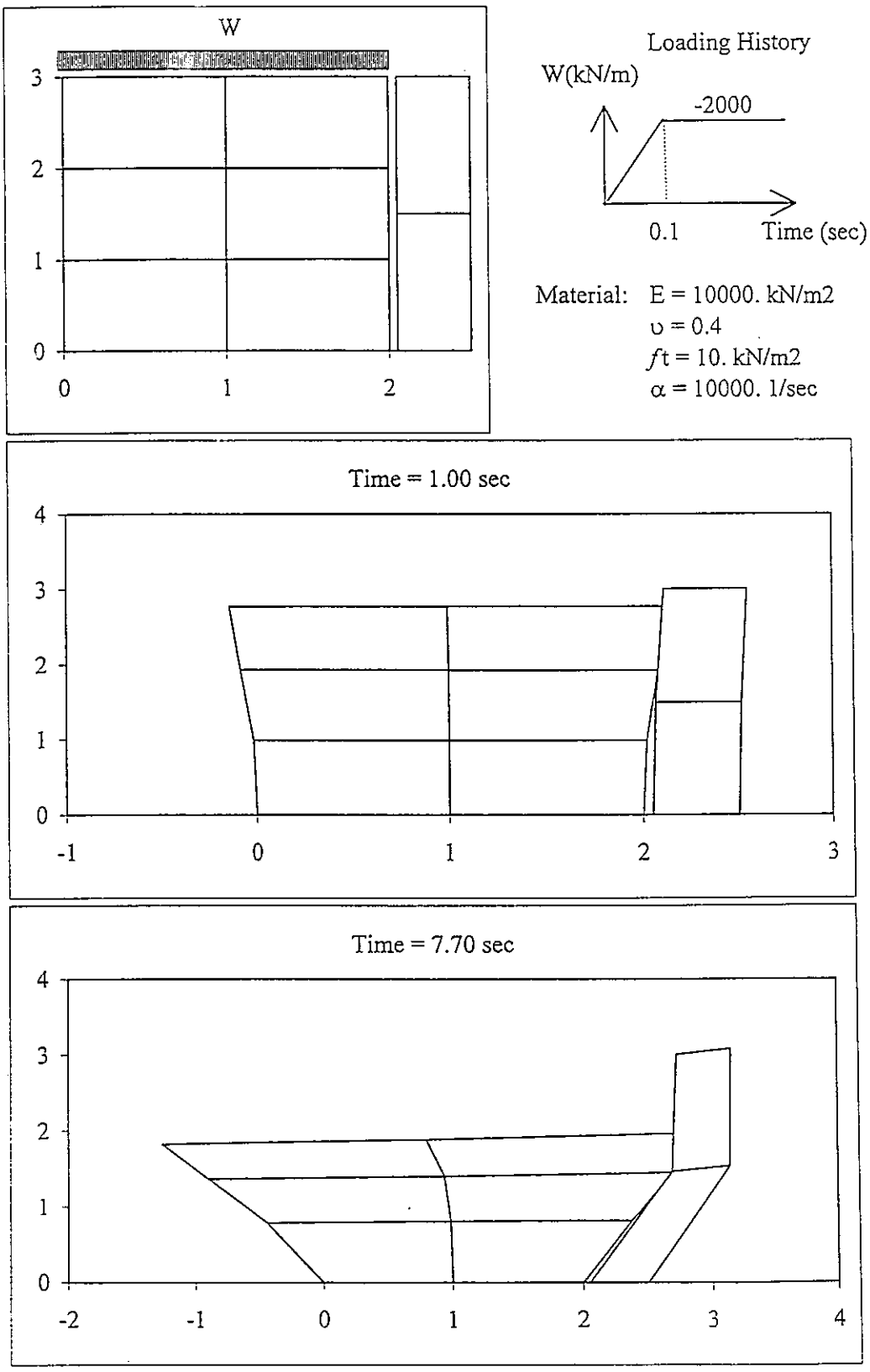

Figure 4. A Patch Test for the Contact

Figure 5A

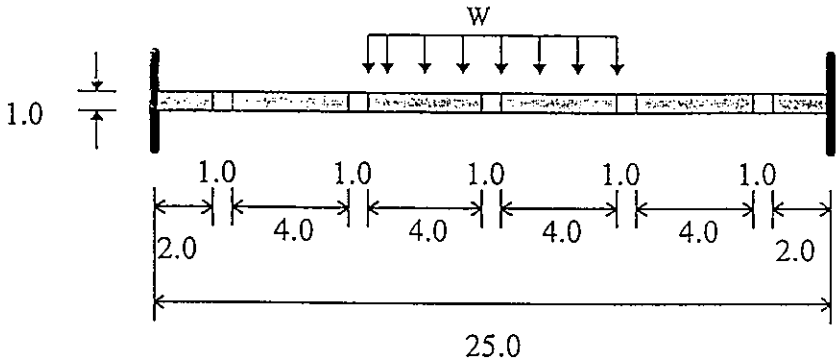

Legend: Rigid Element

Deformable Element

Surcharge, Load-Time Function as

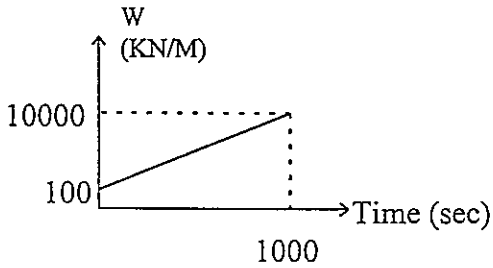

Material Properties :

$E = 100.0 \text{ kN / m}^2$

$\nu = 0.1$

$\rho = 1.0 \text{ kN - sec}^2 \text{ / m}^4$

$c = 10.0 \text{ kN / m}^2$

$\phi = 0.0 \text{ deg.}$

$f_r = 10.0 \text{ kN / m}^2$

Other Data:

$\alpha = 10000.0 \text{ sec}^{-1}$

$\Delta t = 0.00001 \text{ sec}$

$g = 10.0 \text{ m / sec}^2$

Figure 5. A Structure Made of A Mixture of Rigid Solids and Continuum Elements

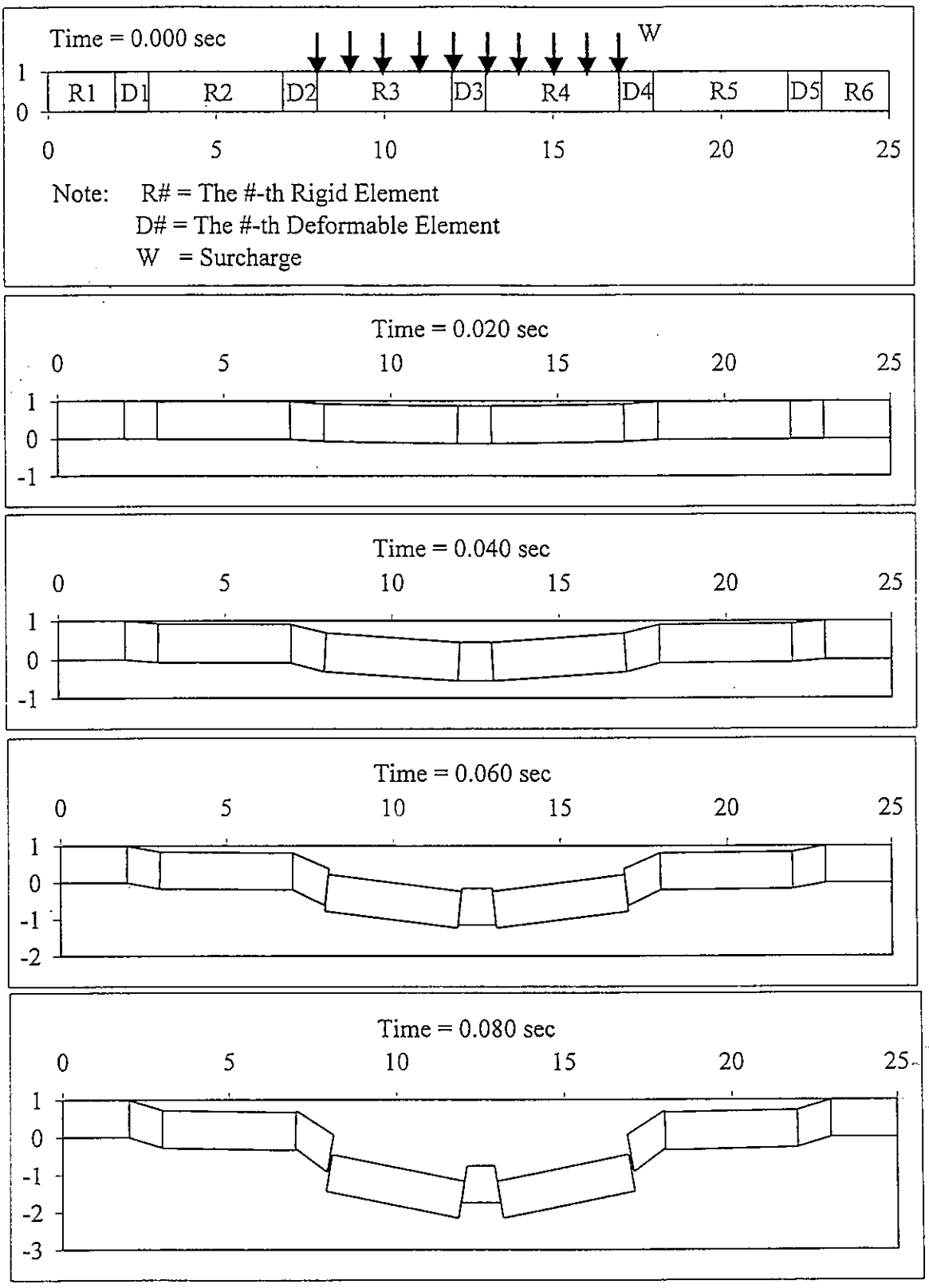

Time History of the Structural Configuration Subjected to An Impact

Figure 5B

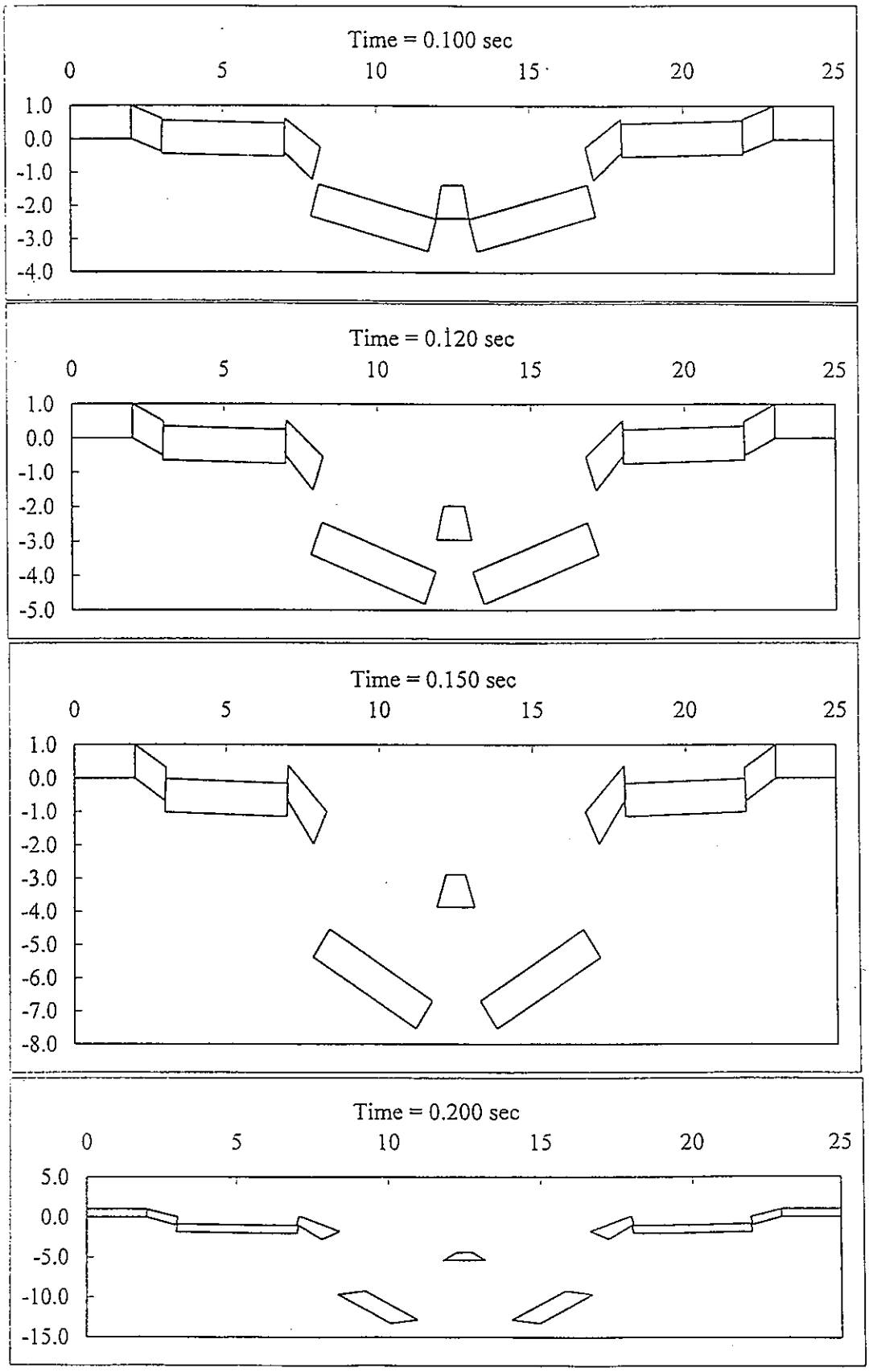
Time = 0.100 sec
0
5
10
15
20
25
1.0
0.0
-1.0
-2.0
-3.0
-4.0
Time = 0.120 sec
0
5
10
15
20
25
1.0
0.0
-1.0
-2.0
-3.0
-4.0
-5.0
Time = 0.150 sec
0
5
10
15
20
25
1.0
0.0
-1.0
-2.0
-3.0
-4.0
-5.0
-6.0
-7.0
-8.0
Time = 0.200 sec
0
5
10
15
20
25
5.0
0.0
-5.0
-10.0
-15.0

Figure 5C

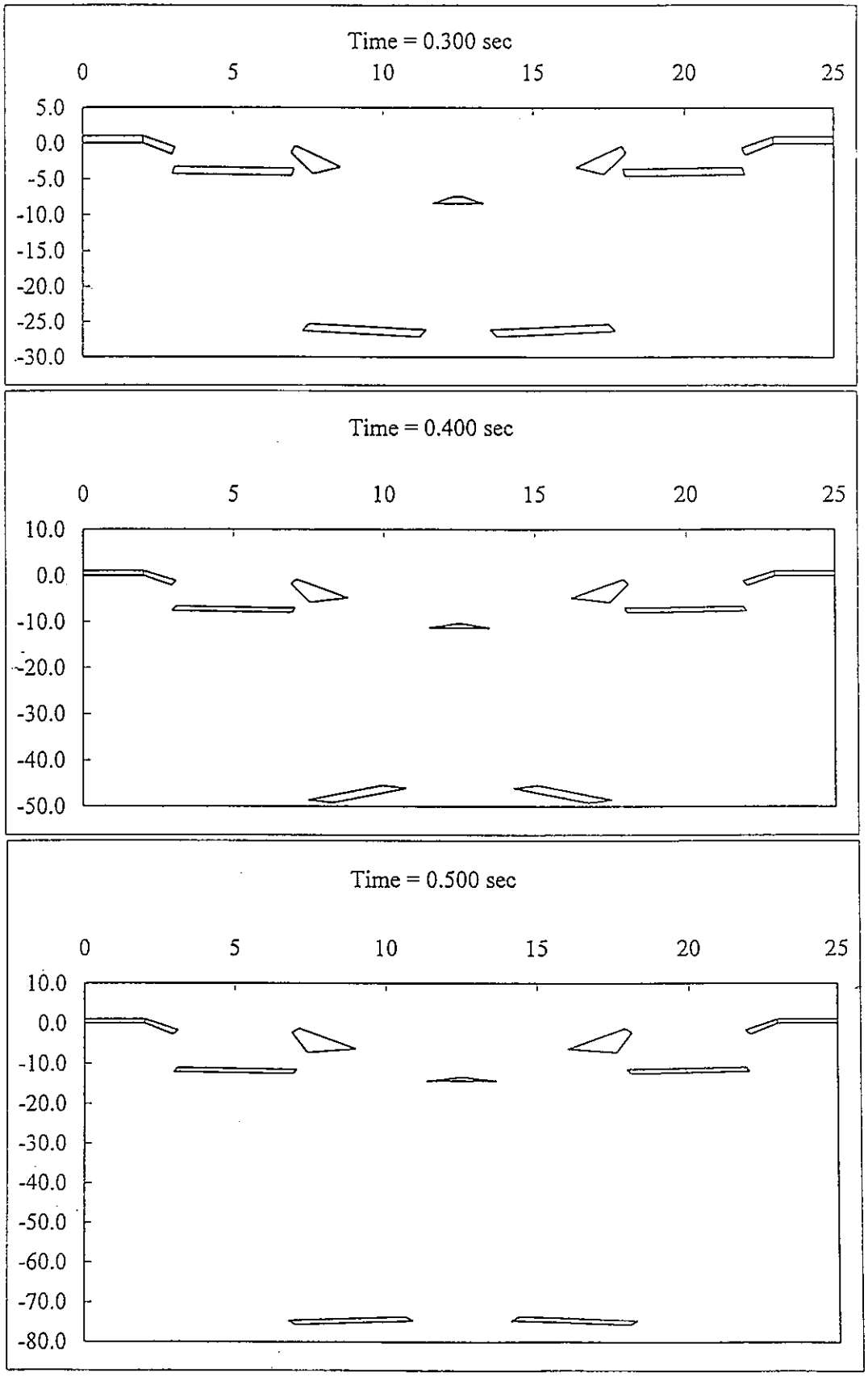
Time = 0.300 sec
0
5
10
15
20
25
5.0
0.0
-5.0
-10.0
-15.0
-20.0
-25.0
-30.0
Time = 0.400 sec
0
5
10
15
20
25
10.0
0.0
-10.0
-20.0
-30.0
-40.0
-50.0
Time = 0.500 sec
0
5
10
15
20
25
10.0
0.0
-10.0
-20.0
-30.0
-40.0
-50.0
-60.0
-70.0
-80.0

Figure 5D

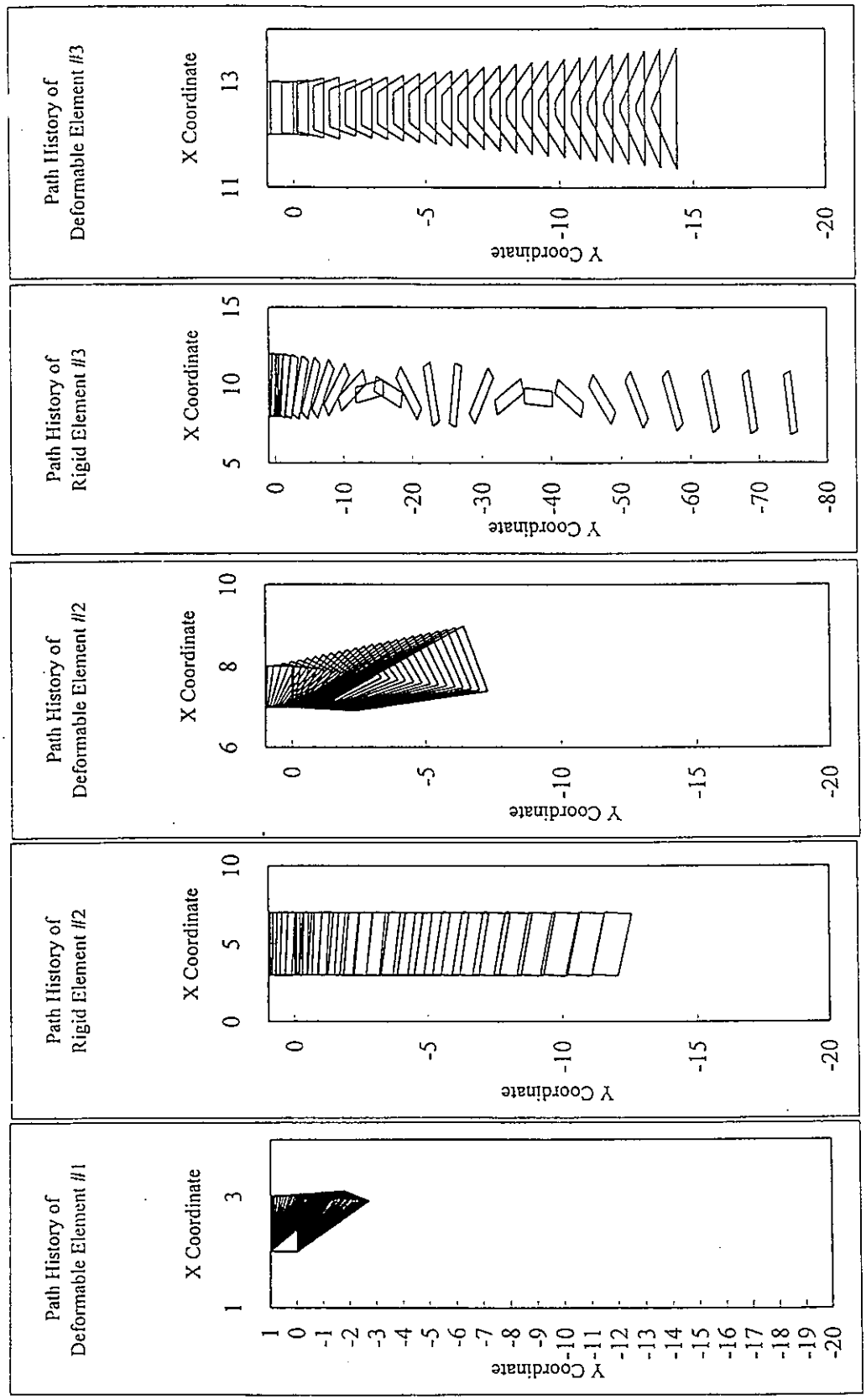

Figure 6. Trajectories of the Elements

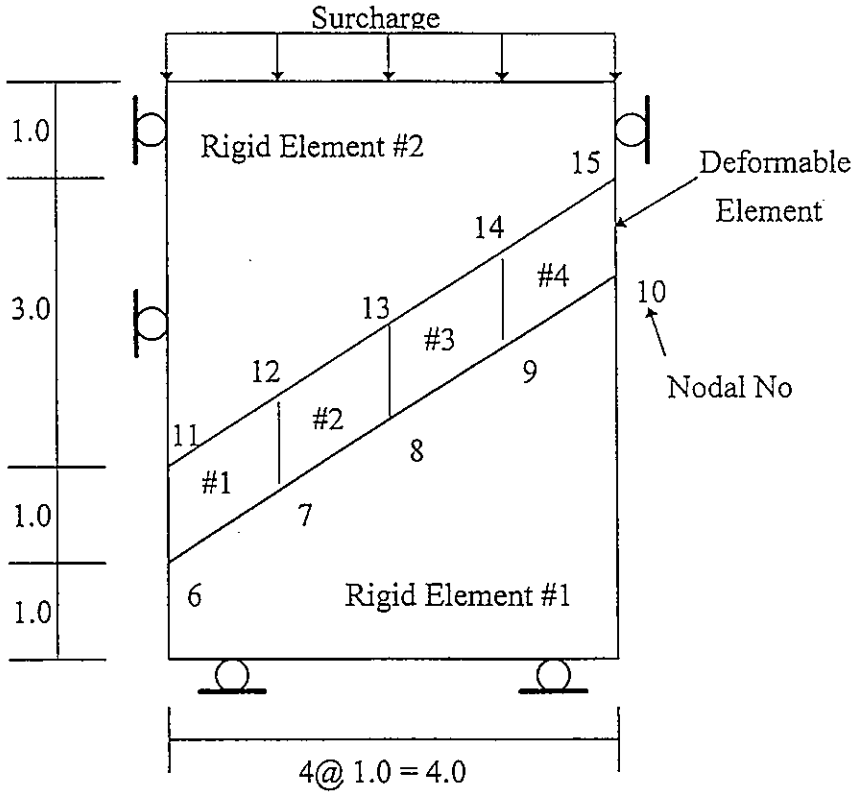

Load History:

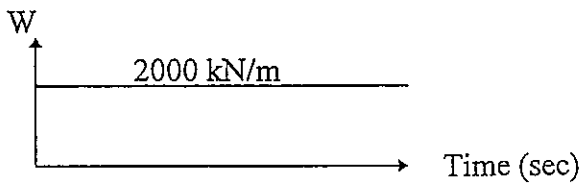

Material Properties:

$E = 10000 \text{ kN / m}^2$

$\nu = 0.3$

$\rho = 10.0 \text{ kN} - \text{sec}^2 / \text{m}^4$

$c = 100.0 \text{ kN / m}^2$

$\phi = 0.0 \text{deg}$

$f_r = 10.0 \text{ kN / m}^2$

Other Data:

$\alpha = 10000.0 \text{ sec}^{-1}$

$\Delta t = 0.00001 \text{ sec}$

$g = 10.0 \text{ m / sec}^2$

Figure 7. An Inclined Bedding in Shear

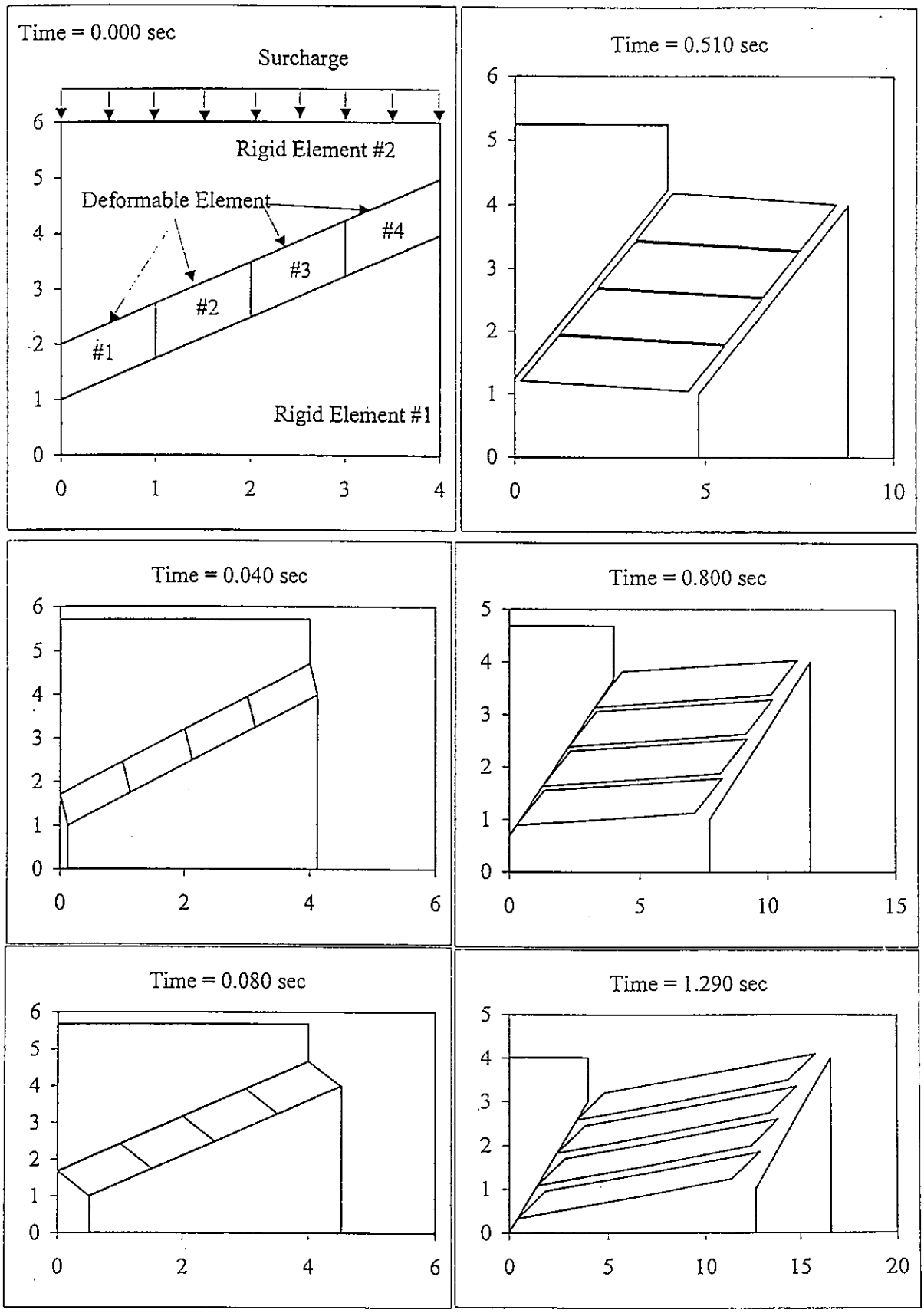

Figure 8 Time Histories of the Structural Configuration

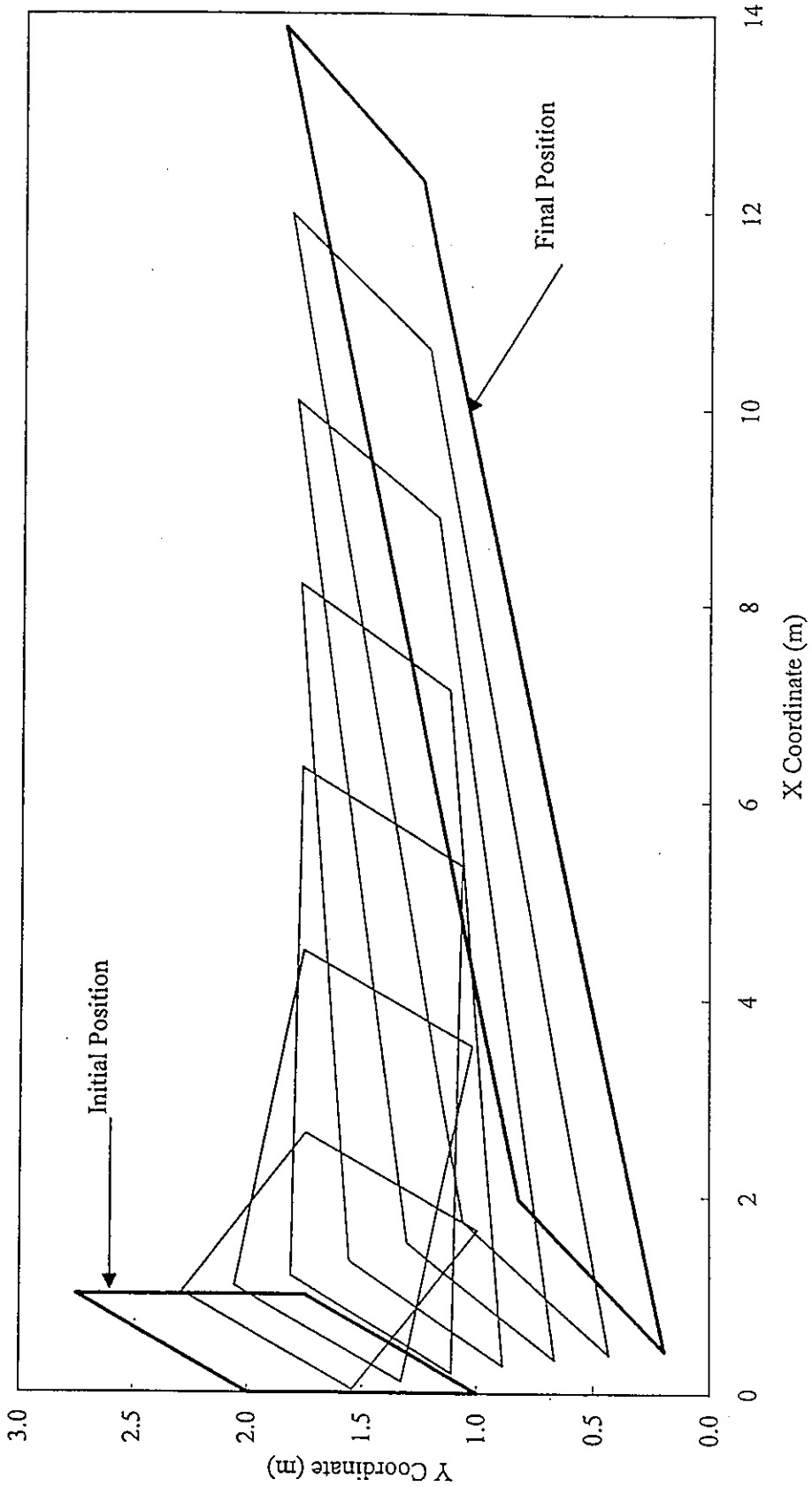

Figure 9. Deformation History of A Continuum Element

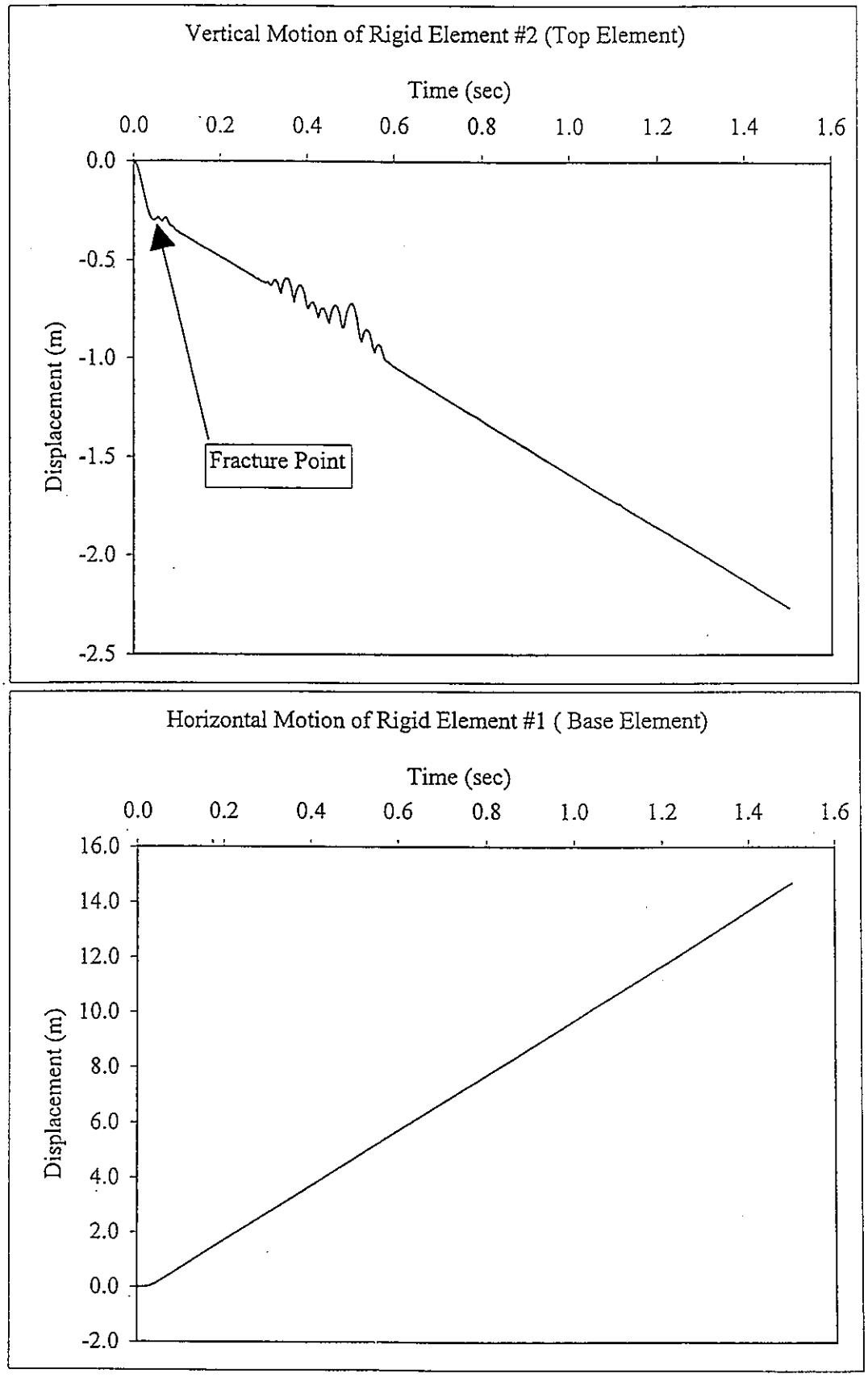

Figure 10. Displacement History of the Rigid Bodies

New Finite Elements for the Analysis of Progressive Discontinuity Problems Based on the Finite Volume Concepts

Hiroshi Takeda
Department of System and Control, Hosei University

Morito Kusabuka
Department of Civil Engineering, Hosei University

Norio Takeuchi
Department of Civil Engineering, Meisei University

Kazuo Sato
Computer Technology System Office, Power and Nuclear Fuel Development Corporation

ABSTRACT: We present new finite elements for the analysis of general solid mechanics problems with/without progressive discontinuity phenomena. Basic formulation of the proposed elements is based on the discrete control surface integration rather the finite element volume integration to simulate natural discontinuity effects. The first part of this paper will be concerned general systematic formulation of the finite volume method and finite volume based finite element method for the solid mechanics problems. As an example of the practical implementations typical triangular element for the two dimensional problems is presented in the second part of this paper. In the last part of this paper, we will extend the proposed method to the meshless analysis.

1. General formulation of the finite volume method for the solid mechanics

1.1. Governing equations and the weak form. Governing equations of the elastic solid are given by

$$\frac{\partial \sigma_{ij}}{\partial x_j} + f_i = 0 \tag{1.1}$$

$$\sigma_{ij} = E_{ijkl}\varepsilon_{kl} \tag{1.2}$$

$$\varepsilon_{kl} = \frac{1}{2}\left(\frac{\partial u_k}{\partial x_l} + \frac{\partial u_l}{\partial x_k}\right) \tag{1.3}$$

where x_j is the material point, σ_{ij} is the stress field, f_i is the body force, E_{ijkl} is the elastic constitutive tensor, ε_{kl} is the strain field and u_i is the displacement field. The weak form of the equilibrium equation (1.1) is expressed by

$$\int_\Omega \overset{*}{u}_i \left(\frac{\partial \sigma_{ij}}{\partial x_j} + f_i\right) d\Omega = 0 \tag{1.4}$$

where $\overset{*}{u}_i$ is arbitrary weight and Ω is the domain of the problem.

1.2. Domain discretization. The domain Ω will be discretized by the sub-domains $\Omega^{(r)}$ as follows

$$\Omega = \bigcup_{r=1}^{R} \Omega^{(r)} : \quad where \quad \Omega^{(r)} \bigcap \Omega^{(q)} = 0 \quad (r \neq q) \tag{1.5}$$

where R is the total number of sub-domains. The discrete counterpart of the weak form (1.4) will be given by

$$\sum_{r=1}^{R} \left(\int_{\Omega^{(r)}} \overset{*}{u}_i \frac{\partial \sigma_{ij}}{\partial x_j} d\Omega + \int_{\Omega^{(r)}} \overset{*}{u}_i \, f_i \, d\Omega \right) = 0. \tag{1.6}$$

Assuming the symmetry of the stress tensor, $\sigma_{ij} = \sigma_{ji}$, and integrating by parts, the first term in the left hand side of (1.6) yields the following equations:

$$\begin{aligned}\int_{\Omega^{(r)}} \overset{*}{u}_i \frac{\partial \sigma_{ij}}{\partial x_j} d\Omega &= \int_{\Omega^{(r)}} \frac{\partial}{\partial x_j}\left(\overset{*}{u}_i\, \sigma_{ij}\right) d\Omega - \int_{\Omega^{(r)}} \frac{\partial \overset{*}{u}_i}{\partial x_j} \sigma_{ij}\, d\Omega \\ &= \oint_{\Gamma^{(r)}} \overset{*}{u}_i\, \sigma_{ij} n_j\, d\Gamma - \int_{\Omega^{(r)}} \frac{\partial \overset{*}{u}_i}{\partial x_j} \sigma_{ij}\, d\Omega \\ &= \oint_{\Gamma^{(r)}} \overset{*}{u}_i\, \sigma_{ij} n_j\, d\Gamma - \int_{\Omega^{(r)}} \overset{*}{\varepsilon}_{ij}\, \sigma_{ij}\, d\Omega \end{aligned} \tag{1.7}$$

where $\Gamma^{(r)}$ is the closed boundary of the sub-domain $\Omega^{(r)}$ and

$$\overset{*}{\varepsilon}_{ij} = \frac{1}{2}\left(\frac{\partial \overset{*}{u}_i}{\partial x_j} + \frac{\partial \overset{*}{u}_j}{\partial x_i}\right). \tag{1.8}$$

Substituting (1.7) into (1.6), we will obtain the discretized version of the weak form of the equilibrium equation:

$$\sum_{r=1}^{R}\left(-\int_{\Omega^{(r)}} \overset{*}{\varepsilon}_{ij}\, \sigma_{ij}\, d\Omega + \oint_{\Gamma^{(r)}} \overset{*}{u}_i\, \sigma_{ij} n_j\, d\Gamma + \int_{\Omega^{(r)}} \overset{*}{u}_i\, f_i\, d\Omega\right) = 0. \tag{1.9}$$

For the latter development, we introduce the following one dimensional arrays to the second order tensor quantities:

$$\{\sigma\} = \begin{Bmatrix} \sigma_{11} \\ \sigma_{22} \\ \sigma_{33} \\ \sigma_{12} \\ \sigma_{23} \\ \sigma_{31} \end{Bmatrix} = \begin{Bmatrix} \sigma_x \\ \sigma_y \\ \sigma_z \\ \tau_{xy} \\ \tau_{yz} \\ \tau_{zx} \end{Bmatrix} \; ; \; \{\varepsilon\} = \begin{Bmatrix} \varepsilon_{11} \\ \varepsilon_{22} \\ \varepsilon_{33} \\ \varepsilon_{12} + \varepsilon_{21} \\ \varepsilon_{23} + \varepsilon_{32} \\ \varepsilon_{31} + \varepsilon_{13} \end{Bmatrix} = \begin{Bmatrix} \varepsilon_x \\ \varepsilon_y \\ \varepsilon_z \\ \gamma_{xy} \\ \gamma_{yz} \\ \gamma_{zx} \end{Bmatrix} \tag{1.10}$$

and one dimensional arrays to the vector quantities:

$$\{\mathbf{f}\} = \begin{Bmatrix} f_1 \\ f_2 \\ f_3 \end{Bmatrix} = \begin{Bmatrix} f_x \\ f_y \\ f_z \end{Bmatrix} \; ; \; \{\mathbf{u}\} = \begin{Bmatrix} u_1 \\ u_2 \\ u_3 \end{Bmatrix} = \begin{Bmatrix} u_x \\ u_y \\ u_z \end{Bmatrix}. \tag{1.11}$$

Applying above notations, the governing equations of the elastic solid is presented by

$$[\mathbf{L}]^T\{\sigma\} + \{\mathbf{f}\} = \{\mathbf{0}\} \tag{1.12}$$

$$\{\sigma\} = [\mathbf{E}]\{\varepsilon\} \tag{1.13}$$

$$\{\varepsilon\} = [\mathbf{L}]\{\mathbf{u}\} \tag{1.14}$$

where

$$[\mathbf{L}] = \begin{bmatrix} \frac{\partial}{\partial x} & 0 & 0 \\ 0 & \frac{\partial}{\partial y} & 0 \\ 0 & 0 & \frac{\partial}{\partial z} \\ \frac{\partial}{\partial y} & \frac{\partial}{\partial x} & 0 \\ 0 & \frac{\partial}{\partial z} & \frac{\partial}{\partial y} \\ \frac{\partial}{\partial z} & 0 & \frac{\partial}{\partial x} \end{bmatrix} \tag{1.15}$$

and $[\mathbf{E}]$ is the constitutive matrix containing the appropriate material properties. In the case of isotropic elastic material, the constitutive matrix $[\mathbf{E}]$ can be written by

$$[\mathbf{E}] = \begin{bmatrix} \bar{E} & \bar{\nu}\bar{E} & \bar{\nu}\bar{E} & 0 & 0 & 0 \\ \bar{\nu}\bar{E} & \bar{E} & \bar{\nu}\bar{E} & 0 & 0 & 0 \\ \bar{\nu}\bar{E} & \bar{\nu}\bar{E} & \bar{E} & 0 & 0 & 0 \\ 0 & 0 & 0 & G & 0 & 0 \\ 0 & 0 & 0 & 0 & G & 0 \\ 0 & 0 & 0 & 0 & 0 & G \end{bmatrix} \tag{1.16}$$

where

$$\bar{E} = \frac{E(1-\nu)}{(1+\nu)(1-2\nu)}\,; \qquad \bar{\nu} = \frac{\nu}{1-\nu}\,; \qquad G = \frac{E}{2(1+\nu)}$$

where E is the elastic constant and ν is the Poisson's ratio.

Using boldface symbols, the weak form (1.9) is presented by

$$\boxed{\sum_{r=1}^{R}\left(-\int_{\Omega^{(r)}}\{\overset{*}{\boldsymbol{\varepsilon}}\}^T\{\boldsymbol{\sigma}\}\,d\Omega + \oint_{\Gamma^{(r)}}\{\overset{*}{\mathbf{u}}\}^T[\mathbf{n}]\{\boldsymbol{\sigma}\}\,d\Gamma + \int_{\Omega^{(r)}}\{\overset{*}{\mathbf{u}}\}^T\{\mathbf{f}\}\,d\Omega\right) = 0} \tag{1.17}$$

where we consider the following rearrangement:

$$\begin{aligned}
\sigma_{ij}n_j &= \begin{bmatrix} \sigma_x & \tau_{xy} & \tau_{zx} \\ \tau_{xy} & \sigma_y & \tau_{yz} \\ \tau_{zx} & \tau_{yz} & \sigma_z \end{bmatrix} \begin{Bmatrix} n_x \\ n_y \\ n_z \end{Bmatrix} \\
&= \begin{Bmatrix} \sigma_x n_x + \tau_{xy} n_y + \tau_{zx} n_z \\ \tau_{xy} n_x + \sigma_y n_y + \tau_{yz} n_z \\ \tau_{zx} n_x + \tau_{yz} n_y + \sigma_z n_z \end{Bmatrix} \\
&= \begin{bmatrix} n_x & 0 & 0 & n_y & 0 & n_z \\ 0 & n_y & 0 & n_x & n_z & 0 \\ 0 & 0 & n_z & 0 & n_y & n_x \end{bmatrix} \begin{Bmatrix} \sigma_x \\ \sigma_y \\ \sigma_z \\ \tau_{xy} \\ \tau_{yz} \\ \tau_{zx} \end{Bmatrix} \\
&= [\mathbf{n}]\{\boldsymbol{\sigma}\}.
\end{aligned} \tag{1.18}$$

1.3. **Classical finite volume method.** In this section, we will present a general formulation of the finite volume method for the solid mechanics problems under considering the computer implementation.

In the finite volume method, each nodal point I has the corresponding sub-domain or control volume $\Omega^{(I)}$ (Fig.1) and weighting function is assumed *to be constant* over the control volume (Fig.2). The weak

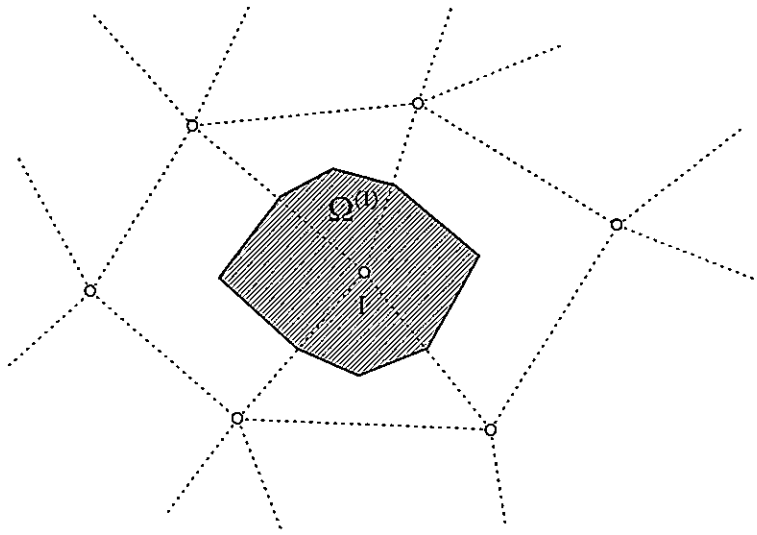

FIGURE 1. Nodal point I and corresponding control volume $\Omega^{(I)}$

form (1.17) can be rewritten for the finite volume method by the following equations:

$$\boxed{\sum_{I=1}^{N}\left(\oint_{\Gamma^{(I)}}\{\overset{*}{\mathbf{u}}\}^T[\mathbf{n}]\{\boldsymbol{\sigma}\}\,d\Gamma + \int_{\Omega^{(I)}}\{\overset{*}{\mathbf{u}}\}^T\{\mathbf{f}\}\,d\Omega\right) = 0} \tag{1.19}$$

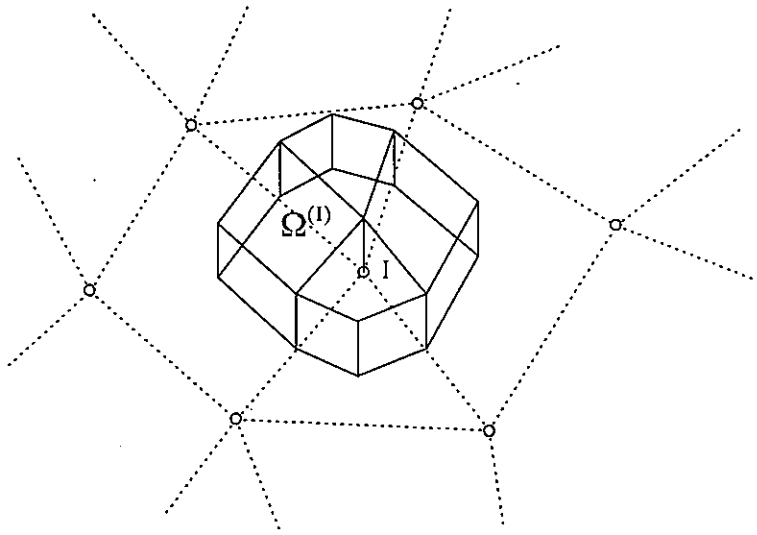

FIGURE 2. Weighting function on the control volume $\Omega^{(I)}$ of the nodal point I

where N is number of total nodes in the domain. Weighting function $\{\overset{*}{\mathbf{u}}\}$ can be replaced by the nodal value $\{\overset{*}{\mathbf{u}}_I\}$ at node I. Therefore the weak form (1.19) can be replaced by

$$\sum_{I=1}^{N}\{\overset{*}{\mathbf{u}}_I\}^T\left(\oint_{\Gamma^{(I)}}[\mathbf{n}]\{\boldsymbol{\sigma}\}\,d\Gamma+\int_{\Omega^{(I)}}\{\mathbf{f}\}\,d\Omega\right)=0. \tag{1.20}$$

Displacements $\{\mathbf{u}\}$ on the boundary $\Gamma^{(I)}$ will be interpolate by displacements $\{\mathbf{u}^{<I>}\}$ at nodal- and the neighbor nodal-displacements:

$$\{\mathbf{u}\}=[\mathbf{N}]\{\mathbf{u}^{<I>}\} \tag{1.21}$$

where $[\mathbf{N}]$ is the interpolation function of the control surface. Applying the strain–displacement relation (1.14), strain tensor will be represented by the displacement array $\{\mathbf{u}^{<I>}\}$ as follows:

$$\{\varepsilon\}=[\mathbf{L}]\{\mathbf{u}\}=[\mathbf{L}][\mathbf{N}]\{\mathbf{u}^{<I>}\}=[\mathbf{B}]\{\mathbf{u}^{<I>}\}. \tag{1.22}$$

where $[\mathbf{B}]$ is the strain-displacement matrix of the control surface. Substituting (1.22) and (1.13) into (1.20), the finite volume weak form of the equilibrium equations will be presented by

$$\sum_{I=1}^{N}\{\overset{*}{\mathbf{u}}_I\}^T\left(\oint_{\Gamma^{(I)}}[\mathbf{n}][\mathbf{E}][\mathbf{B}]\,d\Gamma\{\mathbf{u}^{<I>}\}+\int_{\Omega^{(I)}}\{\mathbf{f}\}\,d\Omega\right)=0. \tag{1.23}$$

Using mesh topology, nodal weighting function $\{\overset{*}{\mathbf{u}}_I\}$ and the displacement array $\{\mathbf{u}^{<I>}\}$ can be represented by the corresponding global nodal arrays $\{\overset{\hat{*}}{\mathbf{U}}\}$ and $\{\hat{\mathbf{U}}\}$ respectively:

$$\{\overset{*}{\mathbf{u}}_I\}=[\mathcal{I}^{(I)}]\{\overset{\hat{*}}{\mathbf{U}}\}\ ;\ \{\mathbf{u}^{<I>}\}=[\mathcal{A}^{<I>}]\{\hat{\mathbf{U}}\} \tag{1.24}$$

where Ith vector component of $\{\overset{\hat{*}}{\mathbf{U}}\}$ and $\{\hat{\mathbf{U}}\}$ are weighting functions $\{\overset{*}{\mathbf{u}}_I\}$ and displacement vector $\{\mathbf{u}_I\}$ at node I respectively, and $[\mathcal{I}^{(I)}]$ and $[\mathcal{A}^{<I>}]$ are boolian matrices whose components are unity or zero. Substituting (1.24) into (1.23), the global version of the weak form can be represented by

$$\{\overset{\hat{*}}{\mathbf{U}}\}^T\left[\sum_{I=1}^{N}[\mathcal{I}^{(I)}]^T\left(\oint_{\Gamma^{(I)}}[\mathbf{n}][\mathbf{E}][\mathbf{B}]\,d\Gamma[\mathcal{A}^{<I>}]\{\hat{\mathbf{U}}\}\ +\int_{\Omega^{(I)}}\{\mathbf{f}\}\,d\Omega\right)\right]=0. \tag{1.25}$$

Since $\{\overset{\hat{*}}{\mathbf{U}}\}$ is an arbitrary nodal array of the weighting functions, one can get following relation:

$$\sum_{I=1}^{N}[\mathcal{I}^{(I)}]^T\left(\oint_{\Gamma^{(I)}}[\mathbf{n}][\mathbf{E}][\mathbf{B}]\,d\Gamma[\mathcal{A}^{<I>}]\{\hat{\mathbf{U}}\}\ +\int_{\Omega^{(I)}}\{\mathbf{f}\}\,d\Omega\right)=\{\mathbf{0}\}. \tag{1.26}$$

(1.26) can be rewritten as

$$\boxed{[\hat{\mathbf{K}}]\{\hat{\mathbf{U}}\} = \{\hat{\mathbf{P}}\}} \tag{1.27}$$

where

$$[\hat{\mathbf{K}}] = \sum_{I=1}^{N} \left([\mathcal{I}^{(I)}]^T [\mathbf{k}^{(I)}] [\mathcal{A}^{<I>}] \right) \tag{1.28}$$

$$\{\hat{\mathbf{P}}\} = \sum_{I=1}^{N} \left([\mathcal{I}^{(I)}]^T \{\mathbf{p}^{(I)}\} \right) \tag{1.29}$$

and

$$[\mathbf{k}^{(I)}] = -\oint_{\Gamma^{(I)}} [\mathbf{n}][\mathbf{E}][\mathbf{B}]\, d\Gamma \tag{1.30}$$

$$\{\mathbf{p}^{(I)}\} = \int_{\Omega^{(I)}} \{\mathbf{f}\}\, d\Omega \tag{1.31}$$

Above development shows that the governing equation of the finite volume method for the elastic problems results in the discretized linear algebraic system of equations (1.24). (1.28) means that the coefficient matrix in the left hand side (global stiffness matrix) $[\hat{\mathbf{K}}]$ can be assembled by each *nodal* contribution $[\mathbf{k}^{(I)}]$ (nodal stiffness matrix). From (1.29), the known vector in the right hand side (global load vector) $\{\hat{\mathbf{P}}\}$ can be also assembled by the nodal contribution $\{\mathbf{p}^{(I)}\}$ (nodal load vector). (1.31) means that the nodal stiffness matrix $[\mathbf{k}^{(I)}]$ can be evaluated *by integrating around the boundary* (control surface) $\Gamma^{(I)}$ of the control volue of the node I. From (1.30), nodal load vecor $\{\mathbf{p}^{(I)}\}$ can be evaluated by integrating the control volume $\Omega^{(I)}$ of the node I.

1.4. **Finite volume based finite element method.** In this section, we will present a general formulation of the finite volume method in the finite element context.

Here we assume that the total domain Ω can be discretized by finite number of element $\Omega^{(e)}$:

$$\Omega = \bigcup_{e=1}^{M} \Omega^{(e)} : \quad where \quad \Omega^{(e)} \bigcap \Omega^{(l)} = 0 \quad (e \neq l) \tag{1.32}$$

where M is total number of finite elements.

Introducing the finite element $\Omega^{(e)}$, control volume $\Omega^{(I)}$ and the boundary $\Gamma^{(I)}$ of node I are expressed as following relation (Fig. 3).

$$\Omega^{(I)} = \bigcup_{e=1}^{m_e^{(I)}} \Omega_I^{(e)} \quad ; \quad \Gamma^{(I)} = \bigcup_{e=1}^{m_e^{(I)}} \Gamma_I^{(e)} \tag{1.33}$$

where $m_e^{(I)}$ is the number of finite elements connected node (I), $\Omega_I^{(e)}$ is the intersection of the control volume $\Omega^{(I)}$ of node I and the finite element $\Omega^{(e)}$, $\Omega_I^{(e)} = \Omega_{(I)} \bigcap \Omega^{(e)}$, and $\Gamma_I^{(e)}$ is the intersection of the closed boundary $\Gamma^{(I)}$ of the control volume $\Omega^{(I)}$ and the finite element $\Omega^{(e)}$, $\Gamma_I^{(e)} = \Gamma_{(I)} \bigcap \Omega^{(e)}$.

Applying above notations, the finite volume version of the weak form (1.19) is rearranged as:

$$\sum_{I=1}^{N} \left[\sum_{e=1}^{m_e^{(e)}} \left(\int_{\Gamma_I^{(e)}} \{\overset{*}{\mathbf{u}}\}^T [\mathbf{n}] \{\boldsymbol{\sigma}\}\, d\Gamma + \int_{\Omega_I^{(e)}} \{\overset{*}{\mathbf{u}}\}^T \{\mathbf{f}\}\, d\Omega \right) \right] = 0 \tag{1.34}$$

(1.34) means that the weak form can be evaluated by assembling nodal contribution which is constructed from element sub-contributions. From the finite element view point, this assembling scheme can be

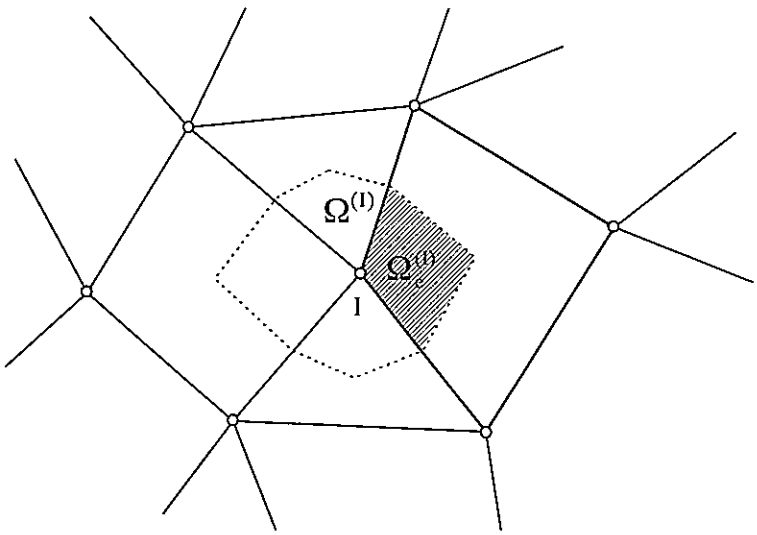

FIGURE 3. **Contribution of finite element (e) to I-th nodal control volume : $\Omega_e^{(I)}$**

modified to the *element wise* assembly form the *nodal wise* assembly as:

$$\boxed{\sum_{e=1}^{M}\left[\sum_{i=1}^{n_e}\left(\int_{\Gamma_i^{(e)}}\{\overset{*}{\mathbf{u}}\}^T[\mathbf{n}]\{\boldsymbol{\sigma}\}\,d\Gamma+\int_{\Omega_i^{(e)}}\{\overset{*}{\mathbf{u}}\}^T\{\mathbf{f}\}\,d\Omega\right)\right]=0} \tag{1.35}$$

where n_e is the number of nodes of finite element (e), $\Omega_i^{(e)}$ is the contribution of element (e) to the control volume of i-th element node, $\Gamma_i^{(e)}$ is the boundary of $\Omega_i^{(e)}$.

For the domain $\Omega_i^{(e)}$ and the boundary $\Gamma_i^{(e)}$, the weighting function is equal to the weighting function at i-th element node as:

$$\{\overset{*}{\mathbf{u}}\}=\{\overset{*}{\mathbf{u}}_i^{(e)}\}. \tag{1.36}$$

Introducing finite element shape functions $[\mathbf{N}]$, displacement vector on the boundary $\Gamma_i^{(e)}$ can be interpolated by the displacement vector at nodes of element (e):

$$\{\mathbf{u}\}=[\mathbf{N}]\{\mathbf{u}^{(e)}\} \tag{1.37}$$

where $\{\mathbf{u}^{(e)}\}$ is the one dimensional array which constituents are element nodal displacement vectors. From above relation, strain tensor on the boundary $\Gamma_i^{(e)}$ will be

$$\{\boldsymbol{\varepsilon}\}=[\mathbf{L}]\{\mathbf{u}\}=[\mathbf{L}][\mathbf{N}]\{\mathbf{u}^{(e)}\}=[\mathbf{B}]\{\mathbf{u}^{(e)}\} \tag{1.38}$$

where $[\mathbf{B}]$ is the standard finite element strain–displacement matrix. Applying the constitutive relations (1.13), stress tensor $\{\boldsymbol{\sigma}\}$ can be represented as:

$$\{\boldsymbol{\sigma}\}=[\mathbf{E}][\mathbf{B}]\{\mathbf{u}^{(e)}\} \tag{1.39}$$

Substituting (1.36) and (1.39) into (1.35), we will get following relations:

$$\sum_{e=1}^{M}\left[\sum_{i=1}^{n_e}\{\overset{*}{\mathbf{u}}_i^{(e)}\}^T\left(\int_{\Gamma_i^{(e)}}[\mathbf{n}][\mathbf{E}][\mathbf{B}]\,d\Gamma\{\mathbf{u}^{(e)}\}+\int_{\Omega_i^{(e)}}\{\mathbf{f}\}\,d\Omega\right)\right]=0 \tag{1.40}$$

Introducing the notations

$$[\mathbf{k}_i^{(e)}]=-\int_{\Gamma_i^{(e)}}[\mathbf{n}][\mathbf{E}][\mathbf{B}]\,d\Gamma \tag{1.41}$$

$$\{\mathbf{p}_i^{(e)}\}=\int_{\Omega_i^{(e)}}\{\mathbf{f}\}\,d\Omega \tag{1.42}$$

(1.40) can be rewritten as:

$$\sum_{e=1}^{M}\left[\sum_{i=1}^{n_e}\{\overset{*}{\mathbf{u}}_i^{(e)}\}^T\left(-[\mathbf{k}_i^{(e)}]\{\mathbf{u}^{(e)}\}+\{\mathbf{p}_i^{(e)}\}\right)\right]=0. \tag{1.43}$$

Weighting functions $\{\overset{*}{\mathbf{u}}_i^{(e)}\}$ at i-th element node can be picked up form the one dimensional array $\{\overset{*}{\mathbf{u}}^{(e)}\}$ of the element nodal weighting functions which has similar arrangement to the element nodal displacement array $\{\mathbf{u}^{(e)}\}$:

$$\{\overset{*}{\mathbf{u}}_i^{(e)}\}=[\mathbf{I}_i]\{\overset{*}{\mathbf{u}}^{(e)}\}. \tag{1.44}$$

Substituting (1.44) into (1.43), we can get the relation

$$\sum_{e=1}^{M}\left[\{\overset{*}{\mathbf{u}}^{(e)}\}^T\sum_{i=1}^{n_e}\left(-[\mathbf{I}_i]^T[\mathbf{k}_i^{(e)}]\{\mathbf{u}^{(e)}\}+[\mathbf{I}_i]^T\{\mathbf{p}_i^{(e)}\}\right)\right]=0. \tag{1.45}$$

Introducing notations

$$\boxed{\begin{aligned}[\mathbf{k}^{(e)}] &= \sum_{i=1}^{n_e}\left([\mathbf{I}_i]^T[\mathbf{k}_i^{(e)}]\right) && (1.46)\\ \{\mathbf{p}^{(e)}\} &= \sum_{i=1}^{n_e}\left([\mathbf{I}_i]^T\{\mathbf{p}_i^{(e)}\}\right) && (1.47)\end{aligned}}$$

(1.45) can be rewritten as:

$$\sum_{e=1}^{M}\{\overset{*}{\mathbf{u}}^{(e)}\}^T\left(-[\mathbf{k}^{(e)}]\{\mathbf{u}^{(e)}\}+\{\mathbf{p}^{(e)}\}\right)=0. \tag{1.48}$$

Using mesh topology, element nodal displacement $\{\mathbf{u}^{(e)}\}$ and element nodal weighting functions $\{\overset{*}{\mathbf{u}}^{(e)}\}$ can be picked up from corresponding global nodal arrays $\{\hat{\mathbf{U}}\}$ and $\{\hat{\overset{*}{\mathbf{U}}}\}$ as:

$$\{\mathbf{u}^{(e)}\}=[\mathcal{A}^{(e)}]\{\hat{\mathbf{U}}\}\ ;\ \{\overset{*}{\mathbf{u}}^{(e)}\}=[\mathcal{A}^{(e)}]\{\hat{\overset{*}{\mathbf{U}}}\} \tag{1.49}$$

where $[\mathcal{A}^{(e)}]$ is the boolian matrix which transforms the global nodal array to the corresponding element nodal aray. Substituting (1.49) into (1.48), the global version of the weak form can be represented by

$$\{\hat{\overset{*}{\mathbf{U}}}\}^T\left[-\sum_{e=1}^{M}\left([\mathcal{A}^{(e)}]^T[\mathbf{k}^{(e)}][\mathcal{A}^{(e)}]\right)\{\hat{\mathbf{U}}\}+\sum_{e=1}^{M}\left([\mathcal{A}^{(e)}]^T\{\mathbf{p}^{(e)}\}\right)\right]=0 \tag{1.50}$$

Considering $\{\hat{\overset{*}{\mathbf{U}}}\}$ is an arbitrary vector, we will get following representations

$$\boxed{[\hat{\mathbf{K}}]\{\hat{\mathbf{U}}\}=\{\hat{\mathbf{P}}\}} \tag{1.51}$$

where

$$\boxed{\begin{aligned}[\hat{\mathbf{K}}] &= \sum_{e=1}^{M}\left([\mathcal{A}^{(e)}]^T[\mathbf{k}^{(e)}][\mathcal{A}^{(e)}]\right) && (1.52)\\ \{\hat{\mathbf{P}}\} &= \sum_{e=1}^{M}\left([\mathcal{A}^{(e)}]^T\{\mathbf{p}^{(e)}\}\right) && (1.53)\end{aligned}}$$

Above development shows that governing equations of the finite volume method with finite element concepts results in the discretized linear algebraic system of equations (1.51) as the classical finite volume method. However the coefficient matrix in the left hand side, global stiffness matrix, $[\hat{\mathbf{K}}]$ can be assembled by each *element* contribution $[\mathbf{k}^{(e)}]$ rather than the nodal contribution as shown in (1.52). The known vector in right hand side, global load vector, $\{\hat{\mathbf{P}}\}$ is also assembled by element wise scheme as shown in

(1.53). From (1.46) and (1.41), the element stiffness matrix $[\mathbf{k}^{(e)}]$ can be evaluated by *integrating around the boundary* $\Gamma^{(e)i}$ rather than integrating over the domain $\Omega^{(e)}$ in the standard finite element method. From (1.47) and (1.42), the element load vector $\{\mathbf{p}^{(e)}\}$ can be evaluated by integrating over the domain $\Omega^{(e)}$ as the standard finite element method.

Progressive discontinuity problems, such as slip phenomena in rocks and crack propagating phenomena in metal sheets, can be simulated naturally by the proposed formulation because of surface integration scheme in stiffness evaluation.

2. Three node triangle element

As an simple example of proposed formulation for the practical implementation, we will show that three node triangle element of the proposed formulation is exactly equivalent to standard finite element version of the triangle element.

2.1. **Geometry and reference number.** In this section, we will use following conventions: element nodes will be referred by $1, 2$ and 3, inter-element boundaries will be referred by $\underline{1}, \underline{2}$ and $\underline{3}$, internal point such as centroid is shown by the symbol O, the line from O to the mid-point of inter-element boundary $\underline{i}$ will be referred by h_i and ortho-normal unit vector to line h_i is referred by $\{\mathbf{n}_i\}$(see Fig.4).

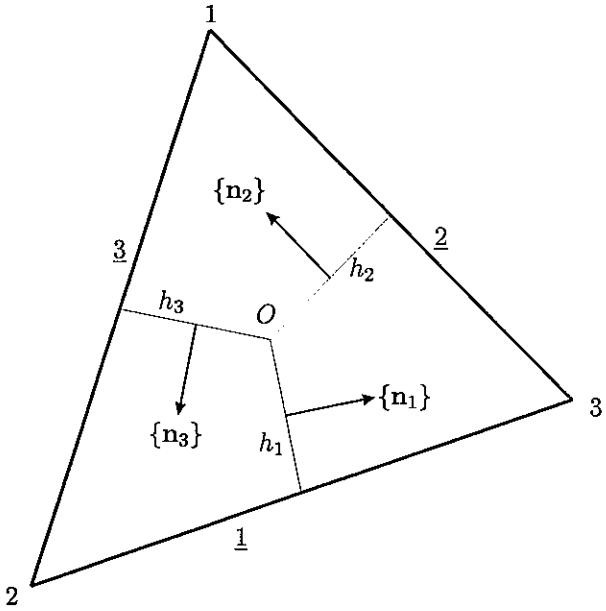

FIGURE 4. Triangle element and references

2.2. **Element stiffness matrix.** the element stiffness matrix $[\mathbf{k}^{(e)}]$ is defined by (1.46) as:

$$[\mathbf{k}^{(e)}] = \sum_{i=1}^{3} \left([\mathbf{I}_i]^T [\mathbf{k}_i^{(e)}] \right) \tag{2.1}$$

If we define element nodal displacement array $\{\mathbf{u}^{(e)}\}$ as

$$\{\mathbf{u}^{(e)}\}^T = [u_1^e, v_1^e, u_2^e, v_2^e, u_3^e, v_3^e] \tag{2.2}$$

where u_i^e and v_i^e are x- and y-components of displacement vector at element node i respectively, and remembering that mapping $[\mathbf{I}_i]$ transforms the element nodal displacement array $\{\mathbf{u}^{(e)}\}$ to the displacement vector at element node i, we will obtain following relations:

$$[\mathbf{I}_1] = \begin{bmatrix} 1 & 0 & 0 & 0 & 0 & 0 \\ 0 & 1 & 0 & 0 & 0 & 0 \end{bmatrix} \tag{2.3a}$$

$$[\mathbf{I}_2] = \begin{bmatrix} 0 & 0 & 1 & 0 & 0 & 0 \\ 0 & 0 & 0 & 1 & 0 & 0 \end{bmatrix} \tag{2.3b}$$

$$[\mathbf{I}_3] = \begin{bmatrix} 0 & 0 & 0 & 0 & 1 & 0 \\ 0 & 0 & 0 & 0 & 0 & 1 \end{bmatrix} \tag{2.3c}$$

The element nodal contributions $[\mathbf{k}_i^{(e)}]$ to the element stiffness matrix $[\mathbf{k}^{(e)}]$ is defined by (1.41) as:

$$[\mathbf{k}_i^{(e)}] = -\int_{\Gamma_i^{(e)}} [\mathbf{n}][\mathbf{E}][\mathbf{B}] d\Gamma \tag{2.4}$$

where matrix $[\mathbf{n}]$ has components n_x, n_y of unit normal vector at the control sub-surface concerned with element node i and defined by following relation:

$$[\mathbf{n}] = \begin{bmatrix} n_x & 0 & n_y \\ 0 & n_y & n_x \end{bmatrix} \tag{2.5}$$

In accordance with that the control sub-surface of element node i is consist of line segments h_j, h_k, where

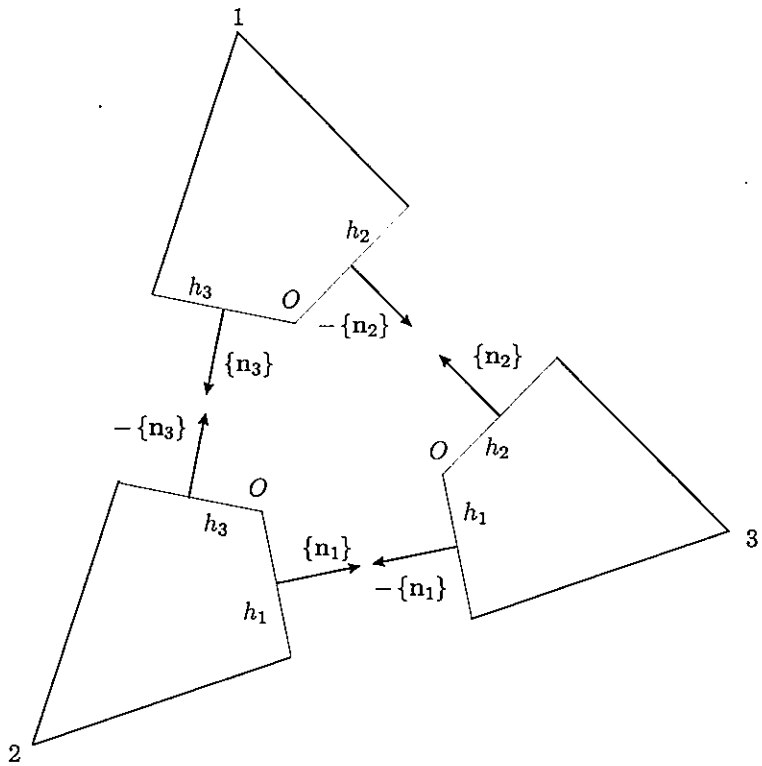

FIGURE 5. Element nodes and corresponding control sub-surfaces

i, j and k are permutations, as shown in Fig.5 and assuming constant material and strain fields, element nodal contribution $[\mathbf{k}_i^{(e)}]$ to the element stiffness matrix $[\mathbf{k}^{(e)}]$ can be obtained by

$$[\mathbf{k}_i^{(e)}] = -\int_{\Gamma_i^{(e)}} [\mathbf{n}] d\Gamma\, [\mathbf{E}][\mathbf{B}] = (h_j[\mathbf{n}_j] - h_k[\mathbf{n}_k])\, [\mathbf{E}][\mathbf{B}] = [\mathbf{A}_i][\mathbf{E}][\mathbf{B}] \tag{2.6}$$

in which if we define one dimensional strain array $\{\varepsilon\}$ as

$$\{\varepsilon\}^T = [\varepsilon_x, \varepsilon_y, \gamma_{xy}] \tag{2.7}$$

and applying the standard constant strain field to the element, strain–displacement matrix $[\mathbf{B}]$ will be defined by

$$[\mathbf{B}] = \frac{1}{2\Delta} \begin{bmatrix} b_1 & 0 & b_2 & 0 & b_3 & 0 \\ 0 & c_1 & 0 & c_2 & 0 & c_3 \\ c_1 & b_1 & c_2 & b_2 & c_3 & b_3 \end{bmatrix} \tag{2.8}$$

where

$$b_i = y_j - y_k \tag{2.9}$$

$$c_i = x_k - x_j \tag{2.10}$$

and Δ is area of the triangle and defined by

$$2\Delta = \begin{vmatrix} 1 & x_1 & y_1 \\ 1 & x_2 & y_2 \\ 1 & x_3 & y_3 \end{vmatrix} \tag{2.11}$$

If we will write the unit normal vector $\{\mathbf{n}_i\}$ as

$$\{\mathbf{n}_i\} = \begin{Bmatrix} n_x^{(i)} \\ n_y^{(i)} \end{Bmatrix} \tag{2.12}$$

the directional matrix $[\mathbf{n}_i]$ will be

$$[\mathbf{n}_i] = \begin{bmatrix} n_x^{(i)} & 0 & n_y^{(i)} \\ 0 & n_y^{(i)} & n_x^{(i)} \end{bmatrix}. \tag{2.13}$$

Referring Fig.4, unit normal vector of the control sub-surfaces can be presented by

$$\{\mathbf{n}_i\} = \begin{Bmatrix} n_x^{(i)} \\ n_y^{(i)} \end{Bmatrix} = \frac{1}{6h_i} \begin{Bmatrix} 2y_i - y_j - y_k \\ -2x_i + x_j + x_k \end{Bmatrix}. \tag{2.14}$$

Matrix $[\mathbf{A}_i]$ in (2.6) will be

$$[\mathbf{A}_i] = (h_j[\mathbf{n}_j] - h_k[\mathbf{n}_k]) = \frac{1}{2}\begin{bmatrix} y_j - y_k & 0 & x_k - x_j \\ 0 & x_k - x_j & y_j - y_k \end{bmatrix} = \frac{1}{2}\begin{bmatrix} b_i & 0 & c_i \\ 0 & c_i & b_i \end{bmatrix}. \tag{2.15}$$

From (2.1), the element stiffness matrix $[\mathbf{k}^{(e)}]$ can be obtained by

$$[\mathbf{k}^{(e)}] = \sum_{i=1}^{3} \left([\mathbf{I}_i]^T [\mathbf{k}_i^{(e)}] \right) = \left(\sum_{i=1}^{3} [\mathbf{I}_i]^T [\mathbf{A}_i] \right) [\mathbf{E}][\mathbf{B}] = [\mathbf{A}][\mathbf{E}][\mathbf{B}] \tag{2.16}$$

where

$$[\mathbf{A}] = \left(\sum_{i=1}^{3} [\mathbf{I}_i]^T [\mathbf{A}_i] \right) = \frac{1}{2}\begin{bmatrix} b_1 & 0 & c_1 \\ 0 & c_1 & b_1 \\ b_2 & 0 & c_2 \\ 0 & c_2 & b_2 \\ b_3 & 0 & c_3 \\ 0 & c_3 & b_3 \end{bmatrix} = [\mathbf{B}]^T \Delta \tag{2.17}$$

From the above consideration, we will get following final conclusion for the three node triangle element.

$$\boxed{[\mathbf{k}^{(e)}]_{(FVM)} = [\mathbf{A}][\mathbf{E}][\mathbf{B}] = [\mathbf{B}]^T[\mathbf{E}][\mathbf{B}]\Delta = [\mathbf{k}^{(e)}]_{(FEM)}} \tag{2.18}$$

where $[\mathbf{k}^{(e)}]_{(FVM)}$ is the stiffness matrix which is derived from the proposed formulation and $[\mathbf{k}^{(e)}]_{(FEM)}$ is the stiffness matrix which is derived from standard finite element formulation.

3. Extension to the meshless analysis

In this section a meshless procedure for the solid mechanics problems is presented. The method is based on the finite volume concepts to establish the simplest inter-nodes mechanical relations. Plane problems will be considered in the practical formulation.

3.1. Control volume and automatic assignment of control surface. Both finite element and finite volume analyses will force to engineers time consuming mesh topological data. Simplest formulation without mesh topological data will be proposed by the finite volume context.

In the beginning, domain occupation ratio Ξ_I of node I is defined by following relation(see Fig.6):

$$\Xi_I = \begin{cases} 1, & \text{if node } I \text{ is allocated in the domain} \\ \frac{1}{2}, & \text{if node } I \text{ is allocated on the edge boundary} \\ \frac{1}{4}, & \text{if node } I \text{ is allocated at edge corner} \end{cases} \tag{3.1}$$

Using the table of domain occupation ratios, we can estimate total number of control volumes as

$$\Xi = \sum_{I=1}^{N} \Xi_I \tag{3.2}$$

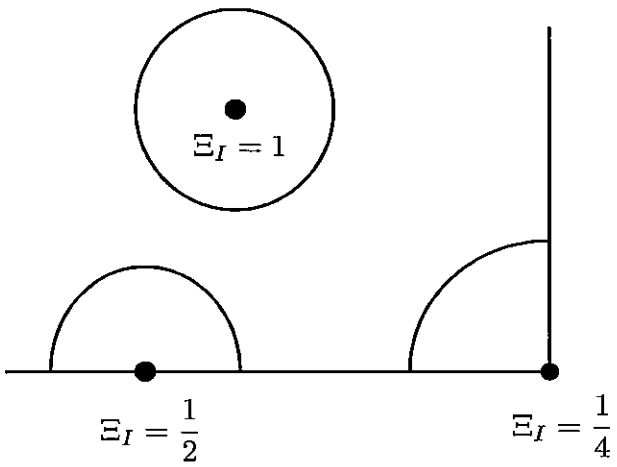

FIGURE 6. **Domain occupation ratio Ξ_I of node I**

where N is the total number of nodes. Mean control volume $\bar{\omega}$ will be evaluated by

$$\bar{\omega} = \frac{\Omega}{\Xi} \tag{3.3}$$

where Ω means total volume of the domain. Assuming circular shaped control volume, mean radius $\bar{r}$ of the control volume will be estimated by

$$\bar{r} = \alpha\sqrt{\frac{\bar{\omega}}{\pi}} \tag{3.4}$$

where α is an input parameter. Neighbor node J of the node I should be satisfied relation

$$\frac{||\mathbf{x}_I - \mathbf{x}_J||}{2} \leq \bar{r} \tag{3.5}$$

where $\mathbf{x}_I$ is a position vector of node I. Mean radius $\bar{r}_I$ of node I is defined by

$$\bar{r}_I = \frac{1}{M_I}\left(\sum_{J=1}^{M_I} \frac{||\mathbf{x}_I - \mathbf{x}_J||}{2}\right) \tag{3.6}$$

where M_I number of neighbor nodes of node I. The mean control volume $\bar{\Omega}_I$ which corresponding to the mean radius $\bar{r}_I$ is obtained by

$$\bar{\Omega}_I = \pi\, \bar{r}_I^2\, \Xi_I \tag{3.7}$$

However the sum of the mean control volume may be generally not equal of the volume of the domain:

$$\sum_{I=1}^{N} \bar{\Omega}_I \neq \Omega. \tag{3.8}$$

To avoid this inconsistency, we will introduce following correction parameter $\aleph$:

$$\aleph = \sqrt{\frac{\Omega}{\bar{\Omega}}}. \tag{3.9}$$

Using this parameter, the radius r_I of the control volume $\Omega^{(I)}$ of node I can be defined by

$$r_I = \aleph\, \bar{r}_I. \tag{3.10}$$

Applying this radius, we can define the control volume $\Omega^{(I)}$ and its surface $\Gamma^{(I)}$ as

$$\Omega^{(I)} = \pi r_I^2 \Xi_I \tag{3.11}$$

$$\Gamma^{(I)} = 2\pi r_I \Xi_I \tag{3.12}$$

These control volumes are satisfied the relation

$$\sum_{I=1}^{N} \Omega_I = \Omega \tag{3.13}$$

Contribution $\Gamma_J^{(I)}$ of the control volume to the neighbor node J will be obtained by

$$\Gamma_J^{(I)} = \frac{\Gamma^{(I)}}{M_I} \qquad or \qquad \Gamma_J^{(I)} = \pi\theta_{IJ} r_I \tag{3.14}$$

where θ_{IJ} is the contribution angle of node J to the node I (see Fig.7).

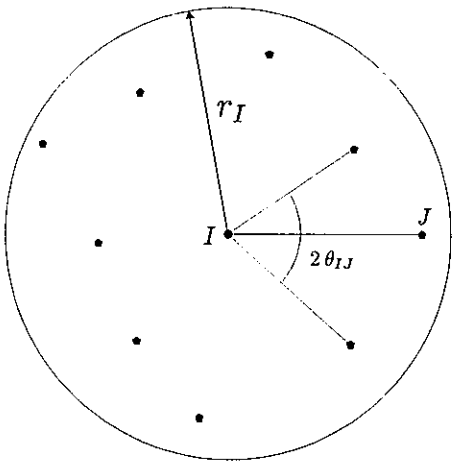

FIGURE 7. **Contribution angle θ_{IJ} of node J to node I**

3.2. **Mechanical relations.** Coefficients relating to node I of the stiffness equations are given in (1.30). We can rearranged the relation for the relations to neighbor nodes as:

$$[\mathbf{k}^{(I)}] = -\oint_{\Gamma^{(I)}} [\mathbf{n}][\mathbf{E}][\mathbf{B}]\, d\Gamma = \sum_{J=1}^{M_I} \left(-\int_{\Gamma_J^{(I)}} [\mathbf{n}][\mathbf{E}][\mathbf{B}]\, d\Gamma \right) = \sum_{J=1}^{M_I} \left(-[\mathbf{n}]_{IJ}[\mathbf{E}][\mathbf{B}]_{IJ}\, \Gamma_J^{(I)} \right) \tag{3.15}$$

where

$$[\mathbf{n}]_{IJ} = \begin{bmatrix} n_x & 0 & n_y \\ 0 & n_y & n_x \end{bmatrix} \tag{3.16}$$

and

$$n_x = \frac{x_J - x_I}{||\mathbf{x}_J - \mathbf{x}_I||}\,; \qquad n_y = \frac{y_J - y_I}{||\mathbf{x}_J - \mathbf{x}_I||}. \tag{3.17}$$

Local strain tensors on the direction from node I to node J can be defined by

$$\begin{Bmatrix} \bar{\varepsilon} \\ \bar{\gamma} \end{Bmatrix} = \frac{1}{||\mathbf{x}_I - \mathbf{x}_J||} \begin{bmatrix} 1 & 0 \\ 0 & 1 \end{bmatrix} \begin{Bmatrix} \Delta\bar{u}_{IJ} \\ \Delta\bar{v}_{IJ} \end{Bmatrix} \tag{3.18a}$$

where $\Delta\bar{u}_{IJ}$ and $\Delta\bar{v}_{IJ}$ are relative displacements directed to node J form node I and its perpendicular, respectively.

We introduce following abbreviation form of (3.18):

$$\{\bar{\varepsilon}\} = [\bar{\mathbf{B}}]\Delta\{\bar{\mathbf{u}}\}. \tag{3.18b}$$

Relative displacements on the inter-element boundaries can be related with the local displacements of both edge nodes as:

$$\begin{Bmatrix} \Delta\bar{u}_{IJ} \\ \Delta\bar{v}_{IJ} \end{Bmatrix} = \begin{bmatrix} -1 & 0 & 1 & 0 \\ 0 & -1 & 0 & 1 \end{bmatrix} \begin{Bmatrix} \bar{u}_I \\ \bar{v}_I \\ \bar{u}_J \\ \bar{v}_J \end{Bmatrix} \tag{3.19a}$$

We introduce the abbreviation form of (3.19a):

$$\Delta\{\bar{\mathbf{u}}\} = [\mathbf{A}]\{\bar{\mathbf{u}}^p\} \tag{3.19b}$$

Relations between local and global displacements at edge nodes are given by

$$\begin{Bmatrix} \bar{u}_I \\ \bar{v}_I \\ \bar{u}_J \\ \bar{v}_J \end{Bmatrix} = \begin{bmatrix} n_x & n_y & 0 & 0 \\ -n_y & n_x & 0 & 0 \\ 0 & 0 & n_x & n_y \\ 0 & 0 & -n_y & n_x \end{bmatrix} \begin{Bmatrix} u_I \\ v_I \\ u_J \\ v_J \end{Bmatrix} \tag{3.20a}$$

where n_x and n_y are given by

$$n_x = \cos\theta_i \ ; \quad n_y = \sin\theta_i$$

where θ_i is the angle between $\{\mathbf{n}_i\}$ and global X direction. We introduce following abbreviation form of (3.20a):

$$\{\bar{\mathbf{u}}^p\} = [\mathbf{T}]\{\mathbf{u}^p\}. \tag{3.20b}$$

Local to global strain relations are given by

$$\begin{Bmatrix} \varepsilon_x \\ \varepsilon_y \\ \gamma_{xy} \end{Bmatrix} = \begin{bmatrix} n_x^2 & -n_x n_y \\ n^2 & n_x n_y \\ 2n_x n_y & n_x^2 - n_y^2 \end{bmatrix} \begin{Bmatrix} \bar{\varepsilon} \\ \bar{\gamma} \end{Bmatrix} \tag{3.21a}$$

Abbreviation form is

$$\{\varepsilon\} = [\mathbf{Q}]\{\bar{\varepsilon}\}. \tag{3.21b}$$

Substituting (3.18b), (3.19b) and (3.20b) into (3.21b), relations between displacements of both edge nodes and the strain tensor on the inter-element boundary are given by

$$\{\varepsilon\} = [\mathbf{Q}][\bar{\mathbf{B}}][\mathbf{A}][\mathbf{T}]\{\mathbf{u}^p\} = [\mathbf{B}_i]\{\mathbf{u}^p\} \tag{3.22}$$

Substituting (3.18a), (3.19a), (3.20a) and (3.21a) into above relations, we will get

$$[\mathbf{B}]_{IJ} = \frac{1}{||\mathbf{x}_I - \mathbf{x}_J||} \begin{bmatrix} -n_x(n_x^2+n_y^2) & 0 & n_x(n_x^2+n_y^2) & 0 \\ 0 & -n_y(n_x^2+n_y^2) & 0 & n_y(n_x^2+n_y^2) \\ -n_y(n_x^2+n_y^2) & -n_x(n_x^2+n_y^2) & n_y(n_x^2+n_y^2) & n_x(n_x^2+n_y^2) \end{bmatrix} \tag{3.23}$$

Considering the identity $n_x^2 + n_y^2 = 1$, final strain-nodal displacement vector on node I to node J can be given by

$$[\mathbf{B}]_{IJ} = \frac{1}{||\mathbf{x}_I - \mathbf{x}_J||} \begin{bmatrix} -n_x & 0 & n_x & 0 \\ 0 & -n_y & 0 & n_y \\ -n_y & -n_x & n_y & n_x \end{bmatrix} \tag{3.24}$$

In this section we are concerned with a meshless analysis based on the finite volume concepts using plane problems as an example. Purpose of the proposed method is to establish the simplest mechanical relations between two discrete nodes.

4. Conclusions

In this paper, we have presented general considerations on the finite volume method to the solid mechanics problems. Especially we have proposed the finite element analysis which has been based on the finite volume context to the progressive discontinuity problems. As an example of practical implementations, the stiffness matrix of three node triangle element has been derived and the equivalence of the element with the standard three node triangle element has been presented. For future development, the extension to the meshless analysis has been tried by the simplest approach.

References

[1] C. Bailey and M. Cress, 'A Finite volume procedure to solve elastic solid mechanics problems in three dimensions on an unstructured mesh', *Int. j. numer. methods eng.*, **38**, 1757–1776 (1995).

[2] T. Belytschko, Y. Kronguz, D. Organ, M. Fleming and P. Krysl, 'Meshless methods: An overview and recent developments',*Comput. Methods Appl. Mech. Engirg.*, **139**, 3–47 (1996).

Finite Element Method for Contact Problem and Its Application to Shield Tunnel Excavation Analysis

Hiroshi Takeda
Department of System and Control, Hosei University

Morito Kusabuka
Department of Civil Engineering, Hosei University

Hiroshi Tanaka
Department of Urban Civil Engineering, Nippon Koei Co., Ltd.

Nobuko Kurokawa
Department of Urban Civil Engineering, Nippon Koei Co., Ltd.

ABSTRACT: We present a generalized formulation for contact problems in the category of widely used displacement-based finite element algorithm, by introducing the perturbed Lagrangian functional and localized mixed scheme. In addition, a shield tunnel excavation analysis method is proposed under the condition of contact between the shield machine and its surrounding ground. This excavation analysis procedure can simulate the shield tunnelling process more accurately than the conventional methods. A numerical example of shield tunnelling is also shown, and its analysis results compare with the measured value in a construction site.

1. INTRODUCTION

Tunnel excavation using shield machines illustrates a typical example of a contact problem. Analyses considering the friction contact between the shield machine and the ground are of great importance in estimating ground subsidence, deformation of existing structures adjacent to the shield tunnel, and earth pressure acting on the shield segment structure. However, many of the conventional excavation analyses based on the finite element method have not expressed such a contact condition properly in terms of mechanics. Therefore, improvement in the accuracy of analysis results, and rapid progress in numerical analyses faithfully reflecting actual construction process have been at a standstill.

In this paper, an attempt is made to attain the following three major objectives in relation to excavation of shield tunnels.

- Show a formulation for general contact problems using widely applied displacement-based finite element algorithm.
- Propose an excavation analysis method that reflects the actual shield tunnel construction process as accurately as possible.
- To evaluate the viability of the proposed analysis method through comparison between ground deformation created during actual shield tunnelling and the numerical results.

2. FINITE ELEMENT METHOD FOR GENERAL CONTACT PROBLEMS

Finite element analyses for contact problems have widely used contact elements such as gap elements, interface elements and joint elements. These elements, however, could not be used for the problems in which two bodies facing each other across the contact interface are displaced considerably along the interface.

An numerical analysis method for such problems was proposed by Simo et al.[1] for the frictionless contact problems, and another by Shyu et al.[2] for the friction contact problems. Both of these algorithms were successfully developed by introducing the concept of contact segment that provides for free contact position between nodes on the contact interface. These methods, however, had several restrictions including the need to have nearly equally divided finite element mesh in both of the bodies contacting each other.

In this section, a method proposed by Simo et al. is generalized using the perturbed Lagrangian functional. The generalization enables analysis of contact problems either between deforming bodies or between a deforming body and a rigid body, with or without friction. In addition, it is possible to freely select finite element mesh divisions for the bodies contacting each other.

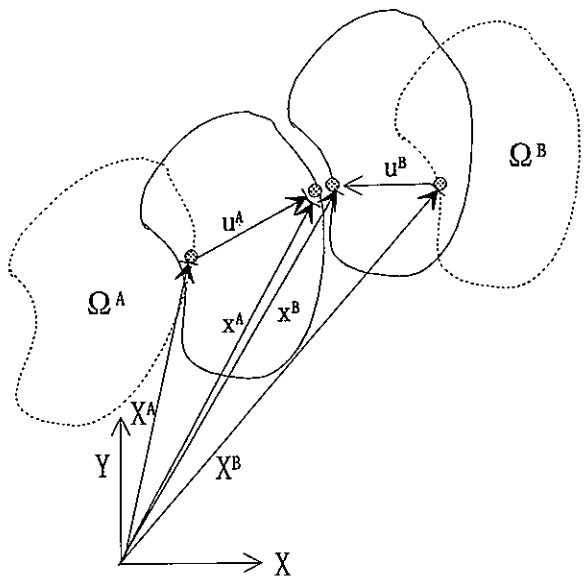

Fig.1 Reference and current configurations for bodies A and B.

2.1. Governing Equations and the Variational Form

As shown in **Fig.1**, the current configurations of bodies A and B, that are expected to contact each other, are represented as follows

$$\mathbf{x}^\alpha = \mathbf{x}^\alpha(\mathbf{X}^\alpha) \quad ; \quad \mathbf{X}^\alpha \in \Omega^\alpha \tag{1}$$

where Ω indicates the reference configuration, $\mathbf{X}$ is the material point in the reference configuration, and $\mathbf{x}$ is the material point in the current configuration. Subscript α represents body A or B. Position vector $\mathbf{x}$ is represented using displacement $\mathbf{u}$ by the following equation.

$$\mathbf{x}^\alpha = \mathbf{X}^\alpha + \mathbf{u}^\alpha \tag{2}$$

Position vector $\mathbf{x}^c$ and unit normal vector $\mathbf{n}^c$ of the contact interfaces are represented by the following

equations.

$$\mathbf{x}^c = \mathbf{x}^A \cap \mathbf{x}^B \tag{3}$$

$$\mathbf{n}^c = \frac{\nabla \mathbf{x}^c(\mathbf{X})}{\| \nabla \mathbf{x}^c(\mathbf{X}) \|} \tag{4}$$

The gap clearance g at the contact interface can be represented by the incremental form as shown below

$$g = [\Delta \mathbf{u}^B - \Delta \mathbf{u}^A] \cdot \mathbf{n}^c + g_0 \tag{5}$$

where g_0 is the gap clearance before an increment. The gap g_0 is represented as

$$g_0 = [\mathbf{u}_0^B - \mathbf{u}_0^A] \cdot \mathbf{n}^c + G \tag{6}$$

where $\mathbf{u}_0^\alpha$ is the displacement before the increment, and G is the gap clearance in the reference configuration.

The state when the gap is open before contact is represented by

$$g = [\Delta \mathbf{u}^B - \Delta \mathbf{u}^A] \cdot \mathbf{n}^c + g_0 > 0 \tag{7}$$

$$\lambda = \mathbf{T}^A \cdot \mathbf{n}^c \equiv -\mathbf{T}^B \cdot \mathbf{n}^c = 0 \tag{8}$$

where $\mathbf{T}$ is the surface traction vector on the contact interface, and λ is the normal component (contact pressure) of the surface traction. The state when the gap is closed after contact is represented by the following equations.

$$g = [\Delta \mathbf{u}^B - \Delta \mathbf{u}^A] \cdot \mathbf{n}^c + g_0 = 0 \tag{9}$$

$$\lambda = \mathbf{T}^A \cdot \mathbf{n}^c \equiv -\mathbf{T}^B \cdot \mathbf{n}^c < 0 \tag{10}$$

Closed gap situation is further divided into a case where there is a slip and the other where there is none. The sticking state where there is no slip is represented as shown below using the incremental relative displacement $\Delta\gamma$ between the contact interfaces

$$\Delta\gamma = [\Delta \mathbf{u}^B - \Delta \mathbf{u}^A] \cdot \mathbf{t}^c = 0 \tag{11}$$

$$\eta = \mathbf{T}^A \cdot \mathbf{t}^c \equiv -\mathbf{T}^B \cdot \mathbf{t}^c \neq 0 \tag{12}$$

where $\mathbf{t}^c$ is the unit normal vector on the contact interface, and η is the tangential component (contact shear stress) of surface traction $\mathbf{T}$. Similarly, the slip state can be represented by following equations.

$$\Delta\gamma = [\Delta \mathbf{u}^B - \Delta \mathbf{u}^A] \cdot \mathbf{t}^c \neq 0 \tag{13}$$

$$\eta = \mathbf{T}^A \cdot \mathbf{t}^c \equiv -\mathbf{T}^B \cdot \mathbf{t}^c = 0 \tag{14}$$

The above contact conditions can be defined as the Kuhn-Tucker conditions and represented by the following equation.

$$g\lambda = 0, \quad \Delta\gamma\eta = 0 \quad on \ \mathbf{x}^c \tag{15}$$

As an incremental variational form in the case where no contact condition is considered, the potential energy functional $\Delta\mathcal{I}$ can consider as

$$\Delta\mathcal{I}^\alpha(\Delta \mathbf{u}^\alpha) \equiv \int_{\Omega^\alpha} \Delta\mathcal{U} dV - \int_{\Omega^\alpha} (\overline{\mathbf{q}}^\alpha + \Delta\overline{\mathbf{q}}^\alpha) \cdot \Delta \mathbf{u}^\alpha dV - \int_{\partial_\sigma \Omega^\alpha} (\overline{\mathbf{T}}^\alpha + \Delta\overline{\mathbf{T}}^\alpha) \cdot \Delta \mathbf{u}^\alpha dS \tag{16}$$

$$\alpha = A, B$$

where $\mathcal{U}$ is an internal energy function, $\overline{\mathbf{q}}^{\alpha}$ is a body force, and $\overline{\mathbf{T}}^{\alpha}$ is the surface force defined on mechanical boundary $\partial_{\sigma}\Omega^{\alpha}$. If a constraint condition of contact is to be incorporated into the above equation, the following perturbed Lagrange functional $\Delta\Pi_{\epsilon}$ is considered using surface forces λ and η on the contact interface as Lagrange multipliers

$$\begin{aligned}\Delta\Pi_{\epsilon}(\Delta\mathbf{u}^{A},\Delta\mathbf{u}^{B},\lambda,\eta) &\equiv \sum_{\alpha=A}^{B}\Delta\mathcal{I}^{\alpha}(\Delta\mathbf{u}^{\alpha}) \\ &+ \int_{\mathbf{x}^c}\lambda g dS - \frac{1}{2\epsilon_{\lambda}}\int_{\mathbf{x}^c}\lambda^2 dS + \int_{\mathbf{x}^c}\eta\Delta\gamma dS - \frac{1}{2\epsilon_{\eta}}\int_{\mathbf{x}^c}\eta^2 dS \end{aligned} \tag{17}$$

where $\epsilon > 0$ is a penalty coefficient[1]. Based on the stationary condition of the functional shown above, the variational equations for finite element formulation of contact problems can be represented as follows

$$\Delta\mathcal{F}_{\mathbf{u}} = \sum_{\alpha=A}^{B}\Delta\mathcal{I}^{\alpha}\overset{*}{\mathbf{u}}^{\alpha} + \int_{\mathbf{x}_s^c}\lambda[\overset{*}{\mathbf{u}}^{B} - \overset{*}{\mathbf{u}}^{A}]\cdot\mathbf{n}^c dS + \int_{\mathbf{x}_s^c}\eta[\overset{*}{\mathbf{u}}^{B} - \overset{*}{\mathbf{u}}^{A}]\cdot\mathbf{t}^c dS = 0 \tag{18}$$

$$\Delta\mathcal{F}_{\lambda} = \int_{\mathbf{x}^c}\overset{*}{\lambda}\cdot\left\{-\frac{\lambda}{\epsilon_{\lambda}} + [\Delta\mathbf{u}^{B} - \Delta\mathbf{u}^{A}]\cdot\mathbf{n}^c + g_0\right\}dS = 0 \tag{19}$$

$$\Delta\mathcal{F}_{\eta} = \int_{\mathbf{x}^c}\overset{*}{\eta}\left\{-\frac{\eta}{\epsilon_{\eta}} + [\Delta\mathbf{u}^{B} - \Delta\mathbf{u}^{A}]\cdot\mathbf{t}^c\right\}dS = 0 \tag{20}$$

where $\dot{\mathbf{u}}$ is a geometrically admissible virtual displacement. $\dot{\lambda}$ and $\dot{\eta}$ are statically admissible virtual surface stresses.

2.2. Finite Element Discretization

In the preceding section, a variational form was shown for general contact problems. As for finite element systems, the discretization schemes for (18)~(20) can be represented by

$$\Delta\mathcal{F}_{\mathbf{u}} \approx \sum_{e=1}^{M}\Delta\mathcal{F}_{\mathbf{u}}^{(e)} + \sum_{s=1}^{L}\Delta\mathcal{F}_{\mathbf{u}}^{(s)} = 0 \tag{21}$$

$$\Delta\mathcal{F}_{\lambda} \approx \sum_{s=1}^{L}\Delta\mathcal{F}_{\lambda}^{(s)} = 0 \tag{22}$$

$$\Delta\mathcal{F}_{\eta} \approx \sum_{s=1}^{L}\Delta\mathcal{F}_{\eta}^{(s)} = 0 \tag{23}$$

where M is the total number of elements. L is the total number of contact segments automatically established according to the contact condition. Subscripts e and s represent a element and a contact segment, respectively. $\Delta\mathcal{F}_{\mathbf{u}}^{(e)}$ is the incremental virtual work of a finite element. Terms of contact segments are represented as shown below using individual segment $\mathbf{x}_s^c$.

$$\Delta\mathcal{F}_{\mathbf{u}}^{(s)} = \int_{\mathbf{x}_s^c}\lambda[\overset{*}{\mathbf{u}}^{B} - \overset{*}{\mathbf{u}}^{A}]\cdot\mathbf{n}^c dS + \int_{\mathbf{x}_s^c}\eta[\overset{*}{\mathbf{u}}^{B} - \overset{*}{\mathbf{u}}^{A}]\cdot\mathbf{t}^c dS \tag{24}$$

$$\Delta\mathcal{F}_{\lambda}^{(s)} = \int_{\mathbf{x}_s^c}\overset{*}{\lambda}\cdot\left\{-\frac{\lambda}{\epsilon_{\lambda}} + [\Delta\mathbf{u}^{B} - \Delta\mathbf{u}^{A}]\cdot\mathbf{n}^c + g_0\right\}dS \tag{25}$$

$$\Delta\mathcal{F}_{\eta}^{(s)} = \int_{\mathbf{x}_s^c}\overset{*}{\eta}\cdot\left\{-\frac{\eta}{\epsilon_{\eta}} + [\Delta\mathbf{u}^{B} - \Delta\mathbf{u}^{A}]\cdot\mathbf{t}^c\right\}dS \tag{26}$$

If it act on the ordinary displacement-based finite element formulation, $\Delta\mathcal{F}^{(e)}$ is re-written as

$$\Delta\mathcal{F}_{\mathbf{u}}^{(e)} = \{\overset{*}{\mathbf{u}}^{e}\}^{T}[\mathbf{k}_T^e]\Delta\{\mathbf{u}^e\} - \{\overset{*}{\mathbf{u}}^{e}\}^{T}\Delta\{\mathbf{p}^e\} \tag{27}$$

[1]The ordinary Lagrange functional having contact conditions as subsidiary conditions can be obtained by $\epsilon \to \infty$

where $\{\overset{*}{\mathbf{u}}^e\}$ is the virtual nodal displacement of the element. $\Delta\{\mathbf{u}^e\}$ is incremental nodal displacement of the element. $[\mathbf{k}_T^e]$ is tangential stiffness matrix of the element. $\Delta\{\mathbf{p}^e\}$ is the equivalent incremental nodal force of the element.

For the whole domain, the following equation is developed through the normal procedure of finite element assembly.

$$\sum_{e=1}^{M} \Delta\mathcal{F}_{\mathbf{u}}^{(e)} = \{\overset{*}{\mathbf{U}}\}^T[\mathbf{K}_T]\Delta\{\mathbf{U}\} - \{\overset{*}{\mathbf{U}}\}^T\Delta\{\mathbf{P}\} \tag{28}$$

$[\mathbf{K}_T]$ and $\Delta\{\mathbf{P}\}$ can be obtained by

$$[\mathbf{K}_T] = \sum_{e=1}^{M}[\mathcal{A}^e]^T[\mathbf{k}_T^e][\mathcal{A}^e] \tag{29}$$

$$\Delta\{\mathbf{P}\} = \sum_{e=1}^{M}[\mathcal{A}^e]^T\Delta\{\mathbf{p}^e\} \tag{30}$$

In the above equation, $\{\overset{*}{\mathbf{U}}\}$ is the virtual nodal displacement, $\Delta\{\mathbf{U}\}$ is the incremental nodal displacement, $[\mathbf{K}_T]$ is the tangential stiffness matrix, and $\Delta\{\mathbf{P}\}$ is the equivalent incremental nodal force. $[\mathcal{A}^e]$ is a logical matrix relating with the connection between e-th element and the nodes in the whole domain, and is satisfied the relation as follows.

$$[\mathcal{A}^e] : \Delta\{\mathbf{U}\} \rightarrow \Delta\{\mathbf{u}^e\} \quad or \quad [\mathcal{A}^e]\Delta\{\mathbf{U}\} = \Delta\{\mathbf{u}^e\} \tag{31}$$

For contact segments, finite element interpolations are used as follows

$$\lambda = [\mathbf{N}_\lambda]\{\lambda^s\} \tag{32}$$

$$\eta = [\mathbf{N}_\eta]\{\eta^s\} \tag{33}$$

$$\Delta\mathbf{u}^B - \Delta\mathbf{u}^A = [\mathbf{N}_\mathbf{u}]\Delta\{\mathbf{u}^s\} \tag{34}$$

$$\overset{*}{\lambda} = [\mathbf{N}_\lambda]\{\overset{*}{\lambda}^s\} \tag{35}$$

$$\overset{*}{\eta} = [\mathbf{N}_\eta]\{\overset{*}{\eta}^s\} \tag{36}$$

$$\overset{*}{\mathbf{u}}^B - \overset{*}{\mathbf{u}}^A = [\mathbf{N}_\mathbf{u}]\Delta\{\overset{*}{\mathbf{u}}^s\} \tag{37}$$

where $[\mathbf{N}_\lambda]$ is the interpolation function for contact pressure, $[\mathbf{N}_\eta]$ is the interpolation function for contact shear stress, $[\mathbf{N}_\mathbf{u}]$ is the interpolation function for relative displacement of the contact interface, and subscript s indicates the value at the points[2] that constitute contact segments.

The following equations are obtained by substituting the above equations to (24)~(26).

$$\Delta\mathcal{F}_{\mathbf{u}}^{(s)} = \{\overset{*}{\mathbf{u}}^s\}^T\left([\mathbf{z}_\lambda^s]\{\lambda^s\} + [\mathbf{z}_\eta^s]\{\eta^s\}\right) \tag{38}$$

$$\Delta\mathcal{F}_{\lambda}^{(s)} = \{\overset{*}{\lambda}^s\}^T[\mathbf{z}_\lambda^s]^T\Delta\{\mathbf{u}^s\} + \{\overset{*}{\lambda}^s\}^T\frac{1}{\epsilon_\lambda}[\mathbf{c}_\lambda^s]\{\lambda^s\} \tag{39}$$

$$\Delta\mathcal{F}_{\eta}^{(s)} = \{\overset{*}{\eta}^s\}^T[\mathbf{z}_\eta^s]^T\Delta\{\mathbf{u}^s\} + \{\overset{*}{\eta}^s\}^T\frac{1}{\epsilon_\eta}[\mathbf{c}_\eta^s]\{\eta^s\} \tag{40}$$

$[\mathbf{z}_\lambda^s]$, $[\mathbf{c}_\lambda^s]$, $[\mathbf{z}_\eta^s]$ and $[\mathbf{c}_\eta^s]$ are represented as shown below, respectively.

$$[\mathbf{z}_\lambda^s] = \int_{\mathbf{X}_s^c}[\mathbf{N}_\mathbf{u}]^T\mathbf{n}^c[\mathbf{N}_\lambda]dS \tag{41}$$

$$[\mathbf{c}_\lambda^s] = -\int_{\mathbf{X}_s^c}[\mathbf{N}_\lambda]^T[\mathbf{N}_\lambda]dS \tag{42}$$

$$[\mathbf{z}_\eta^s] = \int_{\mathbf{X}_s^c}[\mathbf{N}_\mathbf{u}]^T\mathbf{t}^c[\mathbf{N}_\eta]dS \tag{43}$$

$$[\mathbf{c}_\eta^s] = -\int_{\mathbf{X}_s^c}[\mathbf{N}_\eta]^T[\mathbf{N}_\eta]dS \tag{44}$$

[2]It does not generally match the node located on the contact boundary.

The following representation is possible for the whole domain of contact interface by assembling all contact segments[3].

$$\sum_{s=1}^{L} \Delta\mathcal{F}_{\mathbf{u}}^{(s)} = \{\overset{*}{\mathbf{U}}\}^T ([\mathbf{Z}_\lambda]\{\mathbf{\Lambda}\} + [\mathbf{Z}_\eta]\{\mathbf{H}\}) \tag{45}$$

$$\sum_{s=1}^{L} \Delta\mathcal{F}_{\lambda}^{(s)} = \{\overset{*}{\Lambda}\}^T [\mathbf{Z}_\lambda]^T \Delta\{\mathbf{U}\} + \{\overset{*}{\Lambda}\}^T \frac{1}{\epsilon_\lambda} [\mathbf{C}_\lambda]\{\mathbf{\Lambda}\} \tag{46}$$

$$\sum_{s=1}^{L} \Delta\mathcal{F}_{\eta}^{(s)} = \{\overset{*}{H}\}^T [\mathbf{Z}_\eta]^T \Delta\{\mathbf{U}\} + \{\overset{*}{H}\}^T \frac{1}{\epsilon_\eta} [\mathbf{C}_\eta]\{\mathbf{H}\} \tag{47}$$

$[\mathbf{Z}_\lambda]$, $[\mathbf{C}_\lambda]$, $[\mathbf{Z}_\eta]$ and $[\mathbf{C}_\eta]$ are represented as shown below, respectively.

$$[\mathbf{Z}_\lambda] = \sum_{s=1}^{L} [\mathcal{T}^s]^T [\mathbf{z}_\lambda^s][\mathcal{A}_\lambda^s] \tag{48}$$

$$[\mathbf{C}_\lambda] = \sum_{s=1}^{L} [\mathcal{A}_\lambda^s]^T [\mathbf{c}_\lambda^s][\mathcal{A}_\lambda^s] \tag{49}$$

$$[\mathbf{Z}_\eta] = \sum_{s=1}^{L} [\mathcal{T}^s]^T [\mathbf{z}_\eta^s][\mathcal{A}_\eta^s] \tag{50}$$

$$[\mathbf{C}_\eta] = \sum_{s=1}^{L} [\mathcal{A}_\eta^s]^T [\mathbf{c}_\eta^s][\mathcal{A}_\eta^s] \tag{51}$$

in which $[\mathcal{A}_\lambda^s]$ and $[\mathcal{A}_\eta^s]$ represent logical matrixes relating with connection between s-th contact segment and the whole system of contact interface. $[\mathcal{T}^s]$ indicates a matrix showing relation between typical incremental relative displacement of s-th contact segment and incremental nodal displacements. These matrixes are satisfied the relation as follows.

$$[\mathcal{T}^s] : \Delta\{\mathbf{U}\} \rightarrow \Delta\{\mathbf{u}^s\} \quad or \quad \{[\mathcal{T}^s]\}\Delta\{\mathbf{U}\} = \Delta\{\mathbf{u}^s\} \tag{52}$$

$$[\mathcal{A}_\lambda^s] : \{\mathbf{\Lambda}\} \rightarrow \{\lambda^s\} \quad or \quad \{[\mathcal{A}_\lambda^s]\}\{\mathbf{\Lambda}\} = \{\lambda^s\} \tag{53}$$

$$[\mathcal{A}_\eta^s] : \{\mathbf{H}\} \rightarrow \{\eta^s\} \quad or \quad \{[\mathcal{A}_\eta^s]\}\{\mathbf{H}\} = \{\eta^s\} \tag{54}$$

Finally, the following finite element governing equations are obtained for contact problems by substituting (28) and (45)~(47) to (21)~(23).

$$[\mathbf{K}_T]\Delta\{\mathbf{U}\} + [\mathbf{Z}_\lambda]\{\mathbf{\Lambda}\} + [\mathbf{Z}_\eta]\{\mathbf{H}\} = \Delta\{\mathbf{P}\} \tag{55}$$

$$[\mathbf{Z}_\lambda]^T \Delta\{\mathbf{U}\} + \frac{1}{\epsilon_\lambda}[\mathbf{C}_\lambda]\{\mathbf{\Lambda}\} = \{\mathbf{0}\} \tag{56}$$

$$[\mathbf{Z}_\eta]^T \Delta\{\mathbf{U}\} + \frac{1}{\epsilon_\eta}[\mathbf{C}_\eta]\{\mathbf{H}\} = \{\mathbf{0}\} \tag{57}$$

The above equations can be summarized as shown below.

$$\begin{bmatrix} \mathbf{K}_T & \mathbf{Z}_\lambda & \mathbf{Z}_\eta \\ \mathbf{Z}_\lambda^T & \frac{1}{\epsilon_\lambda}\mathbf{C}_\lambda & \mathbf{0} \\ \mathbf{Z}_\eta^T & \mathbf{0} & \frac{1}{\epsilon_\eta}\mathbf{C}_\eta \end{bmatrix} \begin{Bmatrix} \Delta\mathbf{U} \\ \mathbf{\Lambda} \\ \mathbf{H} \end{Bmatrix} = \begin{Bmatrix} \Delta\mathbf{P} \\ \mathbf{0} \\ \mathbf{0} \end{Bmatrix} \tag{58}$$

If $\mathbf{\Lambda}$ and $\mathbf{H}$ are eliminated from the above equation, the equation is represented as

$$[\tilde{\mathbf{K}}_T]\Delta\{\mathbf{U}\} = \Delta\{\mathbf{P}\} \tag{59}$$

[3]Similar to normal finite element assembly.

where $[\tilde{\mathbf{K}}_T]$ is tangential stiffness matrix that takes contact conditions into consideration, and is defined as shown below.

$$[\tilde{\mathbf{K}}_T] = [\mathbf{K}_T] + [\mathbf{K}_T^C] \tag{60}$$

The contribution of contact condition $[\mathbf{K}_T^C]$ for the above tangential stiffness matrix is given by the following equation.

$$[\mathbf{K}_T^C] = -\epsilon_\lambda[\mathbf{Z}_\lambda][\mathbf{C}_\lambda]^{-1}[\mathbf{Z}_\lambda]^T - \epsilon_\eta[\mathbf{Z}_\eta][\mathbf{C}_\eta]^{-1}[\mathbf{Z}_\eta]^T \tag{61}$$

If interpolations for contact pressure and contact shear stress in the contact segment are selected independently for each segment[4], there will be no coupling between contact segments, and inverses of $[\mathbf{C}_\lambda]$ and $[\mathbf{C}_\eta]$ can be obtained by assembling inverses of $[\mathbf{c}_\lambda]$ and $[\mathbf{c}_\eta]$ for each segment. Therefore, $[\mathbf{K}_T^C]$ in the above equation is represented as[5]

$$[\mathbf{K}_T^C] = \sum_{s=1}^{L}[\mathcal{T}^s]^T[\mathbf{k}_t^s][\mathcal{T}^s] \tag{62}$$

where $[\mathbf{k}_t^s]$ is stiffness matrix for contact segment s, and is shown as follows.

$$[\mathbf{k}_T^C] = -\epsilon_\lambda[\mathbf{z}_\lambda^s][\mathbf{c}_\lambda^s]^{-1}[\mathbf{z}_\lambda^s]^T - \epsilon_\eta[\mathbf{z}_\eta^s][\mathbf{c}_\eta^s]^{-1}[\mathbf{z}_\eta^s]^T \tag{63}$$

As discussed above, generalization of numerical algorithm for contact problems becomes possible in the category of widely used displacement-based finite element method, by introducing the perturbed Lagrangian functional and localized mixed scheme.

3. EXCAVATION ANALYSIS PROCEDURE FOR SHIELD TUNNELLING

Excavation analysis of shield tunnelling is one of the typical contact problems. Unless an analysis is made that satisfactorily reflects the condition of contact between the shield machine and segments, and the ground, it is impossible to represent stress state or deformation of the ground surrounding the tunnel.

This section presents a shield tunnel excavation analysis method that reflects not only the contact conditions as described above but also actual construction process.

Fig.2 shows an excavation analysis system that re-creates actual shield tunnel construction process as much as possible. The system consists of two tiers of incremental loops. The outer loop represents excavation of soil elements and one ring of segment insertion, and the inner loop shows the penetration of the shield machine.

As the contact condition should always be satisfied at the boundary between the shield machine and the segment, and the excavation ground, the penetration of the shield machine and elimination of excavation element results in the creation of the new contact interface. Therefore, stress release reflecting supporting effect by the shield machine and the segment is represented without prior assumption of the stress release ratio at the shield face and tail. It is also possible to apply shield thrust force and slurry pressure at the shield face, and apply backfilling injection pressure in the shield tail void.

[4]The method is referred to as the localized mixed method.

[5]$[\mathcal{A}_\lambda^s][\mathcal{A}_\lambda^t]^T = \delta_{st}[\mathbf{I}_\lambda]$ *and* $[\mathcal{A}_\eta^s][\mathcal{A}_\eta^t]^T = \delta_{st}[\mathbf{I}_\eta]$ are considered, where δ_{st} is Kronecker delta. $[\mathbf{I}_\lambda]$ and $[\mathbf{I}_\eta]$ indicate unit matrixes.

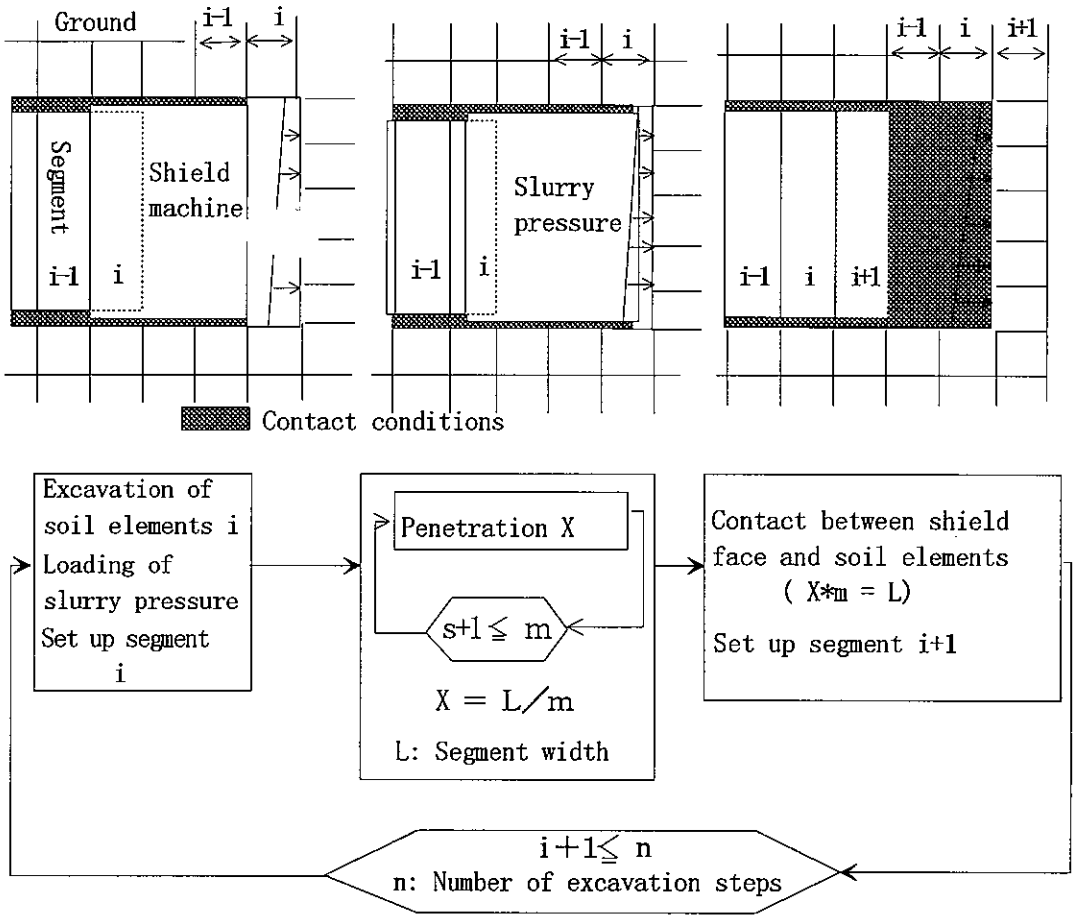

Fig.2 Numerical analysis procedure representing shield tunnelling process.

4. AN EXAMPLE OF SHIELD TUNNEL EXCAVATION ANALYSIS

Fig.3 shows the material properties of ground, and configuration of the tunnel and measurement points for a shield tunnel actually constructed. In the soil material, it was assumed the elasto-plastic constitutive equation with Drucker-Prager yield criterion. Conditions of contact between the shield skin plate and segment, and the ground were considered. The coefficient of friction μ on the contact interface was assumed linear distribution from the shield face to the shield tail within the range between 0.05 and 0.30. The slurry pressure acting on the shield face was assumed the coefficient of earth pressure K = 0.6 for vertical overburden pressure. Grouting ratio of the backfill material in the tail void was assumed 70% based on the results of field investigation. **Fig.4** shows the finite element mesh used for the analysis.

Fig.5 is a comparison of the numerical results and the measured values in construction site. The vertical displacement and horizontal earth pressure in the figure are incremental values occurred by penetration of shield machine. As is obvious from the figure, the numerical results compare well with the measured values. It should, however, be noted that the numerical results greatly vary depending on the evaluation of the contact friction coefficient and the shield face pressure, used in the analysis. The evaluation of the ratio of friction resistance of the shield skin plate and the shield face pressure is a matter of great importance.

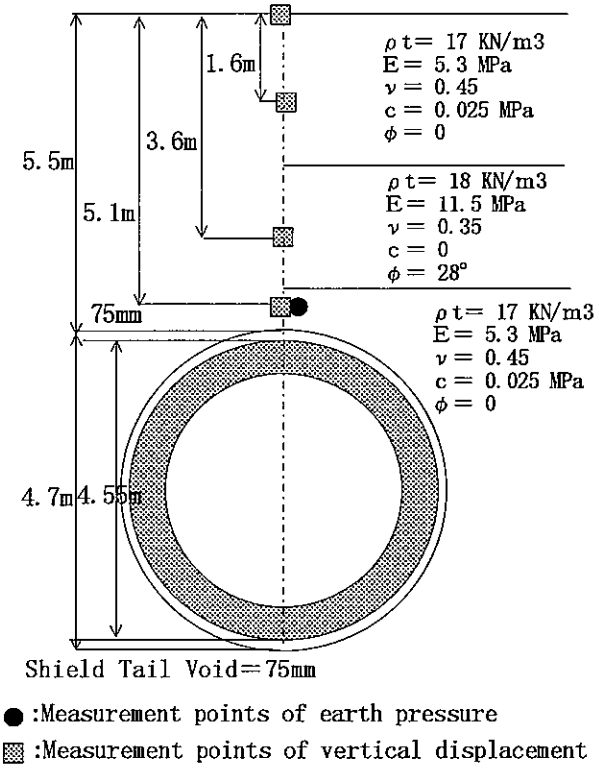

Fig.3 Configuration of the shield tunnel and measurement points, and soil properties.

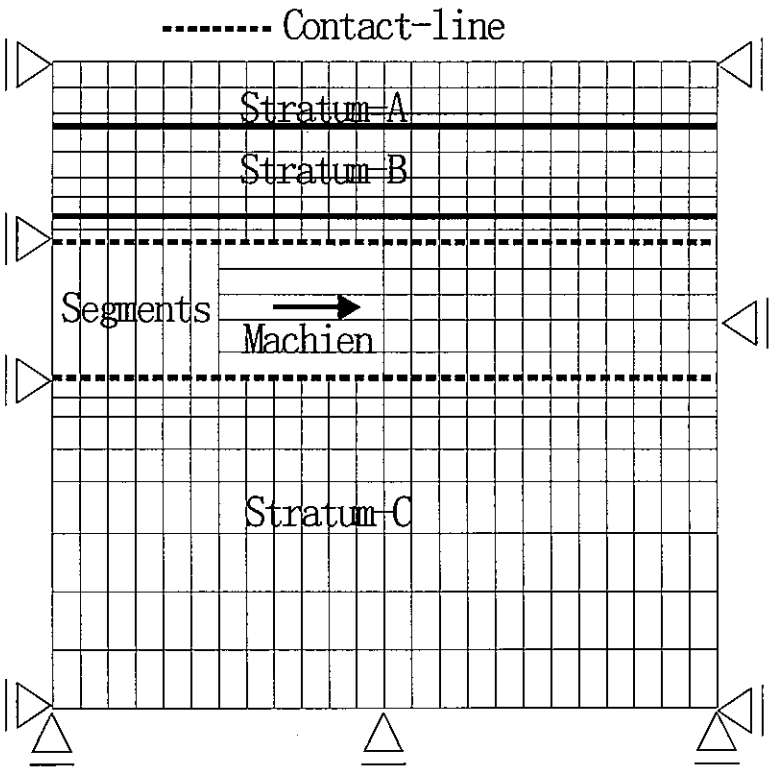

Fig.4 Finite element mesh for the shield tunnel.

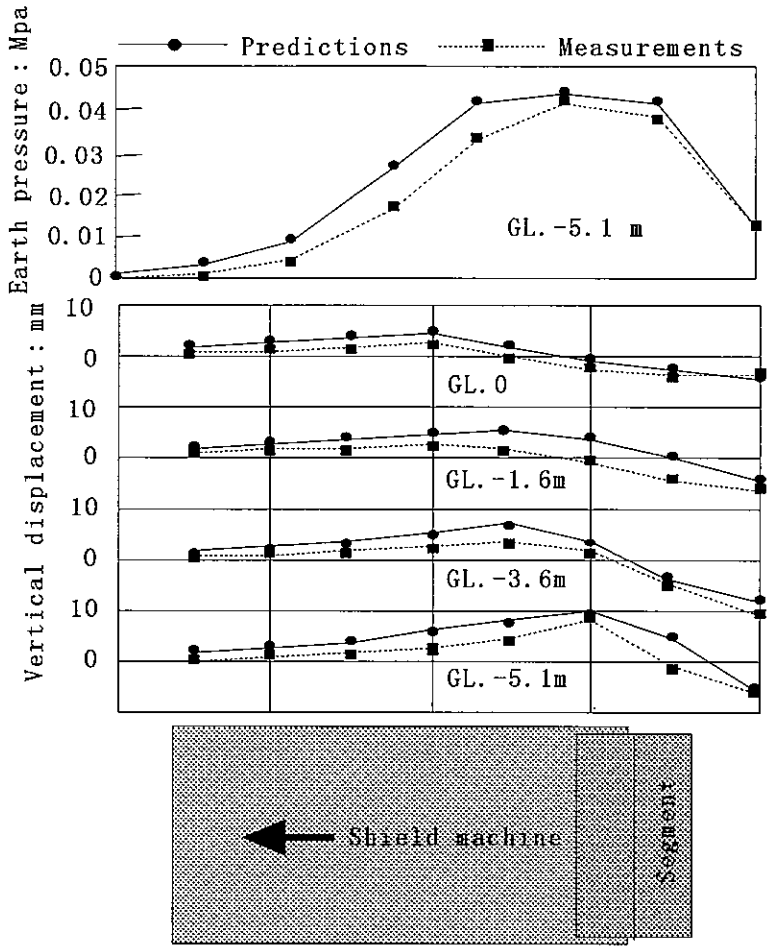

Fig.5 Comparisons of the numerical results and the measured values in construction site.

5. CONCLUSIONS

The generalized governing equations for contact problems has been presented, and the related discretization form has been shown specifically based on the displacement-based finite element algorithm. The proposed method eliminates the restriction under which finite element mesh divisions should be more or less the same on both sides of the expected contact interface, and makes it possible to freely make a general model.

An excavation analysis procedure faithfully reflecting shield tunnel construction process has been proposed, and its viability has been verified through comparison between the numerical results and the measured values in construction site.

REFERENCES

[1] J.C.Simo and T.A.Laursen : An augmented Lagrangian treatment of contact problems involving friction, Comput. Struct., Vol.42, No.1, 1992.

[2] S.C.Shyu. T.Y.Chang and A.F.Saleeb:Friction-contact analysis using a mixed finite element method, Comput. Struct. Vol.32, No.1, 1989.

The movement of rock joint triggered by water diffusion

Xing-jue Shi Dong-mei Li
Dept. of Earth and Space Sciences , Univ. of Science and Technology of China
Hefei ,Anhui , 230026, P.R.C.

ABSTRACT A significant triggering effect was observed after the Landers , California, earthquake of 28 June 1992, but the mechanism of the triggering effect remained largely unclear and the underground water diffusion may be involved the triggering mechanism. To explain the possible mechanism of the movement of rock joints or faults, some simulated experiments had been performed in the laboratory under confining pressure. After injecting the pressurized water into the rock joint, a sequence of stick-slips were observed while the stress decreased successively with each slip. A model of joint movement due to inhomogeneity of water pressure was developed . According to this model, the rock joint surface was divided into the slipped and locked regions, depending on whether or not the local state of stress satisfied the friction criterion. By comparing the experimental data with the model predictions, we found that the joint moved when the average shear stress over the locked region became equal to the value given by the friction criterion. We suggested that the stress transfer owing to the water diffusion may be a viable mechanism of the triggered earthquake.

1. INTRODUCTION

A significant triggering effect was observed after the Landaus , California, earthquake of 28 June 1992. The Landaus example with its clear evidence of remote triggering had given us some guidance to new ways of thinking about what initiated seismic ruptures. It particularly called our attention to the movement of underground water. Cinna Lomnitz [1] tested a 90-years catalog of shallow world earthquake (m>7), Kuo-Liang Wem [2] studied the seismicity in Taiwan region, both of them found the remote triggering was present at high magnitude levels and would be expected to be much more common at lower magnitude. The triggering effect may be a universal feature of the earthquake process.

The mechanism of the triggering effect remained largely unclear. It may be attributed to transient dynamic stresses that might initiate some sort of non-linear time-delayed process and may be related to readjustment directly connected with the stress distribution.

The time delays between mainshock and triggered earthquakes ranged from 3 minute to 33 hours. That suggested the movement of underground fluids was somehow involved in triggering mechanism. Most observed remote triggering events occurred in areas of known faults and geothermal activity. That pointed to magma and water possibly superheated water as obvious fluid suspects.

In order to explain the possible mechanism of the movement of rock joint, some simulated experiments had been performed in the laboratory under the confining pressure to study the movement of rock joint triggered by water diffusion.

Right cylinders of granite, 2.54 cm in diameter and 5.4 cm in length, were sawed into two halves at an angle of 30 degree to the axis of the cylinder. A small hole of 2 mm in diameter was drilled through the upper half of the specimen .This half of the specimen was mounted directly onto a steel piston, which also contained a small hole along its axis, serving as a channel between the sample and an external water reservoir. The sample assembly, including the steel piston and a steel end cap, was covered by a rubber tubing and placed in a triaxial vessel. see figure 1.

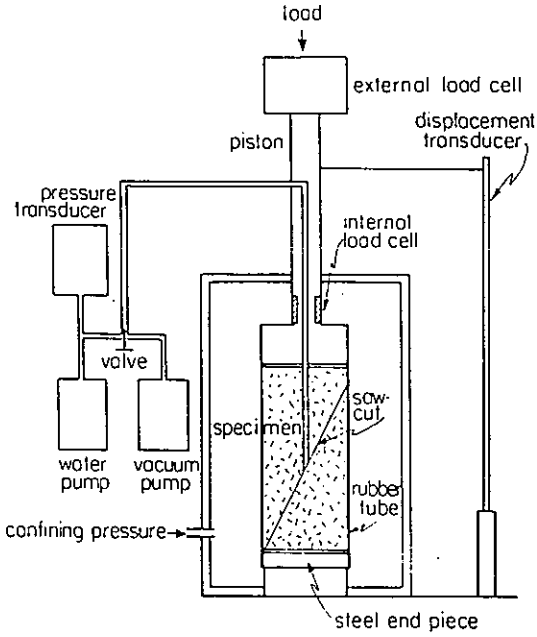

Figure 1 Schematic drawing of experimental setup.

The interior of the sample assembly was first evacuated with a vacuum pump. After a few hours the pump was shut off and pressurized water was injected into the assembly through the hole for saturation.

During the experiment the axial stress, pore pressure , confining pressure, resistance and the displacement of the piston were monitored and recorded.

Before water was injected, the specimen was subjected to a predetermined confining pressure and axial stress such that the stress condition on joint was close to the failure criterion as determined. Water was then injected to the joint instantly through the hole in the specimen. A outside valve was shut off to keep a fixed amount of water in the hole. A series of stick-slip events, usually 3 or 4 sudden movements could be observed within 200 second, each associated with a sudden release of axial stress and a sudden displacement.

3.EXPERIMENTAL RESULTS AND ANALYSIS

Some typical experimental results were in figure 2 and table 1. Before the injection of water, the first two displacements were induced by increasing the axial stress . From the friction criterion we could determine the critical water pressure required to cause frictional instability on the joint surface. If the injected-water pressure was high enough, a sequence of movements would occur some time after injection.

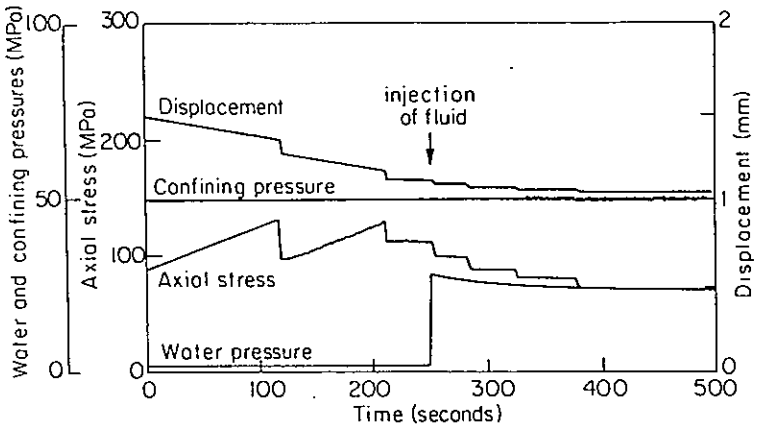

Figure 2 Axial displacement, stress confining pressure and water pressure plotted against time in typical experiment.

table 1 Another typical experimental result

time(s)	$\Delta\sigma(10^8 Pa)$	$\Delta u(\times 10^{-3} mm)$	$\Delta R(\Omega)$
44	0.12	5.98	-0.0147
92	0.16	8.65	-0.0049
153	0.16	9.97	-0.0098
224	0.17	9.97	-0.0049

In the table 1, the time t is measured from the instant of water injection. $\Delta\sigma$ is the axial stress drop. Δu is the movement of rock joint. ΔR is the change of resistance of the whole sample assembly. The change of resistance implied the water diffusion along the rock joint.

On the basis of the experimental observation we developed a model of joint instability due to the water diffusion along the joint surface. By applying Darcy's law and the observed lapse time we get the water pressure in the joint as function of radius of sample at different times.

$$\frac{\partial P}{\partial t} = A\left[\frac{\partial^2 p}{\partial r^2} + \frac{1}{r}\frac{\partial p}{\partial r}\right]$$

The boundary condition are

$$P(r,t)=P_0 \quad \text{for } r<a, \text{ and } \left(\frac{\partial P}{\partial r}\right)_{r=b} = 0 \quad \text{for all } t$$

where a is the radius of the small hole of the upper half of the rock specimen and b is the outer radius of the specimen. $A=k/(\mu\beta\phi)$, k is the permeability of the joint, β is the compressibility of water, μ is the viscosity of water, φ is the porosity of the joint.

In this text we estimated $A=0.4\ cm^2/sec$. The water pressure was as a function of radius at different times are plotted in Fig. 3.

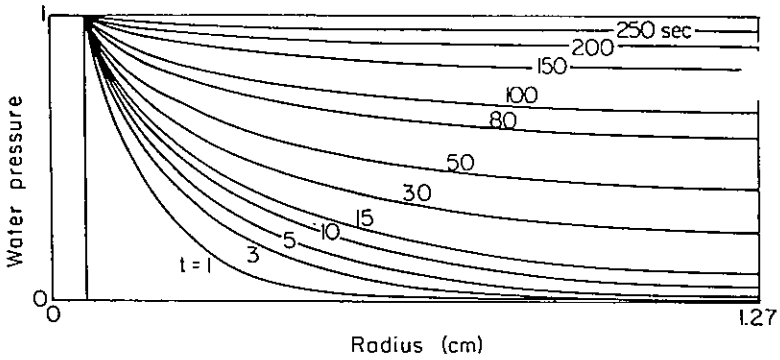

Figure 3 Calculated water pressure on the joint as function of radius at different times following injection of water.

According to this model, the joint surface is divided into the slipped and locked regions, depending on whether or not the local state of stress satisfies the friction criterion. See figure 4.

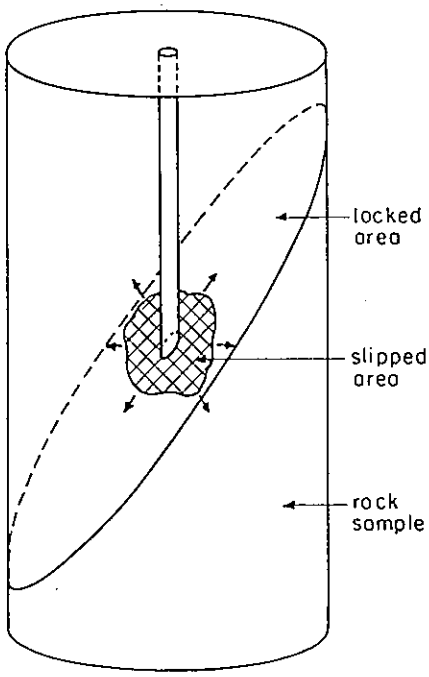

Figure 4. Conceptual model of rock joint after water injection.

At a given instant after water injection, the whole joint maintain the static equilibrium, shear stress on the locked area must increase so as to compensate the decreases in shear stress over the slipped area. as the slipped area expands in size with time due to water diffusion , the average shear stress on locked area must increase with time. The shear stress transfer on joint surface may be formulated by the following equation:

$$\int^{A_{locked}} \tau_l (r,t)\, dA = \tau A - \int^{A_{slipped}} \tau_s (r,t)\, dA$$

where t is the average shear stress over the joint with an area A, t_l (r,t) is the shear stress over locked area, and t_s (r,t) is the shear stress over slipped area and is equal to the frictional strength of the joint given by the friction criterion as follows,

$$\tau s = \mu[\sigma_n - P_w(r,t)]$$

where s_n is the normal stress , $P_w(r,t)$ is pore press on the joint, m is the coefficient of friction.

By using the above formula ,the average shear stress and the average effective normal stress on locked area are plotted in figure 5.

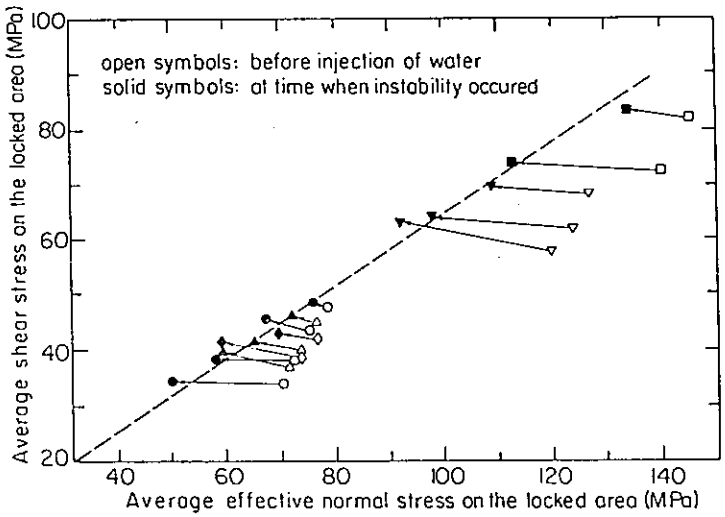

Figure 5 Average shear stress and the average effective normal stress on locked area.

It is seen that the solid symbols, which indicate the average state of stress on locked area at the moment of movement, cluster about the friction criterion. The result demonstrates that the condition for joint movement is that the average state of stress on locked area satisfies the effective friction criterion.

shear stress in the remaining locked region on the joint surface increases with time. This situation may last until a critical state of stress on the joint is met, at which a sudden instability may occur. We suggest that this mechanism of stress transfer may be a viable mechanism of induced movement of rock joint or fault..

By comparing the experimental data with model predictions we show that the critical condition for movement of rock joint is when the average shear stress over the locked region becomes equal to the value given by the friction criterion.

4.CONCLUSION AND DISCUSSION

Most previous studies of frictional properties of rock joint were made on the assumption that the stress was macroscopically uniform, but we think that the same friction criterion may be applicable to both under uniform and nonuniform stress conditions.

When part of the joint weakens and its strength is lowered to the ambient shear stress, movement will occur on that part , and part of the shear stress will be released, in order to maintain an overall equilibrium, the decreased shear stress will be transferred to the locked area of the joint. From figure 5, it is seen that the transferred stress is relatively small .

Assuming the correctness of this model, the mechanism of triggering effect may be that the joint

surface is gradually weakened and unloaded through pore pressure increase and the shear stress is transferred to a few hard asperites, leading to the eventual rupture and sudden release of shear stress. In the field, the wave pressure pulse might rupture seals between previously isolated porous fluid volumes with different hydrostatic pressure. After the resulting transfer of water, whose speed would depend on the permeability and pressure gradients, a joint might find itself immersed in a much higher static pore pressure than it previously had to endure. The delay time between cause and effect may be determined by the permeability around the joint.

We note the experiment in this text is too simple to compare with the actual condition. It need to be improved in a more complete investigation of the problem. In the absence of many improvement, the present result can only be regarded as preliminary.

REFERENCES

Cinna Lomnitz (1996), Search of a worldwide catalog for earthquakes triggered at intermediate distance, Bulletin of the Seismological Society of America, 86,293-298.

Kuo-liang Wen, Igor A. Beresney, and Shih-Nan Cheng (1996), Moderate-magnitude seismicity remotely triggered in the Taiwan region by large earthquakes around the Philippine sea plate, Bulletin of the Seismological Society of America, 86, 843-847.

Study of the Mechanism of Destruction of Rock with a Discrete Inhomogeneity

A.D.Alexeyev, V.N.Revva
A.A.Galkin Physico-Technical Institute of the Ukrainian Academy of Sciences,
340114 Donetsk, Ukraine

Yu.B.Gryadushchi
"Makeyevugol" Coal Mining Association

A.N.Kabanov
Ministry of Coal Industry of Ukraine

ABSTRACT: The experimental investigations of the destruction mechanisms in the rock samples with discrete inhomogeneity have been carried out using the unique three-axis nonequicomponent loading plant. The loading of samples was performed according the $\sigma_1 > \sigma_2 > \sigma_3$ configuration while σ_3 varied within 0–5 MPa, σ_2 within 10–100 MPa, and the σ_1 was increased up to the destruction of sample (700 MPa max). The samples of cubic shape were prepared from the various rock with discrete inhomoheneity. The rock samples featured the different elastic properties and each one contained an artificial disk-type crack placed at a definite angle in respect to the gluing plane. The experiments have allowed us to establish the dependencies of the destroying stresses on the ratio between the elastic constants of the composite samples, crack orientation angle and loading configuration making possible the evaluation of the mechanism of destruction of the rock with a discrete inhomoheneity.

The rock are the typical examples of discrete solids containing the various stress concentrators like the cracks which reduce the strength. A special feature of the rock is a great variety of physical and mechanical properties including the discrete inhomogeneity in the elastic parameters of the rock mass due to its layered structure. This makes important the investigation of the mechanism of defect formation (of crack type) in a medium with discrete inhomogeneity.

The experimental studies on the destruction of samples of the rock with discrete inhomogeneity have been conducted at A.A.Galkin Physico-Technical Institute using an unique three-axis compression plant (TANL plant, USSR Pat. No 128534) [1]. The three-axis drawing of the operating unit of this machine is presented in fig.1.

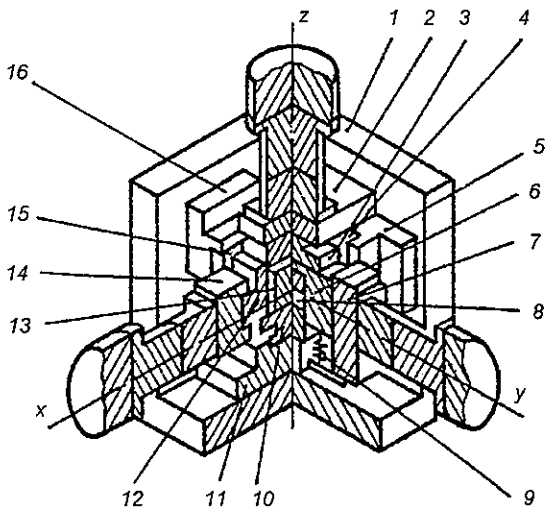

Fig.1. Three-dimension sketch of an operating chamber of the TANL plant

The base *1* bears the rigidly fixed supports *5*, *11*, *16*, providing the movement of the receiving plates *4*, *10*, *15* along the guides. The loading system consist of three hydraulic cylinders oriented along the three mutually orthogonal directions, joining elements and journals *2*, *7*, *14*. These journals conducts the loads developed by the cylinder to the pressing plates *3*, *6*, *12* and, hence, to the sample under investigation *8*. At the same time they guide the movement of the working plates. The working receiving plates *4*, *10*, *15*, and the pressing ones *3*, *6*, *12* are provided with the springs *9*.

The unit operates the following way. When the pistons of hydraulic cylinders move along the mutually orthogonal directions towards the sample *8*, the pressing plates *3*, *6*, *12* together with the receiving ones *4*, *10*, *15* form the closed chamber overlapping each other. For instance, pressing plate *6* (y-axis) slides along the pressing plate *3* and the receiving one *4*. Simultaneously the plate *6* touches plates *12* and *10* moving them along the guides of journal *14*, and, respectively, support *11*. The springs of pressing plate *12* and receiving one *10* are therefore compressed and provide the constant touching of the pressing plate *6* and receiving one *10*. The same scheme of operation is realized during the displacement of the other two pistons (x and z axes). The sample is compressed by the pressing plates *3*, *6*, *12* and the receiving ones *4*, *10*, *15* over the hole area of interface between these plates and the corresponding facets of the sample.

The described configuration provides the always closed volume of the test chamber and the possibility to vary the three mutually orthogonal loads independently. The more detailed description of this plant is given in [1].

The TANL plants of the second generations feature the use of roller bearings between the moving surfaces. The friction is reduced by factor of 50, as is revealed by calculations.

The studies were carried out on the samples of argillite with σ_{compr} = 35 MPa, $E = 10^4$ MPa, Poisson's factor $\nu = 0.23$ and the sandstone (σ_{compr} = 120 MPa, $E = 2.5 \cdot 10^4$ MPa, $\nu = 0.11$) of Donbass.

The samples were cut using a machine saw intended to process the quartz crystals that allowed us to obtain the cubic specimens with great accuracy. The samples with rib size of 60 mm had the deviation in the distances between the parallel planes and the perpendicular ribs less than 0.04 mm, and a convexity of the surface less than 0.03 mm.

The bulk samples were cut by halves. On the dissection surface (gluing plane) there were semicircular cuts 0.7–1.0 mm thick and 155 mm in diameter made by a diamond disk saw. These cuts were oriented at different angles from 50° to 70° with intervals of 5°.

After the treatment by a resonant vibrator with the wedge, fatigue crack was formed at the month of this cut. Then the halves of the sample were glued together by a glue featuring the values of E and ν close to those of a sandstone (sandstone–sandstone configuration) or an argillite (argillite–argillite or sandstone–argillite ones).

The composite samples with an artificial crack at angle of α to the gluing plane were again processed with machine saw in order to enhance the tolerance of orthogonality of the facets (see fig.2)

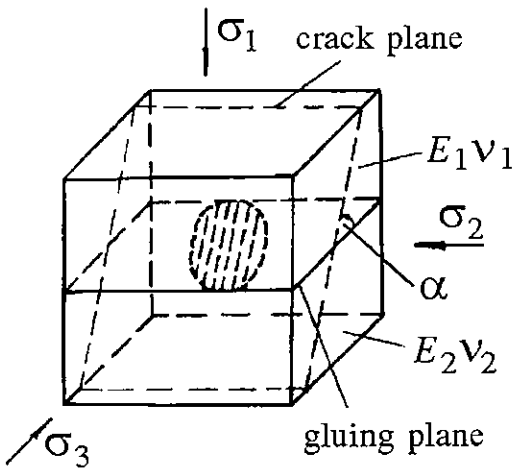

Fig.2. Sample for the studies of rock with discrete inhomogeneity.

The loading was applied according to $\sigma_1 > \sigma_2 > \sigma_3$ configuration. The σ_3 was varied within 0–50 MPa, σ_2 – within 10–100 MPa, and σ_1 was gradually increased up to the destruction of a sample.

Influence of a discrete inhomogeneity (composite samples), crack plane orientation in respect to maximal compressive load (σ_1) on the rock strength in a three-dimensional nonequicomponent stressed state is shown in fig.3 (each points is a mean value over 3–6 tests on TANL plant). The extremal (minimal) value corresponds to the dangerous orientation of a crack at angle of $\beta = 0.5$ arcctg ρ in respect to the main maximal compressive

stress ($\beta = \pi/2 - \alpha$) where ρ is an internal friction factor, $tg\rho_0$ (ρ_0 – internal friction angle). The minimal strength was pointed out at $\alpha = 60°$ in sandstone, and $\alpha = 65°$ in argillite that corresponds to $\rho_0 = 30°$ and 40° respectively. One should note that the values of ρ_0 determined from the envelopes of More circles by the data on rock tests in three-axis stressed state are 32° for sandstone and 38° for argillite.

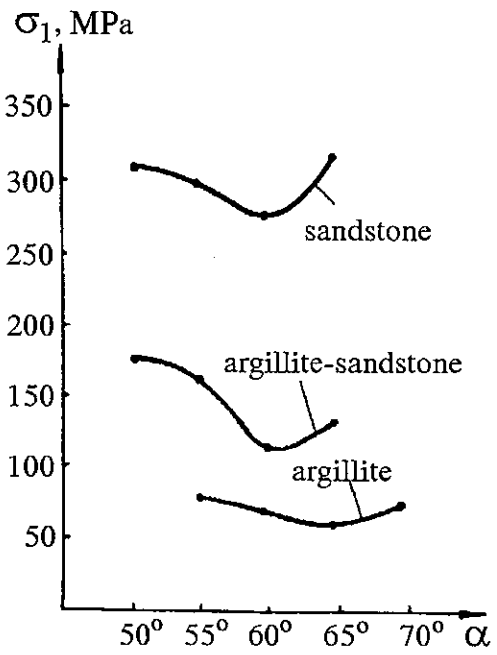

Fig.3. Influence of a discrete inhomogeneity of rock and crack orientation on the destructive stress.

Investigation of the region of plastic deformation in a vicinity of a crack and its deviation from the initial orientation have proved that the destruction of rock in three-axis nonequicomponent field of compressive stresses occurs due to the spread of shift cracks along a plane tilted by an angle of β to the main destructive stress. The similar theoretical conclusion was elaborated by G.P.Cherepanov [2]. The variation of the initial orientation in respect to β angle towards any direction requires the huge loads for destruction so the region of plastic deformation spreads around the cracks. When the crack spreads at ultimate state it moves towards the angle β. The higher the modulus of elasticity, the larger is the difference in the strength of rock with different initial orientations of cracks $\Delta\sigma_1$. For the sandstone samples studied $\Delta\sigma_1 = 50$ MPa while that for the argillite is 23 MPa.

The bulk strength of argillite–sandstone composite samples is close to that of argillite but is not equal to the strengths of the weakest part as assumed on the known strength theories.

REFERENCES

1. *Alexeyev A.D., Revva V.N., Ryazantsev N.A.* Destruction of rock in the bulk field of comressive stresses. – Kiev; Naukova dumka, 1989. – 166 p. (in Russian).
2. *Cherepanov G.P.* On the development of cracks in solids. Applied math. and mechanics, 1966, Vol.3, No1, p.82–93 (in Russian).

Selections of Contact Spring stiffness values in the Numerical Analysis for the System of Rigid Disks

C.P. Wang, J. Sheng, C.Y. Wang, C.L. Lee

Department of Civil Engineering, National Central University
Chungli, Taiwan

ABSTRACT: In a discrete element system, both the normal and shear springs are often used to represent the contact forces among elements in a numerical simulation. It is found that the stiffness of the springs significantly affects the mechanical behavior of a discrete element system. In this paper, an emperical equation for selecting the spring stiffness for a system of rigid disks is proposed. The calculated stiffness depending on the size and density of the disks in contact gives a good and stable result in the numerical simulation.

1 CRITICAL TIME STEP

A critical time step Δt is defined in Eq.(1) for a single degree of freedom system[1] [2]with a particle mass m and a spring stiffness k.

$$\Delta t \leq \frac{T}{\pi} = \frac{2\pi/\omega_n}{\pi} = \frac{2}{\omega_n} = 2\sqrt{\frac{m}{k}} \tag{1}$$

Or, it can be rewritten as

$$k_n \leq 4m/(\Delta t)^2 \tag{2}$$

In employing the explicit time integration scheme, any time step smaller than the critical value from Eq.(1) will result in a numerical convergence[3].

For disks with different sizes and densities, it would be a little difficult to choose a value for the mass in Eq.(1) in order to reflect the influences of different sizes and densities of the disks in contact. Also, it often takes several trials to determine a value for the spring stiffness k.

2 EMPERICAL EQUATION FOR NORMAL SPRING STIFFNESS

A simple system with two disks of same size colliding along their centerline is used here as shown in Fig. 1. The necessary parameters for the analysis and the analytical solutions are given in Table 1. Velocities of two disks before and after the collision are shown in Fig. 2. An error index for the calculated velocity is defined as in Eq.(3).

$$Error(\%) = \frac{v_2' - v_1}{v_1} \times 100\% \tag{3}$$

in which v_1 is the velocity of disk 1 before the collision and v_2 is thevelocity of disk 2 after collision. Analytical solutions of velicities correspond to zero error index. Figures 3 and 4 give the error index for different disk sizes under various contact spring stiffness at time step values of 10^{-4} sec. and 10^{-3} sec. respectively.

Two conclusions can be made from these two figures. First, for a given time step, when the radius of the disk increases an order, the spring stiffness has to increase two orders in order to keep the error index at the same level. This can be expressed by Eq.(4) where k_n is the spring stiffness and r is the disk radius.

$$k_n \alpha (1/\Delta t)^2 \tag{4}$$

Secondly, for a given radius, when the time step value reduces to one tenth, the spring stiffness has to increase two orders in order to keep the error index at the same level. This can be expressed by Eq.(5).

$$k_n \alpha (r)^2 \tag{5}$$

Since the mass of a disk is proportional to the square of its radius, Eqs.(4) and (5) match perfectly with Eq.(2). Taking a disk of radius 1cm and an error index of 1.42% as a reference, Eq.(6) is proposed to determine a normal contactspring stiffness k_n as follows:

$$\frac{k_n}{10^8} = \left(\frac{10^{-4}}{\Delta t}\right)^2 \frac{r^2}{1^2} \frac{\rho}{\rho_0} \tag{6}$$

where ρ is the disk density (g/cm^3), ρ_0 is the density of quartz sand 2.65 (g/cm^3), r is the disk radius (cm) and, 10^8 is in ($dyne/cm$) and 10^{-4} is in second and 1 in (cm) for normalization.

3 EMPERICAL EQUATION FOR SHEAR SPRING STIFFNESS

A simple system of a disk with initial velocity v and zero angular velocity moving on a horizontal plane is used here. The frictional coefficient between the disk and the plane is μ_k. For various disk sizes, Table 2 gives the analytical solutions of the translate velocity v and the angular velocity ω as well as the time t required for full rolling. The corresponding initial velocity is 100 cm/sec.

The same definition of an error index as in Eq.(3) is used here. Figures 5 and 6 give the error index for different disk sizes under various shear spring stiffness at time step values of 10^{-3} sec. and 10^{-4} sec , respectively.

It is found from these figures that the shear spring stiffness is close to the normal one for a same error index. Following a same process as is the case of normal spring stiffness, an emperical equation to determine the shear spring stiffness can be expressed as

$$k_s = \left(\frac{10^{-4}}{\Delta t}\right)^2 r^2 \frac{\rho}{\rho_0} \times 10^8 \tag{7}$$

4 COLLISION OF DISKS WITH DIFFERENT SIZES

The concept of conservation of momentum and energy is used here to analyses the system with two disks of different sizes. Eq.(8) gives the velocity v_2 of disk 2 of radius r_2 after disk 2 is collided with disk 1 of initial velocity v_1 and radius r_1. From Eq.(8), it is clear that $v_2 = 2v_1$ when a approaches inifinity. Figure 7 shows the analytical and numerical solutions for the system and obviously using the smaller disk radius to determine the spring stiffness causes no difficulties.

$$v_2' = \frac{2m_1}{m_1+m_2} v_1 = \frac{2\rho\pi r_1^2}{\rho\pi r_1^2+\rho\pi r_2^2} v_1 = \frac{2a^2}{a^2+1} v_1 \tag{8}$$

5 CONCLUSION

Through comparisons between analytical solutions and numerical results, emperical equations are proposed to determine the contact spring stiffness for a rigid disk system. Later papers will show that the proposed equations for the spring stiffness give good results for both circular and elliptical disks.

6 REFERENCE

[1] Chang, C. S. and K. B. Acheampong ,"Accuracy and Stability for Static Analysis Using Dynamic Formulation in Discrete Element Methods ," 2nd Int. Conf. on DEM, 3.17, (1993).

[2] Cundall, P. A. and O. D. L. Strack ,"A discrete numerical model for granular assemblies, " pp.517-535,(1991).

[3] Lin, Jeen-Shang ,"Notes on Discrete Element Method for Disc Particles,"Workshop on particulate mechanics, Taipei , pp.423-469 , (1991).

Table 1. Parameters and solutions for the disks collision

parameter/solution	value
disk radius (r_1, r_2) cm	(10.0,10.0)
time step Δt sec	1.0E-4
damping ratio (b_n, b_s)	(0.0,0.0)
friction angle,cohesion (Φ, c) $(\deg ree, pa)$	(0.0,0.0)
stiffness (k_n, k_s) $dyne/cm$	(1.0E+10,0.0)
initial velocity of disk 1 (v_x, v_y, ω) $cm/$sec	(100.0,0.0,0.0)
initial velocity of disk 2 (v_x, v_y, ω) $cm/$sec	(0.0,0.0,0.0)
velocity of disk 1 after collision (analytical) (v_x, v_y, ω) $cm/$sec	(0.0,0.0,0.0)
velocity of disk 2 after collision (analytical) (v_x, v_y, ω) $cm/$sec	(100.0,0.0,0.0)
velocity of disk 1 after collision (numerical) (v_x, v_y, ω) $cm/$sec	(-0.392,0.0,0.0)
velocity of disk 2 after collision (numerical) (v_x, v_y, ω) $cm/$sec	(100.392,0.0,0.0)

Table 2.Translate and angular velocities of various disk sizes

disk radius	r=1.0 cm	r=10.0 cm	r=100.0 cm
time for full rotation t (sec)	0.06	0.06	0.06
angular velocityω (rad/sec)	-66.67	-66.67	-66.67
translate velocity v (cm/sec)	66.67	66.67	66.67

(Positive angular vlocity for counter-clock wise rolling)

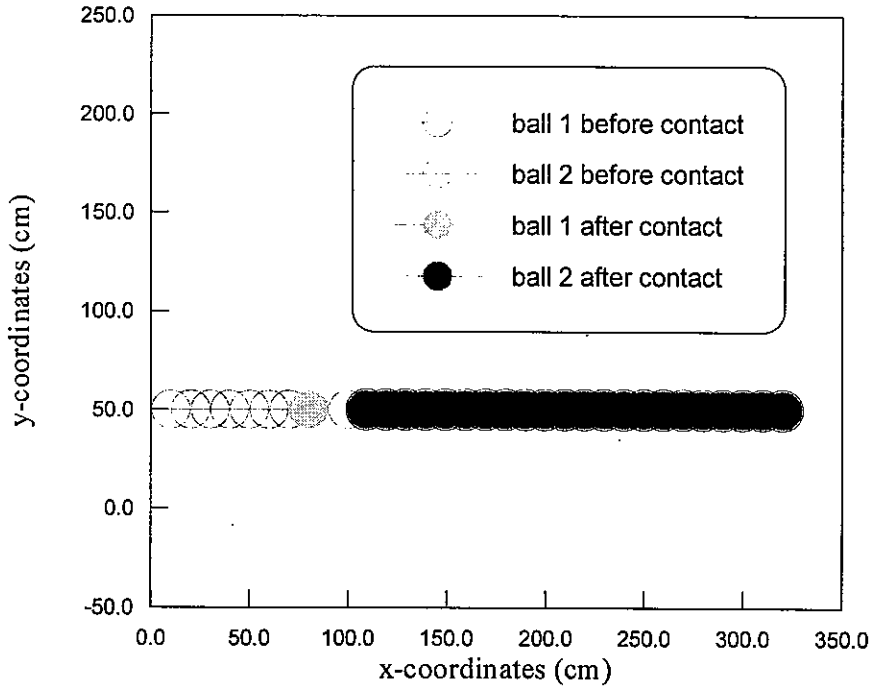

Fig.1 Physical model of two disks collision

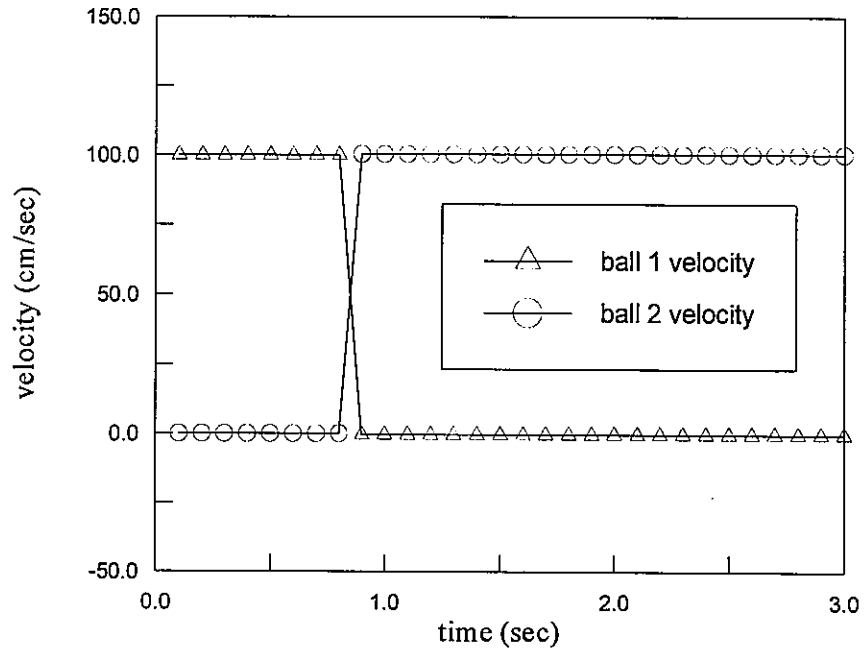

Fig.2 Velocities before and after collision

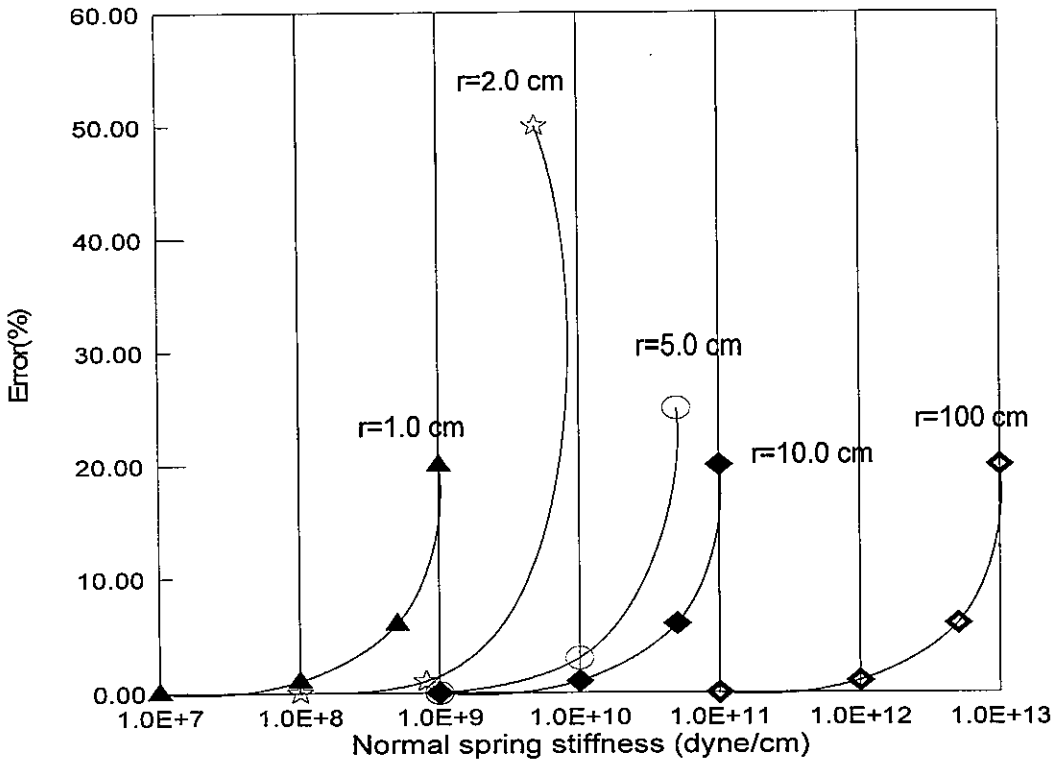

Fig.3 Velocity error under various stiffness and disk sizes (Δ t=1.0 e-4 sec)

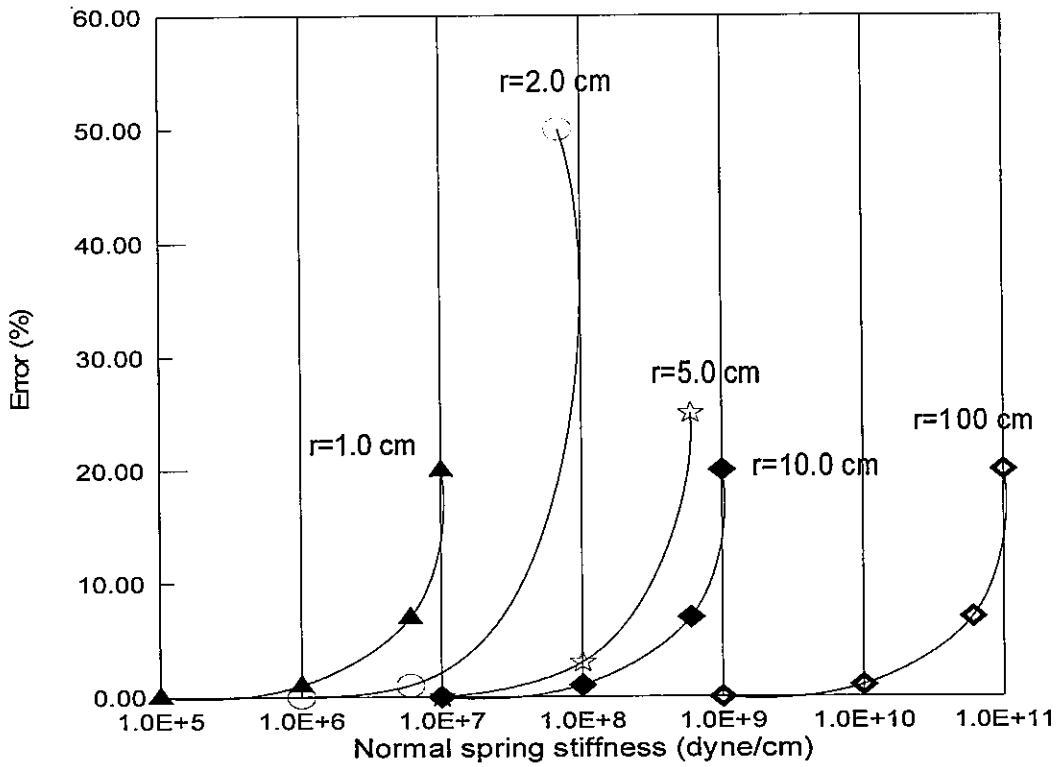

Fig.4 Velocity error under various stiffness and disk sizes (Δ t=1.0 e-3 sec)

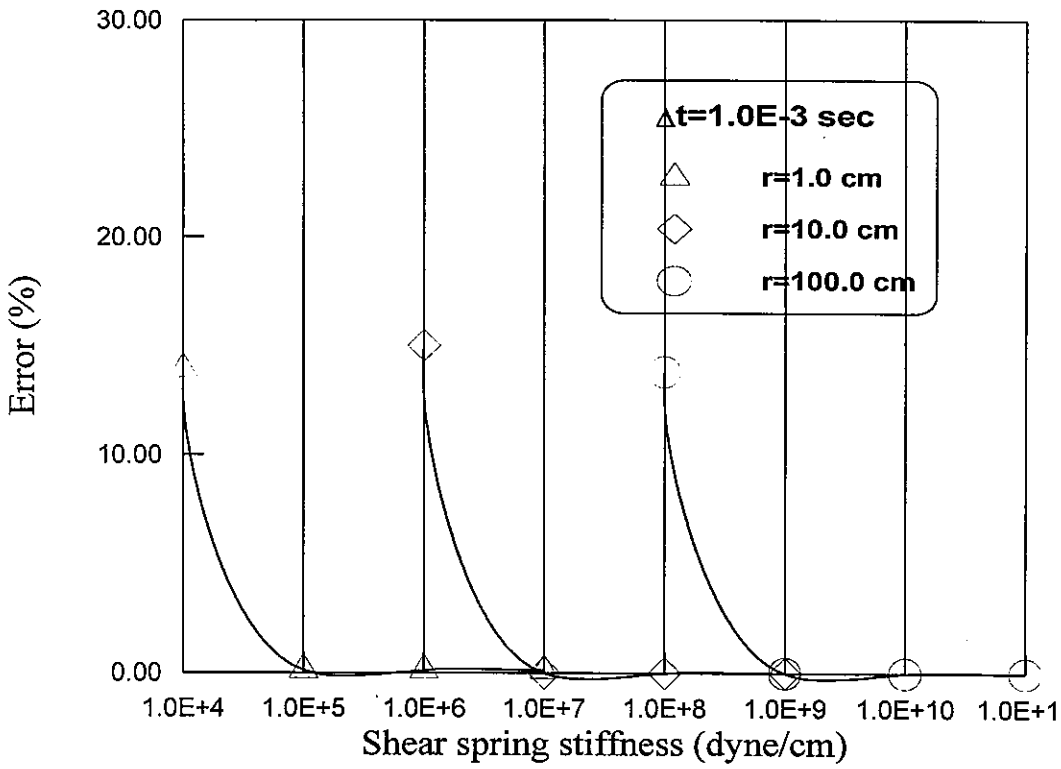

Fig.5 Velocity error under various stiffness and disk sizes (Δ t=1.0e-3 sec)

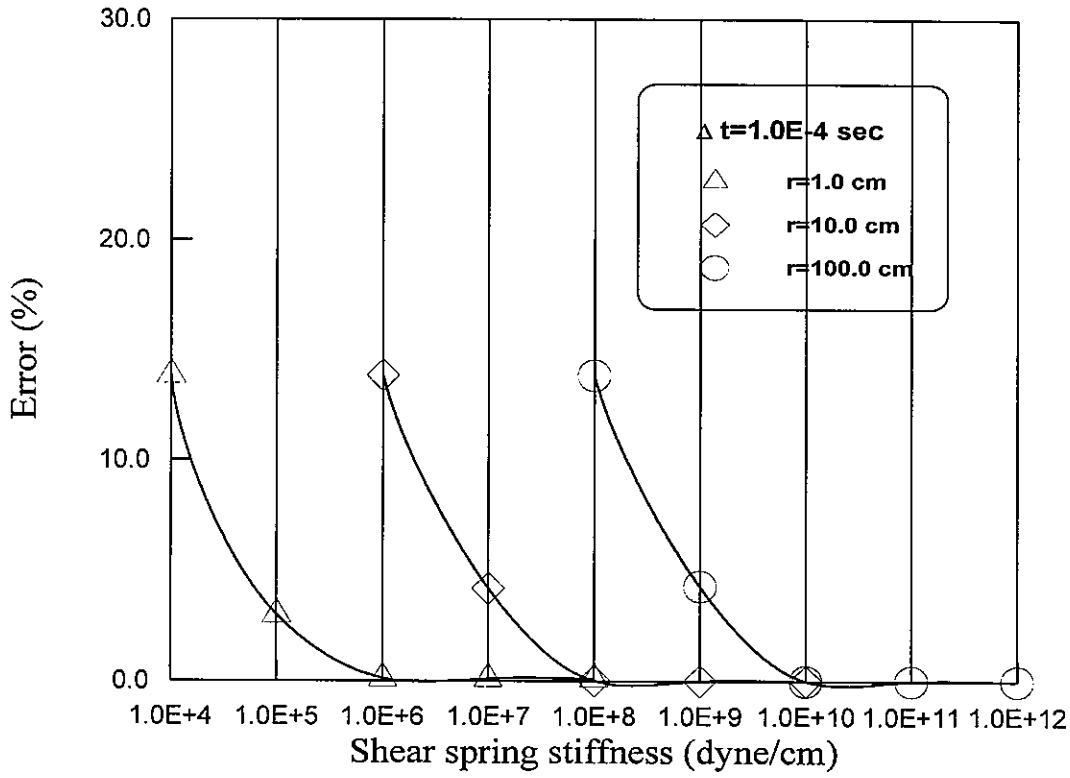

Fig.6 Velocity error under various stiffness and disk sizes (Δ t=1.0e-4 sec)

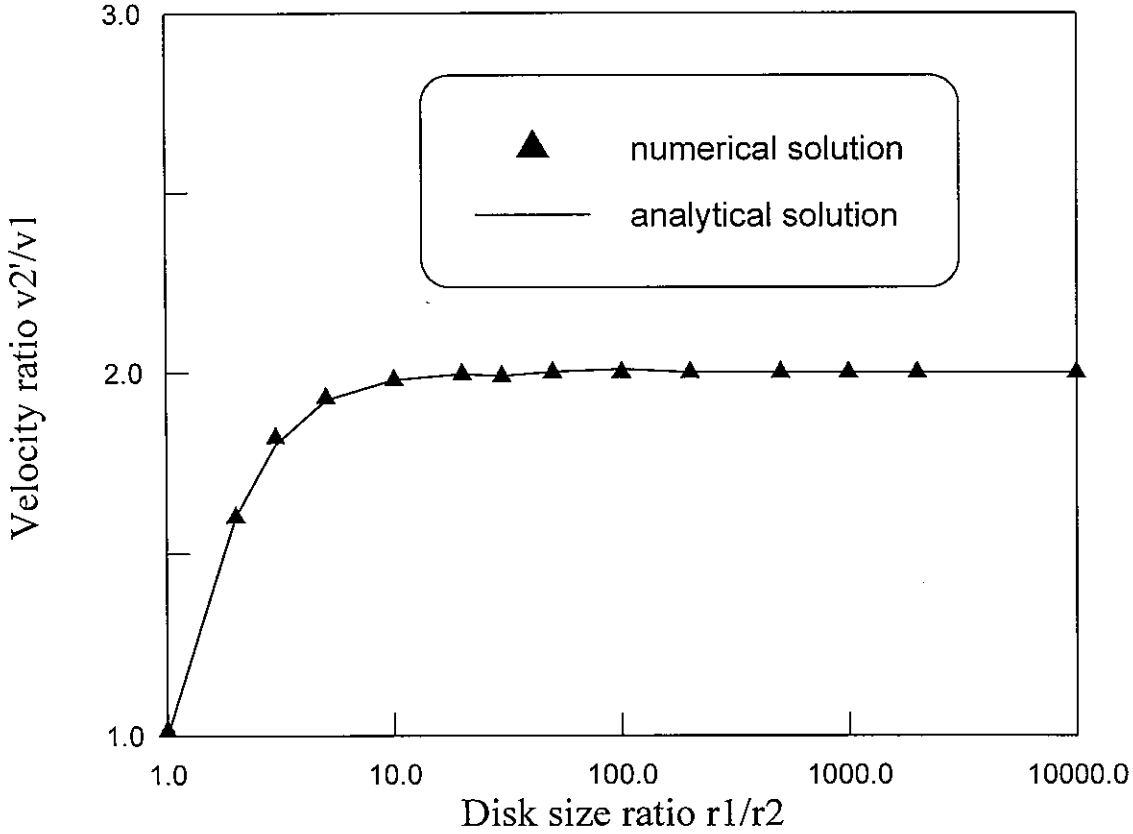

Fig.7 Effect of disk size ratio on velocity ratio

Effect of the asperity damage on the shear behaviour of irregular rock joints

Tetsuro ESAKI, Shouji DU, Yujing JIANG and Yoshinori WADA
(Institute of Environmental Systems, Kyushu University 36, Fukuoka 812-81, Japan)
Jun SUN
(Faculty of Geotechnical Engineering, Tongji University, Shanghai, P.R. China)

ABSTRECT: Asperity damage of joint surface occurs in one or a combination of two mechanisms: asperity wear and asperity shearing. To quantify the degree of asperity damage on joint surfaces during shear process, two cases of shear tests were performed on artificial irregular joints under the conditions of different normal stresses and different shear displacements. Moreover, the roughness surfaces of joints were measured with laser scanning instrument before and after shear test. Based on the results of shear test and the measurement, a new approach is developed for quantifying the relation of the surface roughness and the surface damage of rough joints under the different normal stress and the subscribed shear displacement. Furthermore, a new surface damage criterion is obtained for modeling the irregular rock joints at low normal stresses.

1 Introduction

Recently, various deep underground utilization have drawn the concentrated attention. For the appropriate development of them, it is extremely important to examine and to evaluate the mechanical and hydraulic properties of rock joints. Strength and deformation behaviour and flow properties of a joint depend on its surface roughness. To characterize surface roughness, a number of methods have been suggested in literature (Patton 1966, Barton 1977). However, there is still a large number of problems to solve before having an overall understanding of surface roughness. On the other hand, dilatant deformation gives rise to a joint complex mechanical and hydraulic response. Dilatant deformation is not a purely kinematic phenomenon since the asperity surfaces that are engaged in sliding undergo various forms of damage, or destruction, that are stress and deformation history dependent. Surface damage of rock joints occurs in one or a combination of two mechanisms: asperity wear and asperity shearing. Plesha (1987) proposed an exponential law for surface damage based on his experimental results. Jing (1990) later verified this model by experiments and modified the parameters of the model. However, the surface damage model mentioned above is based on regular joints and don't involve damage status during shear process.

Therefore, in this paper, based on the measurement of rough profiles of irregular rock joints and the results of shear test under different normal stress and subscribed shear displacement, a new approach is, firstly, developed for quantifying the surface roughness of irregular joints. Then, the surface damage of rough joints is evaluated in relation with the different normal stress and subscribed shear displacement. Finally, the damage criterion is developed for modeling the irregular joints at low normal stresses.

2 Joint shear behavior under loading and displacement history

2.1 Direct shear test apparatus and specimens

A shear testing apparatus has been developed, as described in detail by Esaki (1991). This system consists of a direct shear loading

unit with a specially designed shear box, a control and data acquisition unit and an artificial joint creating unit. Using this apparatus, an artificial joint can be created in the rock specimen, and normal and shear stresses can be arbitrarily applied on the joint.

Hard granite specimen from Nangen of Korea and sandstone specimen from Nagasaki of Japan were used in this study. The basic mechanical properties of these two materials are shown in Table 1. The size of specimens is 120mm length, 100mm width and 80mm height. Each specimen has a couple of saw cut slits (width 1mm, depth 10mm) at mid-height of the specimen for creating an artificial joint correctly and easily. Thus, the horizontal area of joint shear plane is 100mm × 80mm.

2.2 Testing procedure

In order to investigate the effect of surface damage on shear behavior of joints, two cases of shear experiment are conducted at two granite and sandstone joints, respectively. In the case 1, as normal loading historical joint, different normal stresses (5, 10, 20, 30MPa for granite specimen of 1# and 2, 5, 10, 20MPa for sandstone 5#) were loaded up on same jointed specimen. And then at every class of normal stress, shear displacement was controlled in steps at a rate of 0.1mm/sec until maximum shear displacement of 20mm. Finally, the normal stress was unloaded and the procedure was repeated in the reverse direction until the beginning point. In the case 2, as displacement historical joint, normal stress of 10MPa for granite 3# and sandstone 7# was loaded up. Shear displacement was controlled at same jointed specimen in steps at a rate of 0.1mm/sec until the different shear displacement of 0.7, 5, 20mm respectively. The irregular rough surfaces of jointed specimens were measured by laser scanning instrument (Fig. 1) before and after each shear process through taking out of jointed specimen from shear box.

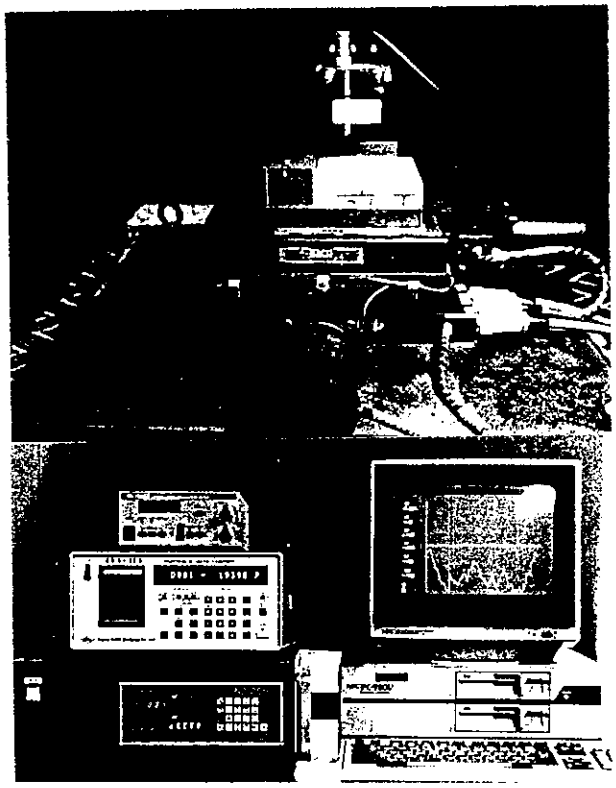

Fig. 1: Photograph of a laser scanning instrument for measurement of joint profiles.

2.3 Experimental results

Shear deformation curves obtained at different constant normal stress and shear displacement for sandstone joints are shown in Figures 1 and 2. Shear stress reaches a rather sharp peak at a relatively small shear displacement as an approximate linear, and then falls to a constant residual value with increasing of shear displacement. Peak and residual shear stress and shear stiffness become larger with increasing of normal stress. Dilatancy will occur when shear stress approaches to peak. It increases at reduced rate with increasing of shear displacement at all normal stress condition. Dilatancy decreases as normal

Table 1: Mechanical properties of rock specimens

Name	Young's Modulus E_t, (GPa)	Specific gravity γ (g/cm^3)	Unixial compressive strength σ_c	Joint wall compressive strength σ_j
Granite	35.71	2.64	190MPa	137MPa
Sandstone	7.81	2.40	72	52

stress increases and surface damage.

In the case 1, as normal loading historical joint, shear deformation curves (Fig.2) show the peak shear stress only at the first class of normal stress of 2MPa. After preceding normal stress history, they don't show peak significantly and the peak shear stresses agree gradually with residual shear stresses. In the case 2, as joints of shear displacement history, peak shear stress and dilatancy decrease gradually as shear displacement increases (Fig.3). After preceding shear displacement of 0.7mm and 5mm, the peak shear stresses agree with residual shear stresses because of the affection of the surface damage.

3 A new approach for quantifying roughness of irregular joints

In general, roughness profiles of irregular rock joints consist of non-stationary and stationary components. To quantify surface roughness in a certain shear direction, firstly, the non-stationary component may be represented by a linear function with a positive or a negative slope ϕ_0, as shown in Fig.4(a), which is estimated through regression analysis in measured profile heights (Kulatilake, 1995). Next, removal of the non-stationary component from actual profile obtains the stationary component of the roughness profile. And then the stationary roughness is quantified by the new fractal model proposed by Du et al.(1997). That is, the average roughness angle U(h) is defined as root mean square of the first derivation increment of two asperity heights separated by a lag distance h:

$$U(h)=\left\{\frac{1}{(N-j)}\sum_{i=1}^{N-j}\left[\frac{Z(x_i+h)-Z(x_i)}{h}(\cos\phi_0)^2-\frac{\sin 2\phi_0}{2}\right]^2\right\}^{1/2} \quad (1)$$

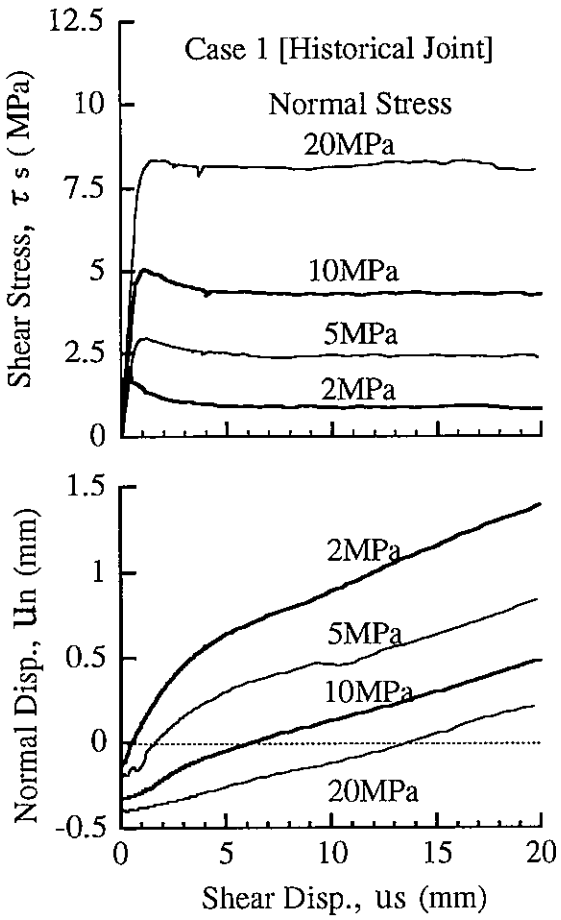

Fig. 2: Shear stress-displacement and normal-shear displacement (dilatancy) curves of a sandstone joint for different normal stresses.

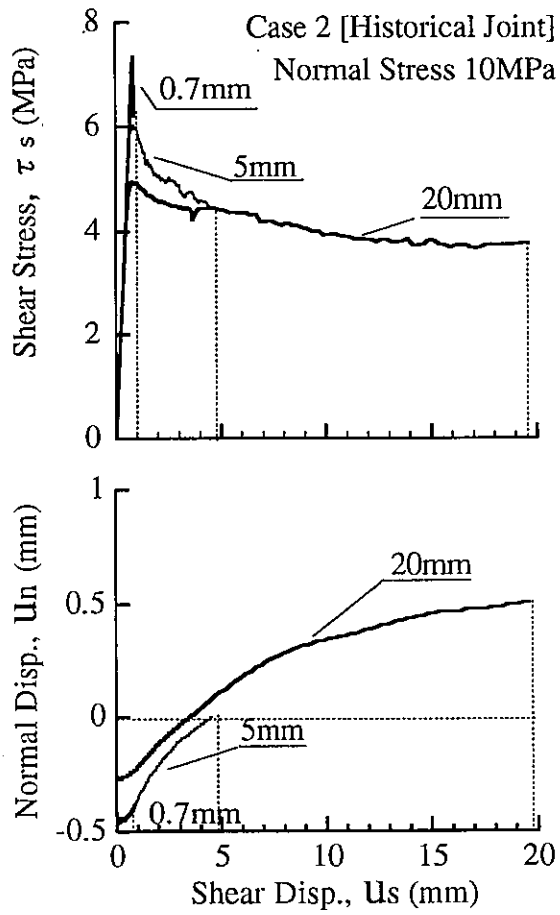

Fig. 3: Shear stress-displacement and normal-shear displacement (dilatancy) curves of a sandstone joint for given shear displacement.

The relation between U(h) and fractal parameters (B and D) can be written as:

$$U(h) = B\,h^{(1-D)} \qquad (2)$$

On a log-log plot of U(h) vs. lags h (Fig.4(b)) , amplitude B is the intercept on U-axis, and $1-D$ is the slope of the plot and D is the fractal dimension. Therefore, the combined fractal parameters (amplitude B and fractal dimension D) can be used to quantify the stationary roughness in practice.

Moreover, since joint surface is three-dimensional, one of the approaches is, therefore, to select several parallel lines on joint surface for measuring the profiles along a certain shear direction. At first, the asperity heights of the profiles is recorded at every 0.05mm up to an accuracy of 0.001mm by laser scanning instrument along each line. Then, the slope (ϕ_0) and fractal parameters (B and D) of each profile are calculated by the above method. Finally, the weighted average values of the slope (ϕ_0) and fractal parameters (B and D) of the several parallel profiles on joint surface are estimated. Therefore, the average roughness angle α of irregular rock joints along shear direction can be given by the following form, which represents the surface roughness of non-stationary and stationary components.

$$\alpha = \phi_0 + U(h) = \phi_0 + B\,h_0^{(1-D)} \qquad (3)$$

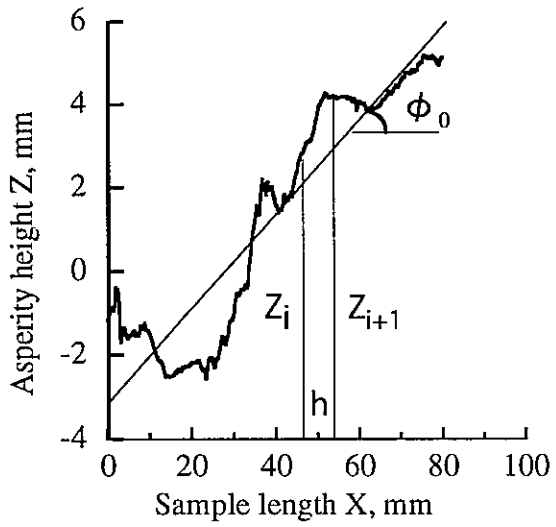

(a) The slope ϕ_0 for non-stationary roughness

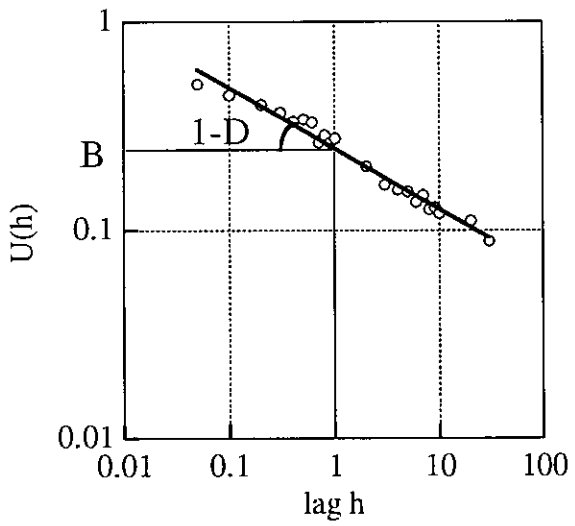

(b) The fractal parameters (B and D)

Fig. 4: The diagram used to calculate statistical and fractal parameters for joint profile.

4 The surface damage analysis

Surface damage (or roughness degradation) appears to be either, or a combination of two mechanisms. The first is wear in which the asperity surfaces are more or less gradually worn away with increasing sliding displacements. The second is asperity shearing which is more catastrophic in that gross of asperities are fractured or sheared from the joint surfaces. Because of damage, surface roughness of rock joints changes as the evolvement of the normal loading and the shear deformation history. The exact manner in which this phenomenon occurs is very complex. Thus, some reasonable assumptions are made so that some features of surface damage can be accounted for. One of the most significant assumptions by Plesha (1987) is that surface damage is a function of the sliding plastic work W^p. An increment of sliding plastic work W^p (i.e. the dissipated energy during shear) is defined by

$$dW^p = dW_s^p + dW_n^p \qquad (4)$$

where $dW_s^p = \tau_s\,du_s^p$ is the increment of shear plastic work and $dW_n^p = \sigma_n\,du_n^p$ is the increment of normal plastic work during shear. The total sliding work accumulated over some sliding history is given by

$$W^p = \int dW^p = \int \tau_s\,du_s^p + \int \sigma_n\,du_n^p \qquad (5)$$

where τ_s, σ_n are the macroscopic (or average) contact stresses in the shear and normal direction of the joint and du_s^p, du_n^p are increments of the irrecoverable sliding displacements in the shear and normal directions.

To quantify the degree of damage, a relative roughness measure R is defined as the ratio between the average roughness angle α of a joint surface that has undergone damage to the average roughness angle α_0 of the same surface that has not. Therefore, the relative roughness measure R is a function of the sliding plastic work W^p, the normal stress σ_n and the joint wall compressive strength σ_j, that is

$$R = \frac{\alpha}{\alpha_0} = f\left(W^p, \sigma_n, \sigma_j\right) \quad (4)$$

Based on the shear test of irregular rock joints at different normal stresses and shear displacements, we focus attention on the mechanism of surfaces damage with special attention to effect of shear displacements and normal stresses. Relative roughness measure R is calculated with joint fracture profiles measured before and after shear test and the plastic work W^p is calculated according to shear deformation curves.

Shown in Fig.5 are results for surface damage (or asperity degradation) as a function of plastic work for the case 2 of preceeding different shear displacements. At initial shear stage, relative roughness measure R decreases very rapidly. It is shown that weak and steep asperities are first fractured and sheared. In this stage, surface damage is very catastrophic and asperities is damaged primarily by shear. After residual shear stress is reached, relative roughness measure R continues to decrease, but the reduced rate is gradually changed to small. It is shown that surface is damaged primarily by wear which is a rather gradual process. It is considered that the damage or degradation of surface asperities caused by shear-off is mainly occured before shear stress reaches to residual state and is about 80% of all damage zones during a shear process. On the other hand, surface damage of sandstone joints is greater than that of granite joints. This

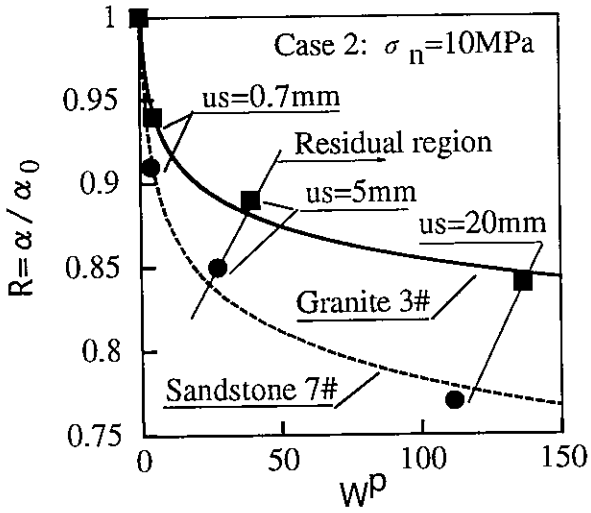

Fig. 5: The effect of shear displacement (or acculated plastic works) on surface damage.

indicates that the harder the rock material is, the greater the damage level becomes. Asperity degradations for the case 1 of preceeding different normal stress are shown in Fig.6. The relative roughness measure R decreases with increase of normal stresses. This indicates that the greater the normal stress is, the greater the damage level is. At the same normal stress level, surface damage of granite joints is less than that of sandstone joints, however, they become similar with decreasing tendency in the relation of the relative roughness measure R and the normal stress level (σ_n/σ_j) (Fig.6(b)).

With the synthetic consideration of the affection of the initial roughness angle α_0, the normal stress σ_n, the joint wall compressive strength σ_j and shear displacement, a new surface damage criterion which takes the following form is suggested for modeling the irregular rock joints at low normal stress level (0-0.4 times wall compressive strength):

$$\alpha = \alpha_0 \exp\left(-c_m\left(\frac{\sigma_n}{\sigma_j}\right)^s (W^p)^t\right) \quad (5)$$

where $\alpha, \alpha_0, \sigma_n, \sigma_j, W_n^p$ are denoted, previously. The coefficients c_m, s and t in the damage criterion are 0.06, 0.14, 0.26, respectively, which are determined by performing multiple regression analysis on the experimental damage results.

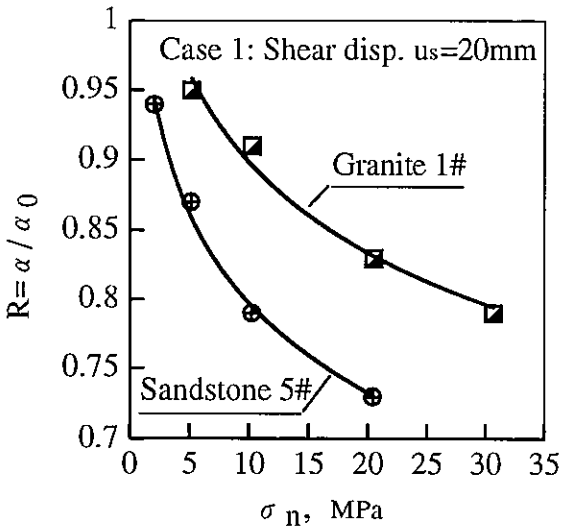

(a) The surface damage vs. normal stress curve

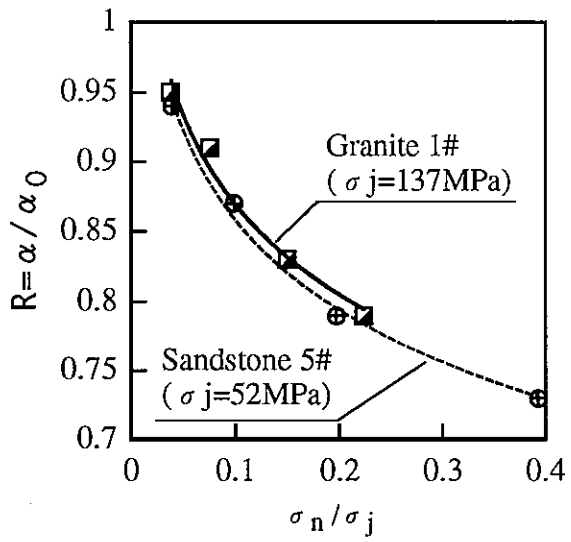

(b) The surface damage vs. normal stress level curve (σ_j : joint wall compressive strength)

Fig. 6: The effect of normal stress (or acculated plastic works) on surface damage.

5 Conclusions

In this study, based on the measurement of rough profiles of irregular rock joints and the results of shear test under the preceeding different normal stresses and subscribed shear displacements, a new approach is developed for quantifying the surface roughness of irregular joints, and the surface damage of rough joints are evaluated in relation with the normal stress and shear displacement. Some significant results are obtained below.

(1) Surface roughness of irregular rock joints can be represented by the average roughness angle α , which is calculated through the slope (ϕ_0) and fractal parameters (B and D) of the several parallel profiles on joint surface.

(2) Surface damage (or roughness degradation) occurs with the history of normal loading and shear deformation process. It is considered that the damage or degradation of surface asperities caused by shear-off is mainly occured before shear stress reaches to residual state and is about 80% of all damage zones during a shear process. On the other hand, surface damage level of sandstone joints is greater than that of granite joints at the same experimental condition.

(3) Based on the results of shear tests, a new surface damage criterion is proposed for modeling the irregular rock joints at low normal stresses.

REFERENCES

Barton N. and Choubey V., The shear strength of rock joints in theory and practice, *Rock Mech*, 10, pp. 1-54, 1977.

Du S., Esaki T., Jiang Y. and Kobayashi K., The relation of fractal characteristics on the rough surface and shear strength of rock joints, *Proc. 28th Symp. Rock Mech.*, Tokyo, Japan, pp. 167-173, Jan. 1997.

Esaki T., Hojo H., Kimula T. and Kameda N., Shear-flow coupling test on rock joints, *Proc. 7th Int. Congr. Rock Mech.*, pp. 389-392, 1991.

Jing L., A two-dimensional constitutive model of rock joints with pre- and after-peak behaviour, *Proc. Int. Con. Rock Joints*, Loen, Norway, pp. 633-638, 1990.

Kulatilake P. H. S. W., Shou G., Huang T. H. and Morgan R. M., New peak shear strength criteria for anisotropic rock joints, *Int. J. Rock. Mech. Min. Sci. & Geomech. Abstr.*, Vol. 32, No. 7, pp. 673-697, 1995.

Patton F. D., Multiple modes of shear failure in rock, *In: Proc., 1st Congress Int. Soc. Rock Mechanics*, Lisbon, 1, pp. 509-513, 1966.

Plesha M. E., Constitutive models for rock joints with ditancy and surface degradation, *Int. J. for Numerical and Analytical Methods in Geomechanics*, Vol. 11, pp. 345-362, 1987.

RESEARCH AND DEVELOPMENT OF NEW DEVICE FOR DISCONTINUITIES' SITE-SURVEY

Tomio Fujikawa [1]
Tosirou Aoki [2]
Takao Hirokawa [3]

ABSTRACT

Recently, new methods for rock mechanics such as Key block theory ,DEM,DDA are becoming increasingly in actual use. As reported in many papers, discontinuities' orientation(strike/dip) plays an important role in rock structure's behavior and stability analysis. To acquire the orientations of discontinuities in rock mass, such as joints ,seams, faults or so, CLINOMETER are usually used. However, this tool tends to have human errors, and is influenced from undulation of discontinuity's face. So the data obtained by this method have often poor reliability to be used for analysis and design .Then we developed a new method which could make site-survey more easy, reliable, and accurate. As a result of this research, a new half-automatic device has been developed. Using the new Device, named "DISCONTINUITY SUEVEYOR" it can be possible to acquire the data within one-third time comparing with CLINOMETER in normal field conditions. Then, according as the excavation work the survey could be done. Also, the poles acquired by the new method on the point diagram concentrate more clearly than the poles obtained by usual CLINOMETER method. Then decision of dominant joints could become more easy and reliable than ever. Accordingly, the results of analysis may be more recognizable.

1. INTRODUCTION

According as being large the scale of structures in rock mass such as under ground power stations , large cutting rock slopes, it has been more and more important to evaluate the discontinuities accurately. At present several methods of analysis and calculations are adopted in the design of NATM or rock slope design where dominated by discontinuities. As you know ,the result of these designs are severely influenced with the values used as the calacteristics of discontinuities in the rock mass. As for us, we have been engaged in the research and development of making key-block system which forecast the rock blocks unstable and quantities of supports rooted in block theory. To make this system applicable in real construction site , we are needed to have new method and device which enables us to acquire the orientations(strike/dip) of joints within very short times. Then we have started to develop new device which plays in stead of today's CLINOMETER used normally by geological engineers.

1. Dr.Eng., Manager. Const. Lab., Civil Eng. Reseach Dept., Tokyu Const. Co., Ltd. (1-16-14, SHIBUYA, SHIBUYA-KU, TOKYO 150, JAPAN)
2. Dr.Eng., Civil Eng. Tech. Dept., Tokyu Const. Co., Ltd. (Same Above)
3. M.S., Civil Eng. Tech. Dept., Tokyu Const. Co., Ltd. (Same Above)

2. SURVEYING SYSTEM USING NEW DEVICE

Items which characterize the rock discontinuities are orientation, position, roughens, continuity, spacing, seepage, etc.. And if we want to do ' design as you go' method such as key block system we have to survey these items within about 15 minuets or so from just after rock excavation to starting of mortal spraying at the face in the construction site. Normally, except the survey of orientation, sketching or photographs are available, and as for the survey of orientation CLINO-METER are available (Photo. 1).

CLINOMETER consists of magnetic needle which points the north, small weight which shows the vertical direction, and the level unit. And then CLINOMETER have some defects, for example, asking the professional skills, tend to have human errors, being necessary about 1 or 2 minuets to obtain one datum, being severely affected the existence of metal equipment.

In order to solve these defects we have made the survey system showed in the fig.1. At the face of excavation, discontinuities' dips/directions are surveyed in succession by the half-automatic device "DISCONTINUITY SUEVEYOR" in a short time. At the same time Photograph are taken by CCD camera. These data are taken into personal computer by way of RS 232C cable. Then by use of CAD system and some mathematical methods, accurate orientations of discontinuities are able to obtain.

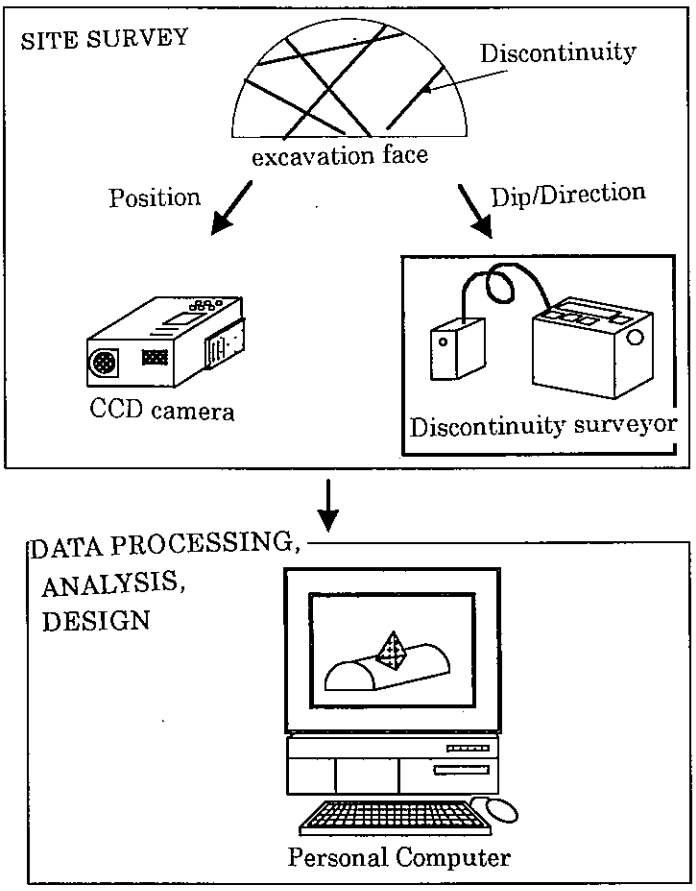

Fig.1 Discontinuity Survey System

3. PRINCIPLE OF THE METHOD

The principle of DISCONTINUITY SUEVEYOR" are basically come from the technology concerning the air plane's attitude control system. This theory is known as strap-down theory which used as the technology to appreciate the three dimensional attitude of air-craft or rocket.

Fig.2 and fig.3 indicate the difference between CLINOMETER and "DISCONTINUITY SUEVEYOR". CLINOMETER is used in static condition at one point in the discontinuity's surface. On the contrary, "DISCONTINUITY SUEVEYOR" is used in dynamic condition tracing the discontinuity's undulate surface.

During the tracing motion the device gets 60 data per second and calculate the average value of data obtained. So the discontinuity's dip/direction are observed more precisely compare with CLINOMETER. Because the data from new devise indicate the direction as a whole direction of discontinuity itself. Phpto.2 shows the units of the "DISCONTINUITY SUEVEYOR" .Fig.4 (a),(b),(c) express the mathematical principle of the new method. Firstly, relative decart coordinates (x,y,z) which move with the sensor unit box are set. In the sensor unit box three gyro sensors which monitor angular velocity around the coordinate axis's and three accelerate sensors those monitor acceleration of the coordinate axis's direction are installed respectively (cf. Fig.(a)). Relative decart coordinates (x,y,z) are corresponded with the earth coordinates (X,Y,Z) ,X axis points north and Y axis points upper direction, at the area where in the normal earth magnetic condition. Then at this time relative decart coordinates (x,y,z) are reset as a initial standard coordinates (X',Y',Z'). The relation between (X,Y,Z) and (X',Y',Z') is calculated from the outputs of three accelerate sensors(cf. Fig.(b)). Then the rotation of the relative decart coordinates (x,y,z) which fixed to the sensor unit box are calculated by using the outputs of three accelerate sensors and three gyro sensors according to the strap-down theory. After sequence calculations, the relation between the relative decart coordinates (x,y,z) and the earth coordinates (X,Y,Z) is able to obtained at every moment.

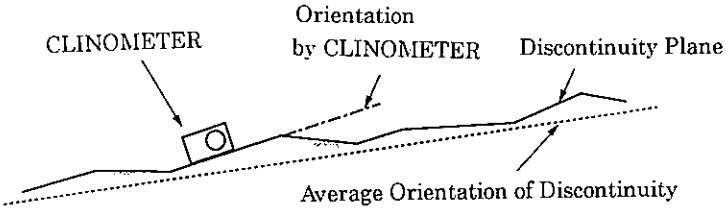

Fig.2 Point Survey with CLINOMETER

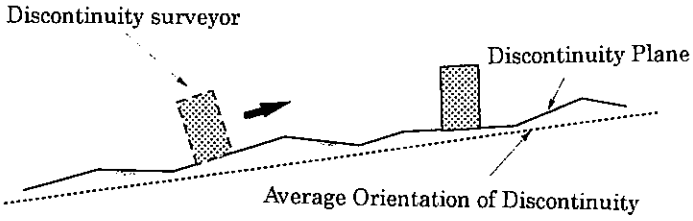

Fig.3 Tracing Survey with New Device

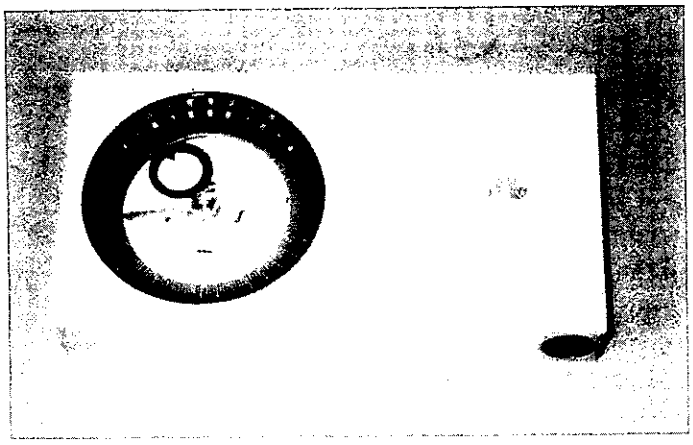

Photo.1 CLINOMETER

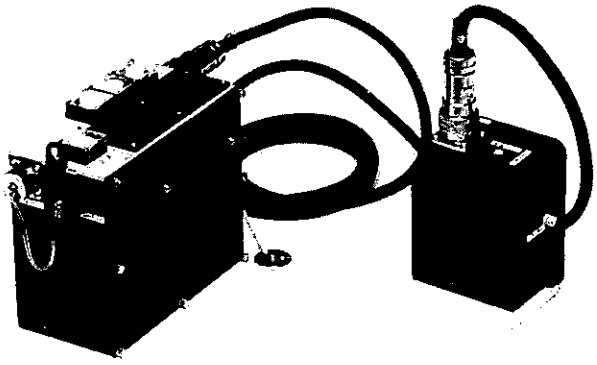

Photo.2 DISCONTINUITY SURVEYOR

4. ELEMENTS AND CHARACTERISTICS OF THE NEW DEVICE

Fig. 5 shows the components the device. The device consists of two parts of units. One is called sensor unit box and the other is called control unit box. Sensor unit box is installed three oscillate gyro sensors, three accelerate sensors and have the switches in order to make start or stop the surveying. The data obtained are sent to the control unit box through the cable. In the control unit box there are data logger , central processing unit (CPU), indicator , battery, and output unit. Fig .6 and Photo. 3 show the situation when the device is used in the rock face. The characteristics of the device are as follows.

- ordinary site engineer or worker is able to survey the joints without any special know-how.
- it is possible to survey about 300 joints at a time.
- the data are not influenced by the near existence of machines or metal materials.
- there is no need to write data in the note at the site.

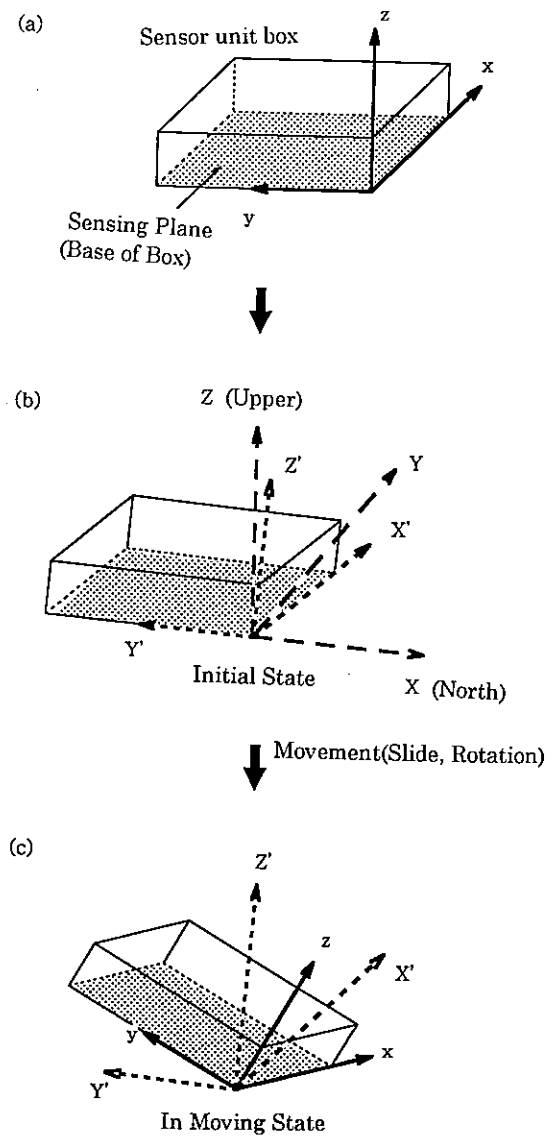

Fig.4 Relation of Coordinates

5. EXPERIMENT TO CONFIRM THE ACCURACY

To confirm the accuracy of the device, the basic experiment was done according to the following procedure.

- setting the sensor unit box to the north
- measure dip/direction three times per 4 slopes which have 30, 45, 60, 75 degrees respectively
- repeat three time about upper process

As a result of the experiment, 9 data were acquired per one slope respectively. And measure the same slopes one time with CLINOMETER to compare with the former data. Fig. 7 (a) indicates one example among these dip data. From this result, concerning dips , values obtained by new device are concentrates clearly. Table 1 shows the result of dips about 4 slopes. The standard deviation σ is between 0.19 degree and 0.31 degree. And then the accuracy of the new device is evaluated as fully contented.

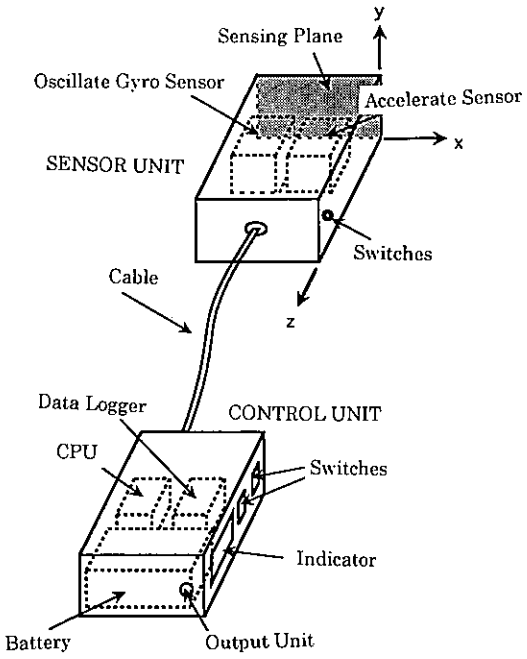

Fig.5 Components of DISCONTINUITY SURVEYOR

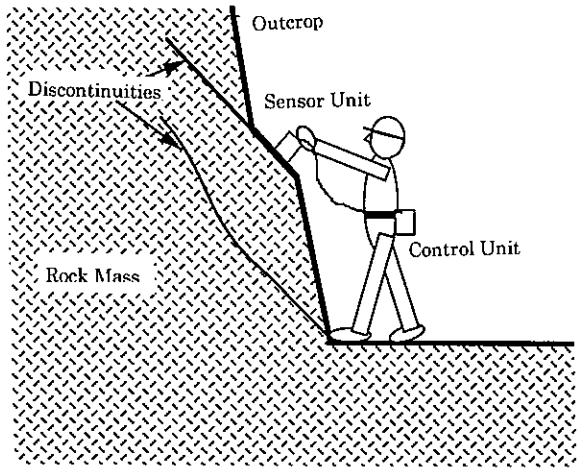

Fig.6 Survey at Excavation Face

Fig. 7 (b) indicates one example among direction data. And table 2 shows the result of directions about 4 slopes. The standard deviation σ is between 1.05 degree and 1.76 degree.

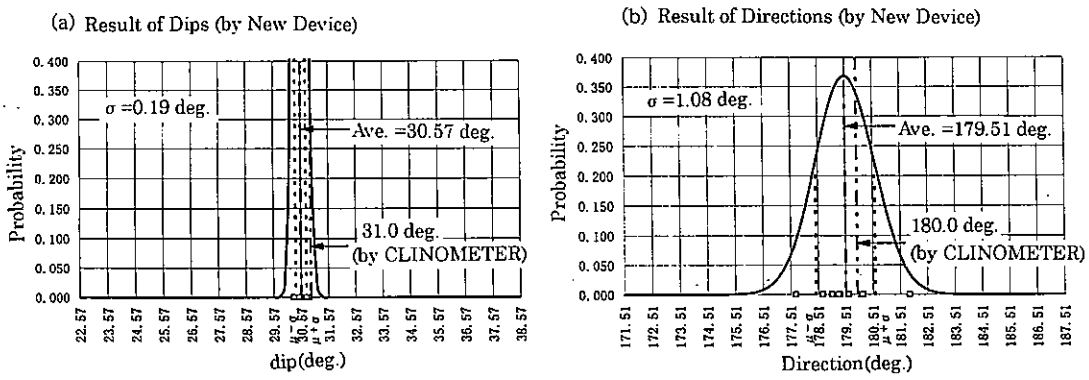

Fig.7 Probability Distribution Map (in case of 30 deg. Slope)

This value is a little large than the case of dips. However the differences between the average value and the value obtained by CLINOMETER are within from 0.49 degree to 0.24 degree. So the accuracy of the new device is evaluated as fully contented as well as dips.

Table 1 Result of Dips

item \ slope	30 deg.	45 deg.	60 deg.	75 deg.
Standard Deviation New Device σ	0.19°	0.22°	0.26°	0.31°
Average of 9 data a	30.56°	46.07°	61.31°	75.52°
Datum of CLINOMETER b	31°	46°	62°	75°
a - b	− 0.44°	+ 0.07°	− 0.69°	+ 0.52°

Table 2 Result of Directions

item \ slope	30 deg.	45 deg.	60 deg.	75 deg.
Standard Deviation New Device σ	1.08°	1.72°	1.76°	1.05°
Average of 9 data a	179.51°	270.24°	359.52°	88.79°
Datum of CLINOMETER b	180°	270°	360°	89°
a - b	− 0.49°	+ 0.24°	− 0.48°	− 0.21°

6. TEST USE IN THE SITE

To reveal the efficiency of the new device, test use has been done at the site of tunnel. Photo. 3 shoes the situation of surveying. In this test 9 data have been got concerning a discontinuity. And several discontinuities were surveyed in the same procedure. Table 3 shows the result of the test survey. From this result, we have judged that the new device has sufficient preciseness and durability.

Table 3 Result of Site Experiment

item \ method		DISCONTINUITY SURVEYOR	CLINOMETER
Survey time for one datum		15 (sec)	39 (sec)
Accuracy (σ)	dip	1.67°	3.00°
	direc.	2.58°	3.70°

Photo.3 Surveying at Real Site

Fig.8 and fig.9 are the result that show the point diagram contour and the surface roughness line concerning one discontinuity's plane. About this plane we obtained 230 point data and 10 tracing data , using by new device, of dip/direction. All data obtained at the points on the plane are easily tend to disperse about 10 degrees. However 10 tracing data obtained by the new device concentrate in almost the same position which shown as ● mark. This result suggests that the dominate orientation of joints are easily decided if we use the new device in the site survey.

7. CONCLUSION

In this paper the new method and new device are generally expressed. We have used the new device in the several sites, and have got fine and reasonable data for design or supervise of excavation. We hope that in near future we/engineer don't need CLINOMETER and personal know-how to decide the dominate orientation of joints.

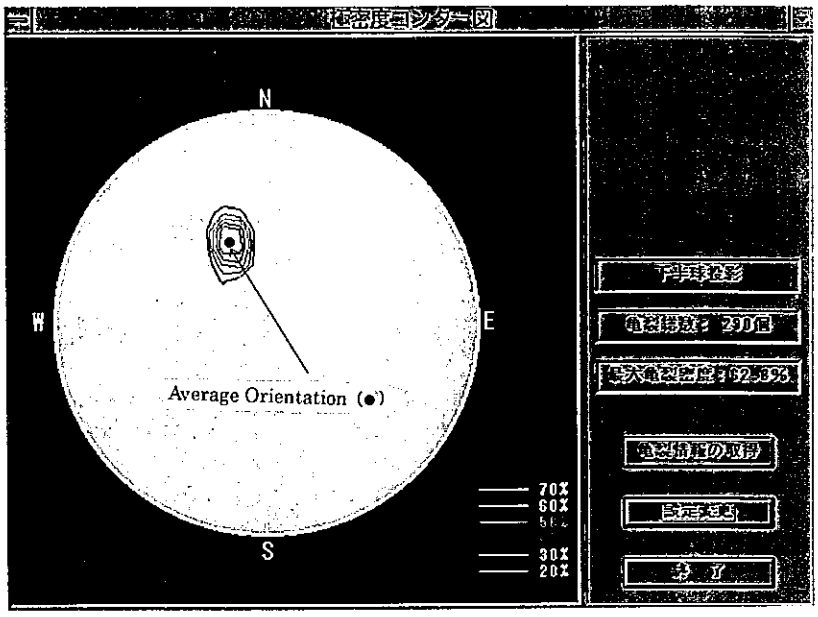

Fig.8 Point Diagram

ACKNOWLEGEMENT:

The authors appreciate fruitful discussion and kind advice with Prof. Ohnishi (Kyoto Univ.) , Mr. Hashmoto and Mr. Motida(Electric Power Development), and Mr. Ohtuka(KCC).

Characterization and behavior evaluation of jointed rock mass in tunnelling

Masayuki Kosugi[1)], Yuki Onodera[2)], Akio Tamai[3)], Wuyi Wang[4)]

1) Dr., National Institute for Resources and Environment, Ibaraki, Japan., 2) Terra Corp., Saitama, Japan.
3) Obayashi Corp., Tokyo, Japan. 4) Dr., Tsukuba University, Ibaraki, Japan.

ABSTRACT: A 30m-long test tunnel with cross section of 4m height and 5m width was excavated at an underground site to validate analytical prediction of jointed rock mass behavior due to tunnelling by means of measuring in-situ joint deformation. Geomechanical properties of joints were investigated in detail in the site rock mass by scanline surveys in surrounding drifts and characterizing test of jointed cores. The results lead to the development of a joint distribution model and joint behavior models. Using these models, DEM simulation was performed to predict jointed rock mass behavior due to tunnel excavation. Furthermore, joint deformations in three dimensions were monitored in the field by means of joint deformeters of rock blocks separated by a joint in a borehole. The measured displacements enable to show the amplitude and the direction of the maximum shearing vector and the aperture of a joint directly.

1. Introduction

While discussing the stability of an underground cavern, it is important to evaluate the deformation of discontinuities and the change of underground water in rock mass. It is also desirable to establish a method to predict and evaluate of rock mass behavior as a problem of discontinuous media. As one way to analyze the problem of discontinuous (jointed) rock mass, Cundall (1980) proposed a distinct element method (DEM) to evaluate rock mass behavior on the basis of deformation along discontinuous boundary. According to characterizing of joints in rock, Barton et al. (1985) and Chryssanthakis and Barton (1992) lead an in-situ behavior model, comparing a behavior simulation with an extensometer readings in-situ of cavern. Kosugi et al. (1992) proposed a method to analytically evaluate the effective support of rock cavern based on the comparison a calculated behavior for jointed rock mass and in-situ measurements of rock joint.

For the purpose of checking practical applicability of the above analytical method for a prediction of jointed rock mass behavior, test tunnelling was performed for in-situ rock blocks (30m×40m×5m) with mapped joints (Kosugi et al., 1994). A joint distribution was determined according to a borahole television (BTV) evaluation, boring core observation, evaluation of joint characteristic and behavior modelling according to experiments of core specimen including a joint. Subsequently, test tunnel was excavated, and joint behaviors around tunnel were measured by newly developed joint deformeters (Kosugi and Ogata, 1988, Kosugi and Tamai, 1993). Then we compared DEM behavior prediction in tunnelling with measurements of joint behavior. In this paper, we report the above mentioned procedure for evaluation of discontinuous rock mass.

2. Rock mass investigation

2.1 Testing site

A topography and a tunnel location are illustrated in **Fig.1**. The site is located in Kamioko mine, about 300km northwest far from Tokyo, where is 850m above sea level, about 200m from the tunnel opening and 175m overburden (about 4.6MPa in stress). The geological features near Kamioka consists of granitic rock and gneiss. There is no large fault around this site, but joints are comparatively well develpoed in the rock mass.

Experimental results for the properties of the site rock are summarized in **Table 1**. The rock mass properties were obtained from an elasticity wave experiment in a borehole. The properties of rock core specimens were determined from tests by means of an elasticity wave, a borehole loading, an uniaxial compression and Brazilian tension. According to AE method, principal stress were determined to be σ_1=5.53, σ_2=3.74, σ_3=2.97MPa respectively, and a normal stress shows almost to be equal to the overburden stress.

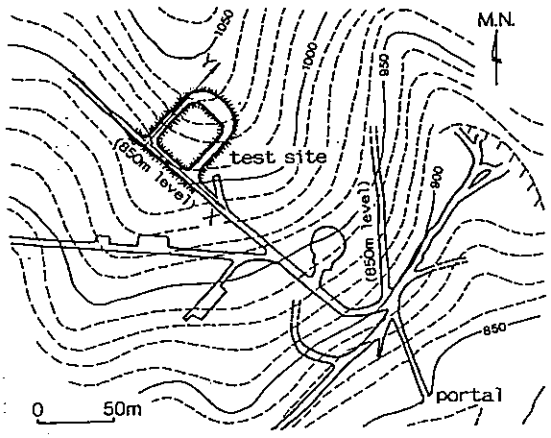

Fig.1 Geography of the underground test site at Kamioka mine

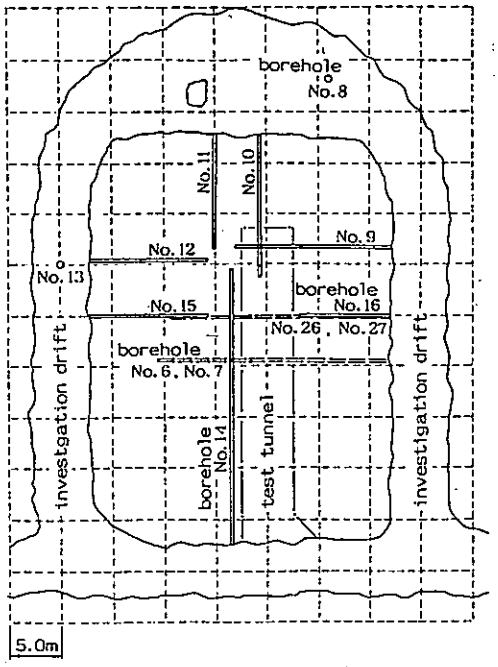

Fig.2 Layout of the underground test site and investigation boreholes

Table 1 Physical and mechanical properties of rock mass and rock specimen

	test num.	value range	average
<Rock Mass Property>			
wave velocity, V_p (km/sec)	8	5.2 ~ 6.2	5.6
V_s (km/sec)	8	2.8 ~ 3.2	3.0
modulus of deformation (GPa)	12	1.3 ~29.1	10.3
modulus of elasticity (GPa)	12	6.4 ~37.8	16.4
<Rock Specimen Property>			
wave velocity, V_p (km/sec)	27	3.3 ~ 5.6	4.9
V_s (km/sec)	27	1.5 ~ 3.2	2.7
modulus of elasticity (GPa)	27	27 ~ 81	51
compressive strength (MPa)	27	38 ~172	92
Poisson's ratio	29	0.12~ 0.43	0.23
tensile strength (MPa)	9	4.2 ~14.4	11.4
shear strength (MPa)	32	6.4 ~20.6	13.3
internal friction angle (°)	3	41 ~ 49	46

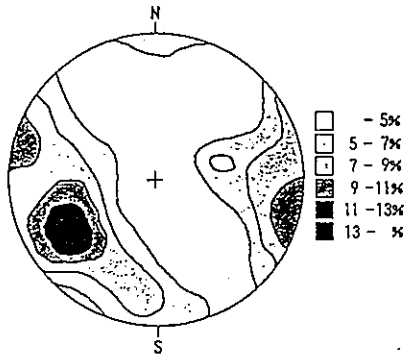

Fig.3 Contours of polar density of investigated joints

2.2 Joint analysis

According to a joint investigation of recovered cores and a BTV obserbation of rock mass circumference, a distribution of rock mass discontinuities was evaluated. A tunnel wall investigation obtained a inclination and an aperture of joint that the trace length is over 1m. An arrangement of the site brock and investigation boreholes is illustrated in **Fig.2**. In this figure, two boreholes, No.8 and 13, are in the vertical direction, and the other, No.6, 7, 26 and 27, are inclined. The joint investigation was performed for core samples with 338m length from 28 boreholes, and the BTV observation for 212m of 13 boreholes. The extreme density which described strike and dip of 2,018 joints was illustrated in **Fig3**. It was recognized that the density is unevenly distributed and concentrated on the around of over 11% density part showed in black in the graph. So it is possible to explain the tendency that many joints distrubute nearby the direction of high density strike and/or dip, and there are also some joints existing accross the direction.

In order to analyze joint aoerture by statistics, we tried to classficate according to the following indexes.

[class 0]: a closed joint, stuck joint, others;
[class 1]: a small joint, aperture below 0.5mm;
[class 2]: a clear joint, aperture from 0.6 to 1.9mm;
[class 3]: an open joint, aperture above 2mm.

Table 2 Joint classification

borehole No.	length (m)	joint classification			
		Class-3	Class-2	Class-1	Class-0
6	25.00	5	20 (25)	49(74)	78 (152)
7	24.10	11	32 (43)	51(94)	74 (168)
9	16.26	8	6 (14)	24(38)	70 (108)
10	15.62	4	14 (18)	7(25)	67 (92)
11	9.08	2	11 (13)	9(22)	32 (54)
12	10.90	3	8 (11)	21(32)	23 (55)
14	26.97	7	21 (28)	142(170)	97 (267)
15	13.96	3	9 (12)	33(45)	64 (109)
16	9.14	2	6 (8)	15(23)	21 (44)
26	20.00	4	15 (19)	64(83)	36 (119)
27	20.01	5	18 (23)	51(74)	31 (105)
total	191.04	54	160(214)	466(680)	593(1273)
average span (m)		3.93	0.99	0.28	0.15

(The total numbers of classified joints are shown in parentheses.)

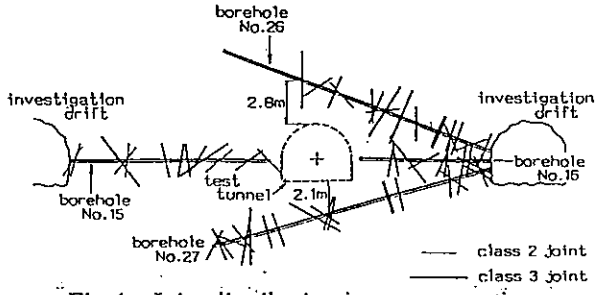

Fig.4 Joint distribution in a cross-section from borehole investigation

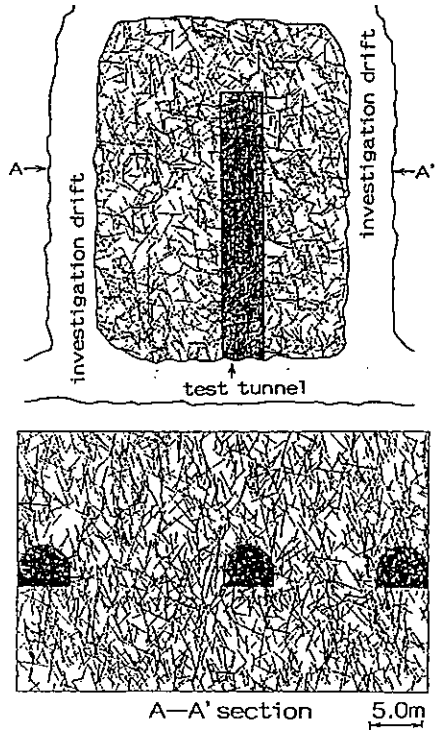

Fig.5 Distributing condition of joints predicted by MonteCalro simulation

The result of the joint classification for 11 boreholes is shown in **Table2**. The average values of joint span which are obtained from a measured borehole length and a total joint number are about 0.3m, 1.0m, 4.0m for each class 1-3. According to Barton's concept of a joint classfication, it is assumed that the values are equal to average length of each classified joint.

2.3 Joint mapping

As an evaluation of discontinuities in rock mass, a joint distribution is shown in **Fig4**, which is developed in a measurement section. In this figure, a long solid line shown on the line of investigation borehole is class 3 joint, and a short solid line is class 2 joint. The dashed line in the centre is a tunnel excavated in test .

In order to presume a joint distribution from the above investigation, we used a probability model to make a quantitative analysis. A general joint distribution led from a MonteCalro simulation based on the joint density in direction (Fig.3) is shown in **Fig.5**. The figure in two dimensions is obtained from a three-dimensional distribution through the mapping of class 2 and class 3 joints.

3. Joint characterizing

3.1 Joint core test

The jointed core samples to be molded by moltal or epoxy/sand mixture in the shape with 100mm in width, 100mm in height, 100-300mm in length was used for a shearing push test (Kosugi et al., 1994). The stress perpendicular to a joint surface was established to be so small as to reduce the damage caused by micro-failuring on a joint surface with shear sliding. We measured for a shear displacement, an aperture and a shear stress while joint shearing.

As an example of the shearing push test results, shear and aperture behaviors of class 1 and class 2 joints are shown in **Fig.6** and **Fig.7** respectively. According to a data-sheet and an evaluating procedure obtained by Kosugi et al. (1991), a joint characterization was performed for a residual friction angle, ϕ_r, a compressive strength of joint surface, JCS_0, and a joint roughness coefficient, JRC_0. A joint length of test samples is in the range from 70 to 300mm. The joint properties of JCS_0 and JRC_0 are corrected for a size effect of a joint sample having a standard joint length, L_{01}=100mm, by means of the following formula (Barton et al., 1985).

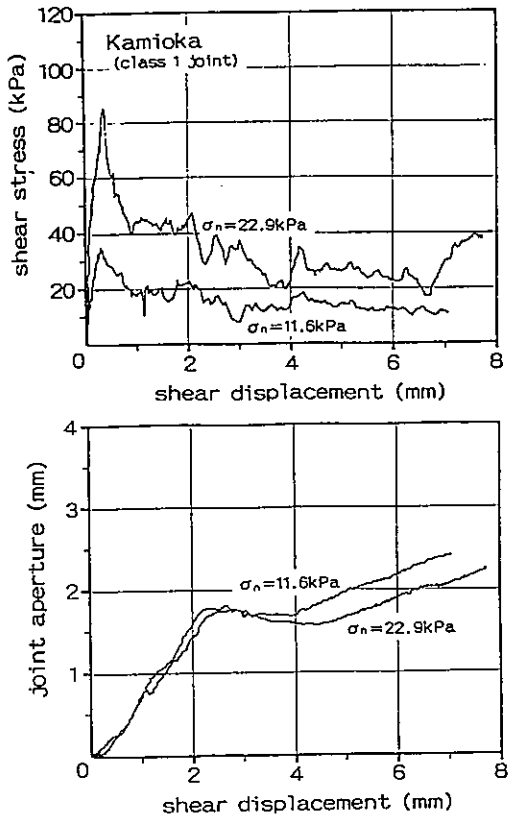

Fig.6 Shear behaviors of class 1 joint

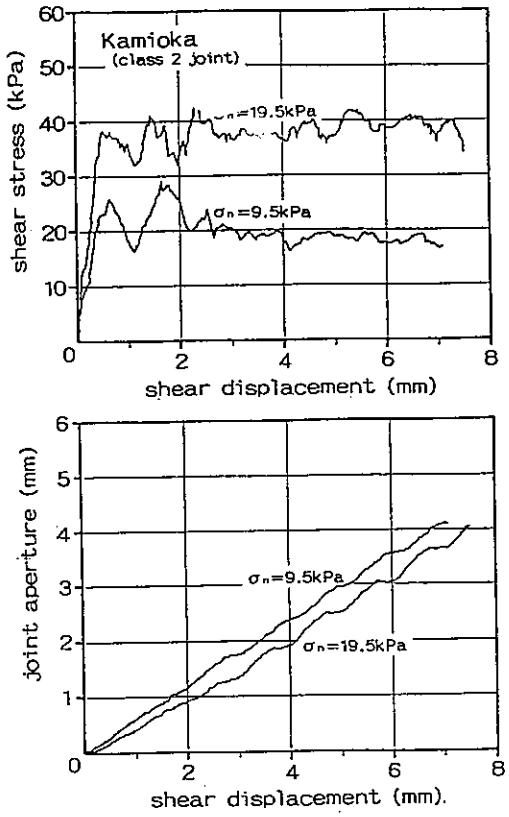

Fig.7 Shear behaviors of class 2 joint

Table 3 Joint characterization for jointed cores in the laboratory

	test num.	L_0 (m)	ϕ_r (°)	JCS_{01} (MPa)	JRC_{01}
Class-0	8	0.055~0.110	28.6	64.2	11.5
Class-1	20	0.053~0.092	26.6	47.8	9.5
Class-2	15	0.041~0.122	27.0	51.0	9.4
Class-3	1	0.066	24.1	37.8	3.3

JCS_{01} and JRC_{01} are calculated for a joint of L_{01}=0.100m.

Table 4 Joint characterization for in-situ scale joints

	L_n (m)	ϕ_r (°)	JCS_n (MPa)	JRC_n
Class-0	0.15	28.6	55.8	10.5
Class-1	0.28	26.6	35.6	7.8
Class-2	0.99	27.0	26.7	6.1
Class-3	3.93	24.1	26.3	2.6

$$JCS_{01} = JCS_0 (L_{01}/L_0)^{-0.03JRCo} \quad (1)$$
$$JRC_{01} = JRC_0 (L_{01}/L_0)^{-0.02JRCo} \quad (2)$$

The average value of each classified joint is shown in **Table 3**. From the result, it is obtained that the every properties tend to show a large value for a stuck joint with a small aperture, and to be small for an open joint (class 3). The residual friction angle is comparatively small between each class. The result shows that it is possible to classify a joint properties according to the joint aperture classification.

In case the length of each classified joint in the field is assumpted to be equal to the average span (Table 2), an in-situ joint properties shown in **Table 4** are obtained by the correction formula (1) and (2) based on the laboratory values (Table3). The results show a quantitative classification of joint properties between classes obiously. In general, it is thought that the residual friction angle, ϕ_r, would be the most useful property without size effect, because it is very difficult to observe an in-situ joint length exactly.

3.2. Joint behavior model

According to a evaluating procedure of a behavior model from Barton et al. (1985), a laboratory joint behavior model comparing with shearing test results is shown in **Fig.8**. The model simulates the

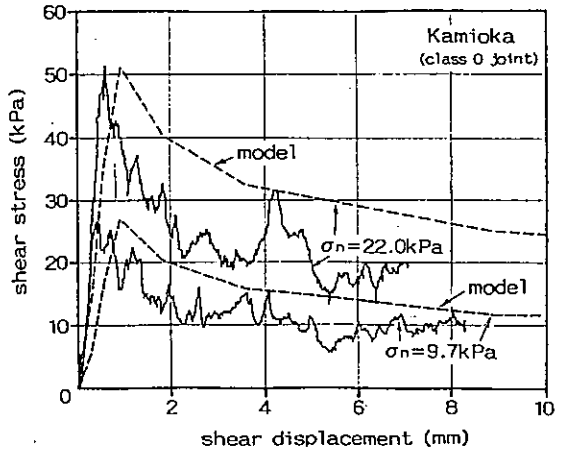

Fig.8 Shear behaviors in push tests and modellings

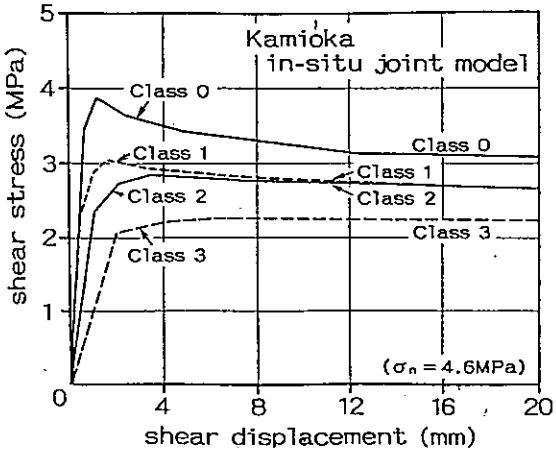

Fig.9 Behavior models for in-situ scale joints

Table 5 Input datum for DEM analysis

JOINT

input data			Class-2	Class-3
JCS₀	laboratory joint wall compressive strength	MPa	51.0	37.8
JRC₀	laboratory joint roughness coefficient	---	9.4	3.3
L₀	laboratory joint length	m	0.10	
Lₙ	in-situ joint length	m	0.99	3.93
Knn	joint normal stiffness	GPa/m	105	(100)
Kss	initial joint stiffness	GPa/m	2.16	1.07
φr	residual friction angle	degree	27.0	24.1
σc	unconfined compressive strength of rock surface	MPa	109.6	

ROCK MASS

input data			site
E	rock mass elastic modulus	GPa	10.3
ν	rock mass Poisson's ratio	---	0.23
ρ	dry density of rock mass	kN/m³	26.6

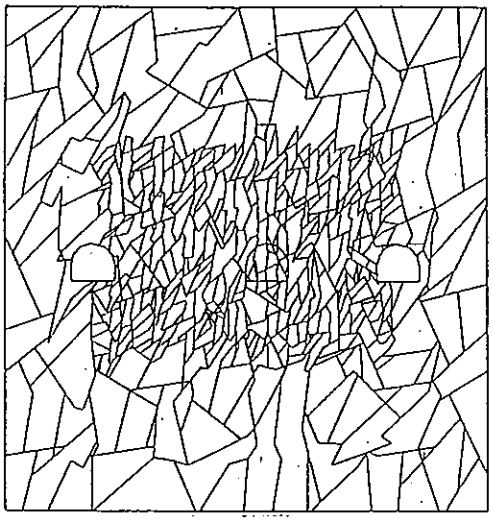

Fig.10 Discontinuous boundaries of joints in DEM analysis

maximum shear stress and a non-linear behavior in residual shearing very well. So, it is recognized that the modelling concept is statistically and qualitatively useful for laboratory behaviors. In the same manner as the above, an in-situ joint behavior model is obtained from the in-situ properties (Table 4) as shown in **Fig.9**. The stress perpendicular to joint surface is assumped to be equal to the overburden pressure,4.6MPa. The model relating to the classified joint property for each class are present. The resulted behavior shows that a class 3 joint is brought by shearing caused by the maximum shear stress with about 50-60% overburden stress. This means that the change of a stress concentrating induced by a tunnel excavating would be happen to cause a joint shearing in the near field of a cavern.

4. Behavior prediction

4.1 Primary conditions for DEM

A DEM simulation program (UDEC-BB, Ver.2.0) was employed to calculate a jointed rock mass behavior, an input datum for this are summarized in **Table 5**. The joint normal stiffness (K_{nn}) in the table are obtained from the following formula, and the initial joint stiffness (K_{ss}) are obtained from the in-situ joint behavior model (Fig.9).

$$K_{nn} = K_{ni}\{1-\sigma_n/(V_m K_{ni}+\sigma_n)\} \qquad (3)$$

In this formula, σ_n is the stress perpendicular to a joint surface, which is assumed to be equal to overburden stress. K_{ni} is the initial normal stiffness of a joint, and V_m is the maximum closure of a joint, both are determined from the experimental joint properties in a laboratory (Vik and Barton, 1988). As to the class 3 joint, due to shortage of experimental data, K_{nn}=100GPa/m is persumed.

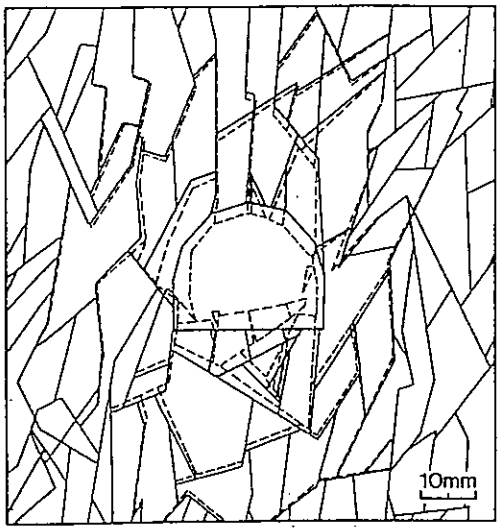

Fig.11 Rock mass deformation in DEM simulation

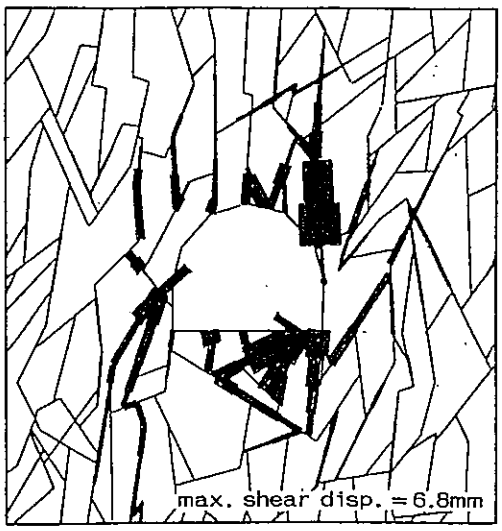

Fig.12 Shear displacements on joints in DEM simulation

The distribution of discontinuities in rock mass around test tunnel was evaluated in three dimensions as shown in Fig.5. It is problem that a deformation of discontinuities under a compressive stress condition is caused by a stress concentration in the ares close to underground cavern (Hungr and Morgenstern, 1980). Here for simplicity, a joint distribution corresponding to an actual observation and a simulation for class 2 and 3 is obtained in the central area (hight 20m x width 30m), and a joint distribution for class 3 is in its surrounding area (hight 55m x width 55m). According the above concept, a distinct element mesh is determined as shown in **Fig.10**.

4.2 DEM simulation

In the analysis, a deformation of jointed rock mass is obtained after repeating calculations to find a converged solution. As the rsults of this simulation, deformations of the rock mass around the test tunnel before and after excavation are displayed in **Fig.11**. The result is characterized by the strong deformation in the right corner of the test tunnel and the fall-down of wall block surrounded by joints. A distribution of joint shearing, of which the degrees of shear displacements are displayed in thickness of the lines above discontinuous boundaries, are showin in **Fig.12**. As to the scale, the maximum displacement of joint shear at the right corner of the test tunnel is 6.8mm. The result shows the shear deformation is strongly dependant upon a joint orientation in the area close to the test tunnel. If we are able to predict a key-joint with a high posibility of large deformation in advance, it becomes possible to consider an effective supporting design in some specific directions (Kosugi et al., 1992).

5. Joint measurement under tunnelling

5.1 Behavior measurement by joint deformeter

For evaluating a joint behavior with the progressing of tunnelling, five joint deformeters were set up in boreholes surrounding the test tunnel, as shown in **Fig.13**. The test tunnel, which has a width of 5.0m and a height of 4.0m, was excavated 1 meter a day by blasting. LVDT sensors in the device are able to measure displacement ranging from 0 to 5mm with the accuracy of 2-4 μm. An in-situ monitoring was conducted using a data logger system with a battery power supply for a month.

The joint deformeter used in this research was newly developed in order to measure the joint behavior in three dimensions (Kosugi et al., 1995). It was settled in a borehole with a diameter of 76mm, in two and three devices for each borehole. A structure of the device is shown in **Fig.14**. The sensor part and the measured part joined together by a setting guide are fastened to the borehole wall by contact pins with springs separately. The relative positional change between the two parts is monitored in three dimensions. These values are tranformed to a vector of shearing and an aperture of a joint. An image from BTV apparatus which is connected with the device make it possible to confirm a certain position of joints in boreholes.

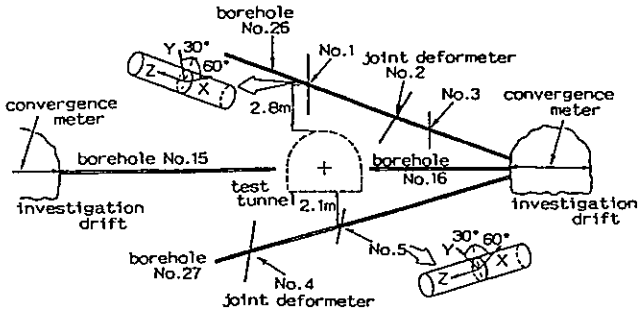

Fig.13 Installed locations of joint deformeters

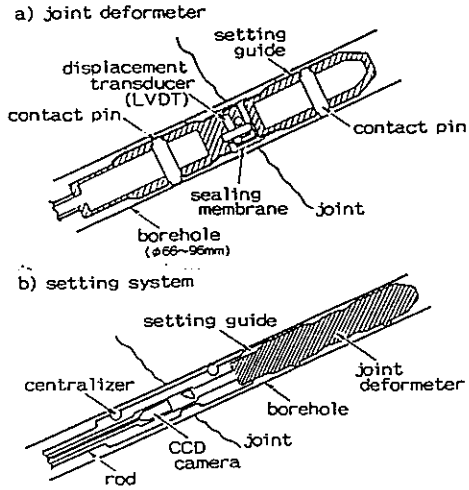

Fig.14 Structure of a joint deformeter

5.2 Joint behavior induced by tunnelling

As the measuring results of joint displacements for the No.1 position at the top part and the no.5 at the lower part of the test tunnel, the relationships between joint displacements and position of tunnelling face are shown in **Fig.15**. Here, the measured values of the X-Y-Z coordinates along to the axes of the deformeter are changed into the l-m-n coordinates based on the joint surface and its normal direction. The n-axis is perpendicular to the joint surface, and the displacement in this direction shows the degree of a joint aperture. Because the l and m-axis are perpendicular to each other within the surface, a vector in the l-m plane shows the maximum shear displacement coressponding to shear stress within the surface of the joint. Besides, the positions of tunnelling face are set in relation to the measuring section immidiately after the tunnel blasting.

The shear stress induced by tunnelling are evaluated according to the maximum shear displacement and the in-situ joint behavior model (Fig.9), as shown in **Fig.16**. Thus, it comes clear that the variation of the shearing stress as comparing with that before tunnelling. It is also suggested that the stress conditions are changed considerally when the tunnelling face is about 5m close to the measuring section. The maximum displacement for the No.1 and No.5 joints are 0.74 and 0.34mm respectively. This displacement was compared with the in-situ behavior model for each joint class, as shown in **Fig.17**. The maximum shear stresses induced for the two joints are in the range of 0.7-0.8MPa which correspond to about 1/4 of the maximum stresses of the joint models and about 1/6 of the overburden stress (4.6MPa). The result shows that there is possibility to represent a remarkable deformation of pre-existing joints connecting with dilation of rock mass, even if it is under a lower stress condition without tensile and/or compressive failures.

6. Comparison of measurement and analysis

The results of the simulation significantly depend upon the setting of input data and initial condition for the analysis. Normally, an input setting was decided first for consistent with an in-situ measuring data, and then used to deduce in-situ properties of rock mass. However, the joint properties obtained from the core experiments and the discontinuous distribution observed in-situ are both constantly mentained in advance, the simulation result is all produced according to these conditions in this report. For this reason, the comparison of the results from the in-situ measurement and the simulation directly reflect the applicability of the joint behavior models as well as the analysis method. But it is thought that considering the calculated displacement probablity is also necessary because of obtaining a rock mass behavior on the basis of the probability in the assumption of the joint distribution.

As a comparison of these results, the direction and the magnitude of joint shearing in the measuring section where the joint deformeters were set are shown in **Fig.18**. As to the No.1 and No.5 joints closely near the test tunnel, it is obtained that both the direction and the magnitude of joint shearing is able to be roughly predicted. The results also show that an in-situ joint measurement is very important to verificate the applicability of a simulating method using discontinuous code for jointed rock mass, because such joint displacements sensitively reflect mocro-deformation in rock masses.

Further investigations which take consideration of joint dilation for a large cavern is required to establish an applicable procedure of behavior prediction for jointed rock mass.

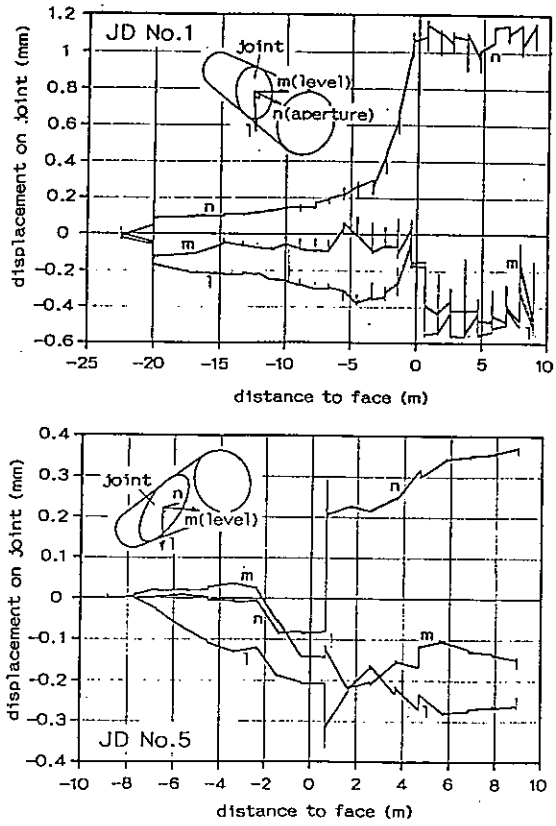

Fig.15 Tunnel advancing and 3-D joint behavior

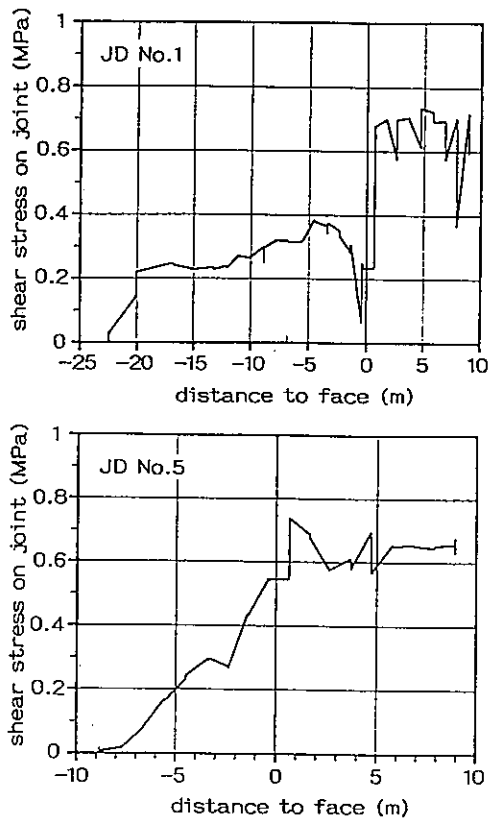

Fig.16 Shear stress derived from joint monitoring

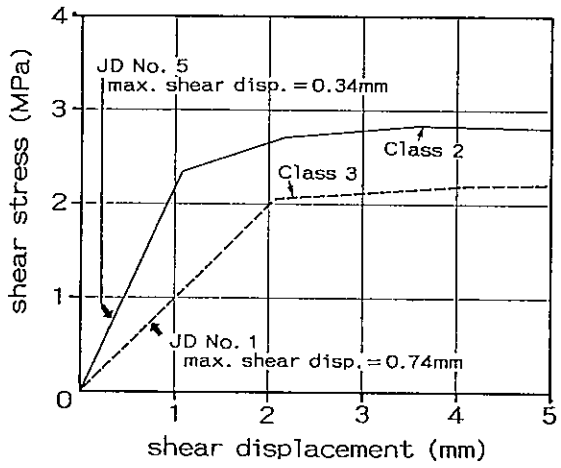

Fig.17 Comparison of maximum shear displacement with the joint behavior models

(Joint Shear) (mm)	Joint Number				
	No. 1	No. 2	No. 3	No. 4	No. 5
in-situ measurement	+0.48	-0.04	-0.15	----	+0.32
DEM for discontinuity	+0.24	-0.58	-0.07	-0.69	+0.20

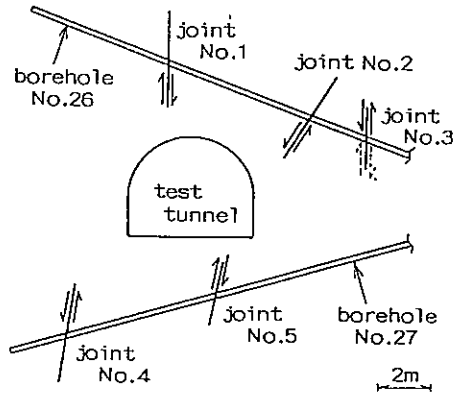

Fig.18 Joint shearing directions and displacements from in-situ measurements and DEM simulation

7. Conclusions

In this report, in order to compare a simulation result for jointed rock mass and in-situ measurement results of a joint behavior, a tunnelling test was conducted in a 30x40m rock mass block in Kamioka site, where the joint behavior was evaluated.

Based on the investigation data of more than 2000 joints recovered from boreholes with 300m length and of drift wall with 140m length, the processes which lead to the joint probability distributions according to the clssification of joint aperture become clear. The boundary conditions for the similation were decided in accordane with the statistical joint distribution, and thus the methods to evaluate the behavior of the rock mass in probability was also proposed.

Jointed cores from the site were used to determine joint properties experimentally. With the correction of size effect according to Barton's concept, an in-situ behavior model of the joints were clarified. It indicates that shearing stress along the joint surface can be easily determined according to the established model and the in-situ joint deformations.

A new joint deformeter was developed for measuring joint deformation in three dimensions in a borehole. Its capabilities were verified from the in-situ measurement for a long time duration. For the in-situ measurement, the behavior of joints were detected with high accuracy under tunnel blasting condition or even setting in groundwater. It shows that the new device can be practically used for monitoring any sensitive indicators of rock mass behavior.

Joint behaviors were simulated using the DEM method which consider various factors around joint. Consistency of the simulation results with the in-situ measurement indicated that the shearing direction and the magnitude of the joint can generally be predicted.

Based on the discussions about an in-situ measurement and a predicting simulation, it is proposeed that an effective supporting is possible to de designed by means of setting the allowable range of joint deformation.

Reference:

Cundall,P.A. : A Generalized Distinct Element Program for Modelling Jointed Rock, Report PCAR-1-80, Contract DAJA 37-79-C-0548, European Research Office, U.S.Army, Peter Cindall Associates, 1980.

Barton,N.C., S.C.Bandis and K.Bakhtar : Strength, Deformation and Conductivity Coupled of Rock Joints, Int. J. Rock Mech. Min. Sci. & Geomech. Abstr., Vol.22, No.3, p.121-140, 1985.

Chryssanthakis,P. and N.Barton : Predicting Performance of the 62m Span Ice Hockey Cavern in Gjovik, Norway, Preprints of ISRM Conf. Fractured and Jointed Rock Masses, Lake Tahoe, LBL-32379, Vol.3, p.624-631, 1992.

Kosugi,M., H.Ishihara and M.Nakagawa : Tunnelling Method Coupled with Joint Monitoring and DEM Analysis, Preprints of ISRM Conf. Fractured and Jointed Rock Masses, Lake Tahoe, LBL-32379, Vol.3, p.765-770, 1992.

Kosugi,M., A.Tamai and H.Ishihara : Development of a New Device to Measure Three Dimensional Behavior of Joints, Journal of Geotechnical Engineering, No.517, p.181-188, 1995.

Kosugi,M. et al. : Joint Mapping and Joint Characterizing at Kamioka Test Site and Development of Joint Deformeter, 9th Symposium on Rock Mechanics, p.731-736, 1994.

Kosugi,M and Y.Ogata : Fracture Deformeter, Application to Japanese Patent Office, No.63-87818, 1988, Patent No.1966585, 1995.

Kosugi,M. and A.Tamai : Joint Deformeter, Application to Japanese Patent Office, No.5-308277, 1993.

Kosugi,M. and A.Tamai : Method and System for Measuring Three-dimensional Displacement, Patent Application No.08/277520 & 08/478680 in the USA, 1994, Patent No.5511429, 1996.

Barton,N. : Recent Experiences with the Q-system of Tunnel Support Design, Proceedimg of the Symposium on Exploration for Rock Engineering, Johannesburg, Vol.1, p.107-117, 1976.

Tuda,T : MonteCalro Method and Simulation, Baifu-kan.

Kosugi,M., G.Vik and N.Barton : Joint Characterization Based on JRC/JCS Indexes, -Studies on Predicting Jointed Rock Mass Behaviour (Part 1)-, Shigen, Vol.3, No.1, p.11-21, 1991.

Vik,G. and N.Barton : Stage I Joint Characterization and Stage II Preliminary Prediction using Small Core Sample, Stripa Project Report, No.88-08, p.1-31, 1988.

Hungr,O. and N.R.Morgenstern : A Numerical Approach to Predicting Stresses and Displacements around a Three-dimensional Pressurized Fracture, Int. J. Rock Mech. Min. Sci. & Geomech. Abstr., Vol.17, p.333-338, 1980.